

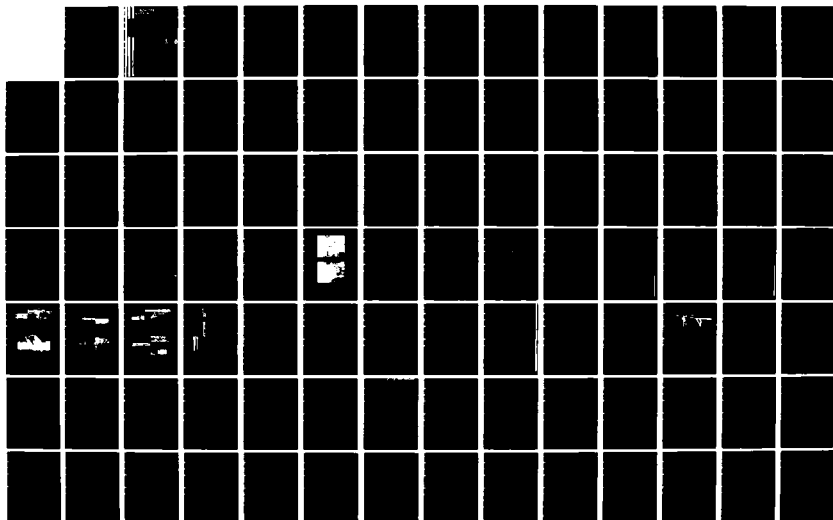
AD-A165 039

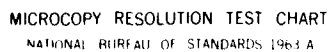
WORKSHOP ON NEW DIRECTIONS IN SOLID STATE POWER
SWITCHES HELD AT FARMINGD. (U) POLYTECHNIC INST OF NEW
YORK FARMINGDALE WEBER RESEARCH INST. B SENITZKY
24 DEC 85 N00014-85-G-0236 F/G 9/5

1/6

UNCLASSIFIED

NL





MICROCOPY RESOLUTION TEST CHART
NATIONAL BUREAU OF STANDARDS 1963 A

Polytechnic Institute of New York



AD-A165 039

FINAL REPORT

WORKSHOP ON NEW DIRECTIONS
IN SOLID STATE POWER SWITCHES

SPONSORED BY

INNOVATIVE SCIENCE AND TECHNOLOGY OFFICE
OF SDIO

OFFICE OF NAVAL RESEARCH

CONDUCTED BY

WEBER RESEARCH INSTITUTE
POLYTECHNIC INSTITUTE OF NEW YORK
FARMINGDALE, NEW YORK 11735

DTIC
ELECTE
FEB 28 1986
S D

ON

AUGUST 28 - 30, 1985

SUBMITTED BY

B. SENITZKY, CHAIRMAN

This work relates to Department of Navy Grant N00014-85-G-0236 issued by the Office of Naval Research. The United States Government has a royalty-free license throughout the world in all copyrightable material contained herein.

DISTRIBUTION STATEMENT A

Approved for public release
Distribution Unlimited

85 12 21 103

DTIC FILE COPY

FINAL REPORT

WORKSHOP ON NEW DIRECTIONS
IN SOLID STATE POWER SWITCHES

SPONSORED BY

INNOVATIVE SCIENCE AND TECHNOLOGY OFFICE
OF SDIO
OFFICE OF NAVAL RESEARCH

CONDUCTED BY

WEBER RESEARCH INSTITUTE
POLYTECHNIC INSTITUTE OF NEW YORK
FARMINGDALE, NEW YORK 11735

ON

AUGUST 28 - 30, 1985

SUBMITTED BY

B. SENITZKY, CHAIRMAN

This work relates to Department of Navy Grant N00014-85-G-0236 issued by the Office of Naval Research. The United States Government has a royalty-free license throughout the world in all copyrightable material contained herein.

TABLE OF CONTENTS

	<u>Page</u>
I. Introduction	
Benjamin Senitzky, Polytechnic Institute of New York	1
II. Program	6
Attendees	10
III. Overview of Space Power Switching Requirements	13
Erich Kunhardt, Polytechnic Institute of New York	
L. Luessen, F. Rose, Naval Surface Weapons Center	
T. R. Burkes, T. R. Burkes, Inc.	
IV. Material Properties	
1. Silicon Carbide as a Potential Candidate for High Power and High Temperature Devices	31
Robert F. Davis, N. Carolina State University	
2. Super-ionic Conductors as High Speed Switches	61
J. F. Scott, Un. of Colorado	
3. Free Carrier Plasma Transport in Photoexcited Semiconductors	74
J. R. Meyer, Naval Research Laboratory	
V. Photoconductive Switching	
1. Picosecond Photoconductors: Problems and Perspectives	120
David H. Auston, AT&T Bell Laboratories	
2. Picosecond Relaxation of Photoexcited Carriers in Disordered Semiconductors	150
Anthony M. Johnson, AT&T Bell Laboratories	
3. Problems of High Power Photoconductive Switching on a Picosecond Time Scale	187
William R. Donaldson and Gerard Mourou	
University of Rochester	
4. Photoconductor Switching: Some Physical Mechanisms	239
Robert B. Hammond, Los Alamos National Laboratory	
5. High Power Photoconductive Switch Applications	286
W. C. Nunnally, Un. of Texas at Arlington	
6. Optically Activated Semiconductors as Repetitive Opening Switches	325
E. A. Chauchard, M. J. Rhee, Chi H. Lee	
University of Maryland	

TABLE OF CONTENTS (continued)

	<u>Page</u>
VI. Non-Photoconductive Switching	
1. MOS Controlled Thyristors (MCT'S)	359
V. A. K. Temple, General Electric Company	
2. Avalanche Breakdown Mechanisms and Application to Switching Devices	371
Michael D. Pocha, Lawrence Livermore Natl. Lab.	
3. Thermal Switches for Pulse Power	405
R. Ford and M. Kahn, Naval Research Laboratory	
VII. Group Discussions	
1. Potential Materials for Solid State Switching	445
Gale R. Sundberg, Chairman NASA Lewis Research Center	
2. Pertinent Relaxation Mechanisms	453
Robert B. Hammond, Chairman Los Alamos National Laboratory	
3. Volume and Surface Breakdown Problems	467
M. D. Pocha, Chairman Lawrence Livermore National Laboratory	
4. Solid State Plasma Transport	470
Erich Kunhardt, Chairman Polytechnic Institute of New York	



Accession For	
NTIS CRA&I	<input checked="" type="checkbox"/>
DTIC TAB	<input type="checkbox"/>
Unannounced	<input type="checkbox"/>
Justification	
By <i>lbr on file</i>	
Distribution/	
Availability Codes	
Dist	Avail and/or Special
<i>A-1</i>	

1. INTRODUCTION

I. INTRODUCTION

B. Senitzky
Weber Research Institute
Polytechnic Institute of New York
Farmingdale, New York 11735

A workshop on New Directions in Solid State Power Switches was conducted on August 28-30, 1985, by the Weber Research Institute of the Polytechnic Institute of New York. The workshop was sponsored by the Innovative Science and Technology Office of SDIO through the Office of Naval Research.

To meet the requirements of pulsed power, a number of switching concepts have been proposed. Foremost among these have been gas discharge switches. Nevertheless, solid state switches may be more desirable because of the potentially higher charge densities and greater speed. The use of solid state devices to switch megavolts and kiloamperes leads us into an operating range in solids which has not been explored.

Much of the enormous body of research in solid state has been directed towards understanding the operation of small low-power devices, and considerably less attention has been given to ultra-high power switches.

One of the primary goals of this workshop was to invite people working in different areas to give papers on their specialties and to establish technical interaction with each other. The general feeling among the participants was that this goal was accomplished. Another goal of our workshop was to identify problems which require further effort. In order to accomplish this, we split up into four working groups which then reported their results to all the participants. Although it was difficult for one to be aware of all the discussions taking place in the individual working groups, it was apparent that there was a high level of agreement among the members of the working groups about the significant problems in their areas.

Our program (Section I) started off with a formulation by R. Junker of the goals of solid-state switching and the need for fundamental research to

support this effort. An overview of space power switching requirements (Section III) was presented by E. Kunhardt, L. Luessen, F. Rose and T. R. Burkes. In this overview some of the pulsed power requirements for particle accelerators, electrically driven lasers, microwave generators and electromagnetic guns were given and the basic physical mechanisms which control the switching characteristics were discussed.

The talks presented are grouped in three sections: Material Properties (Section IV), Photoconductive Switching (Section V) and Non-Photoconductive-Switching (Section VI). In Section IV on Material Properties, there are two talks on new materials (R. Davis and J. Scott) and one talk on photo-excited carriers in semiconductors (J. Meyer). There has been considerably more work done on silicon carbide (R. Davis) than on the super-ionic conductors (J. Scott). As R. Davis points out, silicon carbide is a material which has many technologically significant properties such as high operating temperature, high thermal conductivity, high mobility, high breakdown field, and the technology has advanced to the point where pn junctions have been fabricated.

The second talk by J. Scott discusses optically activated switching in crystals which he terms "super-ionic conductor", where the conductivity decreases with the incident light. The third talk in this group deals with the transport properties of photoexcited semiconductors. In this talk J. Meyer points out that treating electron-hole scattering as similar to electron-ionized impurity scattering can lead to considerable error. This fact is very important for device considerations, and it would seem that further experimental and theoretical work in this area would be quite useful.

The photoconductive switching talks fell into two categories: one class related to high-speed (picosecond) low power devices, and the other class dealt with high power photoconductive switches. D. Auston ("Picosecond Optoelectronics - Problems and Perspective") gives a summary of the work on extremely wide bandwidth picosecond optoelectronic devices and the areas of scientific research that the availability of ultrashort electrical pulses have opened up. He also lists some interesting engineering applications. Since ultrashort pulses require fast relaxation of photoexcited charge carriers,

A. Johnson ("Picosecond Relaxation of Photoexcited Carriers in Disordered Semiconductors") considers disordered semiconductors which have shorter relaxation times than single crystal semiconductors. Because of the picosecond times involved, wideband transmission line structures and electronic correlation measurements with two photoconductors are used. At present the low mobilities encountered in disordered semiconductors cause the "on" state resistance to be rather high although their high dark resistivity and dielectric strength insure a high "off" state resistance. At first glance it would seem that picosecond range phenomena is not of interest in high power photoconductive switching, but as indicated by E. Kunhardt in his overview paper, the maximum switch dissipation occurs during turn-on and turn-off; therefore, the ideal switch should have as rapid a turn-on and turn-off transient as possible. The study of these transients is the subject of the paper by W. R. Donaldson and G. Mourou ("Problems in Picosecond High Voltage Photoconductive Switching"). The authors conducted studies with ultra-fast laser pulses on silicon and gallium arsenide switches which are turned on by a laser pulse and turned off by the electrical discharge of a transmission line. Studies were also conducted on the effect of contacts on the leakage properties of silicon switches.

The next talk entitled "Photoconductor Switching: Some Physical Mechanisms" by Robert B. Hammond relates the physical mechanisms of silicon resistivity, free carrier absorption and electron-hole pair density to such device properties such as risetime, efficiency, on-time and temperature control. The following talk by W.C. Nunnally ("High Power Photoconductive Switch Applications") summarizes the requirements and limitations of very high power photoconductive switching and describes some novel techniques for photoexcitation. The final talk delivered by Chi H. Lee ("Optically Activated Semiconductors as Repetitive Opening Switches" - E. A. Chauehard, M. J. Rhee and Chi H. Lee) analyzes the properties of an opening switch using GaAs and I_n GaAs:Fe which has achieved a turn-off time of 1 ns.

Switching by non-photoconductive techniques is the subject of the talks in Section VI. The first talk by V. Temple ("The MOS Controlled Thyristor, a New Switching Device") considers a new class of power devices which is based on a combination of MOS and thyristor elements. Some of the techniques of dealing with the limitations imposed by surface breakdown, such as bevelling

and field rings are discussed. The next talk by M. Pocha ("Avalanche Breakdown Mechanisms and Application to Switching Devices") considers surface breakdown as well as bulk breakdown in more detail. Both primary and secondary breakdown are discussed, and a diode switch based on the second breakdown phenomenon which has achieved a peak amplitude of 2800 volts (56 amps) and a risetime of less than 0.5 ns is described. The last talk in this session entitled "Thermal Switches for Pulse Power" by M. Kahn and R. Ford was delivered by M. Kahn who considers the requirements for opening switches in inductive storage power supplies. Two types of material: carbon filled polymers and barium titanate are studied, and a detailed discussion of failure mechanisms is presented in this talk.

The second half of the program was devoted to group discussions aimed at identifying needed research directions. G. R. Sundberg chaired the group on Potential Materials for Solid State Switches in Section VII. This group summarized proposed research directions in Table 4.

R. B. Hammond's group considered the various relaxation mechanisms that can play an important role in photoconductive switching: dielectric relaxation, carrier trapping and thermal emission, carrier recombination, carrier transit time related relaxation mechanism, time and intensity dependent optical absorption and filament formation. Many of these mechanisms need further investigation.

Volume and surface breakdown problems were discussed by a group chaired by M. D. Pocha. There was a consensus in the group that surface breakdown was one of the fundamental problems facing high power photoconductive switches and requires further study. Some physical mechanisms that effect surface breakdown such as the ambient surroundings and field inhomogeneities at contacts are also noted.

The Solid State Plasma Transport group, chaired by E. Kunhardt, considered questions such as: (1) Can the dynamics of charge carriers be described by microscopic equations? (2) What is the role of carrier-carrier scattering of high electron densities? (3) What is the mechanism of surface breakdown? It was also agreed that instabilities such as filament formation (microplasmas) and failure mechanisms at contacts deserve more detailed consideration.

In conclusion, I would like to thank R. Junker of ONR for suggesting this workshop and all the participants for the active efforts they expended in presenting the talks, taking part in the working groups and contributing to the interesting discussions.

11. PROGRAM

II. PROGRAM

WORKSHOP ON NEW DIRECTIONS IN SOLID STATE POWER SWITCHES

Wednesday, August 28, 1985

8:30-8:40a.m.	Welcome	B. SENITZKY Polytechnic Institute Farmingdale, N.Y.
8:40-9:00a.m.	Goals of Solid State Switching	R. JUNKER Office of Naval Research Washington, D.C.
9:00-9:45a.m.	Overview of Space Power Switching Requirements and Basic Issues	E. KUNHARDT Polytechnic Institute Farmingdale, N.Y. L. LUESSEN Naval Surface Weapons Center Dahlgren, Va. F. ROSE Naval Surface Weapons Center Dahlgren, Va. T. R. BURKES T. R. Burkes, Inc. Lubbock, Tx.
9:45-10:00a.m.	Break	
10:00-11:00a.m.	Silicon Carbide as a Potential Candidate for High Power and High Temperature Devices	R. DAVIS N. Carolina State University Raleigh, N.C.
11:00-12:00p.m.	Picosecond Relaxation of Photoexcited Carriers in Disordered Semiconductors	A. JOHNSON A T & T Bell Laboratories Holmdel, N.J.
12:00-1:00p.m.	Lunch	
1:00-2:00p.m.	Free Carrier Plasma Transport in Photoexcited Semiconductors	J. MEYER Naval Research Laboratories Washington, D.C.
2:00-3:00p.m.	Physical Mechanisms in Photoconductor Switching	R. HAMMOND Los Alamos National Laboratory Los Alamos, N. Mex.
3:00-3:15p.m.	Break	

WORKSHOP ON NEW DIRECTIONS IN SOLID STATE POWER SWITCHES

PROGRAM

Wednesday, August 28, 1985 (cont'd.)

- | | | |
|---------------|--|---|
| 3:15-4:15p.m. | Picosecond Photoconductors:
Problems and Perspectives | D. AUSTON
A T & T Bell Laboratories
Murray Hill, N.J. |
| 4:15-5:15p.m. | Problems of High Power
Photoconductive Switching
in the Picosecond Time
Scale | G. MOUROU and W. DONALDSON
Laboratory for Laser Energetics
University of Rochester
Rochester, N.Y. |

Thursday, August 29, 1985

- | | | |
|-----------------|---|---|
| 9:00-10:00a.m. | High Power Photo-
Conductive Switch
Applications | W. NUNNALLY
Power Conditioning Laboratory
University of Texas at
Arlington, Texas |
| 10:00-10:15a.m. | Break | |
| 10:15-11:15a.m. | The MOS Controlled
Thyristor, A New
Switching Device | V. TEMPLE
General Electric Corporate
Research and Development Center
Schenectady, N.Y. |
| 11:15-12:00p.m. | Avalanche Breakdown
Mechanisms and Associated
Devices | M. POCHA
Lawrence Livermore National Lab.
Livermore, Ca. |
| 12:00-1:00p.m. | Lunch | |
| 1:00-1:30p.m. | Thermodynamic Change of
State Switching for Pulse
Power | M. KAHN
Naval Research Laboratory
Washington, D.C. |
| 1:30-2:00p.m. | Super-ionic Conductors
as High Speed Switches | J. SCOTT
University of Colorado
Boulder, Col. |
| 2:00-2:15p.m. | Break | |

WORKSHOP ON NEW DIRECTIONS IN SOLID STATE POWER SWITCHES

PROGRAM

Thursday, August 29, 1985 (cont'd.)

2:15-2:45p.m. Optically Activated
Semiconductors as
Repetitive Opening
Switches

C. H. LEE
Un. of Maryland
College Park, Md.

2:45-5:45p.m. GROUP DISCUSSIONS

GROUP I G. SUNDBERG, CHAIRMAN
Potential Materials for
Solid State Switching

GROUP II R. HAMMOND, CHAIRMAN
Pertinent Relaxation
Mechanisms

GROUP III M. POCHA, CHAIRMAN
Volume and Surface
Breakdown Problems

GROUP IV E. KUNHARDT, CHAIRMAN
Solid State Plasma
Transport

Friday, August 30, 1985

9:00-10:00a.m.

GROUP I DISCUSSION

10:00-10:15a.m.

Break

11:15-12:15p.m.

GROUP II DISCUSSION

12:15-1:15p.m.

Lunch

1:15-2:15p.m.

GROUP III DISCUSSION

2:15-2:30p.m.

Break

2:30-3:30p.m.

GROUP IV DISCUSSION

3:30-3:45p.m.

CONCLUDING REMARKS - B. SENITZKY

WORKSHOP ON NEW DIRECTIONS IN SOLID STATE POWER SWITCHES

GROUP CONSTITUENTS

GROUP I Potential Materials for Solid State Switches

R. Davis
R. D. Ford
M. Kahn
W. Nunnally
M. O'Malley
T. Rao
R. Rediker
J. Scott
G. Sundberg, Chairman

GROUP II Pertinent Relaxation Mechanisms

D. Auston
J. Halbout
R. Hammond, Chairman
C. Lee
G. Mourou

GROUP III Volume and Surface Breakdown Problems

T. Burkes
R. Donaldson
M. Pocha, Chairman
B. Senitzky
V. Temple
M. Weiner
F. Zutavern

GROUP IV Solid State Plasma Transport and Modelling

M. Gunderson
K. Jungling
E. Kunhardt, Chairman
J. Meyer
P. Williams

WORKSHOP ON NEW DIRECTIONS IN SOLID STATE POWER SWITCHES

AUGUST 28, 29, 30, 1985

POLYTECHNIC INSTITUTE OF NEW YORK
Route 110, Farmingdale, New York

D. Auston 201/582-3188
Room 1C424
A T & T Bell Labs
Murray Hill, N.J. 07974

Lawrence Bovino 201/544-5404
U.S. Army
Electronics Technology
and Devices Lab
DELET-M.L.
Ft. Monmouth, N.J. 07703

Tommy T. Burkes 805/885-4887
T. R. Burkes, Inc.
P. O. Box 16577
Lubbock, Texas 79490

Robert F. Davis 919/737-3272
N. Carolina State University
Box 79071
Dept. of Material Engineering
Raleigh, N. Carolina 27695

Peter Delfyett 212/690-6960
Physics Department
City College of New York
Rm. J419
138th St. and Convent Ave.
New York, N.Y. 10031

Brian Ditchek 617/890-8460
GTE Laboratories, Inc.
40 Sylvan Rd.
Waltham, MA 02154

W. R. Donaldson 716/275-5101
Laser Lab
University of Rochester
250 E. River Road
Rochester, N.Y. 14623

Dwight Dustin
OSD/SDIP
Att.: ISD
Washington, D.C.
20301-7100

John Farber (RAEV) 702/325-7026
HQ DNA
6801 Telegraph Rd.
Alexandria, Va. 22811

Michael Field 505/844-8918
Sandia National Labs
Div. 5164
P. O. Box 5800
Albuquerque, N. Mexico 87185

Richard D. Ford 202/767-2724
Naval Research Lab
Code 4775 Bldg. 101
Washington, D.C.
20375-5000

A. Guenther 505/844-9856
AFWL/CA
Kirtland AFB
N. Mexico 87117

Martin Gundersen 213/743-6195
University of S. California
SSC 420
MC0484
Los Angeles, Ca.
90089-0484

R. Gunther 919/549-0641
ARO
P. O. Box 12211
4300 S. Miami Blvd.
Research Triangle Park, N. Carolina
27709-2211

Jean'Marc Halbout 914/945-1807
IBM
P. O. Box 218
Yorktown Heights, N.Y. 10598

Robert Hammond 505/667-1813
Los Alamos National Laboratory
MS D429
Los Alamos, N. Mexico 87545

WORKSHOP ON NEW DIRECTIONS IN SOLID STATE POWER SWITCHES

AUGUST 28, 29, 30, 1985

POLYTECHNIC INSTITUTE OF NEW YORK
Route 110, Farmingdale, New York

R. Jain
Amoco Research Center
P. O. Box 400
Naperville, Ill. 60566

Anthony Johnson 201/949-6764
A T & T Bell Labs
Rm. 4D-321
Holmdel, N.J. 07733

Ken Jungling 505/277-6032
University of New Mexico
Papy Hall 218
Albuquerque, N. Mexico 87131

R. Junker
Office of Naval Research
800 N. Quincy
Arlington, VA 22200

Manfred Kahn 202/767-2724
Naval Research Laboratory
Code 4775 Bldg. 101
Washington, D.C.
20375-5000

Erich Kunhardt 516/454-5140
Polytechnic Institute of New York
Route 110, Farmingdale, NY 11735

Hoi Sing Kwok 716/636-3110
Elec. Eng., SUNY
Buffalo, N.Y. 14200

Chi H. Lee 301/454-6852
Elec. Eng., Un. of Maryland
College Park, Md. 20742

L. Luessen, Code F12
Naval Surface Weapons Center
Dahlgren, Va. 22448

Jerry Meyers 202/767-3276
Code 6551, Naval Research Lab
Washington, D.C. 20375

Gerard Mourou 716/275-2092
Laboratory for Laser Energetics
250 E. River Road
Rochester, N.Y. 14623

W. C. Nunnally 817/273-2671
Power Conditioning Laboratory
Un. of Texas
P. O. Box 19016
Arlington, Tx. 76019

Martin O'Malley 505/846-7032
Div. 1248, Sandia Labs
Albuquerque, N. Mex. 87185

Michael D. Pocha 415/422-8664
Lawrence Livermore Natl. Lab
P. O. Box 5504, Mail Stop L156
Livermore, Ca. 94550

Triveni Rao 516/282-5072
Bldg. 535B, Brookhaven Natl. Labs
Upton, N.Y. 11973

Robert Rediker 617/863-5500 x4417
Rm. C325, MIT Lincoln Labs
P. O. Box 73
Lexington, Mass. 02173-0073

F. Rose, Code F12
Naval Surface Weapons Center
Dahlgren, Va. 22448

James Scott 303/492-7365
Dept. of Physics, Un. of Colorado
Campus 390
Boulder, Col. 80309

Benjamin Senitzky 516/454-5085
Polytechnic Institute of New York
Route 110, Farmingdale, NY 11735

Bruce Smith
Directorate of Physics
Bldg. 410
Bolling Air Force Base
Washington, D.C. 20332

WORKSHOP ON NEW DIRECTIONS IN SOLID STATE POWER SWITCHES

AUGUST 28, 29, 30, 1985

POLYTECHNIC INSTITUTE OF NEW YORK
Route 110, Farmingdale, New York

Gale R. Sundberg 216/433-4006 x5233
MS77-4
NASA Lewis Research Center
21000 Brookpark Rd.
Cleveland, Ohio 44135

Victor Temple
General Electric Research
& Development Center
Rm. 1715 AWA
1 River Road
Schenectady, N.Y. 12301

Ihor Vitkovitzky 202/767-2997
Code 4701
Naval Research Labs
4555 Overlook Ave. SW
Washington, D.C.
20375-5000

Maurice Weiner 201/544-5404
U.S. Army
Electronics Technology
and Devices Laboratory
DELET-M.L.
Ft. Monmouth, N.J. 07703

P. F. Williams
Department of Elec. Eng.
University of Nebraska
Lincoln, Neb.
68588-0511

Horst Wittman
AFOSR
Bldg. 410
Bolling AFB
Washington, D.C. 20332

Fred Zutavern 505/846-7032
Sandia National Laboratories
Division 1248
P. O. Box 5800
Albuquerque, N. Mexico 87185

III. OVERVIEW OF SPACE POWER SWITCHING REQUIREMENTS AND BASIC ISSUES

WEBER RESEARCH INSTITUTE
POLYTECHNIC INSTITUTE OF NEW YORK

III. PULSE POWER

A Brief Overview
(with emphasis on
Basic Switching Issues)

E.E. Kunhardt

L. Luessen

F. Rose

T. R. Burkes

Introduction

The term "pulsed power" is synonymous with "power conditioning". It is the manipulation of the time scale in which energy is delivered to a load. This technology finds application in a large number of areas. Table 1 gives a partial list of these areas. Typical load and switching requirements found in pulsed power systems are given in Table 2.¹ A block diagram of a generic pulsed power system with examples of system components is shown in Fig 1. Typical values for the time scales and power levels throughout the system are also shown in the figure. To meet the goals of the SDI program, a number of technological advancements will have to be made in all areas of the pulse power chain. Moreover, and of critical importance to power systems to be operated in space, significant improvements will have to be made in the overall efficiency of the power system. The advancements to be made are predicated to a large extent on our understanding of the basic phenomena underlying this technology and the transfer of this knowledge to the development of system components. Among the principal problems limiting the application of current pulse power system technology to space-based operations of interest to SDI are: a) the rating of switching components, b) deficiency of materials in a space environment and c) efficiency of power system.

TABLE 1. Pulsed Power Applications

Particle Accelerators
Electrically Driven Lasers
 μ Wave Generators
Electromagnetic Guns
Electric Thrusters

In this workshop, we will focus on the first problem. That is, switching devices that will allow the fast and repetitive transfer of energy from the energy storage device to the load (the switch in Fig 1). To meet the diverse requirements, as

shown in table 2, a number of switching concepts have been proposed.² In them, a gas, a solid, or a liquid serves as the switching medium.

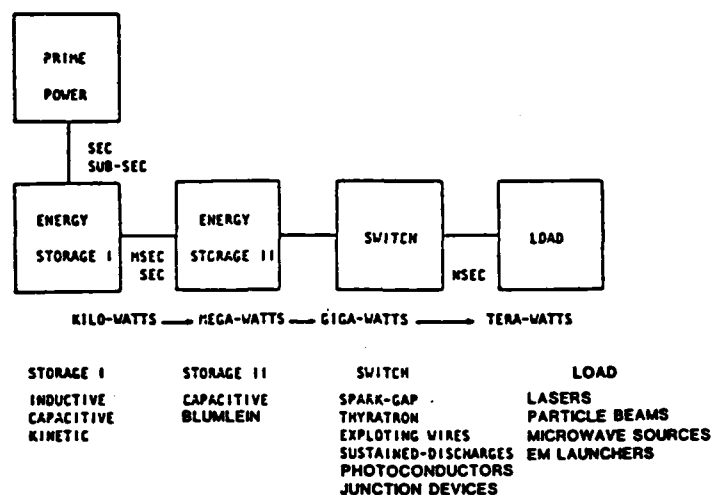


Fig. 1. Block Diagram of Pulse Power System.

TABLE 2. Pulsed Power Requirements

Load Requirements	Directed Energy		
	Charged Particle Beam	Laser	EM Propulsion
V_{oc}	0.1 - 1 MV	10 - 20 KV	5 - 10 KV
I_{peak}	10 - 100 KA	20 KA	1 - 5 MA
Rep-rate	~ 10 KHz (Burst)	100 Hz	100 - 500 Hz
Life (shots)	$10^6 - 10^8$	10^8	$10^6 - 10^8$
Switch Requirements			
Conduction	20 μs	100 μsec	1 sec
Opening times	< 1 μsec	~ μsec	100 μsec
Hold-off times	2 - 5 μsec	100 μsec	1 - 5 msec

Present Switching Needs

Two areas of application are presently receiving considerable attention. These are: (1) repetitive switches, and (2) opening switches for use with inductive storage. Opening switches may also operate repetitively. The requirements of these two technologies are slightly different, as shown below. A schematic diagram of a system that utilizes inductive store is shown in Fig. 2a.

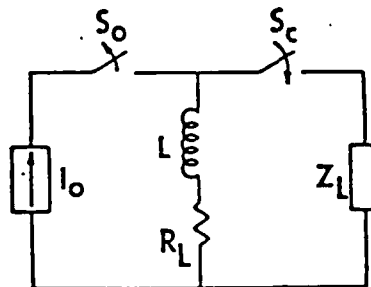


Fig. 2a. Inductive Energy Store Circuit.

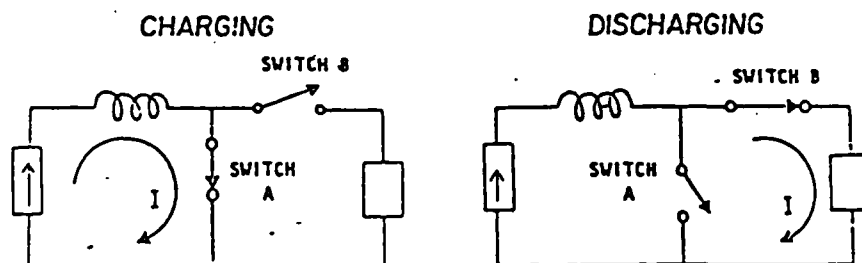


Fig. 2b. Cycle of Inductive Circuit.

The procedure for delivering energy to the load for one cycle of operation is shown in Fig. 2b. The center stage in this process is taken by switch A in the figure; it is a closing/opening switch. Initially, switch A is closed and energy is stored at a slow rate in the inductor. On command, switch A is made to open shortly after the closure of switch B, and energy is delivered to the load. There is a great interest in developing a closing/opening switch for use with inductive energy storage. The energy density in inductive store is much higher than in capacitive store. Thus, for equal total stored energy, inductive store requires

less volume.

The switching requirements for a system not using inductive storage but operating repetitively are less demanding. A schematic diagram of such a system is shown in Fig. 3. The procedure for delivering energy to the load in one cycle is as follows. Initially, the capacitor, C , is charged to a voltage V_0 by the DC supply.

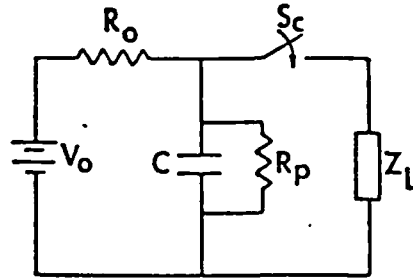


Fig. 3. Capacitive Energy Store Circuit.

On command, switch S_c is closed and the energy stored in the capacitor is quickly delivered to the load. After the transfer, it is desirable for the switch S_c to fully recover its insulating properties so that the capacitor can be recharged to the desired potential, V_0 . Note that this switch does not have to "open" but to "recover" (in actual applications the DC supply V_0 , is momentarily isolated from the load to allow the switch to begin the recovery process. That is, there is a period of zero current at the load).

Since the switch forms an intricate part of the pulsed power system, it may not, in general, be possible to predict its behavior from investigation of isolated switches. This is particularly so in the case of opening/closing switches where the voltage generated by the circuit during the opening phase (in Fig. 2 note that the change in current creates a voltage $L di/dt$ which appears across the switch) affects the performance of the switch. However, by directing the research on the basic issues common to a category of switches (and perhaps all switches), considerable contributions can be made towards developing new

concepts and assessing their feasibility. Breakthroughs in pulse power technology rely on the quantitative understanding of these basic issues.

Workshop Objectives

The goals of this workshop are: a) Identify physics concepts that may be utilized for switching. Examples of switching concepts are photo-conductivity and p-n junctions. And (b) given the concept, identify the physics issues whose understanding may help assess the fundamental limitations of a given concept and guide the development of the switch technology.

General Desired Switch Characteristics

Consider the simple circuit shown in Fig. 3. When the switch in the circuit is operated repetitively, it follows the cycle shown in Fig. 4. In each of these stages, a number of physics issues (which may be common to all switches) need to be addressed. Example of these issues are given in the figure.

The voltage (electric field) V_s , current I , and power loss P_L ($V_s I$), in the switch in one cycle of operation are shown in Fig. 5. Note that the slower the switch turns on and off, and the greater the on-state voltage V_o , the greater the power losses in the switch. For an efficient switch, power losses should be minimized. To do so, we need to look at the behavior of the carrier density and drift velocity as a function of electric field. The desired behavior is schematically shown in Fig. 6. In the on-state, where the field is low, the carrier density and drift velocity are high and the carrier loss rate is negligible. Thus, very little energy is being used to compensate for loss of carriers. As the switch opens (recovery phase), the electric field and carrier loss rate increase, while the carrier density and drift velocity decreases. The increase in the carrier loss rate and the decrease in drift velocity with increasing electric field, drives the switch to the off-state. It is desirable to tailor the transport properties and rate constants of the switching medium to conform, in general, with

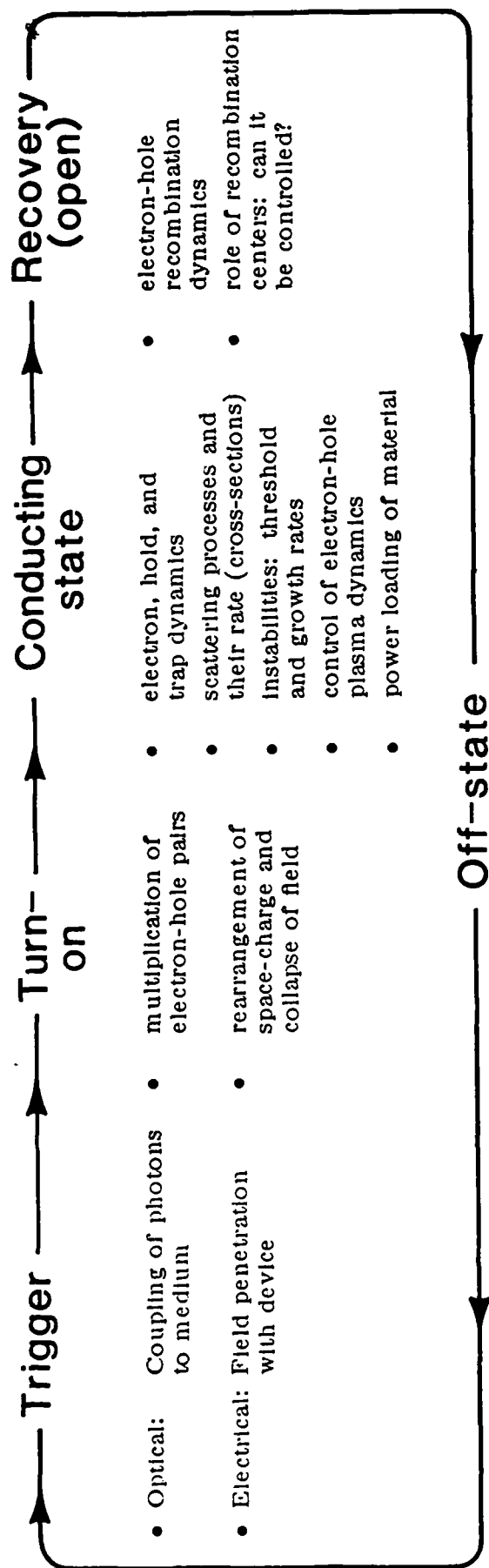


Fig. 4. A Switch Under Repetitive Operation. Physics Issues.

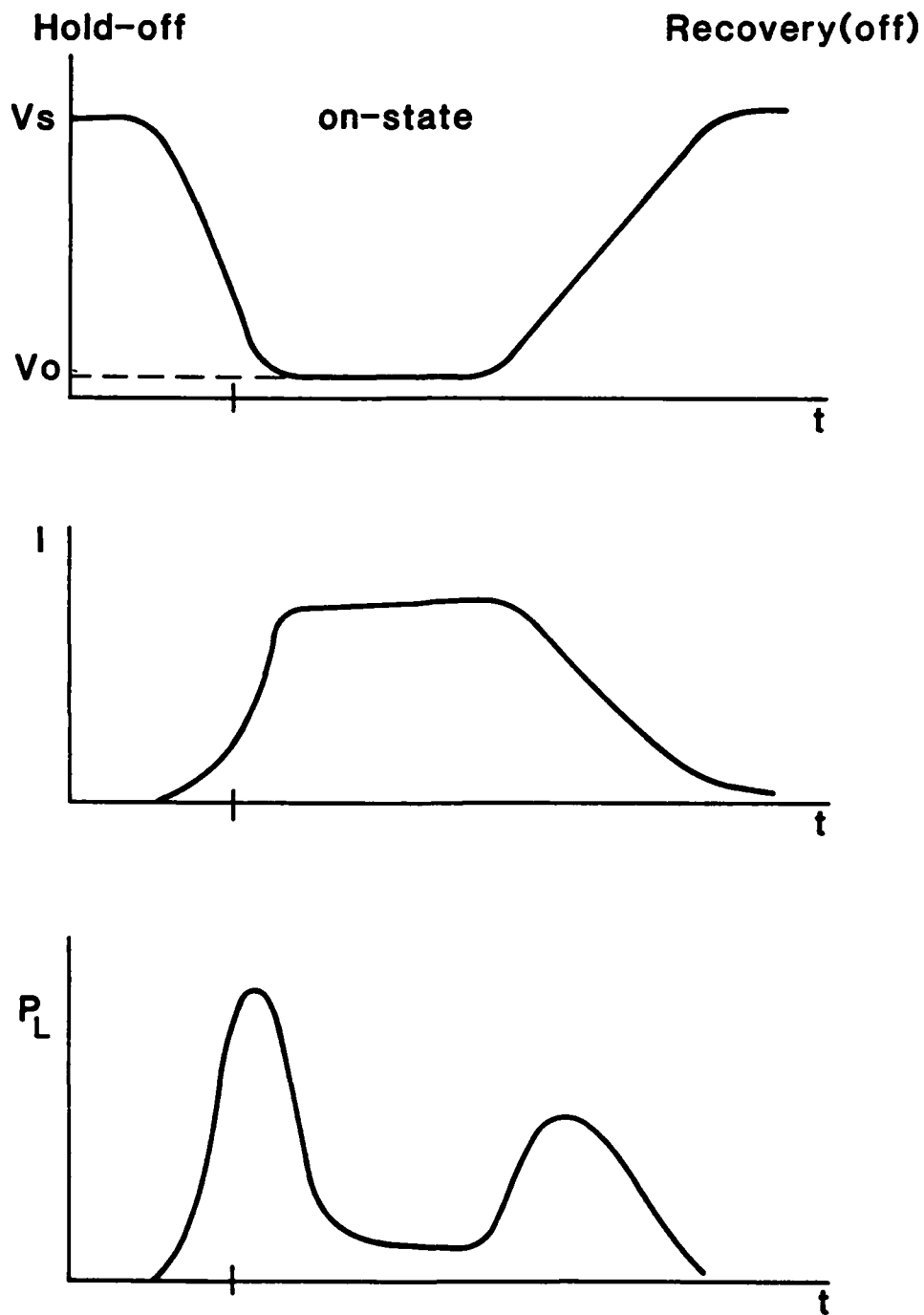


Fig. 5. Behavior of Switch Variables During one Cycle of Operation

Fig. 6. A point that needs further consideration is whether or not the behavior shown in Fig. 6 results in high losses in the turn-on stage. That is, the switch is turned on by driving the medium from the high-loss region (high field) to the low-loss region. To assess this loss, the carrier production mechanism and its dependence with field also needs to be considered. If the production mechanism is internal (i.e. avalanching), then it may also influence the recovery phase; however, if it is external, then it can be made operative in the turn-on stage only without influencing the recovery. This is a desirable characteristic.

Some Basic Physics Issues

To give a better physical perspective of the switch, the circuit in Fig. 4 has been re-drawn and shown in Fig. 7. The switch, in general, consists of two metal electrodes separated by the switching medium. This medium is initially an insulator; it is transformed into a good conductor while closing, and returns to the insulating state while opening. Vacuum, gases, liquids, and solids have been used as switching medium. In a vacuum switch, the medium is in essence the vapor of the electrode material; and thus, for our purpose, may be considered a type of gas switch. A similar statement may be said about liquids in that conduction (and in most cases breakdown) occurs in the vapor of the liquid. There is no liquid switch where conduction occurs in the liquid state. Thus, a liquid switch is also "gas-like". There are three general characteristics of solid and "gas-like" switching medium that need to be considered. These are: a) the nature of the transfer of the electrons from the metal electrode to the medium (i.e. nature of contacts, b) carrier dynamics and c) survivability of medium under switching conditions. A summary of these characteristics is given in Table 3. The remainder of the paper will be devoted to identifying some physics issues that are associated with a solid state medium.

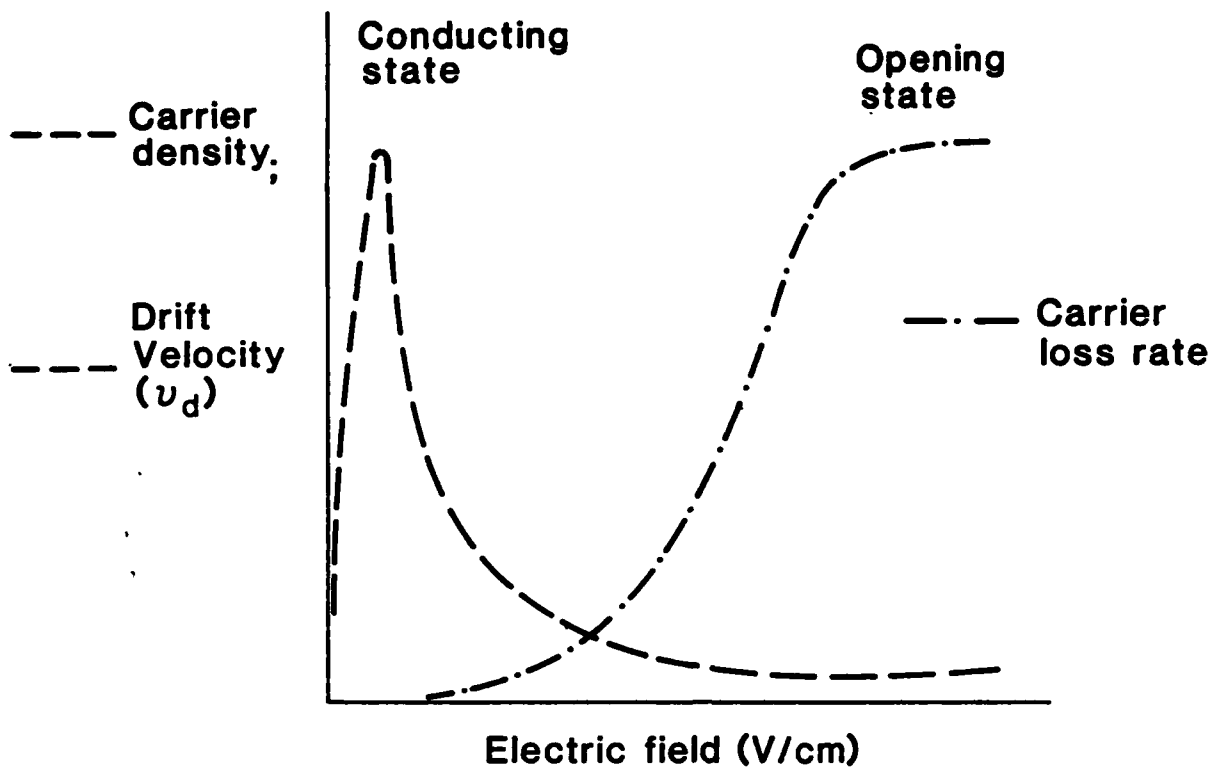


Fig. 6. Desired Field Dependence of Switch Parameters.

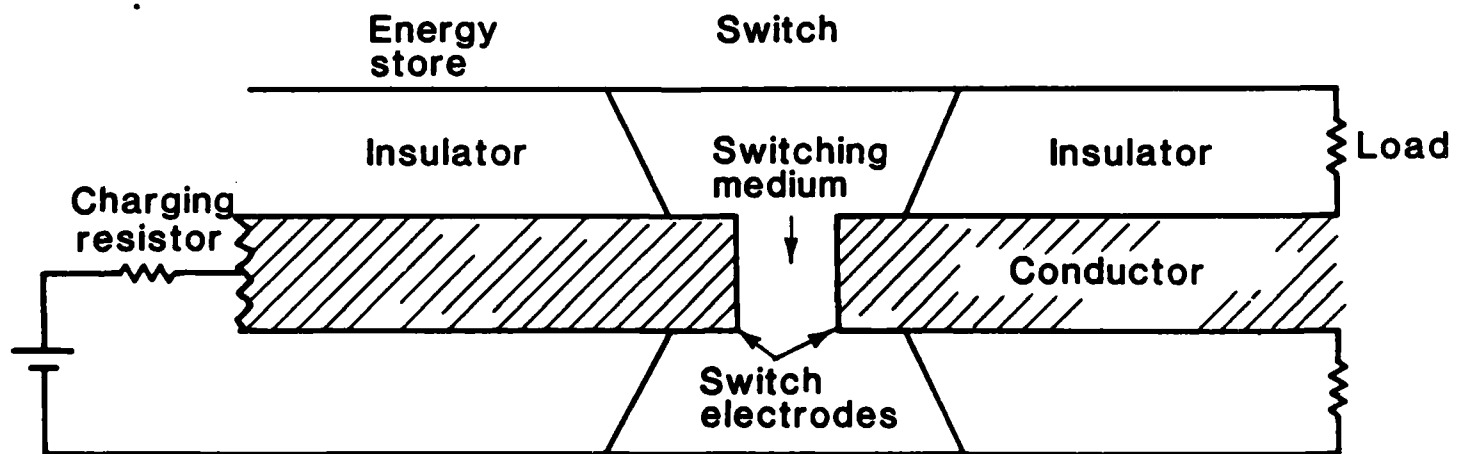


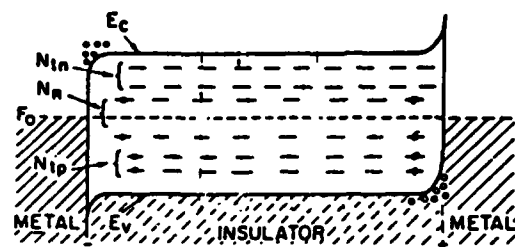
Fig. 7. Coaxial - Switch Geometry.

TABLE 3. General Characteristics of Switching Medium

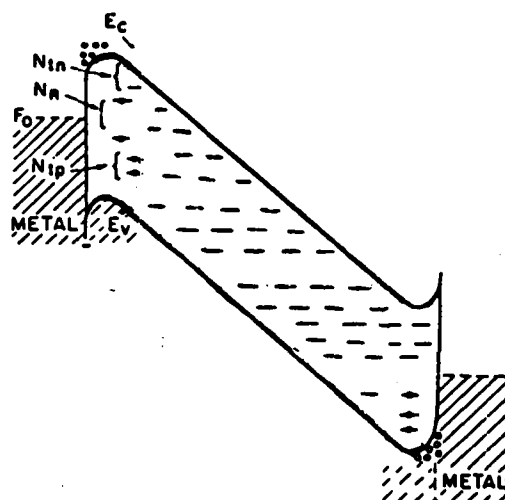
Conducting State	Carrier Injection Mechanism (Contact Area)	Carrier Dynamics Governed by	Material Survivability: is it "self-healing?"
"Gas-like"			
diffuse discharge	Ion impact on cathode, although it is thermionic when using heated cathodes (very lossy).	Carrier-neutral gas interactions (weakly ionized gas) and coulomb interactions (strongly ionized gas).	Yes
filamentary discharge (arc)	Thermionic and field emission (very destructive).	Coulomb interactions	Yes
Solid State			
Uniform current	tunneling (very efficient)	Carrier-impurity and	No
filamentary channel(s)		carrier-carrier interactions	

Let a (homogeneous) solid medium fill the switch region shown in Fig. 7. Usually, the solid medium only fills the inter-electrode space, so that consideration must be given to the possibility of breakdown along the solid surface. Although this does not affect the behavior of the switch, it usually determines the maximum operating voltage. Electrode shaping and/or separation of the solid surfaces are techniques which are employed to reduce the possibility of surface breakdown. These will be discussed in other talks. Note that electrode shaping may also be desirable to create a uniform field pattern in the on-state of the switch to lower the probability of transition from a uniform current state into a (destructive) filamentary channel.

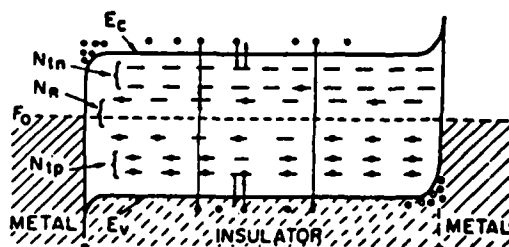
The energy-band diagram for the switch (with no field present) is shown in Fig. 8a.³ In this figure E_c and E_v are the conduction and valence-band edges



(a)



(b)



(c)

Fig. 8

Schematic energy-band diagram for double injection into an insulator with injecting contacts.

(a) Applied field = 0

(b) Applied field \neq 0

(c) Applied field collapses due to plasma formation in the bulk

respectively; N_{t_e} and N_{t_h} are the densities of electron and hole traps (impurities in general), respectively; N_R is the density of recombination centers; F_0 is the Fermi level; and ψ is the interface energy barrier. When the external field is applied to the switch, the bands bend resulting in the diagram shown on Fig. 8b.

The first question that arises regards the size of ψ . Is it necessary for ψ to be low (ohmic contacts) for the switch to be: a) efficient and b) stable for long pulse operation? Let's defer this to later discussions. Note in Fig. 8b that the region the carriers need to tunnel is narrow so that it appears that no matter what ψ is, there is a copious supply of carrier. Assuming this is the case, electrons and holes injected from respective contacts into the medium (plasma injection) proceed to the respective collecting contacts, and, assuming $N_{t_e} = N_{t_h} = N_R = 0$ will only be lost in the medium if direct recombination occurs. In this case, the steady state, an electron-hole plasma exists in the medium, the field across it is nearly zero (except maybe at the contacts), the current through the medium may be as large as desired and the losses (due to phonon scattering and direct recombination) may be made as low as desired (by cooling the medium and decreasing the operating current density). The energy band diagram for this situation is shown in Fig. 8c. This medium (and contacts), of course, would not be a switch since any time a field is present across the medium, a current would flow, i.e., it does not hold off any voltage. Thus, the questions we need to ask are:

1. what is the role of (a) the contacts; (b) traps, and (c) recombination centers in shaping the space-charge in the hold-off state and in the on-state, and,

2. what are the losses in the various regions due to field redistribution during and after turn-on of the switch?

To answer these questions, we need to understand carrier dynamics at high carrier densities. This involves a description of the carrier distributions, trap dynamic, and space-charge fields. Moreover, depending on the level of description, knowledge of the scattering rates or cross-sections is also required. If an external source is used to affect the carrier concentration, the coupling of this source to the medium need also be considered. Given that, we understand the carrier dynamics so that we can answer the two questions posed above; we then ask, can we control the carrier dynamics? This may be done either actively (by using external means such as a laser) or passively (by purposely introducing impurities in the medium by using an inhomogeneous medium, such as junction devices, or microscopic design of the lattice, such as creating lattice channels). This topic is rather exciting and one that we may spend some time discussing in this workshop.

With regard to junction devices, they are in general characterized by having regions where very high fields can exist and where avalanche growth and the formation micro-plasmas may take place. How this occurs and how it propagates needs to be addressed. In this context, the role of defects needs to be assessed.

A final topic that I would like to discuss is that of instabilities. That is, given that the switch has been made to turn on and is carrying a uniform current, how long can we continue doing this without destroying the medium? In general, instabilities cause a redistribution of the current density, creating filamentary channels where the current density may be sufficiently high to destroy the medium. The question is then what may cause a "constriction" instability? What are the threshold conditions and the growth rate for the

instability. Since these very much depend on the properties of the medium, I defer the details of the discussion to later on in the workshop. However, there are some general remarks that can be made. The temperature profile for a diffuse and filamentary current channels (in steady-state) are shown in Fig. 9. The radius of the channel is R . In both cases $\partial_r T \leq 0$, whereas $\frac{\partial^2 T}{\partial r^2} < 0$ for a diffuse channel and $\frac{\partial^2 T}{\partial r^2} > 0$ for a constricted channel. Thus, we may ask - under what condition can $\partial^2 T / \partial r^2$ be greater than zero? This would imply a constricted state. To further explore this, we must look at the energy balance equation. It may be written as

$$\frac{\partial^2 T}{\partial r^2} = \frac{1}{\kappa} \left[(u - \sigma E^2) - \frac{\kappa}{r} \partial_r T - \frac{d\kappa}{dT} \left(\frac{\partial T}{\partial r} \right)^2 + \rho C_p V_z \partial_z T \right]$$

where κ = thermal conductivity; $\kappa = \kappa(T)$

σ = electrical conductivity

ρ = density of material

C_p = specific heat

V_z = drift velocity, and

u = energy radiated.

Thus, $\partial^2 T / \partial r^2$ may be greater than zero if:

- (a) $u > \sigma E^2$, that is, if radiation losses are greater than the local $\underline{J} \underline{E}$ heating.
- (b) if $\frac{d\kappa}{dT} < 0$, that is, if there is a maximum in the thermal conductivity as a function of pressure, and
- (c) convection at a contact where $V_z \partial_z T$ may be > 0 . In addition to the above, magnetic pinch effects ($\underline{J} \times \underline{B}$) and wall effect also need to be considered.

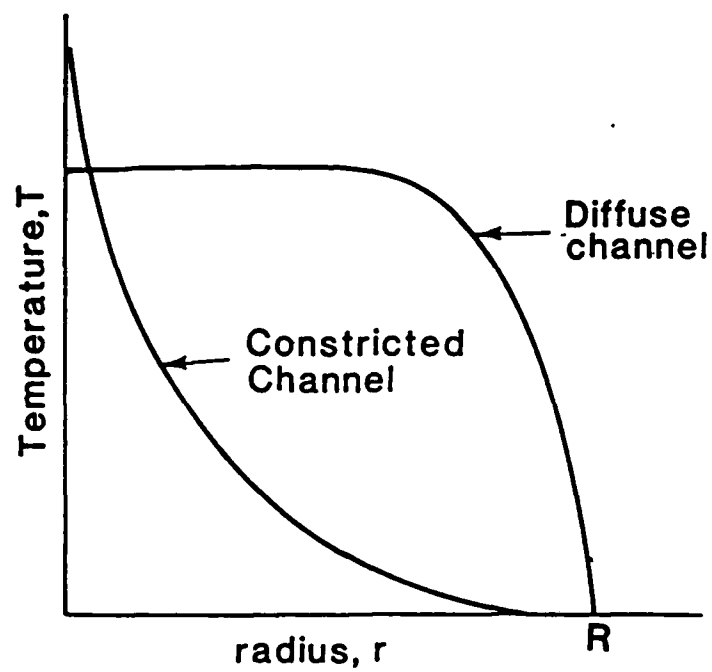


Fig. 9. Temperature Profile of Diffuse and Constricted Channels.

Concluding Remarks

In this paper, I have tried to present an overview of pulse power systems requirements and switches in particular. This will serve as background for those not familiar with pulse power, and a review for those who are in the field. I have then discussed some fundamental physics issues whose understanding may lead to significant breakthroughs in the use of solid medium for pulse power switching. The questions I would like to pose to the participants are: (a) what are the exciting physics concepts that we need to be looking at, and (b) what are the physics issues?

References

1. M.F. Rose and A.U. Hyder, "Pulsed Power Requirements," Proc. U.S. Army Research Office Workshop on Diffuse Discharge Opening Switches, pp. 20-28, Tamarron, CO, 1982.
2. T.R. Burkes, J.P. Craig, M.O. Hagler, M. Kristiansen and W.W. Portnoy, "A Review of High Power Switch Technology," IEEE Trans. Elect. Devices, ED-26, pp. 1401-1409, 1979.
3. M.A. Lampert and P. Mark, Current Injection in Solids (Academic Press, New York, 1968).
4. I.P. Shkarofsky, T.W. Johnston and M.D. Bachynski, The Particle Kinetics of Plasmas, (Addison-Wesley, Reading, MA, 1966).

IV. MATERIAL PROPERTIES

Silicon Carbide as a Potential Candidate for High
Power and High Temperature Devices

Robert F. Davis

North Carolina State University

Department of Materials Engineering

Raleigh, NC 27695

Silicon carbide (SiC) is the only compound species that exists in the solid state in the Si-C system. However, it can occur in the cubic (C), hexagonal (H) or rhombohedral (R) structures. It is also classified as existing in the beta (β) and alpha (α) modifications. The beta, or cubic, form crystallizes in the zinc-blende or sphalerite structure; whereas, a large number (approximately 170) of the alpha modifications occur in the hexagonal or rhombohedral forms known as polytypes. Silicon carbide intrinsically possesses extreme hardness, very good thermal and mechanical properties as well as excellent resistance to oxidation, corrosion, thermal shock and radiation, since the bonding between Si and C atoms possesses a highly covalent character with an ionic contribution of approximately 12%.

Beta silicon carbide (β -SiC) is currently being examined throughout the world as a candidate material for use in specialized applications such as high temperature, high frequency, high power or high speed devices. Because of its excellent thermal conductivity and high breakdown field, the integration of devices from this material could be achieved with very high densities. The reasons for the interest in this material are its special physical and electronic properties such as a high melting point ($T_m=3103K$), high thermal conductivity ($\rho_T=3.9W/cm-deg$), wide band gap ($E_g=2.3$ eV at 300K), high breakdown electric field ($E_b=2.5 \times 10^6$ volts/cm), high saturated drift velocity ($V_{sat}=2 \times 10^7$ m/s) and a small dielectric constant ($K=9.7$). In addition, the electron Hall mobility

of high purity undoped beta-SiC has been estimated from theoretical calculations to be approximately $1300 \text{ cm}^2/\text{V s}$ and has been measured to be $1000 \text{ cm}^2/\text{V-s}$ at 300K. Most recently, an electron mobility of more than $10^4/\text{cm}^2/\text{V-s}$ has been observed in β -SiC thin films by electron cyclotron resonance. Because of the smaller amount of phonon scattering in the cubic material, the electron mobility is greater than that of alpha-SiC, thus beta-SiC is currently considered more desirable than any of the alpha polytypes for a number of device applications. In fact, Johnson developed a simple theoretical relationship between the breakdown voltage, the saturated drift velocity and the power and frequency limits of transistors. Using the data for these parameters, Johnson's "figure of merit" shows β -SiC to be more than three orders of magnitude better than Si for high power applications.

Research at NCSU and elsewhere around the world has most recently concentrated on growing thin films of β -SiC on single crystal Si and on other substrates. In the case of Si, a two step growth process involving the initial conversion of the Si surface to SiC via its reaction with a C-containing gas at high temperature and the subsequent deposition of SiC from C- and Si-containing gases entrained in H_2 . The formation of the $\approx 40\text{nm}$ thick converted surface layer ameliorates the approximately 20% and 22% mismatch in coefficients of thermal expansion and lattice parameter, respectively, so that a thick SiC film can be deposited having very smooth surfaces.

However, in spite of the above efforts, near interfacial misfit dislocations, stacking faults and residual strain occur in the β -SiC film to a width of $\approx 3\mu\text{m}$. The concentrations of these defects drops rapidly beyond this distance but are not eliminated even to a thickness of $20\mu\text{m}$. Although these thick as-grown films

lack perfection, they are suitable for the additional studies conducted at NCSU regarding (1) the addition of the n- and p-type dopants of N and P and B and Al, respectively, both during growth and via ion implantation, (2) annealing studies on the as-grown and implanted materials, (3) oxidation and reactive ion etching research and (4) development of simple devices. This will be briefly described below.

Raman spectra of the as-grown and doped films reveal that residual stress exists in those films which is not completely relieved until the samples are heated to approximately 2073K for 300s. The solubility limits at the growth temperature of 1630K of the n-type impurities of N and P are $2 \times 10^{20}/\text{cm}^3$ and $4 \times 10^{17}/\text{cm}^3$, respectively; for the p-type dopants of Al and B these values are $4 \times 10^{19}/\text{cm}^3$ and $2 \times 10^{18}/\text{cm}^3$, respectively. The majority carrier concentration of the n-type materials is approximately one-half an order of magnitude less than the atomic concentration; however, for the p-type materials, this difference expands to 2 orders of magnitude for Al and 3 orders of magnitude for B.

Implantation results show conclusively that the solid phase epitaxy (SPE) and the resulting microstructure and electrical activity of the films are improved if they are amorphized during implantation. However, although SPE can be accomplished at temperatures as low as 1873K, ionization of the carriers is not maximized until $\approx 2073\text{K}$. As a result of the low solubility limits of most of the dopants, there exists a narrow window wherein amorphization is accomplished without resultant precipitation during rapid thermal annealing. There is little migration of the implanted N and P during the 300s anneal at 2073K; however, there is a measurable decrease in the maximum of the Al peak and the B peak disappears as a result of the rapid diffusion rate of this small atom.

Finally, Schottky barrier diodes using Au as the contact material and p-n junctions using N and Al introduced consecutively during growth or N implanted into an Al-containing sample and TaSi_2 and a 94%Au3%Al4%Ta alloy as the ohmic contact materials for the n- and p-type materials, respectively, have been fabricated from the in situ doped and implanted films. Ongoing studies of oxidation and reactive ion etching have also allowed the fabrication of mesa structures.

In summary, the principal problem at the moment in the advancement of SiC is the lack of a suitable substrate. Nevertheless, the growth of thick ($>15\mu\text{m}$) films of the material with relatively defect free near-surface regions have allowed basic research regarding dopant introduction, solubility limit determination, ion implantation and rapid thermal annealing, oxidation and reactive ion etching and the fabrication of simple devices to be investigated.

Table 2.1.4 Keyes' Figure of Merit for
Selected Semiconductors

Semi- conductor	$\sigma_T(300K)$ (W/cm-deg)	v_s (cm/sec)	K (Dimen- sionless)	$\sigma_T(v_s/K)^{1/2}$ (W/cm ^{1/2} - s ^{1/2} deg)	Figure of Merit (Dimensionless)
Si	1.5	1.0×10^7	11.8	13.8×10^2	1.0
GaAs	0.5	2.0×10^7	12.8	6.3×10^2	0.5
InP	0.7	2.0×10^7	14.0	8.4×10^2	0.6
α -SiC	3.9	2.0×10^7	10.0	55.1×10^2	4.0
β -SiC	3.9	2.5×10^7	9.7	62.6×10^2	4.5

Table 2.1.3 Johnson's Figure of Merit for
Selected Semiconductors.

Semiconductor	E (V/cm)	v_s (cm/sec)	$(Ev_s)/2\pi$ (V/sec)	Figure of Merit (Dimensionless)
Si	3×10^5	1.0×10^7	9.5×10^{11}	1.0
GaAs	4×10^5	2.0×10^7	25.0×10^{11}	6.9
InP	6×10^5	2.0×10^7	38.0×10^{11}	16.0
6H-SiC	40×10^5	2.0×10^7	250.0×10^{11}	694.4
β -SiC	40×10^5	2.5×10^7	320.0×10^{11}	1137.8

VIEWGRAPHS

SILICON CARBIDE AS A POTENTIAL CANDIDATE
FOR HIGH POWER AND HIGH TEMPERATURE DEVICES

ROBERT F. DAVIS

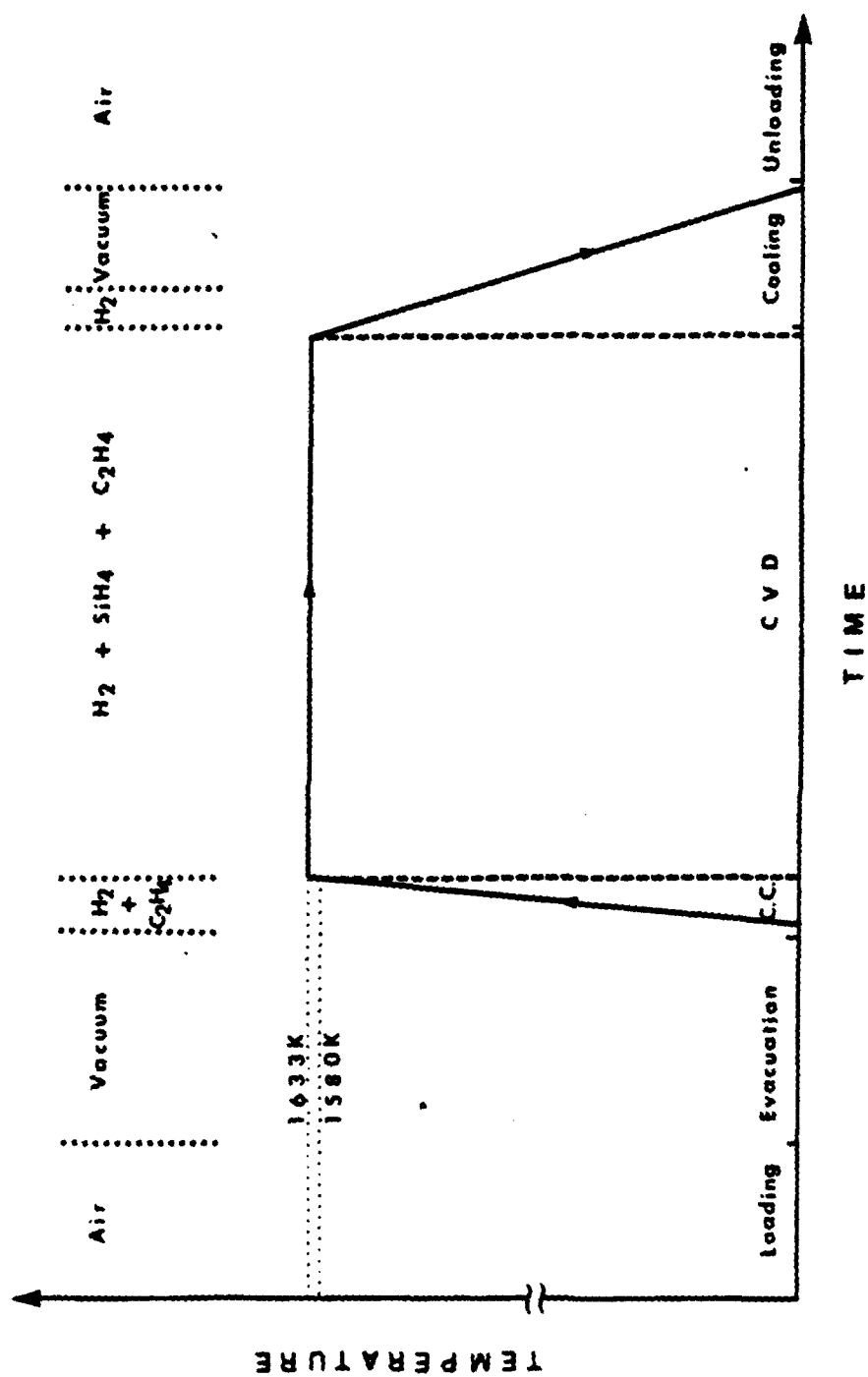


Figure 3.1.2 Schematic diagram for the growth sequence employed to grow of monocrystalline beta-SiC thin films.



Figure 4.2.2 SEM micrographs of surface pits in the converted layer produced in the period of 150 s; (a) sample is normal to electron beam and (b) sample is tilted 45° from the electron beam.

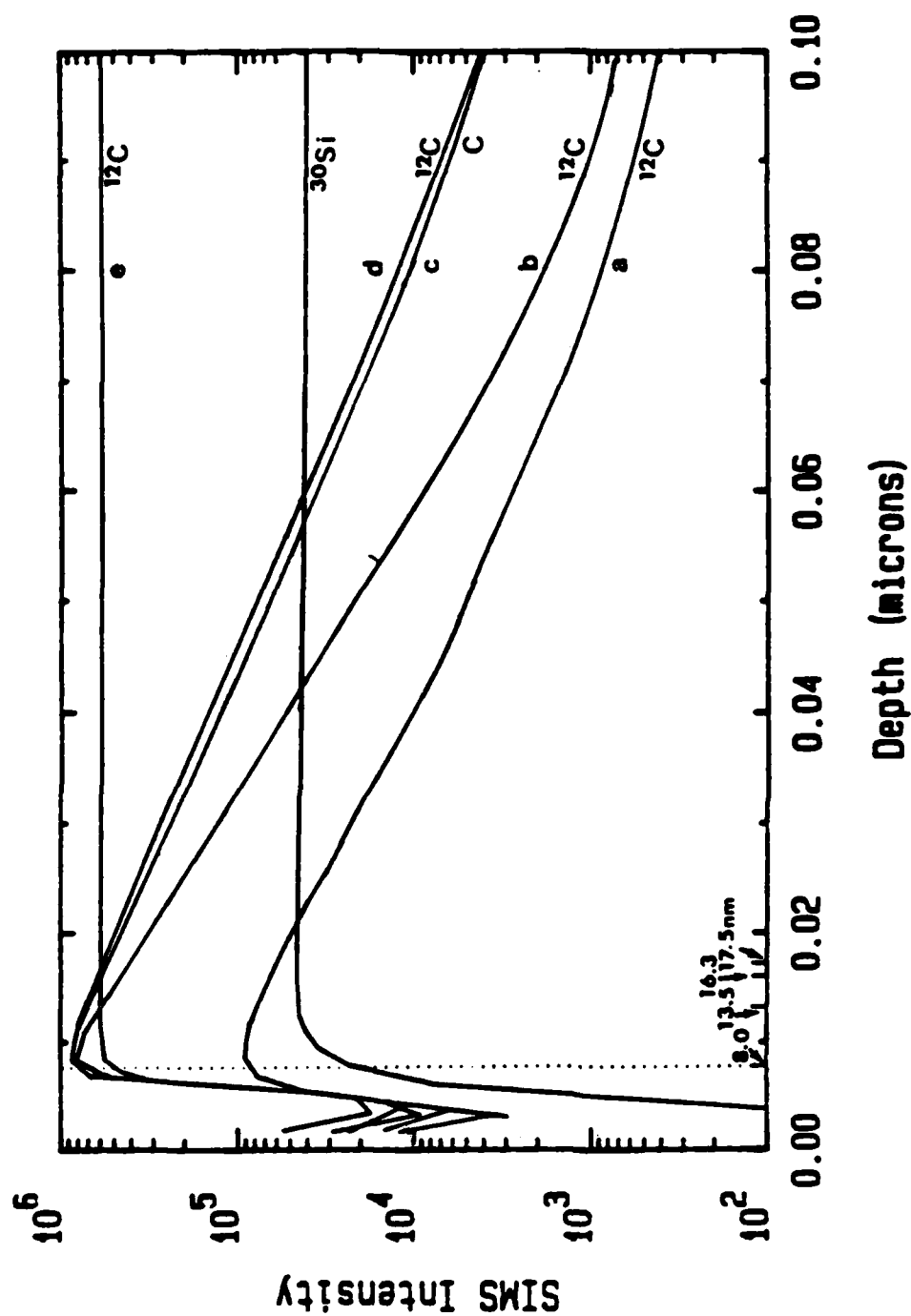


Figure 4.2.6 SIMS depth profiles of Si (mass 30) and C (mass 12) in the converted layers. (a) the 120 s sample, (b) the 150 s sample, (c) the 180 s sample, (d) the 210 s sample and (e) the beta-SiC thin film.

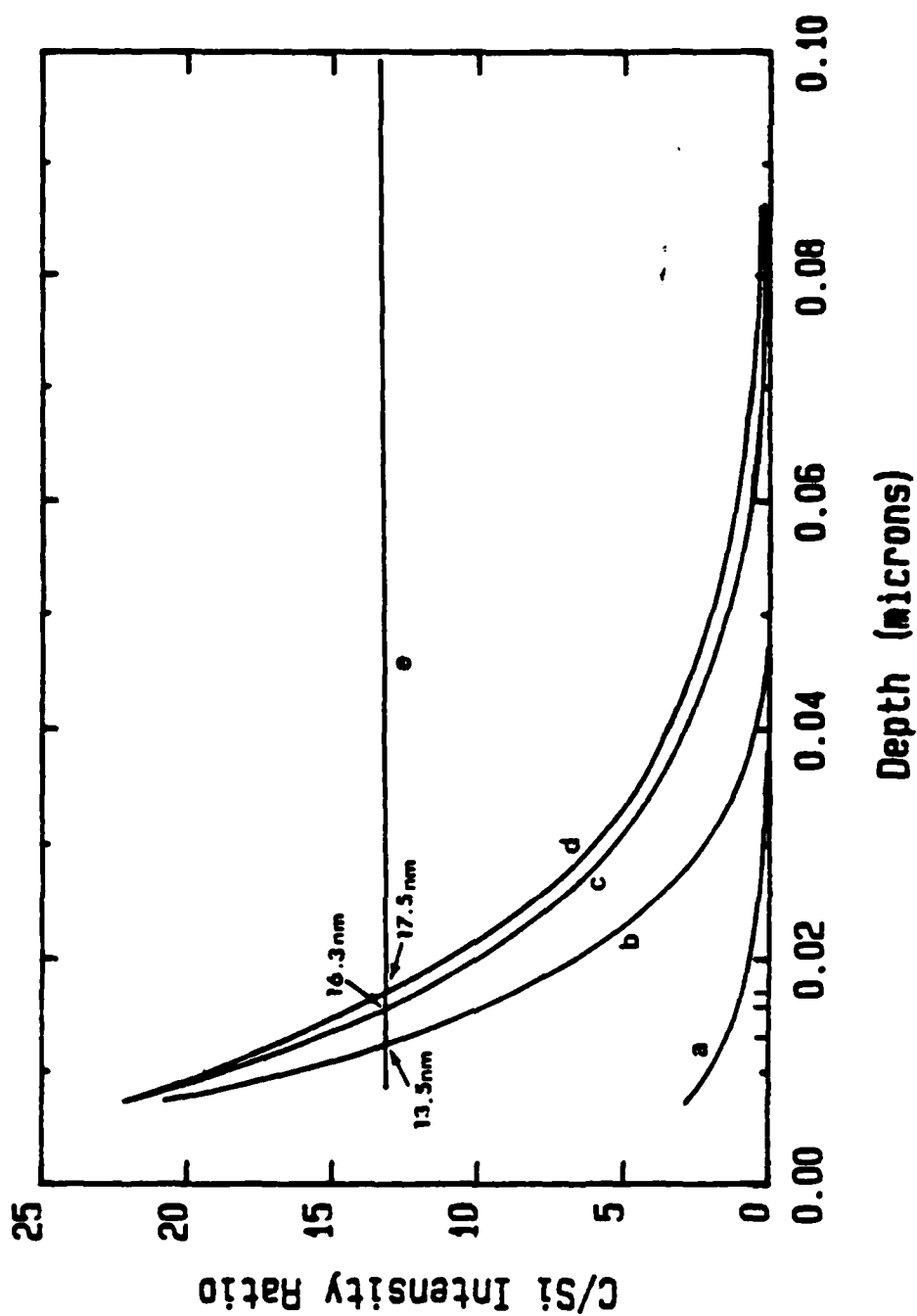
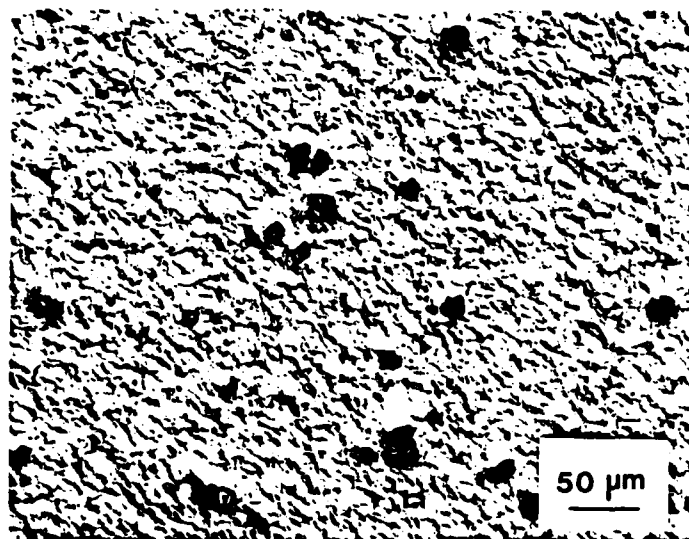
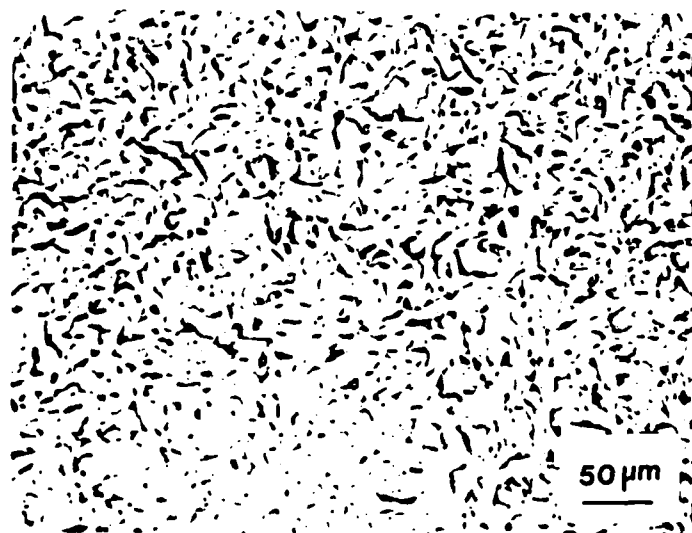


Figure 4.2.7 The C/Si intensity ratio as a function of depth derived from Figure 4.2.6. (a) the 120 s sample, (b) the 150 s sample, (c) the 180 s sample, (d) the 210 s sample and (e) the γ -SiC thin film.



(a)



(b)

Figure 2. Optical micrographs of the final β -SiC surface of the large area samples produced under the Si/C gas flow ratios of (a) 0.89 and (b) 1.05. The black particles shown in (a) are believed to be SiC formed by homogeneous nucleation in the gas phase.

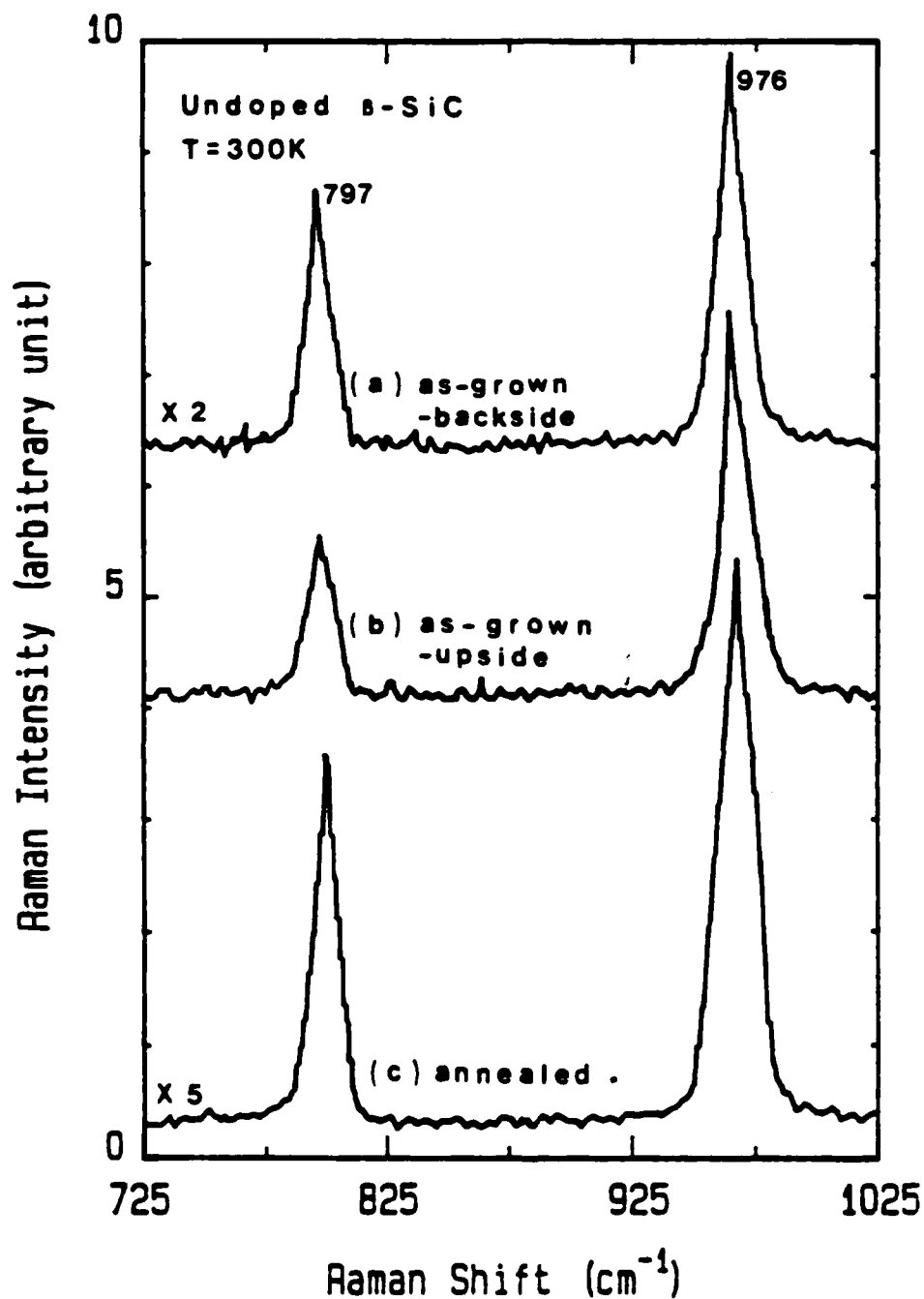


Figure 4.3.22 Raman spectra of an as-grown and undoped beta-SiC film at 300K obtained without the presence of the Si substrate: (a) from the backside (interface between Si and SiC) of the as-grown sample, (b) from the upside (surface) of the as-grown sample and (c) the same sample annealed at 2073K for 300 s.

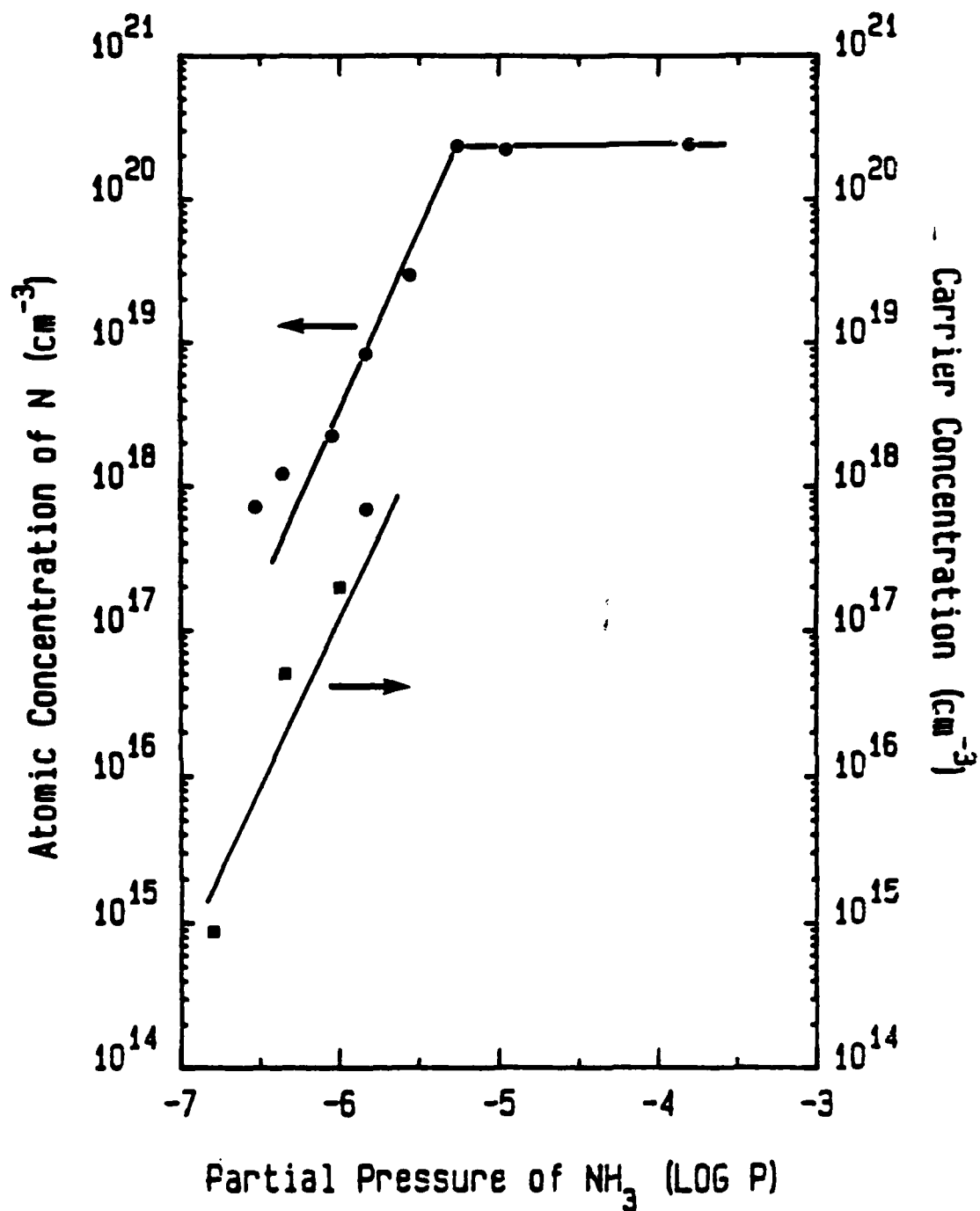


Figure 4.4.7 Atomic concentration of N and n-type carrier concentration of the doped beta-SiC films vs the partial pressure of NH_3 in the gas stream. The films were grown under the conditions noted in the caption of Figure 4.4.6.

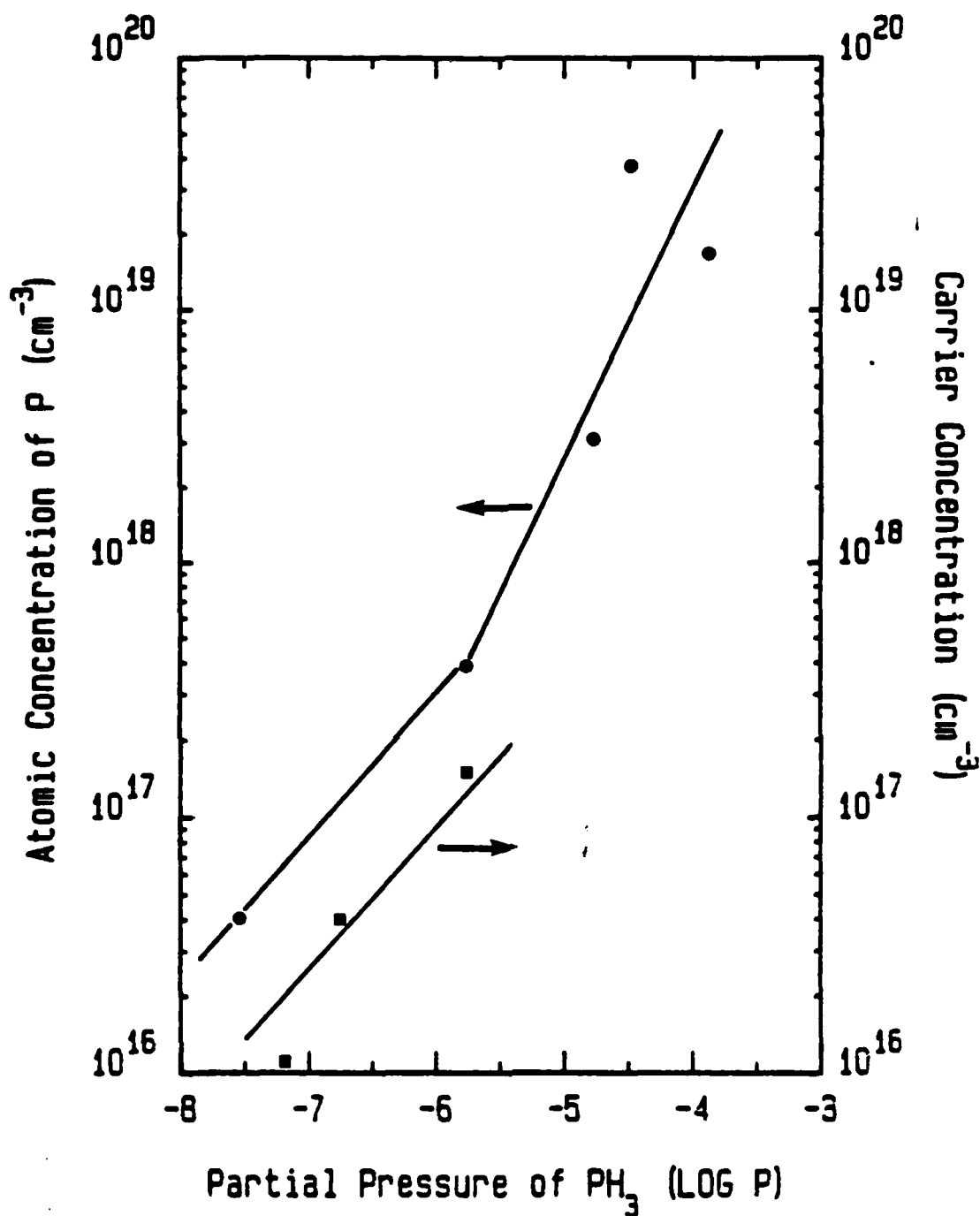


Figure 4.4.8 Atomic concentration of P and n-type carrier concentration of the doped $\beta\text{-SiC}$ films vs the partial pressure of PH_3 in the gas stream. The films were grown under the conditions noted in the caption of Figure 4.4.6.

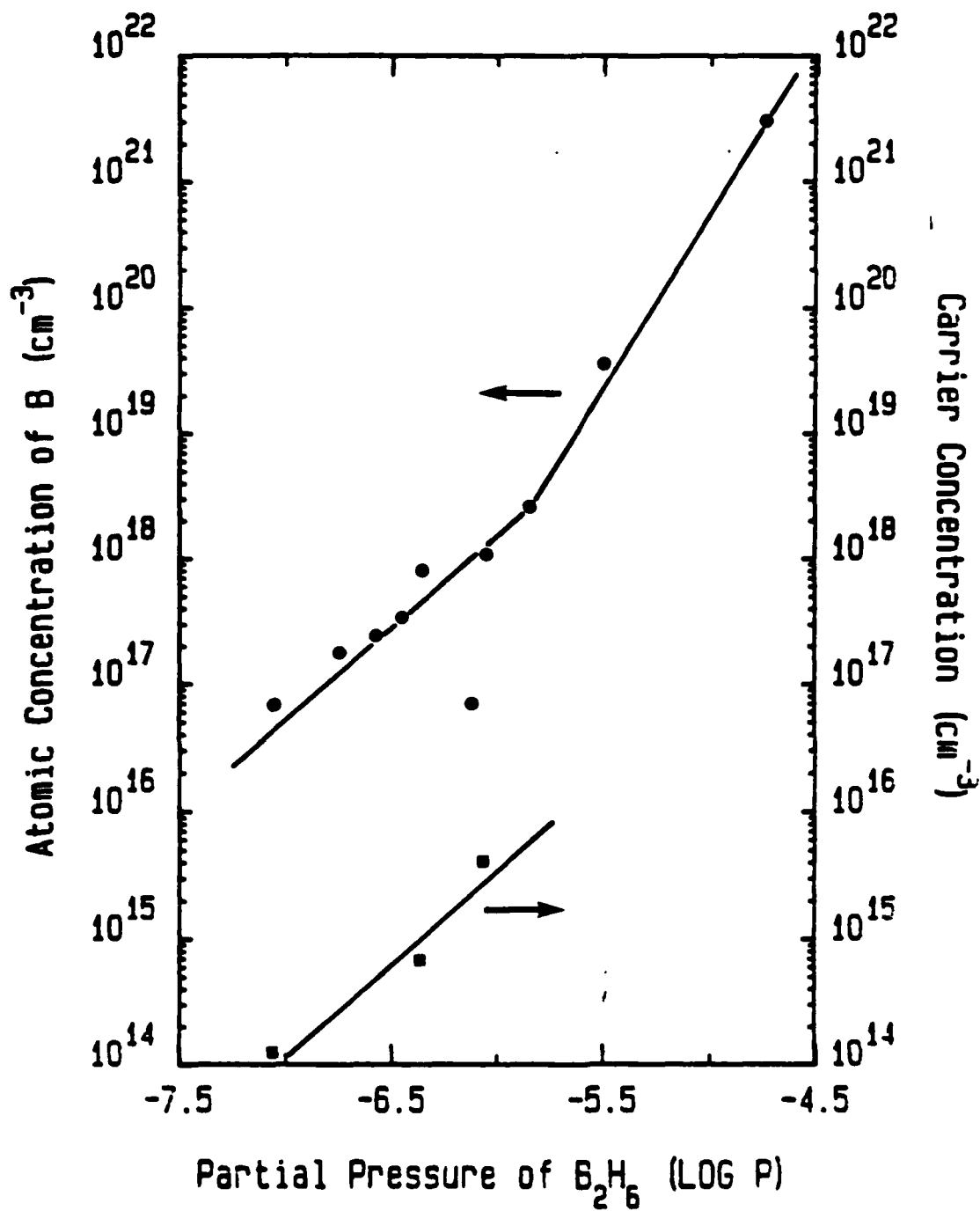


Figure 4.4.9 Atomic concentration of B and p-type carrier concentration of the doped beta-SiC films vs the partial pressure of B_2H_6 in the gas stream. The films were grown under the conditions noted in the caption of Figure 4.4.6.

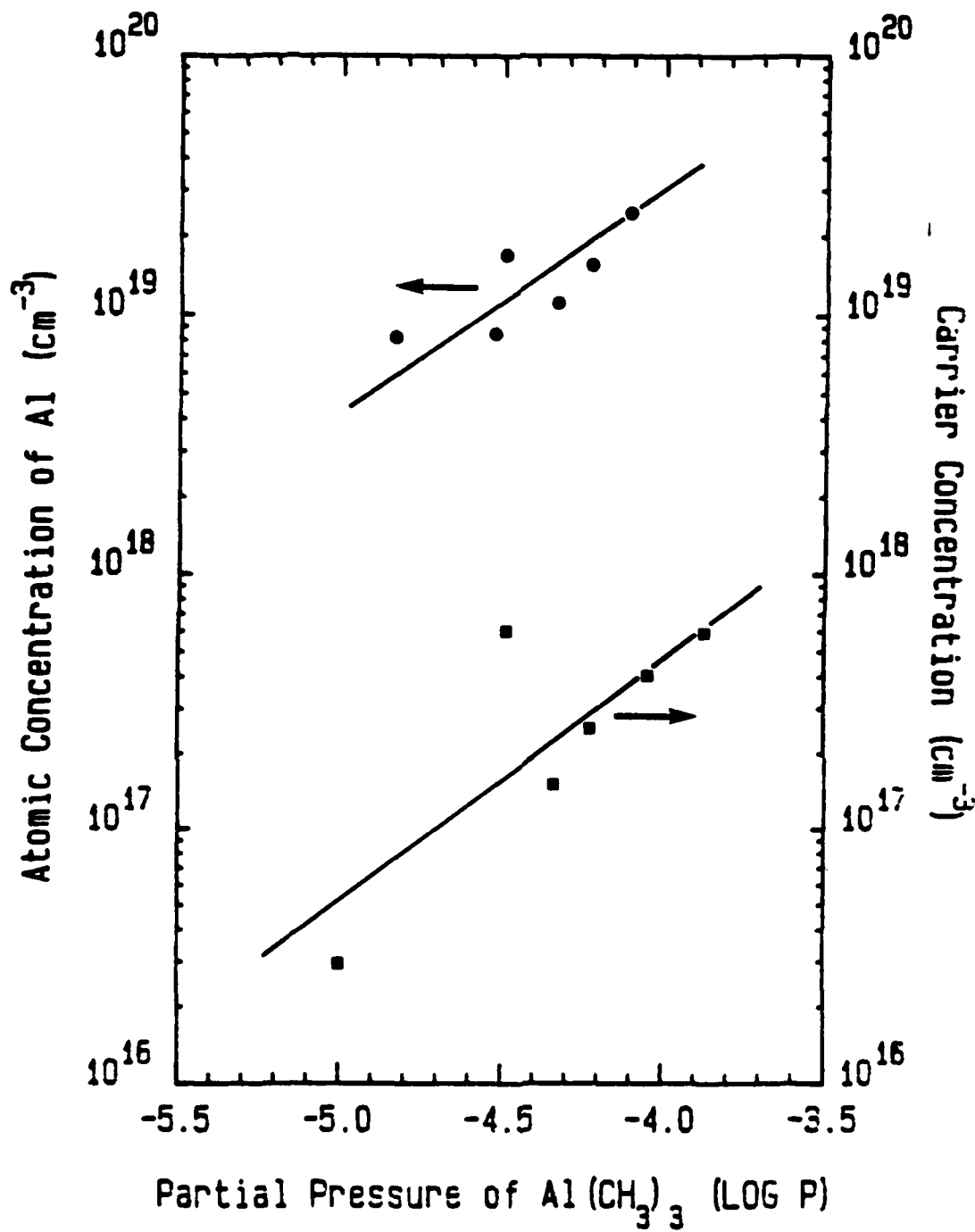


Figure 4.4.10 Atomic concentration of Al and p-type carrier concentration of the doped beta-SiC films vs the partial pressure of $\text{Al}(\text{CH}_3)_3$ in the gas stream. The films were grown under the conditions noted in the caption of Figure 4.4.6.

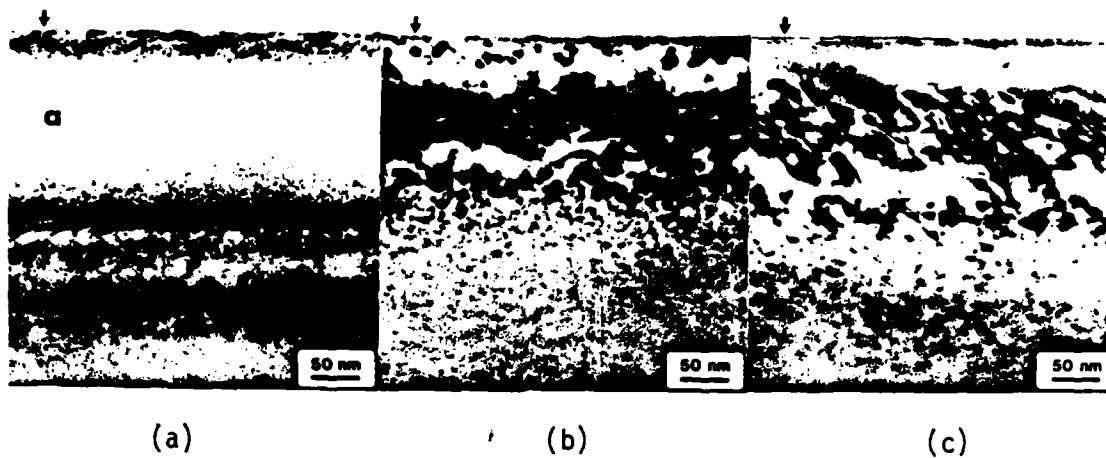


Figure 18. XTEM micrographs showing the surface of a sample which has been double implanted with Al to a peak concentration of 1×10^{20} Al/cm³. (a) As-implanted; (b) annealed at 1873K; (c) annealed at 2073K for 300s.

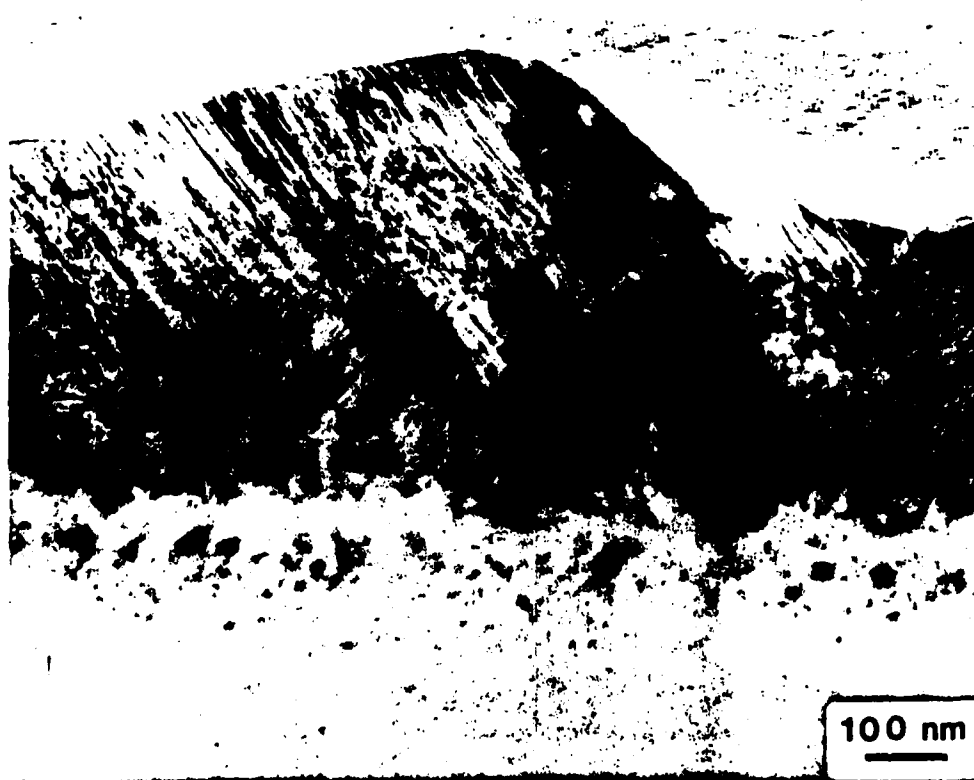


Figure 19. XTEM micrograph of a sample which has been double implanted with P to a peak concentration of 1×10^{20} P/cm³ and subsequently annealed at 1973K for 300s. The surface appears rough as a result of polycrystalline regrowth.

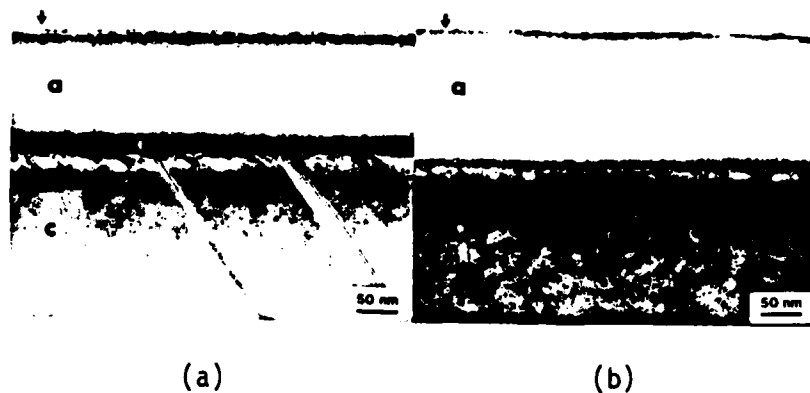


Figure 20. XTEM micrographs comparing the amorphous layers (denoted a) created by ion implantation of P in β -SiC at (a) room temperature and (b) at the temperature of LN_2 into crystalline β -SiC (denoted c).

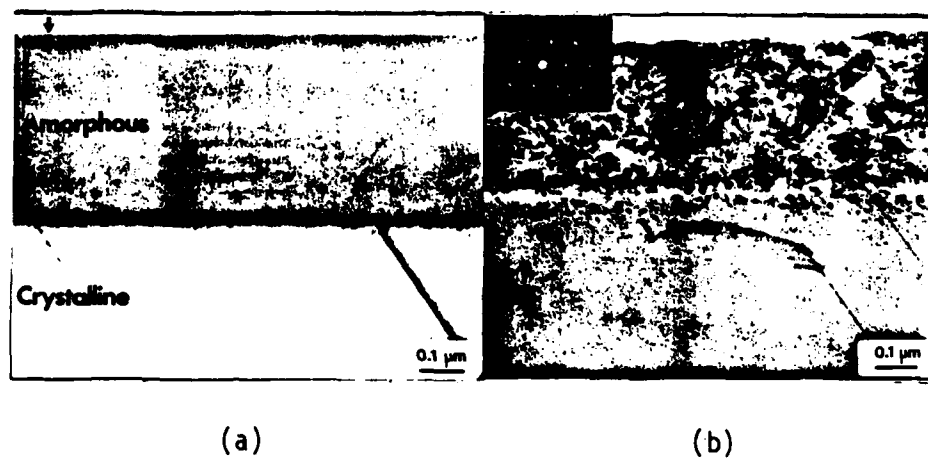


Figure 21. XTEM micrographs and diffraction pattern of (100) β -SiC which has been triple implanted with Si to a peak concentration of $1 \times 10^{20} \text{ Si/cm}^3$. (a) As-implanted; (b) annealed at 1973K for 300s. (The diffraction pattern is near [011] and of the microtwinning and highly faulted layer).

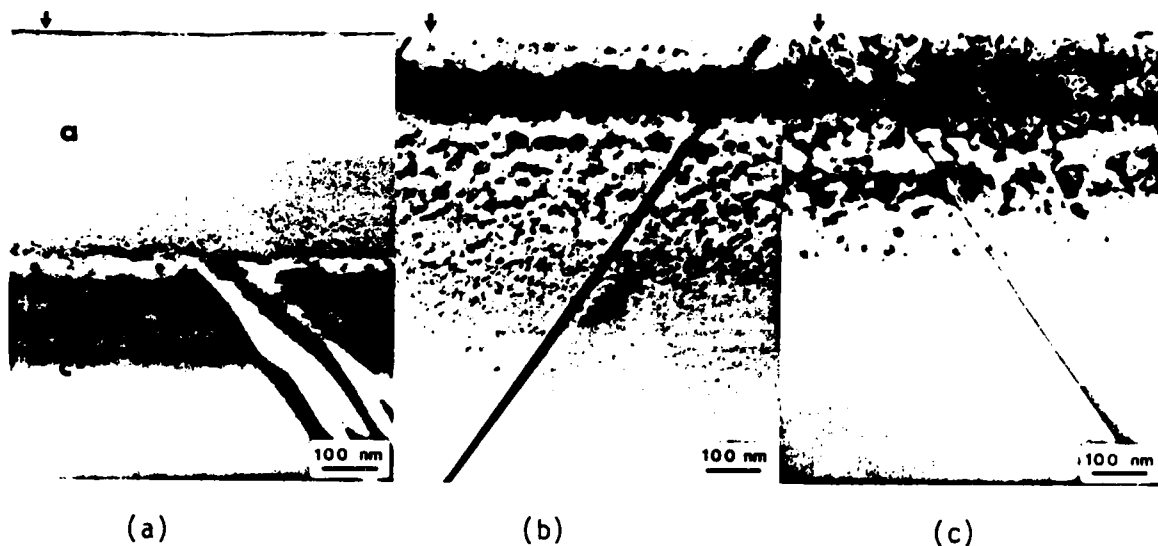


Figure 22. XTEM micrographs comparing the regrowth properties of samples implanted with equal atom concentrations ($1 \times 10^{20}/\text{cm}^3$) of Si (b, center) and Si + C (c, right). The as-implanted amorphous layer is also shown (a).

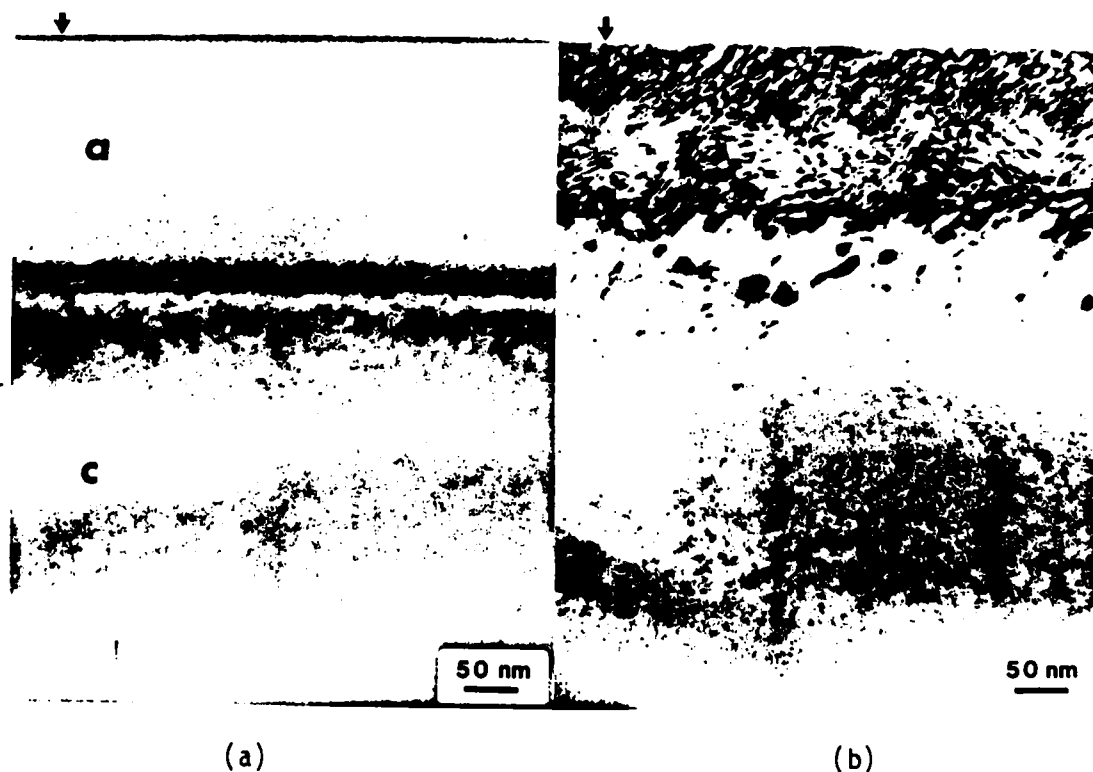


Figure 23. XTEM micrographs showing the surface of a sample which has been single implanted with both Si and C to a peak concentration of 1×10^{20} implanted SiC/ cm^3 . (a) As-implanted; (b) annealed at 1973K for 300s.

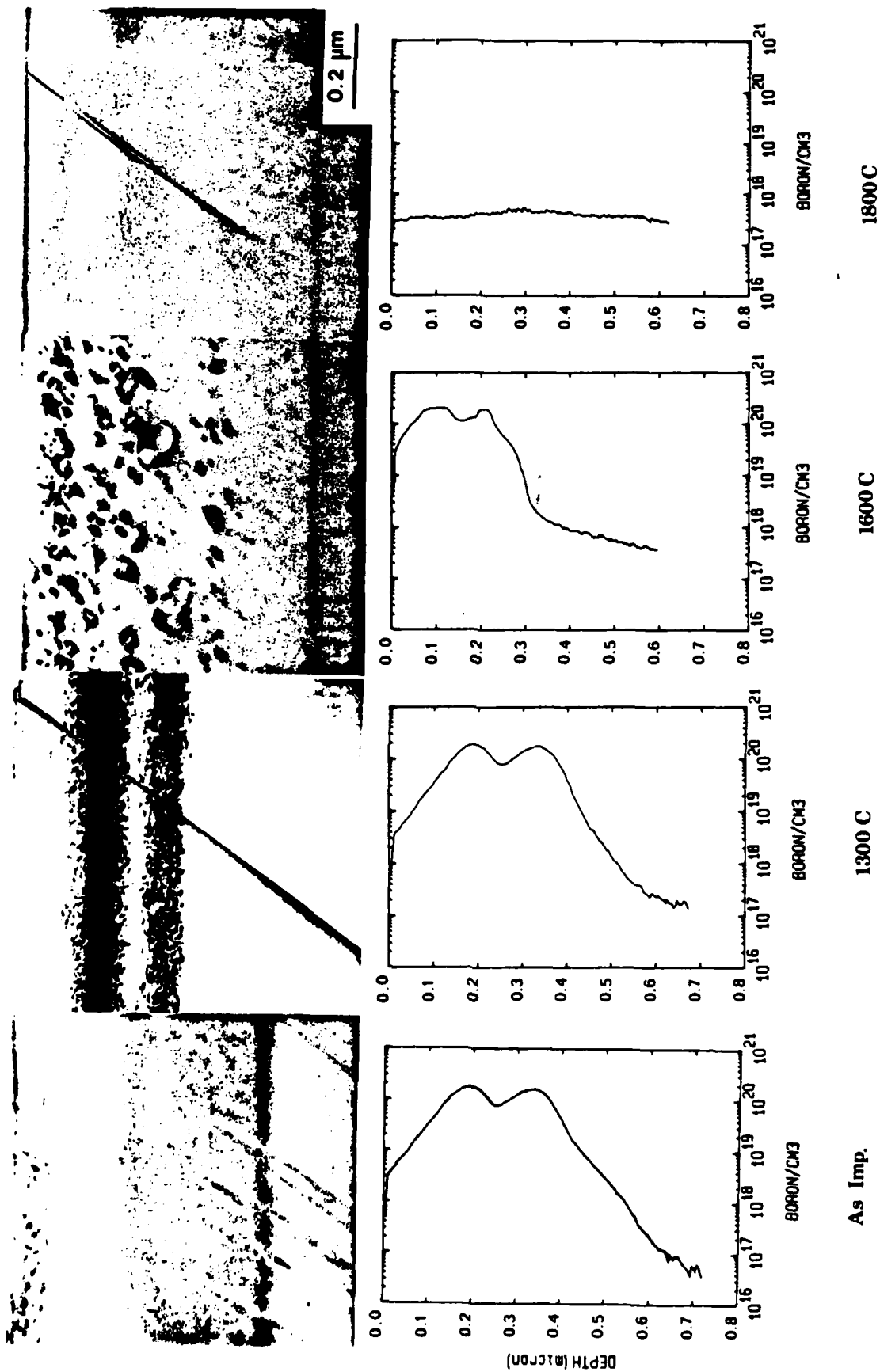


Figure 24. Cross-sectional transmission electron micrographs and complementary SIMS profiles of β -SiC films previously implanted with B at 200 and 120 keV with doses of 2×10^{15} and $1 \times 10^{15} \text{ cm}^{-2}$, respectively and annealed at various temperatures. The annealing time at each temperature was 300s.

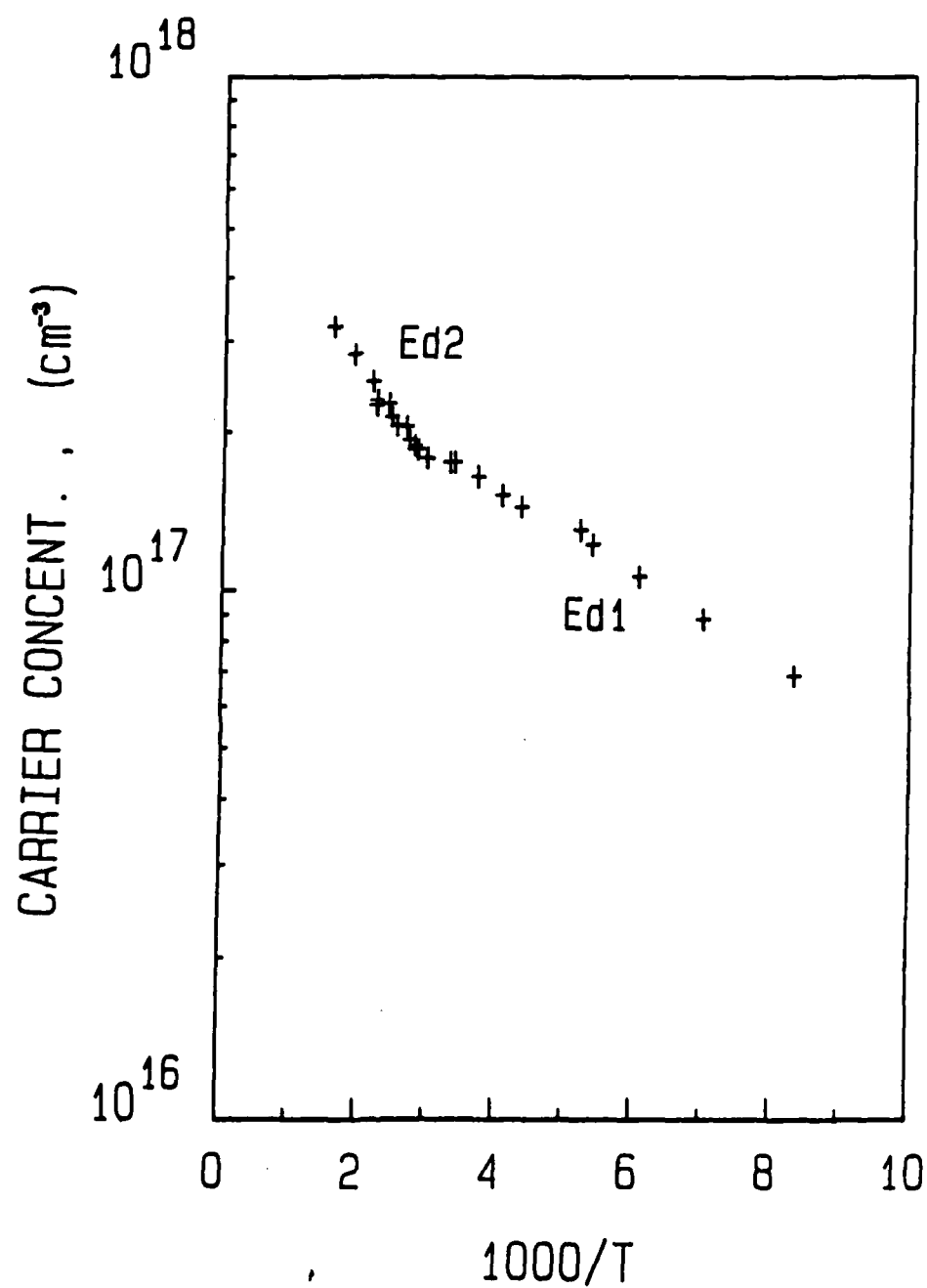


Figure 27. Carrier concentration as a function of reciprocal temperature of an unintentionally doped n-type β -SiC film.

Table IV. Ionization energies in undoped β -SiC having n-type character.

Sample	n_d at 300K	Ed_1	Temp.	Ed_2	Temp.	Remark
	(cm^{-3})	(ev)	(K)	(ev)	(K)	
840705	1.5×10^{18}	21	150-300	52	330-700	Dual
840509	1.75×10^{17}	16	110-290	47	300-700	N^+
840917	1.8×10^{18}	21.4	77-570	-	-	Implant
Rosengreen(1)	2.2×10^{17} (a)	33	100-500	90(b)	500-560	Solution Growth
Aivazova(2)	7×10^{13} (c)	49	100-250	70	250-700	Thermal Decomp.
Yoshida(3)	4×10^{17} (d)	44	100-1000	-		CVD

(a) It is assumed that the SiC is not compensated, since N could not be determined by ESR.

(b) Only a portion of these samples possessed a deeper donor level (Ed_2).

(c) Heavily compensated; N was determined ESR.

(d) In this determination, it was assumed that the material was compensated.

(1) A. Rosengreen, Mat. Res. Bull. 4 (1969) 5355.

(2) L. S. Aivazova, S. N. Gorin, V. G. Sidyakin, and I. M. Shvarts, Sov. Phys. Semicond., 11 (1977) 1069.

(3) S. Yoshida, E. Sakuma, S. Misawa, S. Gonda, Bull. Elect. Research Soc., Japan 21 (1984) 61.

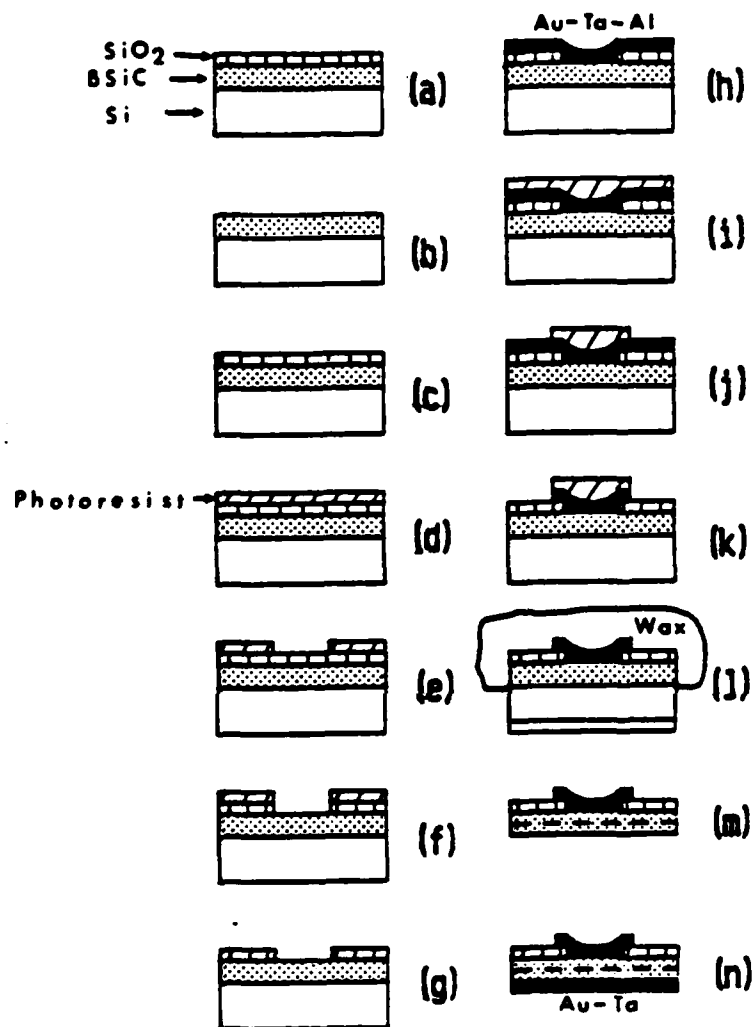


Figure 3.5.2 Step-wise procedure for the fabrication of a p-n junction diode in beta-SiC thin films.

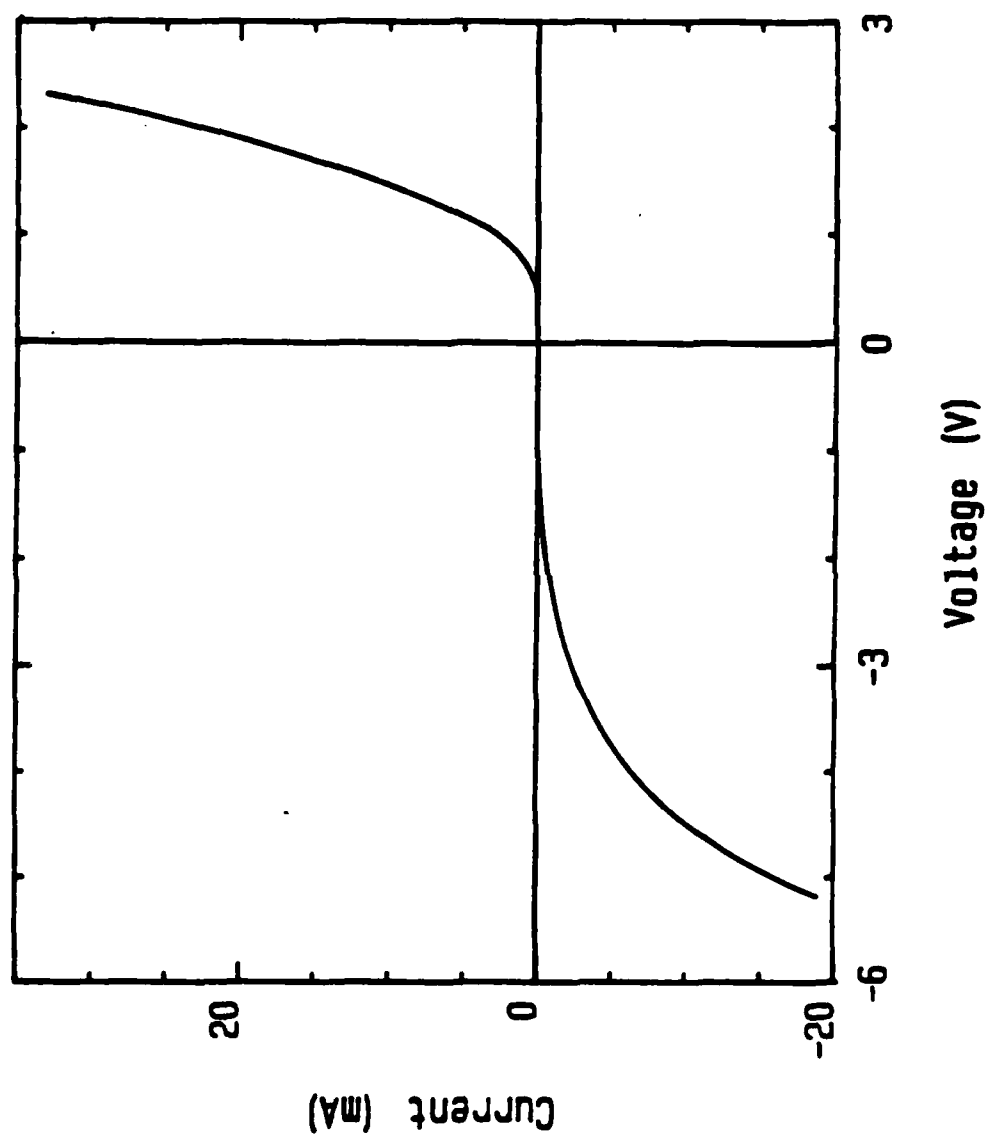


Figure 4.4.27 The I-V characterization of the p-n junction diode which was -
fabricated by in situ doping of sequentially deposited beta-SiC
films with Al and N.

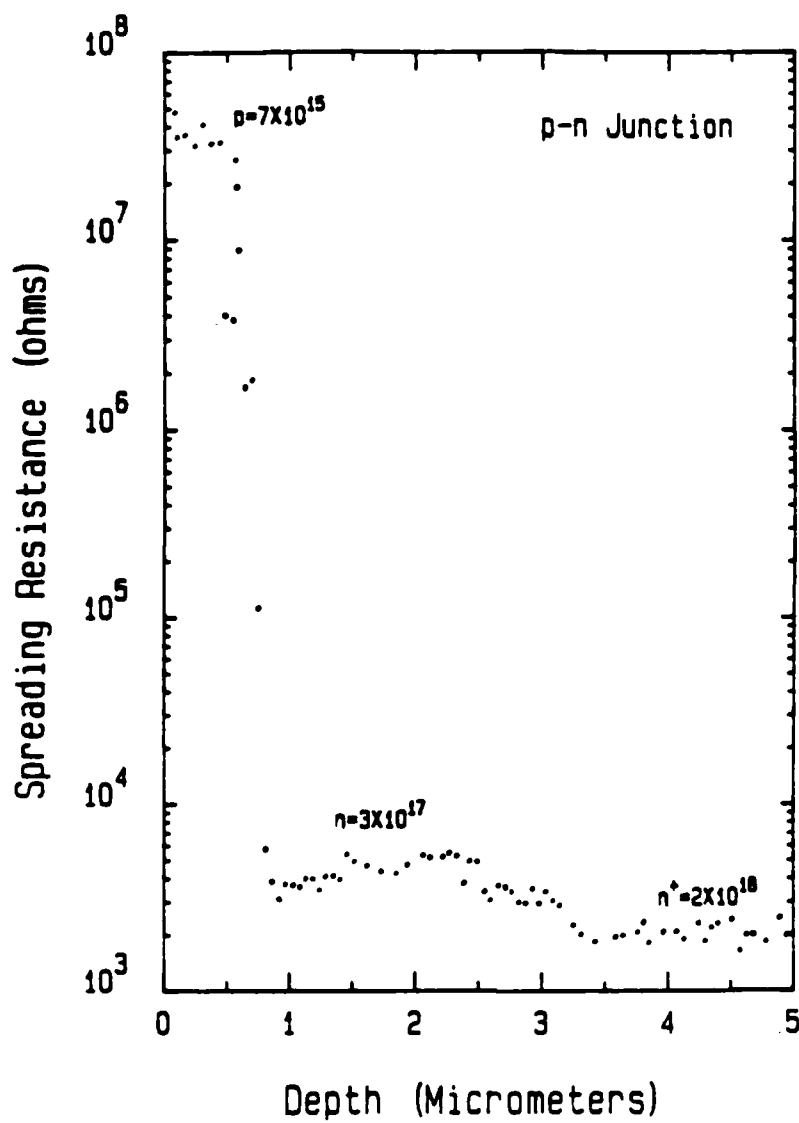
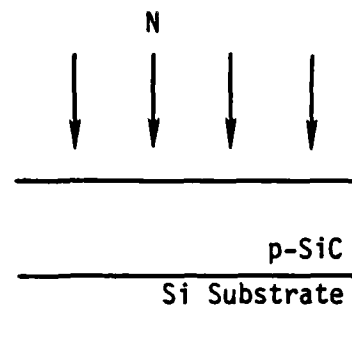
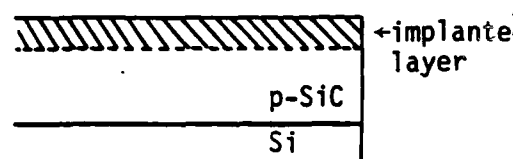


Figure 4.4.29 Spreading resistance profile vs depth of the p-n junction diode which was doped with Al and N during growth.

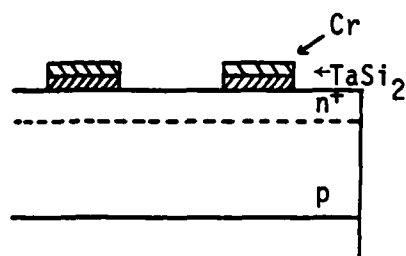
1. Implantation of N into p-type SiC.



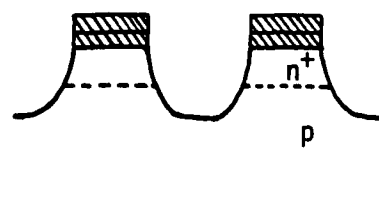
2. Anneal at 1200°C for 300 sec.



3. Deposit TaSi₂ and Cr through mask.



4. RIE etching.



5. Oxidation.

6. Angle lapping and ohmic contact application for p-type layer.

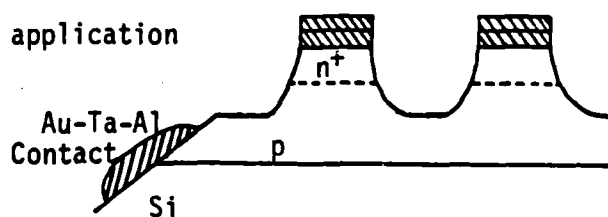
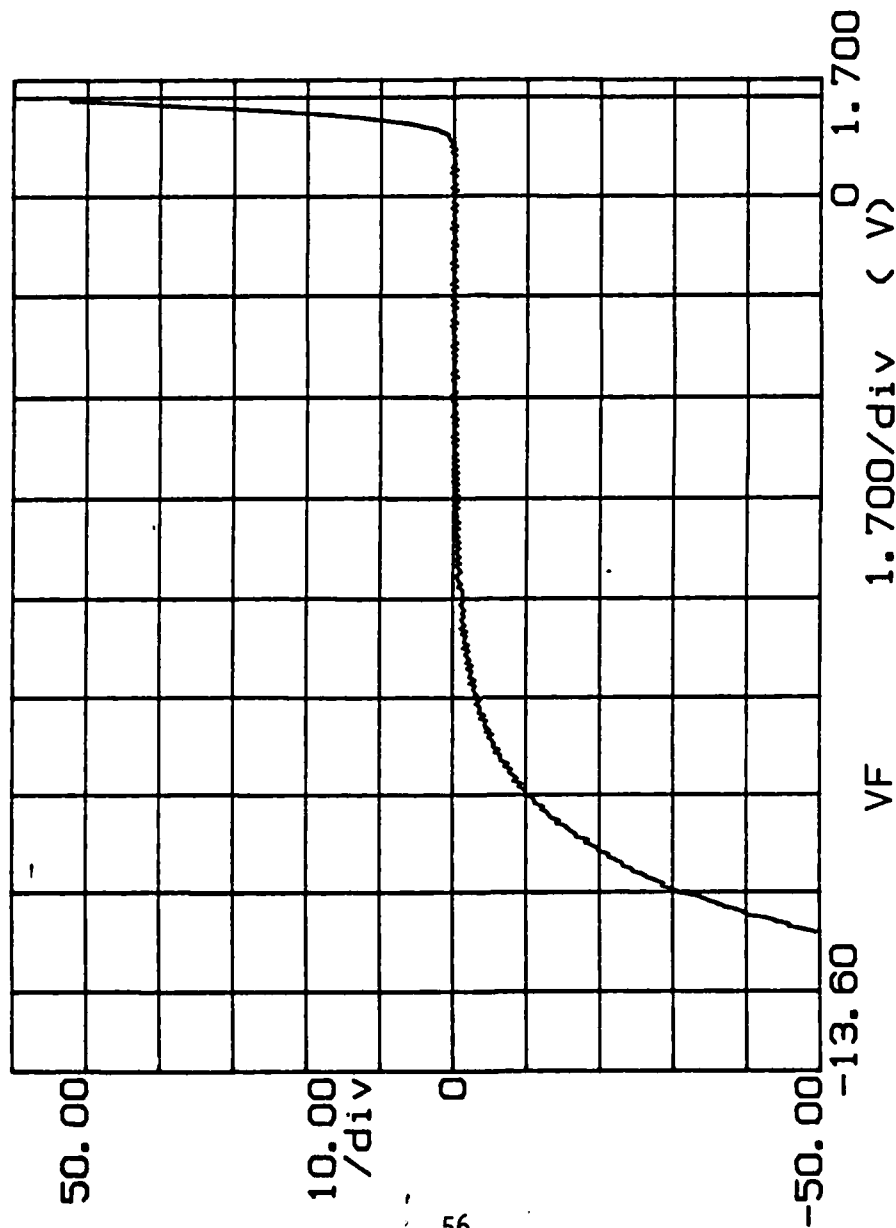


Figure 25. Schematic diagram of the fabrication steps employed to make a n^+p junction in a β -SiC film containing Al (introduced during growth) and N (introduced via dual ion implantation).

***** GRAPHICS PLOT *****
N+P IMP. DIODE

IF (μA)



Variable:
VF -Ch1
Linear sweep
Start -15.000V
Stop 4.0000V
Step .0500V
Constant:
V -Ch3 .0000V

Figure 26. Curve showing the I-V characteristics of the p-n junction produced by the dual N implantation into an Al-containing β -SiC film.

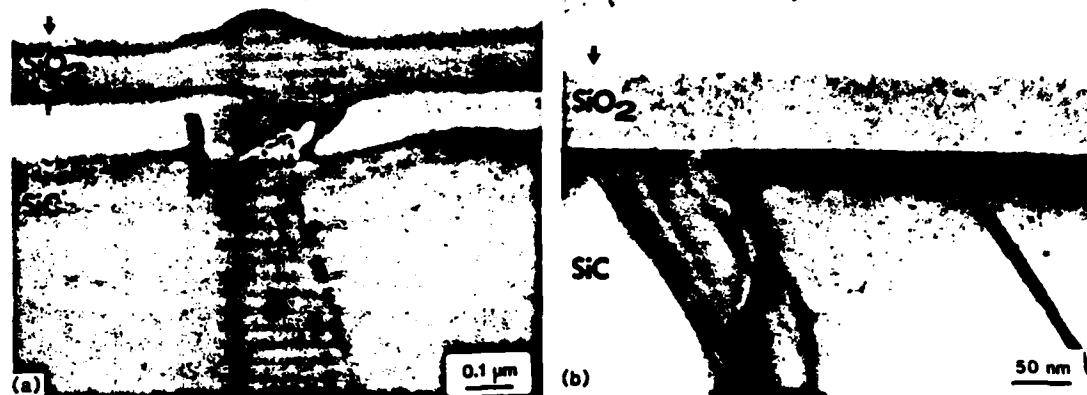


Figure 28. XTEM micrographs of thermally oxidized (100) β -SiC; (a) wet oxide layer, grown at 1273K for 180 ks, showing preferential oxidation at a dislocation band. (The white layer beneath oxide and the dark spots are caused by ion milling effects.), (b) dry oxide layer, grown at 1473K for 3.6 ks, revealing lack of preferential oxidation at a dislocation band.

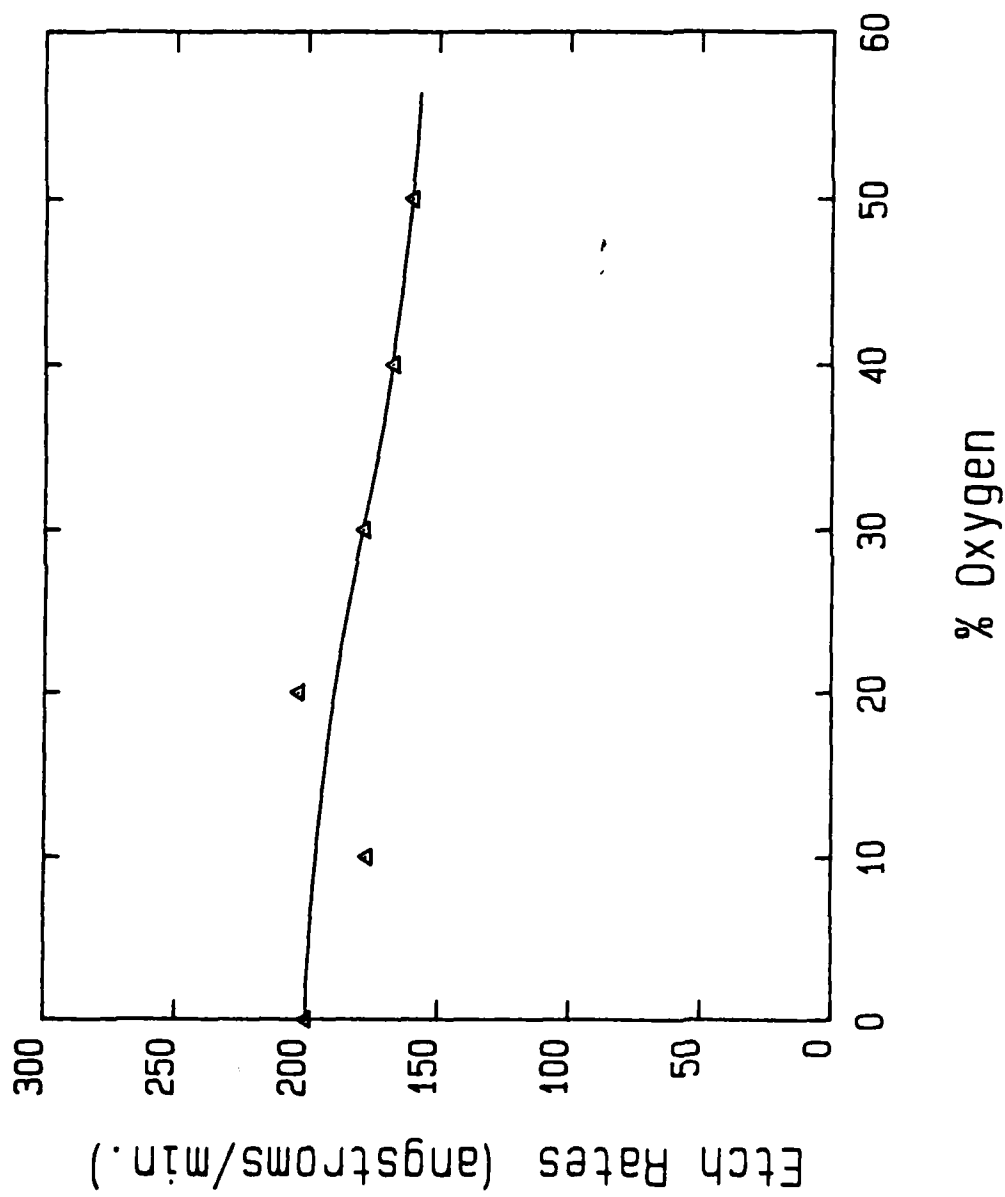


Figure 33. SiC etch rate vs. % oxygen in CF_4 for reactive ion etching at 100 watts and 20 mTorr.

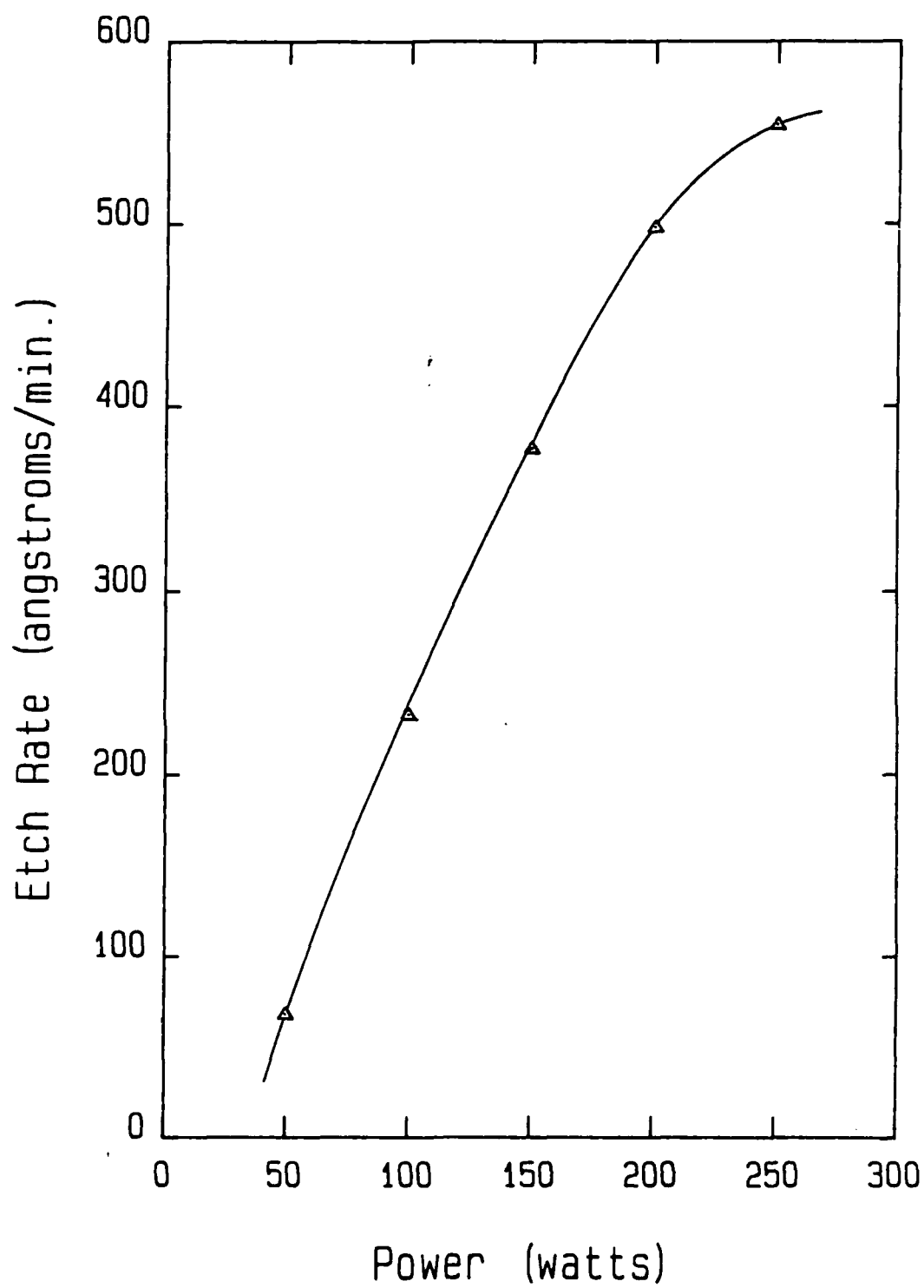


Figure 34. SiC etch rate vs. RF power for reactive ion etching in 40 mTorr pure CF_4 .

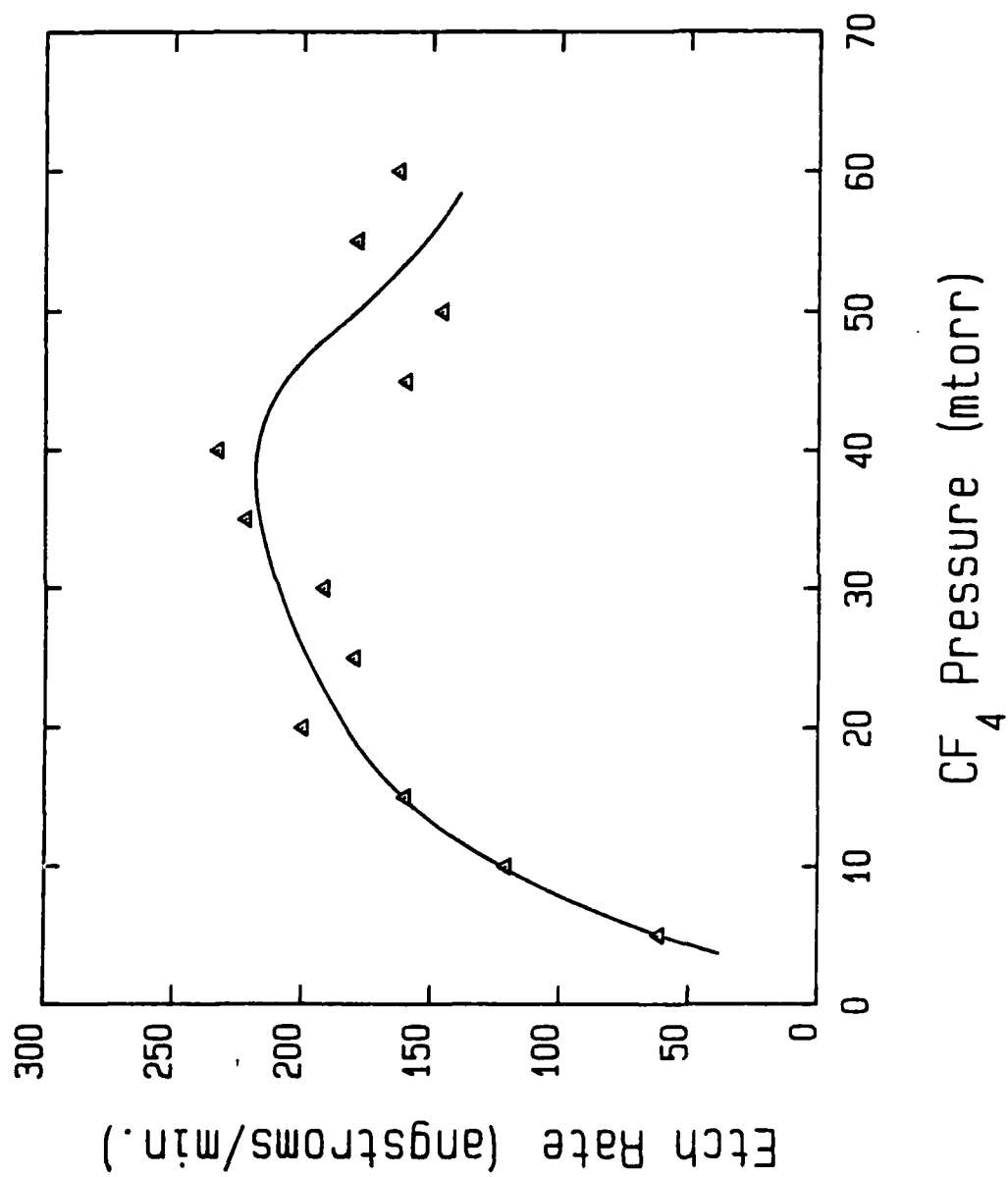


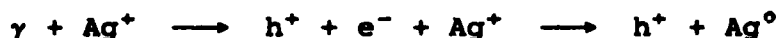
Figure 35. SiC etch rate vs. pressure for reactive ion etching at 100 watts in pure CF_4 .

Superionic Conductor High-Speed Switches

J. F. Scott
 Condensed Matter Laboratory
 Department of Physics
 University of Colorado
 Boulder, Colorado 80309-0390

We have discovered a novel and unexpected optical switching¹ in $\text{Ag}_{13}\text{I}_9\text{W}_2\text{O}_8$: The conductivity decreases by a full order of magnitude when the specimens are illuminated with low intensity ($1\text{W}/\text{cm}^2$) blue or green light. This is to be contrasted with the increase in conductivity under illumination exhibited by most solid state materials.

The mechanism² is hypothesized to be



i.e., a laser photon excites an electron-hole pair; the electron neutralizes a silver ion, removing one carrier from the superionic conductor; the hole that remains has negligible mobility. The process is observed to be approximately independent of temperature from -74°C to $+37^\circ\text{C}$.

This process would be uninteresting, except as a novelty, were it not for two facts: 1) it is reversible; 2) it is very fast.

In order to test its reversibility, we have switched it on and off with a mechanical chopper $\sim 10^6$ times. A very small amount ($\ll 1\%$) of neutral silver plates out on the surface, but no degradation in the size of the (negative) photoconductivity

charge is noted. It would be of interest to perform further studies to see if the silver surface plating is inherently self-limiting or if it poses an intrinsic limitation on the use of this effect as an optical switch.

We have made preliminary measurements of switching speed with an N₂-pumped dye laser. These serve only to set an upper limit of a few ns; the real speed of the process may be very much faster.

In order to make certain that the observed change in apparent conductivity is not instead due to a photovoltaic response, we have reversed the polarity of the d.c. current measured through the illuminated specimen. The same behavior was noted. Since the photovoltaic current develops with a particular sign along a unique crystallographic axis, this shows that the effect is photoconductive and not photovoltaic.

References

1. F. Habbal, J. A. Zvirgzds, and J. F. Scott, *J. Chem. Phys.* 69, 4984 (1978).
2. J. F. Scott, Light Scattering near Phase Transitions, edited by H. Z. Cummins and A. P. Levanyuk (North Holland: Amsterdam, 1983), p. 332.

VIEWGRAPHS

SUPERIONIC CONDUCTOR HIGH-SPEED SWITCHES

J. F. SCOTT

Site type ^a	τ , Å ³
AO	22.3
AO6	22.2
AO6	32.4
AO7	23.1

^a Note: c, b, and / as de

are in these sites at re structure of $\text{Ag}_3\text{I}_{16}\text{W}$ form polyhedra with number, 56, of these f duction passageways. tant to the conducti 1-O polyhedra are al ductivity: 23.1 " or trapped in 12 of then the Ag⁺ ions are in w sites (see Table V). T duction passageways could possibly be c passageways. (It sh are 28 empty 1-O pol are too close to fillo being close, 2.9 to 3.2

The total number c conduction passagew number of mobile A 23.2 or 44.5 " of the The ratio of sites to A passageways is 6.3, a parable with that of total volume of the to that of the unit cel of $\pi\text{-AgI}$, but compar (6, 8). However, if (Fig. 3) of $\text{Ag}_3\text{I}_{16}\text{W}$ than those of both 3 may be attributed to conduction passag and the lower mol polyhedra.

Our conductivity not go to the meth

example of (1) is: Suppose there is an Ag⁺ ion initially in an iodide tetrahedron belonging to a wheel centered at (0, 1, 1). It can move into the neighboring icosahedron in the [110] direction and then into the wheel centered at (1, 1, 1). Because of the pseudosymmetry plane at $y = 0$, the Ag⁺ ion can turn and move in the [110] direction, first entering an icosahedron and then reaching the wheel centered at (0, 1, 1), i.e., one unit cell away from the initial wheel. In this manner, by moving first in the [110] and then in the [110] direction, the Ag⁺ ion has effectively traveled in the [010] direction. An example of (2) is: by utilizing mixed 1-O polyhedra, one direct route is AO9 → AO9* → AO7* → AO8* → A7 → A11* → A10 → A11 → A1* → AO8 → AO7 → AO9 (in the next cell). An alternate route is AO9 → AO9* → AO10 → A5 → A6 → A12* → A11* → A10 → A11 → A12 → A6* → A5* → AO10* → AO9 (in the next cell).

For conduction (effectively) in the [100] direction, an Ag⁺ ion originally in a wheel centered at (0, 1, 1) can first move up the icosahedron in the [110] direction and then into the wheel centered at (1, 1, 1) as described above. The Ag⁺ ion can turn in the [110] instead of the [110] direction, move through another icosahedron and reach the wheel centered at (1, 1, 1), a unit *a* from the initial wheel. In this manner only the iodide polyhedra would be involved. Again a more direct route involving also 1-O polyhedra is AO9 → AO7 → AO6 → A8 → A7 → A12* → A11* → A12* → A7* → A6 → AO4 → AO6* → AO7* → AO9 (in the next cell).

Discussion

In $\text{Ag}_3\text{I}_{16}\text{W}_2\text{O}_{16}$, the tetratingstate ion replaces eight iodide ions. The number of Ag⁺ ions in the formula seems large relative to the number of iodide ions. The 90 iodide polyhedra by themselves cannot accommodate the 52 Ag⁺ ions in the unit cell. In fact, only a small proportion, 23.4 " of the Ag⁺ ions

cannot go through the wall, because to do so, they must go into sites AO15, AO15*, AO16, AO16*, which is apparently forbidden. The Ag⁺ ions could, however, leave the AO2 → AO2* sites on a single side of the wall by entering sites AO5 (AO5*) or AO11 (AO11*), the latter being in a conduction passageway the AO5 (AO5*) may be called by-pass sites (see below).

Thus far we have discussed 36 1-O polyhedra which are all in the wall region. Of the remaining 84 sites, namely AO3-AO13 and AO4*-AO13* (see Tables I and III), 12, AO3, AO13, and AO13*, are vacant because they are close, 2.92, 3.01, and 3.14 Å, respectively, to the W1 atom. Nevertheless, then the remote possibility that Ag⁺ ions do through these. (In $\text{Ag}_3\text{W}_2\text{O}_{16}$ (13) the nearest Ag⁺ W distance is 3.40 Å.) Of the 72 remaining sites, 16, AO5, AO5*, AO12, and AO12*, may be called by-pass sites, like AO2 and AO2*, because they are not directly in conduction passageways. The remaining 56 sites, AO4, AO4*, AO6-AO11, AO6*-AO11*, are clearly in conduction passageways. This is actually consistent with their relatively low fraction occupancies, i.e., $f = 0.5$; the occupancies of the by-pass sites are $0.5 < f < 1.0$.

The tilting of the $(\text{W}_2\text{O}_{16})^{4-}$ anions from the (100) plane (Fig. 4) causes the terminal oxygen atoms O5 to be at a distance of 3.78 Å from O5* of the neighboring $(\text{W}_2\text{O}_{16})^{4-}$ ions (Fig. 5). Together with 16, 17, 18, the O5 and O5* atoms form four tetrahedra, sites AO9, AO9*, AO9*, AO9*. Sites AO10, AO10*, AO10, AO10* share faces with these four connecting them with iodide tetrahedra. These 16 1-O sites are important, but they are not *g*lucely required for conduction in the *a*-an directions; that is, these sites permit more direct routes than just the pure iodide polyhedra alone.

Conduction Pathways

In the [001] direction, conduction is through the wheel-iodide octahedron-wheel-... (Fig. 9)

Fig. 8. The arrangement of iodide ions in a "wheel." Each such wheel contains 30 iodide tetrahedra.

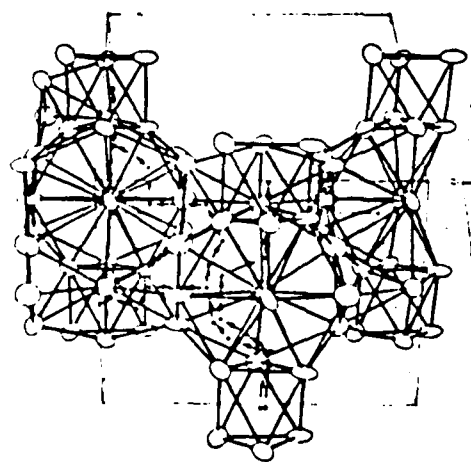


Fig. 9. Iodide arrangement looking down the wheel axis. One complete wheel is shown at the top. To show clearly a particular route in the [001] direction, only two spokes of the wheel at $\pm \frac{1}{2}$ are included.

hedron. All but 12 of the 88 tetrahedra involve an I9 and/or an I10.

Surrounding each $(\text{W}_2\text{O}_{16})^{4-}$ ion, there are 60 polyhedra which are formed from both I⁺ ions and O atoms. Of the 120 1-O polyhedra in the unit cell, 8 are the filled octahedra which occur only in the wall region. The remaining 112 1-O polyhedra are either tetrahedra or five-cornered polyhedra. Of these, 28 are also

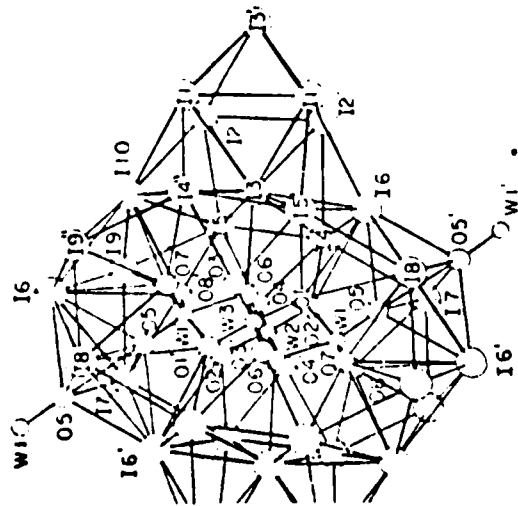


Fig. 4. A stereoscopic view of the complete iodide arrangement is shown in Fig. 7; atoms O7 and O8 (from the tetrahedron or two state ions) are included because they are at two corners of an icosahedron, of which there are four per unit cell; atom O5 is included because it is part of the mixed 1-O tetrahedra that are in conduction passageways. The icosahedra involve all the independent iodide ions except 12. There are thus 10 iodide tetrahedra per icosahedron; the sites are designated 44, 48 and 44', 48'. The 10 mixed 1-O tetrahedral sites are designated 404, 408, 404', 408' (see Tables I and II).

In the [010] direction, the icosahedra are linked by the mixed 1-O tetrahedra formed from 16, 110, O7, and O8 (site 403 in Table II). In the [100] direction, the icosahedra share corners 17 and 18; the width of the icosahedron is the 19, 19' distance, approximately $a/2$. The icosahedra are not directly linked to each other by a single operation of a prime. There tetrahedron (or two state ions) are included because they are at two corners of an icosahedron, of which there are four per unit cell; atom O5 is included because it is part of the mixed 1-O tetrahedra that are in conduction passageways. The icosahedra involve all the independent iodide ions except 12. There are thus 10 iodide tetrahedra per icosahedron; the sites are designated 44, 48 and 44', 48'. The 10 mixed 1-O tetrahedral sites are designated 404, 408, 404', 408' (see Tables I and II).

at $-0.2 < z < 0.2$ called the "wall" in the text. O3, O3', O4, O4' are involved in the formation of mixed 1-O octahedra; O6 and O6' are included to help show the orientation of the $(W_2O_{10})^{8-}$ ion. The other 10 oxygen atoms per $(W_2O_{10})^{8-}$ ion are not shown. For O-I connections or those involved in the formation of the mixed 1-O octahedra, see Fig. 5. The pure iodide octahedra are shaded.

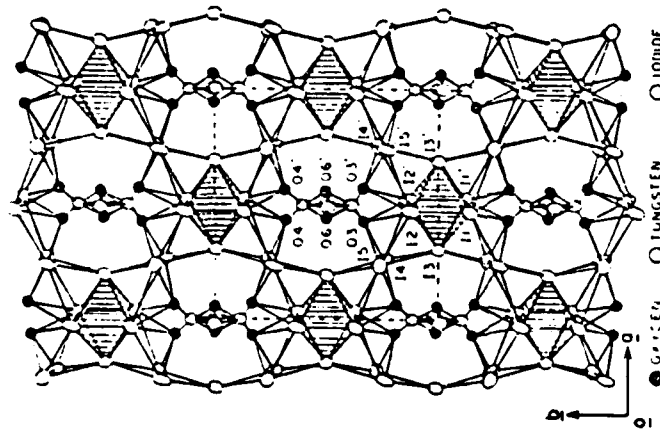
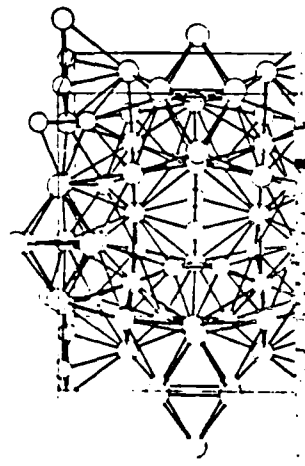
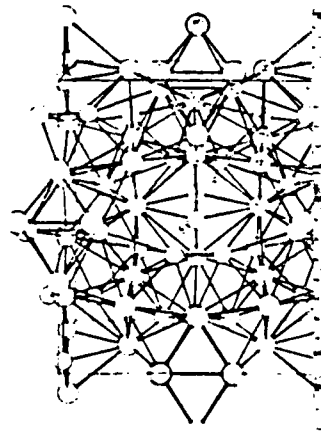


Fig. 6. The structure in the region $-0.2 < z < 0.2$ called the "wall" in the text. O3, O3', O4, O4' are involved in the formation of mixed 1-O octahedra; O6 and O6' are included to help show the orientation of the $(W_2O_{10})^{8-}$ ion. The other 10 oxygen atoms per $(W_2O_{10})^{8-}$ ion are not shown. For O-I connections or those involved in the formation of the mixed 1-O octahedra, see Fig. 5. The pure iodide octahedra are shaded.



not themselves in the icosahedra. One of these faces of the octahedron is 11, 12, 13, connecting it to one icosahedron via $A2 \rightarrow A3 \rightarrow A4$ and to another icosahedron via $A2 \rightarrow A3' \rightarrow A4'$. The symmetry equivalent octahedral face 11', 12', 13' similarly connects the octahedron to two icosahedra on the other side of the wall. The remaining two equivalent faces 11', 12, 13' and 11', 12', 13, open to iodide tetrahedra which are part of an array of iodide ions that form a "wheel" composed of face-sharing iodide tetrahedra (Fig. 8).

The wheel has three hexagonal rims as shown in Figs. 8 and 9 and consists of 20 I^- ions forming 30 tetrahedra each. There are two such wheels per unit cell. All the crystallographically nonequivalent I^- ions are involved in each wheel. As indicated above, wheels in neighboring cells, in the [001] direction, are linked by the iodide octahedra (Fig. 9). Each wheel shares 19 corners with four other wheels. The 19 corners are the centers of the icosahedra. Twelve of the 30 tetrahedra in each wheel belong to two neighboring icosahedra (6 in each). An I^- tetrahedron that involves any 19 belongs to the icosahedron; if an I^- tetrahedron involves any 110, it belongs to the wheel; if it involves both an 19 and an 110, it is in both the wheel and the icosahedron. If the I^- tetrahedron involves neither an 19 nor an 110, it is a connecting tetrahedron between the icosahedron and the iodide octa-

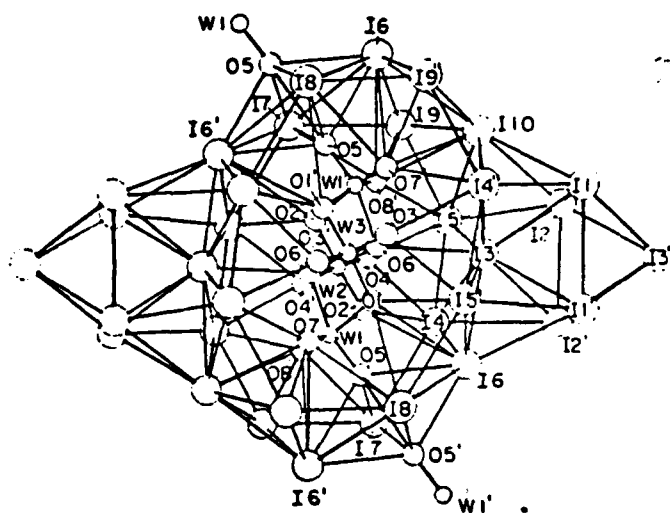


FIG. 5. The surroundings of the $(W_4O_{16})^{8-}$ ion looking down the b -axis (which passes through W2 and W3). The iodide octahedra above and below the $(W_4O_{16})^{8-}$ ion are omitted. Parts of neighboring $(W_4O_{16})^{8-}$ ions are included.

the operation of a twofold axis by a single prime and one obtained by the operation of a twofold screw axis by a double prime. There is one independent iodide octahedron (or two equivalent iodide octahedra) in the unit cell, formed by 11, 12, 13, and 11', 12', 13'. The centers of the octahedra are at $0, \frac{1}{2}, 0$ and $\frac{1}{2}, 0, 0$. Four faces of a single octahedron share faces with mixed I-O octahedra (Fig. 6). The mixed I-O octahedra share only edges or corners with other mixed octahedra. Thus each block of five octahedra separates two pairs of $(W_4O_{16})^{8-}$ ions in the a - and b -directions (Fig. 6). The $(W_4O_{16})^{8-}$ ions, the blocks of octahedra, and the I-O polyhedra between the two, form a wall about (001) planes at $-0.2 < z < 0.2$ (Fig. 6). The mixed I-O octahedra, AO14 and AO14*, are fully occupied by Ag^+ ions, in contrast with the low fractional occupancy, 0.14, of the iodide octahedra (AI in Table I). The I-O polyhedra AO1, AO2, AO2*, AO1', AO2', AO2* also have high occupancy (see Tables I and III); therefore conduction through the wall is most likely to occur via the AI (octahedral) sites.

The network formed from the 88 iodide tetrahedra (22 independent tetrahedral sites, Table I) lies between the walls, i.e., in the region

$0.2 < z < 0.8$ (see Fig. 4). A stereoscopic view of the complete iodide arrangement is shown in Fig. 7; atoms O7 and O8 (from the tetrating-state ions) are included because they are at two corners of an icosahedron, of which there are four per unit cell; atom O5 is included because it is part of the mixed I-O tetrahedra that are in conduction passageways. The icosahedra involve all the independent iodide ions except 12. There are thus 10 iodide tetrahedra per icosahedron; the sites are designated A4-A8 and A4*-A8*. The 10 mixed I-O tetrahedral sites are designated AO4-AO8, AO4*-AO8* (see Tables I and III).

In the [010] direction, the icosahedra are linked by the mixed I-O tetrahedra formed from I6, I10, O7, and O8 (site AO3 in Table II). In the [100] direction, the icosahedra share corners 17 and 18; the width of the icosahedron is the 19-19' distance, approximately $a/2$. The icosahedra are not directly linked to each other in the [001] direction; however, they are linked to iodide octahedra in the wall (see above) through iodide tetrahedra. The four faces of an iodide octahedron not shared with mixed I-O octahedra are shared with connecting iodide tetrahedra, two on each side of the wall. These connecting tetrahedra are

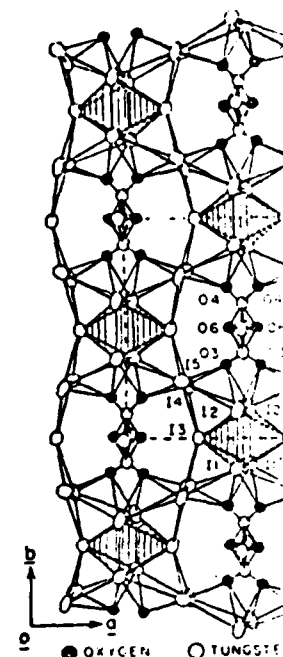


FIG. 6. The structure in the "wall" in the text. O5 and O6* are included to help show $(W_4O_{16})^{8-}$ ion. The other 10 $(W_4O_{16})^{8-}$ ions are not shown, other than those involved in the I-O octahedra, see Fig. 5. The octahedra are shaded.

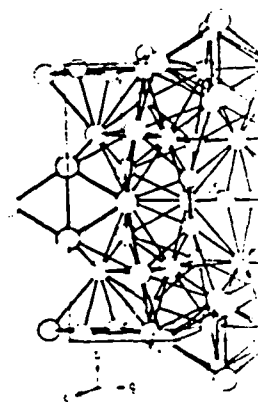


FIG. 7. Stereoscopic view of the complete iodide arrangement. The iodide octahedra and the four mixed I-O octahedra have labels outside the octahedra and the four mixed I-O octahedra have labels outside the octahedra.

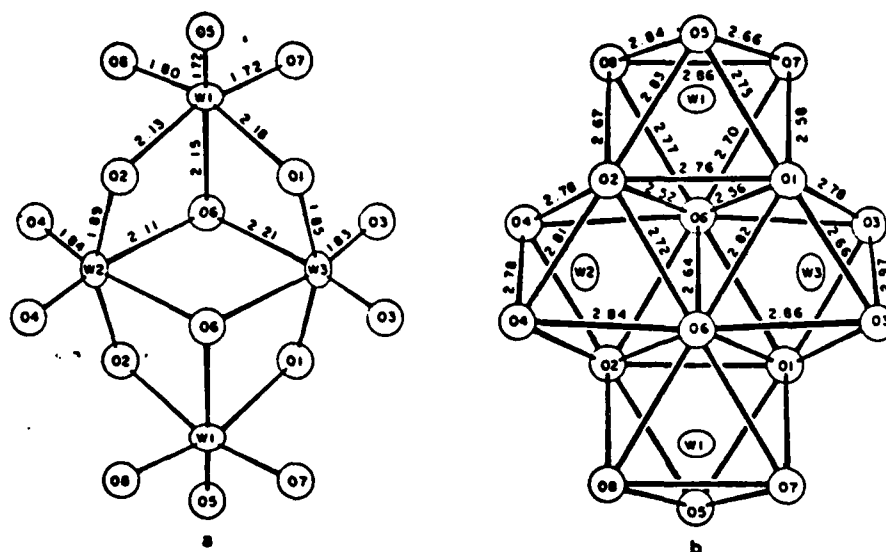


FIG. 1. The $(W_4O_{16})^{8-}$ ion in $Ag_{26}I_{18}W_4O_{16}$: (a) W-O distances, (b) O-O distances. Note that the $(W_4O_{16})^{8-}$ ion in $Ag_{26}I_{18}W_4O_{16}$ is enantiomorphous to that in $Ag_8W_4O_{16}$ (see Ref. (13)).

most relevant to this paper is the appearance of a new $(W_4O_{16})^{8-}$ complex as shown in Fig. 1. This complex has point symmetry 2 (or C_2) and is the tungstate entity that occurs in the solid electrolyte.

Conductivity

Experimental

The $Ag_8W_4O_{16}$ used in the preparation of the solid electrolyte was produced by adding a concentrated solution of sodium tungstate to one of silver nitrate in essentially stoichiometric proportions. The precipitate, which is highly insoluble in water, was washed with H_2O (by decantation) approximately 30 times, then filtered through a Büchner funnel and dried in an oven at $110^\circ C$.

The pure solid electrolyte $Ag_{26}I_{18}W_4O_{16}$ cannot be prepared by melting inasmuch as it melts incongruently. Some of the compound is obtained by melting, but in this case AgI and the compound with nominal chemical formula $Ag_3I(WO_4)_2$ are always present. (If this compound contains $(W_4O_{16})^{8-}$ entities, which is likely, then its formula should be written $Ag_{10}I_2W_4O_{16}$.) The chemical equation

for the decomposition is



Thus even a slight decomposition causes a large amount of AgI to be present. This gives a sensitive probe for purity of the solid electrolyte with respect to unreacted AgI. The latter can be seen in the powder X-ray diffraction photograph, although there are subtleties because of overlap of AgI lines with those of the solid electrolyte (see Appendix). The conductivity measurements are extremely sensitive to the presence of AgI, probably to a small fraction of a percent.

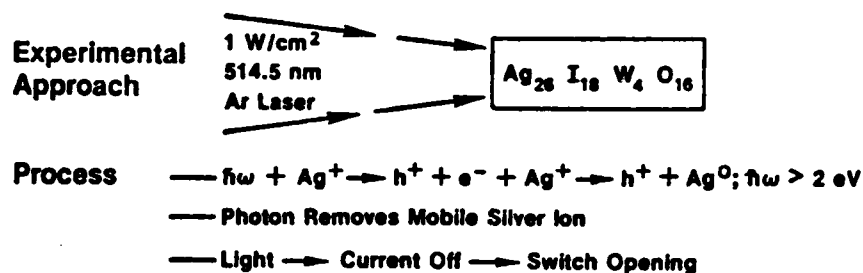
Rapid melting of the thoroughly mixed ingredients in the ratio $4AgI:Ag_2WO_4$ and quenching gives $Ag_{26}I_{18}W_4O_{16}$ plus $Ag_{10}I_2W_4O_{16}$ but no AgI, of course. In this case, the $Ag_{10}I_2W_4O_{16}$ can be detected by powder X-ray diffractometry (see Appendix).

A polycrystalline specimen of the solid electrolyte cannot be prepared by solid state reaction in a reducing atmosphere! In fact, the preparation requires a substantial overpressure of oxygen because at the reaction temperature of $280^\circ C$ the solid electrolyte appears to have a relatively high oxygen vapor

pressure. It has been found that $Ag_8W_4O_{16}$ itself decomposes to temperatures exceeding $280^\circ C$ in the solid electrolyte. The solid electrolyte must be substantially less oxygen than $Ag_8W_4O_{16}$ if we are primarily interested in the stoichiometric specimen. The effort in determining the thermodynamics of the system opposing reaction of oxygen pressure with AgI and $Ag_8W_4O_{16}$ is the solid electrolyte and the decomposition with respect to oxygen is never observed, so the reaction is not involved in the main reaction involving the tetra-tungstate changing its valence. For example, suppose to $(W_4O_{16})^{8-}$. The reduction of 2 in the atoms; this of course having two W^{6+} and one W^{4+} . This also implies the existence of a reduced cerium that melt $Ag_8W_4O_{16}$ in Takahashi *et al.* (14) extended time period (but not free iodine) case of silver tungstate is conceivable that this some tetra-tungstate ions. Then, some themselves to the ion. This is only plain the observation. The discussion of considerable work on polycrystalline n gave us assurance the electrolyte was to make the average conductivity shock this conclusion, the work

DISCOVERY OF INVERSE PHOTOELECTRIC EFFECT IN SUPERIONIC CONDUCTORS

New Opening Switch



Normal Photoelectric Effect

Light \rightarrow Current On \rightarrow Switch Closing

Applications Switch Opening
 Solid State Batteries

Figure 6: Schematic diagram for the photoexcitation process hypothesized in silver iodide tungstate.

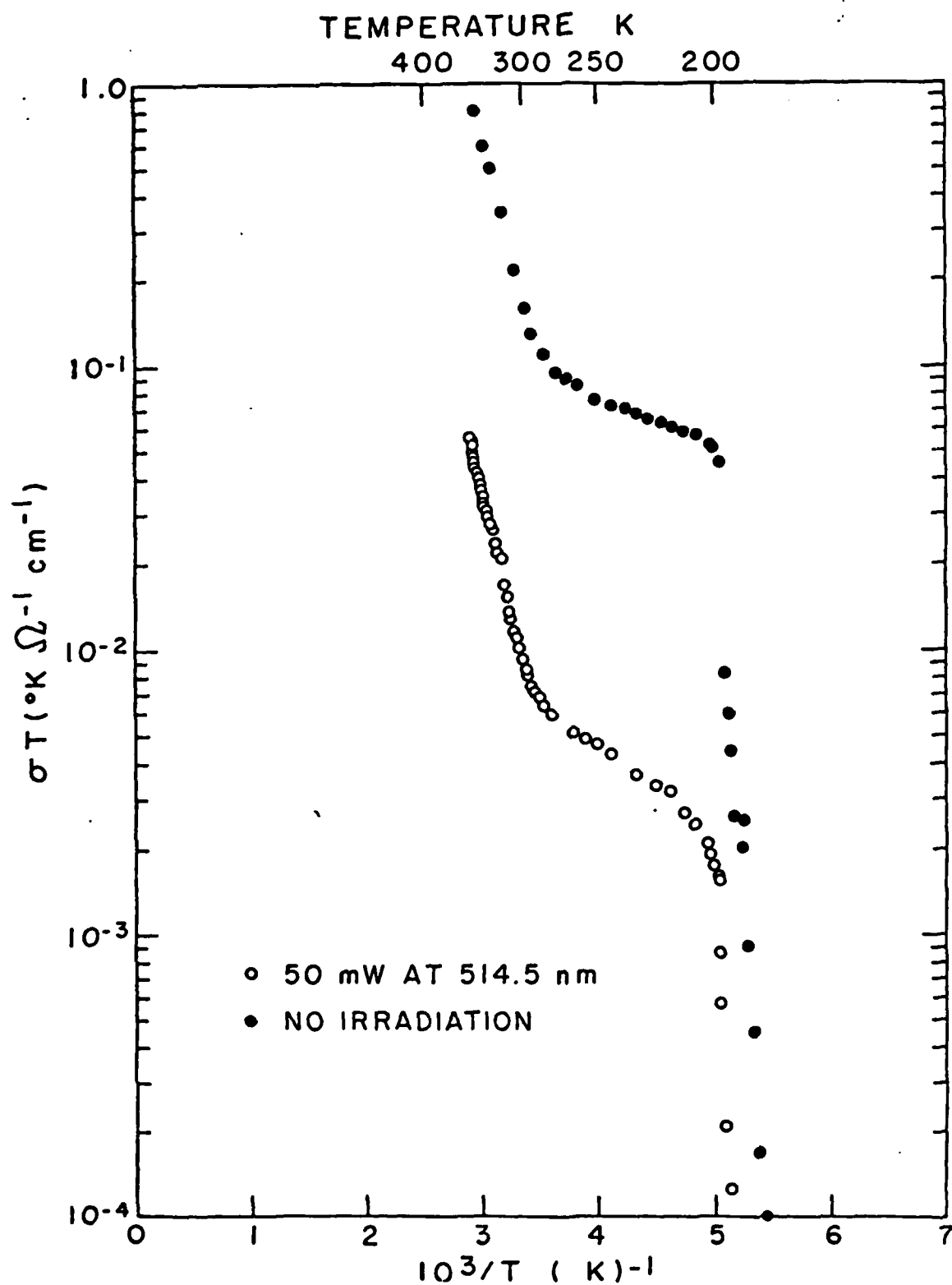
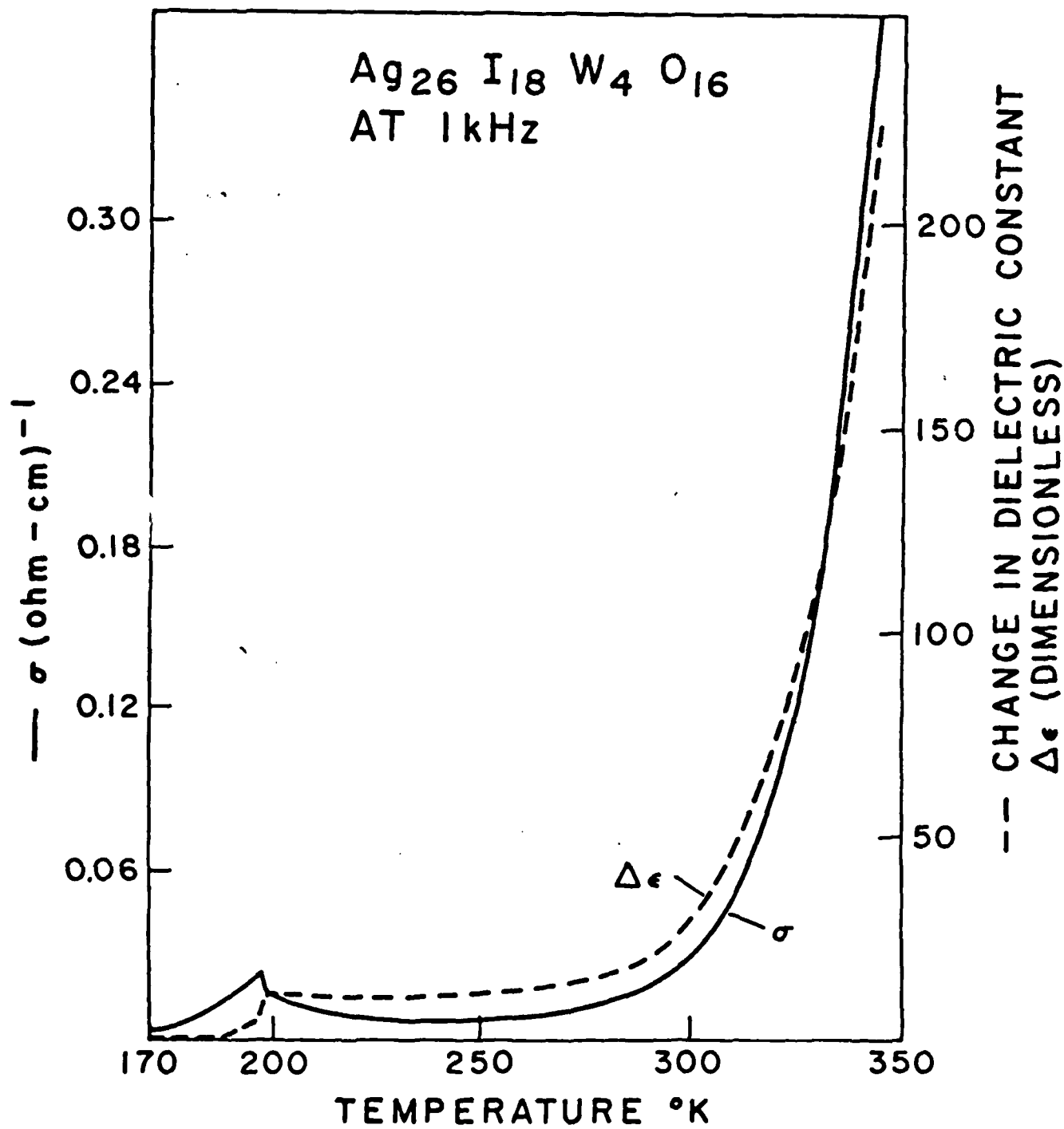


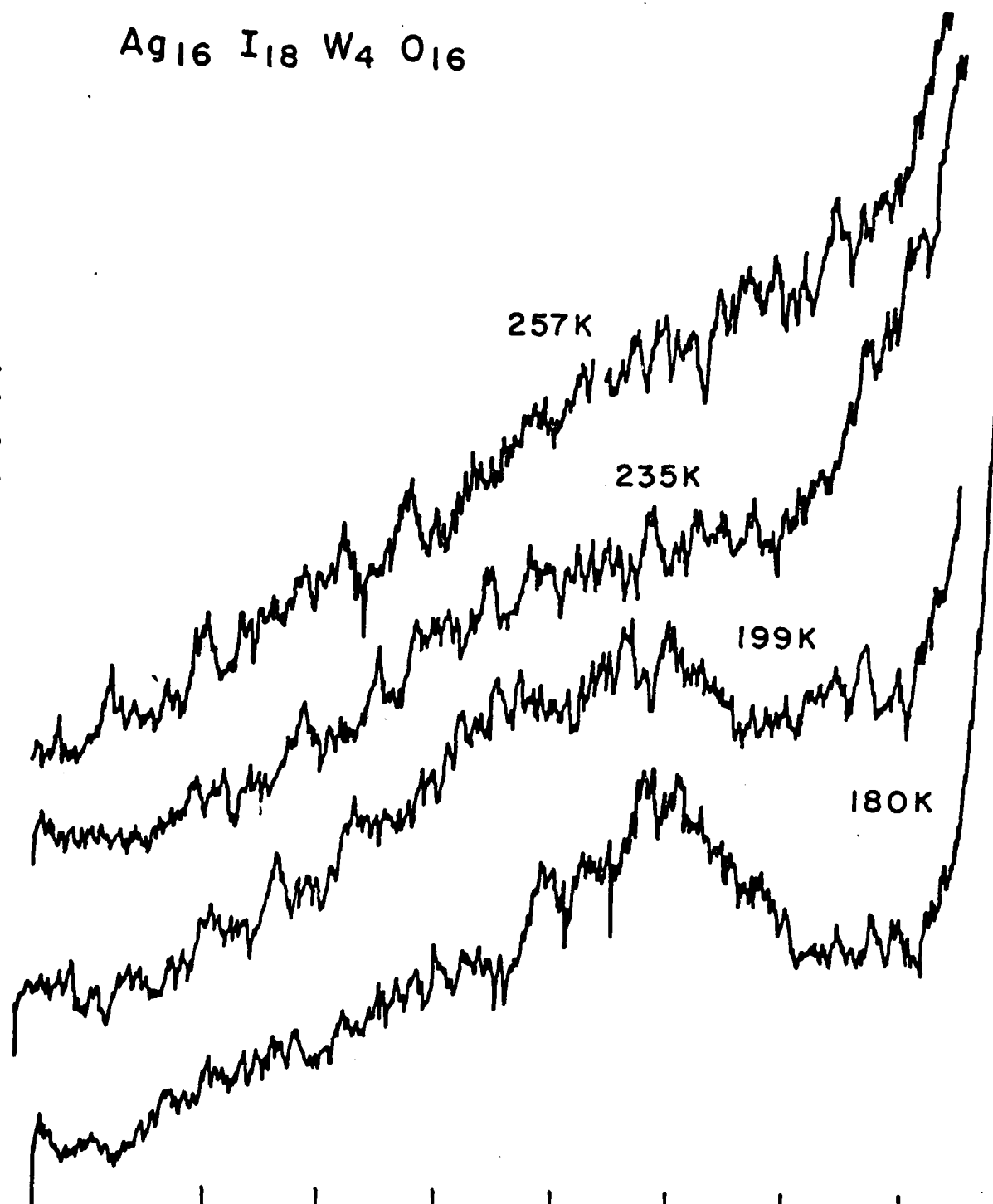
Figure 1: Electrical conductivity of $\text{Ag}_{26}\text{I}_{18}\text{W}_4\text{O}_{16}$ as a function of temperature, with and without 1 W/cm^2 of 514.5 nm illumination.

$\text{Ag}_{26} \text{I}_{18} \text{W}_4 \text{O}_{16}$
AT 1 kHz



Ag₁₆ I₁₈ W₄ O₁₆

SCATTERING INTENSITY



40 35 30 25 20 15 10

FREQUENCY SHIFT (cm⁻¹)

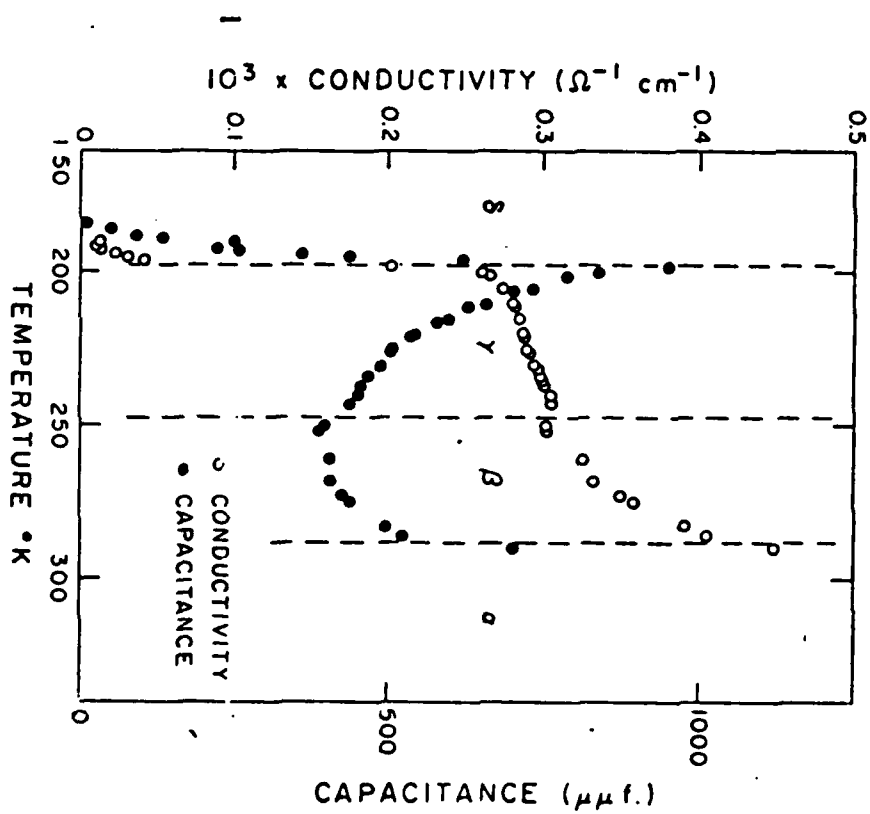
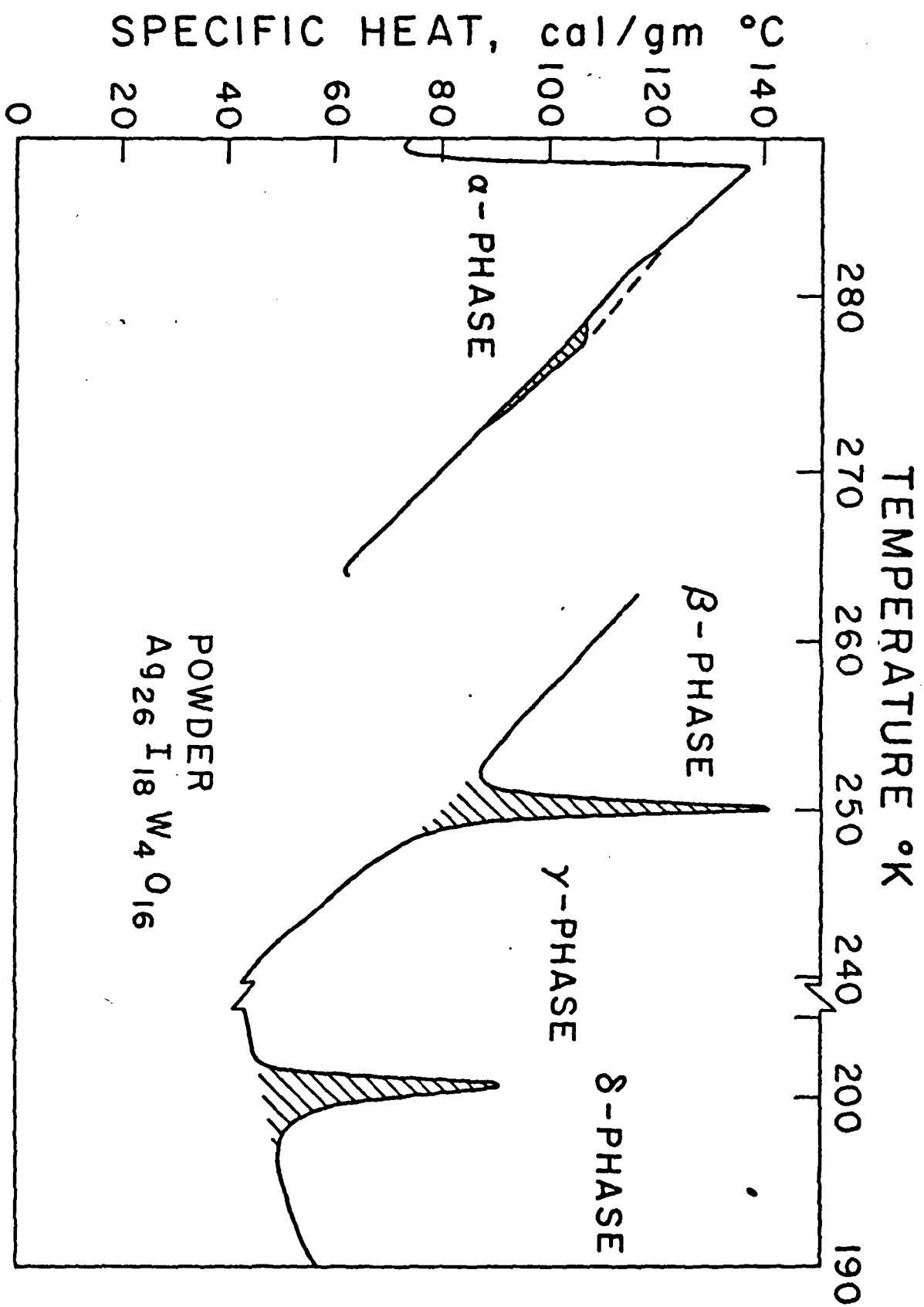


FIG. 1. Dielectric data and conductivity values for $\text{Ag}_2\text{S}_{10}\text{W}_4\text{O}_{16}$ showing four phases; Ref. 4.



JCP-010200-144-Fig. 2-410

$\text{AgI} \cdot \text{WO}_3$ shown in Fig. 3 is a silver ion conductivity and is $0.047 \pm 0.001 \text{ (ohm} \cdot \text{cm)}^{-1}$ at 25°C . The activation energy for conduction obtained from the Arrhenius plot is 3.6 kcal/mole, which is comparable to the values of the other high ionic conductivity solids (1). The high ionic conductivity and low activation energy suggest that the silver ions in this new compound may be statistically distributed in the lattice taking an averaged structure.

X-ray diffraction.—The results of the x-ray diffraction of the samples carried out at room temperature using nickel filtered $\text{Cu-K}\alpha$ radiation are listed in Table II. In the composition range of 0–18 m/o Ag_2WO_3 , the diffraction peaks due to γ -phase silver iodide appeared. The lines due to Ag_2WO_3 were observed in the samples containing 67 m/o or more Ag_2WO_3 . The lines due to β - AgI and Ag_2WO_3 were not observed in the samples containing 20–67 m/o Ag_2WO_3 . The patterns of the samples containing 20, 33, and 67 m/o Ag_2WO_3 showed that the new phases were formed in these compositions. These patterns, however, are too complex to determine the crystal structure only by the powder x-ray diffraction analysis.

Phase diagram of the system $\text{AgI-Ag}_2\text{WO}_3$.—The results of the DTA of the system $\text{AgI-Ag}_2\text{WO}_3$ in the temperature range of $20^\circ\text{--}200^\circ\text{C}$ are shown in Fig. 4. Although the DTA of this system showed an endothermic peak at 147°C in the heating process in the composition range of 0–17.5 m/o of Ag_2WO_3 , which is due to the transformation of silver iodide from β to α phase, the peak did not appear at this temperature in the samples of 20 and 22.5 m/o Ag_2WO_3 . Another endothermic peak at 150°C appeared in the composition range of 25–60 m/o Ag_2WO_3 . These results correspond to those of the electrical conductivity measurements shown in Fig. 3. In the samples containing more than 67 m/o of Ag_2WO_3 , however, no peaks were observed at these temperatures. The endothermic peaks at 3° , 290° , and 348°C were also observed in the composition ranges of 0–20, 20–67, and 50–90 m/o of Ag_2WO_3 in the heating process.

Figure 5 shows the phase diagram of the system $\text{AgI-Ag}_2\text{WO}_3$ determined by the x-ray diffraction measurements and the differential thermal analysis. In this system, there are three intermediate compounds at the compositions of 20, 33, and 67 m/o of Ag_2WO_3 , which may be written as $\text{Ag}_4\text{I}_3\text{WO}_3$, $\text{Ag}_3\text{I}_2\text{WO}_3$, and Ag_2IWO_3 , respectively, at room temperature. $\text{Ag}_4\text{I}_3\text{WO}_3$ and $\text{Ag}_3\text{I}_2\text{WO}_3$ incongruently melt at 293° and 348°C , respectively. Ag_2IWO_3 decomposes to $\text{Ag}_4\text{I}_3\text{WO}_3$ and $\text{Ag}_3\text{I}_2\text{WO}_3$ above 150°C . The melting

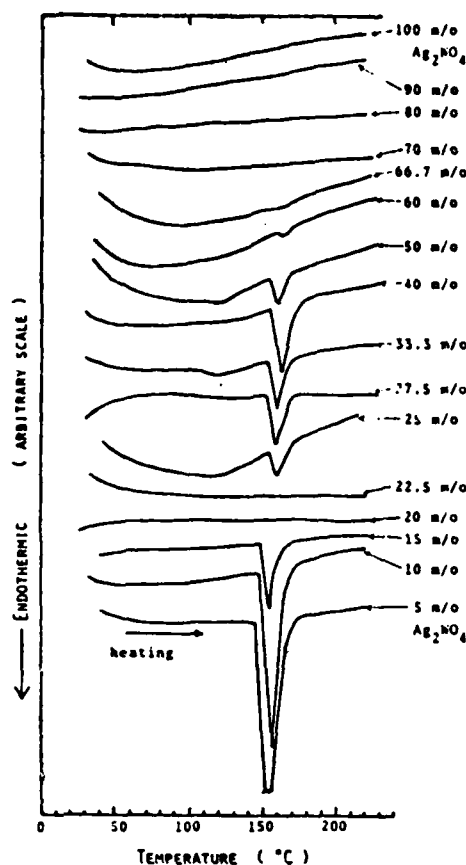


Fig. 4. DTA curves of the system $\text{AgI-Ag}_2\text{WO}_3$ in the heating process in the temperature range of $20^\circ\text{--}200^\circ\text{C}$.

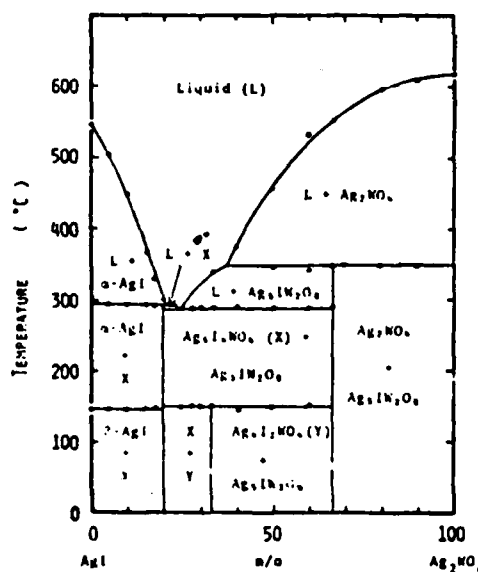


Fig. 5. Phase diagram of the system $\text{AgI-Ag}_2\text{WO}_3$.

point of Ag_2WO_3 is $620^\circ \pm 5^\circ\text{C}$, and the eutectic composition is estimated to be 25 m/o Ag_2WO_3 at 290°C .

Galvanic cell.—The high ionic conductivity solid electrolytes have been mainly used in solid-electrolyte galvanic cells (5–10). In these applications, the solid electrolyte should have a high ionic conductivity, high stability for the cathode material, and low electrode polarization. Figure 6 shows the result of the change of the internal resistance of the cell, Graphite/ $\text{AgI} \cdot \text{WO}_3 + \text{I}_2$ /Graphite, with time. A mixture of 1.3g of the electrolyte and 0.3g of iodine was used. The

Table II. Powder x-ray patterns for the system $\text{AgI-Ag}_2\text{WO}_3$

WO_3 I	Ag_2IWO_3 I	$\text{Ag}_3\text{I}_2\text{WO}_3$ I	$\text{Ag}_4\text{I}_3\text{WO}_3$ I	$\gamma\text{-AgI}$ I		
W	4.17	VW	4.31	W	3.75	VS
W	3.97	W	3.79	S	2.25	VW
VW	3.77	VW	3.48	W	1.13	VW
W	3.62	VW	3.02	M	3.79	MWB*
W	3.22	MW	2.94	M	3.68	MB
M	3.06	M	2.87	MW	3.48	MSB*
VS	2.99	S	2.71	M	3.18	MB
M	2.86	M	2.31	M	2.96	MB
W	2.80	MB*	2.25	VW	2.92	M
VW	2.72	MW	1.97	MW	2.87	M
VW	2.66	M	1.92	W	2.71	SB*
VW	2.50	W			2.56	WB
VW	2.37	W			2.46	W
S	2.30	W			2.38	WB
W	2.21	W			2.31	MB
	2.16	W			2.18	MB
	2.13	VW			1.93	WB
	2.04	W				
	2.01	W				
	1.87	VW				
m/o WO_3	66.7 m/o	33.3 m/o	20 m/o	0 m/o		
0, 50, 70 m/o	80, 50, 40 m/o	30, 25 m/o	17.5, 10, 5 m/o			
Mixed pattern	Mixed pattern	Mixed pattern	Mixed pattern			

MB, MWB, MSB, and SB: B means that the peak is rather broad.

IV. 3

Free Carrier Plasma Transport in Photoexcited Semiconductors

J. R. Meyer
Code 6551
Naval Research Laboratory
Washington, D. C. 20375

SUMMARY

As is well known, the intense laser irradiation of a semiconductor can lead to the generation of a high-density electron-hole plasma. As a consequence, the conductivity of the semiconductor may increase by many orders of magnitude within nanoseconds or even picoseconds, limited primarily by the rise time of the laser pulse. In recent years this phenomenon has been exploited in the development of a new generation of ultra-fast high-power switches.

Since the switching mechanism is photoconductive, a number of important switch performance parameters depend strongly on the mobility of the laser-excited electrons and holes. These include the on-resistance, the transmission coefficient (in the case of microstrip transmission lines) and the switch efficiency. Also depending on the free carrier mobilities is the ambipolar diffusion length, which determines the penetration depth of the plasma in cases where excitation at photon energies well above the bandgap leads to a very short optical absorption depth. In this paper we summarize the present theoretical understanding of free carrier transport in semiconductors at high optically-excited carrier densities.

The most obvious difference between unipolar and bipolar transport is the introduction of electron-hole scattering as an important mobility-limiting mechanism at high excitation levels. The simplest way of dealing with this additional mechanism is to treat the electron-hole events analogously to ionized impurity scattering using Brooks-Herring theory. The e-h mobility can then be combined with the phonon and ionized impurity components using Matthiessen's Rule within the relaxation-time approximation. However, this approach can lead to considerable error because it ignores several important differences between low-density and high-density bipolar transport.

For example, while electron-ion and electron-hole events both involve charged-center scattering, the screening of the interactions by lattice ions and free carriers must be treated differently in the two cases. In the case of scattering by a stationary impurity, the screening medium has an indefinite amount of time to respond to the ion charge. However, in the electron-hole case, the interacting particles are traveling through the medium with a finite center-of-mass velocity v_{cm} . The effectiveness of the screening is therefore limited by the frequency-response of the screening medium, and the interactions are stronger than in the electron-ion

case. A detailed treatment of the dynamic screening [1] of carrier-carrier interactions leads to the simple result: $U(\vec{q}) = V(\vec{q})/\epsilon(\vec{q}, \omega = \vec{q} \cdot \vec{v}_{cm})$, where $V(\vec{q})$ and $U(\vec{q})$ are the bare and screened Coulomb potentials in momentum space and $\epsilon(\vec{q}, \omega)$ is the total dielectric constant due to screening by core electrons, lattice ions, and free carriers. (In the case of scattering by ionized impurities, $v_{cm} = 0$ and one recovers the usual zero-frequency result). It is shown in Ref. [1] that in certain limits the electron-hole scattering mobility has a relatively simple form. For the case of high-density plasmas generated by 10.6 μm irradiation in $\text{Hg}_{1-x}\text{Cd}_x\text{Te}$ [2], it has been verified that the calculated electron mobilities differ significantly from experimental values unless the screening of electron-hole interactions is properly treated by the dynamic theory.

Another important effect which is present only in the bipolar transport case is electron-hole drag. This occurs when an applied electric field causes the electrons to "drift" in one direction and the holes in the other. While this effect cannot be treated within the relaxation time approximation, it is straightforwardly accounted for if one employs Kohler's variational method [3] to solve the Boltzmann equation. Other advantages of the Kohler method are that it accurately combines the scattering due to multiple elastic and inelastic scattering processes, including electron-electron and hole-hole scattering. Electron-hole scattering may be incorporated using Brooks-Herring theory [4,5] or the dynamic screening theory discussed above [2].

The Kohler formalism may also be used to calculate the ambipolar diffusion coefficient D at high optically-excited carrier densities [6]. One finds that to first order the additional electron-hole scattering has no effect on D , although higher orders can give a small decrease (usually less than 20%). This result is not surprising when one considers that in contrast to the drift transport case considered above, the electrons and holes diffuse in the same direction. Electron-hole scattering simply redistributes momentum within the diffusing free carrier system, but does not impede the system as a whole. For the case of germanium, it has been verified that the drift mobility decreases far more than the diffusion mobility when high densities of electrons and holes are optically-injected into the material [5,7].

A further factor influencing the conductivity at high carrier densities is the formation of excitons, which are not electrically conducting because they have no net charge. Since the statistical factors favoring exciton formation go as the square of the carrier density, the fraction of optically-generated carriers which form excitons increases dramatically at high excitation levels. However, at sufficiently high densities the screening length becomes short enough that the bound state vanishes, i.e., the system passes through an exciton Mott transition [8]. Although the occurrence of the Mott transition appears to be verified by experimental luminescence data on Si and GaP [9,10], the detailed nature of the transition remains uncertain [5,11].

Experimentally, combined electron and hole mobilities have been determined for germanium at temperatures between 21 and 300 K and plasma densities between 10^{14} and $3 \times 10^{17} \text{ cm}^{-3}$ [5]. At 300 K, the mobility decreases monotonically with increasing carrier concentration to roughly a factor of two below the low-density value at 10^{17} cm^{-3} . The mobility decrease becomes larger at low temperatures, reaching nearly two orders of magnitude at 21 K. Furthermore, rather than a monotonic decrease one observes a minimum mobility at intermediate carrier densities. At plasma densities above the minimum, the mobility increases due to the effects of both free carrier screening and the Mott transition. A similar increase is predicted for 300 K at carrier densities higher than those investigated experimentally. For silicon, the most relevant data from the literature would appear to be that of Ref. [12], in which the Hall mobility was measured at 300 K for electron-hole densities up to about 10^{18} cm^{-3} . However, an inadequate analysis of the effects of mixed conduction on the Hall data did not allow a reliable estimate of the drift mobility as a function of carrier density. Photo-transport measurements have also been performed on CdSe at temperatures between 100 and 300 K [13]. While a decrease in the high-density mobility is reported, the magnitude of the decrease unfortunately contains considerable experimental uncertainty. Beyond these experiments, we are aware of few reliable high-density ($n > 10^{17} \text{ cm}^{-3}$) mobility measurements on wide-gap semiconductors at temperatures above 20 K.

Summarizing, we have briefly discussed a number of phenomena which do not affect semiconductor free carrier transport properties in the absence of optical excitation but which may become quite important at high laser-generated carrier concentrations. While many of the processes are well understood theoretically and present models usually give good agreement with experiment in regions where comparisons have been made, the most general calculations have not yet been performed for the materials and carrier concentrations of greatest relevance to switch performance and design. Furthermore, almost no reliable experimental drift mobility data presently exist for the region $T > 20 \text{ K}$ and $n > 10^{17} \text{ cm}^{-3}$. An examination of the high-density transport properties in a wider range of materials is clearly called for in order to investigate possible new directions for switch optimization. It should also be mentioned that nearly all previous theoretical and experimental transport work at high optically-excited carrier densities has dealt with the limit of low electric fields. A detailed investigation of high-field effects on the plasma conductivity is indicated.

References

- [1] J. R. Meyer and F. J. Bartoli, Phys. Rev. B 28, 915 (1983).
- [2] F. J. Bartoli, J. R. Meyer, C. A. Hoffman, and R. E. Allen, Phys. Rev. B 27, 2248 (1983).
- [3] M. Kohler, Z. Phys. 124, 772 (1948); 125, 679 (1949).
- [4] J. Appel, Phys. Rev. 122, 1760 (1961); 125, 1815 (1962).
- [5] J. R. Meyer and M. Glicksman, Phys. Rev. B 17, 3227 (1978).
- [6] J. R. Meyer, Phys. Rev. B 21, 1554 (1980).
- [7] A. L. Smirl, S.C. Moss, and J. R. Lindle, Phys. Rev. B 25, 2645 (1982).
- [8] G. B. Norris and K. K. Bajaj, Phys. Rev. B 26, 6706 (1982).
- [9] J. Shah, M. Combescot, and A. H. Dayem, Phys. Rev. Lett. 38, 1497 (1977).
- [10] H. Maaref, J. Barrau, M. Brousseau, J. Collet, J. Mazzaschi, and M. Pagnet, Phy. Stat. Sol. (b) 88, 261 (1978).
- [11] O. Hildebrand, E. O. Goebel, K. M. Romanek, and H. Weber, Phys. Rev. B 17, 4775 (1978).
- [12] Yu. Vaitkus, V. Grivitskas, and Yu. Storasta, Fiz. Tekh. Poluprov. 9, 1339 (1975) [Sov. Phys. Semicond. 9, 883 (1975)].
- [13] R. Baltramiejunas, V. Grivickas, J. Storasta, and J. Vaitkus, Phys. Stat. Sol. (a) 19, K115 (1973).

VIEWGRAPHS

FREE CARRIER PLASMA TRANSPORT
IN PHOTOEXCITED SEMICONDUCTORS

J. R. MEYER

FREE CARRIER PLASMA TRANSPORT IN PHOTOEXCITED SEMICONDUCTORS

J. R. MEYER

NAVAL RESEARCH LABORATORY

CODE 6551

(202)-767-3276

FREE CARRIER TRANSPORT AT HIGH EXCITATION

- o SWITCH OPERATION INVOLVES LASER-GENERATION OF HIGH DENSITY
E-H PLASMAS
- o HIGH-DENSITY TRANSPORT DOMINATED BY EFFECTS NOT ENCOUNTERED
NEAR EQUILIBRIUM

MECHANISMS AT HIGH E-H DENSITIES (1)

- o E-H SCATTERING
- o SCREENING BY PLASMA
- o DYNAMIC SCREENING OF E-H INTERACTIONS
- o CORRECTIONS TO BROOKS-HERRING SCATTERING THEORY

MECHANISMS AT HIGH E-H DENSITIES (2)

- o ELECTRON-HOLE DRAG
- o EXCITON EFFECTS
- o AMBIPOLAR DIFFUSION MOBILITY
- o HOT-CARRIER EFFECTS
- o HIGH E-FIELD PROPERTIES

MOBILITY-DEPENDENT SWITCH PARAMETERS

PHOTOCONDUCTIVITY: $\Delta\sigma = \Delta ne(\mu_e + \mu_p)^2$

o ON-RESISTANCE

o MICROSTRIP TRANSMISSION COEFFICIENT

o SWITCH EFFICIENCY

AMBIPOLAR DIFFUSION DEPTH: $L \approx \alpha^{-1} + L_0$

SCREENED COULOMB POTENTIAL

SCATTERING POTENTIAL

$$V(\vec{r}) = -\frac{e^2}{\kappa_0 r} \exp(-r/\lambda_D)$$

SCREENING LENGTH (DINGLE-MANSFIELD)

$$\lambda_D^{-2} = \frac{4\pi e^2}{\kappa_0 k_B T} \left[n \frac{\sigma_{i-1}(\eta_e)}{\sigma_i(\eta_e)} + \rho \frac{\sigma_{i-1}(\eta_p)}{\sigma_i(\eta_p)} \right]$$

BORN APPROXIMATION

POTENTIAL IN MOMENTUM SPACE

$$V(\vec{q}) = \int d^3r \exp(i\vec{q} \cdot \vec{r}) V(\vec{r})$$
$$= \frac{4\pi e^2}{\kappa_0(q^2 + \lambda_s^{-2})}$$

BORN SCATTERING AMPLITUDE

$$f(\theta) = \frac{m^*}{2\pi\hbar} V(\vec{q})$$
$$\vec{q} = \vec{k}(1 - \cos\theta)$$

BROOKS-HERRING THEORY

SCATTERING CROSS SECTION

$$\sigma(\theta) = |f(\theta)|^2$$

$$\rightarrow \frac{4 \lambda_s^4}{a^2 [1 + 2k^2 \lambda_s^2 (1 - \cos \theta)]^2}$$

MOMENTUM-TRANSFER CROSS SECTION

$$\sigma_T = 2\pi \int_0^\pi \sigma(\theta) (1 - \cos \theta) \sin \theta d\theta$$

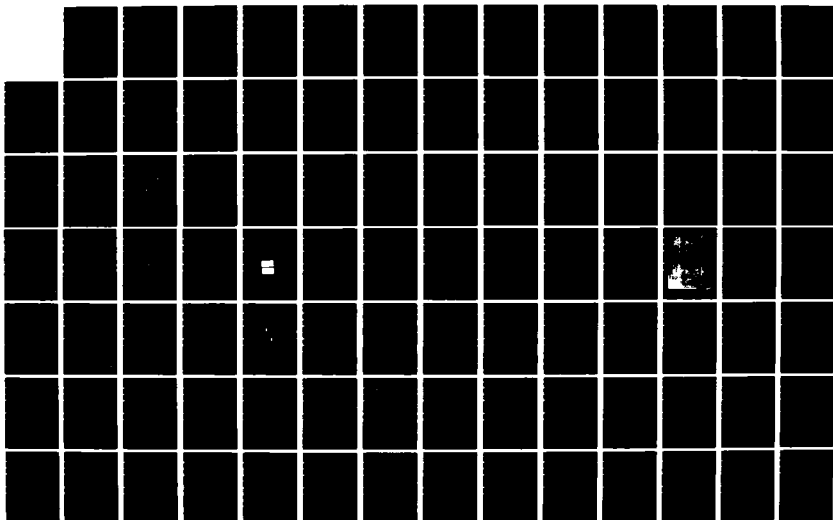
AD-A165 039

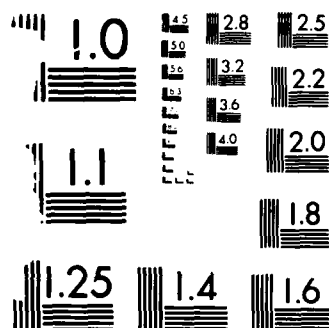
WORKSHOP ON NEW DIRECTIONS IN SOLID STATE POWER
SWITCHES HELD AT FARMINGD. (U) POLYTECHNIC INST OF NEW
YORK FARMINGDALE WEBER RESEARCH INST. B SENITZKY
24 DEC 85 N00014-85-G-0236 F/G 9/5

2/6

UNCLASSIFIED

ML





MICROCOPY RESOLUTION TEST CHART
NATIONAL BUREAU OF STANDARDS 1963-A

RELAXATION-TIME APPROXIMATION

RELAXATION TIME

$$\tau(E) = [N v \sigma_T(E)]^{-1}$$

MOBILITY

$$\mu_i = \frac{4e}{3\pi^{1/2} m^* \sigma_i^{1/2} (k_B T)^{5/2}} \int_0^\infty E^{3/2} f_0(1-f_0) \tau_i(E) dE$$

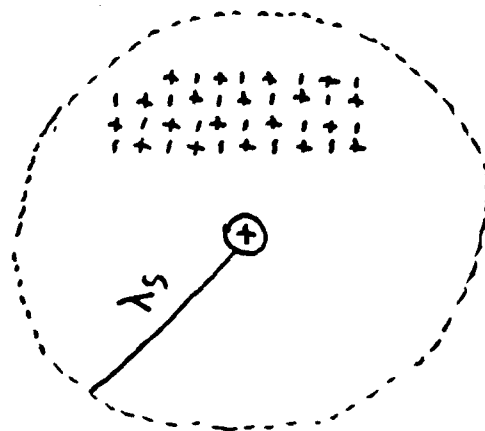
MATTHIESSEN'S RULE

$$\mu = \left[\sum_i \frac{1}{\mu_i} \right]^{-1}$$

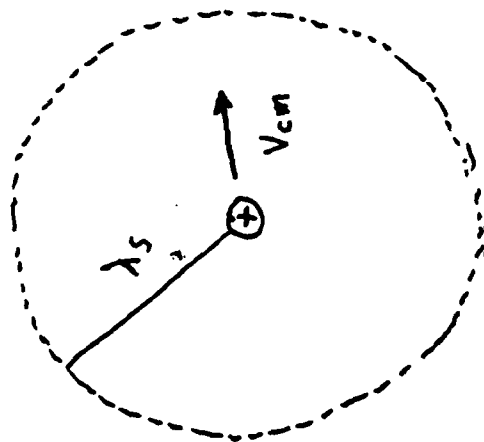
CORRECTIONS TO BROOKS-HERRING THEORY

- o SCATTERING CROSS SECTIONS FROM PARTIAL WAVE PHASE SHIFT METHOD
- o BETTER SCATTERING POTENTIAL
- o MULTI-PARTICLE SCATTERING
- o INHOMOGENEOUS FREE CARRIER DENSITIES

DYNAMIC SCREENING



Donor



Hole

$$\tau \approx \frac{\lambda_s}{V_{cm}}$$

$$\omega \approx \frac{V_{cm}}{\lambda_s}$$

BARE POTENTIAL IN REST FRAME OF SCREENING MEDIUM

$$V(\vec{r}, t) = \frac{-e^2}{|\vec{r} - \vec{v}_{cm} t|}$$

$$\begin{aligned} V(\vec{r}, t) &= \int d^3r \exp(i\vec{q} \cdot \vec{r}) V(\vec{r}, t) \\ &= -\frac{4\pi e^2}{q^2} \exp(i\vec{q} \cdot \vec{v}_{cm} t) \end{aligned}$$

$$V(\vec{q}, \omega) = -\frac{4\pi e^2}{q^2} \delta(\omega - \vec{q} \cdot \vec{v}_{cm})$$

SCREENED POTENTIAL IN REST FRAME OF SCREENING MEDIUM

$$U(\vec{q}, \omega) = \frac{V(\vec{q}, \omega)}{\epsilon(\vec{q}, \omega)}$$

$$U(\vec{q}, t) = - \frac{4\pi e^2 e^{i\vec{q} \cdot \vec{v}_{cm} t}}{q^2 \epsilon(\vec{q}, \omega = \vec{q} \cdot \vec{v}_{cm})}$$

$$U(\vec{r}, t) = -4\pi e^2 \left(\frac{1}{2\pi}\right)^3 \int \frac{d^3 q \exp[-i\vec{q} \cdot (\vec{r} - \vec{v}_{cm} t)]}{q^2 \epsilon(\vec{q}, \omega = \vec{q} \cdot \vec{v}_{cm})}$$

SCREENED POTENTIAL IN CENTER-OF-MASS FRAME

$$U(\vec{r}') = -4\pi e^2 \left(\frac{1}{2\pi} \right)^3 \int \frac{d^3 q \exp(-i\vec{q} \cdot \vec{r}')}{q^2 \epsilon(q, \omega = \vec{q} \cdot \vec{v}_{cm})}$$

$$U(\vec{q}) = - \frac{4\pi e^2}{q^2 \epsilon(\vec{q}, \omega = \vec{q} \cdot \vec{v}_{cm})}$$

$$q \approx \lambda_s^{-1} \Rightarrow \omega \approx \frac{v_{cm}}{\lambda_s}$$

DIELECTRIC CONSTANT

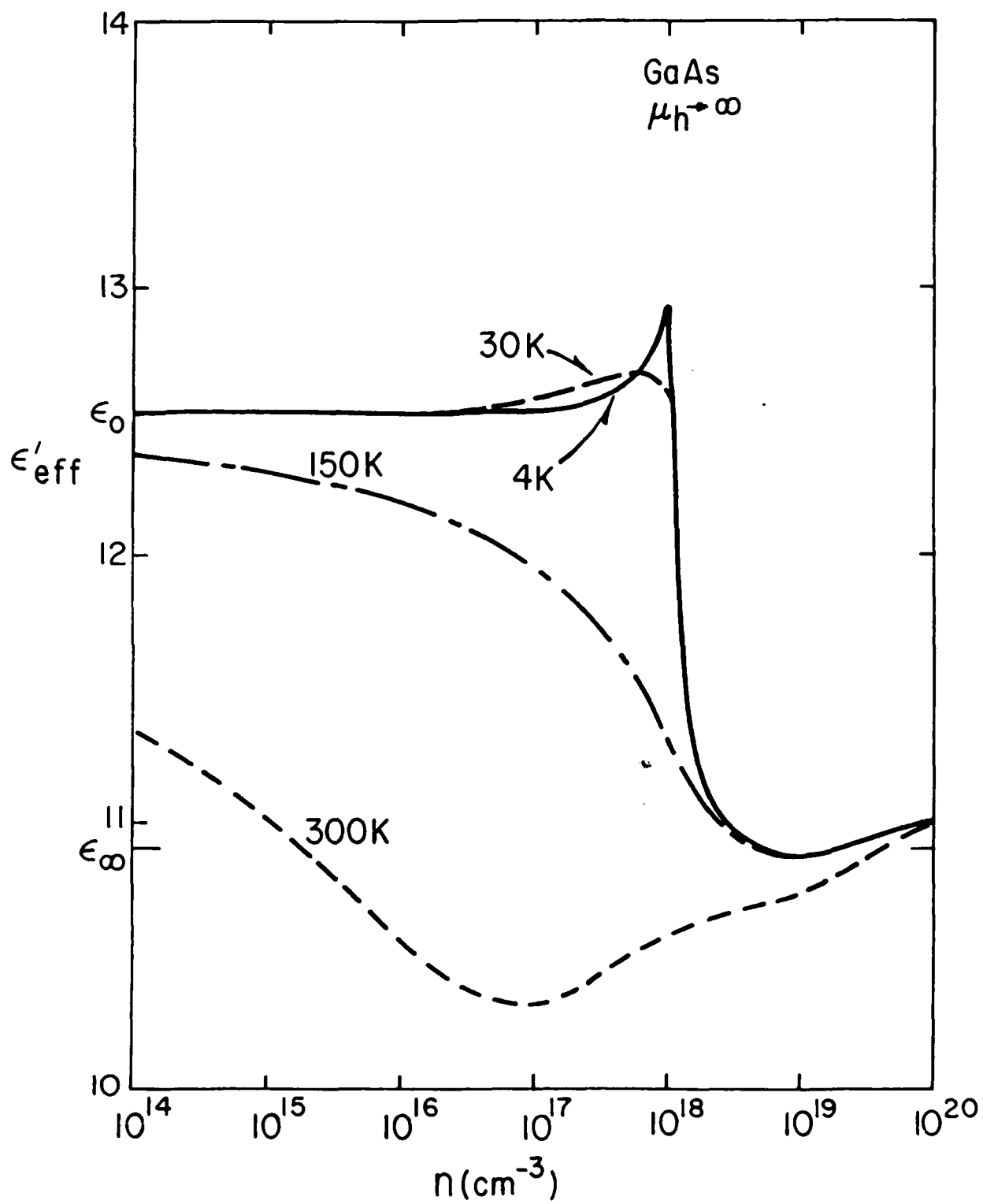
$$\epsilon(\vec{q}, \omega) = \epsilon_{\infty} + \epsilon_L(\vec{q}, \omega) + \epsilon_e(\vec{q}, \omega) + \epsilon_h(\vec{q}, \omega)$$

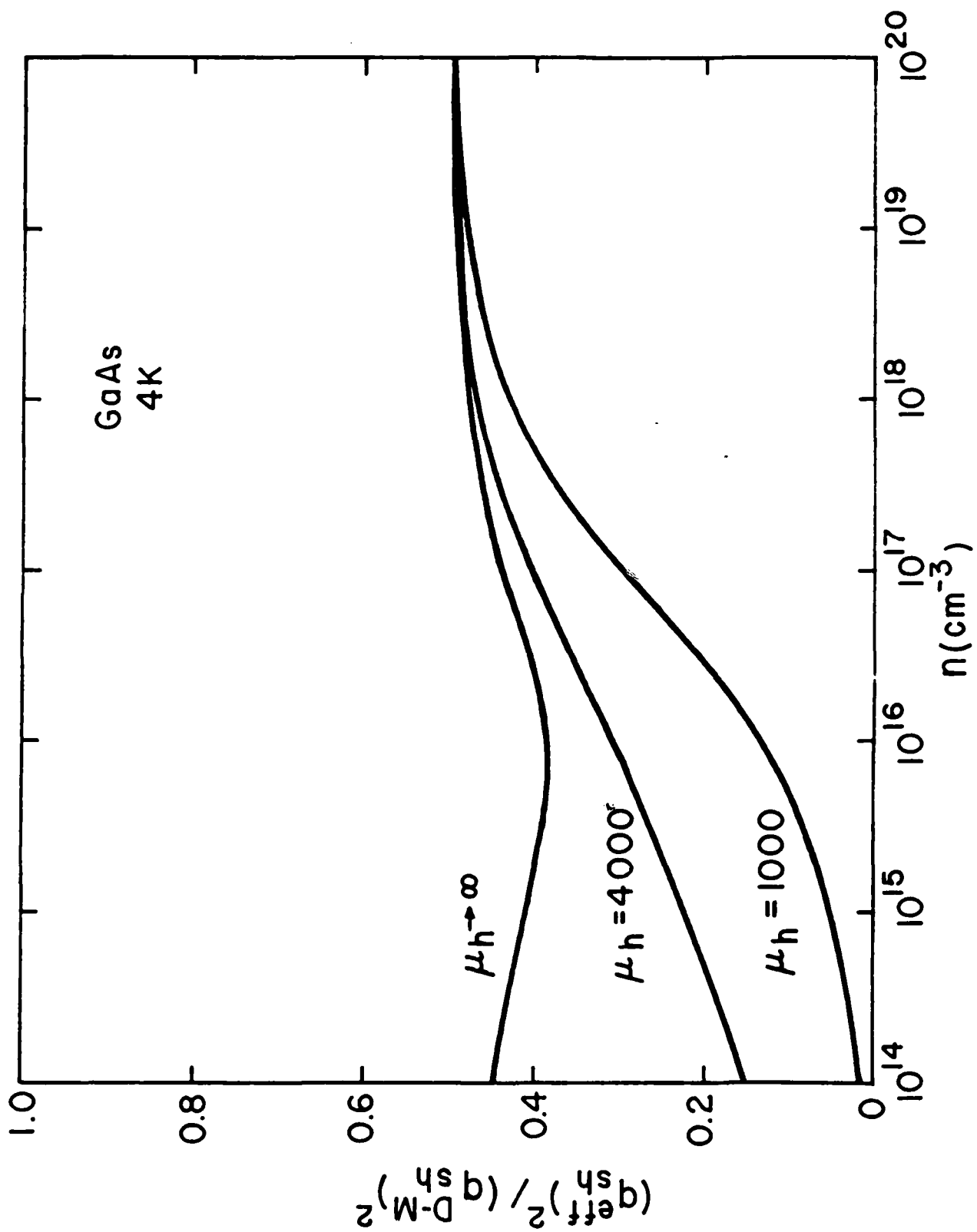
LATTICE

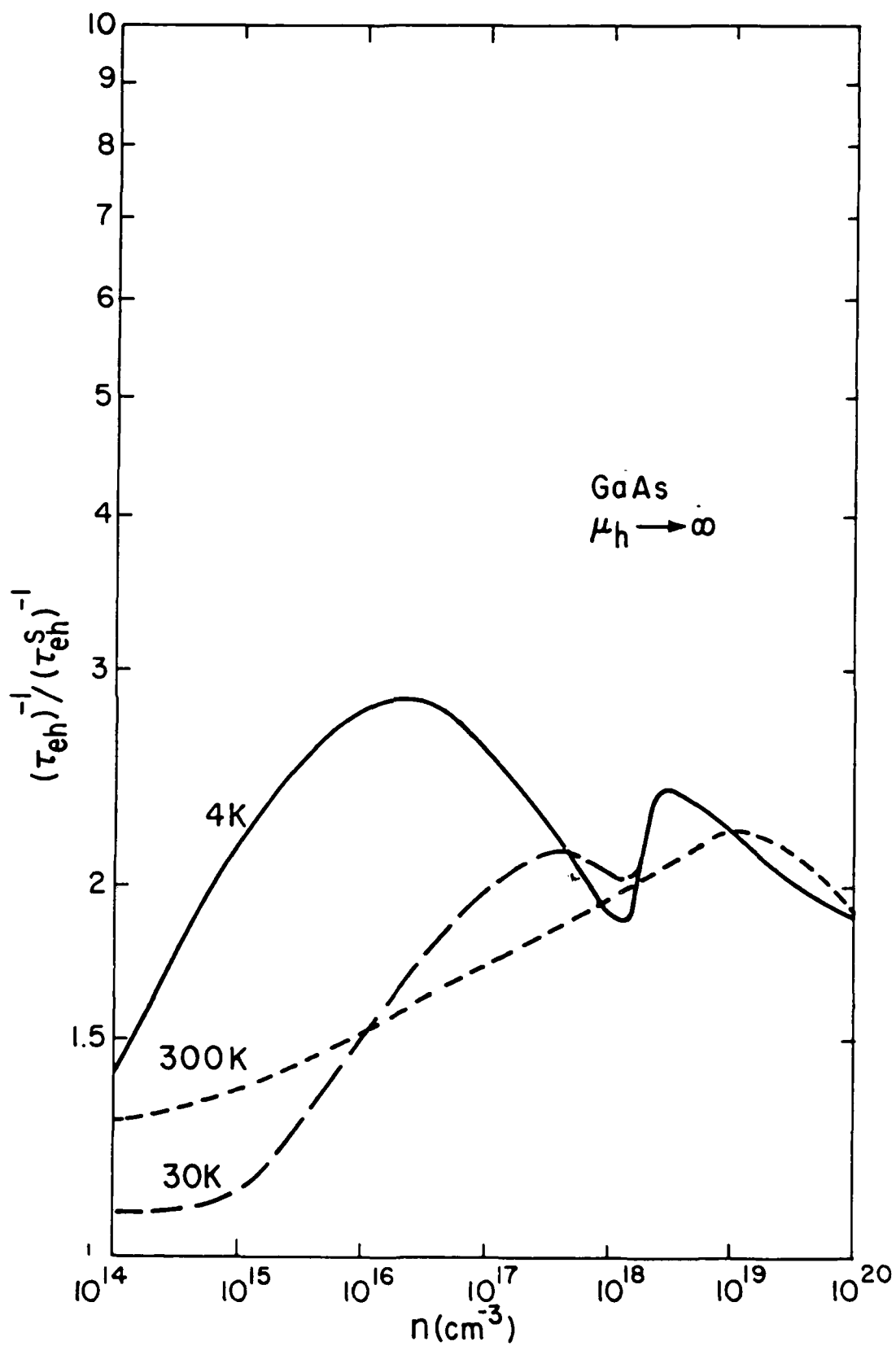
$$\epsilon_L(\omega) = \frac{(\epsilon_0 - \epsilon_{\infty}) \omega_x^2}{\omega_x^2 - \omega^2 + i\omega\Gamma}$$

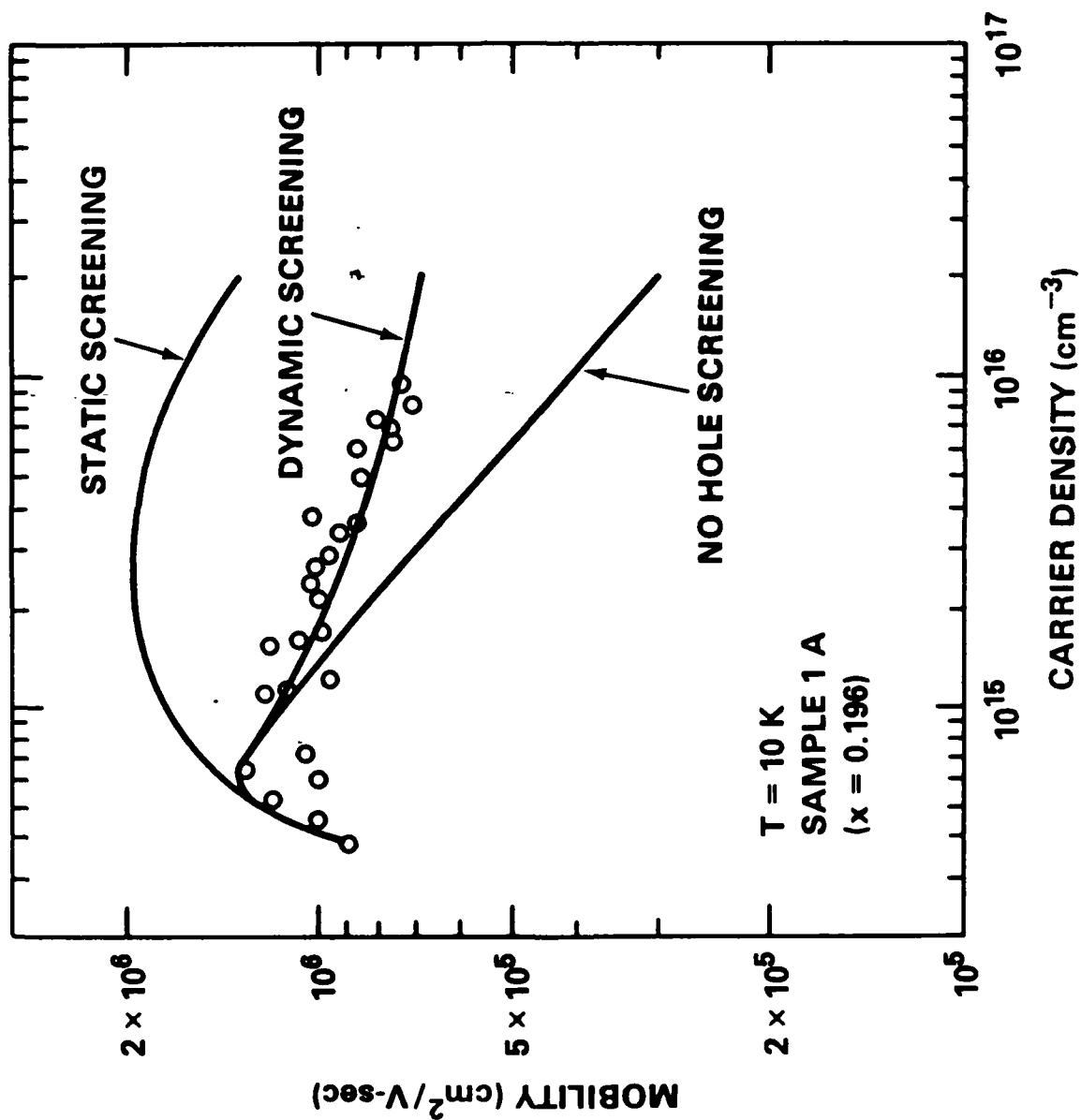
FREE CARRIER (RPA)

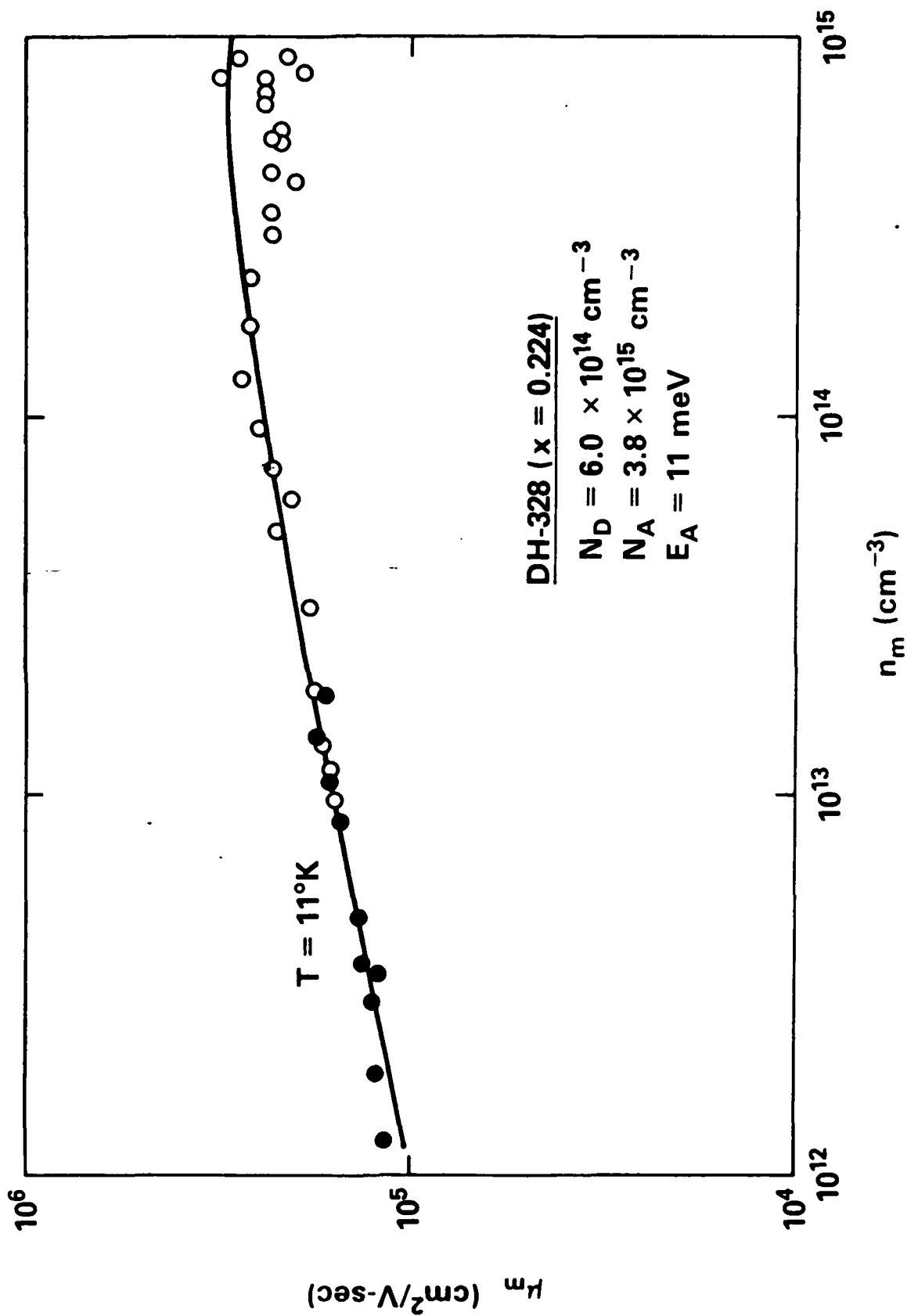
$$\epsilon_e(\vec{q}, \omega) = \frac{4\pi e^2}{q^2} \sum_{\vec{k}} \frac{f_{0i}(\vec{k}) - f_{0i}(\vec{k} + \vec{q})}{E_i(\vec{k} + \vec{q}) - E_i(\vec{k}) - \hbar\omega - \frac{1}{2}i\hbar\Gamma_i}$$

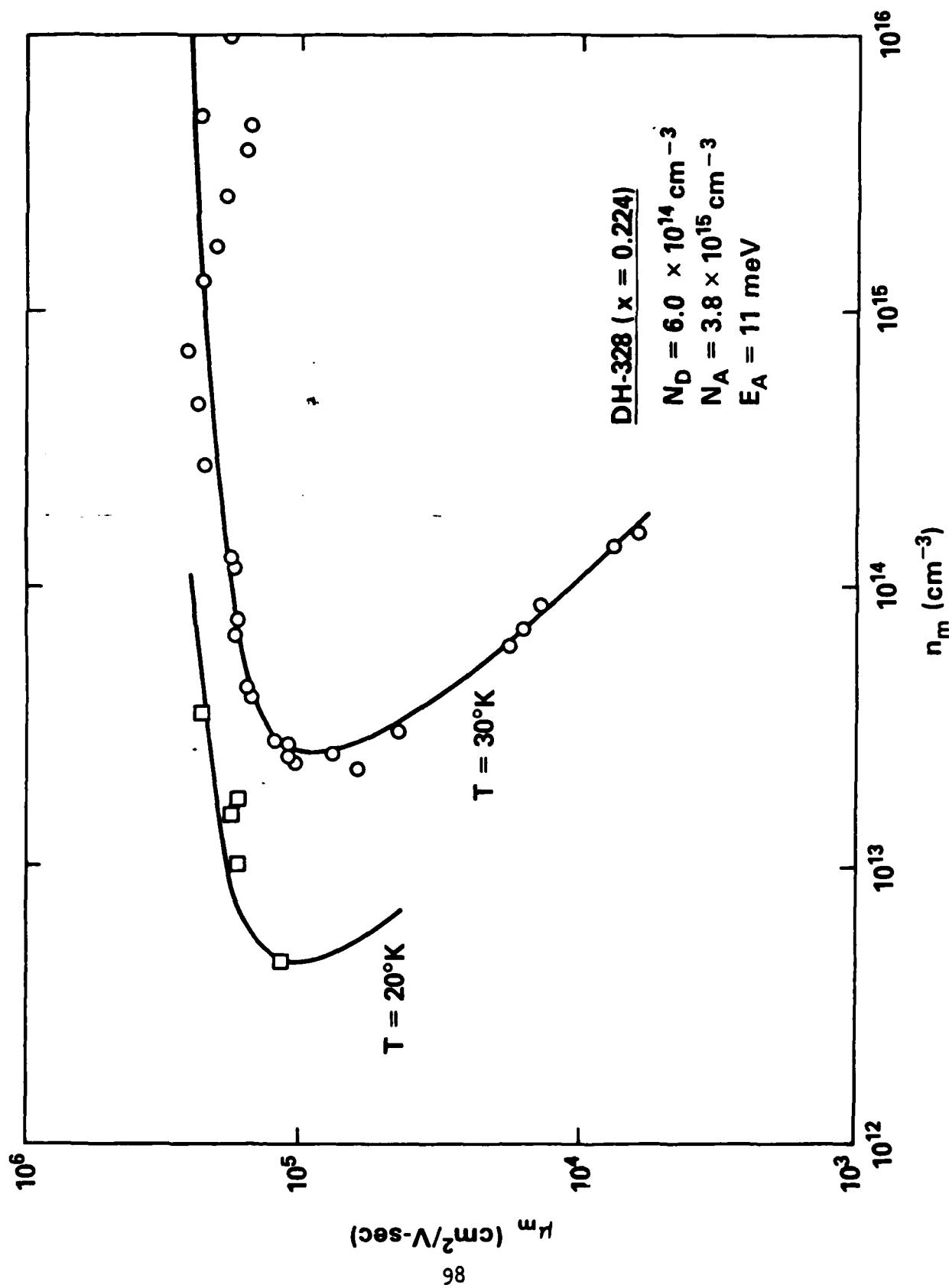




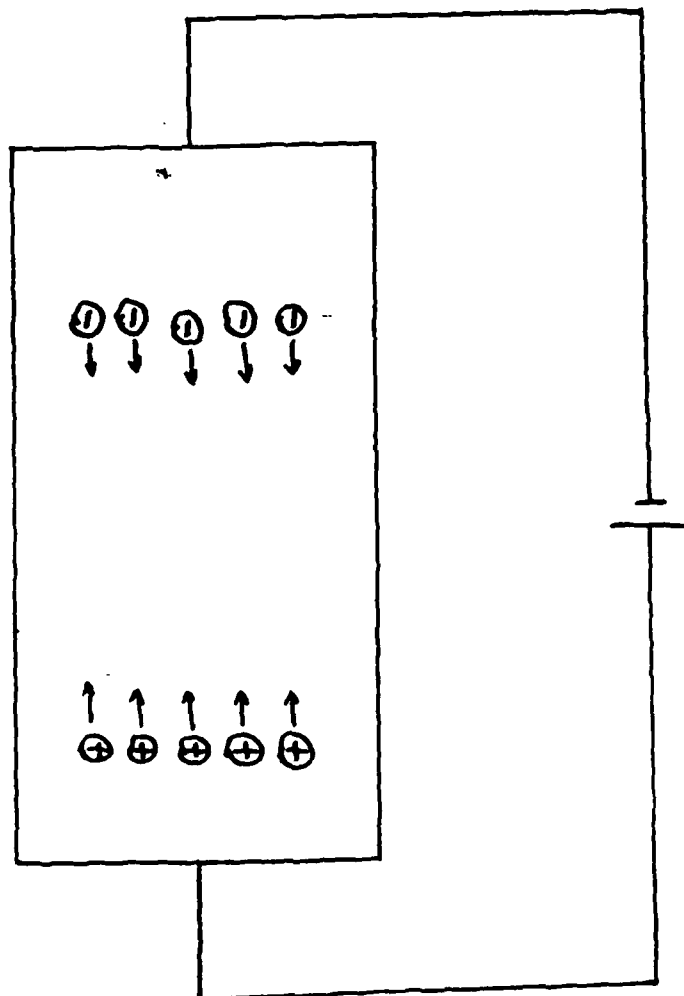








ELECTRON-HOLE DRAG



BOLTZMANN EQUATION

$$\frac{\partial f(\vec{v})}{\partial t} = \left[\frac{\partial f(\vec{v})}{\partial t} \right]_{\text{field}} + \left[\frac{\partial f(\vec{v})}{\partial t} \right]_{\text{grad}} + \left[\frac{\partial f(\vec{v})}{\partial t} \right]_{\text{coll}} \rightarrow 0$$

$$\left[\frac{\partial f(\vec{v})}{\partial t} \right]_{\text{field}} = \frac{\partial f(\vec{v})}{\partial E} \vec{F} \cdot \vec{v}$$

$$\left[\frac{\partial f(\vec{v})}{\partial t} \right]_{\text{grad}} = \vec{v} \cdot \vec{\nabla} \eta \frac{\partial f(\vec{v})}{\partial E}$$

LINEARIZATION OF BOLTZMANN EQUATION

$$\left[\frac{\partial f(\vec{v}_i)}{\partial t} \right]_{coll} = - \frac{1}{k_B T} \left(\frac{m^*}{2\pi\hbar} \right) \int d^3 v_2 f_{01} (1 - f_{02}) \sum_Y W_Y (\vec{v}_1 \rightarrow \vec{v}_2) [\Phi(\vec{v}_1) - \Phi(\vec{v}_2)]$$

$$f(\vec{v}_i) = f_0(\vec{v}_i) - \frac{\Phi(\vec{v}_i)}{k_B T} - \frac{\partial f_0(\vec{v}_i)}{\partial E_i}$$

$$\Phi(\vec{v}_i) = e \vec{F} \cdot \vec{v}_i \tau(E_i)$$

KOHLER VARIATIONAL METHOD

$$\tau_n(E_i) = \sum_s c_{ns} E_i^s$$

BOLTZMANN EQUATION

$$\sum_s \sum_{n=e,h} c_{ns} \Gamma_{rs}^{mn} = \beta_{mr}$$

102

$$\sigma = - e^2$$

$$\begin{vmatrix} 0 & \beta_{eo} & \beta_{ho} & \beta_{ei} & \beta_{hi} & \dots \\ \beta_{eo} & \Gamma_{eo}^{ee} & \Gamma_{eo}^{eh} & \Gamma_{eo}^{ee} & \Gamma_{eo}^{eh} & \dots \\ \beta_{ho} & \Gamma_{ho}^{eh} & \Gamma_{ho}^{hh} & \Gamma_{ho}^{ee} & \Gamma_{ho}^{eh} & \dots \\ \beta_{ei} & \Gamma_{ei}^{ee} & \Gamma_{ei}^{eh} & \Gamma_{ei}^{ee} & \Gamma_{ei}^{eh} & \dots \\ \beta_{hi} & \Gamma_{hi}^{eh} & \Gamma_{hi}^{hh} & \Gamma_{hi}^{ee} & \Gamma_{hi}^{eh} & \dots \\ \vdots & \vdots & \vdots & \vdots & \vdots & \vdots \end{vmatrix} \quad \left| \Gamma_{rs}^{mn} \right|$$

CONDUCTIVITY FROM VARIATIONAL METHOD

- o A FEW S ADEQUATE FOR NEARLY EXACT SOLUTION TO LINEARIZED
BOLTZMANN EQUATION
- o VALID FOR INELASTIC PROCESSES AND MULTIPLE SCATTERING MECHANISMS
- o INCLUDES E-E, H-H, AND E-H SCATTERING (ALSO LIGHT HOLES)
- o MAY INCLUDE INTERBAND HOLE TRANSITIONS
- o ACCOUNTS FOR E-H DRAG

SCATTERING INTEGRALS Γ_{rs}^{mn}

ARB DEGENERACY	DYNAMIC SCREENING	ARB m_h/m_e	MULTIFOLD INTEGRALS
NO	NO	YES	1
YES	NO	YES	5
YES	YES	YES	6
YES	YES	NO	3

SPATIAL DISTRIBUTION OF PHOTOEXCITED CARRIERS

$$n(z) = \frac{g \tau_R}{1 - L_D^2 \alpha^2} [e^{-\alpha z} - L_D \alpha e^{-z/L_D}]$$

$$\begin{array}{c} \rightarrow \\ L_D \alpha \ll 1 \end{array} \quad g \tau e^{-\alpha z}$$

$$\begin{array}{c} \rightarrow \\ L_D \alpha \gg 1 \end{array} \quad \frac{g \tau e^{-z/L_D}}{1 + L_D \alpha}$$

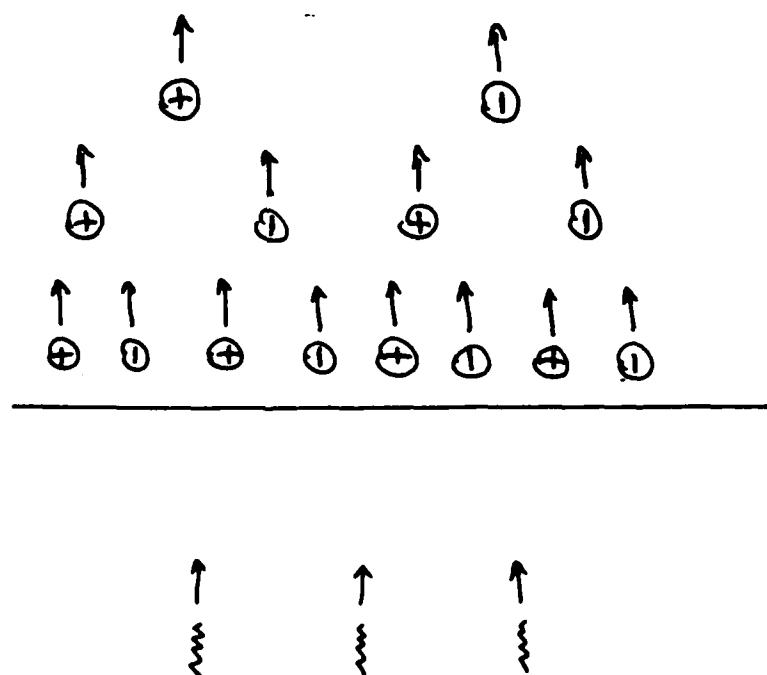
AMBIPOLAR DIFFUSION LENGTH

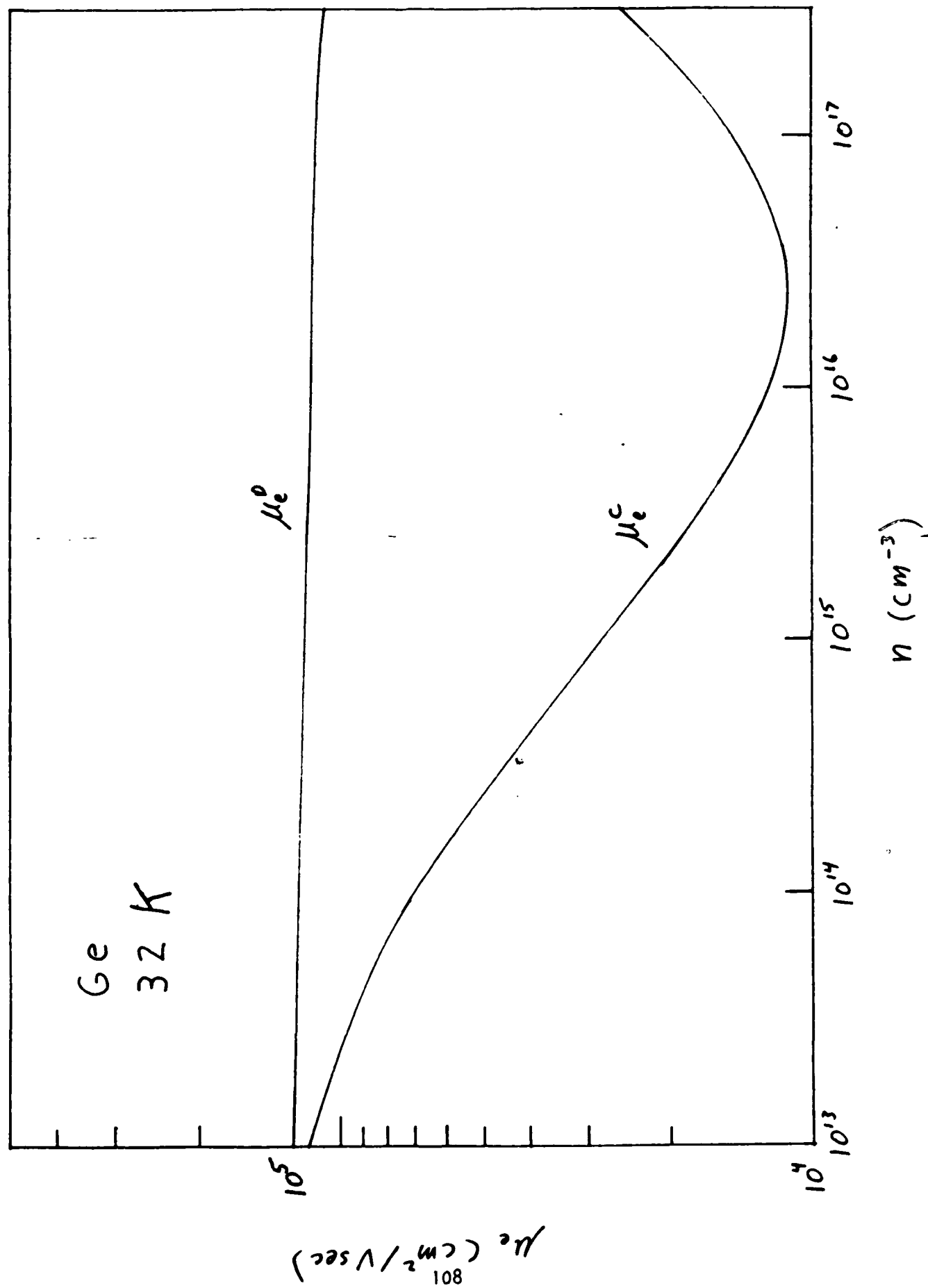
$$L_D = (D \tau_R)^{\frac{1}{2}}$$

$$D = \frac{k_B T}{e} \left[p \frac{\sigma_{h-\frac{1}{2}}(\eta_e)}{\sigma_{h-\frac{1}{2}}(\eta_p)} + n \frac{\sigma_{h-\frac{1}{2}}(\eta_p)}{\sigma_{h-\frac{1}{2}}(\eta_e)} \right] \frac{\mu_e^0 \mu_p^0}{(n \mu_e^0 + p \mu_p^0)}$$

$$\mu_i^0 \approx \mu_i^0$$

AMBIPOLAR DIFFUSION





EXCITON DENSITY

CONDUCTIVITY

$$\sigma = n e (\mu_e + \mu_p) \neq n_T e (\mu_e + \mu_p)$$

TOTAL CARRIER DENSITY

$$n_T = n + n_{ex}^- + n_{ex}^+$$

EXCITON DENSITY

$$n_{ex}^{\pm} = n^2 \left(\frac{2\pi\hbar^2}{k_B T} \right)^{3/2} \left[\frac{(m_T^{\pm})^{2/3} (m_L^{\pm})^{1/3}}{m_{eT}^{2/3} m_{eL}^{1/3} (m_h + m_d)} \right]^{3/2} \exp(E_x^{\pm} / k_B T)$$

EXCITON MOTT TRANSITION

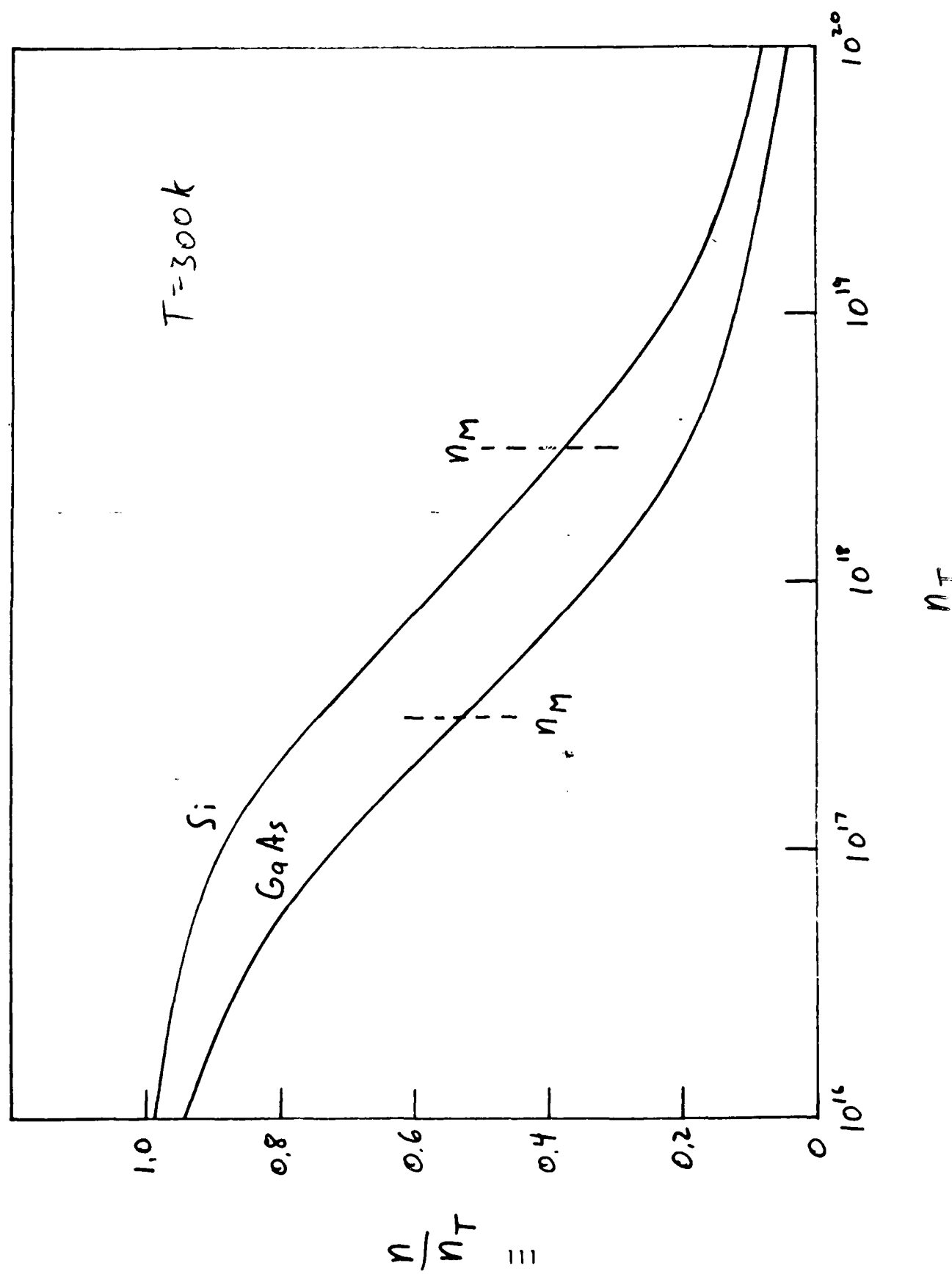
E_x VANISHES WHEN

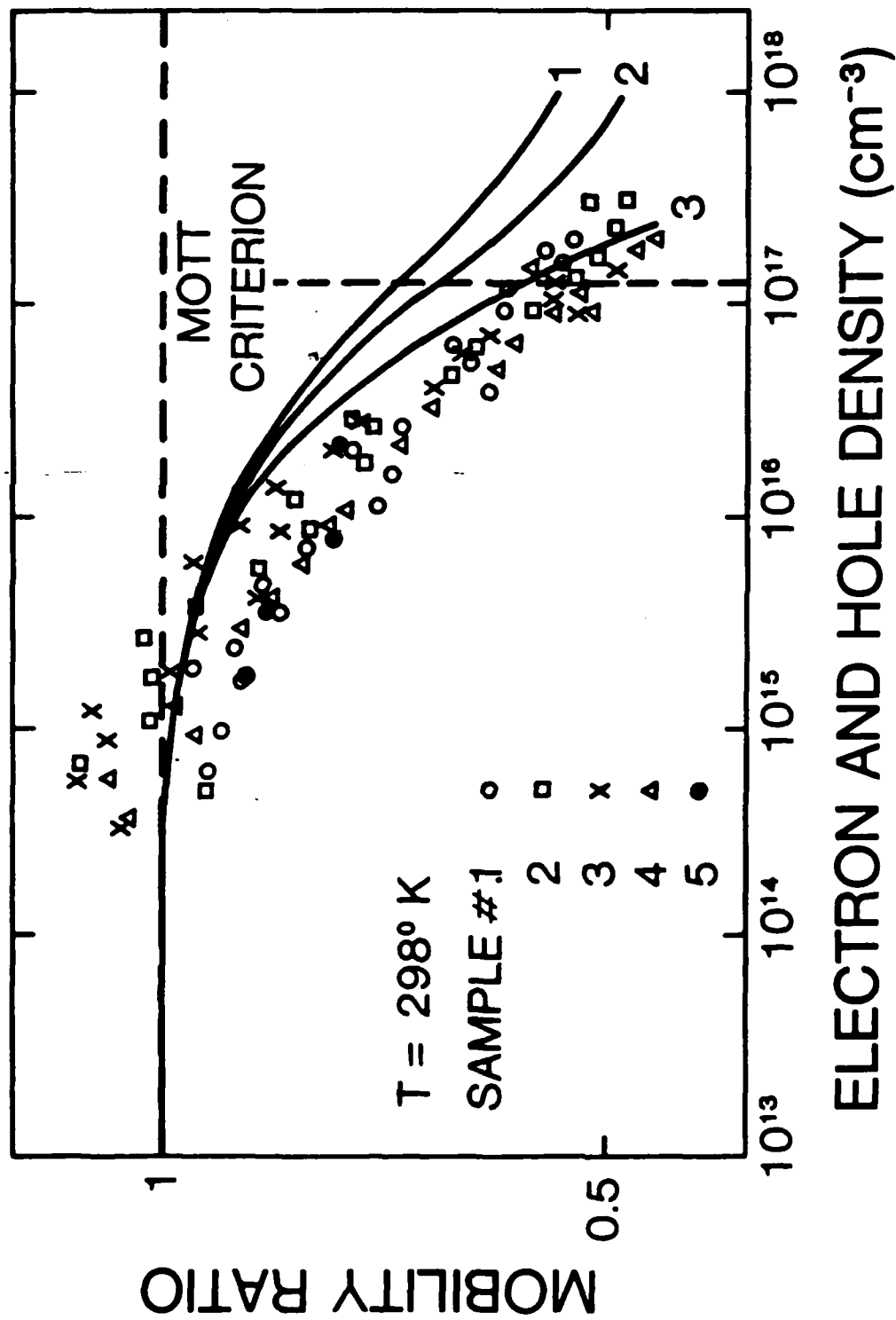
$$\lambda_s \lesssim R a_0 \quad 0.5 \lesssim R \lesssim 1$$

MOTT TRANSITION DENSITY ($R=1$)

$$n_M \approx \frac{E_x^2}{2\pi R^2} \left(\frac{\kappa_0}{e^2} \right)^3 k_B T \left[\frac{\sigma_{\frac{1}{2}}(\eta_e)}{\sigma_{-\frac{1}{2}}(\eta_e)} + \frac{\sigma_{\frac{1}{2}}(\eta_p)}{\sigma_{-\frac{1}{2}}(\eta_p)} \right]$$

Si AND GaP LUMINESCENCE DATA ($T \lesssim 77$ K) SHOW DISAPPEARANCE OF
EXCITON STRUCTURE WHEN $n \gtrsim n_M$

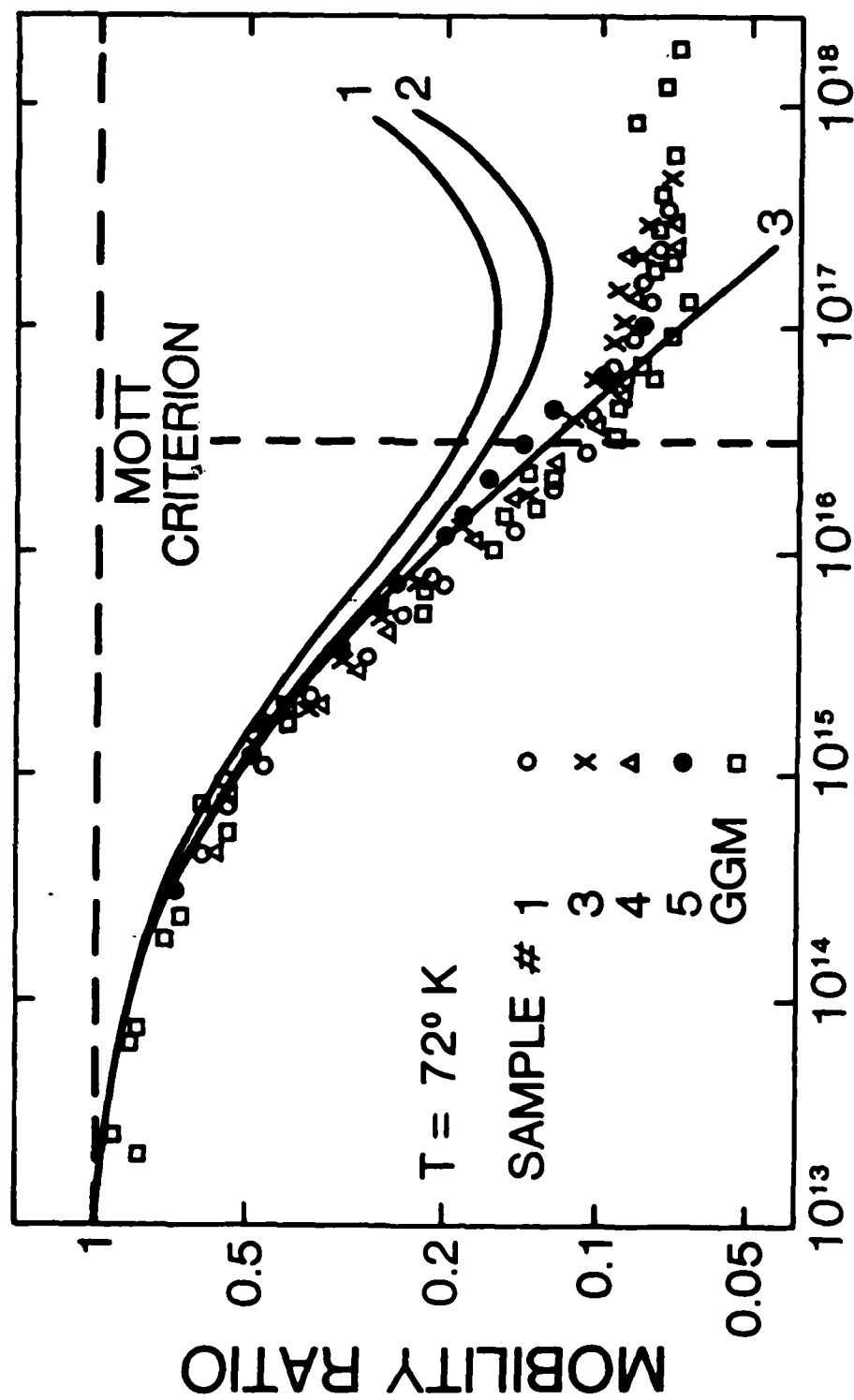




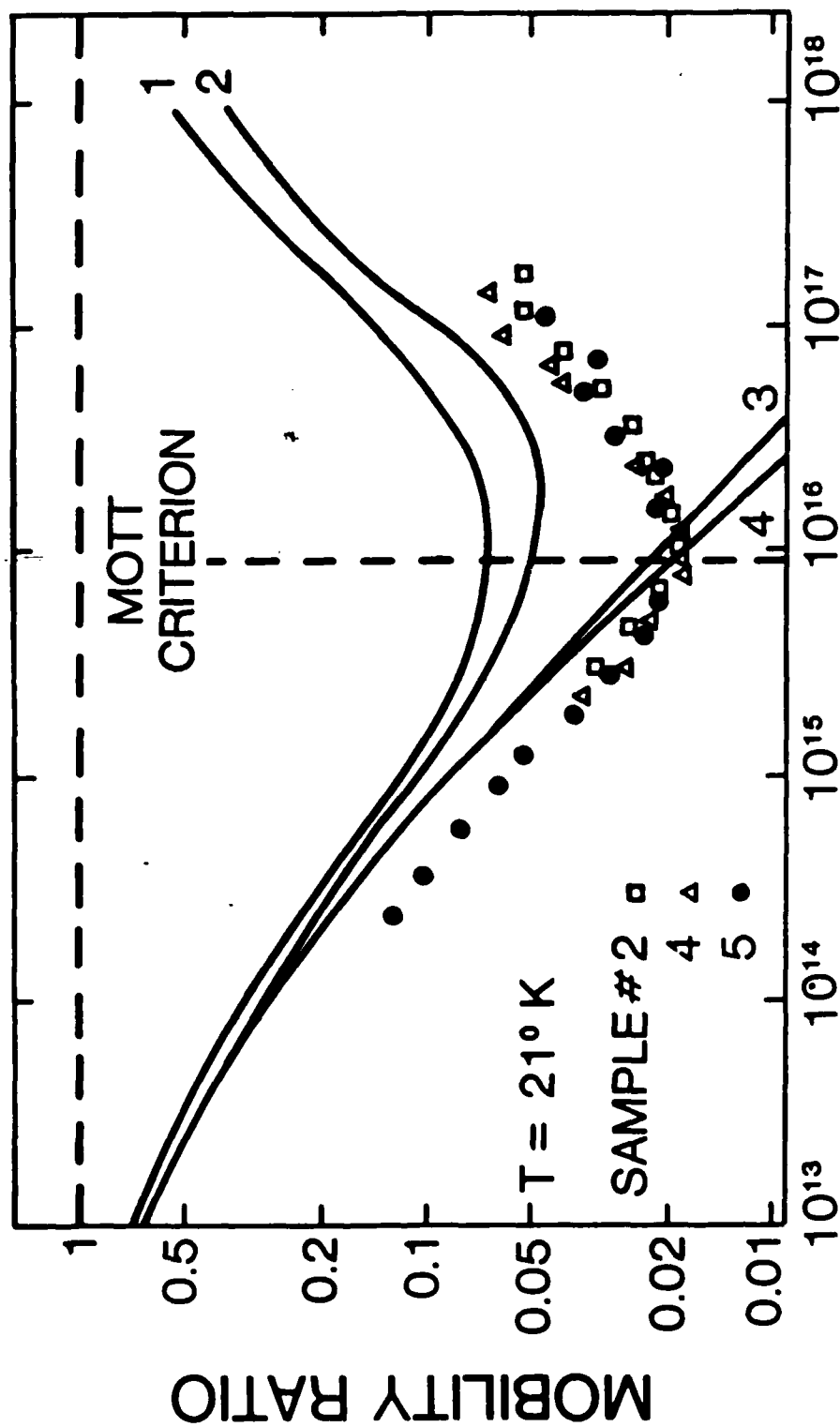
35

HIGH-DENSITY MOBILITY EXPERIMENT IN Ge ($21 < T < 300$ K)

- o FOUR-PROBE CONDUCTIVITY MEASUREMENT
- o PLASMA DENSITIES DETERMINED FROM $3.39 \mu\text{m}$ ABSORPTION
- o UNIFORMITY ACHIEVED FOLLOWING AMBIPOLAR DIFFUSION THROUGH
SAMPLE DEPTH



ELECTRON AND HOLE DENSITY (cm^{-3})



OTHER EXPERIMENTAL WORK

- o SEVERAL STUDIES CONSIDER ONLY $T < 20$ K (E-H DROPLETS, ETC.)
- o BALTRAMIEJUNAS ET AL. (1973) - CdSe AT 100-300 K
 μ DECREASED BY 1.7-5 AT 10^{17} cm^{-3} (LARGE UNCERTAINTY)
- o VAITKUS ET AL. (1975) - Si AT 300 K
LARGE DECREASE IN μ_h , BUT INADEQUATE REDUCTION OF μ_v
DID NOT ACCOUNT FOR EXCITONS
COMPARED WITH FLETCHER THEORY (1957)

46 27

HIGH-DENSITY PLASMA TRANSPORT - THEORY

- o DYNAMIC SCREENING OF E-H INTERACTIONS
- o ELECTRON-HOLE DRAG
- o EXCITON EFFECTS
- o AMBIPOLAR DIFFUSION MOBILITY

REQUIRED FUTURE WORK - THEORY

- o FURTHER INVESTIGATE VALIDITY OF SINGLE-SITE THEORY
- o EXCITON EFFECTS - MOTT TRANSITION
- o HIGH E-FIELD EFFECTS
- o MOST GENERAL CALCULATIONS NOT YET PERFORMED FOR MATERIALS OF GREATEST
PRESENT INTEREST
- o EXAMINE TRANSPORT IN WIDER RANGE OF MATERIALS TO DETERMINE POSSIBLE NEW
DIRECTIONS FOR SWITCH OPTIMIZATION

411 42

REQUIRED FUTURE WORK -- EXPERIMENT

o AT HIGH BIPOLAR PLASMA DENSITIES ($n > 10^{17} \text{ cm}^{-3}$), ALMOST EVERYTHING
REMAINS TO BE DONE

V. PHOTOCONDUCTIVE SWITCHING

PICOSECOND PHOTOCONDUCTORS: PROBLEMS AND PERSPECTIVES

David H. Auston

AT&T Bell Laboratories
Murray Hill, NJ

Picosecond photoconductors have proven to be valuable optoelectronic devices having a wide range of applications¹. Although their very high speed of response is the property that accounts for most applications, there are a number of additional properties that are equally important. Their very high power handling capability has recently been exploited for pulsed power applications in which electrical signals as large as 100 kV and 2kA have been switched by optoelectronic switching². The extremely large dynamic range of photoconductors is determined on the low end by their noise level which is sufficiently low that signals as small as $1 \mu V/\sqrt{Hz}$ can be measured by optoelectronic sampling¹. This sensitivity, combined with their jitter-free response to optical triggering has enabled complete optoelectronic instrumentation systems to be developed for the measurement of high speed electronic devices and circuits with picosecond precision³. This approach has greatly extended the capability for making high speed electronic measurements beyond conventional techniques such as sampling oscilloscopes that are limited to rise-times of 25 ps.

In addition to high speed of response, picosecond photoconductors have the complementary property of very large base bandwidth. For example, a rise-time of 1 ps corresponds to a base bandwidth of approximately 300 GHz. This property has been extensively exploited for millimeter-wave and far-infrared applications. A novel example of this approach is the utilization of picosecond photoconductors as Hertzian dipoles for generating monopulse and single cycles of radiation in the millimeter-wave and far-infrared spectral range⁴. Reciprocity enables these same devices to be used as detectors of electromagnetic pulses so that a complete transmission system can be made having precise timing in which both the transmitting and receiving dipoles are triggered by picosecond optical pulses. Although these experiments have thus far been done with low voltage photoconductors, it is clearly possible to scale up in intensity, enabling very large electromagnetic pulses to be generated and detected. In related work, it has been shown that electro-optic materials can be used to generate and detect electromagnetic pulses with bandwidths extending as high as 5THz⁵.

Some of the problems and challenges that remain are [1] an improved understanding of electrical contacts to photoconductors under conditions of very high bias voltage and illumination intensity, [2] improvements in materials to achieve a better compromise between speed and sensitivity, [3] the development of better circuits having very large base bandwidths for handling extremely short electrical transients, [4] improved circuit models that can describe both the radiative and lumped circuit element properties of picosecond photoconductors, and [5] new methods of dealing with very high voltage transients to prevent dielectric breakdown. These and other problems will ensure that picosecond photoconductors will continue to be a vital and exciting topic of research.

References

- [1] see, for example: D. H. Auston, "Picosecond Photoconductors: Physical Properties and Applications," in *Picosecond Optoelectronic Devices*, ed C. H. Lee, Academic Press, New York (1984).
- [2] W. C. Nunnally and R. B. Hammond, "Optoelectronic switch for pulsed power", chapter 12 of *Picosecond Optoelectronic Devices*, ed C. H. Lee, Academic Press, New York (1984).
- [3] D. H. Auston and P. R. Smith, "Picosecond Optical Electronics for High Speed Instrumentation," *Laser Focus*, April 1982, pp. 89-93.
- [4] D. H. Auston and K. P. Cheung, "Picosecond Photoconducting Hertzian Dipoles," *Appl. Phys. Lett.*, **45**, pp. 284-286 (1984).
- [5] D. H. Auston, K. P. Cheung, J. A. Valdmanis, and D. A. Kleinman, "Cherenkov Radiation from Femtosecond Optical Pulses in Electrooptic Media", *Phys. Rev. Lett.*, **53**, pp. 1555-1558 (1984).

VIEWGRAPHS

PICOSECOND PHOTOCONDUCTORS:
PROBLEMS AND PERSPECTIVES

D. H. AUSTON

TOP
DO NOT AFFIX OVERLAYS ALONG THIS SURFACE

**PICOSECOND PHOTOCONDUCTORS:
PROBLEMS AND PERSPECTIVES**

K. P. Cheung
J. A. Valdmanis
D. A. Kleinman
P. R. Smith

DO NOT AFFIX OVERLAYS ALONG THIS SURFACE

OUTLINE

- Basic Concepts.
- Devices.
- Physical Properties.
- Circuit Models.
- Speed of Response.

TOP
DO NOT AFFIX OVERLAYS ALONG THIS SURFACE

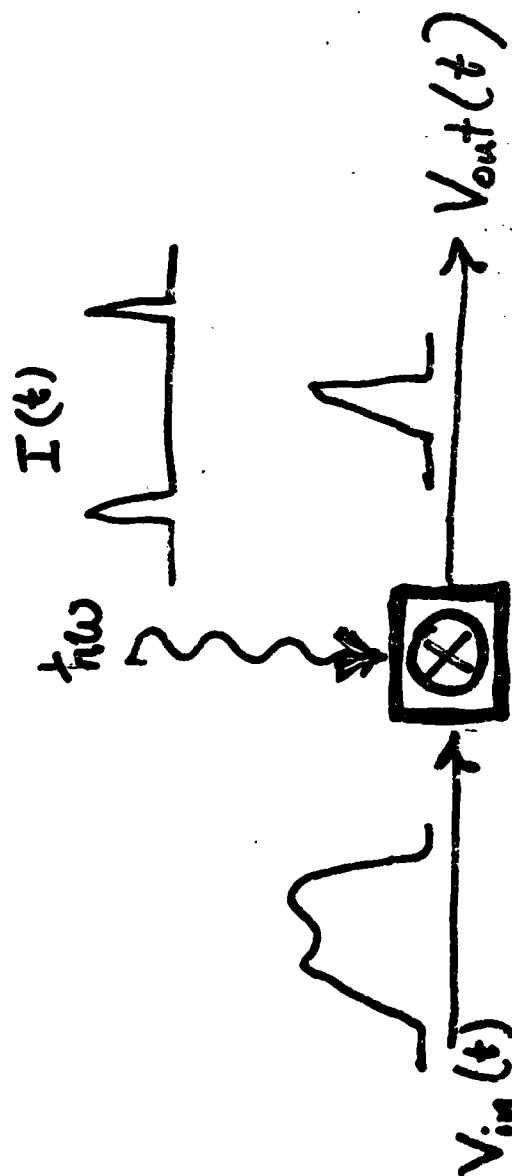
OPTOELECTRONIC MECHANISMS

- Photoconductivity(o-e).
- Electro-optic effect(e-o).
- Optical rectification(o-e).
- Impurities in polar crystals(o-e).
- Electro-absorption(e-o).
- Faraday rotation(m-o).
- Inverse Faraday effect(o-m).
- Pyroelectricity(o-t-e).

CHARACTERISTICS OF PHOTOCONDUCTORS

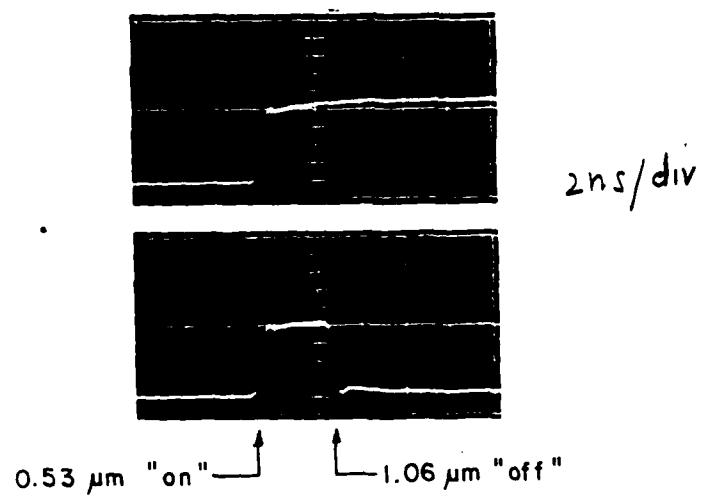
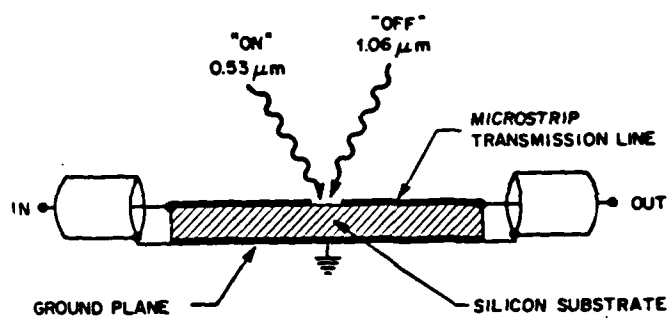
- Very high speed($< 1\text{ps}$).
- Very high power(100kV, 2kA).
- Low noise($< 1\mu\text{V}/\sqrt{\text{Hz}}$).
- Large bilinear dynamic range(160db).
- Jitter-free.
- Wide spectral range($h\nu > E_g$).
- Flexible operating environment.

TOP
DO NOT AFFIX OVERLAYS ALONG THIS SURFACE



APPLICATIONS OF PHOTOCONDUCTORS

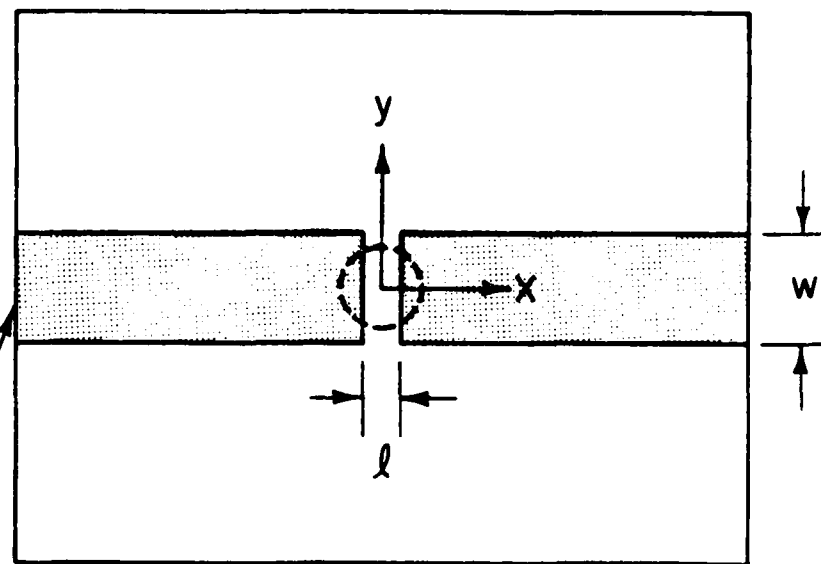
- Electrical impulse generators.
- Electrical Sampling gates.
- RF burst generators.
- RF mixers.
- Frozen wave generators.
- Transmitting and receiving Hertzian dipoles.
- Microwave and millimeter wave modulators.
- Optical detectors.
- Far-infrared detectors.
- Pulsed power.
- Picosecond instrumentation systems.



PICOSECOND ELECTRONIC SWITCH

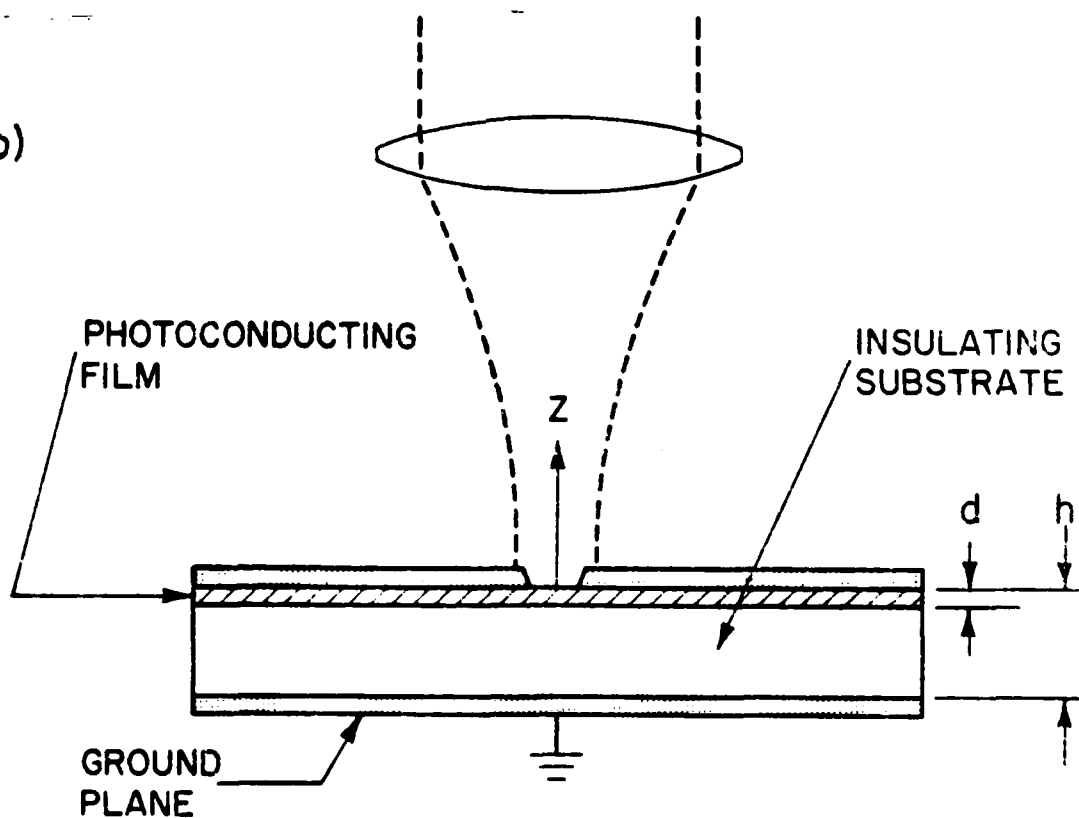
TOP
DO NOT AFFIX OVERLAYS ALONG THIS SURFACE

(a)



MICROSTRIP ELECTRODES

(b)



PHOTOCONDUCTIVITY

$$\sigma [x, y, z] = [1 - R] \frac{\alpha e \mu}{\hbar \omega} \epsilon [x, y] e^{-\alpha z}$$

$$\epsilon [x, y] = \frac{2 \epsilon_p}{\pi w_0^2} \exp \left[- \frac{2 [x^2 + y^2]}{w_0^2} \right]$$

PHOTOCONDUCTANCE

$$G = \frac{1}{V_g^2} \int d^3x \sigma \underline{E} \cdot \underline{E}$$

DIELECTRIC RELAXATION

LOCAL: $\tau = \frac{\epsilon}{\sigma}$

MACROSCOPIC: $\tau = \frac{C}{G} = \frac{\int d^3 x \epsilon \underline{E} \cdot \underline{E}}{\int d^3 x \sigma \underline{E} \cdot \underline{E}}$

RELAXED FIELD

$$\nabla \cdot \mathbf{j} = - \frac{\delta \rho}{\delta t} = 0$$

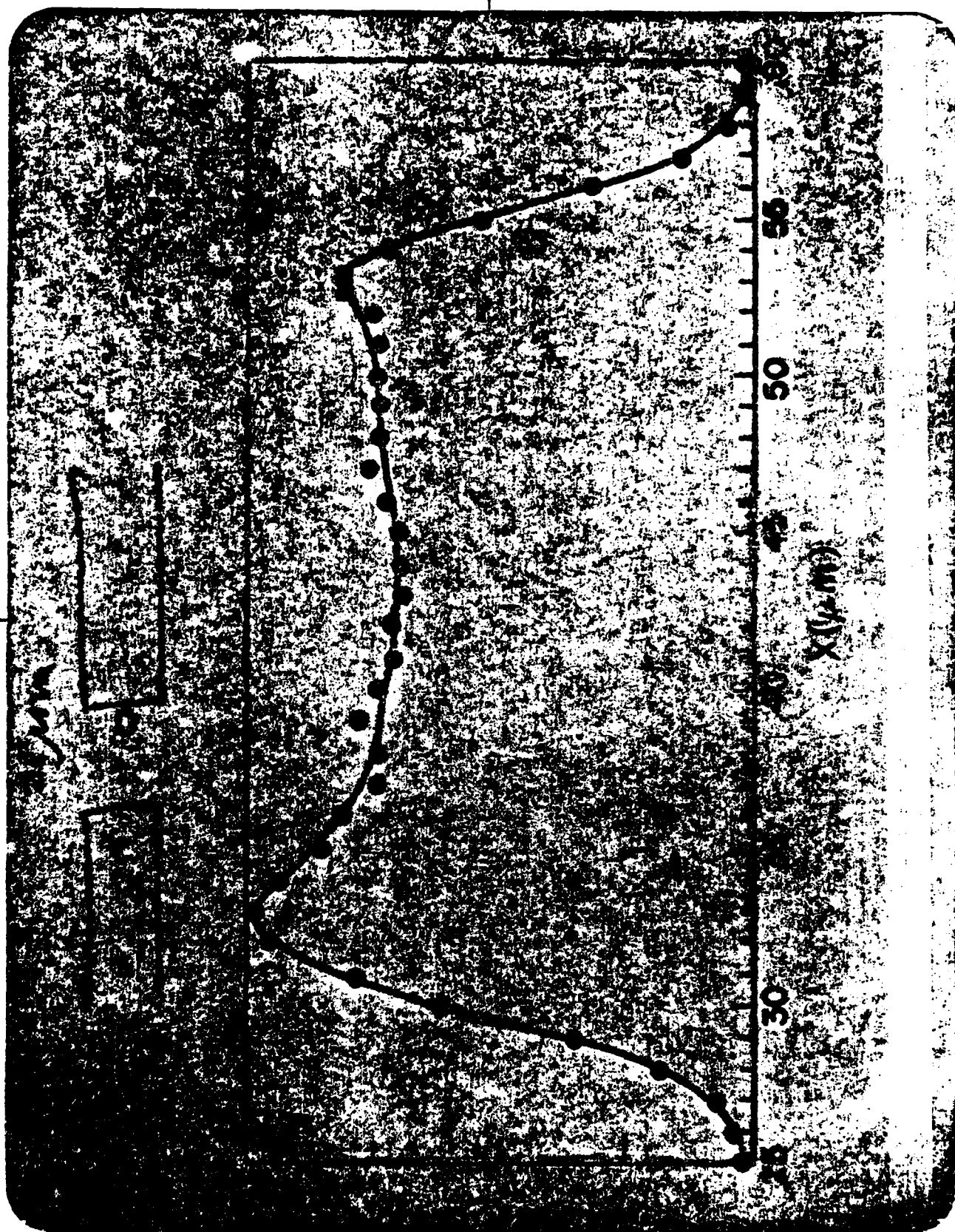
$$E[\mathbf{x}] \propto \frac{1}{\sigma[\mathbf{x}]}$$

$$G = \int \int d\mathbf{x} d\mathbf{y} \left[\int \frac{d\mathbf{x}}{\sigma[\mathbf{x}]} \right]^{-1}$$

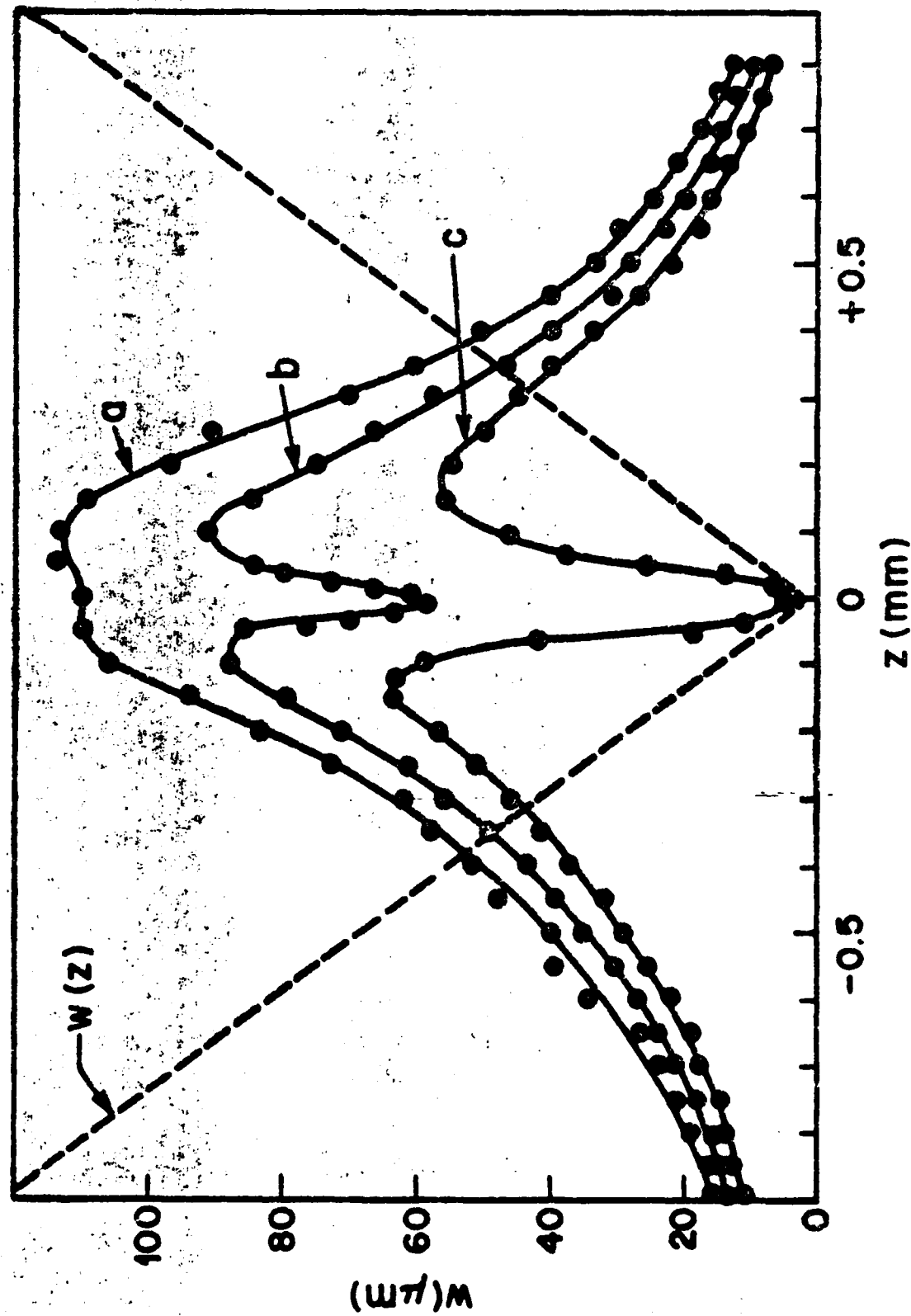
STATIC FIELD

$$E[x] = \frac{2V_g}{\pi Q} \sqrt{1 - \left(\frac{2x}{Q}\right)^2}$$

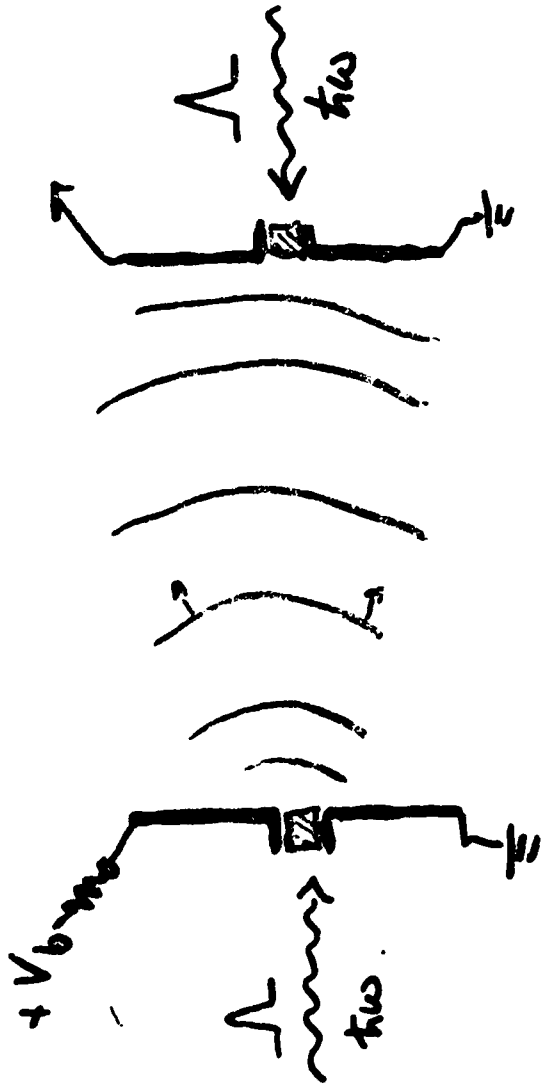
DO NOT AFFIX OVERLAYS ALONG THIS SURFACE



TOP
DO NOT AFFIX OVERLAYS ALONG THIS SURFACE



PHOTOCONDUCTING HERTZIAN DIPOLES



$$E \sim \frac{1}{4\pi\epsilon} \left\{ \vec{P}_{13} + \frac{\vec{P}_{12}}{c r^2} + \ddot{\vec{P}}_{12} \right\}$$

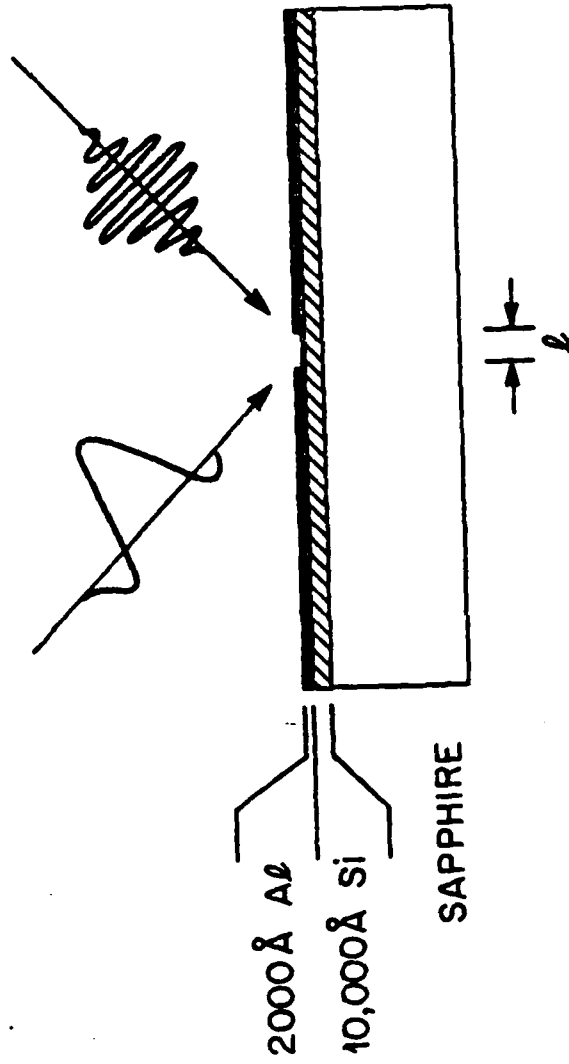
RADIATION EFFICIENCY

$$\eta_{RAD} = \frac{W_{rad.}}{W_{switch}} = \frac{1}{4\pi\epsilon^2} \frac{l^2}{z_0^2 c^2} \frac{1}{\epsilon_p^2}$$

$$= 1$$

$$\text{if } \epsilon_p \sim 1 \text{ ps}$$

$$l \sim 1 \text{ mm}$$



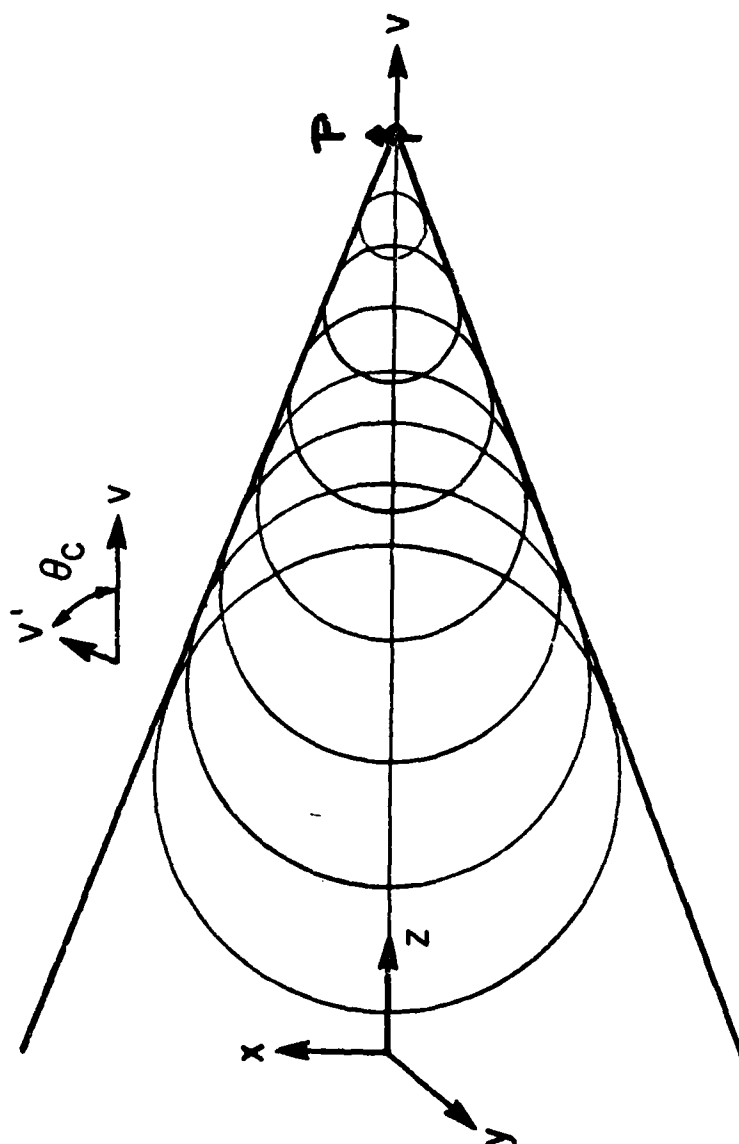
DO NOT AFFIX OVERLAYS ALONG THIS SURFACE

OPTICAL RECTIFICATION NONLINEAR SUSCEPTIBILITY

$$P_i(\omega=\omega_1-\omega_2) = \chi_{ijk} E_j(\omega_1) E_k^*(\omega_2)$$



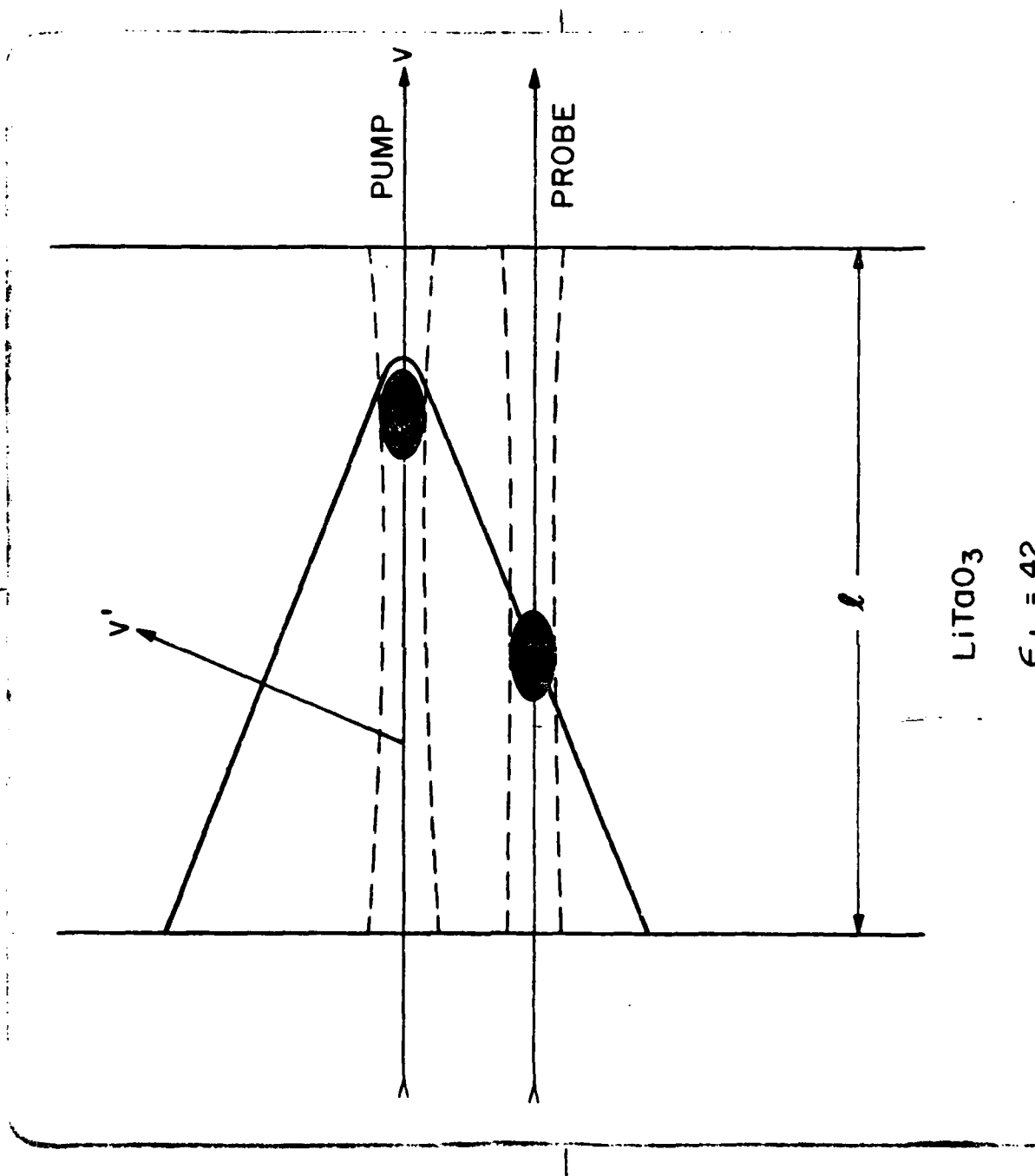
DO NOT AFFIX OVERLAYS ALONG THIS SURFACE



NOTES:

SEQUENCE NO. _____

TOP
DO NOT AFFIX OVERLAYS ALONG THIS SURFACE



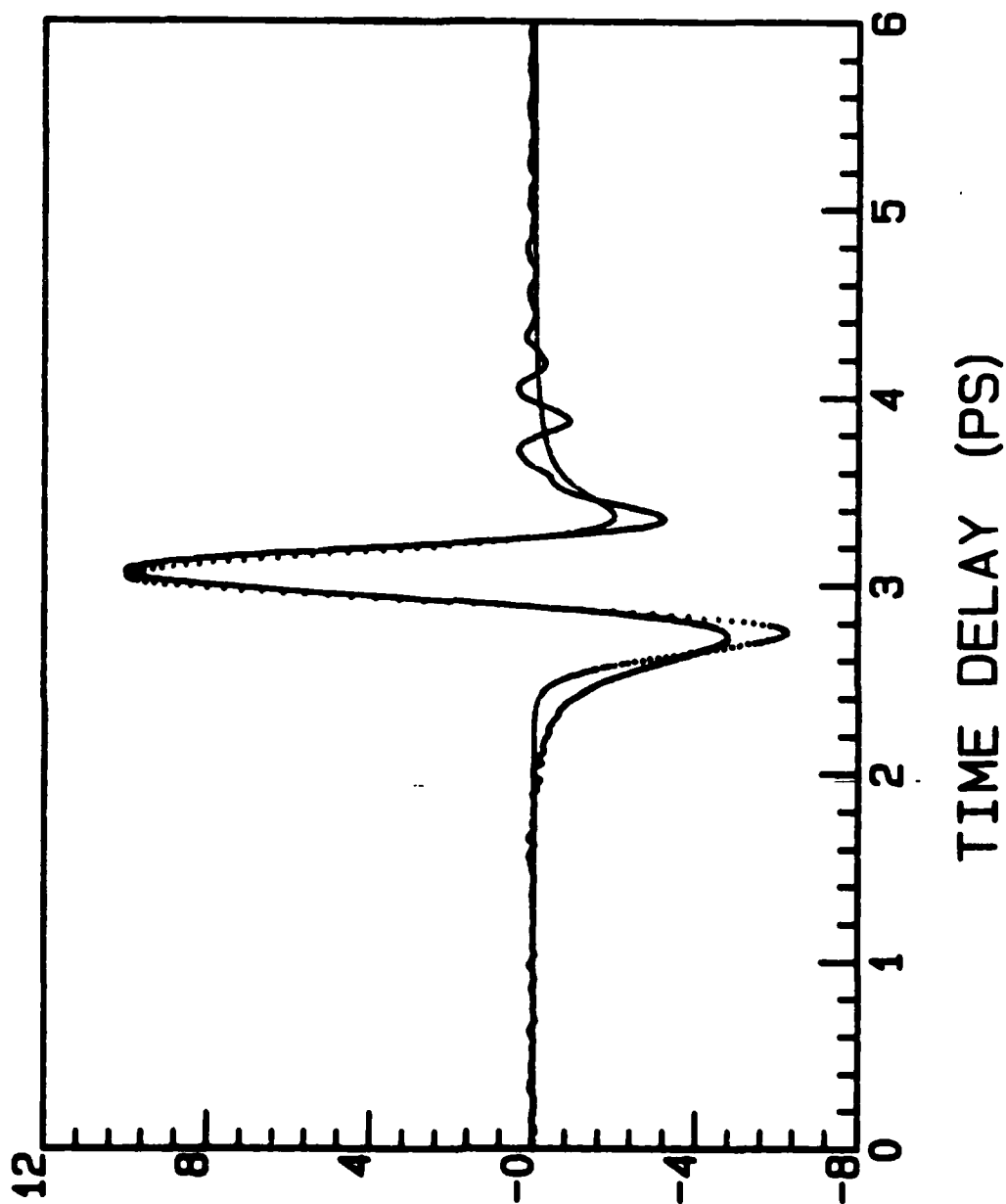
LiTaO_3

$\epsilon_{dc} = 42$

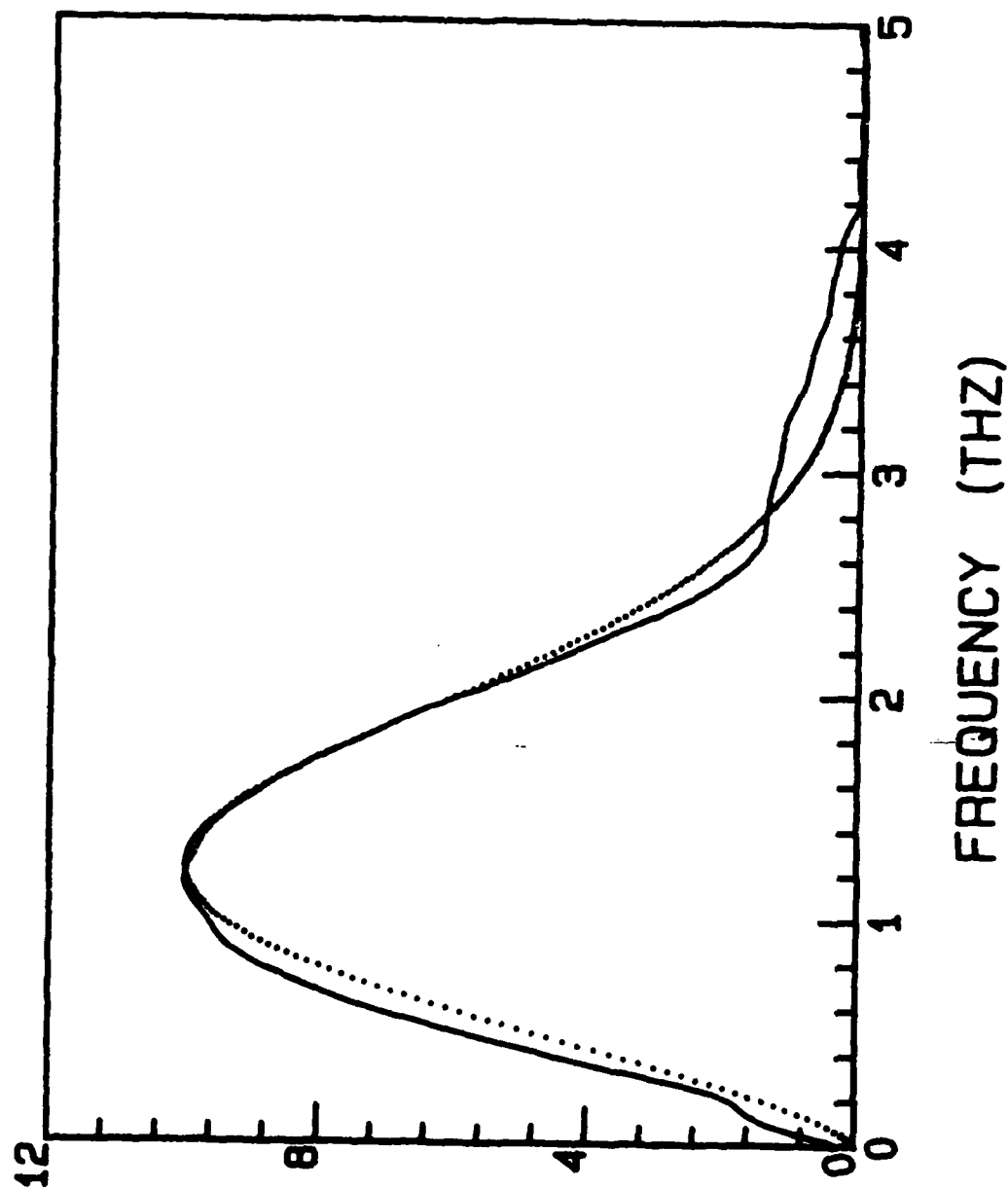
$\epsilon_{op} = 4.8$

DO NOT AFFIX OVERLAYS ALONG THIS SURFACE

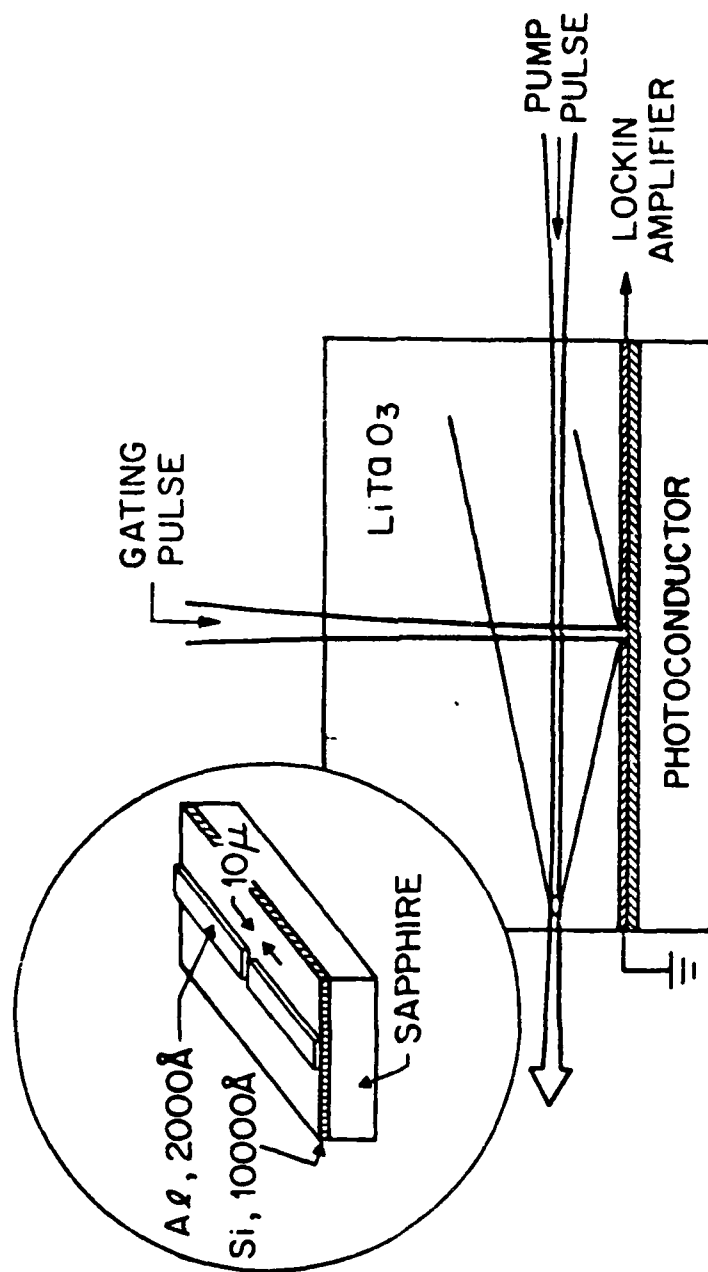
EO CERENKOV WAVEFORM

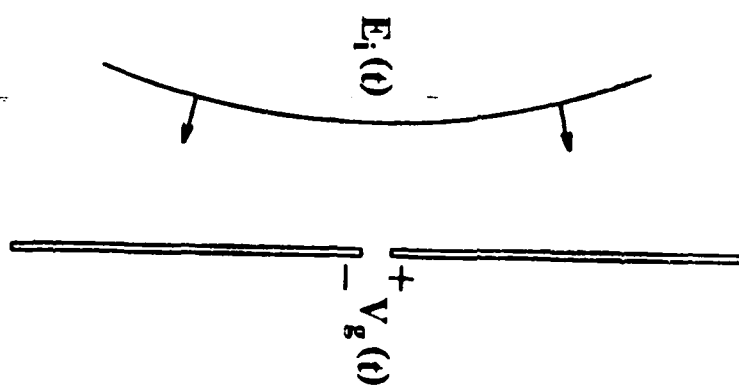


FREQUENCY SPECTRUM

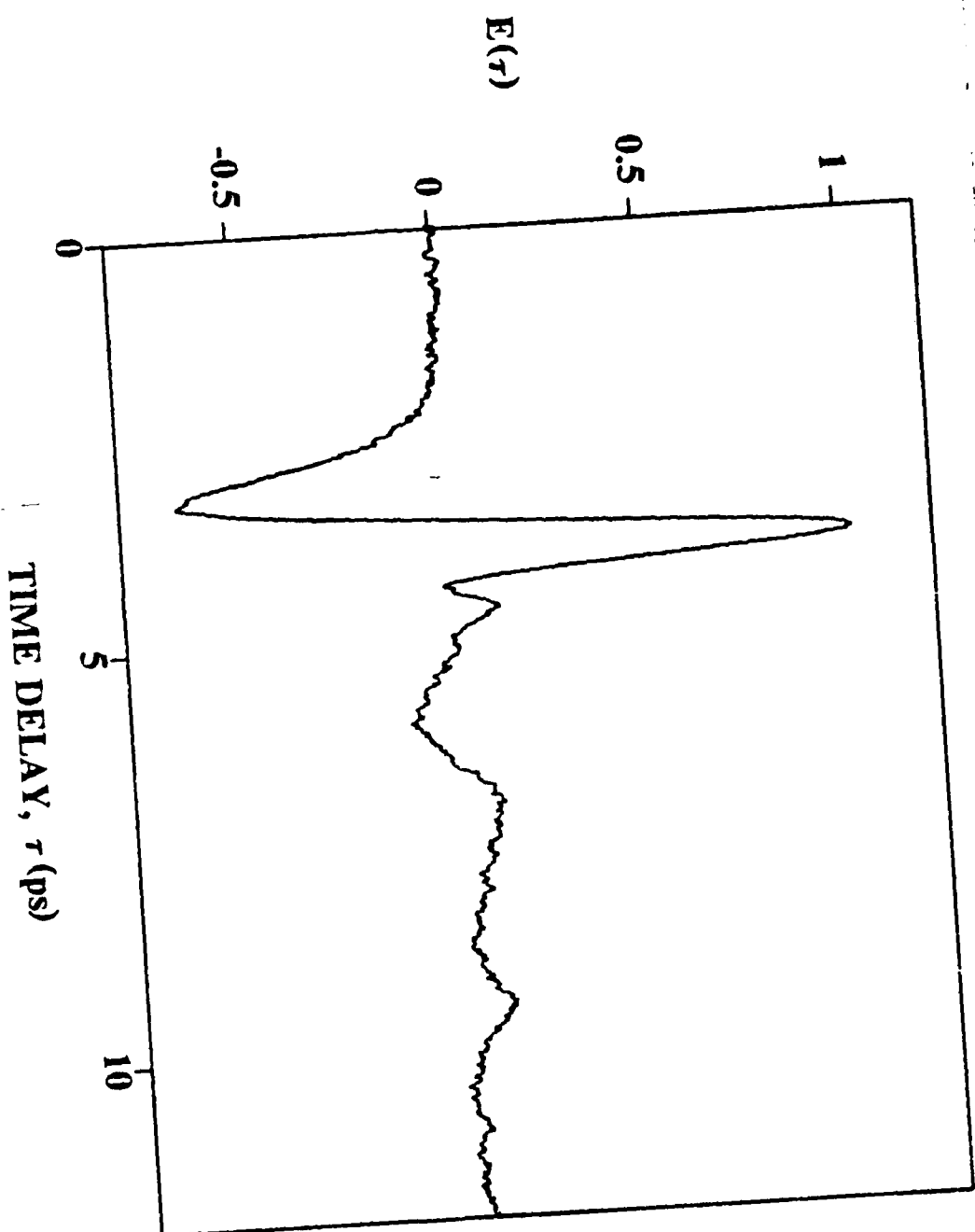


771

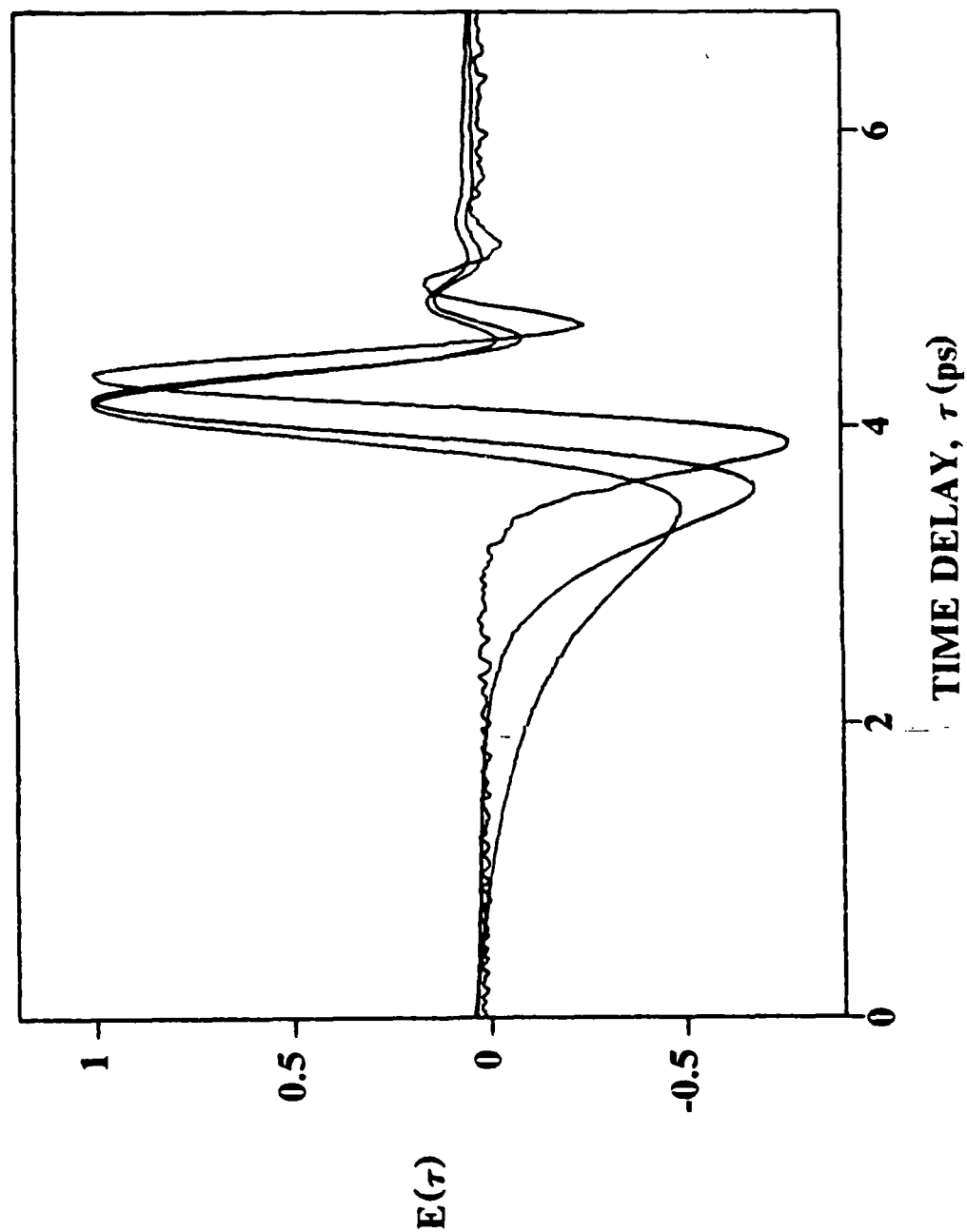




DO NOT AFFIX OVERLAYS ALONG THIS SURFACE



TOP
DO NOT AFFIX OVERLAYS ALONG THIS SURFACE



TOP

DO NOT AFFIX OVERLAYS ALONG THIS SURFACE

CONCLUSIONS

- Photoconductors are flexible, high speed circuit elements.
- Circuit Models have limited range of validity.
- Dielectric relaxation affects response.
- Photoconductors are effective radiating antennas.
- Response times can be less than one picosecond.

ions as a means of introducing a predetermined defect density into crystalline silicon-on-sapphire films without making the material amorphous [3]. With ion doses ranging from 10^{13} to 3×10^{15} ions cm^{-2} , we measured carrier relaxation times ranging from 100 to 8 psec and carrier mobilities ranging from 100 to 12 cm^2/Vsec . Recently [6], we made the first measurements of picosecond photoconductivity in thin films of polycrystalline CdTe grown by photon-assisted Organometallic Chemical Vapor Deposition (OMCVD). The fastest of these photoconductors had a carrier relaxation time of 3.7 psec and a carrier mobility of 59 cm^2/Vsec .

In summary, disordered semiconductors can provide a relatively cheap source of ultrahigh speed photoconducting devices without sophisticated diode structures or ultrapure semiconductors. In many instances, disordered semiconductors possess high dark resistivity and high dielectric strength in addition to the defect structure facilitating Ohmic behavior.

References

- [1] D. H. Auston, P. Lavallard, N. Sol, and D. Kaplan, "An amorphous silicon photodetector for picosecond pulses," Appl. Phys. Lett. 36, 66 (1980).
- [2] A. M. Johnson, D. H. Auston, P. R. Smith, J. C. Bean, J. P. Harbison, and A. C. Adams, "Picosecond transient photocurrents in amorphous silicon," Phys. Rev. B23, 6816 (1981).
- [3] P. R. Smith, D. H. Auston, A. M. Johnson, and W. M.

- Ausgustyniak, "Picosecond photoconductivity in radiation-damaged silicon-on-sapphire films," Appl. Phys. Lett. 38, 47 (1981).
- [4] A. P. DeFonzo, "Picosecond photoconductivity in germanium films," Appl. Phys. Lett. 39, 480 (1981).
- [5] W. Margulis and W. Sibbett, "Picosecond CdSe photodetector," Appl. Phys. Lett. 42, 975 (1983).
- [6] A. M. Johnson, D. W. Kisker, W. M. Simpson, and R. D. Feldman, "Picosecond photoconductivity in polycrystalline CdTe films prepared by uv enhanced OMCVD," Proceedings of the Topical Meeting on Picosecond Electronics and Optoelectronics, March 13-15, 1985, Incline Village, Nevada, to be published by Springer-Verlag.
- [7] D. H. Auston, A. M. Johnson, P. R. Smith, and J. C. Bean, "Picosecond optoelectronic detection, sampling, and correlation measurements in amorphous semiconductors," Appl. Phys. Lett. 37, 371 (1980).
- [8] See for example, A. M. Johnson and W. M. Simpson, "Tunable femtosecond dye laser synchronously pumped by the compressed second harmonic of Nd:YAG," J. Opt. Soc. Am. B 2, 619 (1985).
- [9] A. M. Johnson, A. M. Glass, D. H. Olson, W. M. Simpson, and J. P. Harbison, "High quantum efficiency amorphous silicon photodetectors with picosecond response times," Appl. Phys. Lett. 44, 450 (1984).

VIEWGRAPHS

PICOSECOND RELAXATION OF PHOTOEXCITED CARRIERS
IN DISORDERED SEMICONDUCTORS

A. M. JOHNSON

TOP
DO NOT AFFIX OVERLAYS ALONG THIS SURFACE

Picosecond Relaxation Of Photoexcited Carriers In Disordered Semiconductors

Anthony M Johnson

AT&T Bell Laboratories
Holmdel, New Jersey

NOTES:

TOP
DO NOT AFFIX OVERLAYS ALONG THIS SURFACE

EV
(UHV - EVAPORATED
a-Si)

$N_f \sim 10^{19} - 10^{20} \text{ cm}^{-3}$

5 ps

11 ps FWHM

$\tau_f = 4 \text{ ps}$

11 ps

FWHM

5.0 ps

6.6 ps/11

1.5 ps

propagate
delay

$\tau = 4 \text{ ps}$

5 mV

noise

of 6%

NOTES:

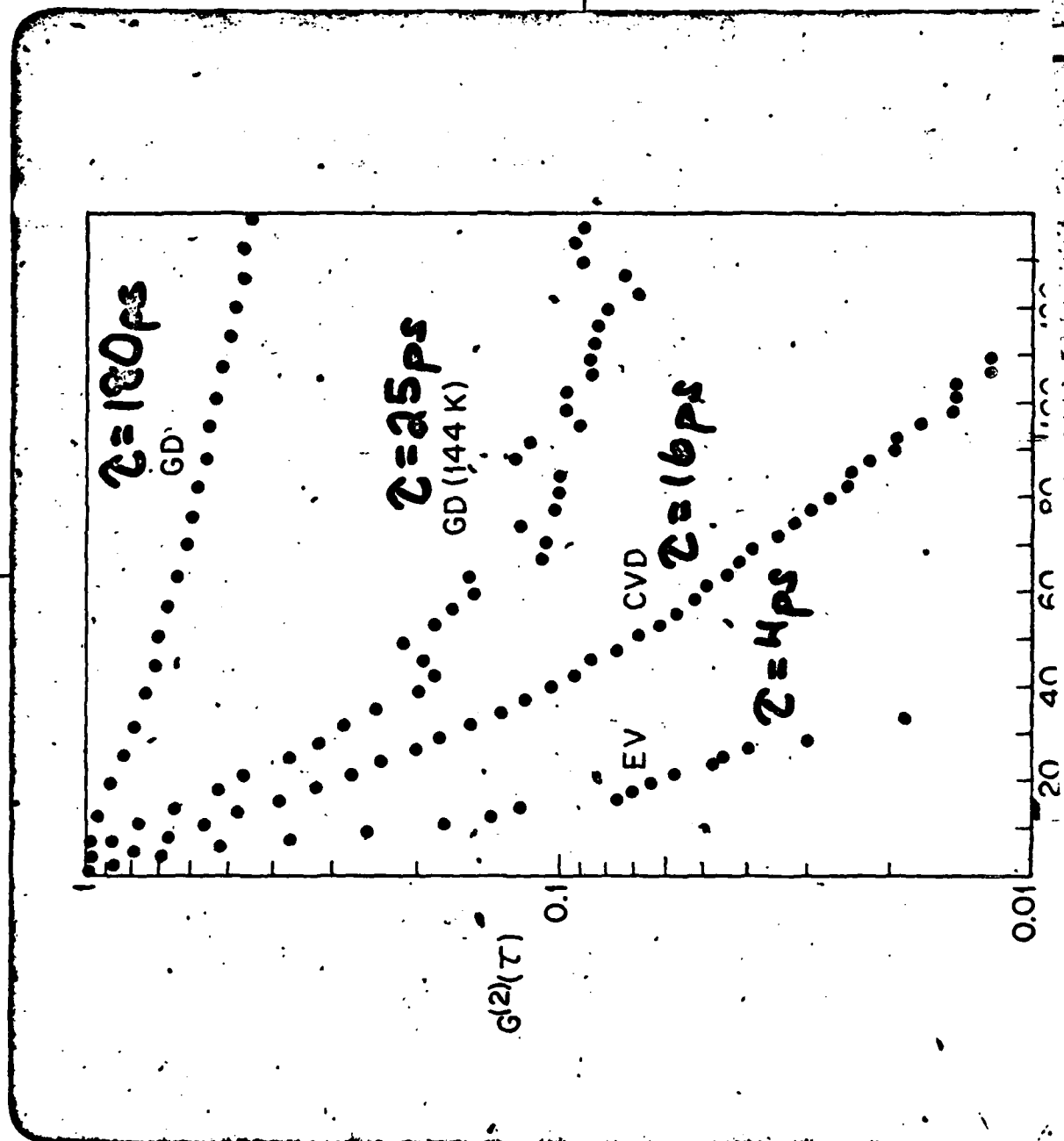
(18)

SEQUENCE NO. _____

TOP

DO NOT AFFIX OVERLAYS ALONG THIS SURFACE

20



GD 200ps (21)

GD (144) 25ps

CVD 16

EV 4

NOTES:

TOP
DO NOT AFFIX OVERLAYS ALONG THIS SURFACE

Photoconductivity

$$Q = \int i(t) dt ; i(t) = i_0 e^{-t/\tau}$$

$$Q = \eta (1-R) (1-e^{-\alpha d}) \frac{e}{h\nu} \mu_r \epsilon_p \frac{V_p^2}{d^2}$$

TOP
DO NOT AFFIX OVERLAYS ALONG THIS SURFACE

Amorphous Silicon

Sample	N_t (cm^{-3})	f_d ($\Omega\text{-cm}$)	μ_{2r} (cm^2/V)	r_r (ps)	μ (cm^2/Vs)
EV	10^{19-20}	2800	4.2×10^{-12}	4	1.1
CVD	10^{18-19}	9.2×10^6	2.3×10^{-11}	16	1.4
GD	$< 10^{16}$	10^8	3.2×10^{-10}	180	1.8

NOTES:

TOP
DO NOT AFFIX OVERLAYS ALONG THIS SURFACE

23

Photoconductivity In Disordered Semiconductors

- High Defect Density Semiconductors Tend To Exhibit Ohmic Behavior
- Small Metal-Semiconductor Schottky Barrier Width
- Efficient Tunneling Through Thin Barrier
- Linear Photoconductor \rightarrow Transport Parameters

Picosecond Photoconductivity in Radiation Damaged Semiconductors

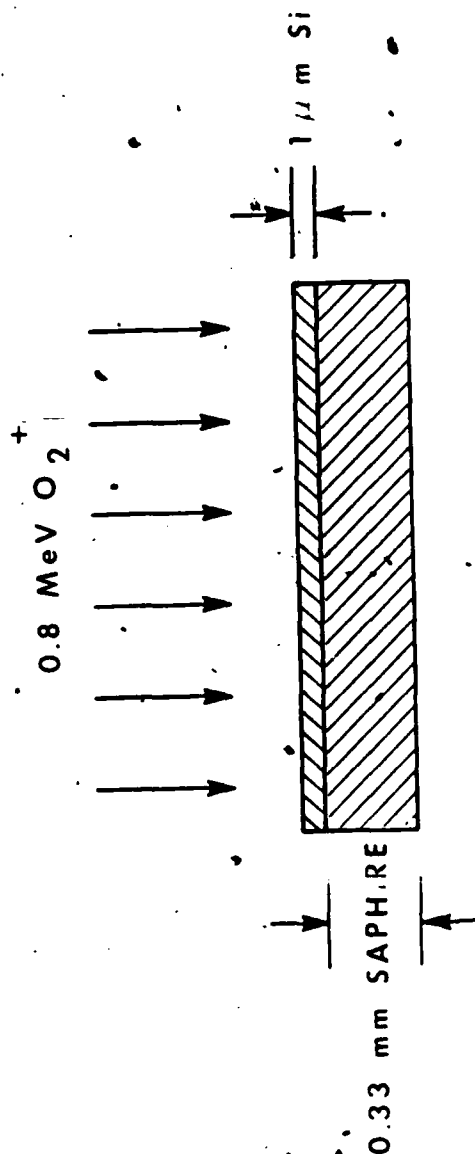
SOS - Smith, Auston, Johnson & Augustyniak (1981).

InP - Foyt, Leonberger & Williamson (1982).

GaAs - Auston & Smith (1982).

InGaAs - Downey, Martin, Mahary &
Lonnier (1985).

Silicon-On-Sapphire



Undamaged SOS: $\tau_p \sim 750 \text{ ps}$
 $\mu \sim 200 \text{ cm}^2/\text{Vs}$

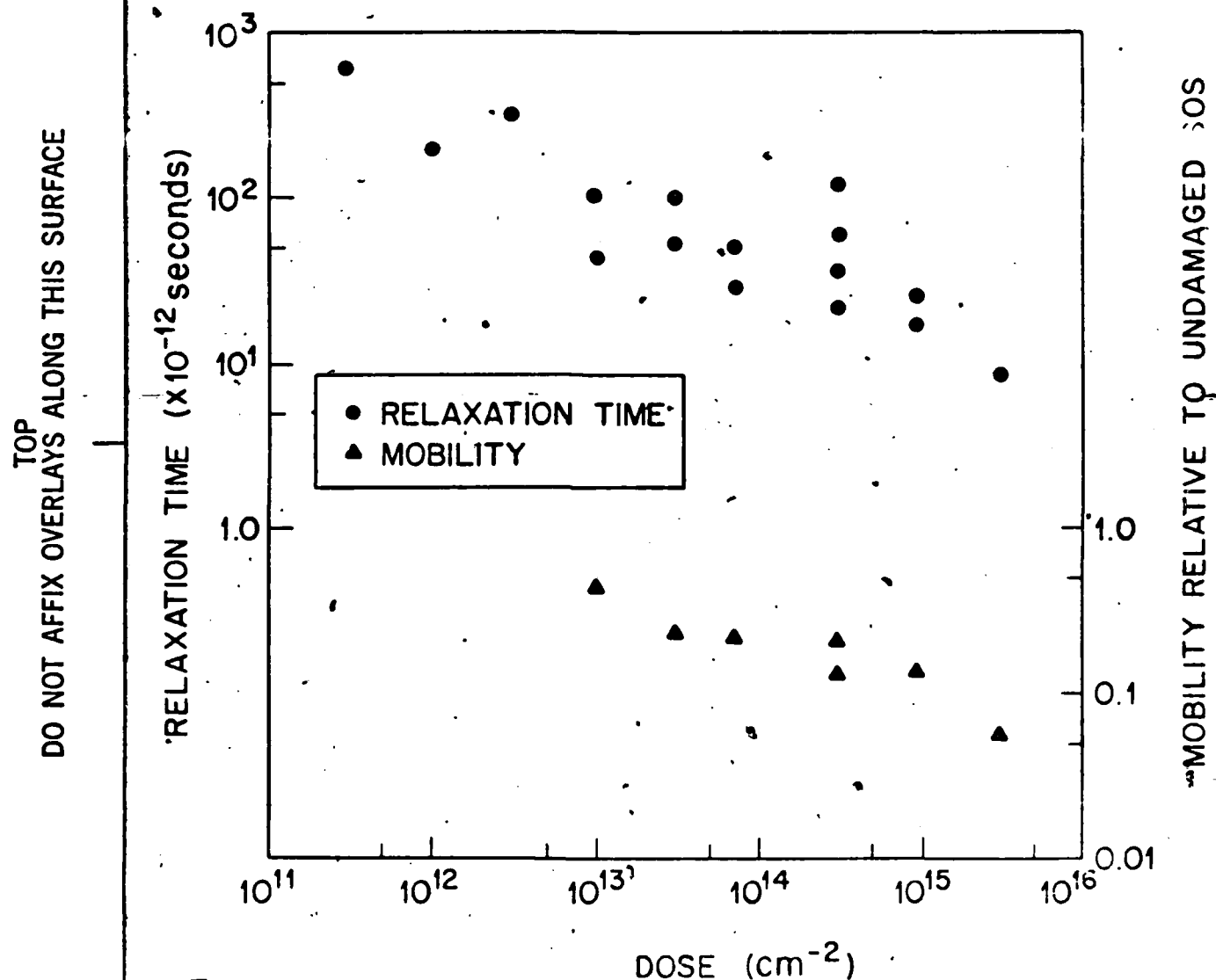


SEQUENCE NO. _____

VG. NO. _____

$$\tau_r = 22 \text{ ps}$$

Radiation-Damaged Silicon-On-Sapphire



Ex: Dose $3 \times 10^{14} \text{ cm}^{-2}$
 $\mu = 40 \text{ cm}^2/\text{Vs}$
 $\tau_r = 22 \text{ ps}$

Undamaged SOS: $\tau_r \sim 750 \text{ ps}$

$\mu \sim 200 \text{ cm}^2/\text{Vs}$

NOTES:

28

TOP
DO NOT AFFIX OVERLAYS ALONG THIS SURFACE

Picosecond Photoconductivity In Polycrystalline Semiconductors

Ge - DeFonzo (1981)

CdSe - Margulis & Sibbett (1983)

RD-Si - Hammond & N. Johnson (1985)

CdTe - Johnson, Kisker, Simpson,
& Feldman (1985)

TOP
DO NOT AFFIX OVERLAYS ALONG THIS SURFACE

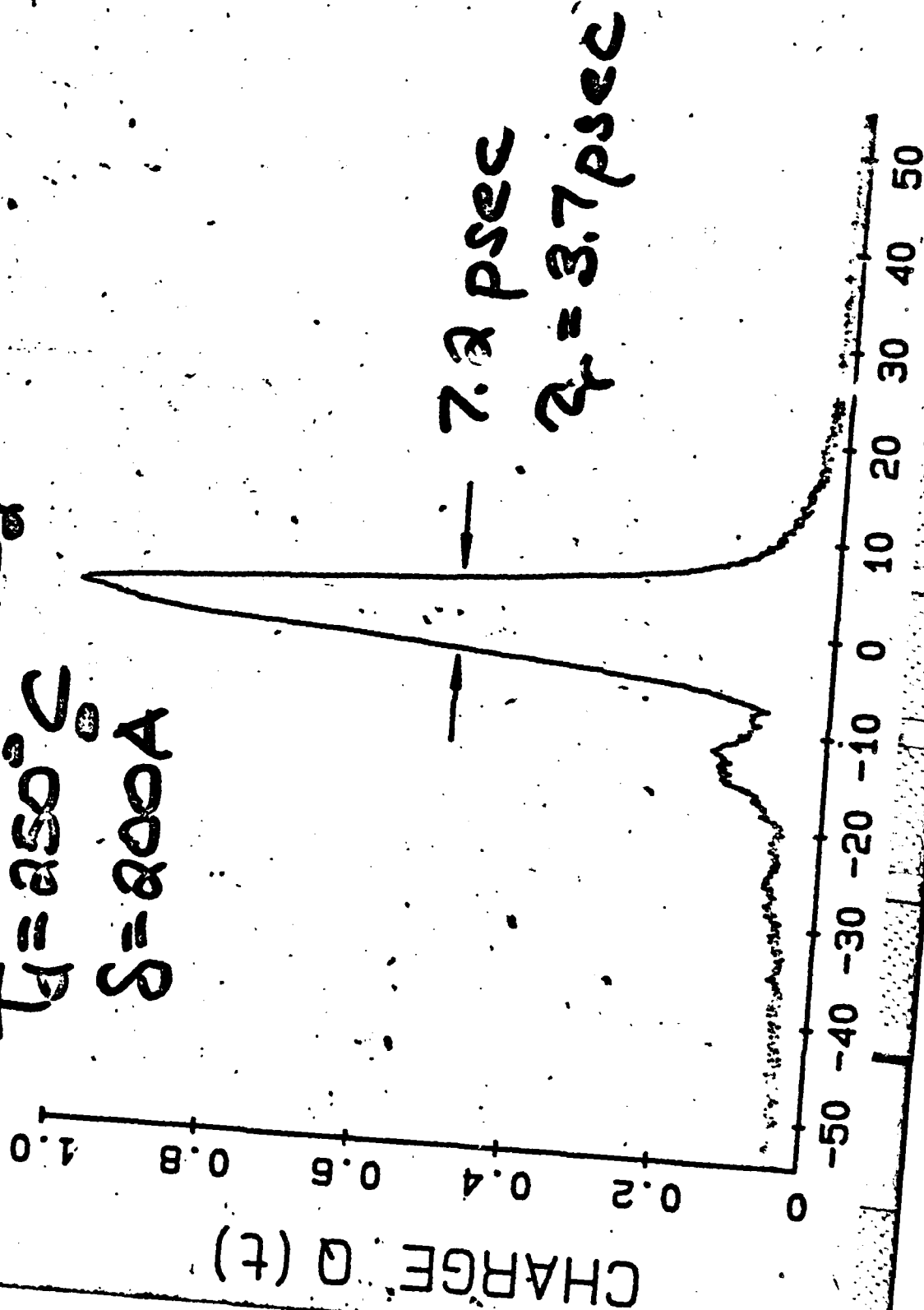
OMCVD CdTe

- 200Å Grain Polycrystalline CdTe On GaAs + SiO₂
- Single Crystal CdTe On (100) GaAs
- Variable Dark Conductivity With Cd/Te Ratio In Gas Phase
- Visible-Infrared Tunable Band Gap With The Incorporation Of Hg \rightarrow Hg_{1-x}Cd_x

NOTES:

TOP
DO NOT AFFIX OVERLAYS ALONG THIS SURFACE

CdTe on SiO₂
T_d = 250°C
S = 200 Å



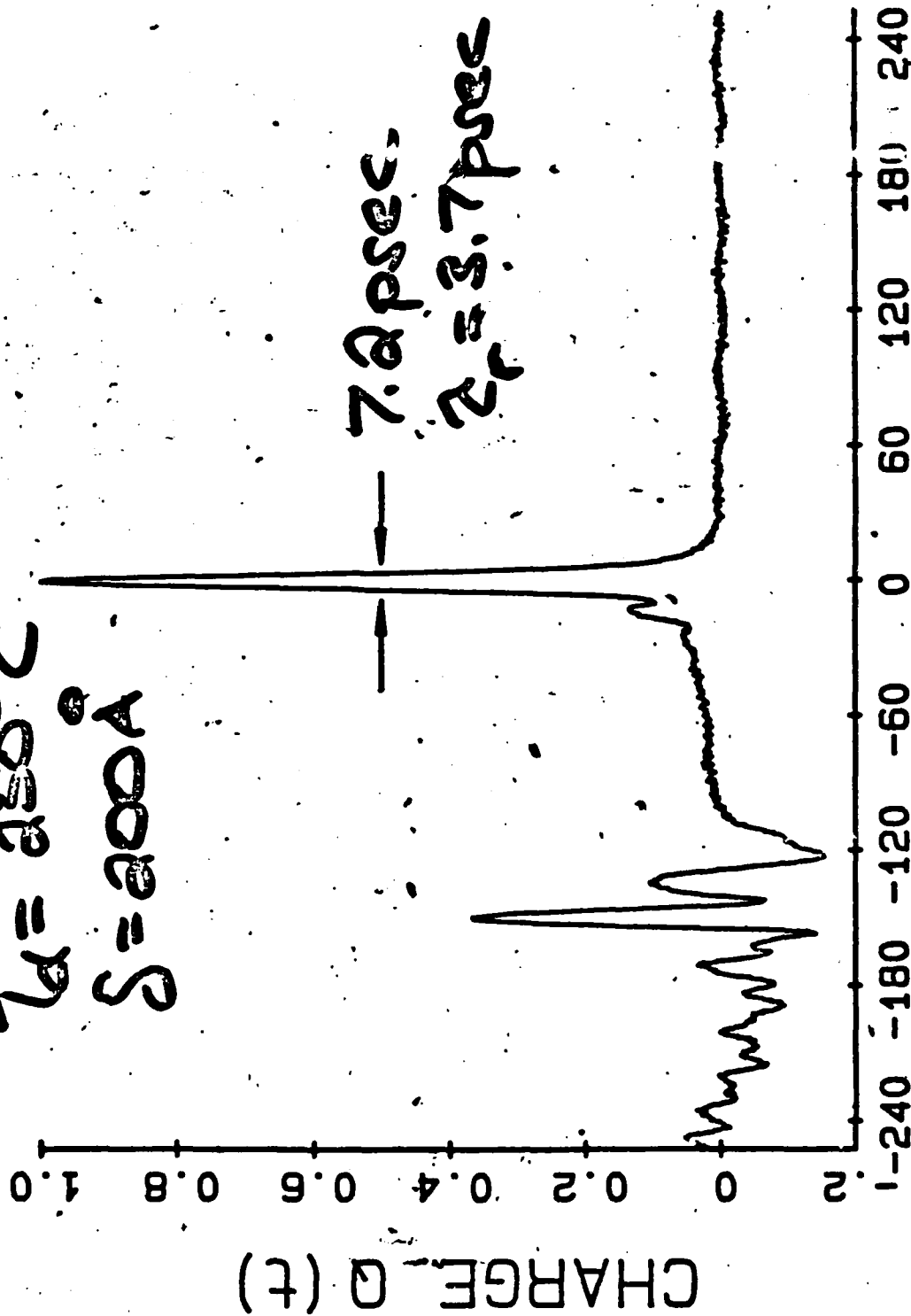
33

TOP
DO NOT AFFIX OVERLAYS ALONG THIS SURFACE

CdTe on SiO₂

T_a = 250°C

S = 200 Å



Reflection
separation
149.58 ps

$\epsilon = 3.78$

T_d ~ 6.5 ps

~ 16.5 ps

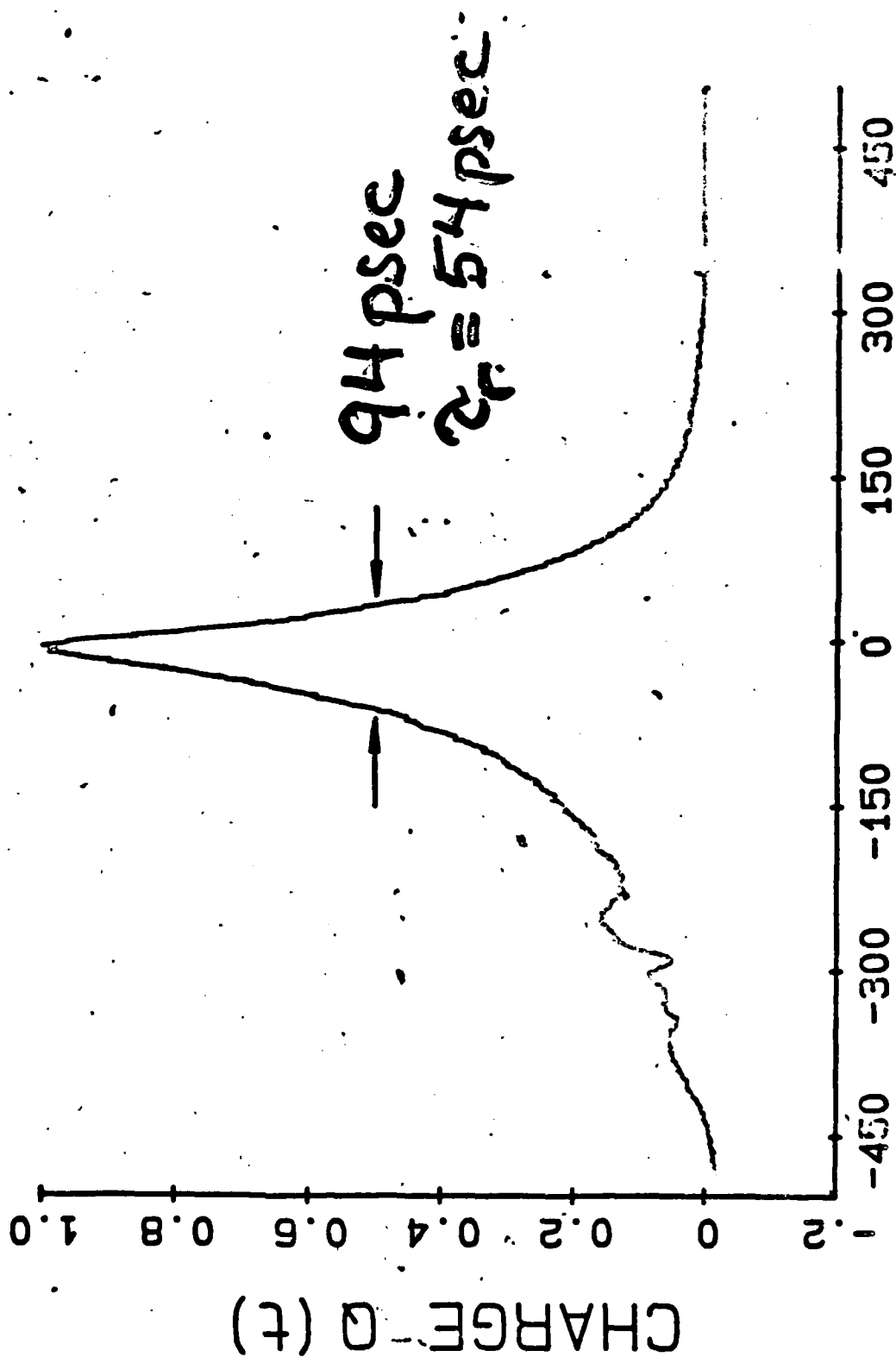
NEI ΔV (nsec)

NOTES:

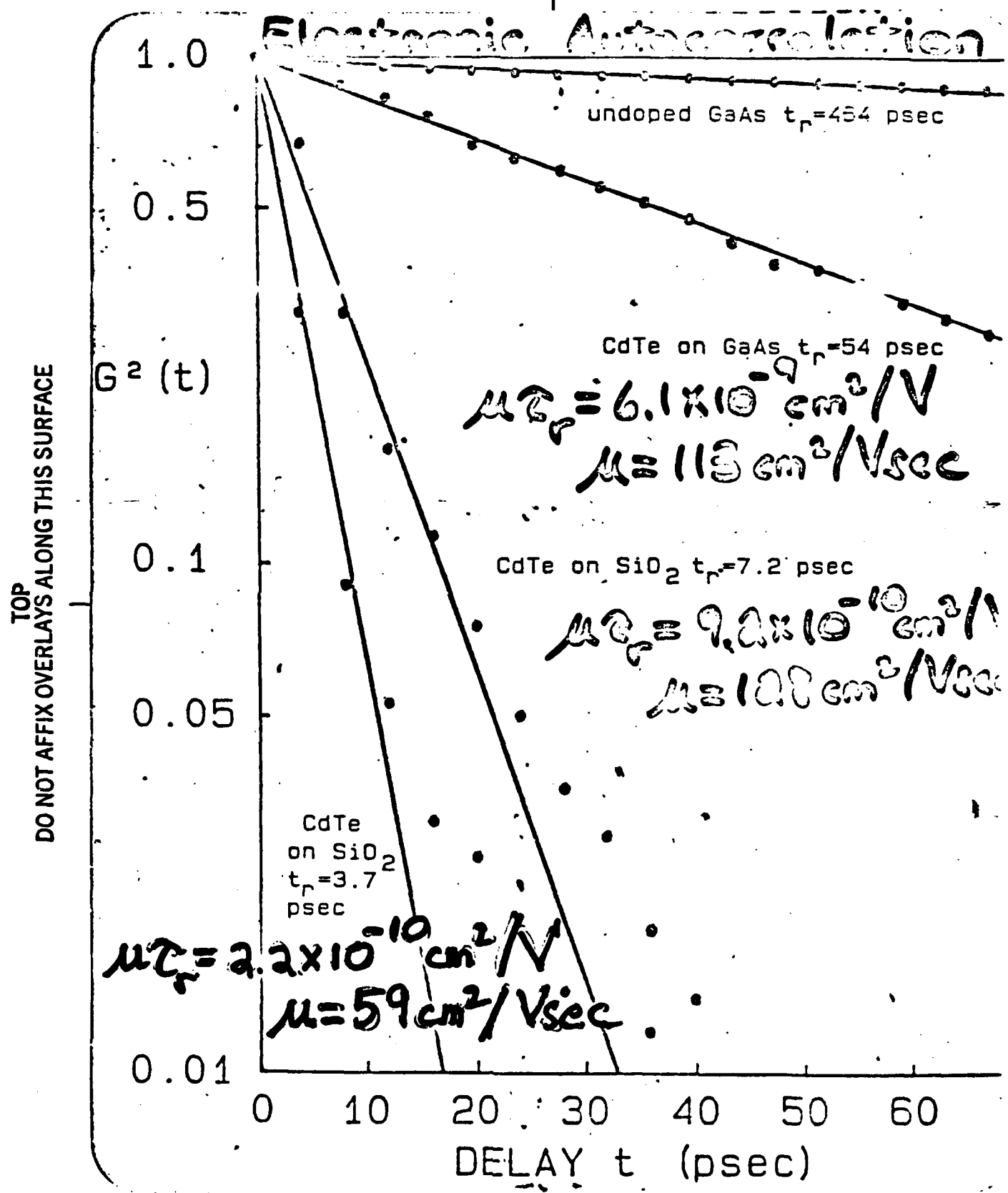
35

TOP
DO NOT AFFIX OVERLAYS ALONG THIS SURFACE

Single Crystal CdTe on GaAs



(13) - (24)



Speed & Sensitivity Comparable to

NOTES:

TOP
DO NOT AFFIX OVERLAYS ALONG THIS SURFACE

OMICVD CdTe

(°C)	Substrate	(Å) Grain Size	(Ω-cm) S _d	(ps) τ _i	(cm ² /Vs) μ
250	SiO ₂	200	(a) 3 × 10 ⁷	3.7	59
350	SiO ₂	>200	(b) 2 × 10 ⁶	7.2	128
350	GaAs	—	—	54	113

(a) $V_b = 60V$, $l = 15\mu m$.

TOP
DO NOT AFFIX OVERLAYS ALONG THIS SURFACE

Model Of Carrier Mobility In Polycrystalline Silicon Solar Cells [Toshi & Srivastava, JAP 56, 2375 (1997)]

$$\frac{1}{\mu^*} = \frac{(D-S)}{\mu_e D} + \frac{S}{D \mu_{gb}}$$

$$D \sim 200 \text{ \AA}$$

$$S \sim 5 \text{ \AA}$$

$$\mu_e \sim 1000 \text{ cm}^2/\text{Vs}$$

$$\mu_{gb} \sim 1 \text{ cm}^2/\text{Vs}$$

$$\mu_{\text{directional}} \sim 10^3 \text{ cm}^2/\text{Vs}$$

NOTES:

39

TOP
DO NOT AFFIX OVERLAYS ALONG THIS SURFACE

Garcin Boundary Recombination
[Goch, Fishman, & Peng, JAP 51, 416 (1992)]

$$\frac{1}{\tau_{eff}} = \frac{1}{\tau} + \frac{1}{\tau_{eff}}$$

$$\tau_{eff} \sim 4 \mu s$$

$$\mu \sim 10 \text{ cm}^2/\text{Vs}$$

$$D = \mu kT/e \sim 1.5 \text{ cm}^2/\text{s}$$

Surface

TOP
DO NOT AFFIX OVERLAYS ALONG THIS SURFACE

Disordered Semiconductors

- Wigner-Seitz Potentials
- High Dark Resistivity
- High Dielectric Strength
- Fermi Behavior
- Enhanced Absorption
- Simple Construction

NOTES:

TOP
DO NOT AFFIX OVERLAYS ALONG THIS SURFACE

Some Relevant Relaxation Times

1. Thermalization Time: $\tau_t \sim \frac{\Delta E}{\hbar \omega_0^2} \sim 10^{-13} - 10^{-12}$ s
(Hot Carriers)

2. Capture Time: $\tau_c \sim \frac{1}{N_t \sigma_c v} \sim 10^{-12} - 10^{-9}$ s
(Trapping)

3. Thermal Emission Time: $\tau_e \sim v^{-1} e^{E/kT}$
 $\sim 10^{-12} - 10^{-5}$ s

4. Recombination Time: $\tau_r \sim 10^{-9} - 10^{-3}$ s

5. Dielectric Relaxation Time: $\tau_d \sim \epsilon \epsilon_0$
 $\sim 10^{-12} - 10^{-4}$ s

2

phonon freq
 $\omega_0 \sim 10^{13}$ Hz

$\sigma_c \sim 10^{-15}$ cm²
 $v \sim 10^7$ cm/s

attempt freq
 $\nu \sim 10^{12}$ Hz

$\epsilon_0 = 8.85 \times 10^{-14}$ F/cm

NOTES:

3

TOP
DO NOT AFFIX OVERLAYS ALONG THIS SURFACE

Photoconductivity In Disordered Semiconductors

- Amorphous Semiconductors
- Radiation-Damaged Semiconductors
- Small-Grain Polycrystalline Semiconductors

• Large Density of Defects

• Trapping And Recombination

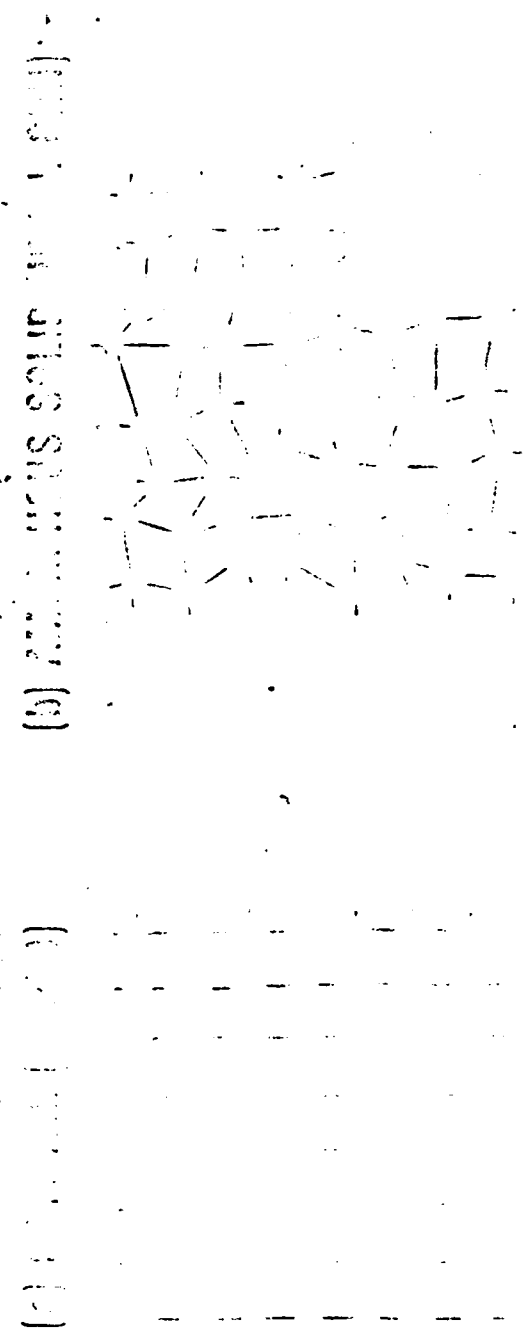
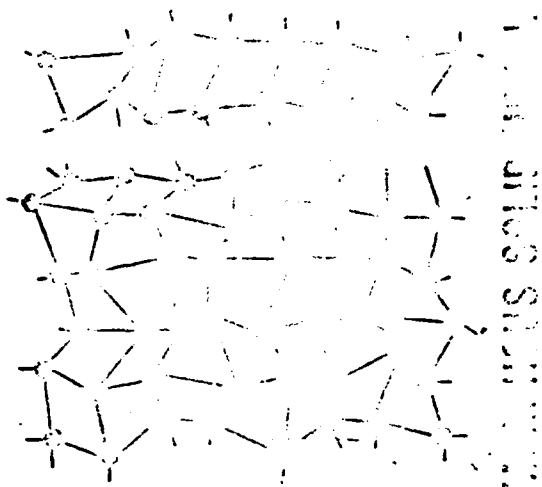
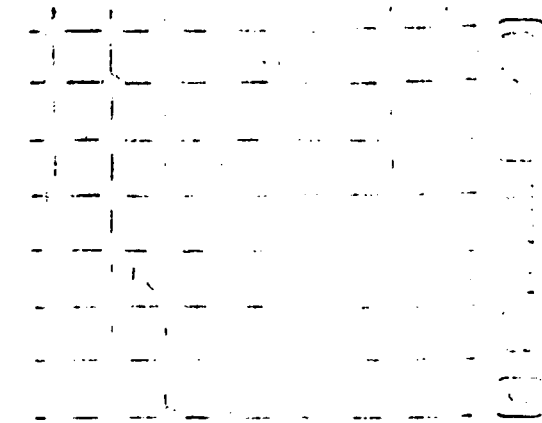
Continued

Other methods of achieving fast photoconductor decay are the use of compensating impurities such as Fe in InP

NOTES:

TOP
DO NOT AFFIX OVERLAYS ALONG THIS SURFACE

CRYSTAL STRUCTURES



47

Infinite
nonperiodic
~~array~~ 3-D
array
interline
atoms
short range
order above
each atom
chem bond
total
similar
bond
angles
lengths
4-Fold
coordination
structure
Defects
vacancies
dangling
bonds
microvoids

NOTES:

3

TOP

DO NOT AFFIX OVERLAYS ALONG THIS SURFACE

SEQUENCE NO.

5 23

DENSITY OF STATES

EXTENDED STATES

$$\mu \sim 1-10 \text{ cm}^2/\text{Vs}$$

LOCALIZED STATES

$$\mu \sim 10^3 - 10^4 \text{ cm}^2/\text{Vs}$$

States lie in
bands
lack of long
range order
→ band tailing

Spatial randomness
of atomic
potential
intrinsic
disorder

→ Anderson
localization

States in gap
due to

Anderson
localization
and structural
defects which
depend upon
material
preparation.

Above the
mobility edge

NOTES:

TOP
DO NOT AFFIX OVERLAYS ALONG THIS SURFACE

Temporal Resolution?

Ex: Chemical Vapor Deposited CdS

Capture Time:
(dangling)

$$\tau_c \sim \frac{1}{N_d \sigma_c}$$

$$N_d \sim 10^{19} \text{ cm}^{-3} \quad (\text{dangling bonds})$$

$$\sigma_c \sim 10^{-15} \text{ cm}^2$$

$$\tau_c \sim \left(\frac{1}{10^{19} \times 10^{-15}} \right) \sim 10 \text{ cm}^{-1}$$

$$\tau_c \sim 10^{-10} \text{ s}$$

6

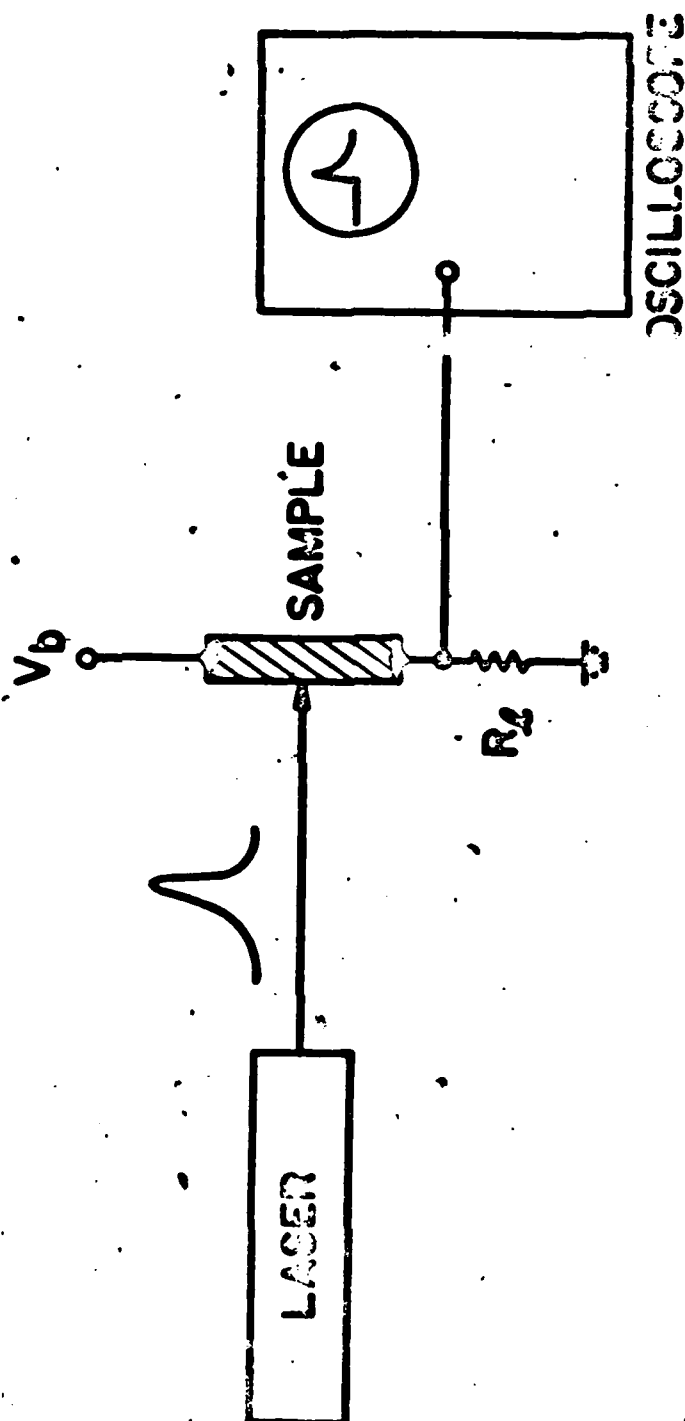
For a state
whose electronic
wave function
is localized
to within
a few Å
(\sim a lattice
constant)
 \sim capture
cross section
is a few-
square-Å
 $\sim 10^{-15} \text{ cm}^2$

NOTES:

9

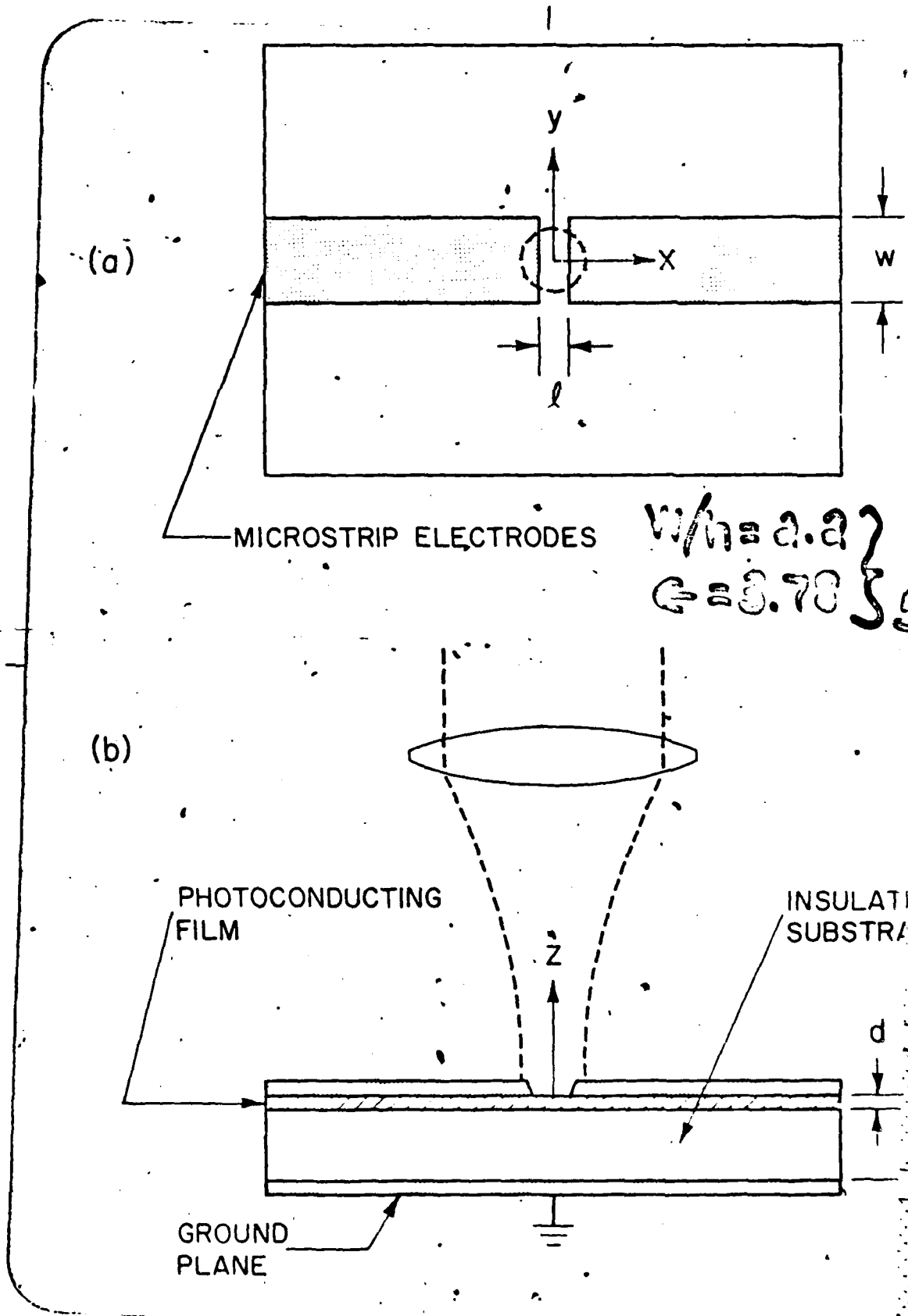
TOP
DO NOT AFFIX OVERLAYS ALONG THIS SURFACE

PHOTOCONDUCTIVITY (THE TRADITIONAL APPROACH)





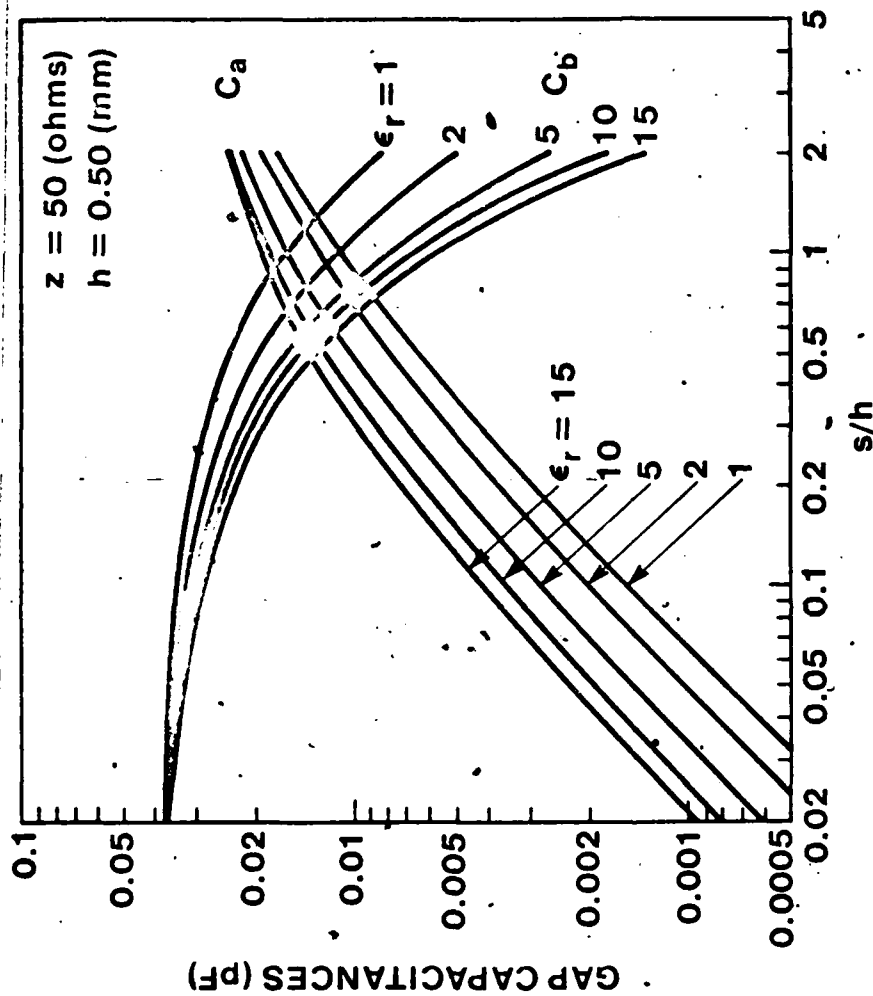
SEQUENCE NO. _____
 VG. NO. _____



between the two center microstrips.

Shunt capacitance C_a (microstrip to ground) associated with the fringing effect of the edge of the strip.

For the value $s/h = 0.1$ $C_b = C_g$ is nearly independent of the dielectric constant, ϵ_r , but C_b varies considerably as a function of h . Thus for $h = 0.25$ mm we estimate $C_b = C_g = 0.002$ pF



FROM: M. MAEDA: IEEE TRANS. MICROWAVE THEORY TECH.
MTT-20, 390 (1972)

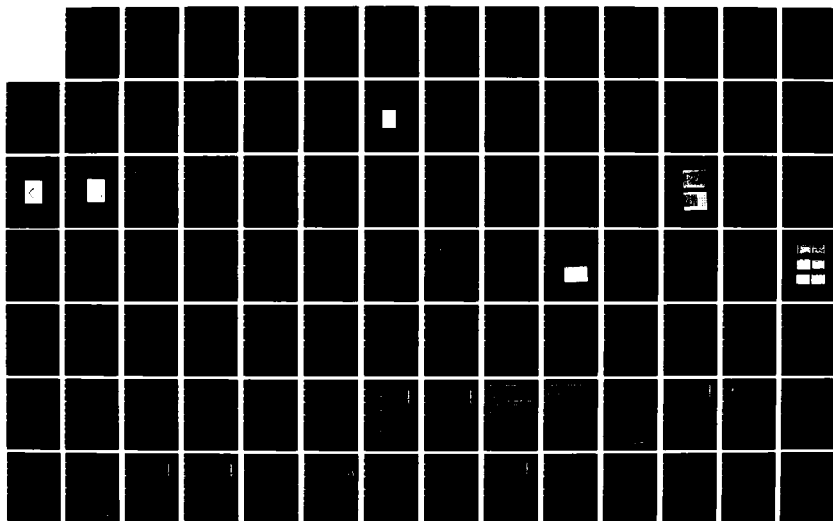
AD-A165 039

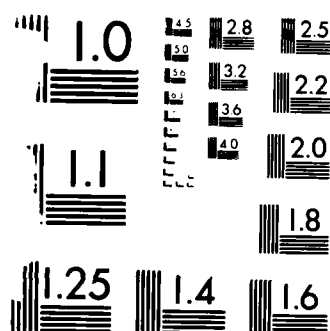
WORKSHOP ON NEW DIRECTIONS IN SOLID STATE POWER
SWITCHES HELD AT FARMINGD. (U) POLYTECHNIC INST OF NEW
YORK FARMINGDALE WEBER RESEARCH INST. B SEMITZKY
24 DEC 85 N00014-85-G-0236 F/G 9/5

3/6

UNCLASSIFIED

NL

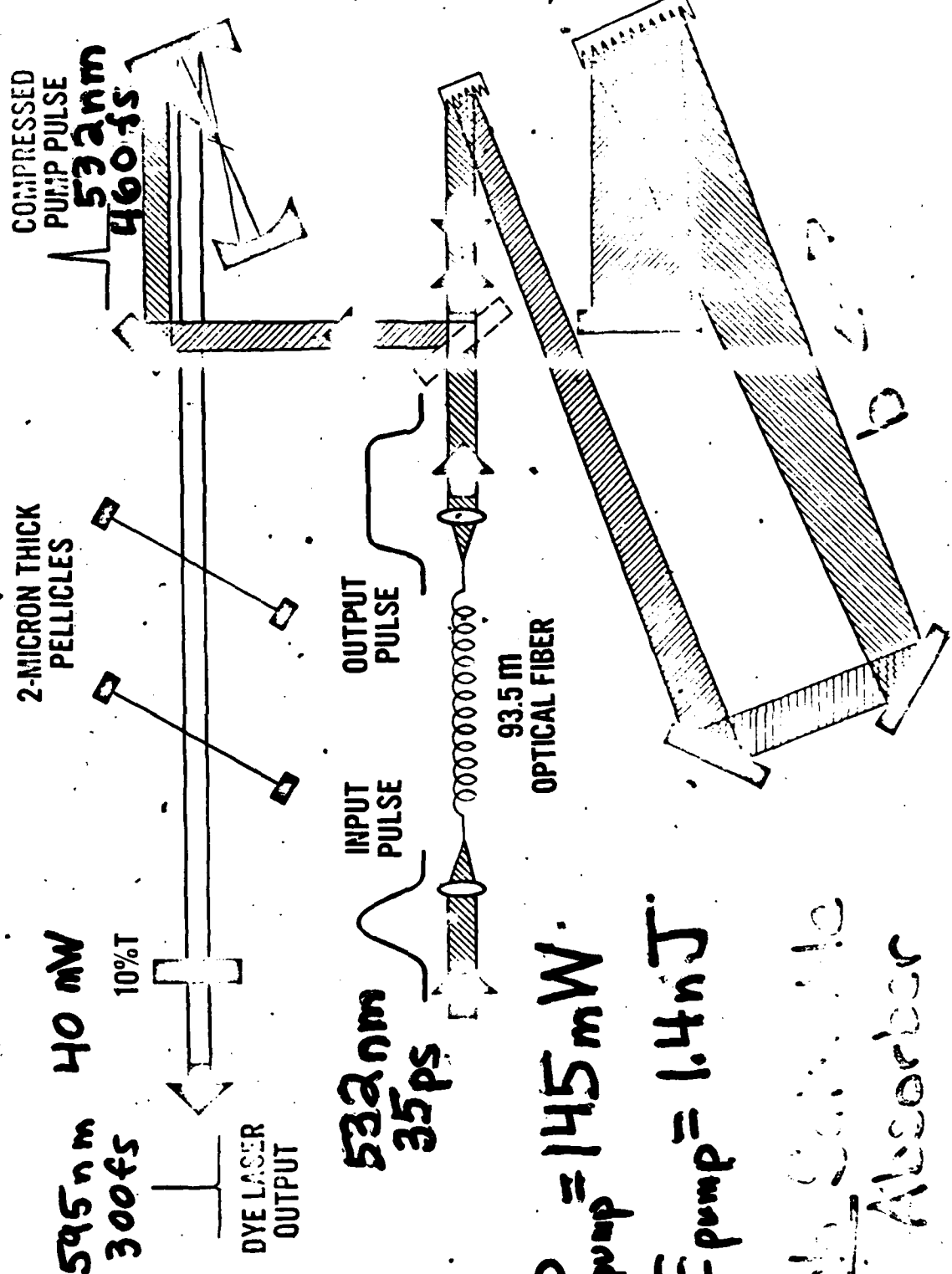




MICROCOPY RESOLUTION TEST CHART
NATIONAL BUREAU OF STANDARDS 1963 A

TOP
DO NOT AFFIX OVERLAYS ALONG THIS SURFACE

Ultrashort Pulse Pumped Dye Laser



$$P_{\text{pump}} = 145 \text{ mW}$$

$$E_{\text{pump}} = 1.4 \text{ nJ}$$

10% T
Absorber

Span of defect densities
ESR lower limit
delineate high from low

unpaired spins > density
6.7

ESR14 (7-70)

MATERIALS

ESR*

Glow-Discharge-Deposited
a-Si:H (GD a-Si:H)

$\sim 10^{16} \text{ cm}^{-3}$

Chemical Vapor-Deposited
a-Si (CVD a-Si)

$10^{18} - 10^{19} \text{ cm}^{-3}$

Ultra-High Vacuum-Evaporated
a-Si (UHV a-Si)

$10^{19} - 10^{20} \text{ cm}^{-3}$



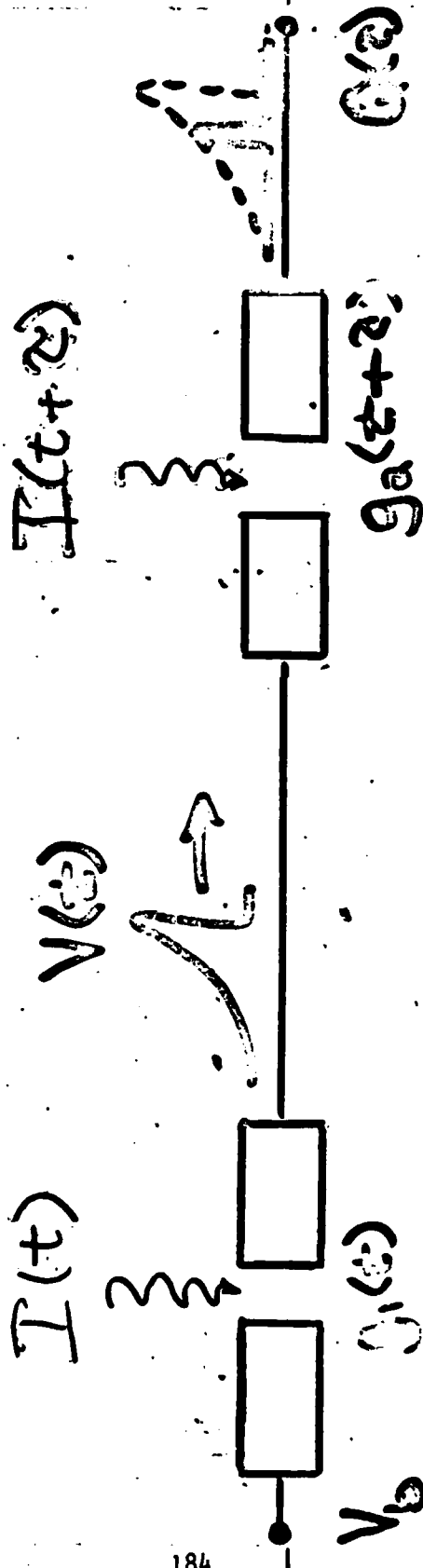
Bell Laboratories

SEQUENCE NO. _____
VG. NO. _____

* Approximate spin densities noted in the literature.

DO NOT AFFIX OVERLAYS ALONG THIS SURFACE

Electronic Correlation (Sampling)



$$Q_1(t) \sim Q(t) \sim V_b Z_0 \int_{-\infty}^{\infty} g_1(t) g_2(t+\tau) dt$$

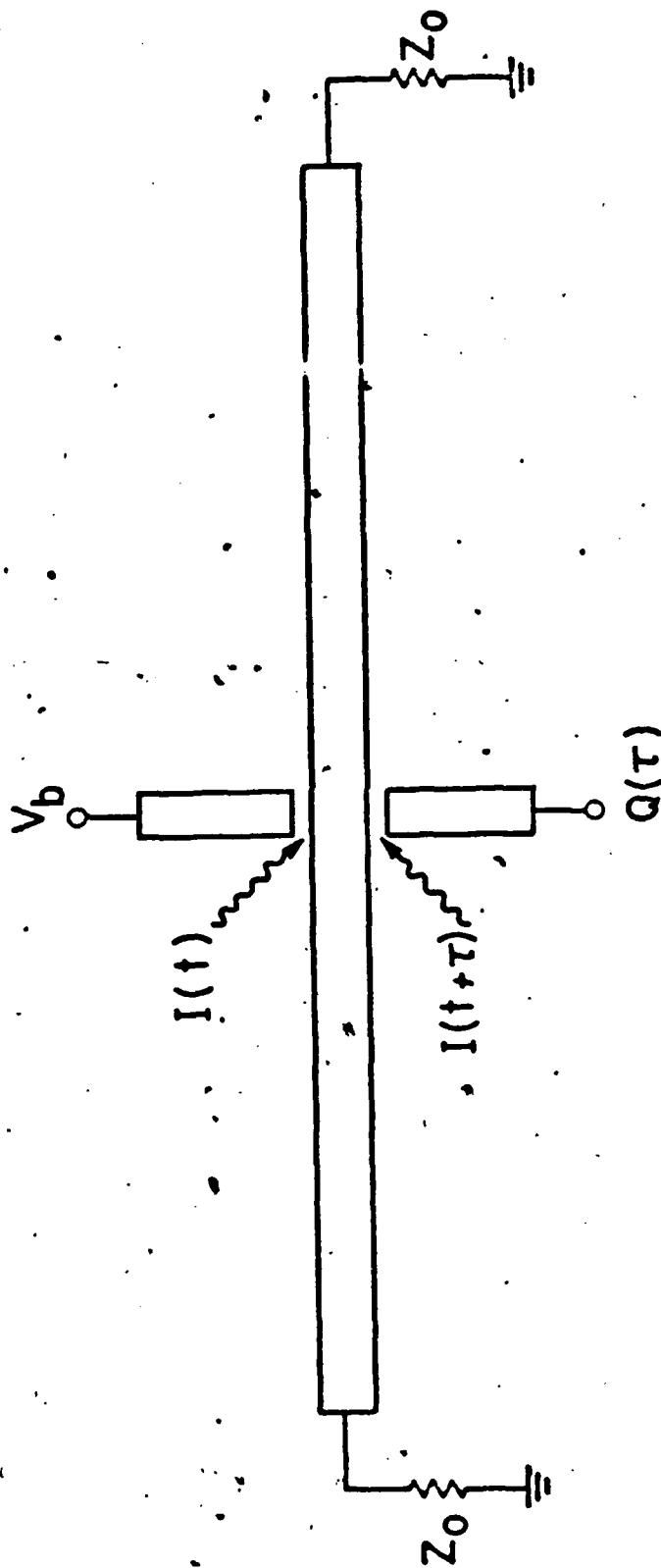
One of the photoconductors provides bias and the output signal from it is used to bias the second photoconductor. The quantity measured is the total charge produced at the output of the 2nd photoconductor as a function of the relative delay between the two optical pulses.

NOTES:

17
(9) (20)

TOP
DO NOT AFFIX OVERLAYS ALONG THIS SURFACE

Electronic Autocorrelation



SEQUENCE NO. _____

18

TOP
DO NOT AFFIX OVERLAYS ALONG THIS SURFACE

NOTES:

$\tau = 16 \text{ ps}$

27 ps FWHM

$\epsilon = 3.78$

$T_d \approx 85 \text{ eV}$
ps/in

$\sim 33 \text{ eV}$
ps/cm

$T_d \approx 65 \text{ ps/cm}$
 $\sim 165 \text{ ps/in}$

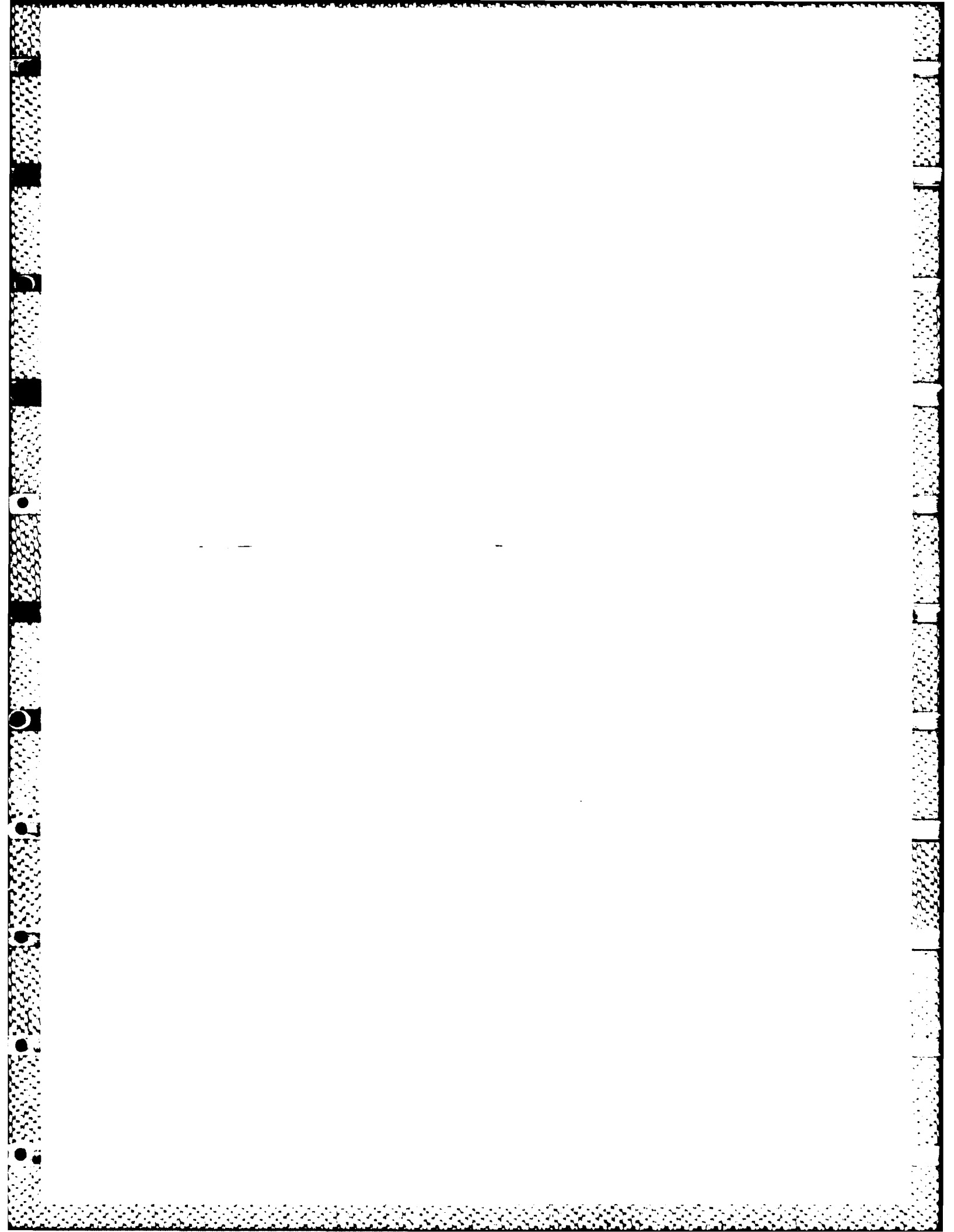
CVD
(LPCVD a - Si)

$N_2 \sim 10^{13} \text{ cm}^{-3}$

27 ps FWHM

$\tau_c \approx 16 \text{ ps}$

$\rightarrow \quad \leftarrow 20 \text{ ps}$



**Problems of High Power Photoconductive Switching on a
Picosecond Time Scale**

William R. Donaldson and Gerard Mourou

LABORATORY FOR LASER ENERGETICS
University of Rochester
250 East River Road
Rochester, New York 14623-1299

High voltage photoconductive switching is a technology which can deliver extremely fast rise time electrical pulses. The electrical pulses generated in this manner have found a variety of applications including the shaping of optical pulses¹ and the development of jitter free streak cameras.² The speed of this process is due to the almost instantaneous absorption of light in the bulk of a semiconductor. The amount of power that can be switched can be increased by increasing the volume of photoconducting material. This can only be accomplished by increasing the energy of the excitation beam. Thus the characteristics of the electrical signal are fundamentally dependent on the laser driver. The shorter risetime of the optical signal will cause the photoconductive state to be established sooner thus reducing the resistive heating during turn on. The benefits of going to an optical trigger pulse of few picoseconds are that we increase the electrical bandwidth and significantly reduce the possibility of switch damage due to dynamic switching energy.

The rise time of the electrical pulse is limited by FWHM of the laser pulse. The laser driver must therefore produce a very high energy short optical pulse. The Laboratory for Laser Energetics has an ongoing program of development of regenerative amplifiers.³ These amplifiers work by seeding a Q-switched laser cavity with a short pulse from a cw mode locked Nd:YAG laser. This is accomplished by

using very fast electronic drivers for the intracavity Pockels cell. A continuously pumped amplifier cavity can obtain 1 mJ of optical energy in a 100 ps pulse at a 1 kHz repetition with a pulse stability of better than 1%. The performance of this system can be improved by passing the mode locked seed pulse through an optical fiber. The group velocity dispersion (GVD) in the fiber will introduce a frequency chirp on the seed pulse which will be impressed upon the amplified pulse. The amplified pulse can then be compressed with a grating pair⁴ to a duration of 15 ps. GVD is not the only process occurring in the fiber. The intense light pulse induces self phase modulation which increases the optical bandwidth. The narrow gain bandwidth of Nd:YAG cannot amplify the entire spectrum of the input pulse and thus limits the ultimate amount of compression. Shorter pulses can be obtained by using Nd doped silicate glass as the amplifying medium, because the glass has a wider gain bandwidth. This system can produce 2 mJ, 1.5 ps pulses at 10 Hz.⁵ The limited repetition rate is due to the difficulty of extracting heat from the glass rod. With further amplification stages it should be possible to obtain 50 mJ/pulse. Thus we now have high energy picosecond laser sources to drive photoconductive switches.

Although the ultimate system parameters such as the rise time and the switched power are determined by the laser system, it is very important to optimize the material parameters to efficiently use the laser power. The materials that we are considering are intrinsic silicon and GaAs. The maximum density of photo induced carriers in these materials is about $10^{17}/\text{cc}$. At 1.06 μm , assuming that an electron-hole pair is created for each incident photon, this means that 5×10^{-2} cc of semiconductor volume can be brought into the saturated photoconductive state for each mJ of absorbed optical radiation. The switching voltage will determine the width of the semiconducting gap because the surface breakdown of the semiconductor

material is about 100 kV/cm. The next material parameter that must be considered is the absorption depth. At 1.06 microns this is about 0.1 cm. Ideally, the absorption depth should equal the thickness of the switch. If the switch is thinner than the absorption depth, then some of the light will not be absorbed. If the switch is thicker than the absorption depth the excess length will not be utilized. Since rise times of a few picoseconds are being considered it is necessary to make the electronic structures as small as possible to minimize dispersion. The geometry of the photoconductive switch is thus determined by the available laser power which sets the maximum volume and the material parameters which set the minimum dimensions. The electrical circuit must then be designed around the switch to efficiently couple the pulse into the load that is to be driven. This is a difficult task due to the conflicting requirements of compact size to accommodate the high frequencies and the need for large spacing to prevent electrical breakdown. Some of these problems may be alleviated by the reduced electrical breakdown associated with ultrashort pulses.

These difficult design problems can only be overcome if we understand how the electrical pulses propagate through the system. However, the electrical bandwidth is much larger than conventional electronic diagnostic equipment. The only way to measure these pulses is to use optical techniques. Mourou and Valdmanis⁶ have demonstrated that subpicosecond rise time electrical signals of a few millivolts can be measured by using optical pulses to sample the electrical field in an electro-optical crystal placed in proximity to the electrical circuit. The electrical field causes a change in the birefringence of the crystal which produces a change in the polarization of the light passing through the crystal. It is this change in polarization which is detected. The high fields associated with power photoconductive switching will make this technique easier to use than the mV signals which have previously been detected.

Another advantageous feature of this technique is the noncontacting probe, which will not load the circuit and increase the rise time. The isolation provided by the optical sampling means that the detectors can be made immune from EMI generated by the switch. Finally, by using fast optical detectors such as streak cameras it should be possible to obtain diagnostics on single shot events.⁷

The advent of short pulse high energy lasers has made possible the generation of high voltage electrical pulses with rise times of few ps. These pulses will reduce the joule heating of the photoconductive switches during their turn on time. Such systems will have many applications in areas such as PFNs and laser accelerators.

REFERENCES

1. G. Mourou and W. Knox, Appl. Phys. Lett. 36, 623 (1980).
2. W. Knox and G. Mourou, Opt. Commun. 37, 203 (1981).
3. I. N. Duling III, T. Norris, T. Sizer, P. Bado, and G. A. Mourou, J. Opt. Soc. of Amer. B 2, 616 (1985).
4. E. B. Treacy, IEEE J. Quantum Electron. QE-5, 454 (1969).
5. D. Strickland and G. Mourou, to be published in Opt. Commun.
6. J. A. Valdmanis, G. Mourou, and C. W. Gabel, Appl. Phys. Lett. 41, 211 (1982).
7. S. Williamson and G. Mourou, Topical Meeting on Picosecond Electronics and Optoelectronics. Springer-Verlag (1985).

ACKNOWLEDGEMENT

This work was supported by the Air Force Office of Scientific Research contract AFOSR-84-017S and by the Sponsors of the Laser Fusion Feasibility Project at the Laboratory for Laser Energetics which has the following sponsors: Empire State Electric Energy Research Corporation, General Electric Company, New York State Energy Research and Development Authority, Northeast Utilities Service Company, Ontario Hydro, Southern California Edison Company, The Standard Oil Company, and the University of Rochester. Such support does not imply endorsement of the content by any of the above parties.

VIEWGRAPHS

PROBLEMS IN PICOSECOND
HIGH VOLTAGE PHOTOCONDUCTIVE SWITCHING

W. DONALDSON and G. MOUROU

**Problems in Picosecond
High Voltage Photoconductive
Switching**

by

William R. Donaldson

and

Gerard Mourou

Laboratory for Laser Energetics

University of Rochester

Outline

I Introduction

II Laser driver

High energy, short pulse

III Material and circuit geometry

IV Diagnostics

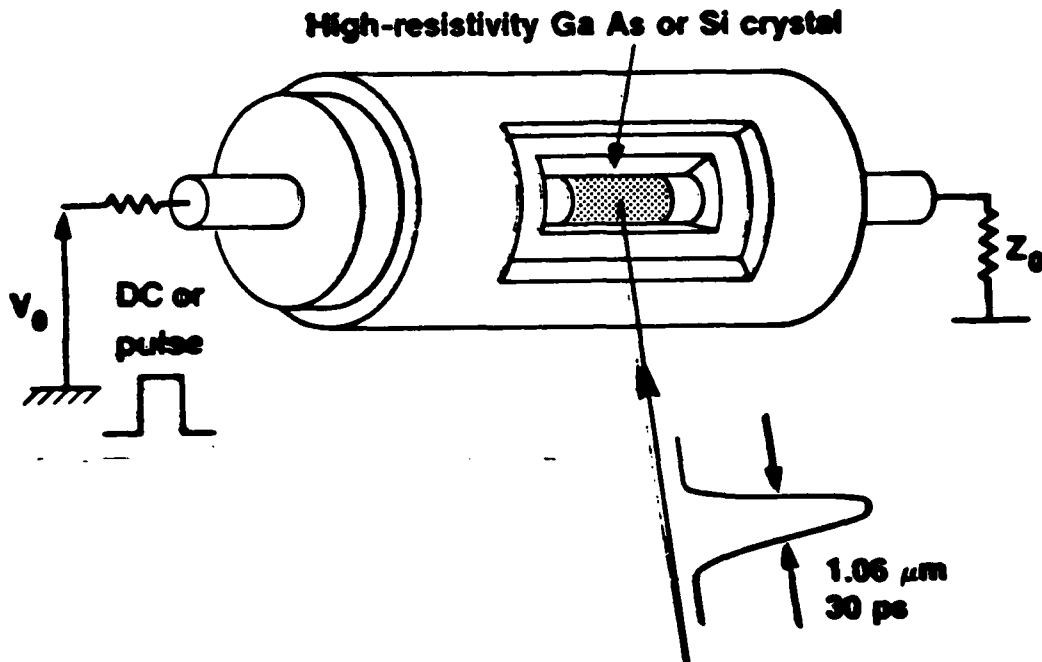
Opto-electronics

Pockels effect

V Conclusion

HIGH-POWER, LASER-ACTIVATED SEMICONDUCTOR SWITCH

USA
LLE



Semiconductor conductivity:

"Off" state $\sigma \propto n_i$

"On" state $\sigma(t) \propto \int_{-\infty}^t P_{\text{opt}}(t') dt'$

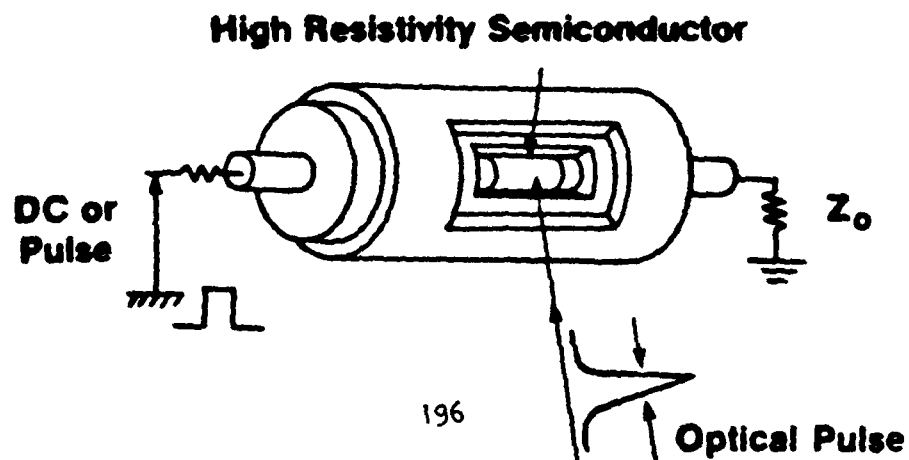
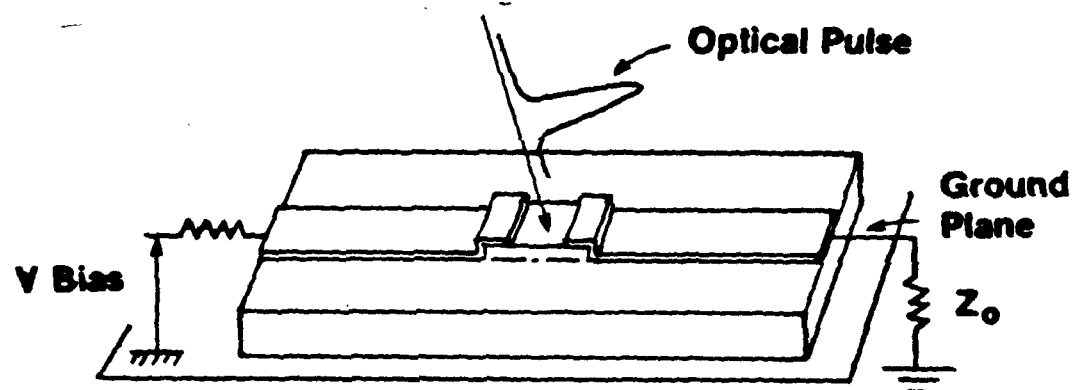
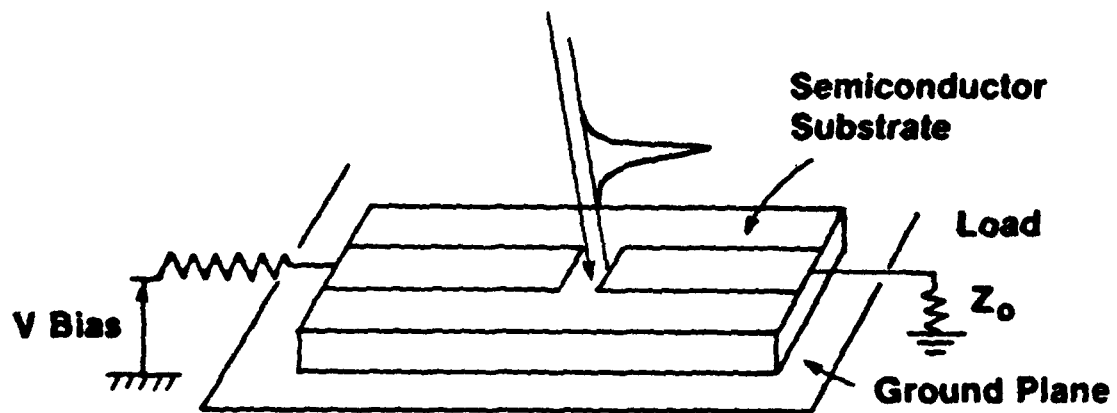
$$V = V_0 \frac{Z_0}{2Z_0 + r}$$

$$r \propto \frac{1}{\int_{-\infty}^t P(t') dt'}$$

62-485

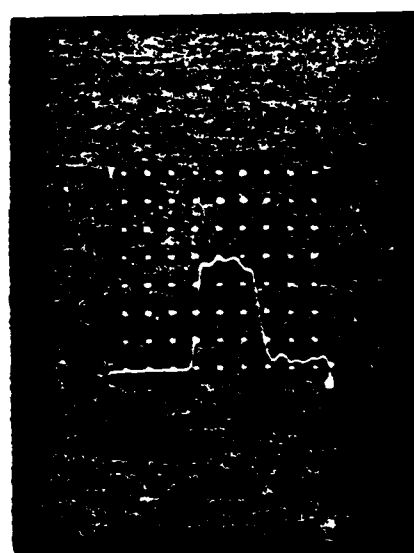
Photoconductive Switch Geometries

UR
LLE



DC HIGH VOLTAGE SWITCHING AT CRYOGENIC TEMPERATURE

UR
LLE



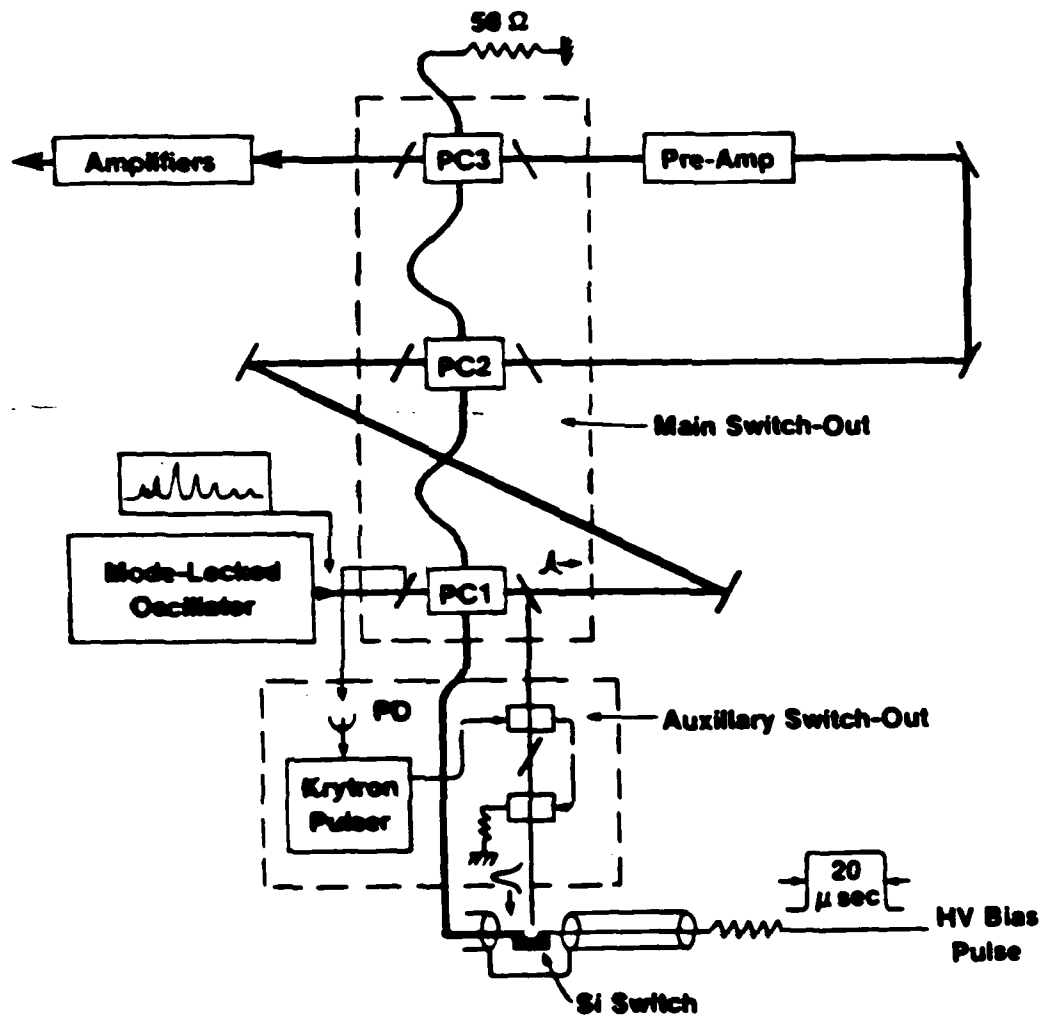
1 kV

500 ps/div

E741

OMEGA SINGLE-PULSE SWITCH-OUT

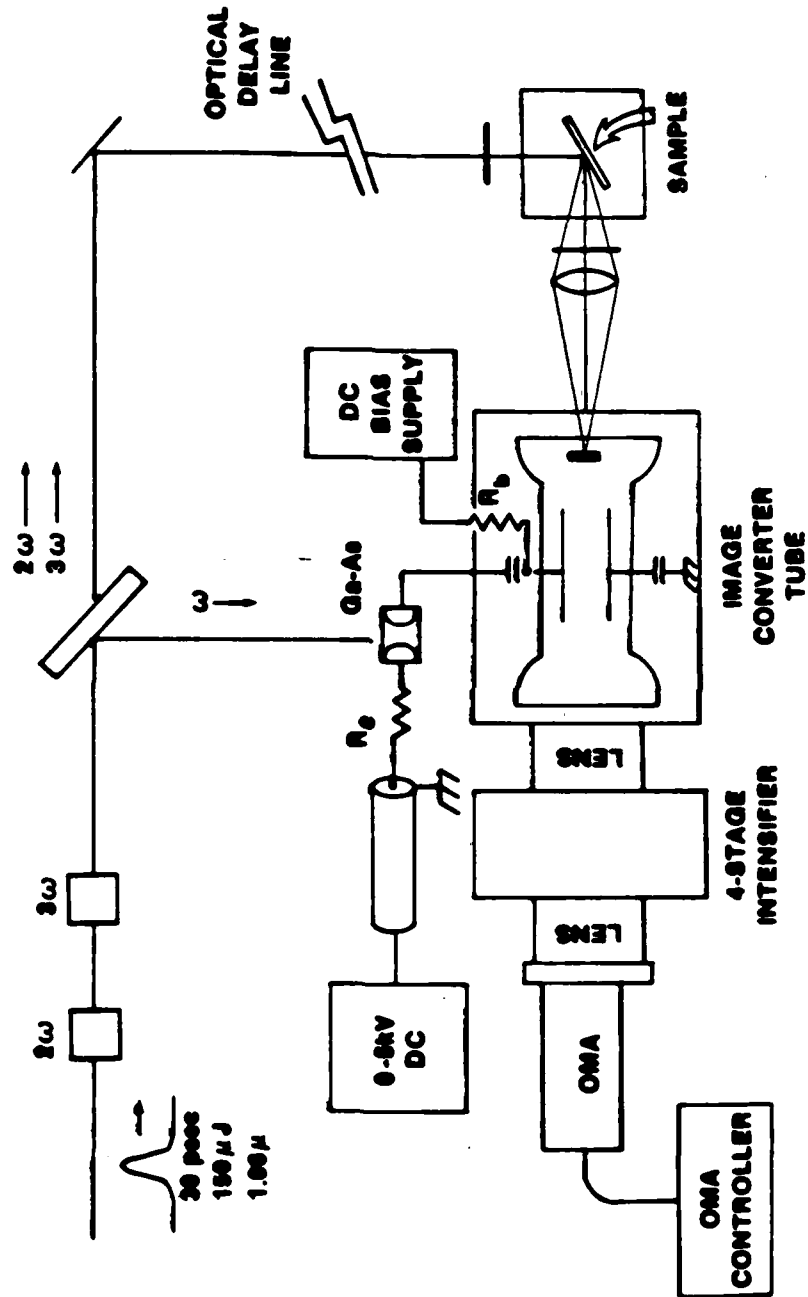
UFR
LLE



E743

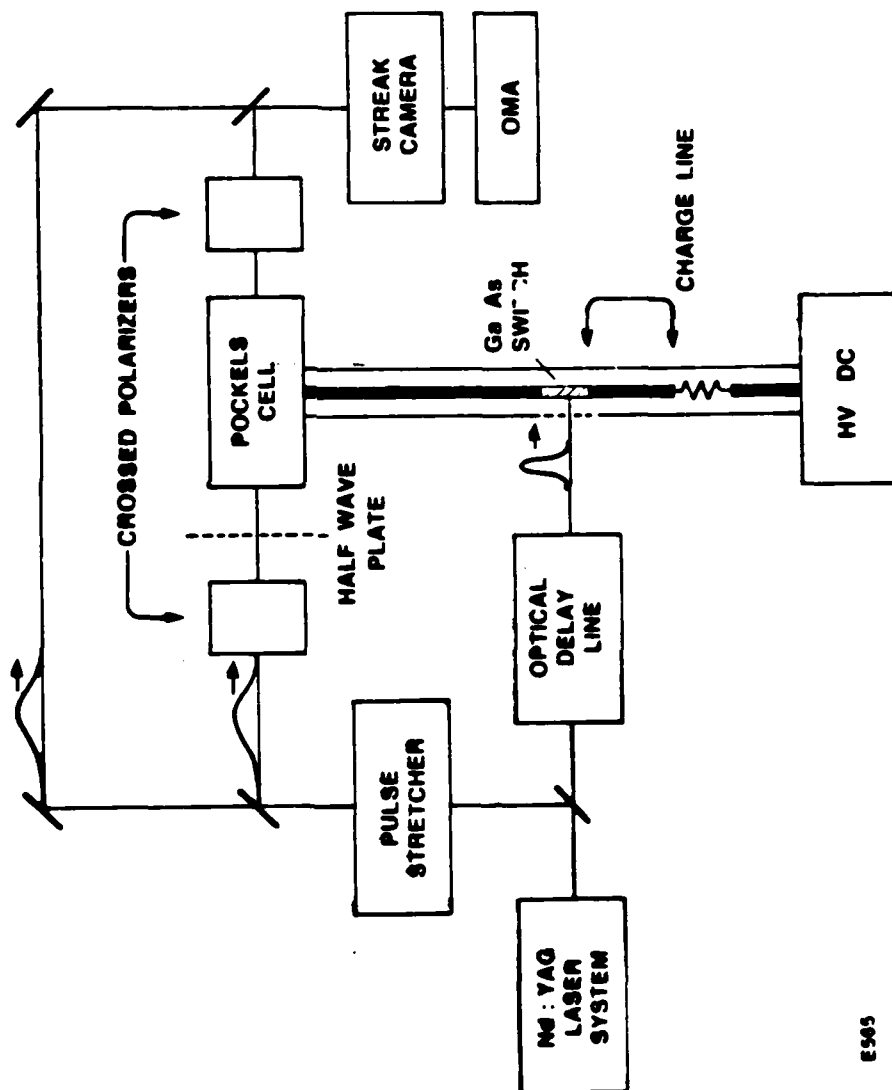
STREAK CAMERA DRIVEN BY DC-BIASED Ge-As

UFR
LLE



E1000

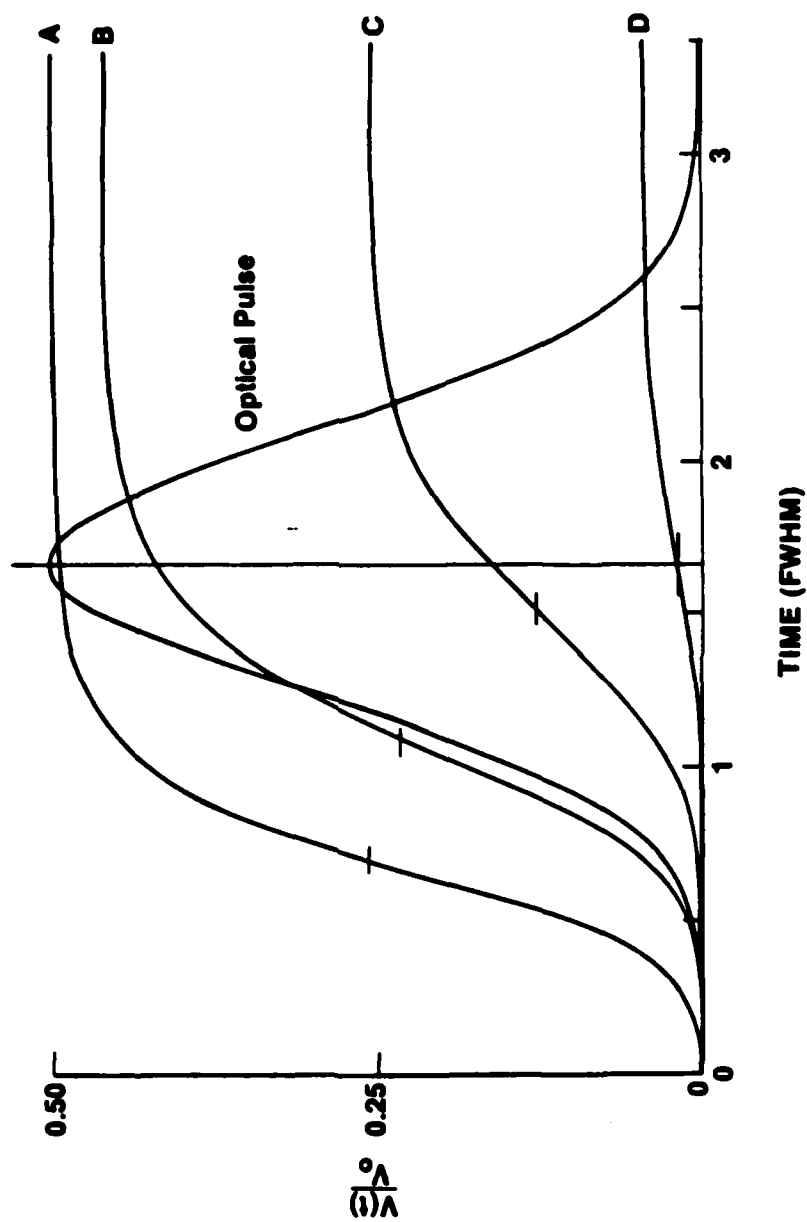
BLOCK DIAGRAM OF THE EXPERIMENTAL SETUP



E505

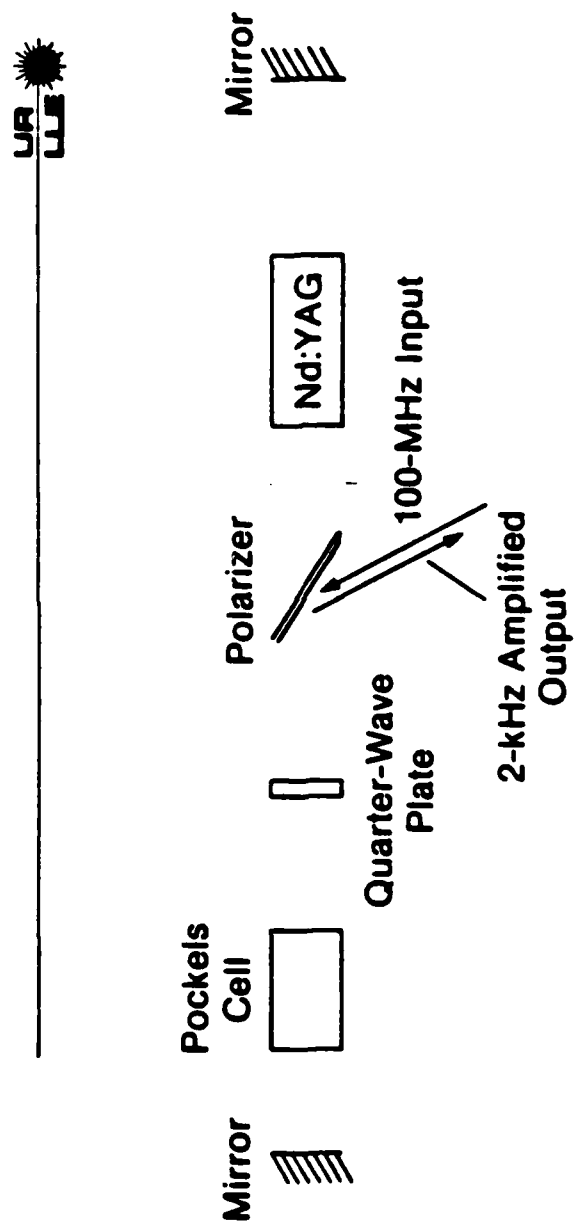
SWITCHING FUNCTION RELATIVE TO THE OPTICAL PULSE

U.S. AIR FORCE



E6558

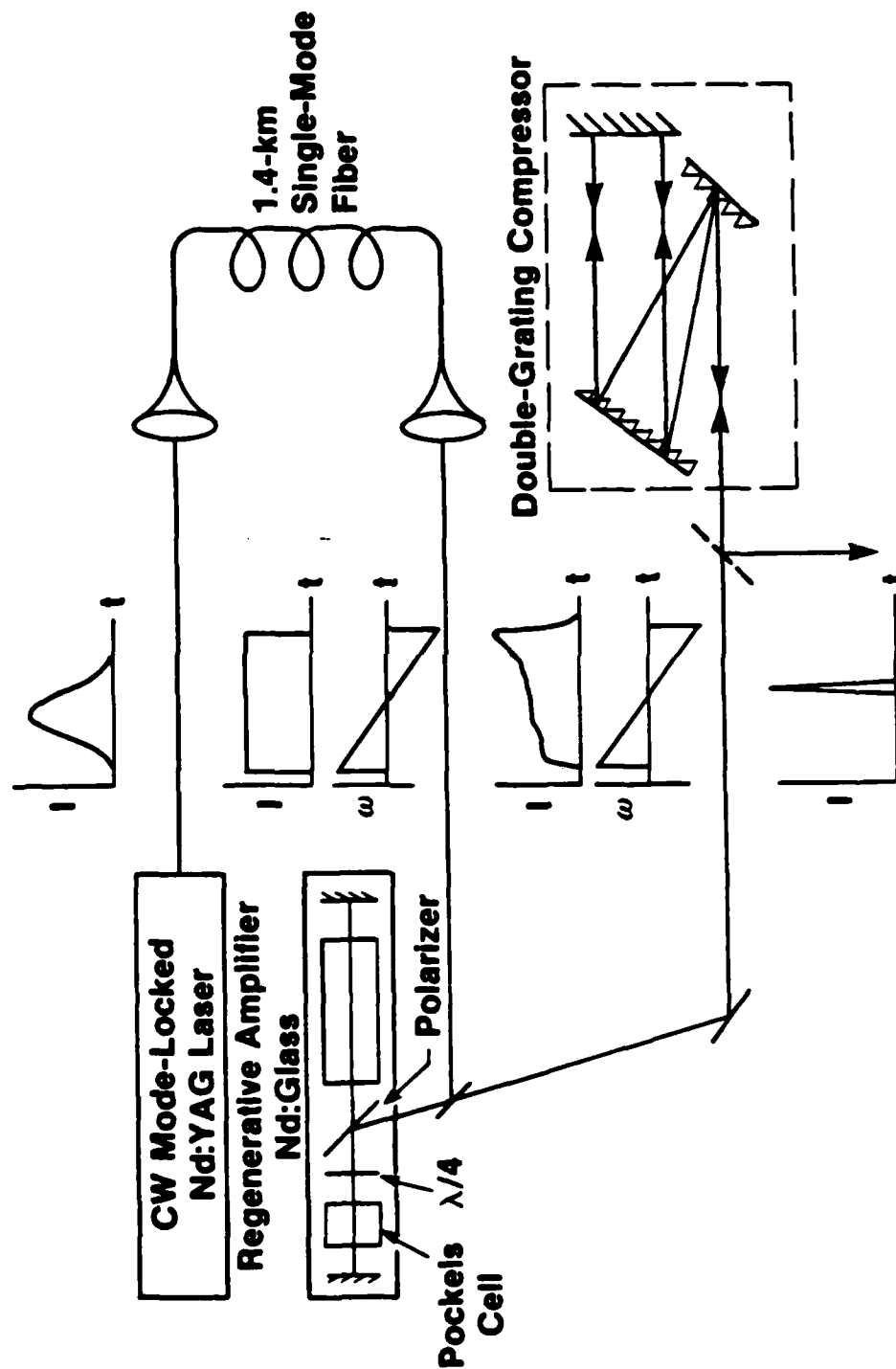
Schematic Representation of the Regenerative Amplifier



E3423

Amplifier and Compression System

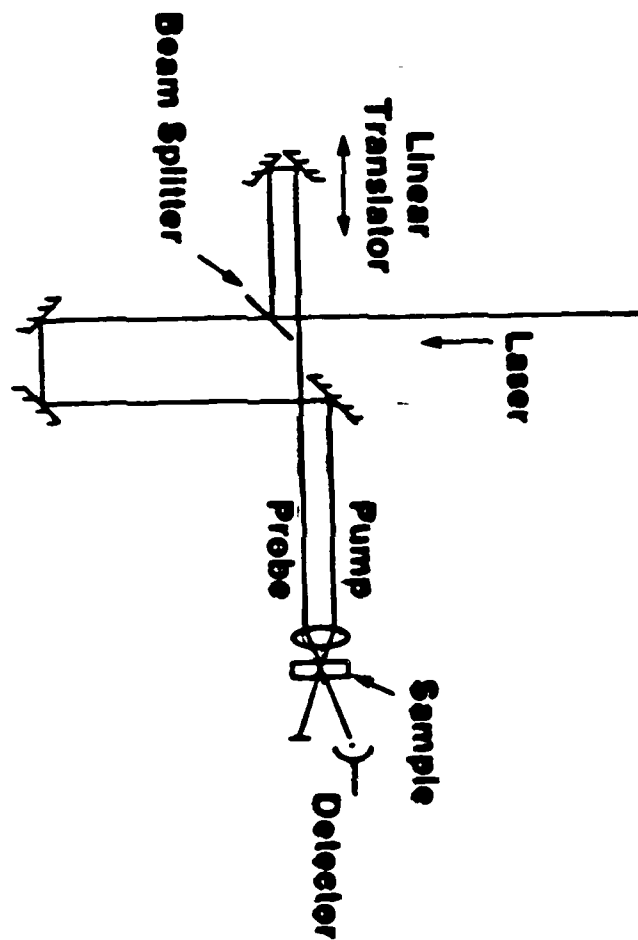
UR
LLE



E3614

Pump-Probe Experimental Setup

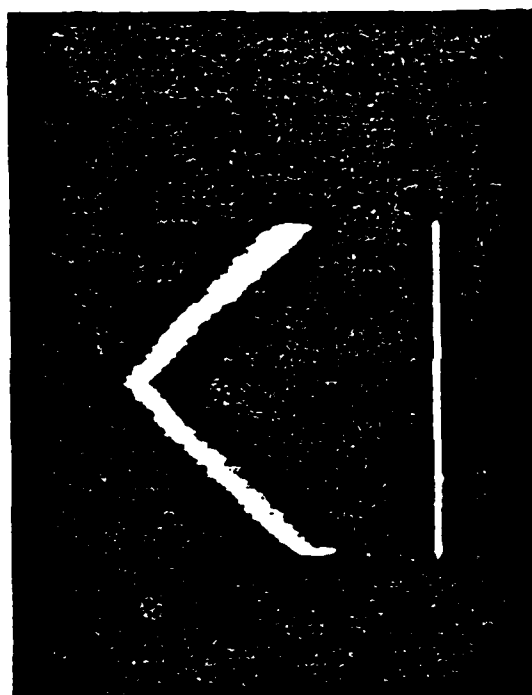
U_A
L_{AS}



E3560

**Autocorrelation of Stretched
Pulse from Fiber**

UR
LLE

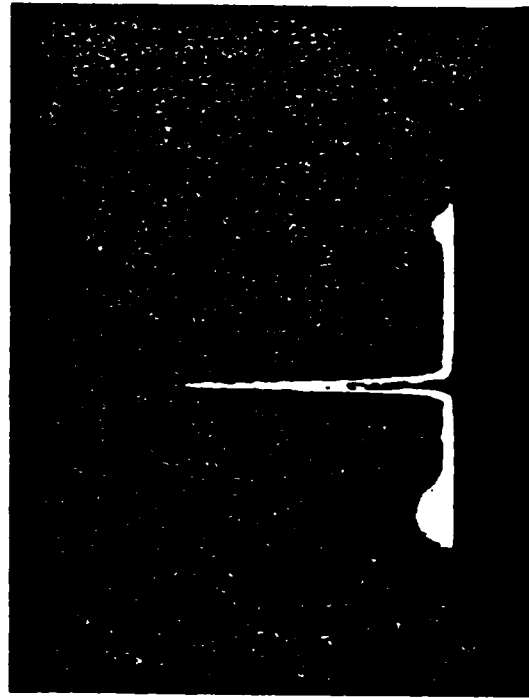


Full Scale = 300 ps

E3554

Autocorrelation of Compressed Pulse

UFA
LLE

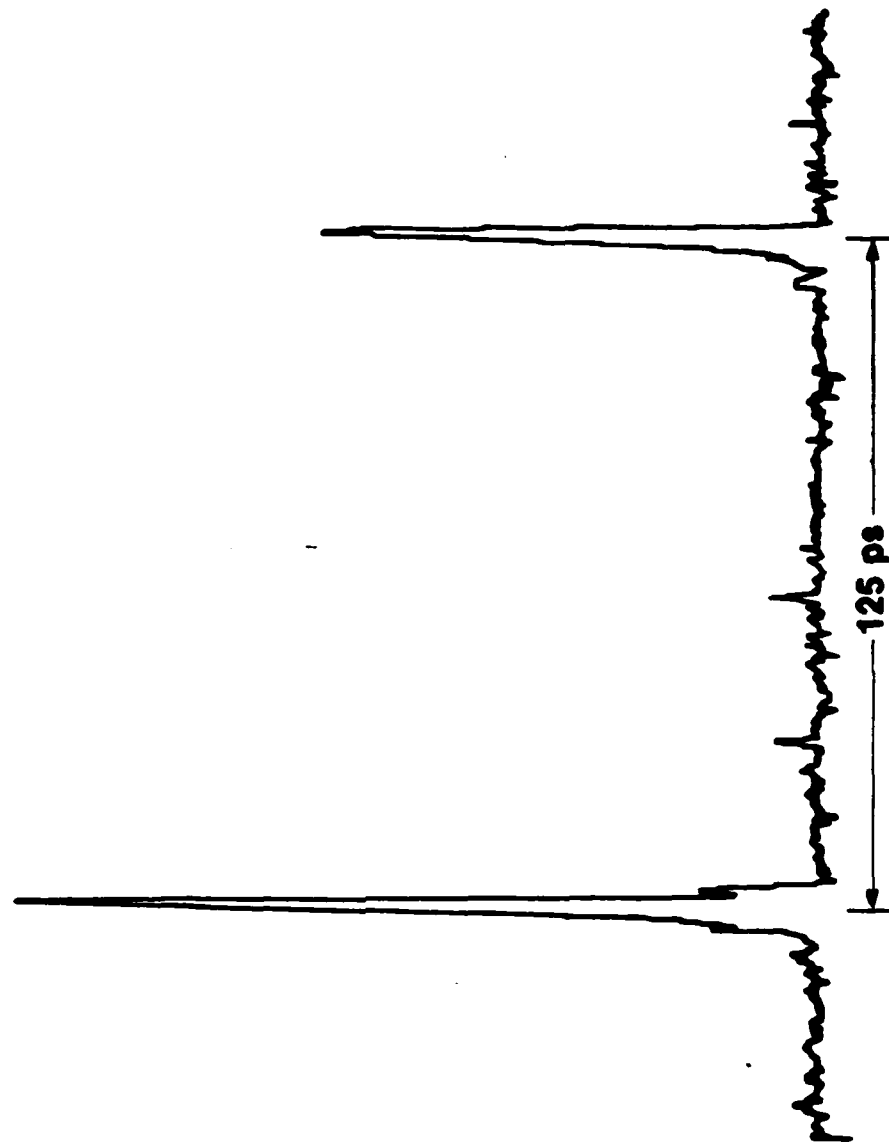


Full Scale = 60 ps

E3561

Streak Camera Trace of Compressed, Amplified Pulse

UFR
LLE



E3615

Regenerative Amplifiers

Laser Parameters

High Repetition Rate System

1 mJ
1 kHz
100 ps

Low Repetition Rate System

2 mJ
10 Hz
2 ps

**What is the maximum volume of
semiconductor material that can be
made to photoconduct?**

Assumptions:

Maximum carrier density: $10^{17}/\text{cc}$

**Every photon yields an electron-hole
pair**

Uniform illumination of the bulk

Result:

**$5 \times 10^{-2} \text{ cc/mJ}$
or $2.5 \text{ cc @ } 50 \text{ mJ}$**

At 10^{17} carriers/cc the conductivity is:

$$ne\mu$$

$$\text{Si: } \mu = 2000 \text{ cm/V sec}$$

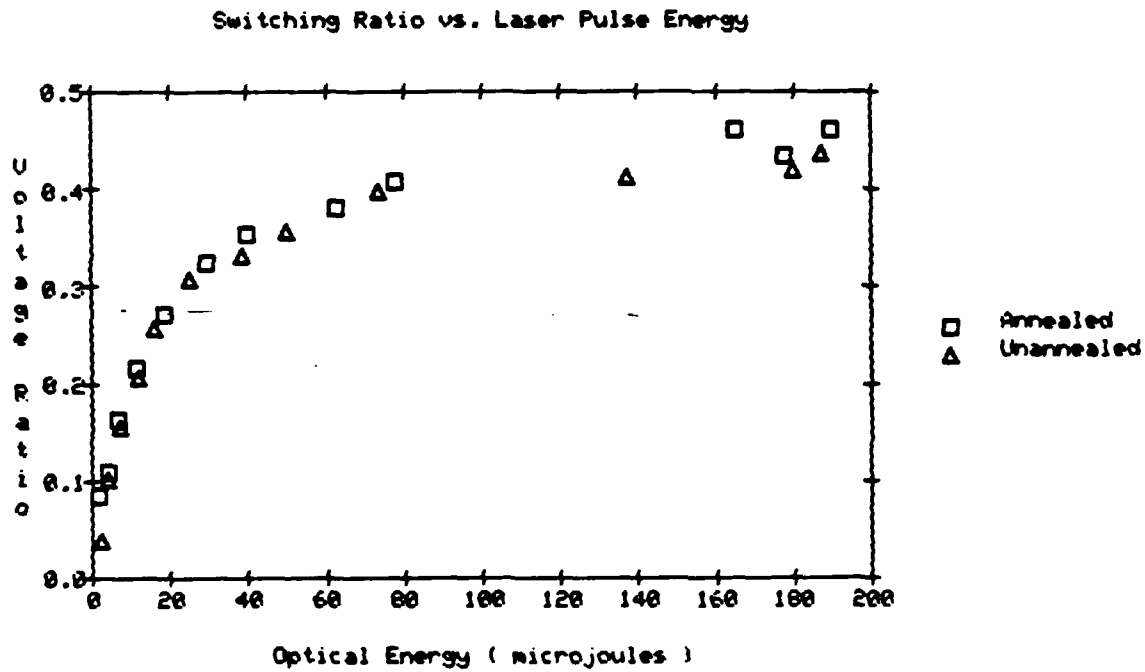
$$\text{GaAs: } \mu = 9000 \text{ cm/V sec}$$

$$\sigma = 32 \text{ (1/ohm cm) for Si}$$

$$\sigma = 144 \text{ (1/ohm cm) for GaAs}$$

Figure 4

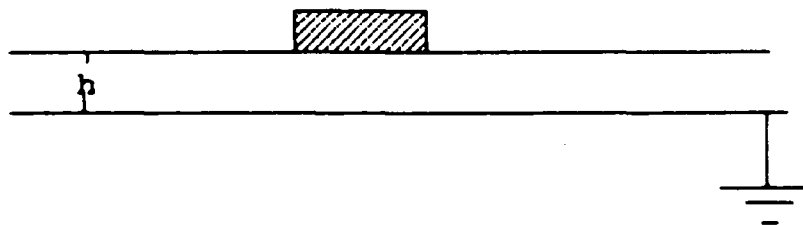
Comparison of Switching Efficiency
Between Laser Annealed Al Contacts on Si
and Unannealed Contacts



The cut-off frequency for a microstrip transmission line is:

$$f = (c/2\pi h) \tan^{-1} (\epsilon_r) \sqrt{2/(\epsilon_r - 1)}$$

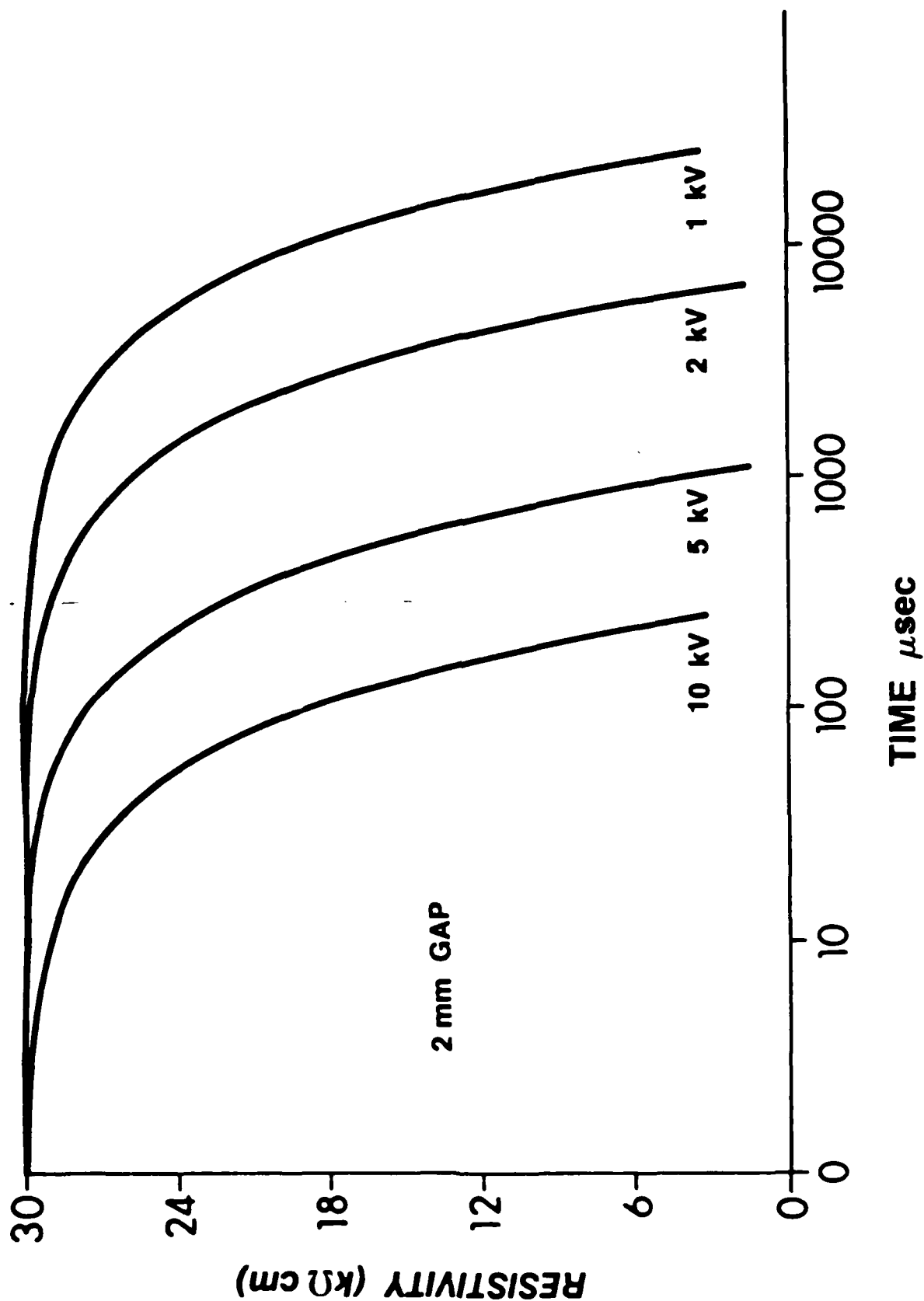
Therefore the thickness of the microstrip line must be as small as possible to obtain the highest frequency response.



1 Bahl and d Trivedi, "Designer's Guide to Microstrip Line" Microwaves, 174 (may, 1977)

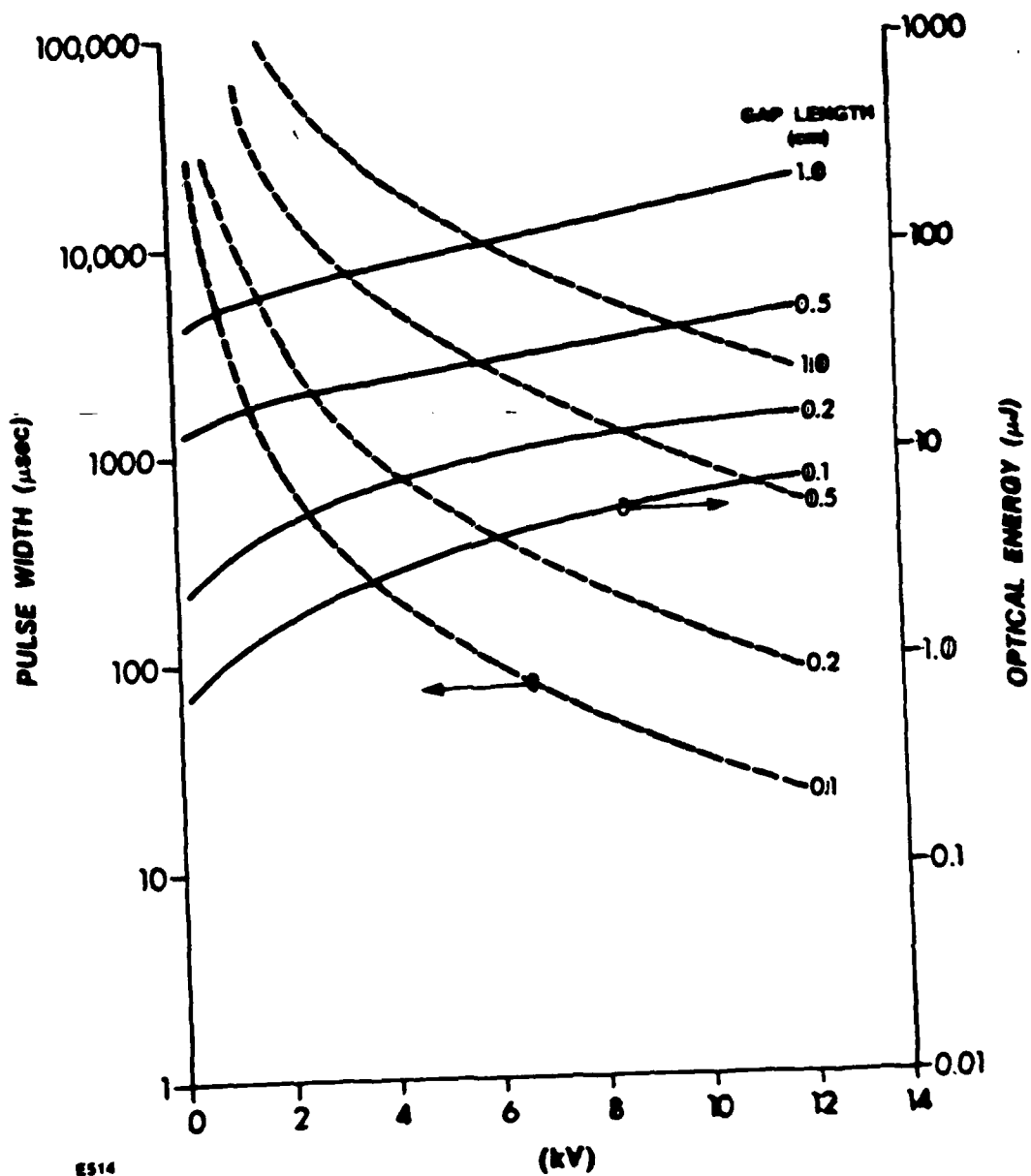
THERMAL RUNWAY IN NEARLY INTRINSIC Si

UA
LLE



E513

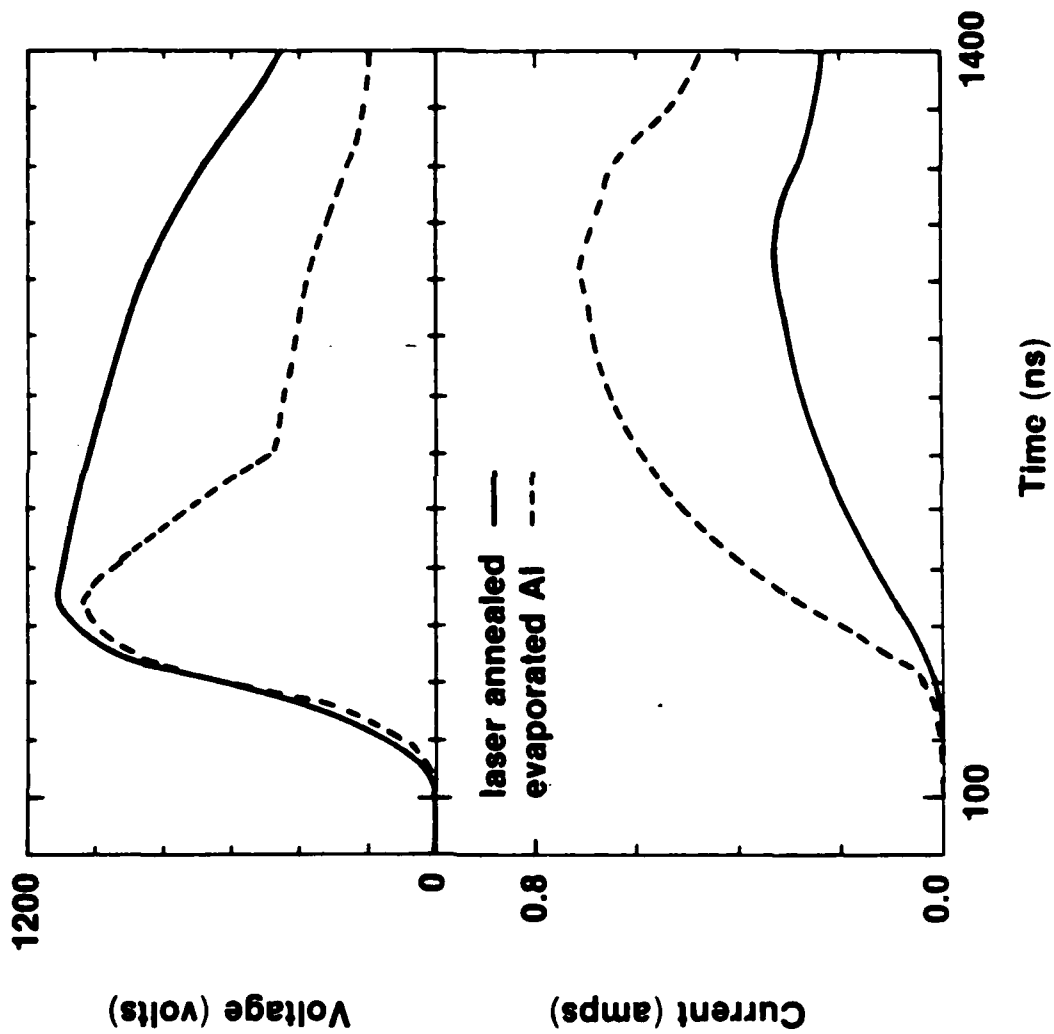
THERMAL RUNWAY IN NEARLY INTRINSIC SI



E514


Pulsed-Leakage Current and Bias Voltage of Si Switches

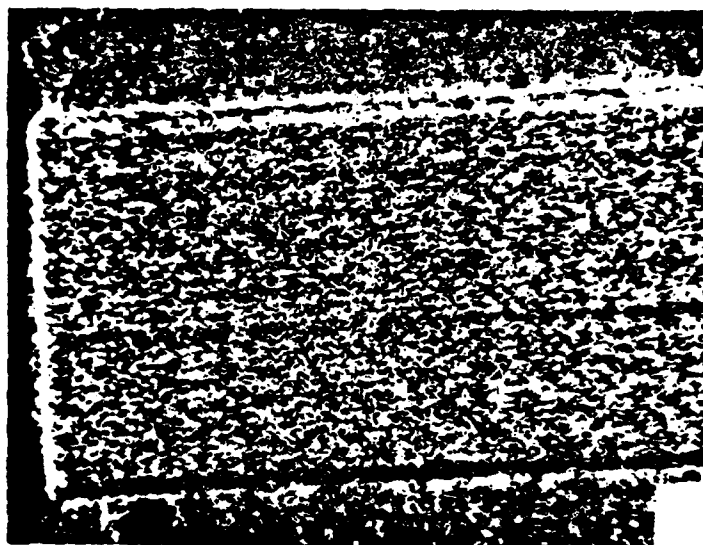
UFR
LLE



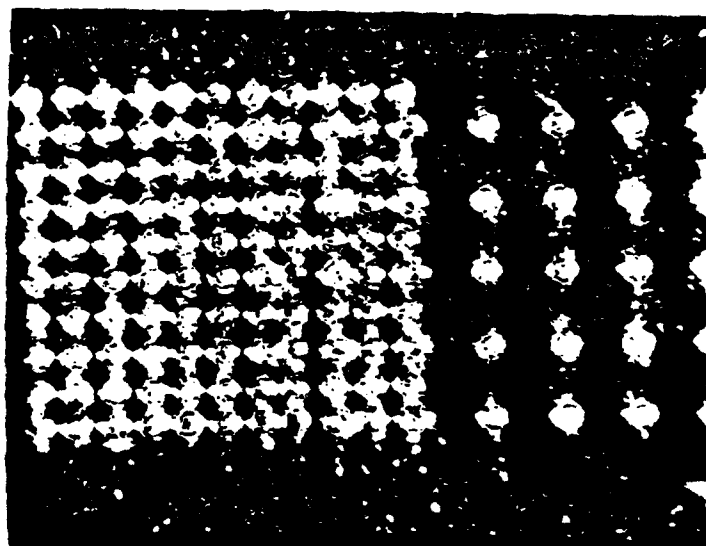
E3387

Optical Micrographs Showing the Effects of Laser Annealing of 3000-Å Au Film on Si

UP
LLE 



25- μ m
spot separation



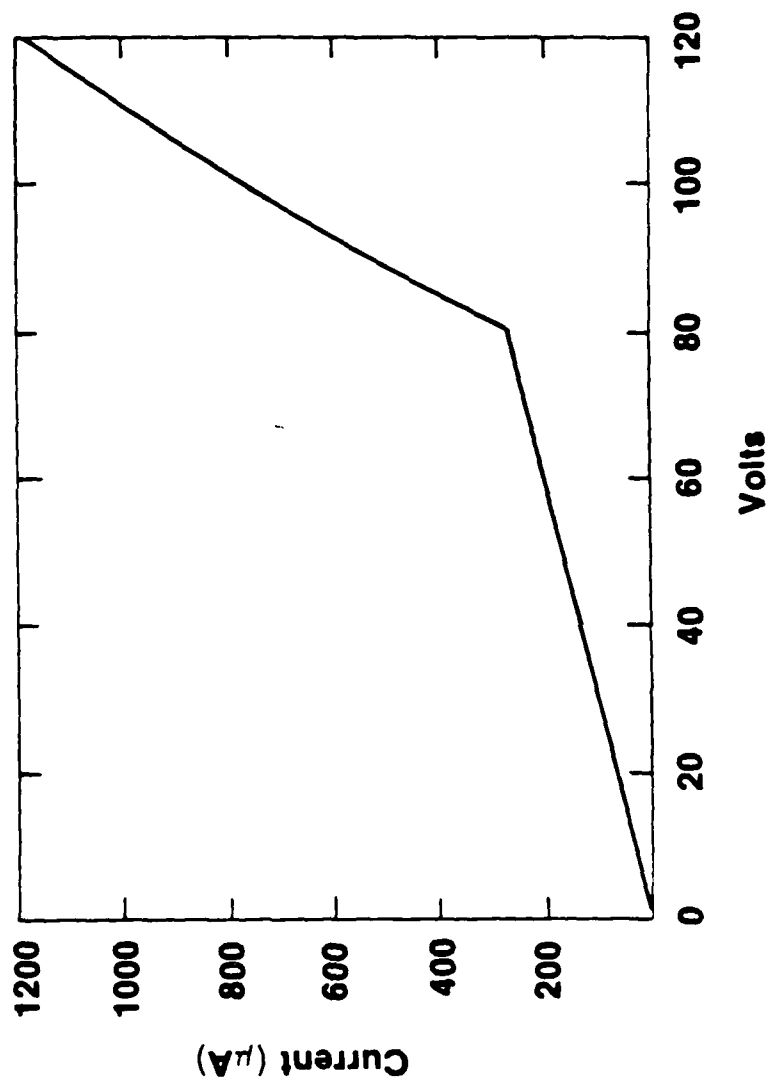
100- μ m
spot separation

200- μ m
spot separation

E3591

I-V Characteristic of Laser-Annealed Au on Si 2-mm Gap

U A
L L E

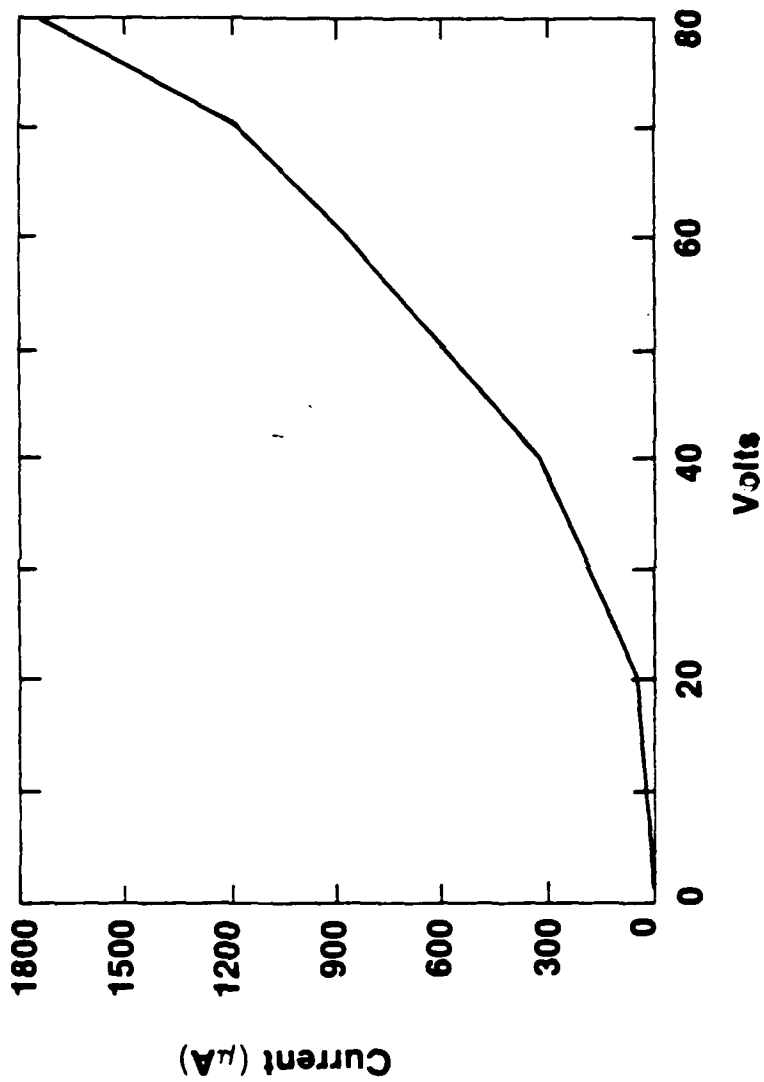


At 80 V the laser-annealed contact switches from the ohmic to injected current regime.

E3593

I-V Characteristic of Al Evaporated on Si
2-mm Gap

UR
LLE

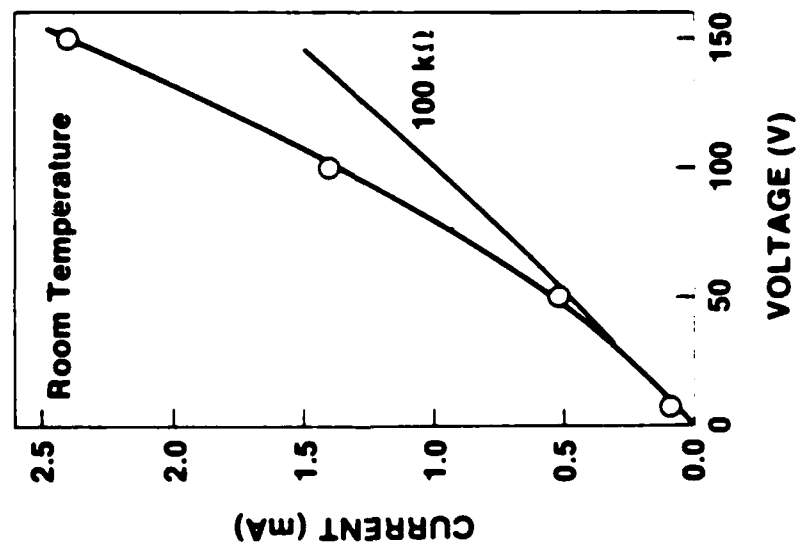
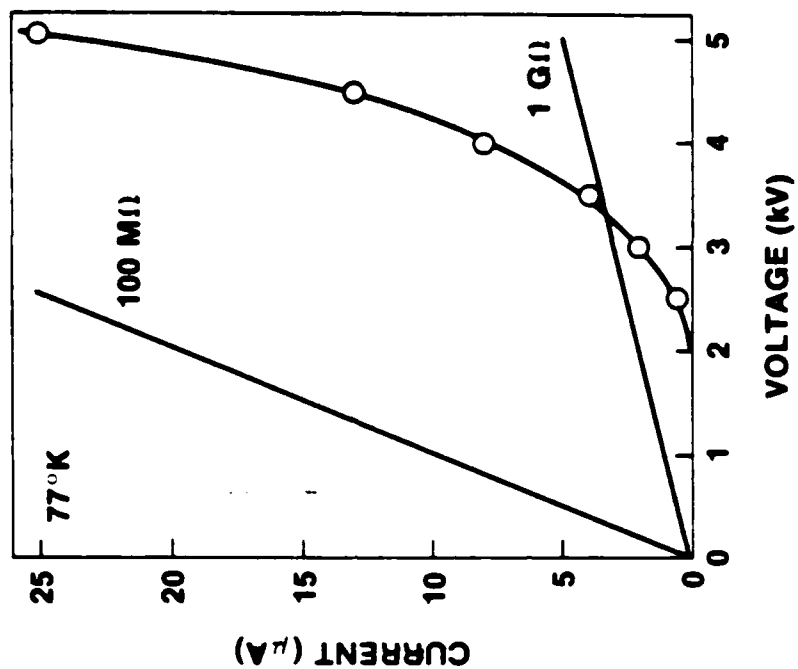


The nonprocessed contact is not ohmic.

E3592

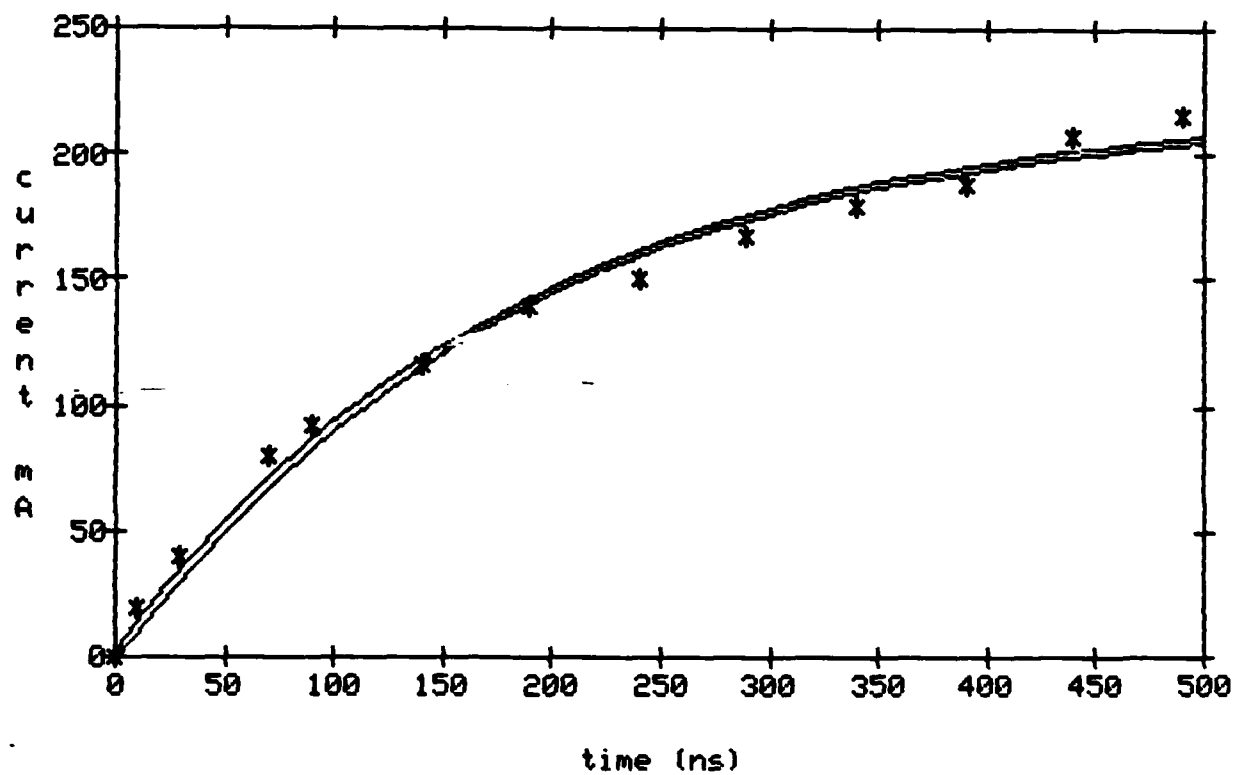
IV CURVE CHARACTERISTICS FOR Au-DOPED SILICON

UJR
LLE



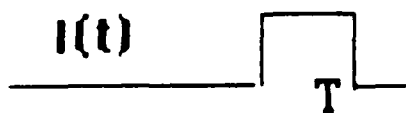
E554

RISE TIME OF CURRENT FOR A 8KV VOLTAGE PULSE



Affect of turn on time on switch heating

Assume a square pulse in time



$$E_A = I_0 T$$

$$E_A(t) = I_0 t$$

$$r(t) = hvLV_0 / (2v_s e E_A)$$

$$E_j = \int \frac{V_0^2 dt}{r(t)}$$

$$E_j = \frac{V E_0 e v_s T}{hvL}$$

$$E_A = 1 \text{ mJ} \quad V_0 = 10 \text{ kV}$$

$$v_s = 10^7 \text{ cm/sec} \quad \text{Volume} = 5 \times 10^{-2} \text{ cc}$$

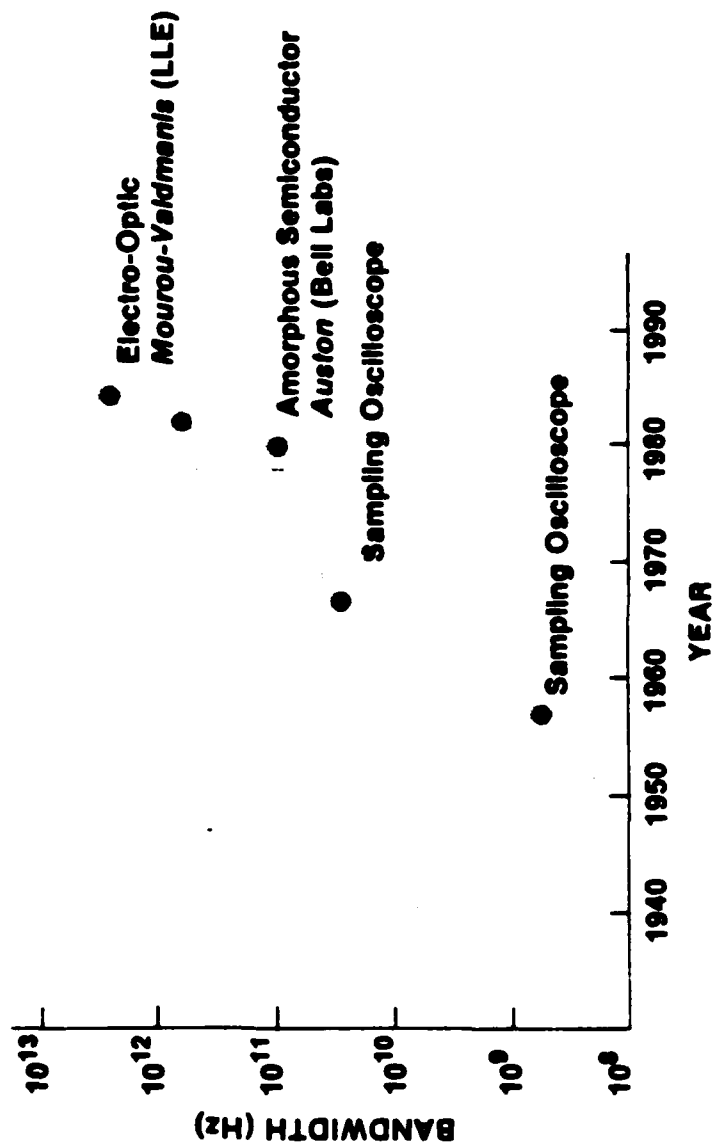
$$T = 100 \text{ ps} \quad C_p = 0.17 \text{ cal/gm}^\circ\text{K}$$

$$\Delta \text{Temp} = 0.5^\circ\text{C} \quad L = 0.2 \text{ cm}$$

Time	$\Delta \text{Temperature } ^\circ\text{C}$
1ps	0.005
1ns	5.0
10ns	50

PROGRESS IN HIGH-SPEED ELECTRICAL SIGNAL SAMPLING

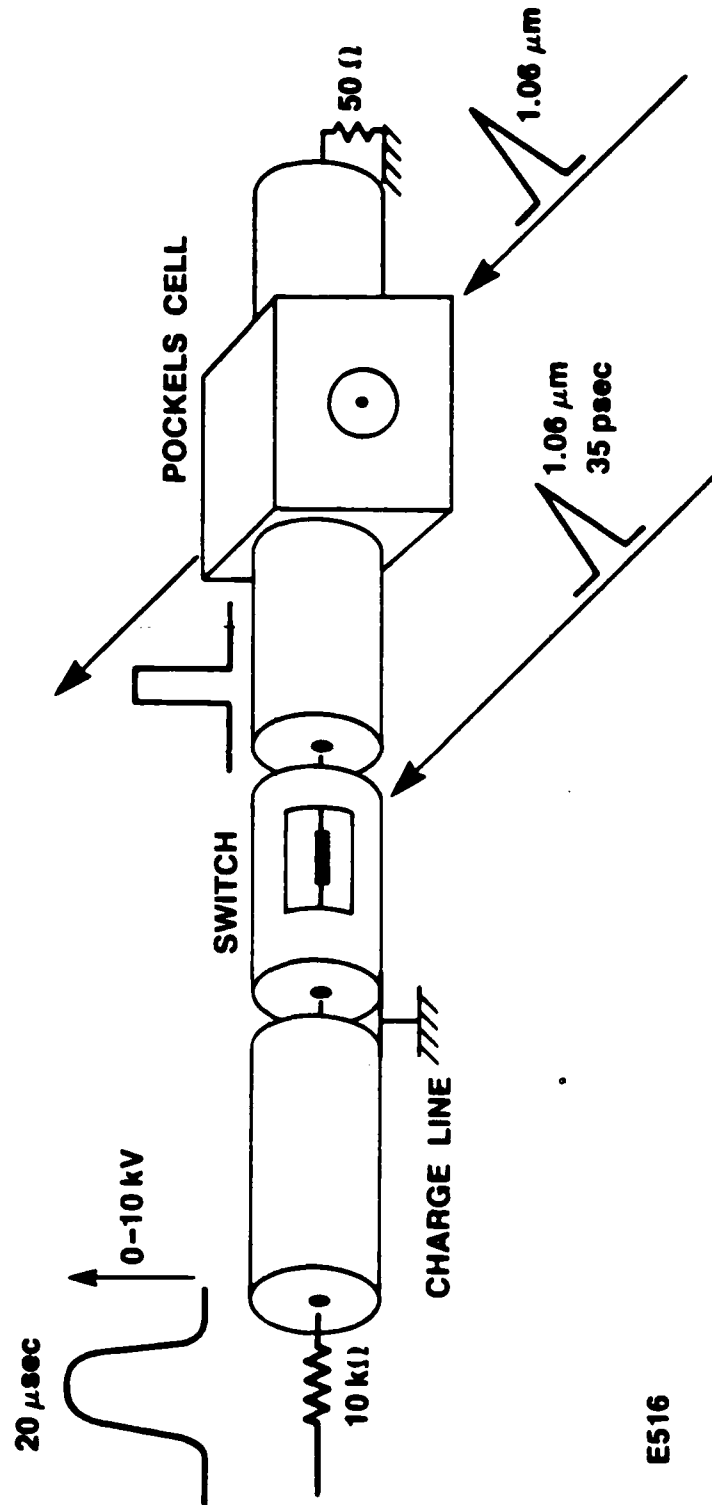
LJR
LLE



E2867

ELECTRICAL RISETIME MEASUREMENT

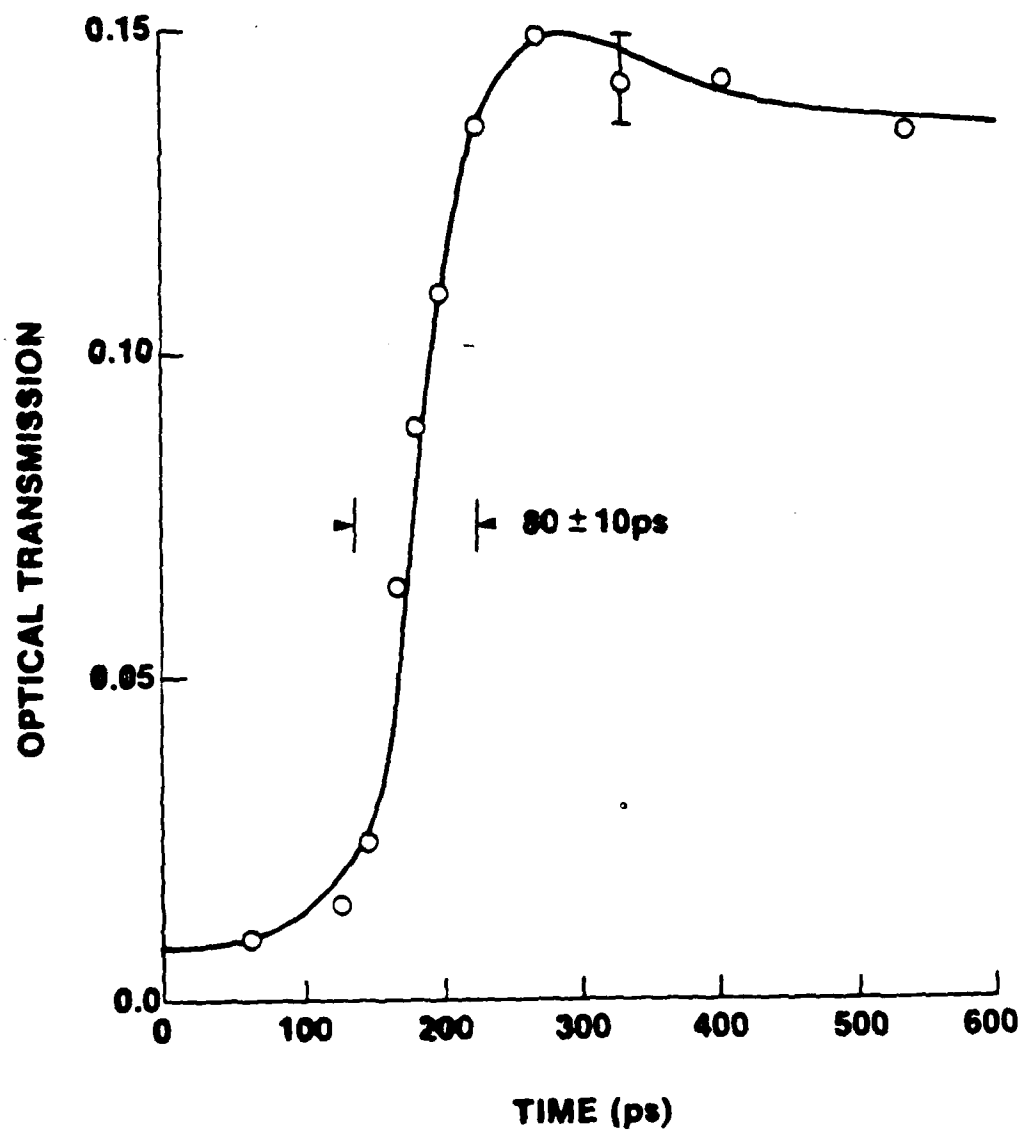
UR
LLE



E516

OPTICAL TRANSMISSION OF A FAST POCKELS CELL DRIVEN BY A LASER- ACTIVATED SI SWITCH

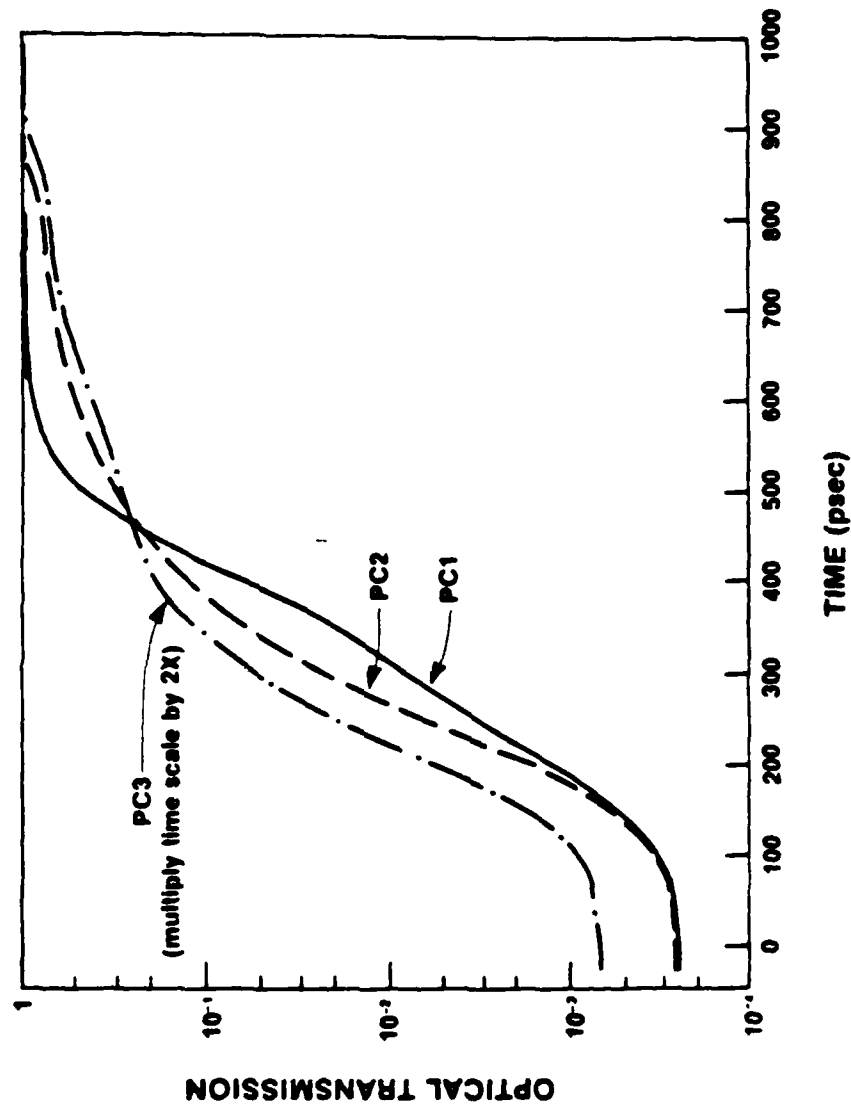
UR
LLE



E517

ZETA SWITCH-OUT POCKELS CELL TRANSMISSION

UPR
LLR



E744

PICOSECOND ELECTROOPTIC SAMPLING SYSTEM



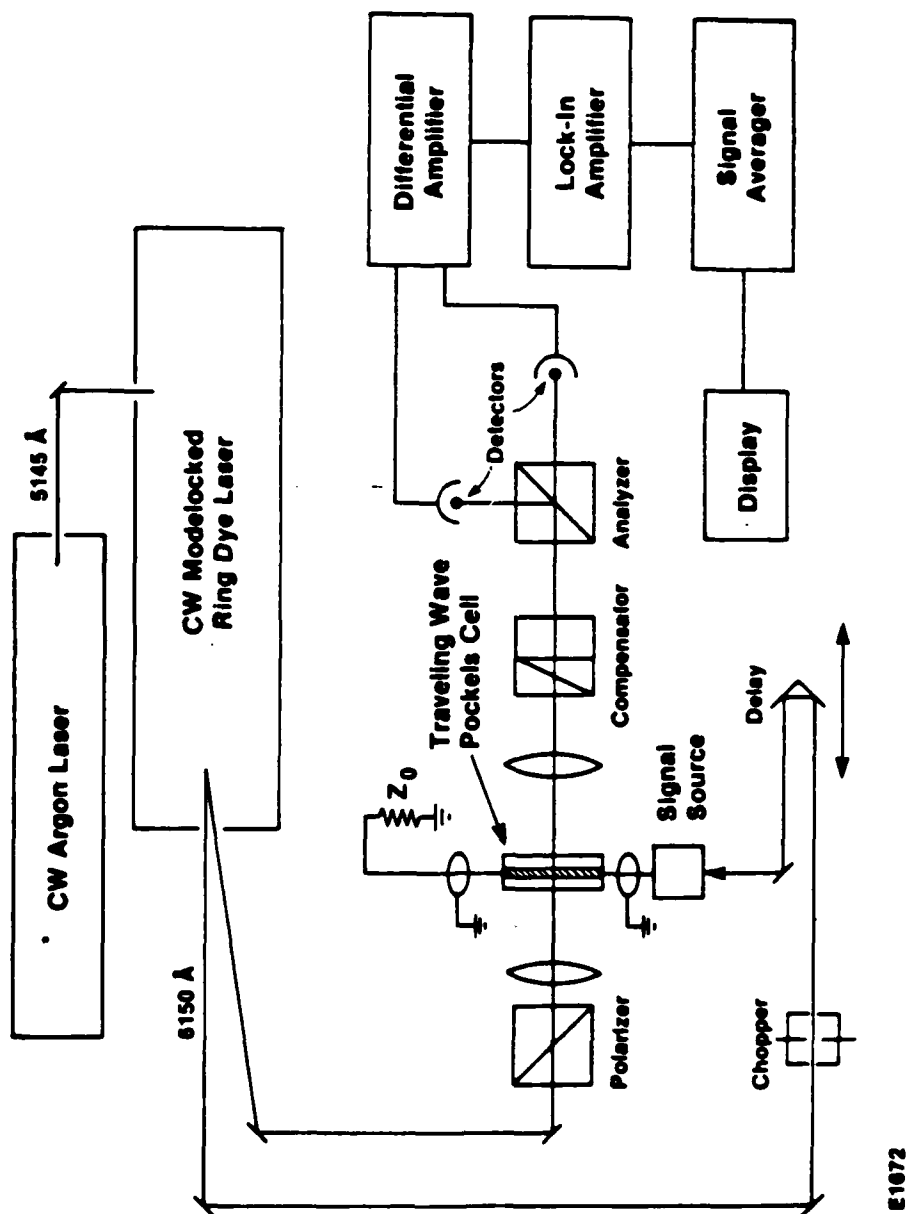
A system for the characterization of ultrafast electrical transients based on the inherent simplicity, reliability, and ultrahigh bandwidth capability of the Pockels effect

- **Demonstrated performance to date:**
 - Temporal resolution** ~ 0.5 psec or 1 THz
 - Sensitivity** < 50 μ V
- **Potential system performance:**
 - Temporal resolution** < 0.2 psec
 - Sensitivity** < 50 μ V

E1775

PICOSECOND SAMPLING SYSTEM

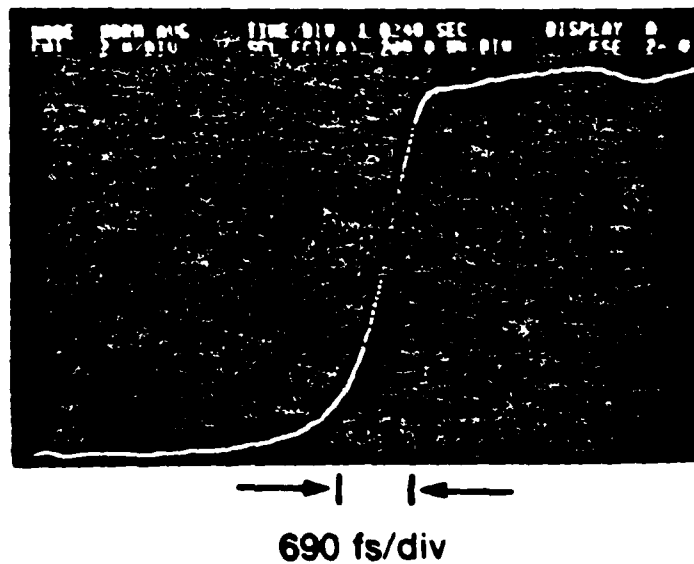
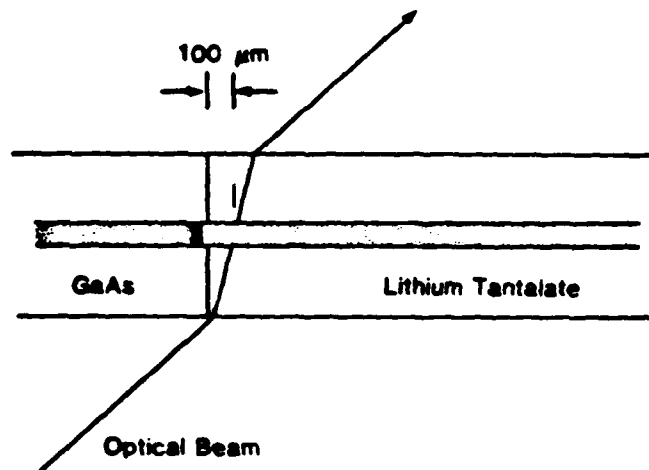
100
100
100



E1072

TRACE OF 550-fs EFFECTIVE RISE TIME AND THE ASSOCIATED ELECTRODE GEOMETRY

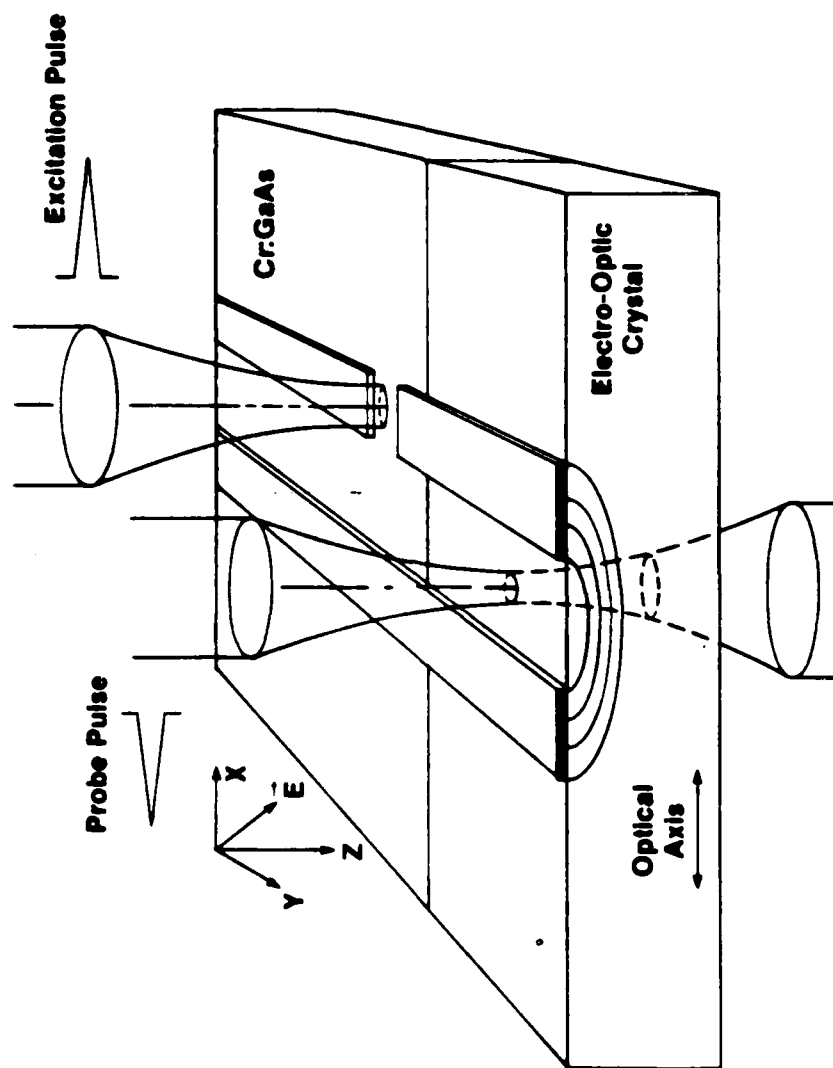
U
LLE



E2794

ELECTRO-OPTIC SAMPLER USING COPLANAR PARALLEL STRIPLINE

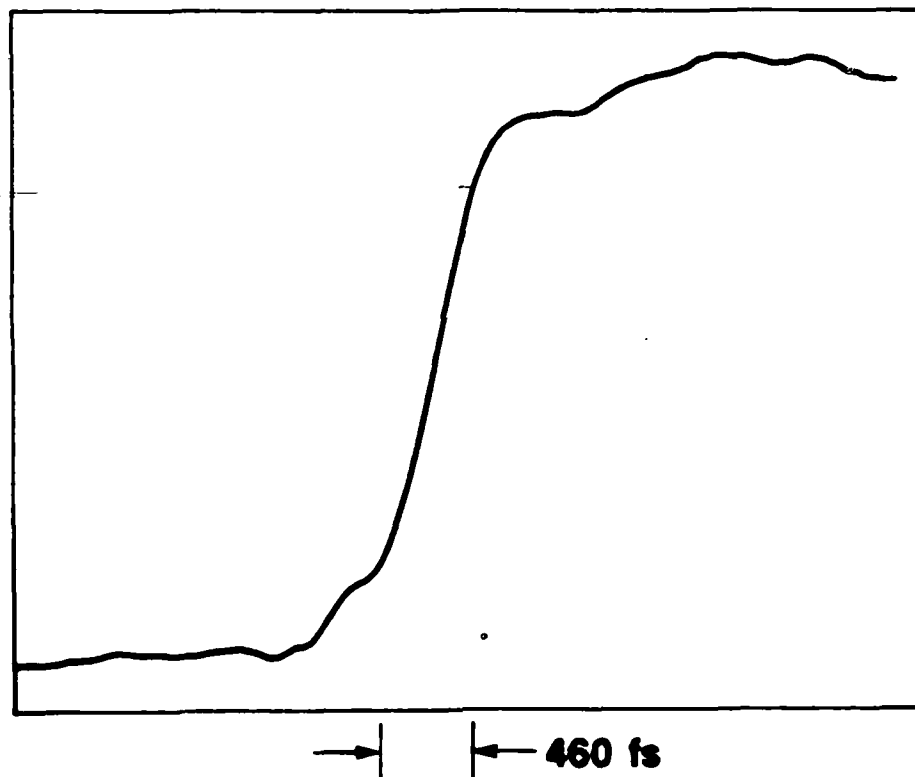
UR
LLE



E2876

TEMPORAL RESPONSE OF COPLANAR STRIP ELECTRO-OPTIC SAMPLER

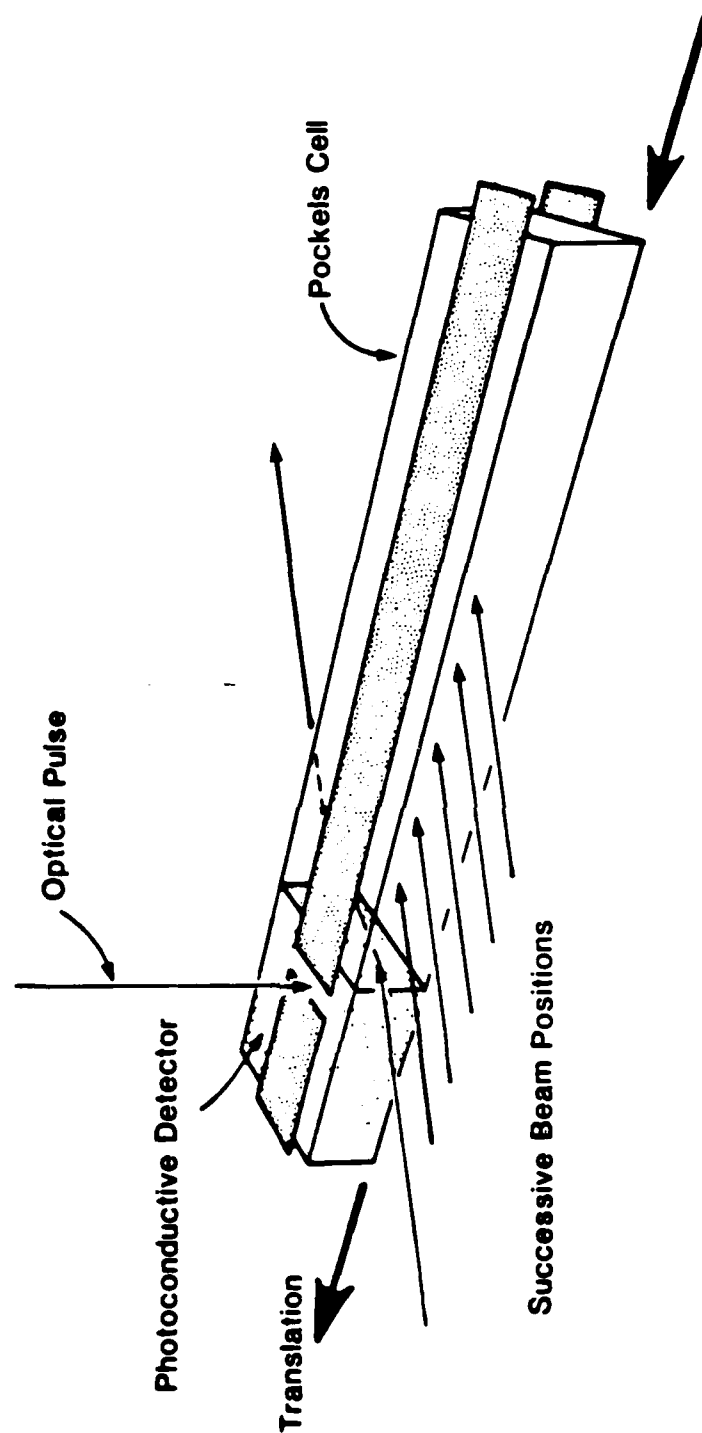
UR
LLE 



E2847

GEOMETRY FOR INVESTIGATING STRIP- LINE DISPERSIVE EFFECTS

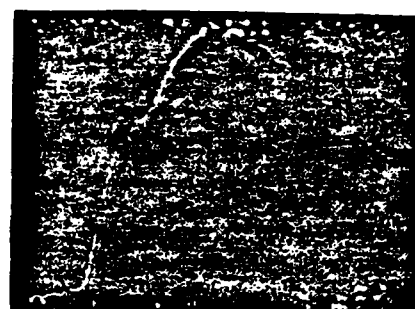
UR
LLE



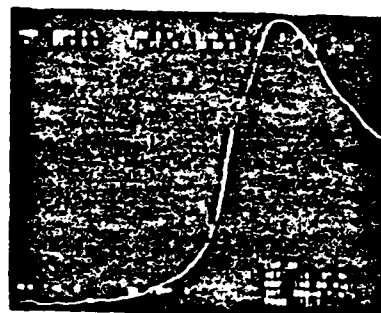
E2800

PROGRESSIVE DISPERSION IN THE 200- μ m THICK MODULATOR

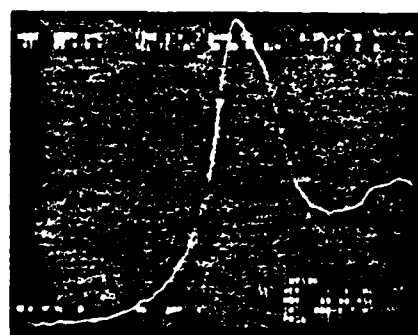
UR
LLE



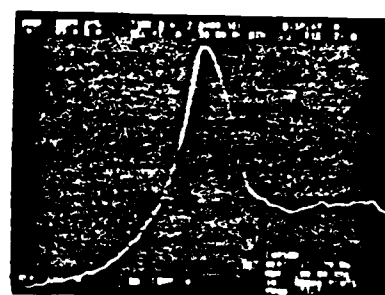
1.4 ps/div
rise time = 3.1 ps at 0 mm



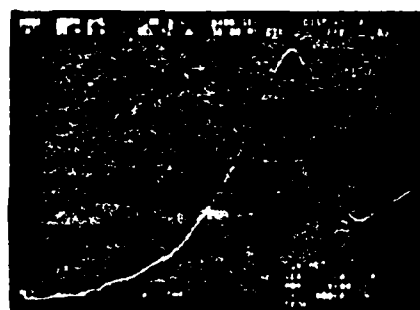
4 ps/div
4.4 ps at 0.4 mm



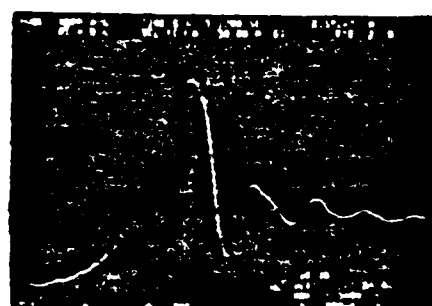
4 ps/div
7.0 ps at 1.2 mm



4 ps/div
8.9 ps at 1.9 mm



4 ps/div
14 ps at 3.6 mm

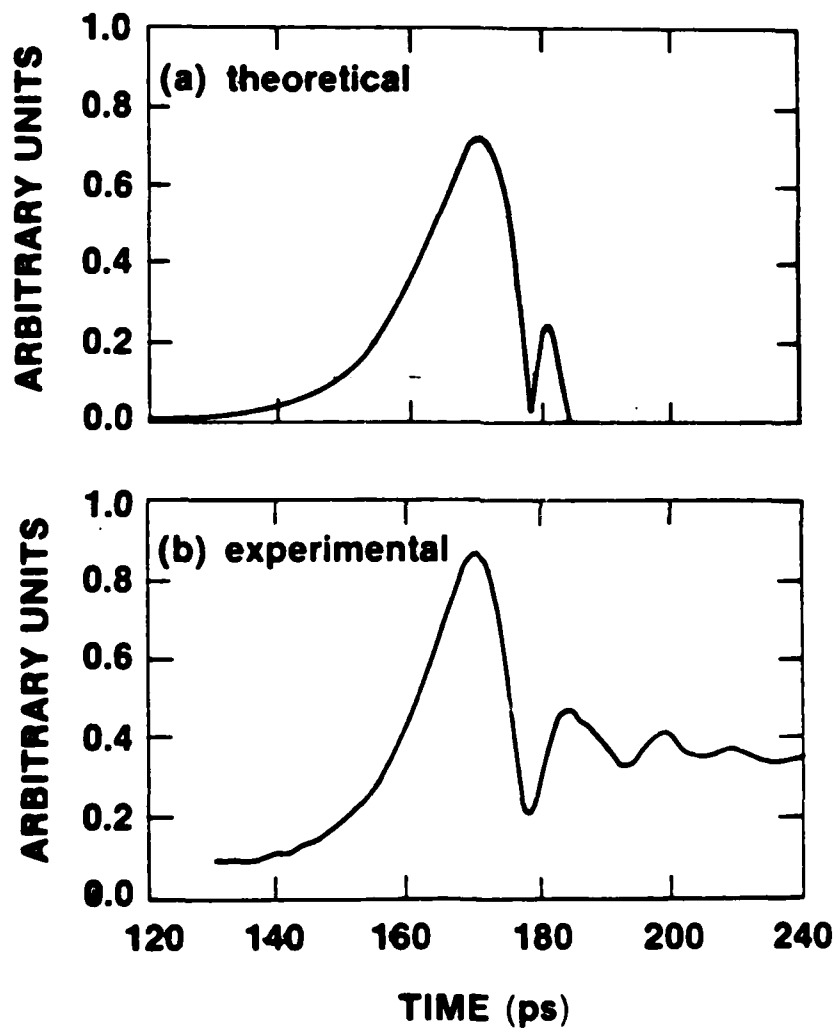


10 ps/div
21 ps at 6.2 mm

E2802

DISPERSION OF AN ASYMMETRIC PULSE ON MICROSTRIP TRANSMISSION LINES

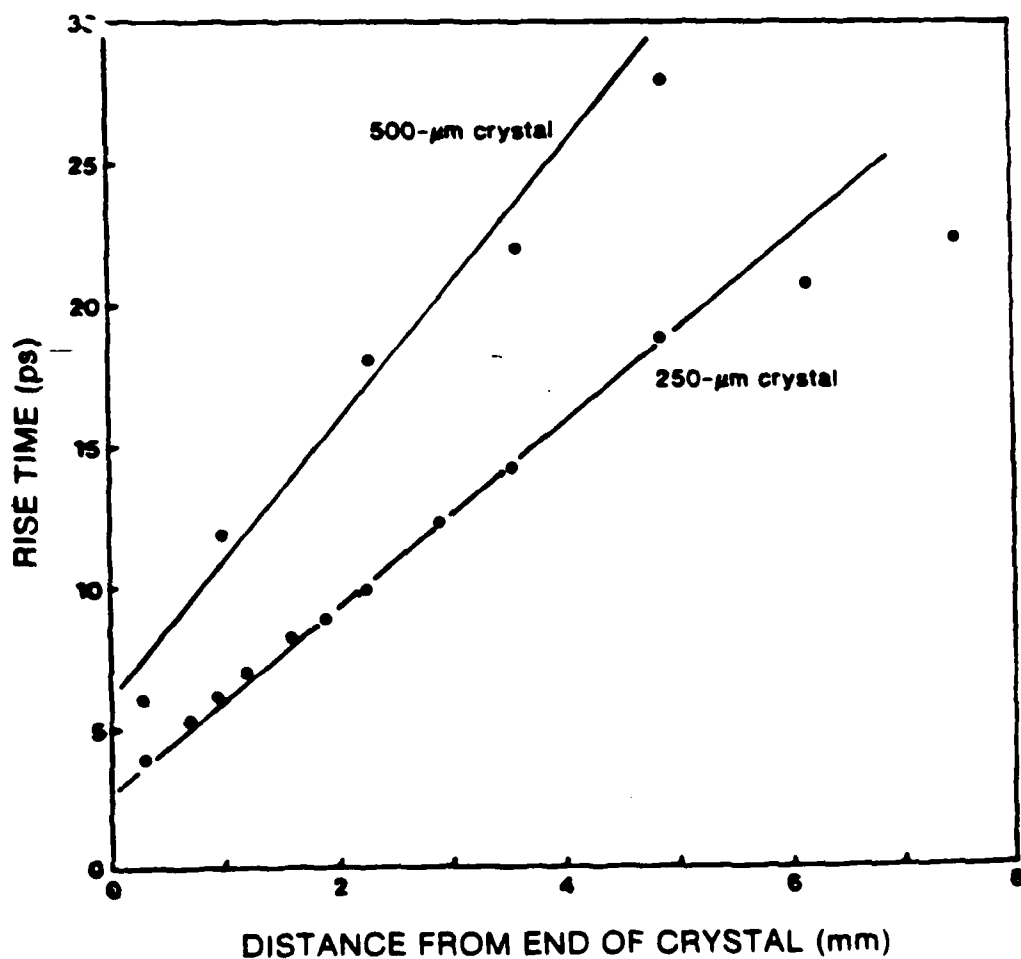
UR
LLE



E2852

COMPARISON OF THE DISPERSIVE EFFECTS FOR THE 500- μm AND 200- μm THICK MODULATORS

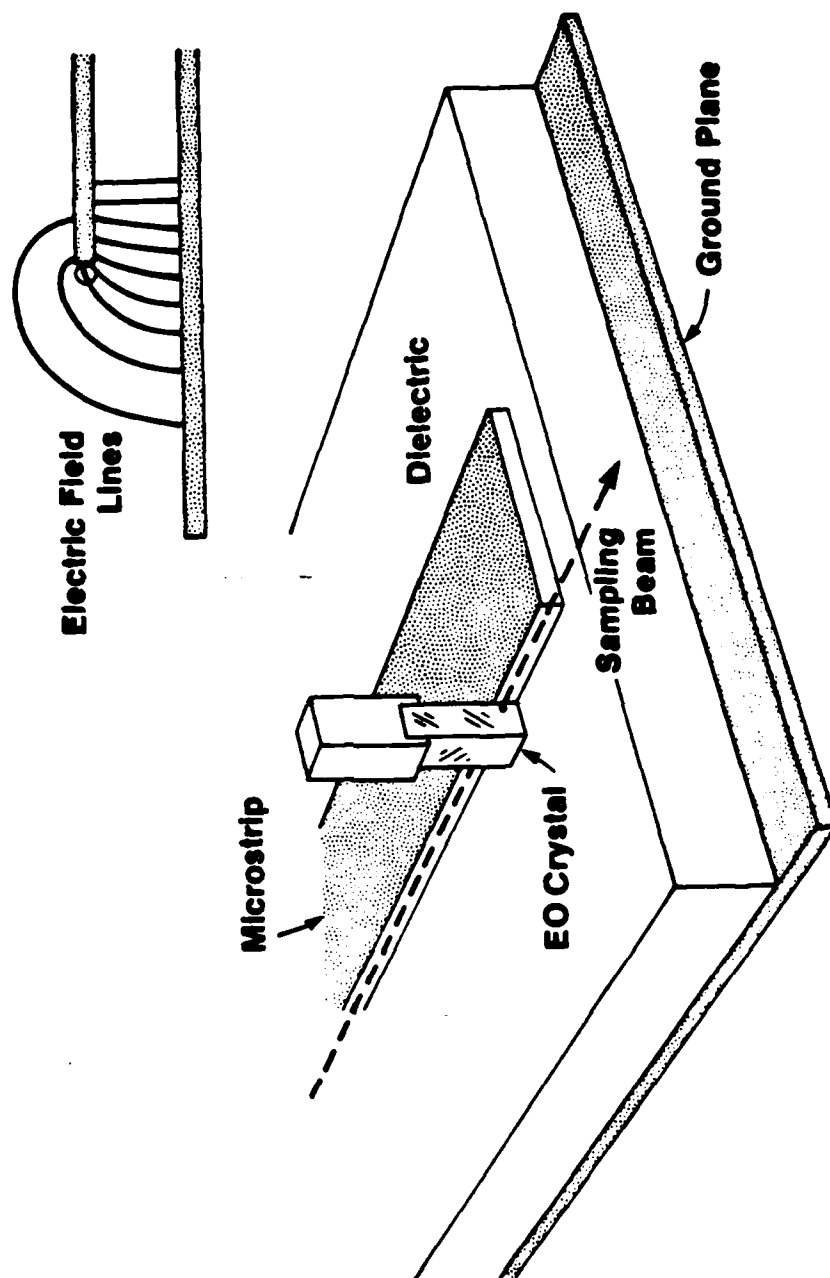
UR
LLE 



E2804

ELECTRODELESS ELECTRO-OPTIC SAMPLING

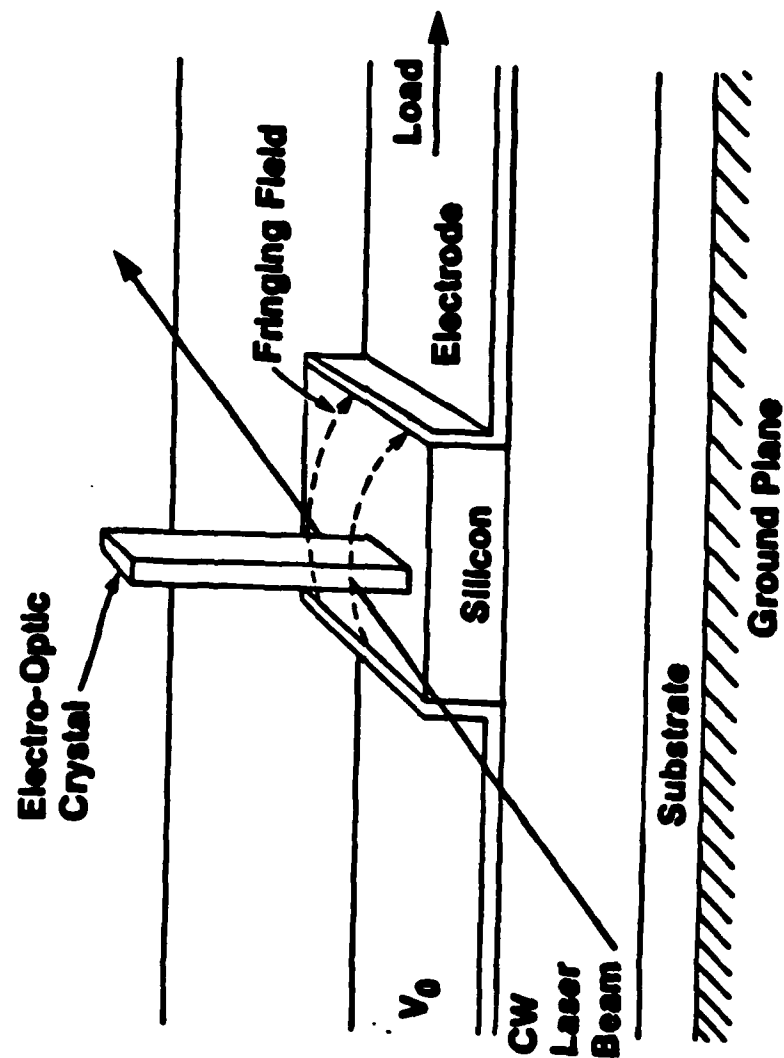
UPL
LLR



E2352

FIELD MEASUREMENT WITH AN ELECTRO-OPTIC TECHNIQUE

U.S. AIR FORCE
AFOSR-84-0000

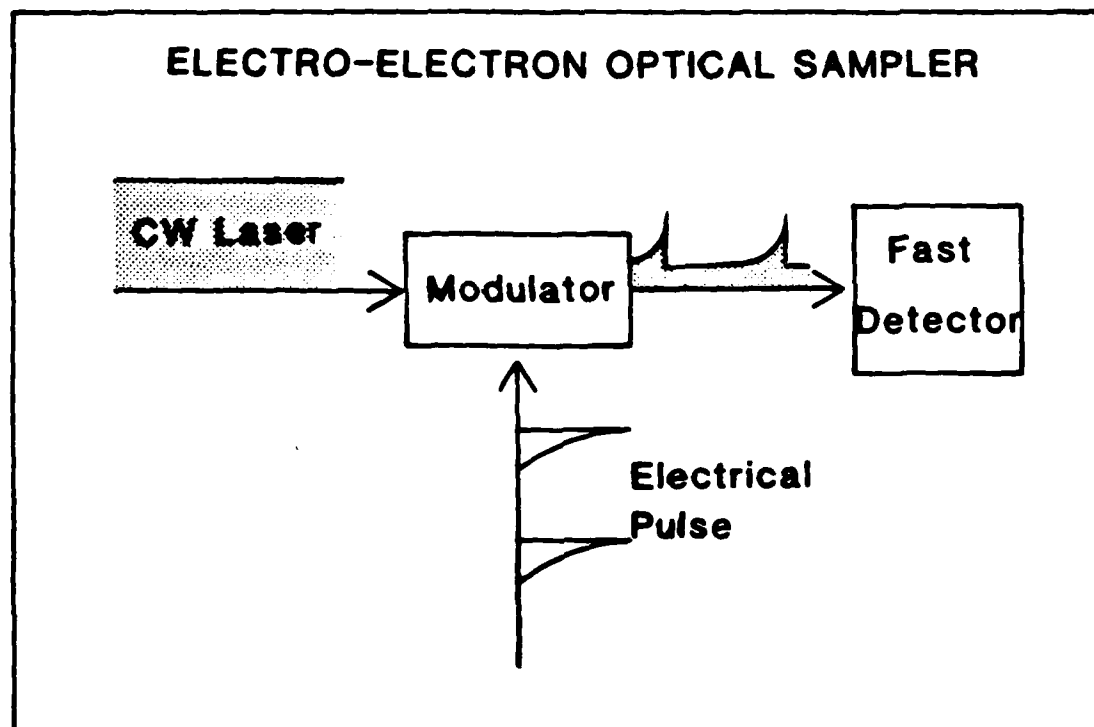
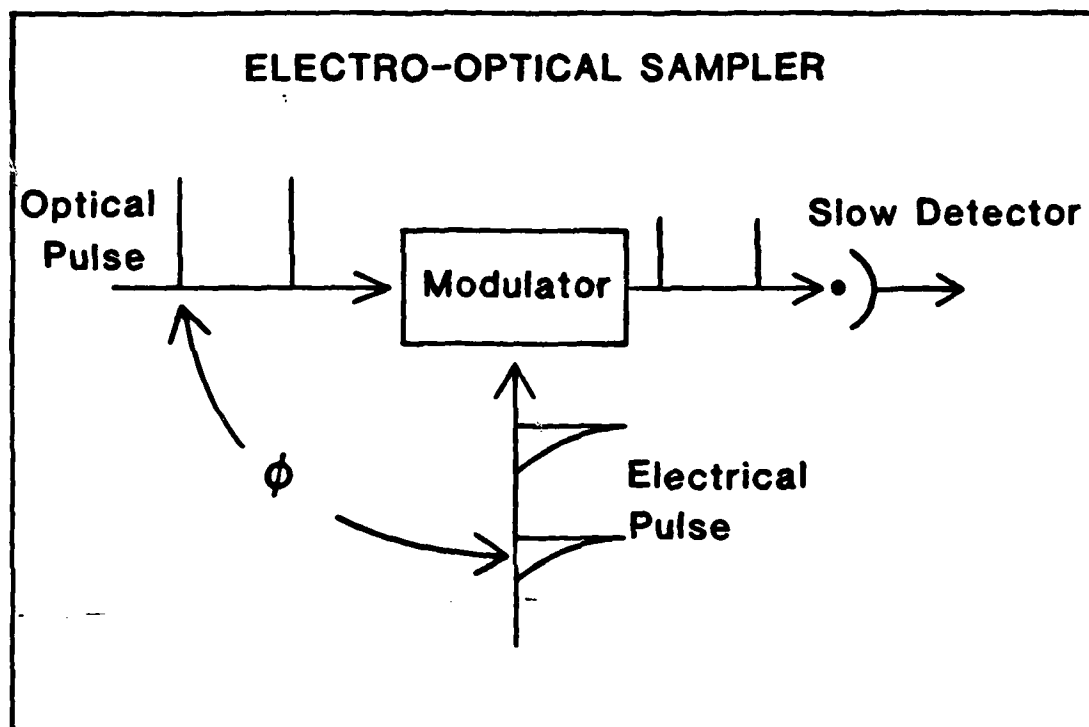


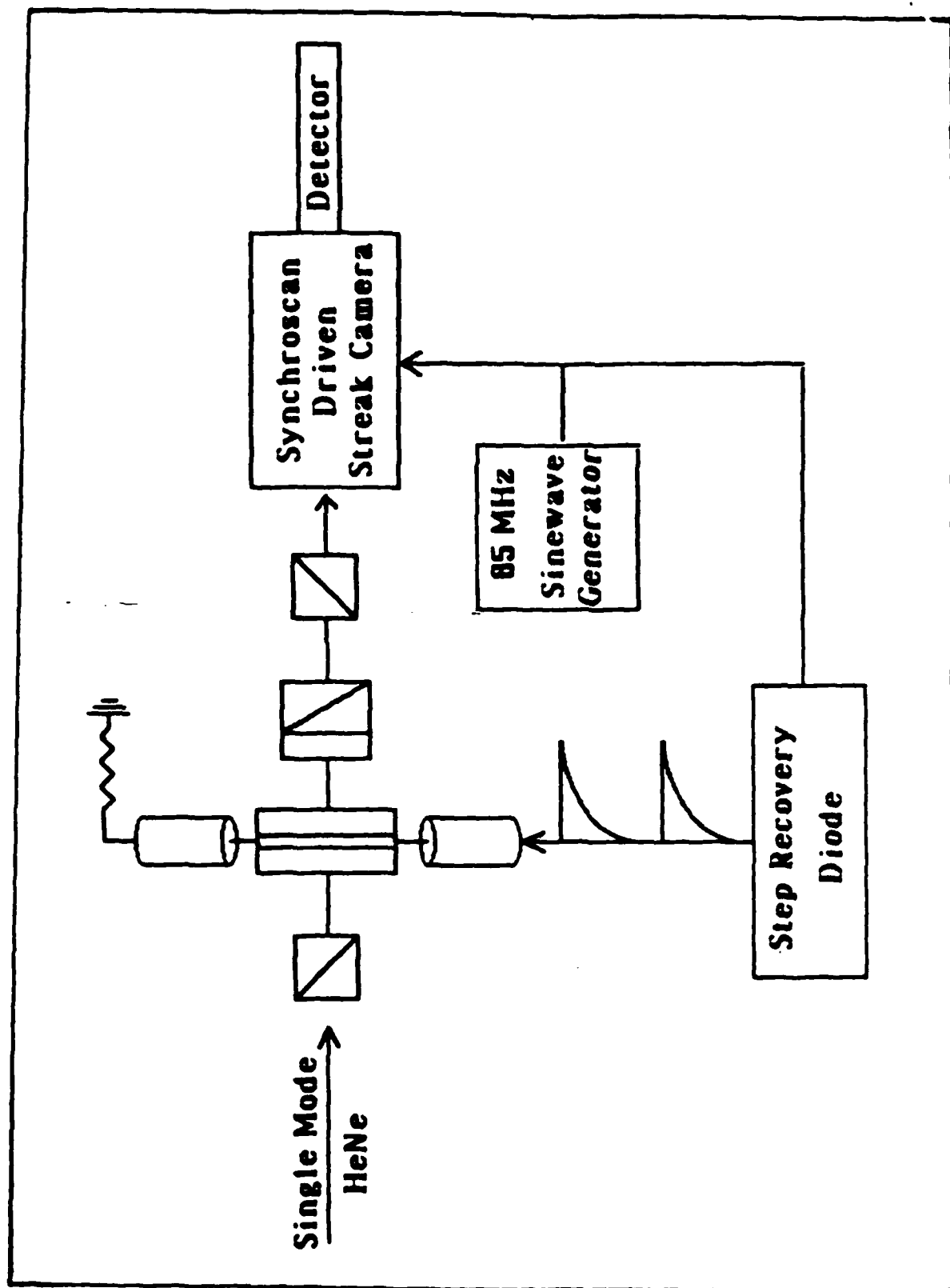
E2604

Figure 9

Converse Approaches to Picosecond Electrical Sampling

UR
LLE





PHOTOCONDUCTOR SWITCHING: SOME PHYSICAL MECHANISMS

Robert B. Hammond

Electronics Division

Los Alamos National Laboratory

Los Alamos, NM 87545

Introduction

At Los Alamos we have studied fast-risetime pulse generation with silicon photoconductors excited by Nd:glass laser pulses. We have achieved pulse risetimes of ~1 nsec, currents of several thousand amps, and square-pulse durations of 200 nsec into 25 ohm loads. Because of the intrinsic scalability of photoconductor power switches, much higher powers are possible. In this paper we discuss some of the physical mechanisms important in photoconductor power switching that affect pulse risetime, switching efficiency, pulse duration, control of photoconductor temperature, and switch size.

Silicon is attractive as the photoconductor switch material because large, high-quality crystals are readily available, it has an indirect bandgap and thus long carrier lifetime to permit long pulse length, it has well understood and controllable properties, and it has long absorption length, permitting large conductive volumes and thus large currents, at 1.06 μm the wavelength of readily available Nd lasers.

Risetime

We assume that the PCPS is in a coaxial transmission-line-pulser geometry where the photoconductor replaces the center conductor of the coax. Pulse risetime is determined by the duration of the excitation laser pulse, the inductance/line-impedance ratio, L/Z ; and the time for optical absorption.

Since Nd laser pulses can be made as short as 10 ps with ease, laser pulse length is not important. Also, optical-absorption time is ~10 ps for a 1-mm absorption depth in silicon and so is generally not a limit. Inductance is thus the normal limit to achievable risetime in photoconductor power switch design.

Efficiency

Photoconductor on-resistance is determined by the relation:

$$R_{on} = L^2 / [N_{eh} q (\mu_e + \mu_h)]$$

where L is the photoconductor length, N_{eh} is the total number of electron-hole pairs produced by the laser pulse, q is the electronic charge, and μ_e , μ_h are the electron and hole mobilities of the photo-excited carriers. In order to reduce the on-state resistance one wants to decrease the length of the photoconductor (maximize its electric field breakdown strength); increase the number of carriers produced by the laser (maximize carrier-production efficiency); have high carrier mobilities; and make sure that all the carriers are used to carry current.

Breakdown strength can be improved by careful surface preparation and providing long surface paths between electrodes. To maximize carrier production an efficient laser is needed. Flash-lamp-pumped Nd lasers are not efficient, but very efficient semiconductor-laser-pumped Nd lasers have been demonstrated. The energy cost per electron-hole pair in silicon at the Nd laser wavelength is just 1.17 eV. One cannot let free carrier absorption steal photons, however. This limits carrier density to less than 10^{18} cm^{-3} at room temperature and less than 10^{16} cm^{-3} at 77K, see figures 1 and 2. Also one must be sure that all photoexcited carriers are within a skin depth

of the photoconductor surface. This criterion also limits carrier density, see figure 3. Carrier mobilities can be enhanced by using pure material and reducing temperature, see figure 4.

On-time

The photoconductor relaxes to its non-conductive state by several mechanisms. First, carriers can be lost by bulk or surface trapping and recombination. Second, they can be lost by recombination at the electrodes. Third, the build-up of space charge in the photoconductor can shield the carriers from the applied bias. Despite the many studies of photoconductivity in semiconductors over the past 40 years there have been no studies of these effects for the conditions occurring in photoconductor power switching. The excitation conditions of the photoconductor power switch are high-optical-excitation-level and non-steady-state. It is important to study these conditions to determine the limits to on-time in photoconductor power switching.

An important limit to photoconductor on-time is imposed by Auger recombination of electrons and holes in the bulk. Because of this limit, long on-time is incompatible with high electron-hole pair density, see figure 5.

Temperature Control

Because semiconductors have conductivities that increase exponentially with increasing temperature, it is important to control the photoconductor temperature so that it does not become conductive from heating and experience "thermal runaway", see figure 6. It is also important to fabricate the photoconductor from high resistivity material to minimize dark current heating. The highest resistivity that silicon can have is its intrinsic resistivity. This is 2.3×10^5 ohm-cm at room temperature. This

resistivity can be achieved using Au-compensated n-type material, see figure 7, or by using Li-compensated p-type material. The heating in the photoconductor during conduction is of course minimized by minimizing the on-state resistance. This will be a design trade-off since lowering on-resistance requires more photons in the excitation laser pulse. We are fortunate, however, that semiconductors have very high thermal conductivities, see figure 8, and thus make it relatively easy to remove excess heat.

Summary and Outlook

Silicon photoconductors excited by Nd-laser pulses are promising as high-speed, high-power closing switches. Fundamental studies of the important physical mechanisms in photoconductor on-time and breakdown strength are needed. Development of efficient semiconductor-laser-pumped Nd lasers will be important to future applications. Optimization of PCPS design for room temperature and low temperature operation should be performed to look at system trade-offs.

References

- 1) W. C. Nunnally and R. B. Hammond. "Optoelectronic Switch for Pulsed Power," in Picosecond Optoelectronic Devices, C. H. Lee, ed.; Academic Press, Orlando, 1984, pp. 374-398.
- 2) Robert B. Hammond. "Extremely Fast Risettime Switches," in Proceedings of the Workshop on Solid State Switches for Pulsed Power, Jan. 12-14, 1983; Tamarron, Colorado; pp. 222-257.

- 3) W.C. Munnally and R. B. Hammond. "80-MW Photoconductor Power Switch," *Applied Physics Letters*, Vol. 44, pp. 980-982, 1984.
- 4) P. Siffert and A. Coche. "Behaviour of Lithium in Silicon and Germanium," in Semiconductor Detectors, G. Bertolini and A. Coche, eds.; Wiley Interscience, New York, 1968, pp. 27-52.
- 5) C. Jacoboni, C. Canali, G. Ottaviani, and A. A. Quaranta, "A Review of Some Charge Transport Properties of Silicon," *Solid State Electronics*, Vol 20, p. 77, 1977.
- 6) M. G. Holland, "Phonon Scattering in Semiconductors from Thermal Conductivity Studies," *Physical Review*, Vol 134, p. A471, 1964.

ABSORPTION LENGTH IN SILICON

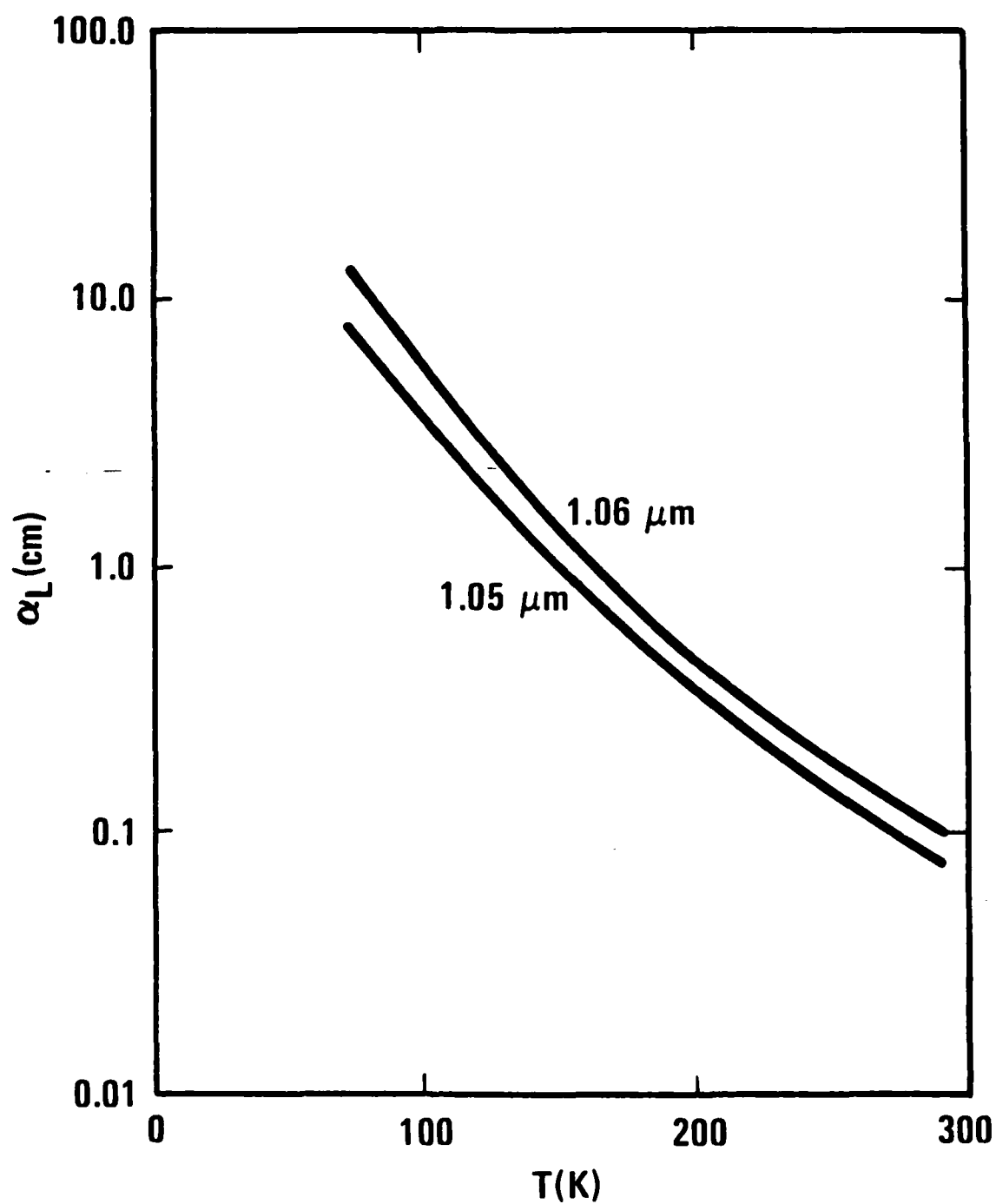


FIGURE 1

Si FREE-CARRIER ABSORPTION DEPTH

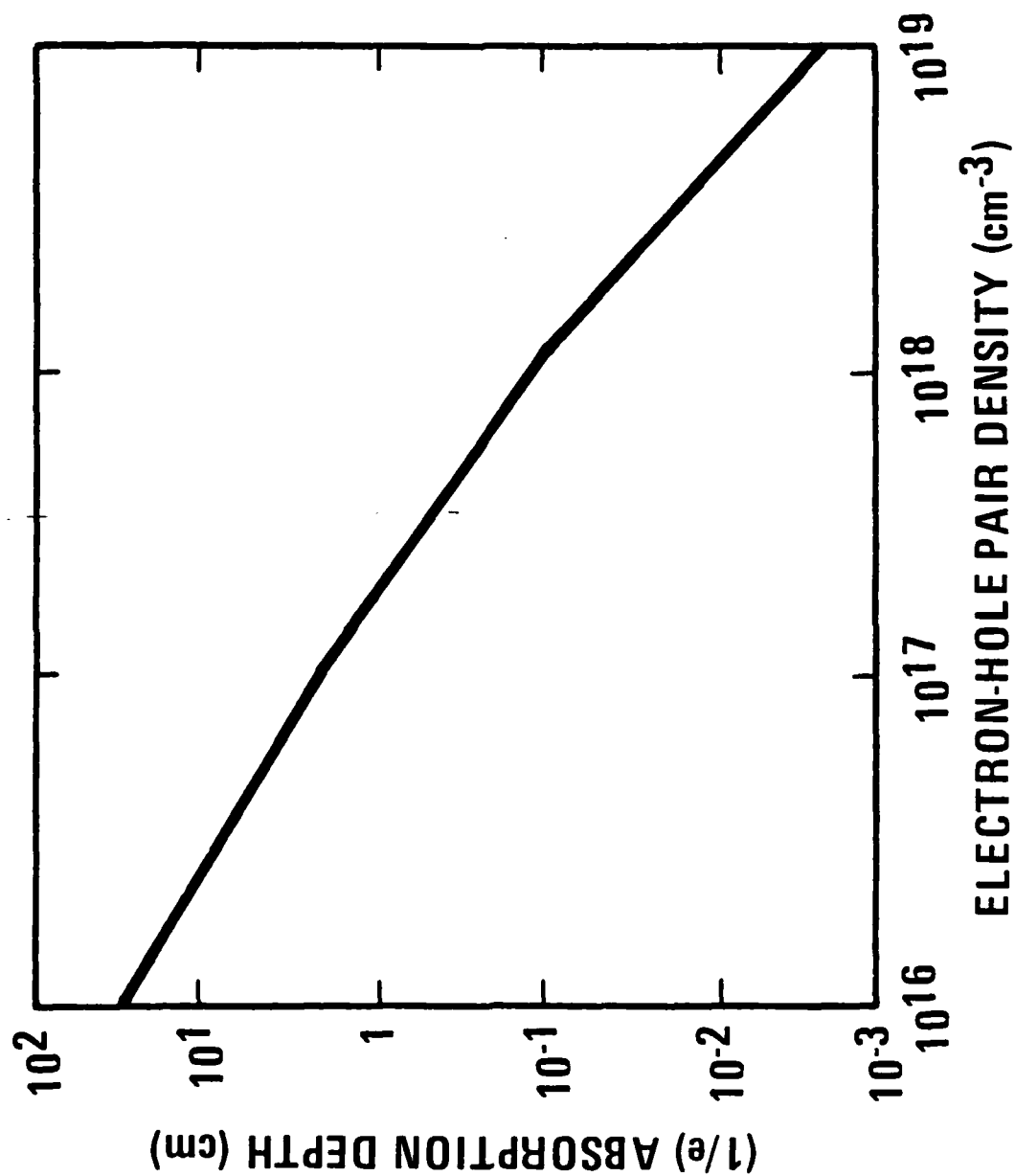


FIGURE 2

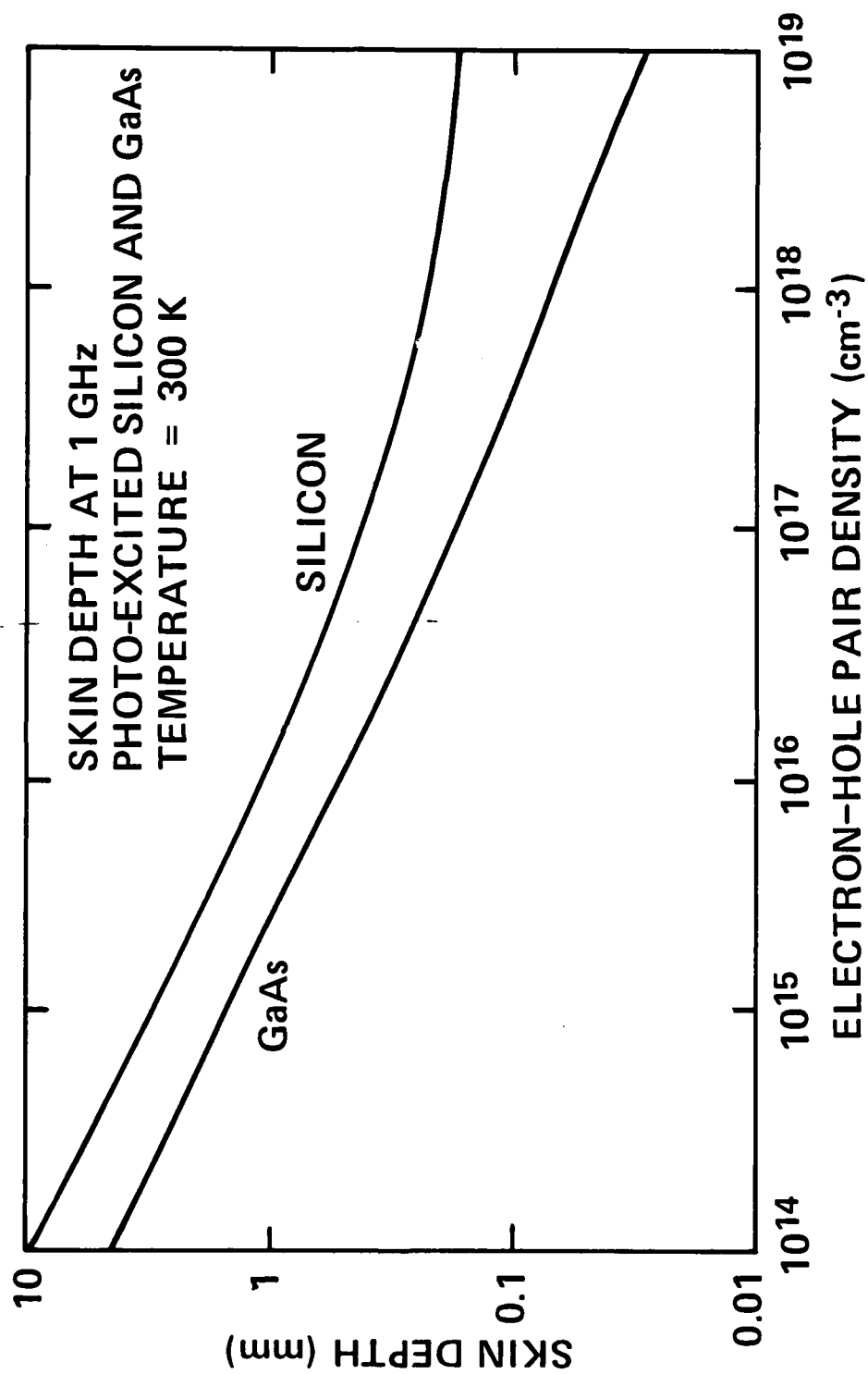


FIGURE 3

SILICON ELECTRON MOBILITY

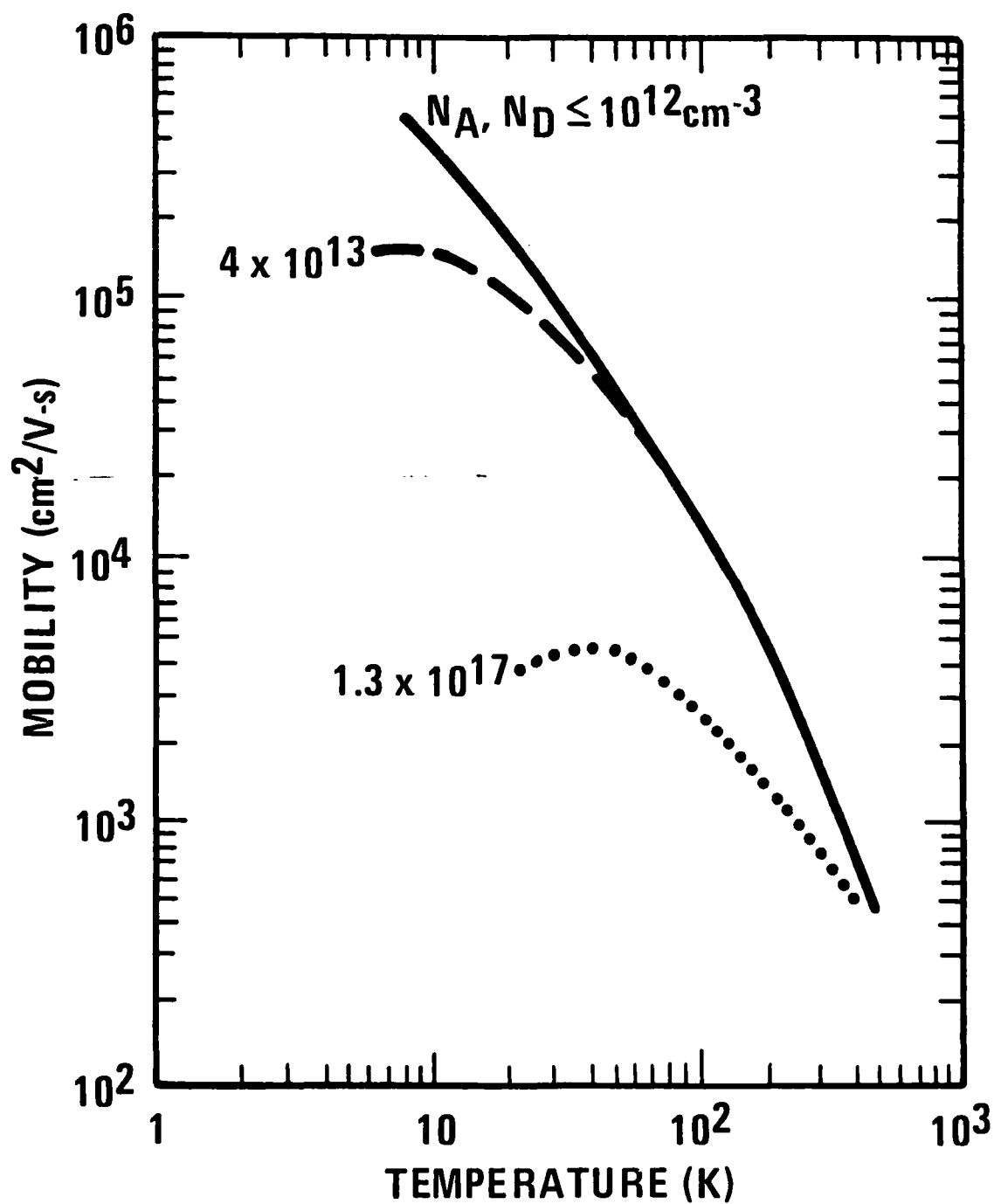


FIGURE 4

AUGER RECOMBINATION IN OPTICALLY EXCITED Si

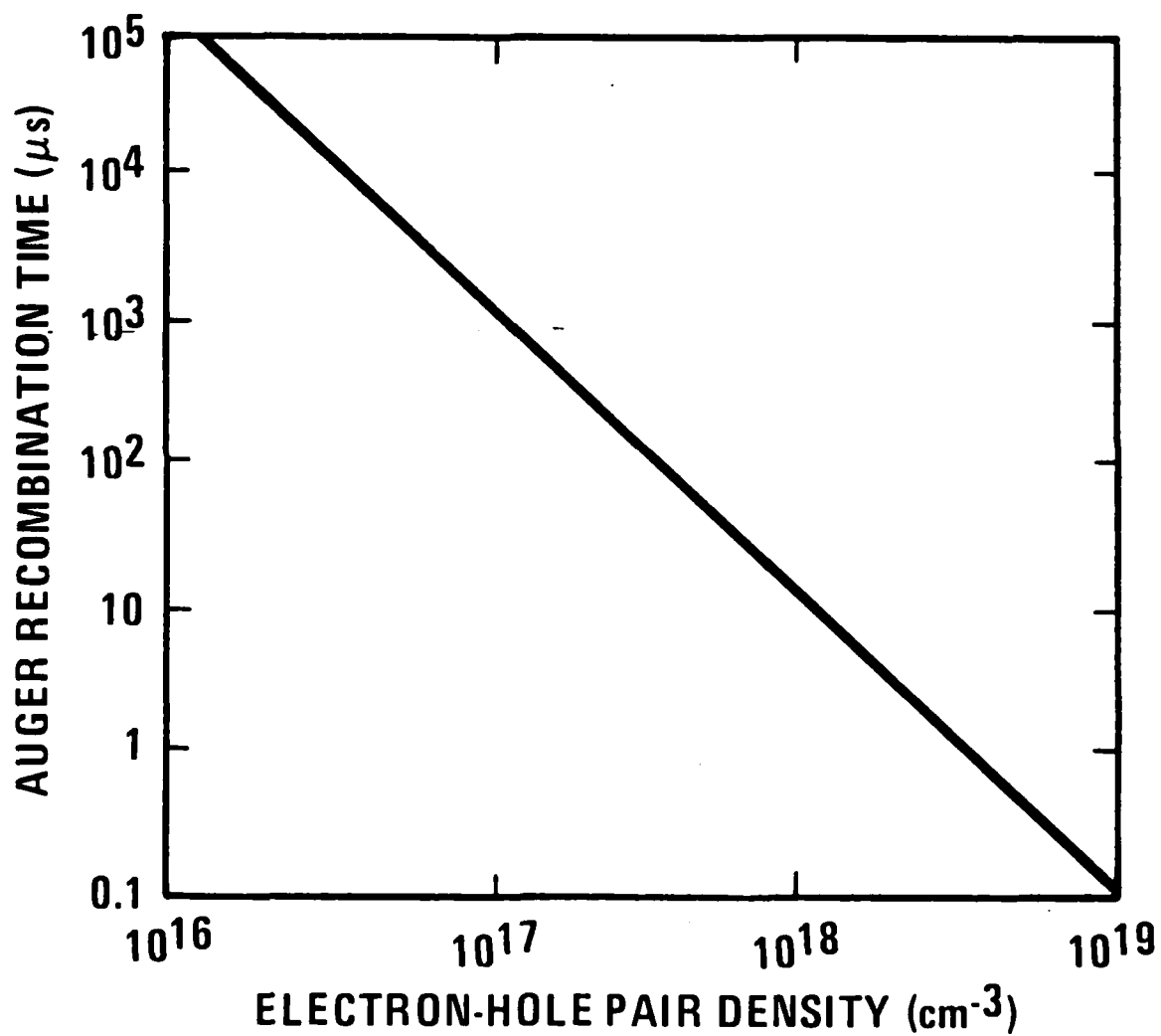


FIGURE 5

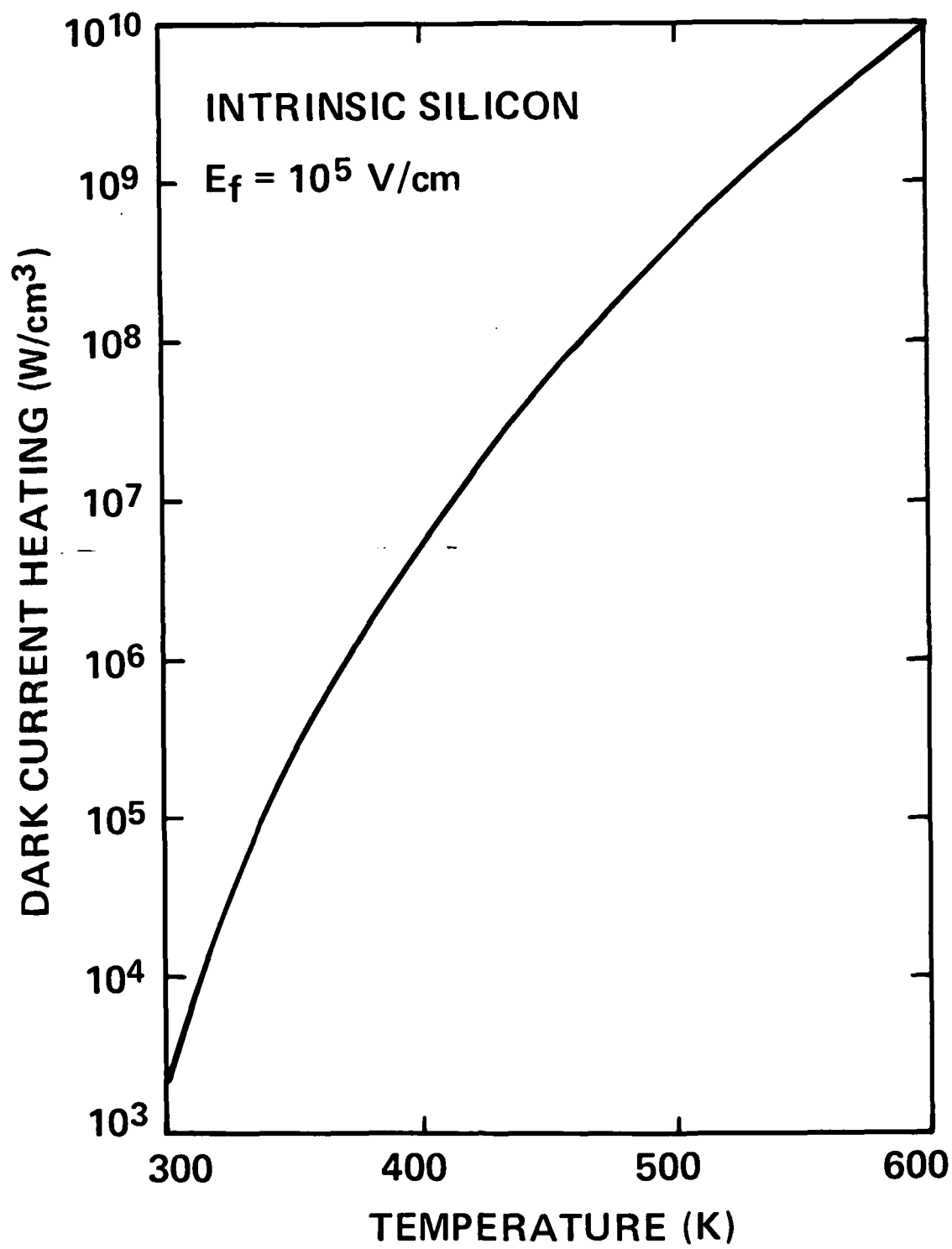
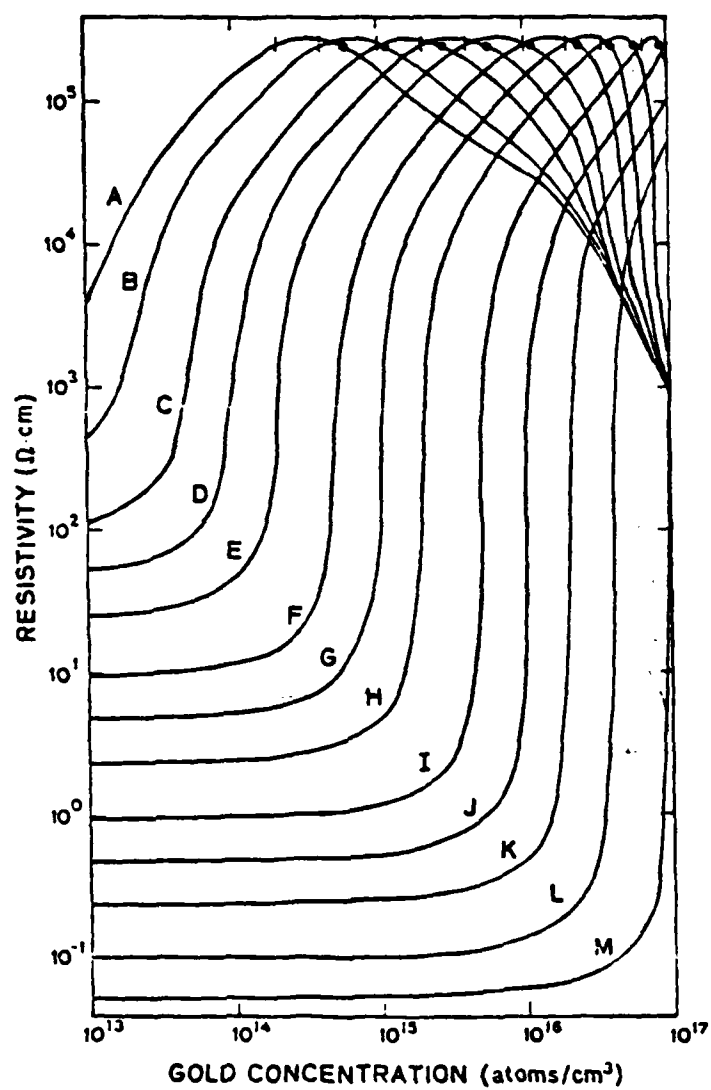


FIGURE 6



$N_D = 10^{13} \text{ cm}^{-3}$, A
 $N_D = 10^{14} \text{ cm}^{-3}$, D
 $N_D = 10^{15} \text{ cm}^{-3}$, G
 $N_D = 10^{16} \text{ cm}^{-3}$, J
 $N_D = 10^{17} \text{ cm}^{-3}$, M

FIGURE 7

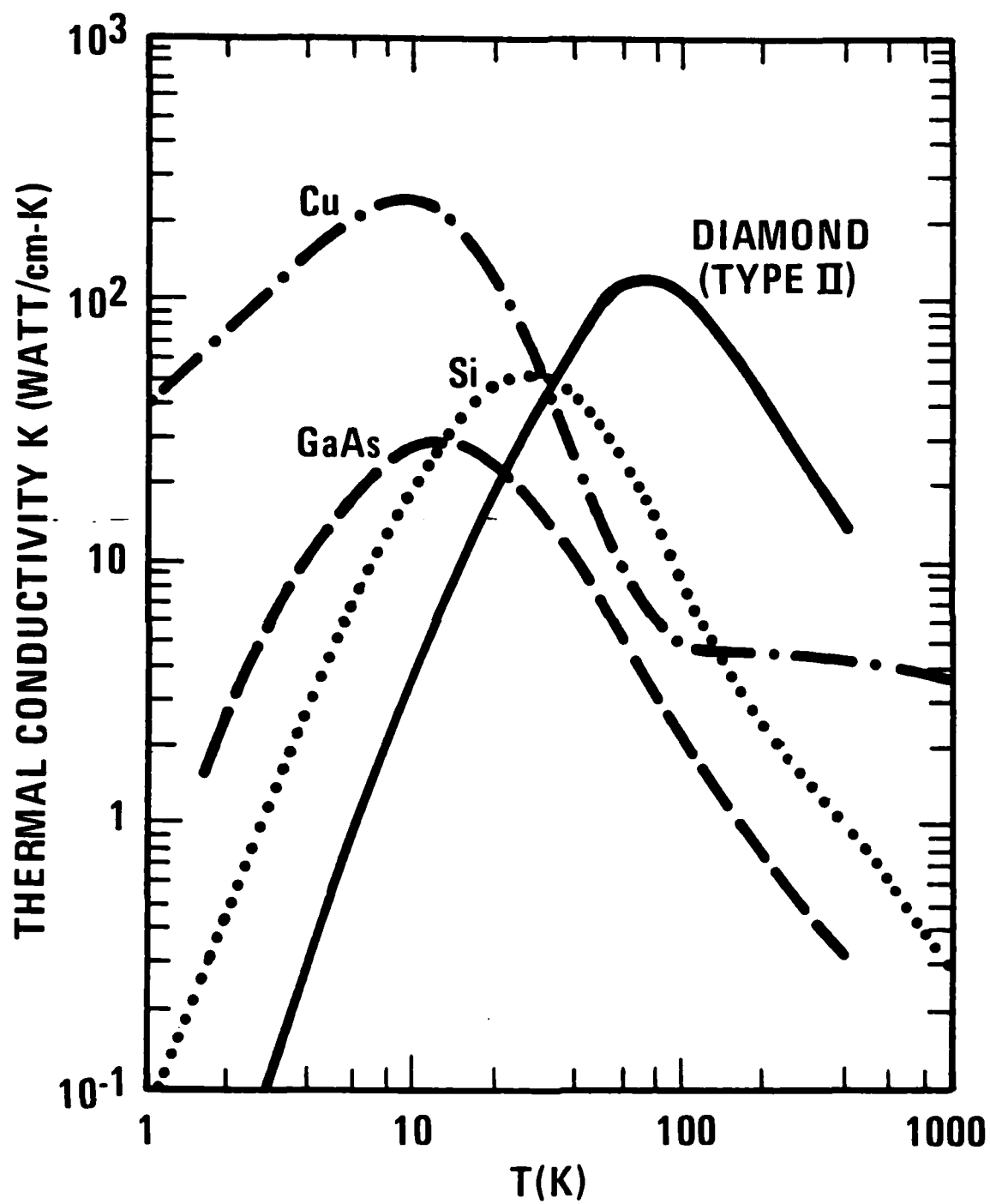


FIGURE 8

VIEWGRAPHS

PHOTOCONDUCTOR SWITCHING:
SOME PHYSICAL MECHANISMS

R. B. HAMMOND

**PHOTOCONDUCTOR SWITCHING:
SOME PHYSICAL MECHANISMS**

**ROBERT B. HAMMOND
LOS ALAMOS NATIONAL LABORATORY**

179-500200

Los Alamos
ELECTRONICS DIVISION

OVERVIEW/SUMMARY

- POWER SWITCHING
 - Risetime
 - Switching Efficiency
 - On-Time
 - Temperature Control
 - Switch Dimensions
- PULSE GENERATION ON INTEGRATED CIRCUITS
 - Silicon
 - GaAs

002805-7-66

Los Alamos
ELECTRONICS DIVISION

FAST-RISETIME, HIGH-POWER, CLOSING SWITCH

- Fast risetime at very high power
 - carrier transit times \Rightarrow risetime
 - optical control / precise time
 - flexible geometry / low inductance
- Solid-state reliability
- Large, High-Quality Crystals
 - available, inexpensive
- Indirect Bandgap
 - long carrier lifetime
- Well understood, Controllable properties
- Good match \rightarrow Nd:YAG laser

HIGH μ , σ_{eh}

254

(SMALL $E_G \Rightarrow$ LOW E_B
HIGH n)

FAST RISE TIME, HIGH-POWER Closing Switch

- Rise time $\rightarrow 1 \text{ nsec}$ ($\alpha_L \approx 10 \text{ cm}$)
- Bias $\rightarrow 10^5 - 10^6 \text{ V}$
($L = 1 \text{ to } 10 \text{ cm}$)
- Pulse Length $\rightarrow 10 \text{ nsec to } 100 \mu\text{sec}$
 $\tau_{\text{relax}} \approx 1 \mu\text{sec}$
- Room Temperature / Low Temperature

PHOTOCONDUCTOR POWER SWITCHING

PHYSICAL MECHANISMS (DESIGN CONSIDERATIONS)

- **RISETIME:** short-pulse source
circuit limits-geometry
- **SWITCHING EFFICIENCY:** source efficiency
carrier-production efficiency
carrier mobility
bias
contact resistance
- **ON-TIME:** lifetime
sweep-out
- **TEMPERATURE CONTROL:** resistivity
 R_{on}
thermal conductivity
- **SWITCH VOLUME:** current density
breakdown strength

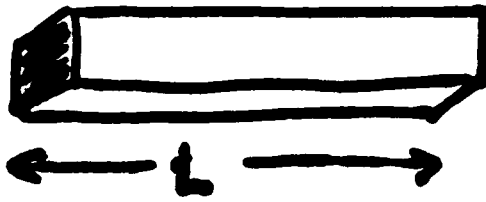
RISETIME

- Excitation Pulse Length
- Circuit Limits: $\tau = L/R$
- Absorption Time

994-908280

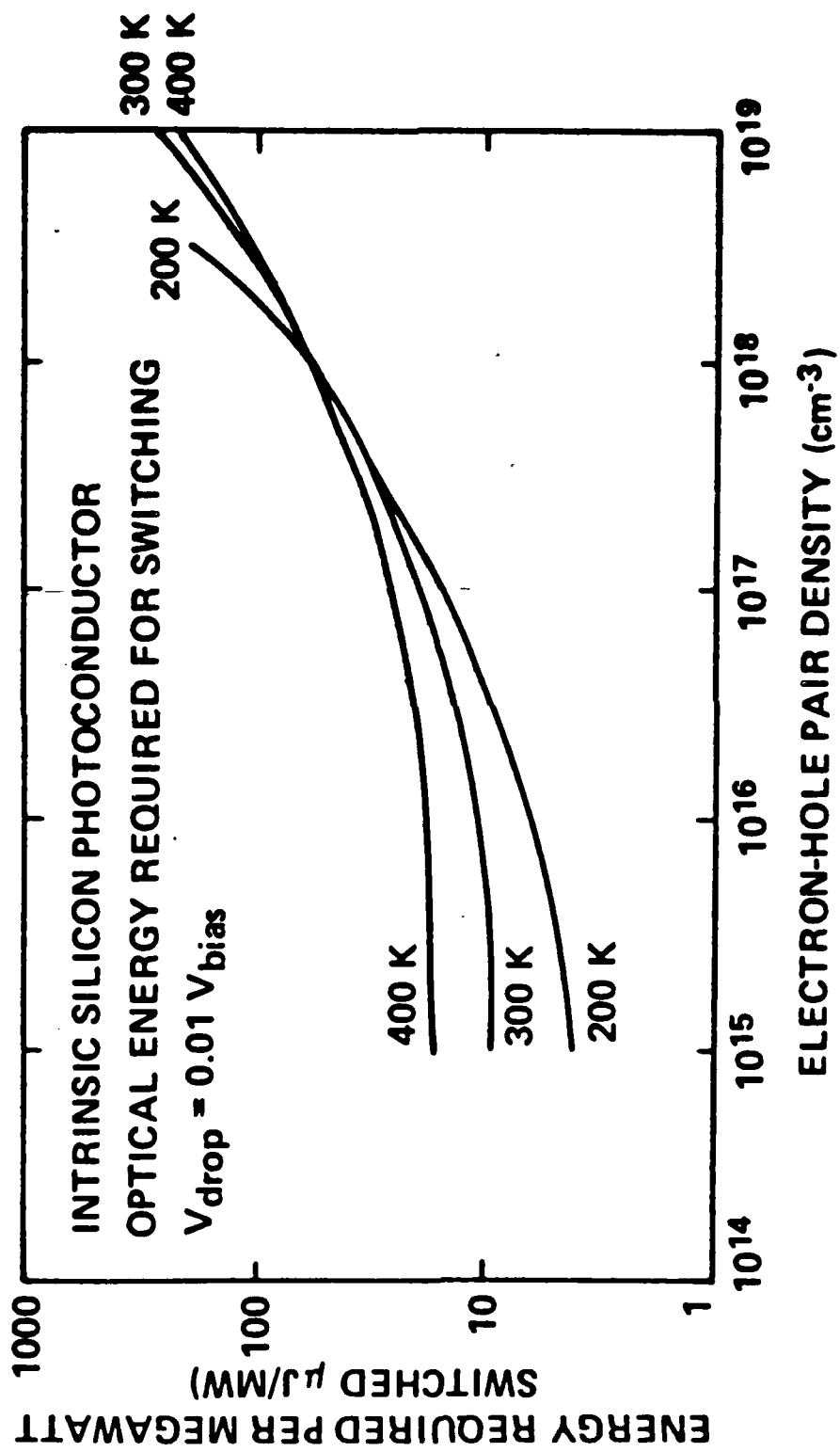
Los Alamos
ELECTRONICS DIVISION

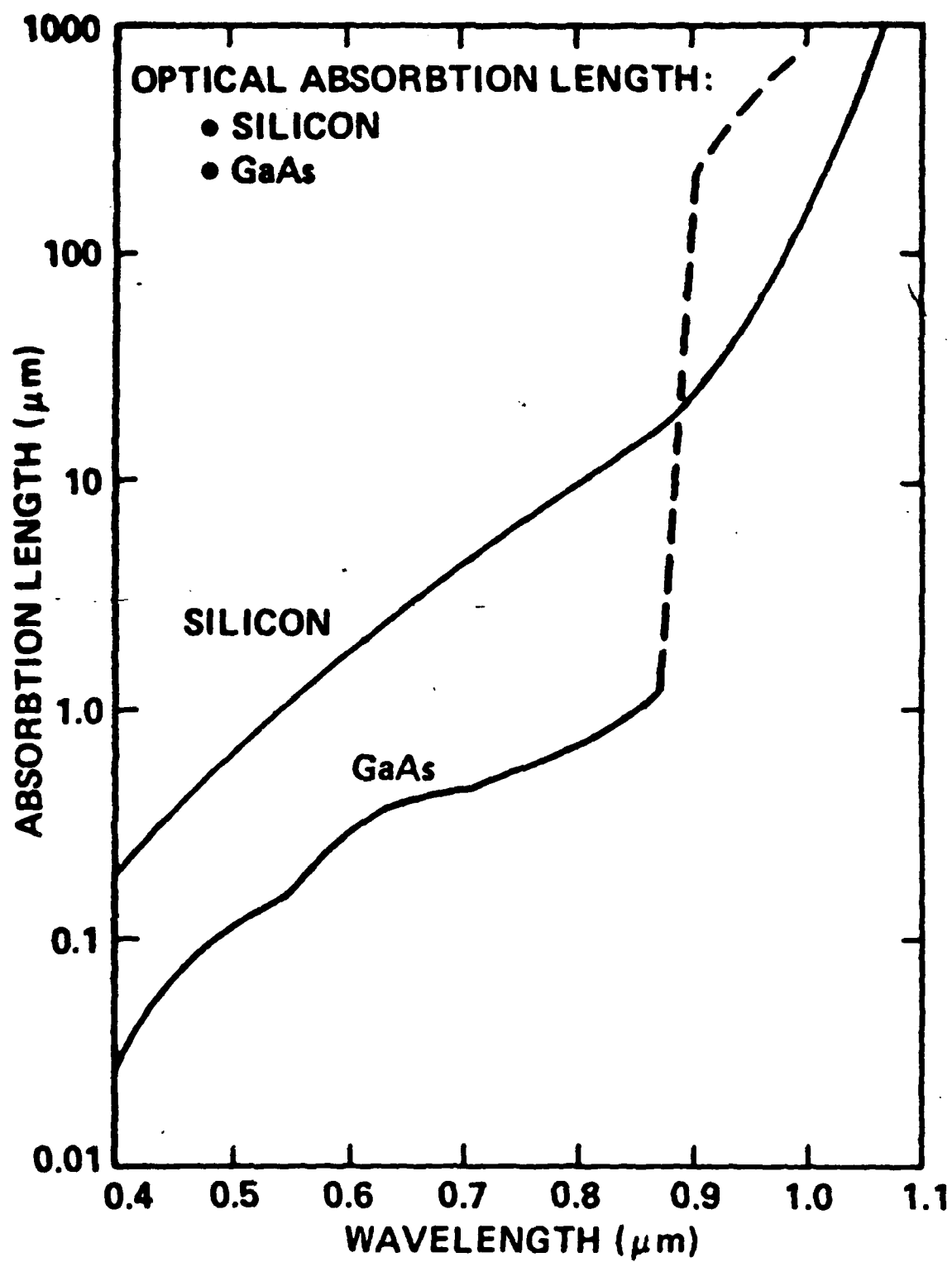
EFFICIENCY



$$R_{OH} = \frac{L^2}{N_{ch} e (\mu_e + \mu_h)}$$

- Minimize L (maximize E_b)
- Maximize N_{ch} (maximize carrier-production efficiency)
- Maximize μ_e, μ_h





SWITCHING EFFICIENCY

SOURCE

- High total efficiency: $\frac{P_{OUT}}{P_{IN}}$

SOURCE/PHOTOCONDUCTOR INTERACTION

- Efficient carrier production:
 - low average energy per e-h pair,
- Long adsorption length:
 - large conductive volume \rightarrow high current
- Skin depth \leftrightarrow Absorption length

PHOTOCONDUCTOR

- High current per carrier:
 - high carrier mobilities: μ_e, μ_h
- High bias, V_b
 - high breakdown strength:
- Low contact resistance

SOURCE EFFICIENCY

- Semiconductor—Laser—Pumped
Nd:YAG, Nd glass
- Electron beam

000000-0000

Los Alamos
ELECTRONICS DIVISION

CARRIER-PRODUCTION EFFICIENCY

- Losses of Excitation Energy

Reflection \rightarrow AR Coating

Free Carrier Absorption \rightarrow Bound Carrier Density
— TRADE OFF —

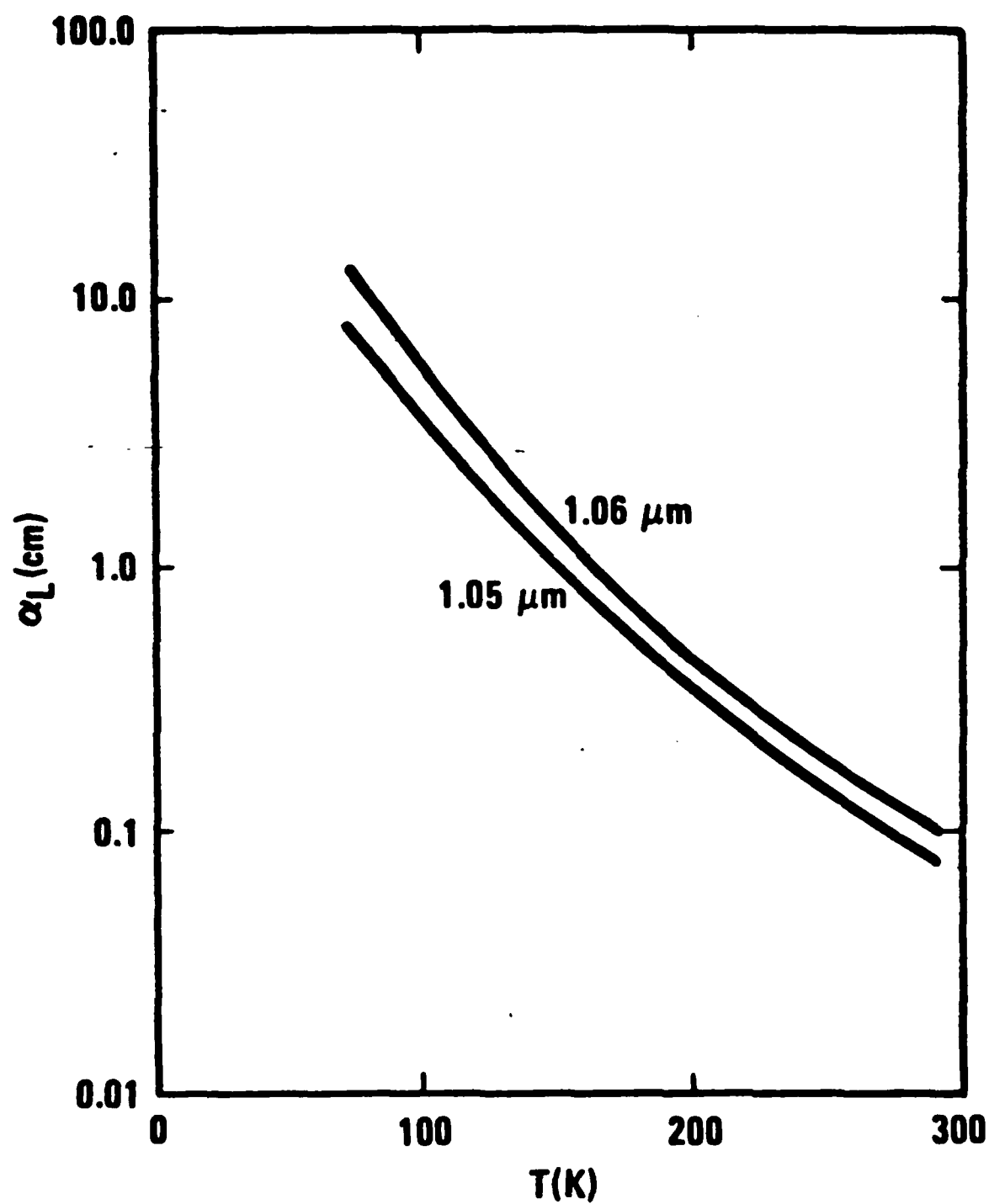
Active Volume \rightarrow Skin Depth

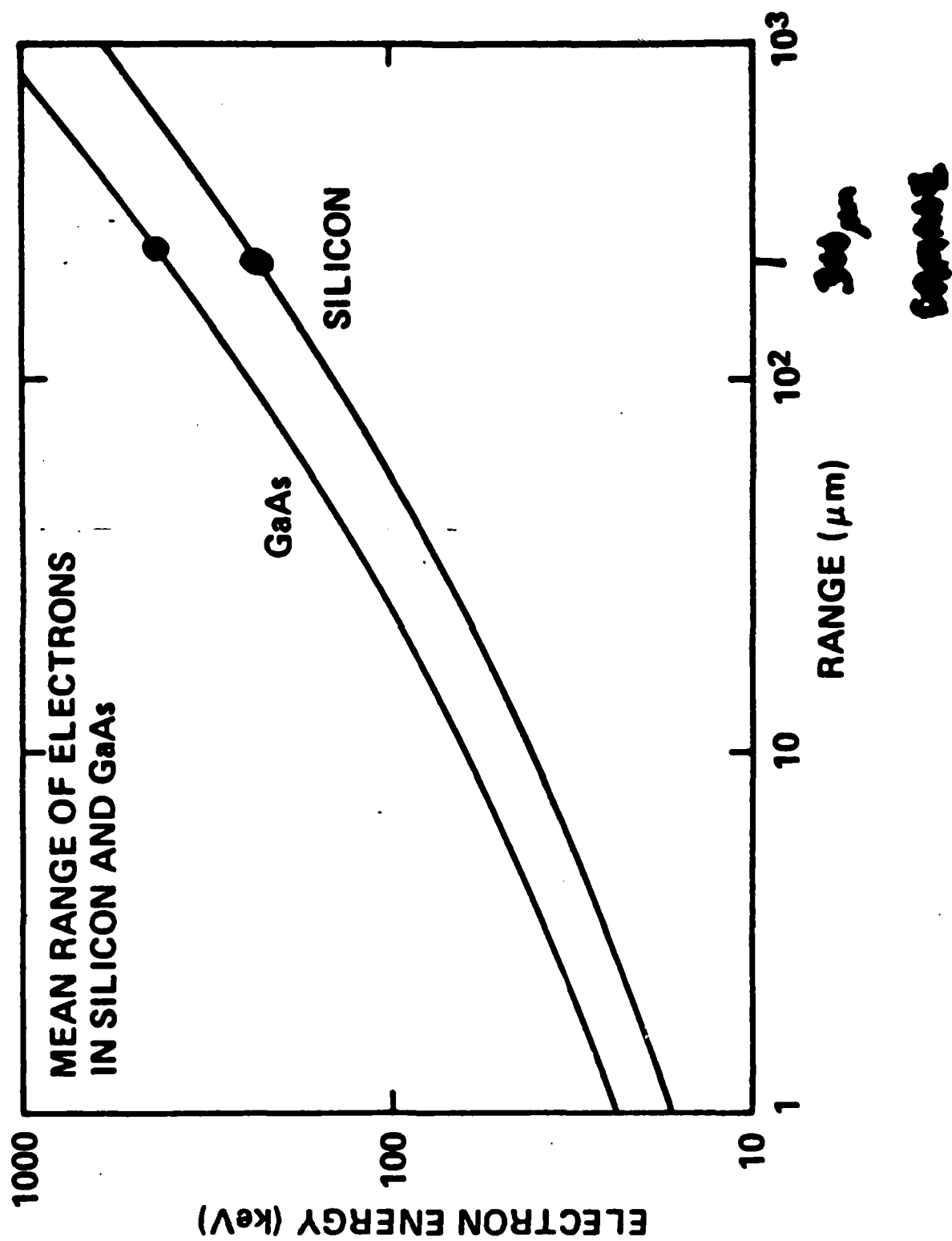
- Average Energy/e-h pair

- 1) Extrinsic Optical Absorption
- 2) Near-Band-Gap Optical Absorption
- 3) Electron-Beam

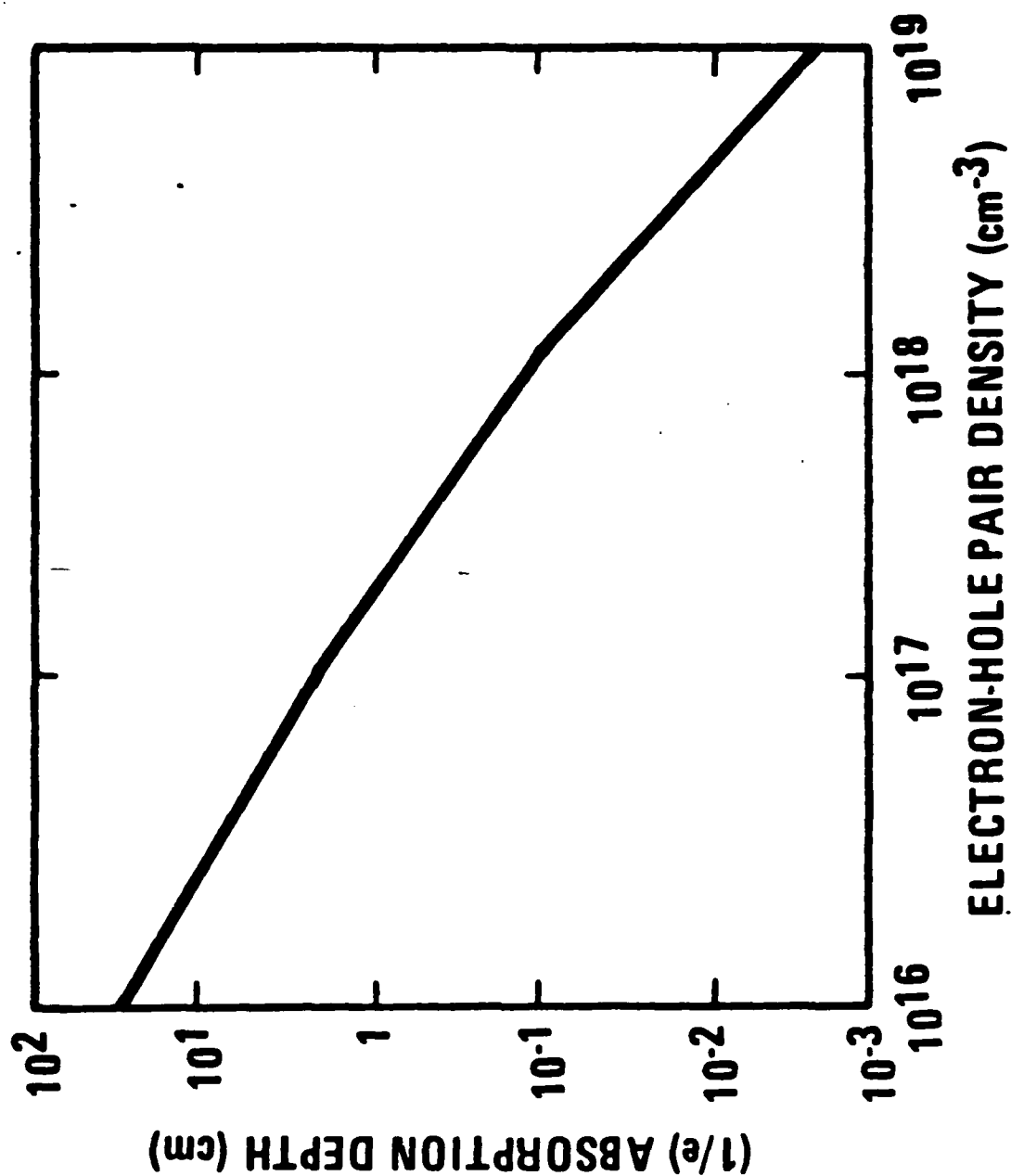
Los Alamos
ELECTRONICS DIVISION

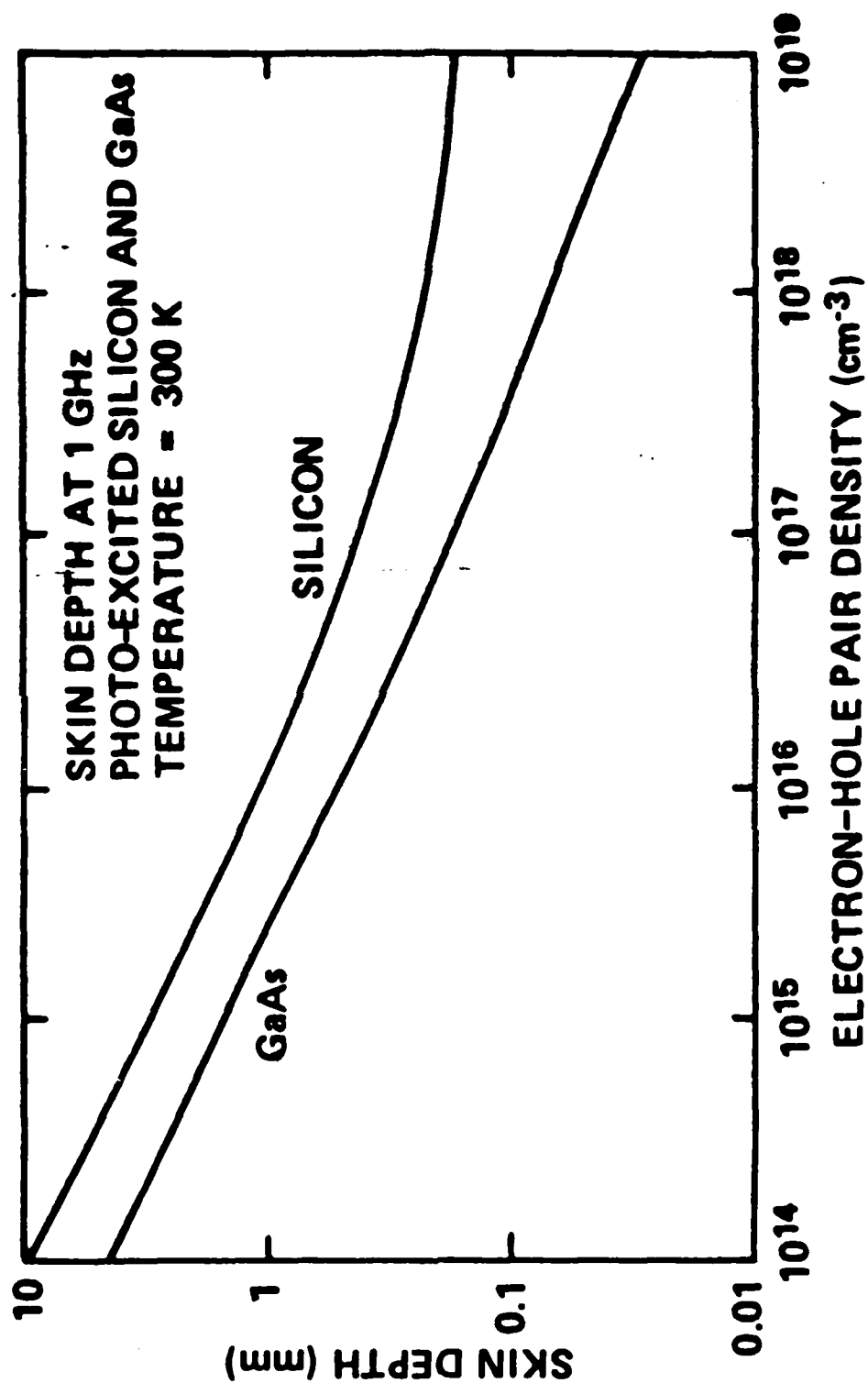
ABSORPTION LENGTH IN SILICON





SI FREE-CARRIER ABSORPTION DEPTH



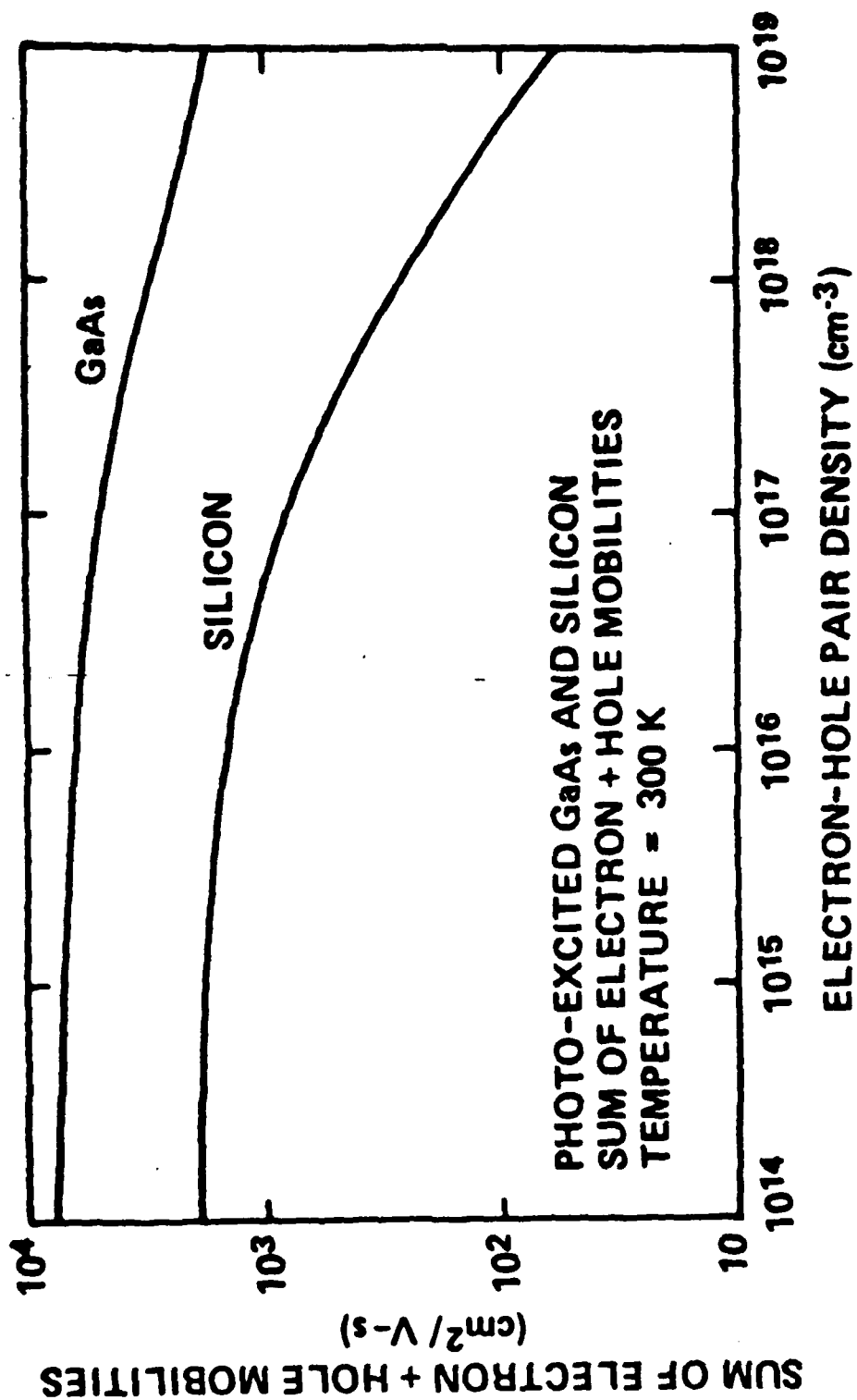


CARRIER MOBILITY

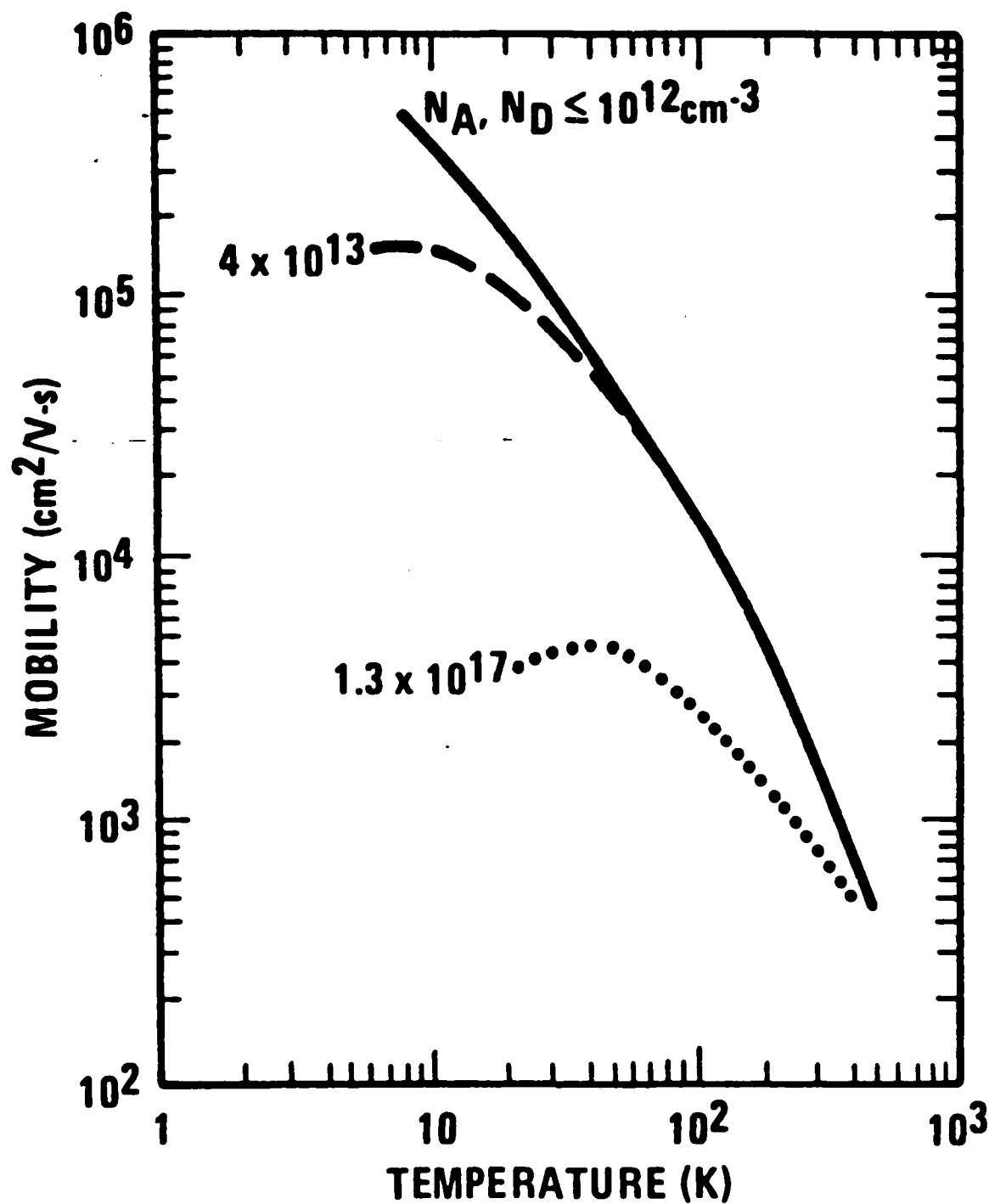
- Hole-electron Scattering
 - Bounds carrier density
 - Trade Off →
- Ionized-impurity Scattering
 - Pure material
 - Trade Off →
- Acoustic-phonon Scattering
 - Lower temperature
- Effective Masses
 - Material choice

002085-14 10

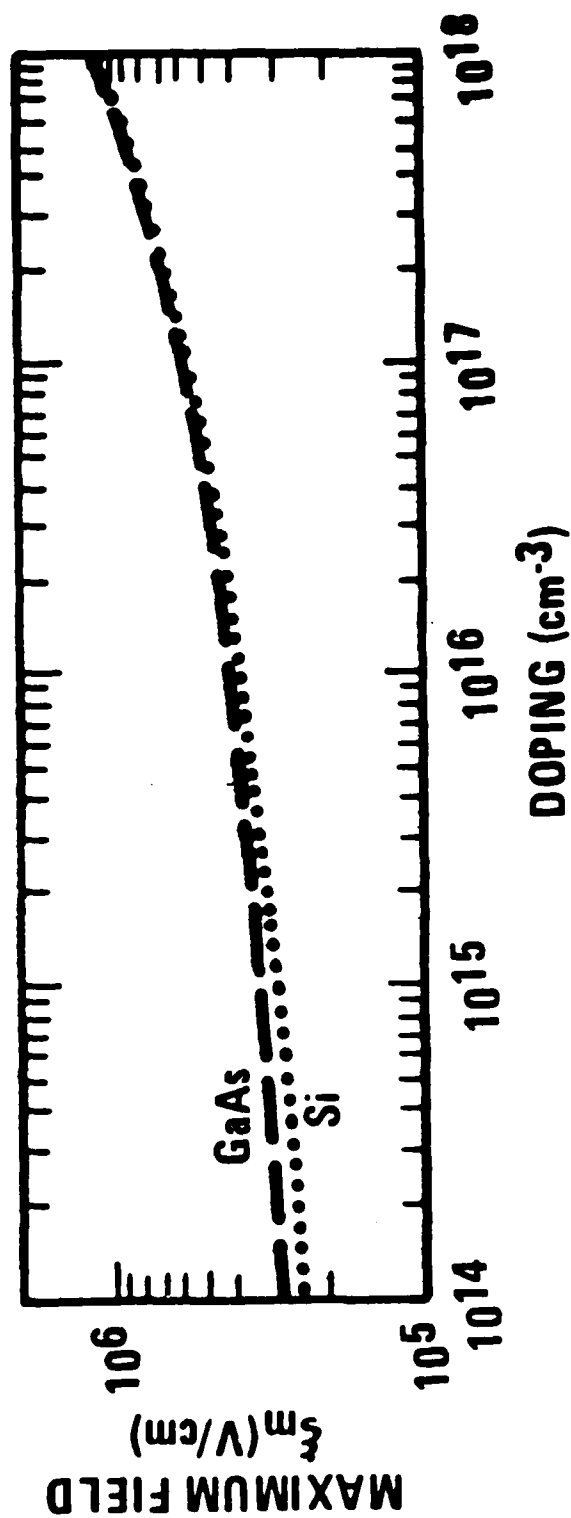
Los Alamos
ELECTRONICS DIVISION



SILICON ELECTRON MOBILITY



BULK AVALANCHE BREAKDOWN STRENGTH



IMPACT IONIZATION

Generation Rate:

$$G = \alpha_n n V_d$$

Electron density:

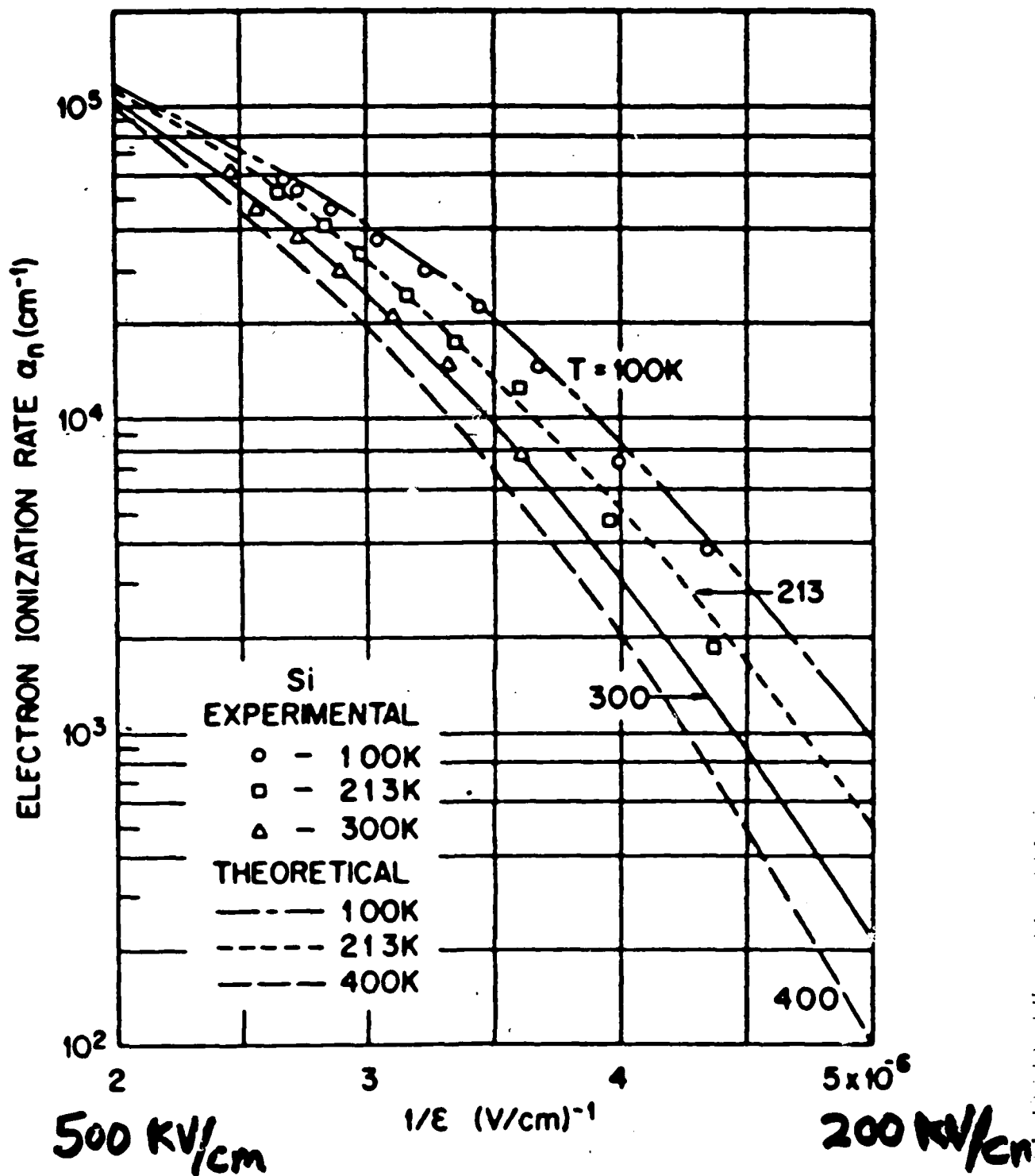
$$n(\tau) = n_0 e^{\alpha_n V_0 \tau}$$

Off-state:

$$n_0 \geq n_i$$

$$\tau \sim 10 \mu\text{sec}$$

$$\Rightarrow \alpha_n \lesssim .01 \text{ cm}^{-1}$$



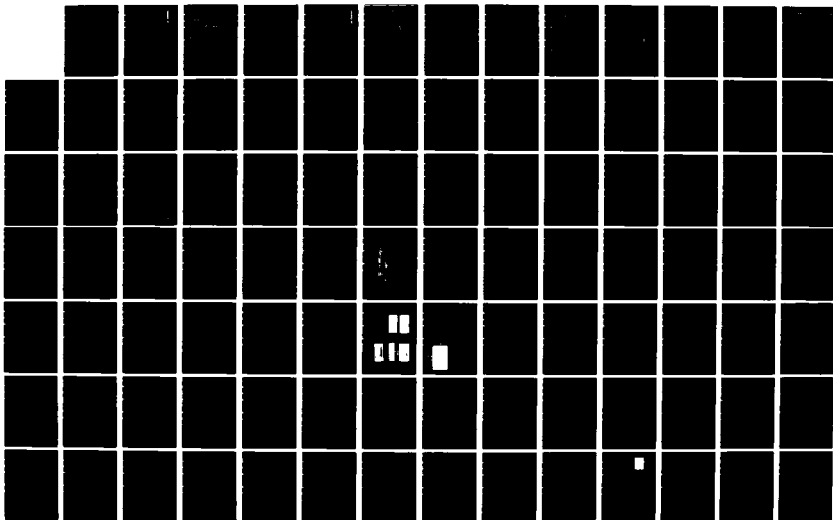
AD-A165 039

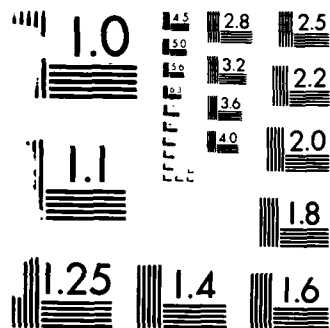
WORKSHOP ON NEW DIRECTIONS IN SOLID STATE POWER
SWITCHES HELD AT FARMINGD. (U) POLYTECHNIC INST OF NEW
YORK FARMINGDALE WEBER RESEARCH INST. B SEMITZKY
24 DEC 85 N00014-85-G-0236 F/G 9/5

4/6

UNCLASSIFIED

NL





MICROCOPY RESOLUTION TEST CHART
NATIONAL BUREAU OF STANDARDS-1963-A

SWITCH ON-TIME

- Carrier Trapping and Recombination
 - Indirect-gap material
 - Low deep-level density
 - Trade Off-
- Carrier Sweep-out
 - Electron injecting contacts
 - Photoconductive gain

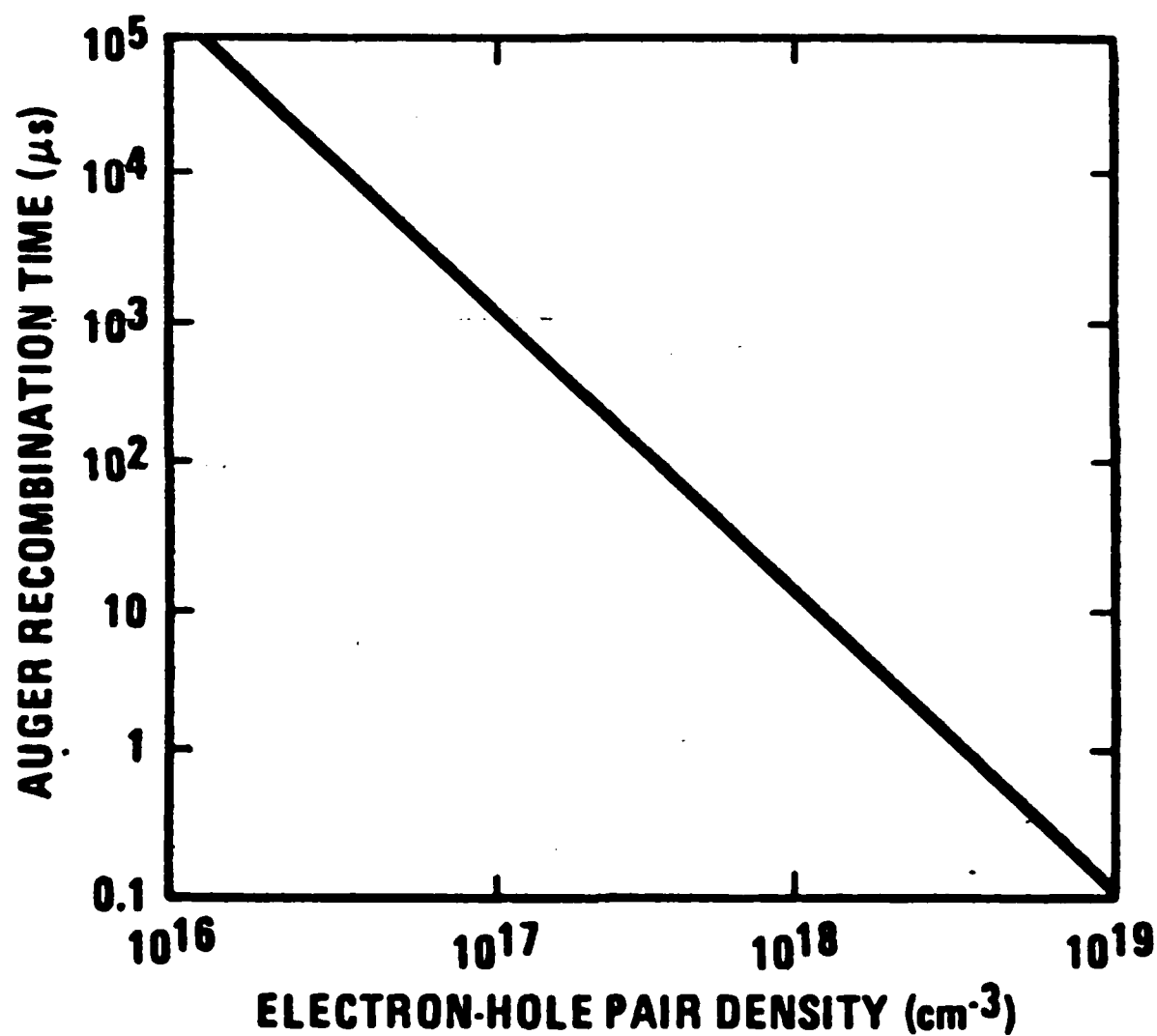
21 94-308200

Los Alamos
ELECTRONICS DIVISION

SWITCH RECOVERY to R_{OFF}

- Bulk Trapping and Recombination
 - Surface Recombination
 - Sweep-out / Contact Recombination
 - Space-charge Build-up
- Carrier transit time

AUGER RECOMBINATION IN OPTICALLY EXCITED Si



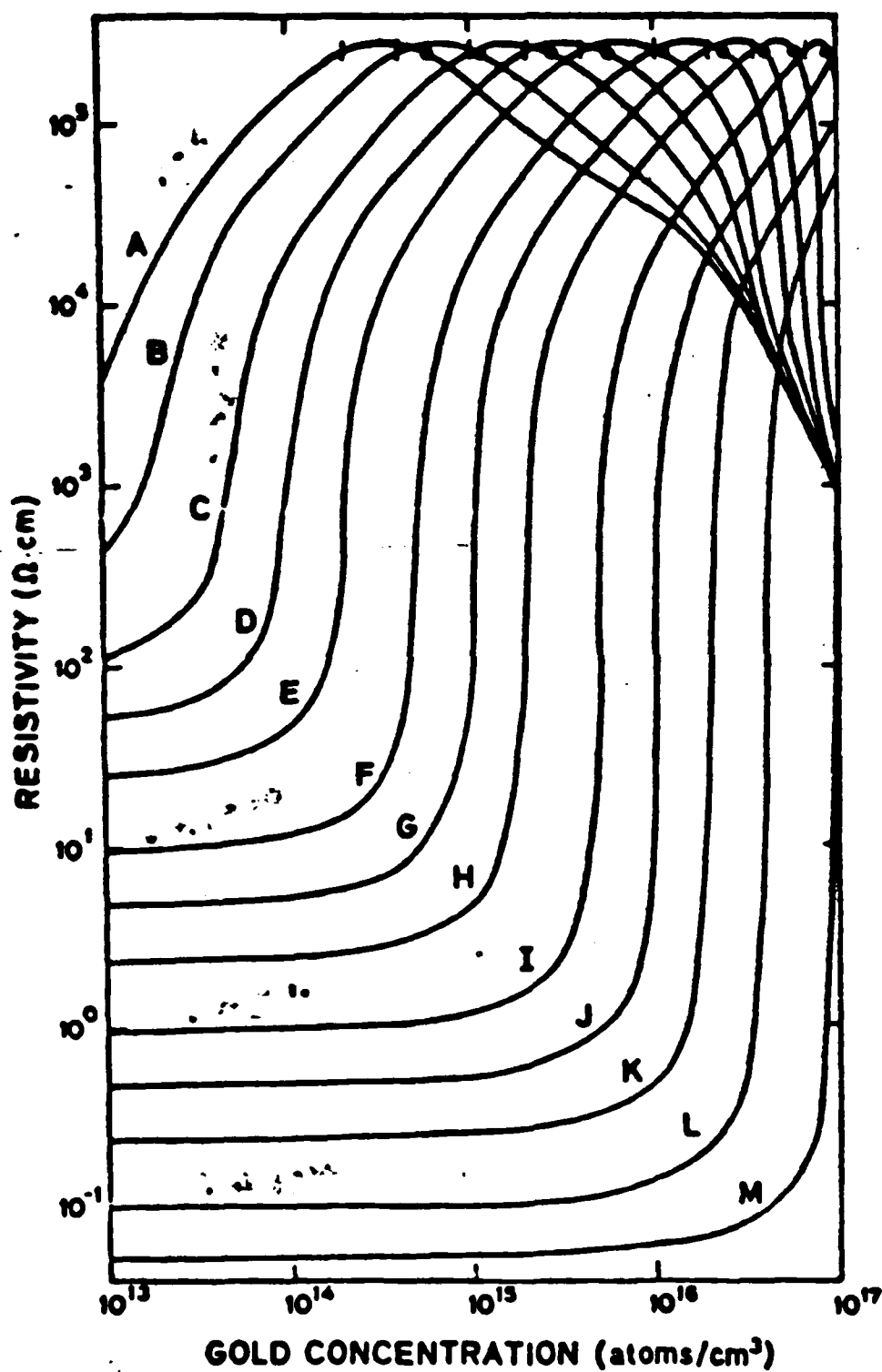
TEMPERATURE CONTROL

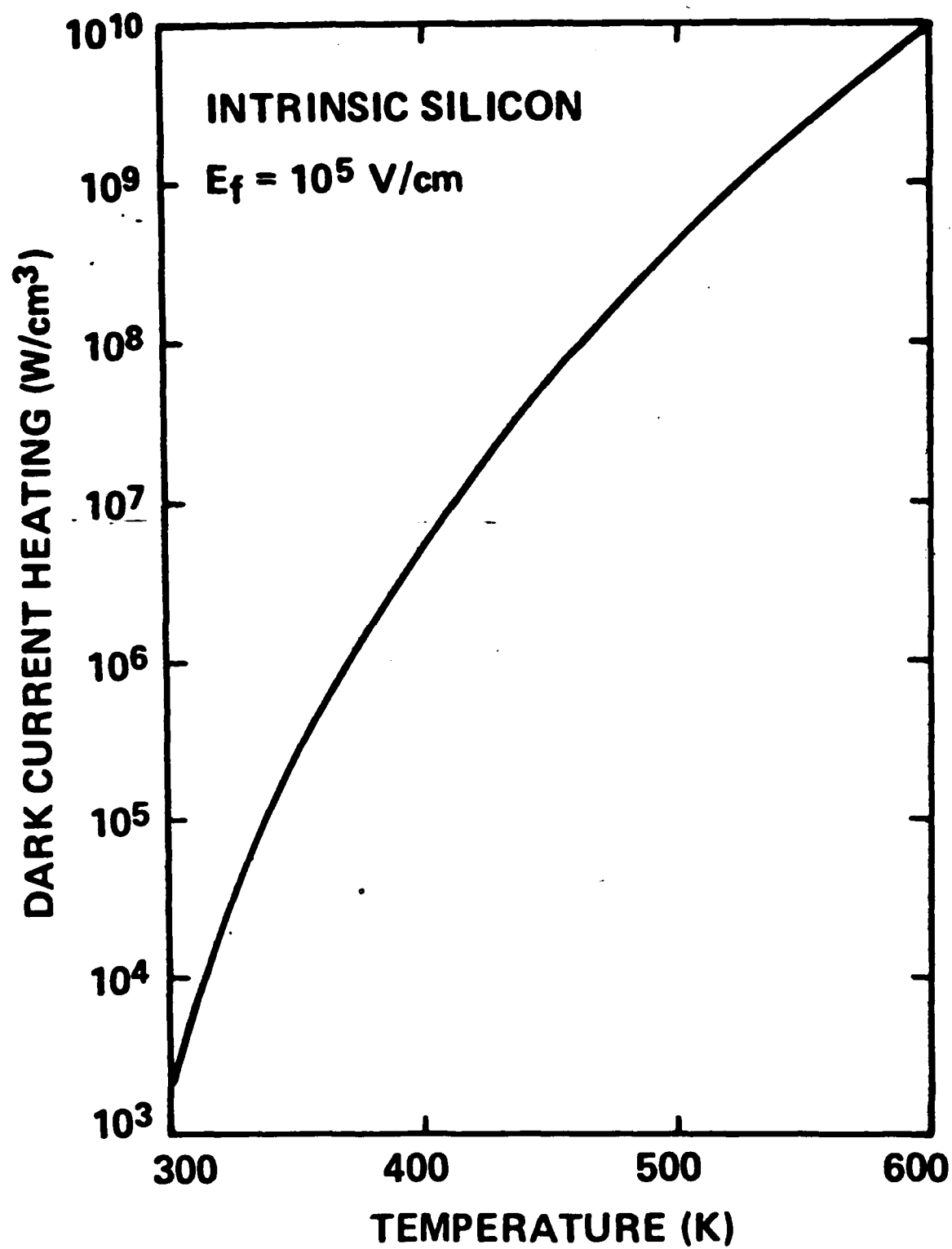
- Dark Current Heating
 - High resistivity material
 - compensation
 - low temperature
 - Pulsed bias
- On-state Heating, $j^2\rho$
 - Trade Off-
- Thermal Conductivity
 - Material choice
 - Temperature

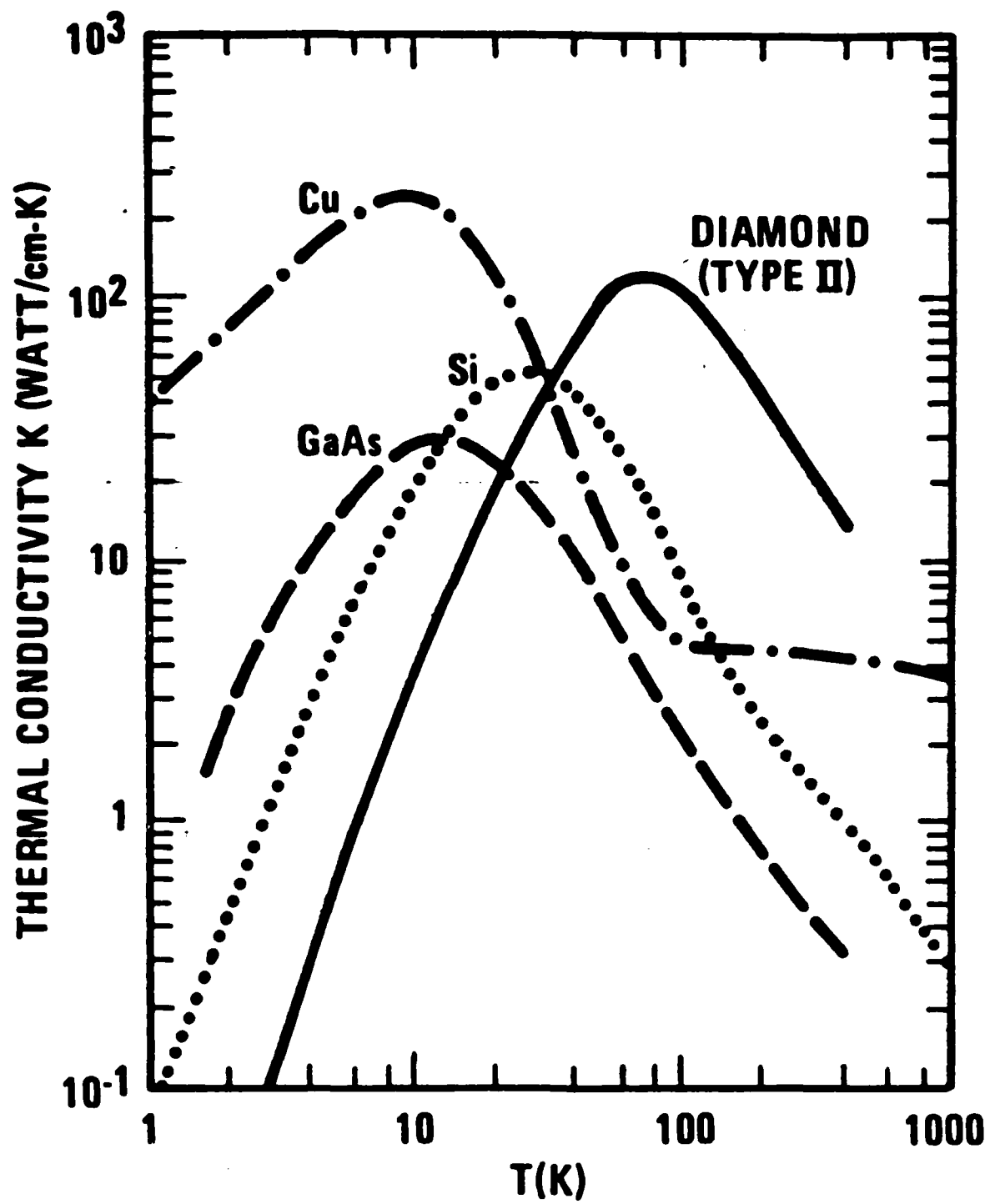
OR2086-1-15 13

Los Alamos
ELECTRONICS DIVISION

Au COMPENSATION, n:Si



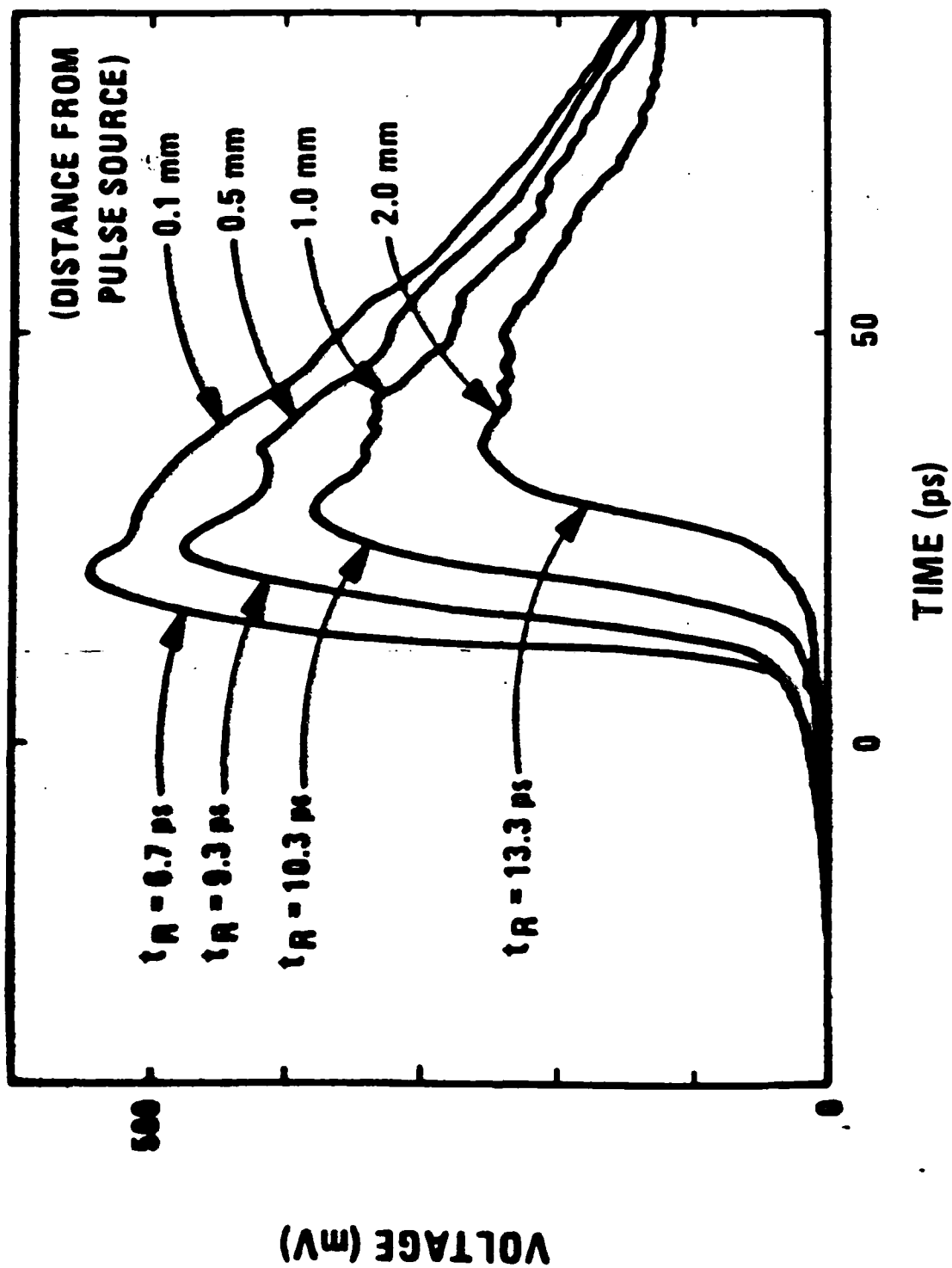


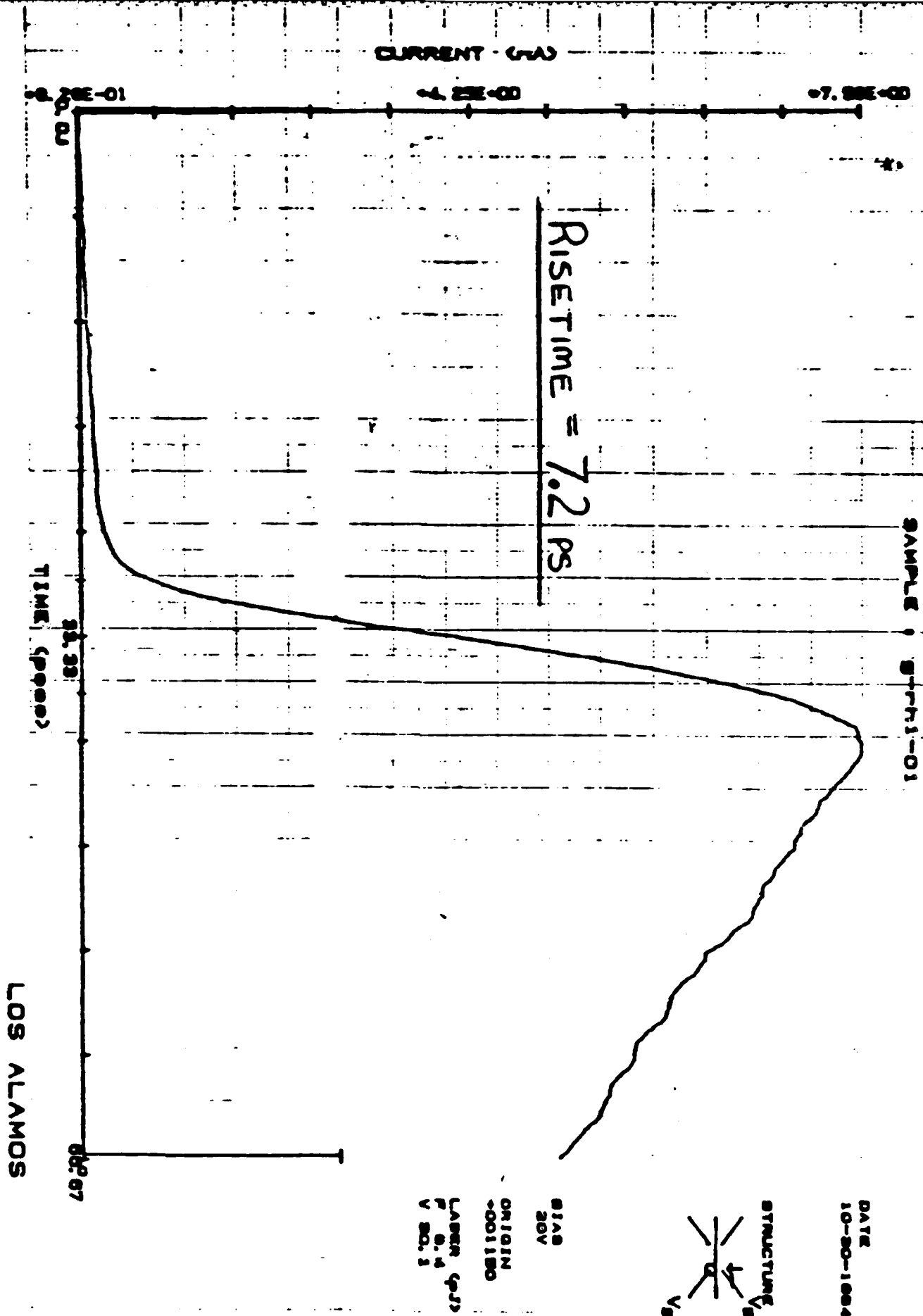


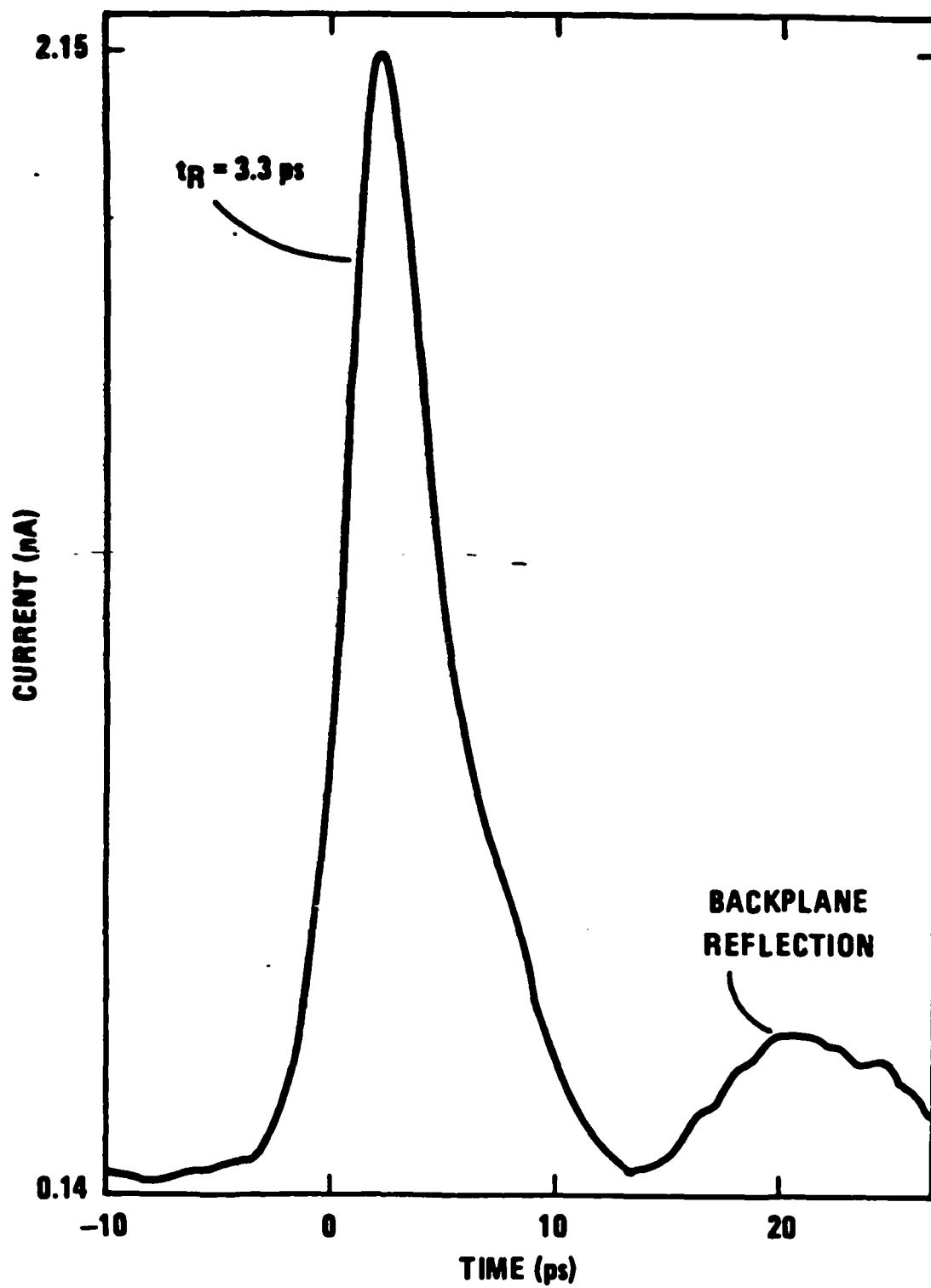
PULSE GENERATION -

Si/GaAs Integrated Circuits

- Low Power: mV to V, mW
- Normally $Z_0 C_{gy}$ limits risetime
(inductance ?)
- Efficiency important
 - Logic-level pulses
 - Semiconductor laser







PROBLEM AREAS - POWER SWITCHING

- Long On-time ~ / HIGH EFFICIENCY
- HIGH BIAS
 - Surface Breakdown
 - Impact Ionization
 - long devices / low T
- EFFICIENT Nd:YAG
- STABILITY OF Si:Li
- THERMAL MANAGEMENT

HIGH POWER PHOTOCONDUCTIVE SWITCH APPLICATIONS

W. C. NUNNALLY

POWER CONDITIONING LABORATORY
P.O. BOX 19016, (817) 273-3409
ENERGY CONVERSION RESEARCH CENTER
UNIVERSITY OF TEXAS AT ARLINGTON
ARLINGTON, TX 76019

INTRODUCTION

The use of photoconductors for very high power switches was initially demonstrated at the Los Alamos National Laboratory with funding from the Chief Scientist of the Air Force Weapons Laboratory, Kirtland AFB, NM and from the Naval Surface Weapons Center, Dahlgren, VA. A single, silicon photoconductive switch operating at a voltage of 150 kV has been used to switch a 225 MW pulse of 200 nS duration into a matched resistive load using only 20 mJ of 1.06 micron laser energy.

Photoconductive power switches have specific advantages that permit them to be used in applications where no other switching technology can function as well. In addition, the advantages of photoconductive switches make other approaches to power conditioning possible. However, in other applications, photoconductors are at a disadvantage when compared with conventional switches. Photoconductive switches are not a universal switching solution, but they have a performance advantage that is unique. Indeed, the advantages of photoconductive switches may make some applications possible that have previously been unattainable.

ADVANTAGES

The major advantages of photoconductive power switches over conventional solid state switches are:

1. Minimum resistive closure time that is dependent on an external optical source such as a laser and permits the fastest possible risetimes at high voltages.
2. Distributed conduction of switched current that makes minimum inductance possible and thus minimum circuit limited risetimes.
3. Bulk resistive voltage holdoff that grades the applied voltage across the entire device and permits one device to be used for very large voltages.
4. The direct optical control of many parallel, series or sequential switches with sub-nS precision and high voltage isolation.
5. Photoconductive switches do not rely on junctions for voltage hold off and thus have bidirectional current capability.
6. Photoconductive switches represent the ideal diffuse discharge gas switch but with the advantages of an order of magnitude less control energy and the possibility of removing thermal energy directly from the conducting medium in situ to promote repetitive operation.

DISADVANTAGES OF PHOTOCONDUCTIVE POWER SWITCHES

The disadvantages of photoconductive power switches include:

1. The electrical pulse length of photoconductive switches is limited to a fraction of the photoconductor carrier recombination time in an impulse triggered system and thus the realizable pulse lengths are limited to about 1 microsec.
2. The electrical pulse length can be increased in a pulse modulation system, but only by increasing the optical energy required for operation. The optical sources required for very high power electrical pulses are not presently available.
3. The pulse rate at which a photoconductor can be operated is limited by the average power of available optical sources and by the rate at which the resistively deposited thermal energy can be removed from the photoconductor material.
4. Large photoconductors are difficult to fabricate.
5. Present day photoconductive switches are not as rugged as conventional spark gaps.

AREAS FOR FUTURE DEVELOPMENT

The following areas for development are necessary to improve the state of the art in photoconductive power switches:

1. Determine the cause of surface flashover in photoconductors to increase the operational electric field and reduce the required optical energy.
2. Determine methods of increasing the intrinsic resistivity of available silicon while maintaining long recombination times.
3. Determine methods of fabricating semi-insulating GaAs with much longer recombination times.
4. Develop additional sources of high power optical energy with high pulse rates such as injection laser diodes, etc to permit higher pulse rate operation of photoconductive switches.
5. Develop method of fabricating large photoconductor geometries with high mobility, long recombination times and high bulk resistivities.
5. Develop ideal photoconductor for switching with high mobility, desired optical band gap, high bulk resistance and long carrier lifetimes using superlattices.

VIEWGRAPHS

APPLICATION OF PHOTOCONDUCTIVE POWER SWITCHES

W. C. NUNNALLY

APPLICATION OF PHOTOCONDUCTIVE POWER SWITCHES

W. C. NUNNALLY

POWER CONDITIONING LABORATORY
ENERGY CONVERSION RESEARCH CENTER
UNIVERSITY OF TEXAS AT ARLINGTON

WORKSHOP ON NEW DIRECTIONS
IN

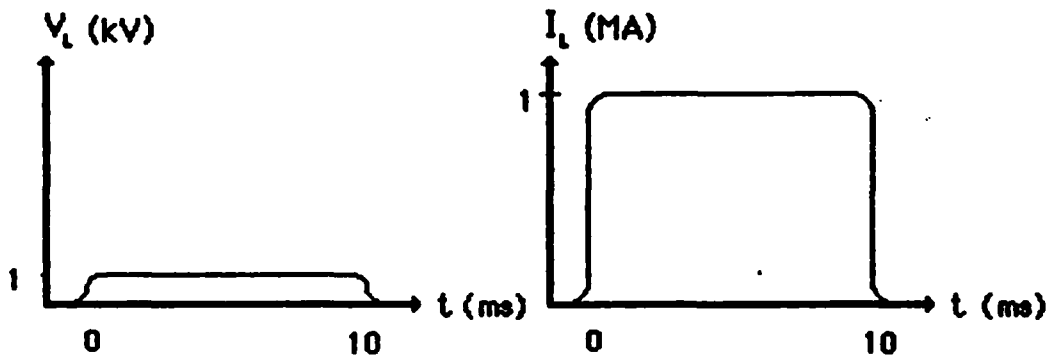
SOLID STATE POWER SWITCHES

• AUGUST 28,29,30, 1985
FARMINGDALE, NEW YORK

UTA-ECRC-PCL
ELECTRICAL ENGINEERING

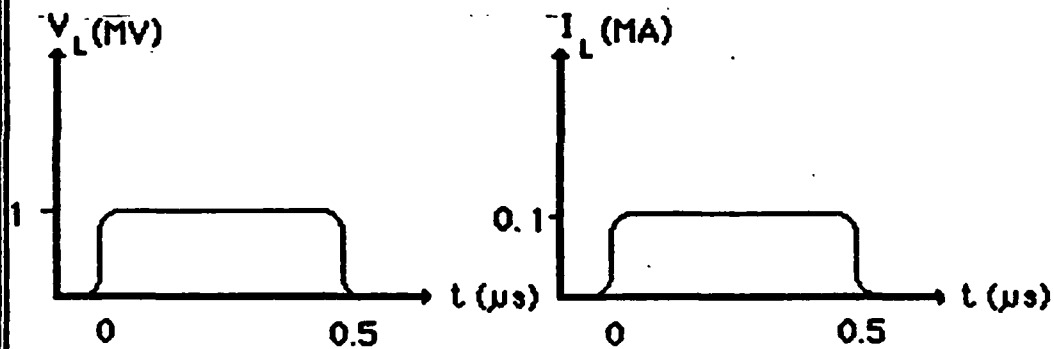
KEW: EM LAUNCHERS

PULSE RATE = 10 Hz



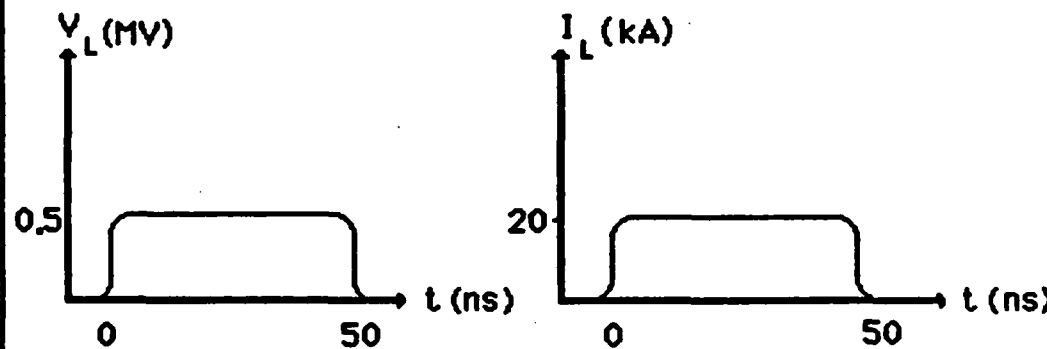
DEW:E-BEAM PUMPED LASER

PULSE RATE = 100 Hz



DEW: INDUCTION ACCEL.

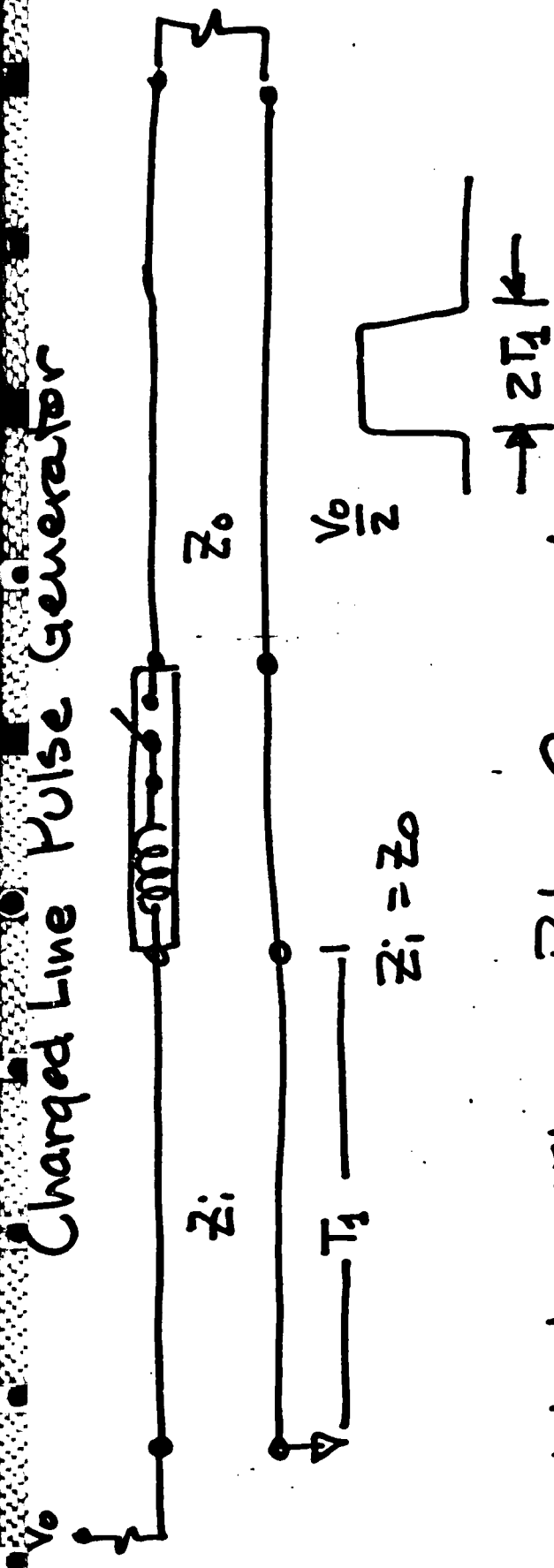
PULSE RATE = > 10 kHz



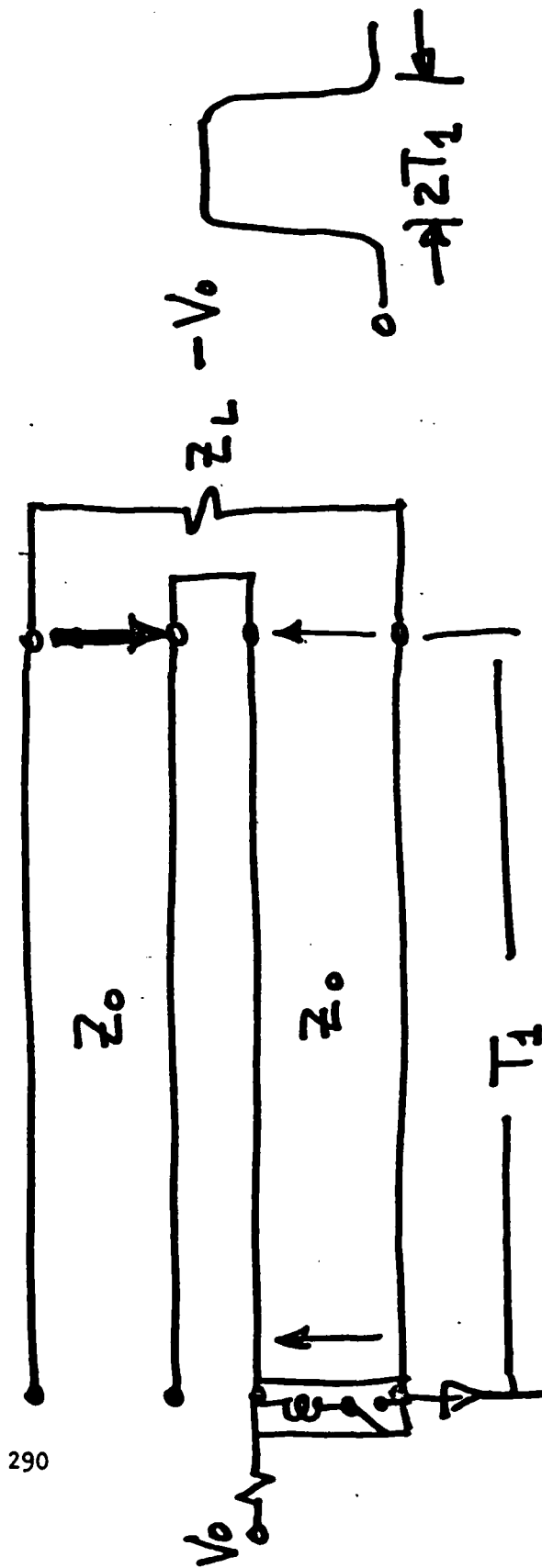
UTA-PCL

289 ELECTRICAL ENGINEERING

Charged Line Pulse Generator



Blumlein Tline Pulse Generator



GENERAL SWITCHING REQUIREMENTS

O HIGH RATE OF CARRIER GENERATION

⊕ SHORT RESISTIVE PHASE

O MINIMUM INDUCTANCE

⊕ CIRCUIT RESPONSE LIMIT

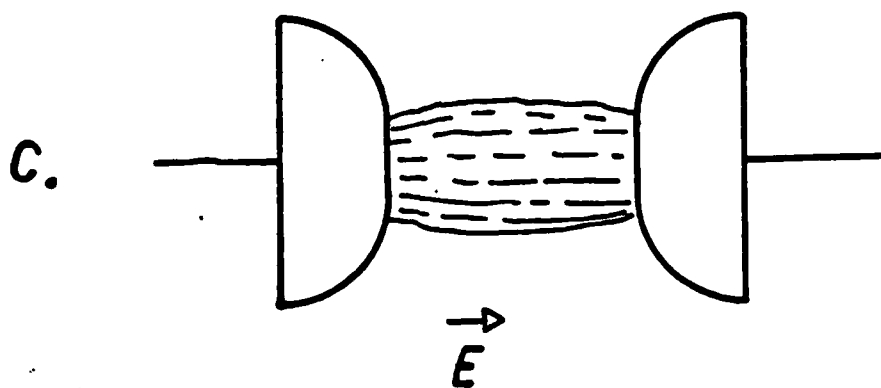
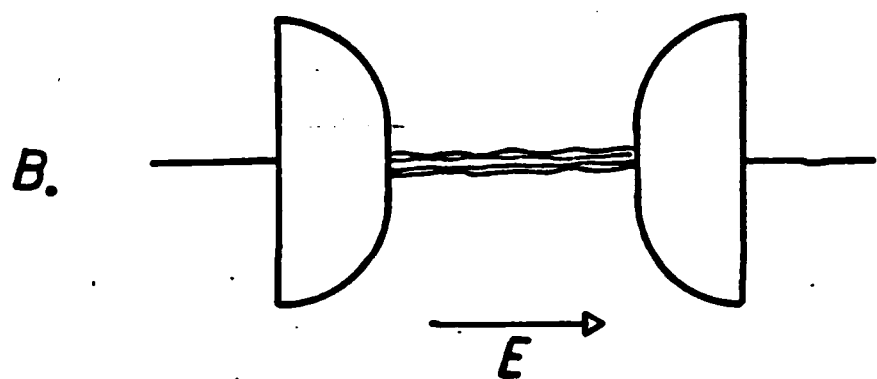
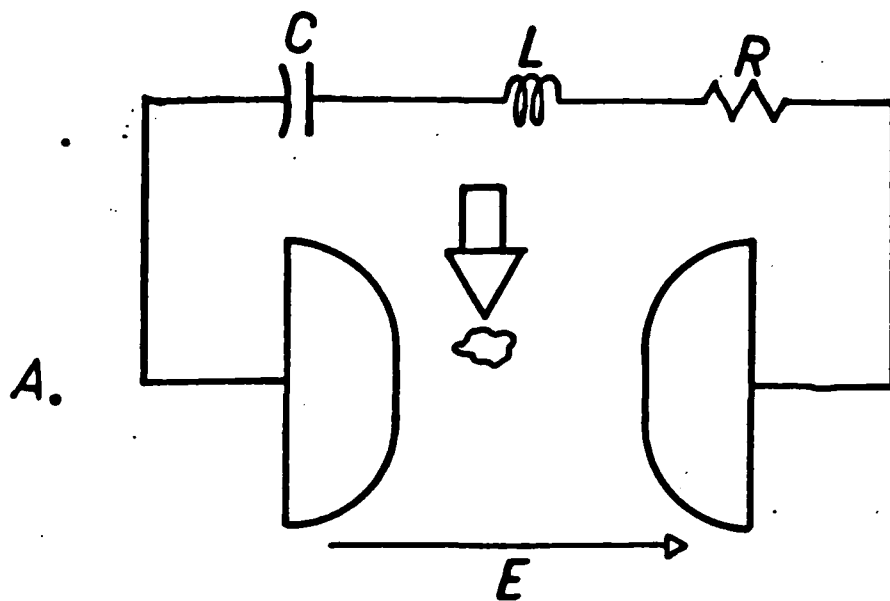
O PRECISE CONTROL

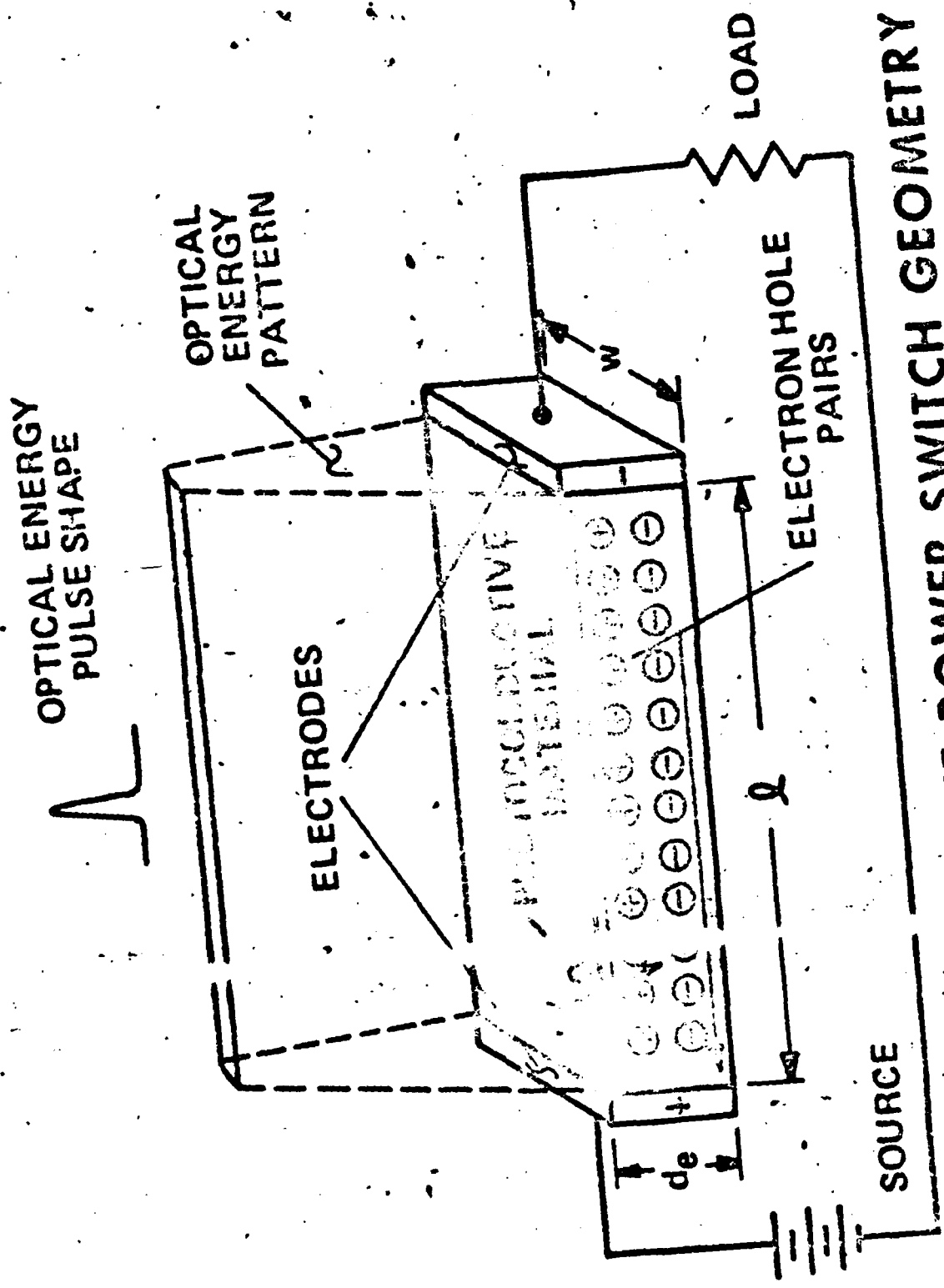
⊕ LOW JITTER

O FAST RECOVERY

⊕ HIGH PULSE RATE

UTA-ECRC-PCL
ELECTRICAL ENGINEERING

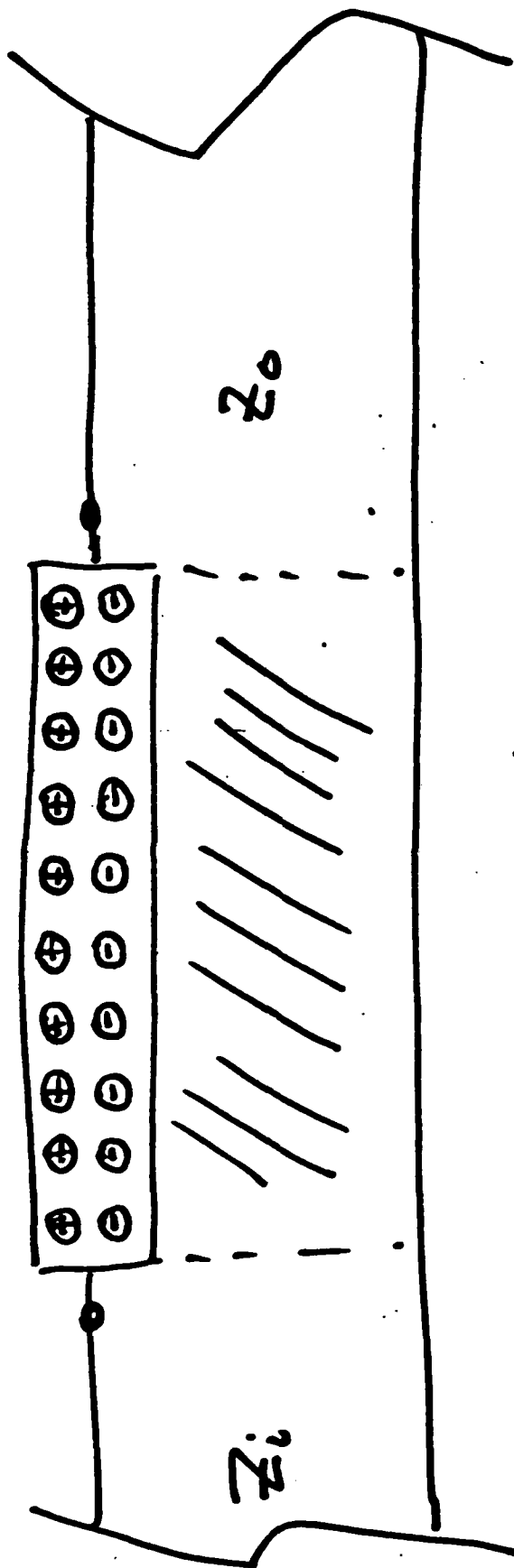
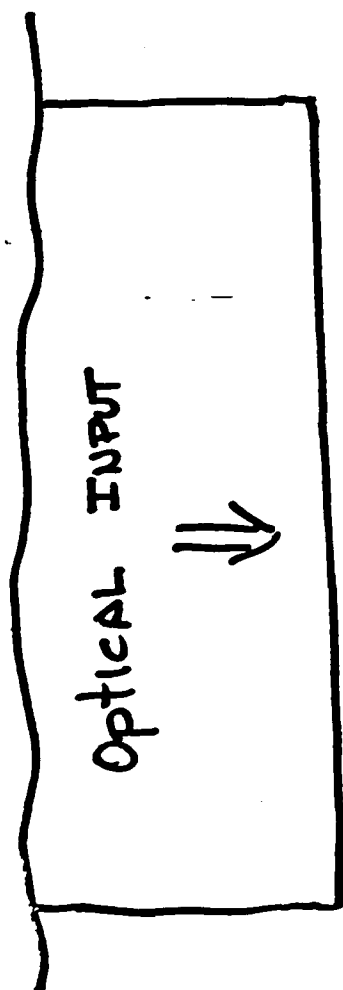




PHOTOCONDUCTIVE POWER SWITCH GEOMETRY

Los Alamos

Los Alamos National Laboratory, University of California

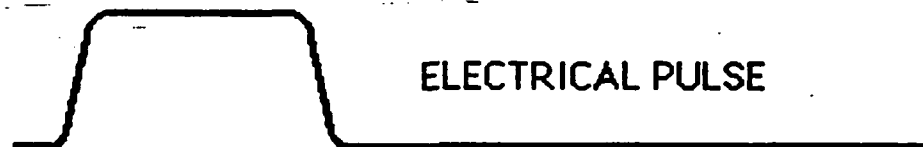
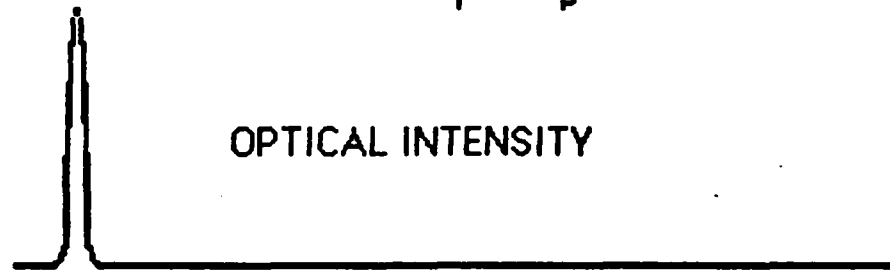


$$\tau_r \propto \frac{L}{(Z_i + Z_0)}$$

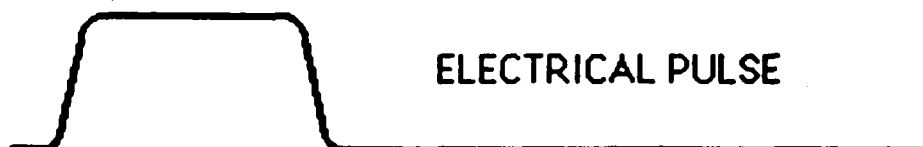
Carrier energy cost - band gap energy

PHOTOCONDUCTIVE SWITCH: MODES OF OPERATION

IMPULSE TRIGGERING $T_r \gg T_p$



PULSE MODULATION $T_r \ll T_p$



UTA-ECRC-PCL

295 ELECTRICAL ENGINEERING

Large
 $\bar{E} = E_0$

$$R_{OFF} = \frac{\rho_B l}{A} = \frac{\rho_B l}{w t}$$

\Rightarrow large ρ_B

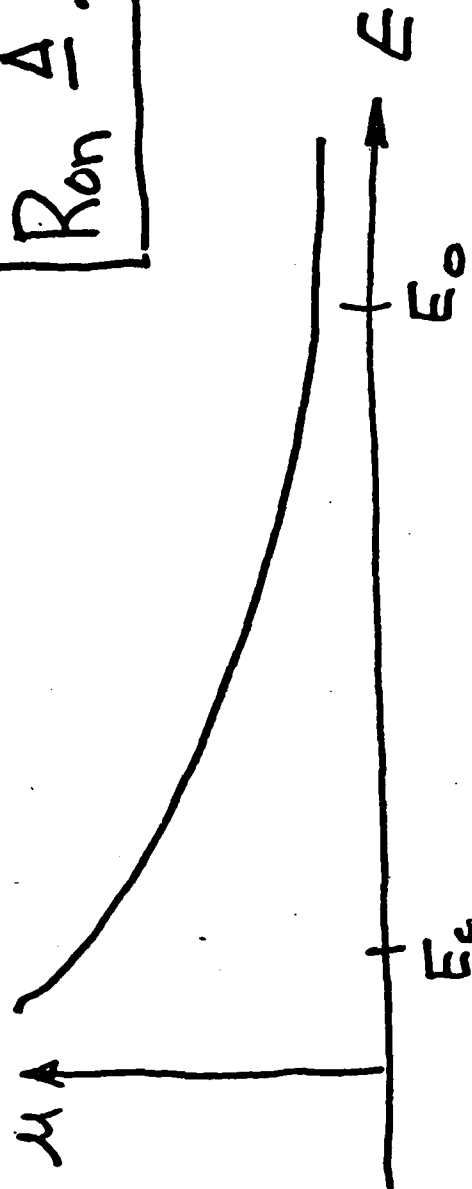
Small

$\bar{E} = E_c$

$$R_{ON} = \frac{l^2 E_x}{(1-r)\mu e E_c}$$

$\tau_r \gg \tau_P$

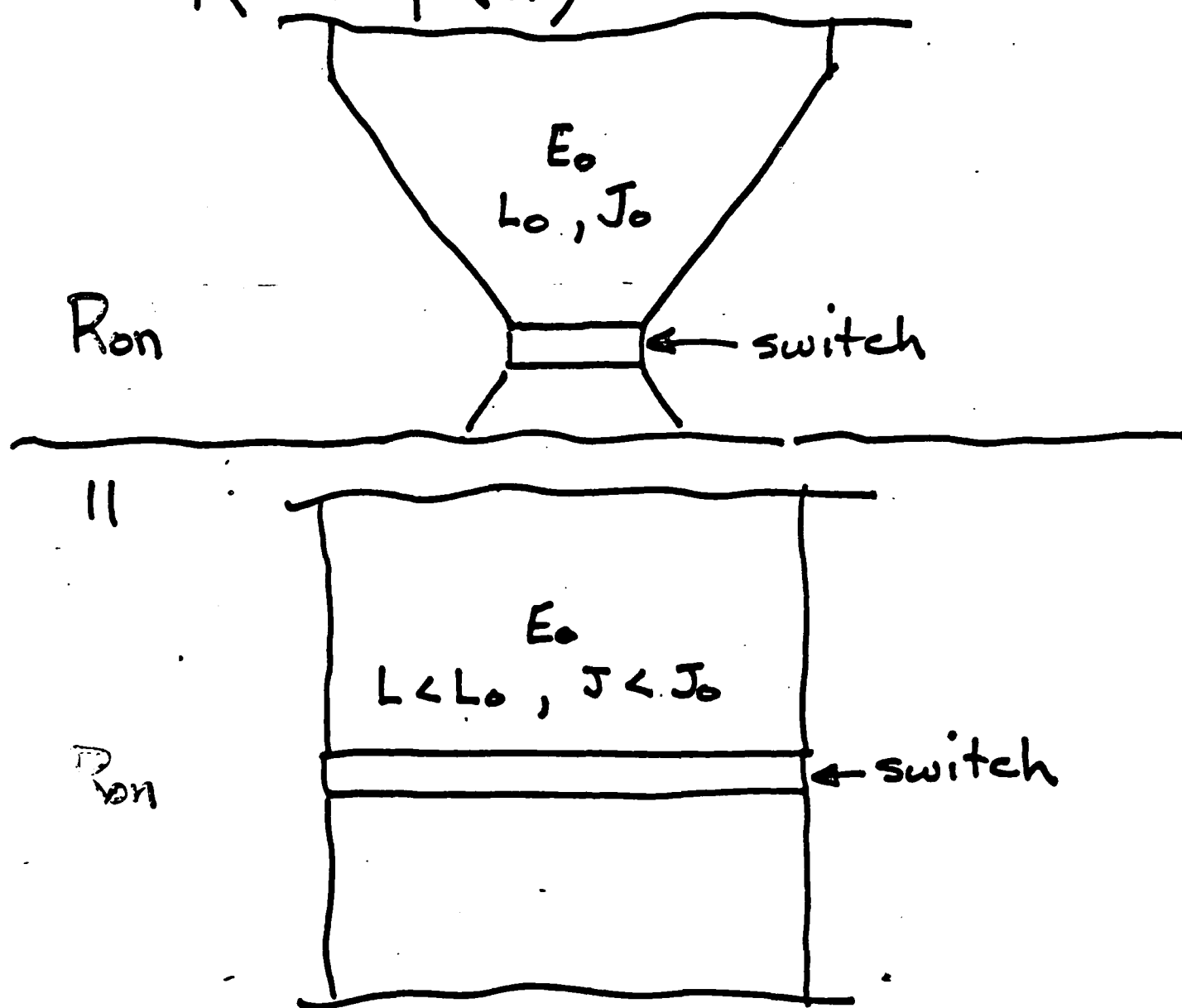
$R_{on} \approx 0.1 Z$



Photoconductor Inductance

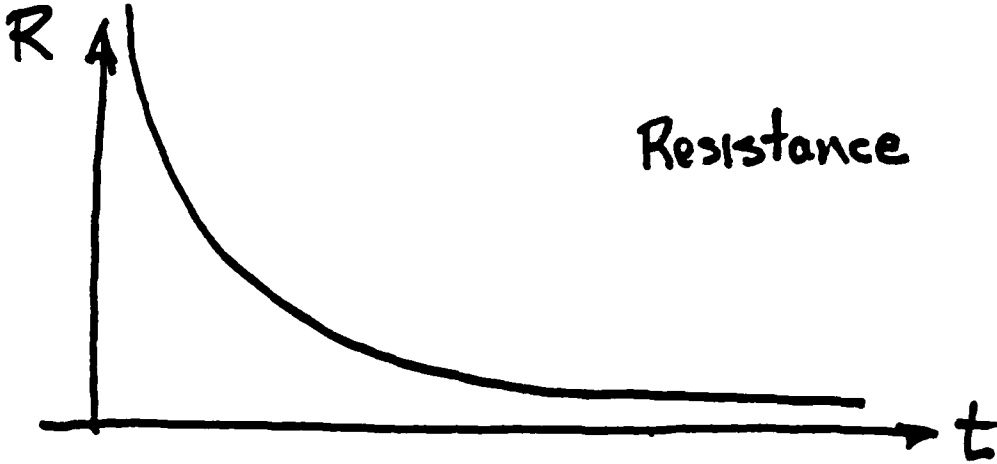
$\&$
Current Density

$$R \neq f(w) \quad (\mu = \text{const})$$

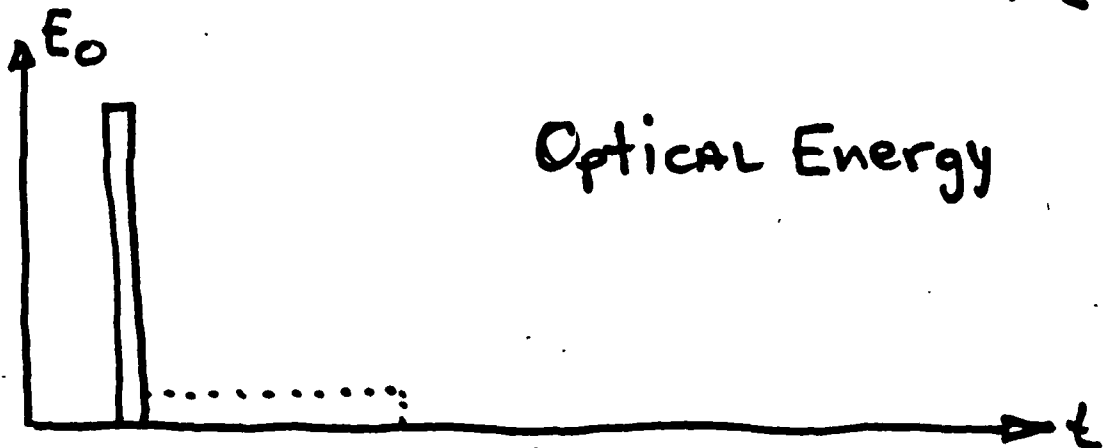
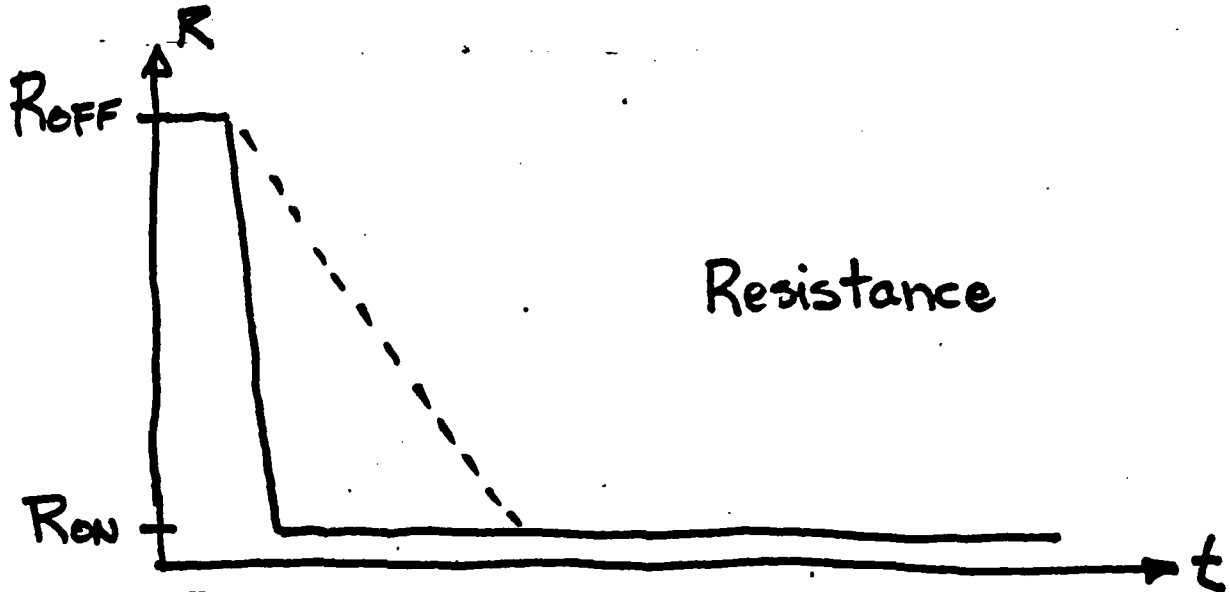


Resistive Phase Comparison

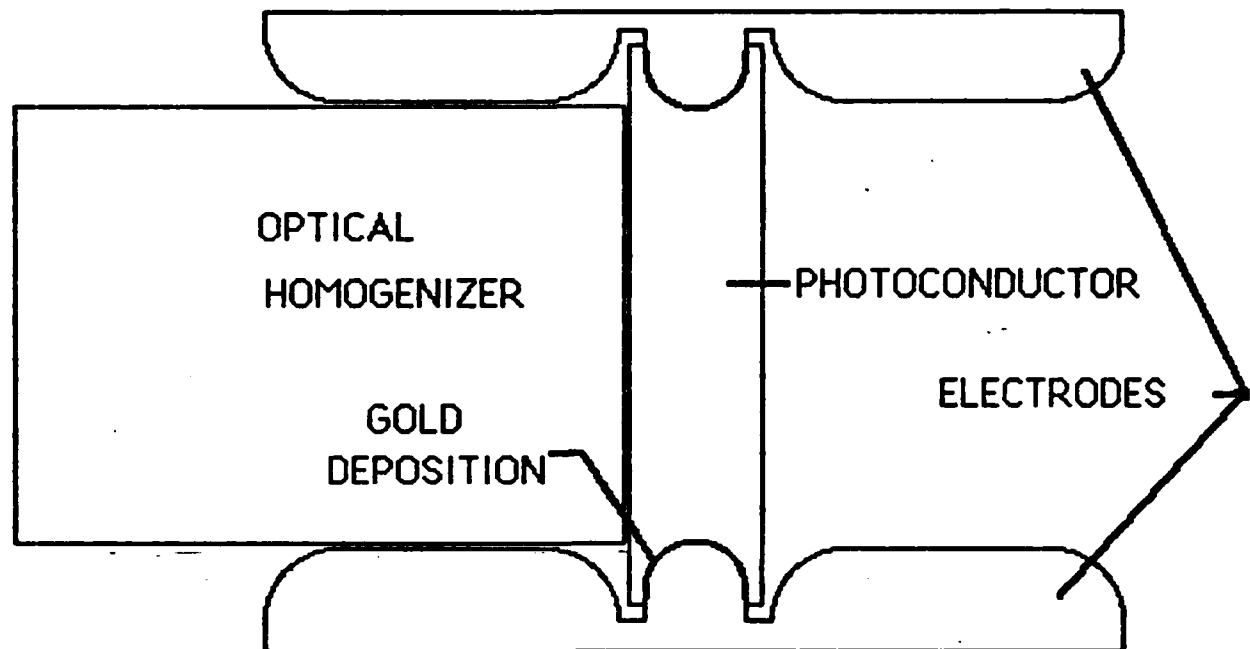
Spark Gap



• Photoconductor



PHOTOCONDUCTIVE SWITCH ELECTRODE GEOMETRY



UTA-ECRC-PCL
ELECTRICAL ENGINEERING

THE MAXIMUM CURRENT DENSITY
IS LIMITED BY THE MAXIMUM
CARRIER DENSITY

$$J_{\max} = n_{p-\max} e \mu E_c$$

$$\text{FOR SILICON} \quad J_{\max} = 50 \text{ kA/cm}^2$$

Electronics Division

Los Alamos

THE UNIVERSITY OF MICHIGAN LIBRARY

ANALYTICAL CHEMISTRY

$$\frac{1}{\lambda} = \frac{1}{\lambda_0} + \frac{1}{\lambda_d} + \frac{1}{\lambda_e}$$

$$\frac{1}{\lambda} = \frac{1}{\lambda_0} + \frac{1}{\lambda_d} + \frac{1}{\lambda_e}$$

$$\frac{1}{\lambda} = \frac{1}{\lambda_0} + \frac{1}{\lambda_d} + \frac{1}{\lambda_e}$$

THE MAXIMUM OPTICAL ENERGY DENSITY SHOULD BE LIMITED TO PRODUCE THE MAXIMUM CARRIER DENSITY

$$\frac{E_L}{w l} = \frac{n_{p-max} E_{\lambda} d e}{(1-r)}$$

FOR SILICON $\frac{E_L}{w l} = 10 \text{ mJ/cm}^2$

2 JOULES OF OPTICAL ENERGY WILL SWITCH 1 MV AT 50 KA

Electronics Division

Los Alamos

UNCLASSIFIED

210 kW
 2000 K (0.1 cm) 0.1 cm
 20 kA
 100 kW
 200 ns
 100 mJ
 2000
 200

Reproduced from
 best available copy.

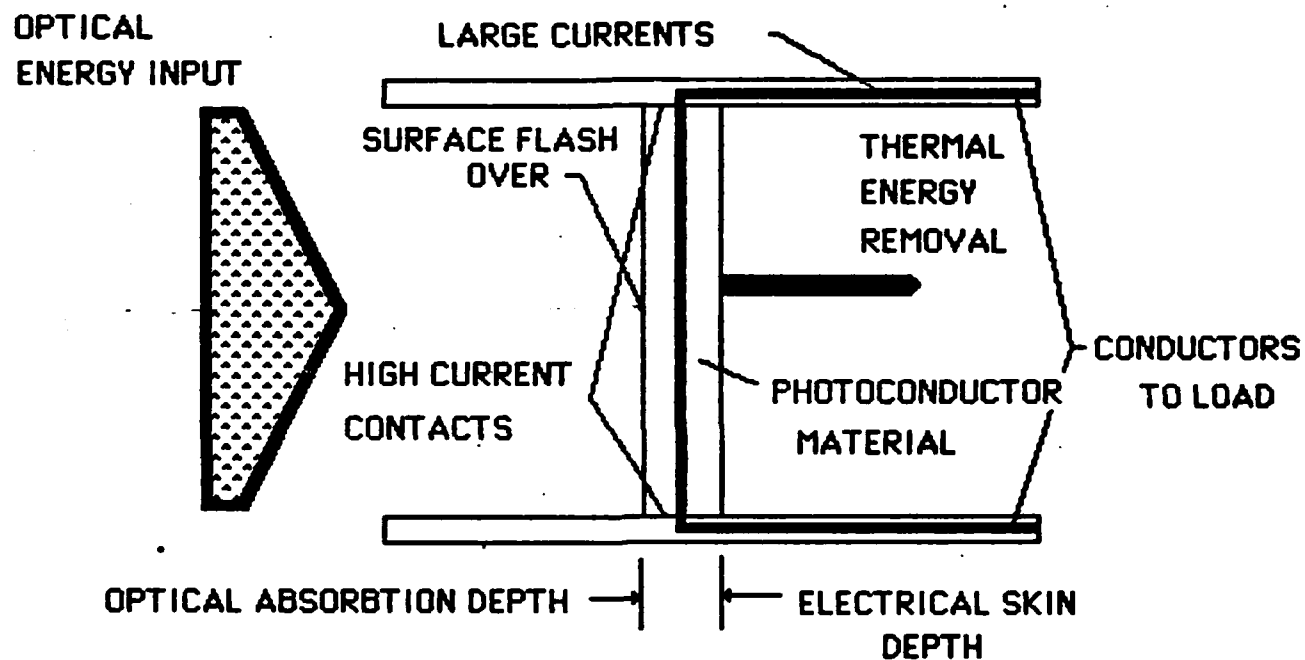
DEMONSTRATED SCALING PARAMETERS

- ⊕ 50 kV PER CM LENGTH
- ⊕ 5 kA PER CM WIDTH
- ⊕ 10 mJ PER SQUARE CM
- ⊕ 2 J OF PHOTONS WILL SWITCH 1 MV AT 50 kA

Electrical Engineering

UTA-PCL

MECHANICAL CONSIDERATIONS



UTA-ECRC-PCL
ELECTRICAL ENGINEERING

PULSE CHARGE LIMITATIONS

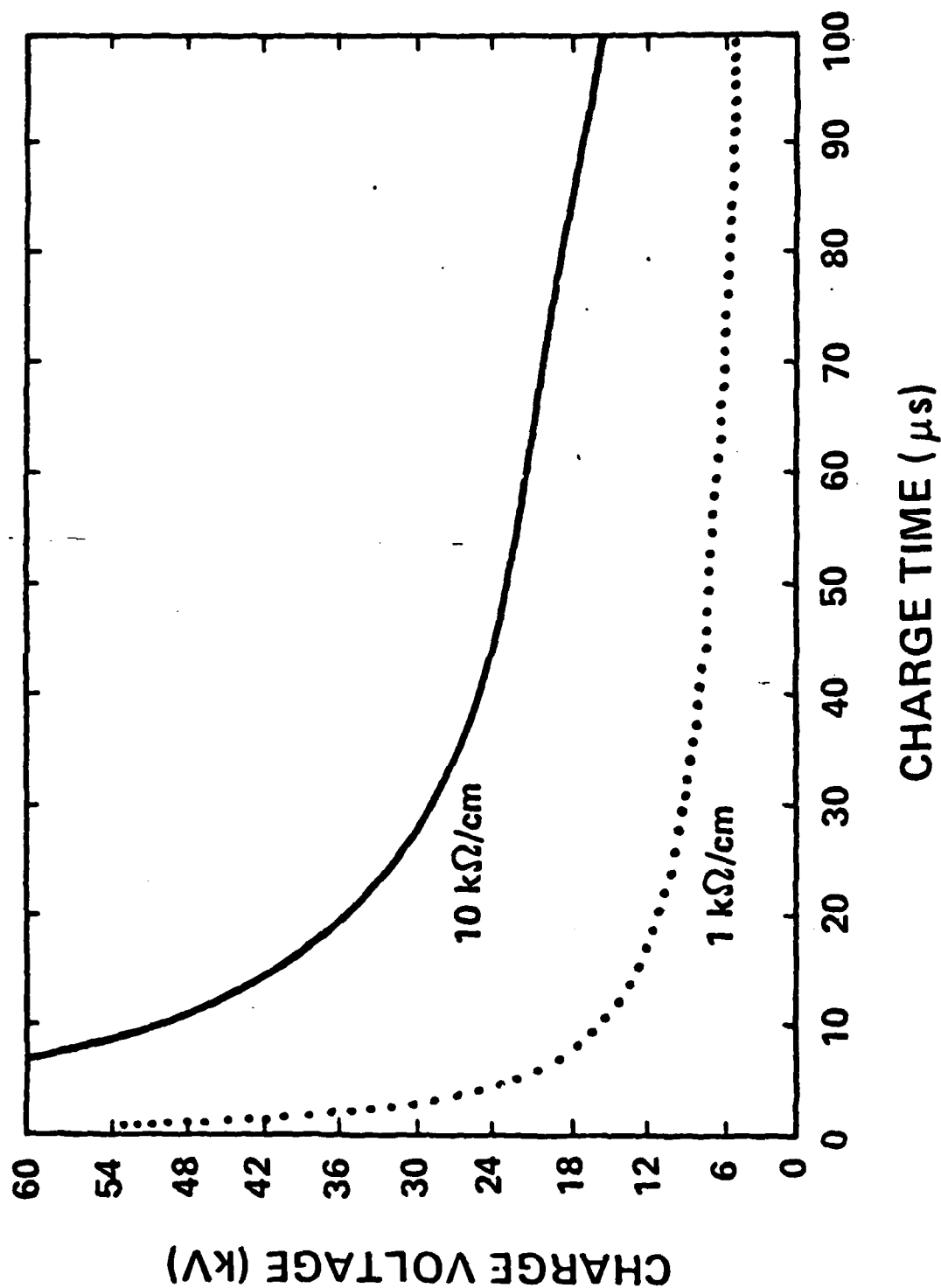
⊕ THERMAL RUNAWAY

⊕ CIRCUIT DECAY TIME

Electronics Division

Los Alamos

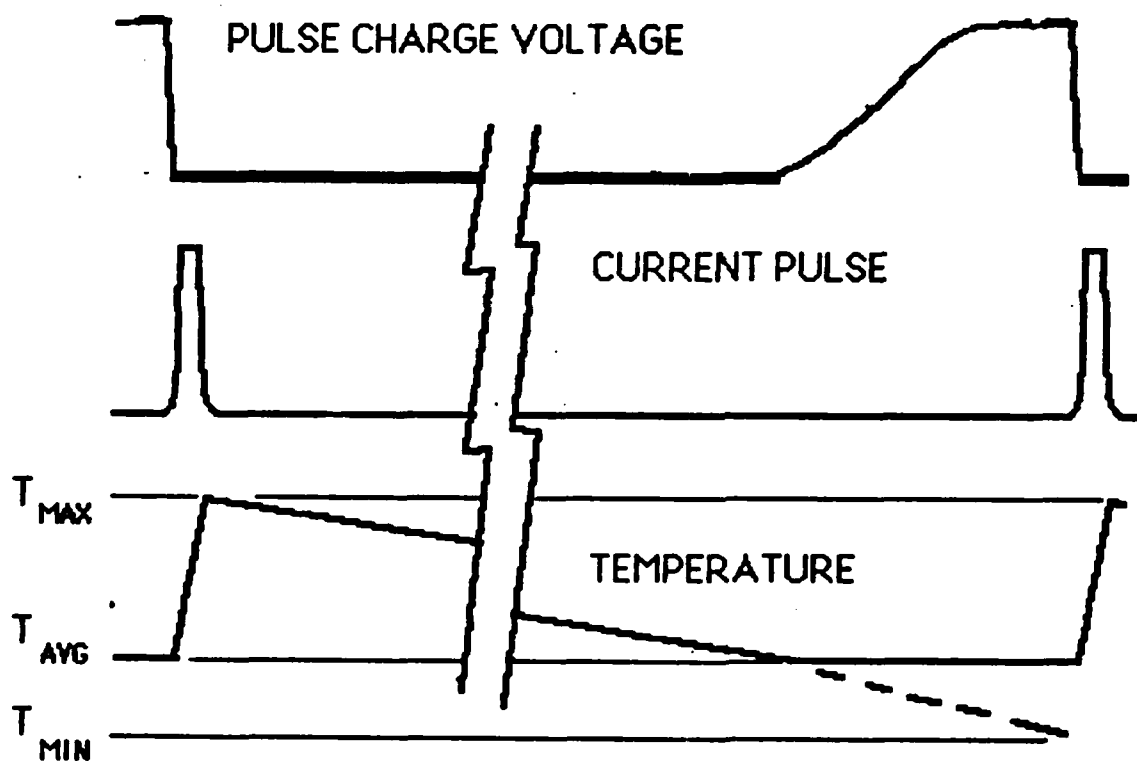
PULSE CHARGE VOLTAGE vs TIME FOR SILICON PCPS



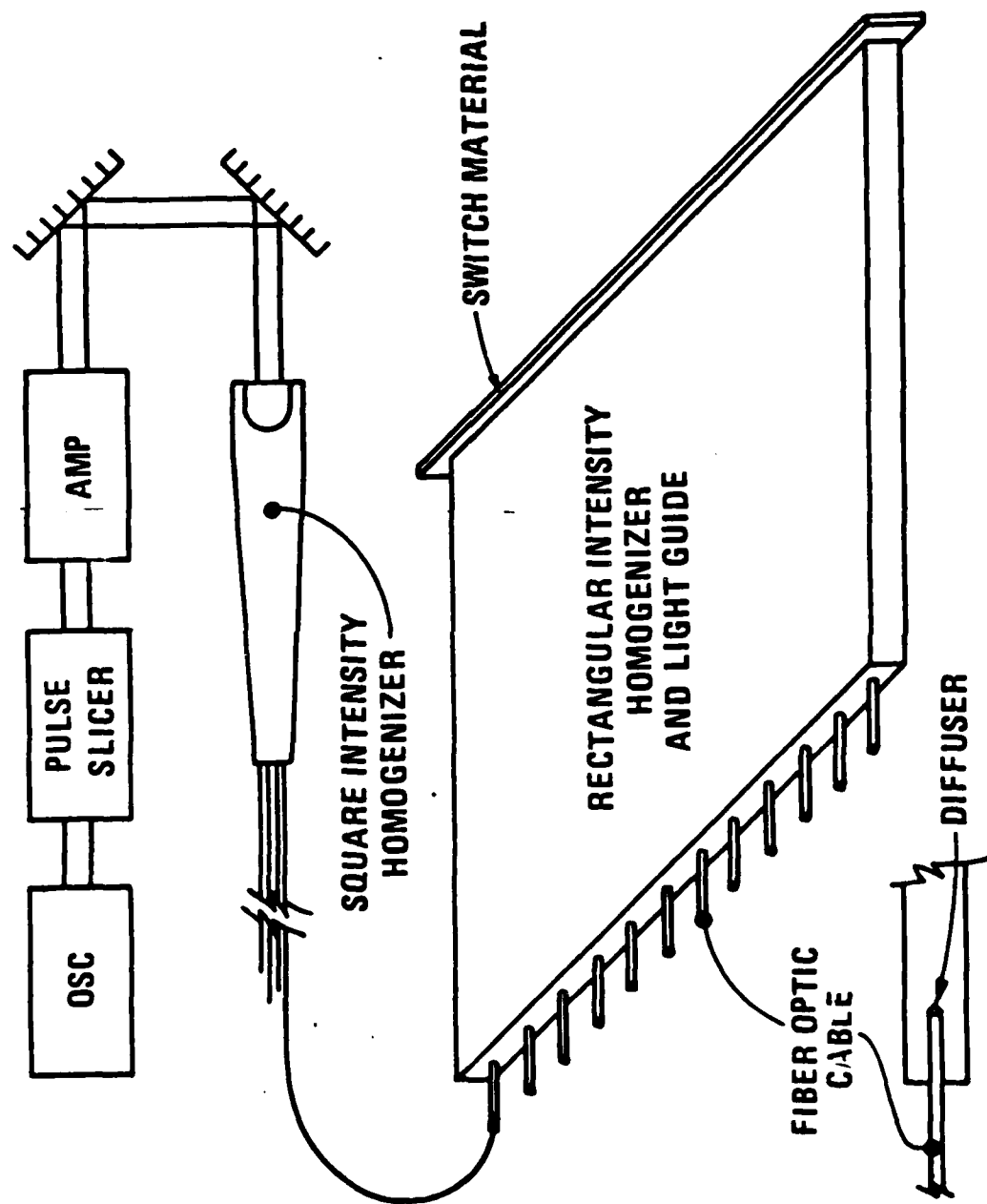
Los Alamos

Los Alamos National Laboratory/Operated by University of California

PHOTOCONDUCTIVE SWITCH: THERMAL CONSIDERATIONS, REPETITIVE OPERATION

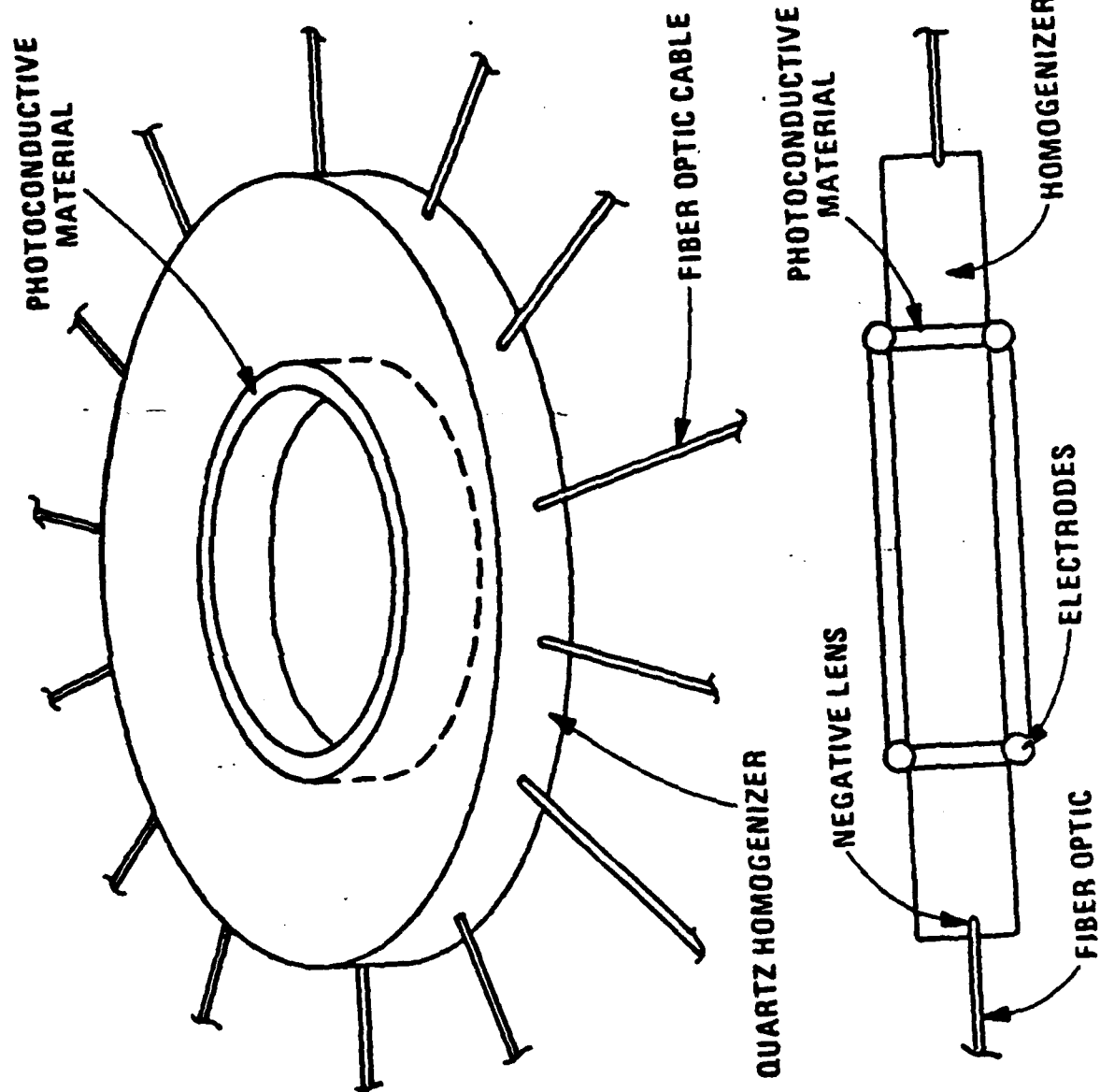


UTA-ECRC-PCL
ELECTRICAL ENGINEERING

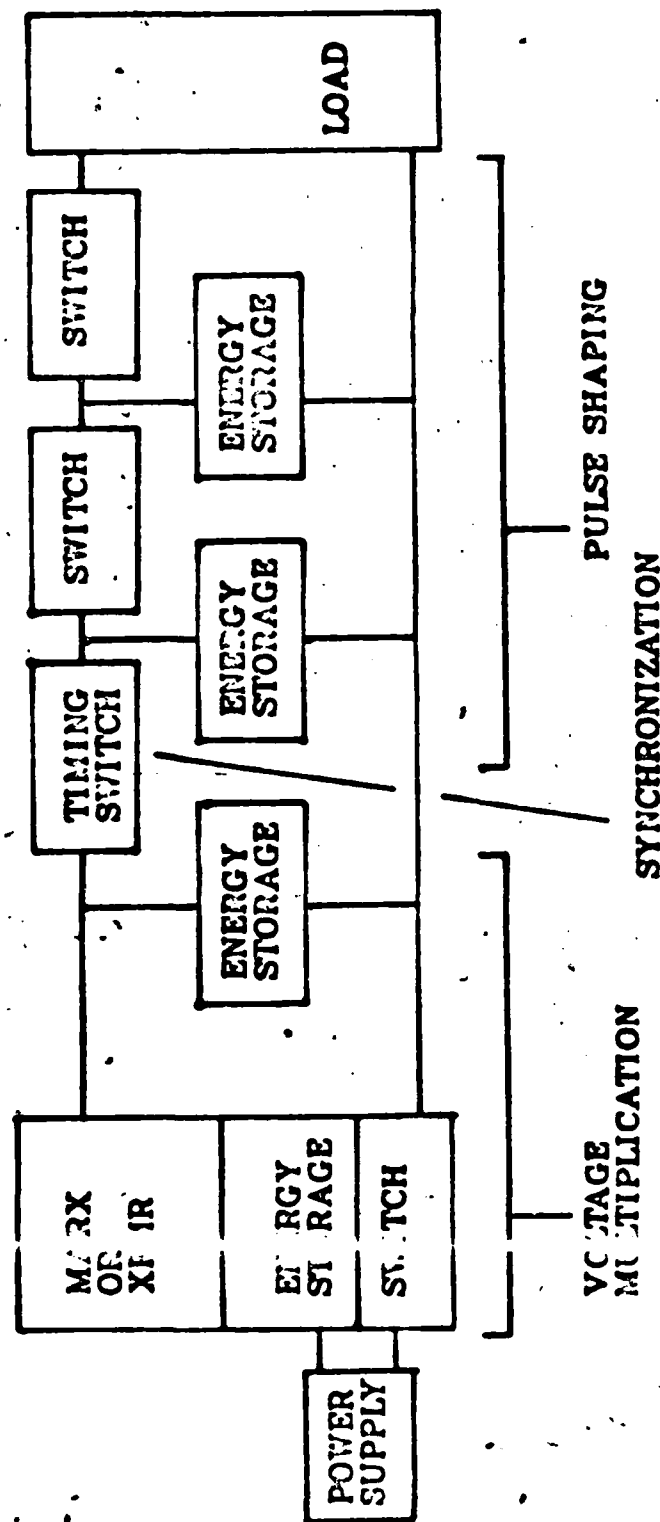


UNIFORM PCPS ILLUMINATION SYSTEM

Los Alamos



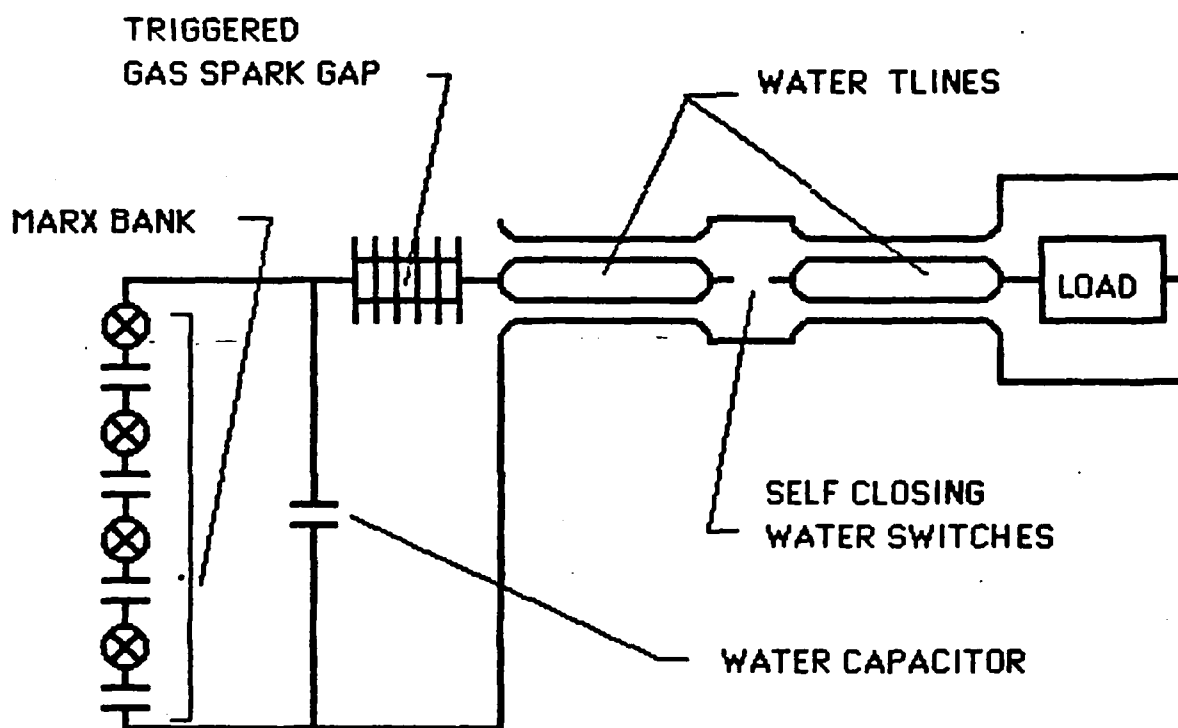
CONVENTIONAL POWER CONDITIONING



Electronics Division

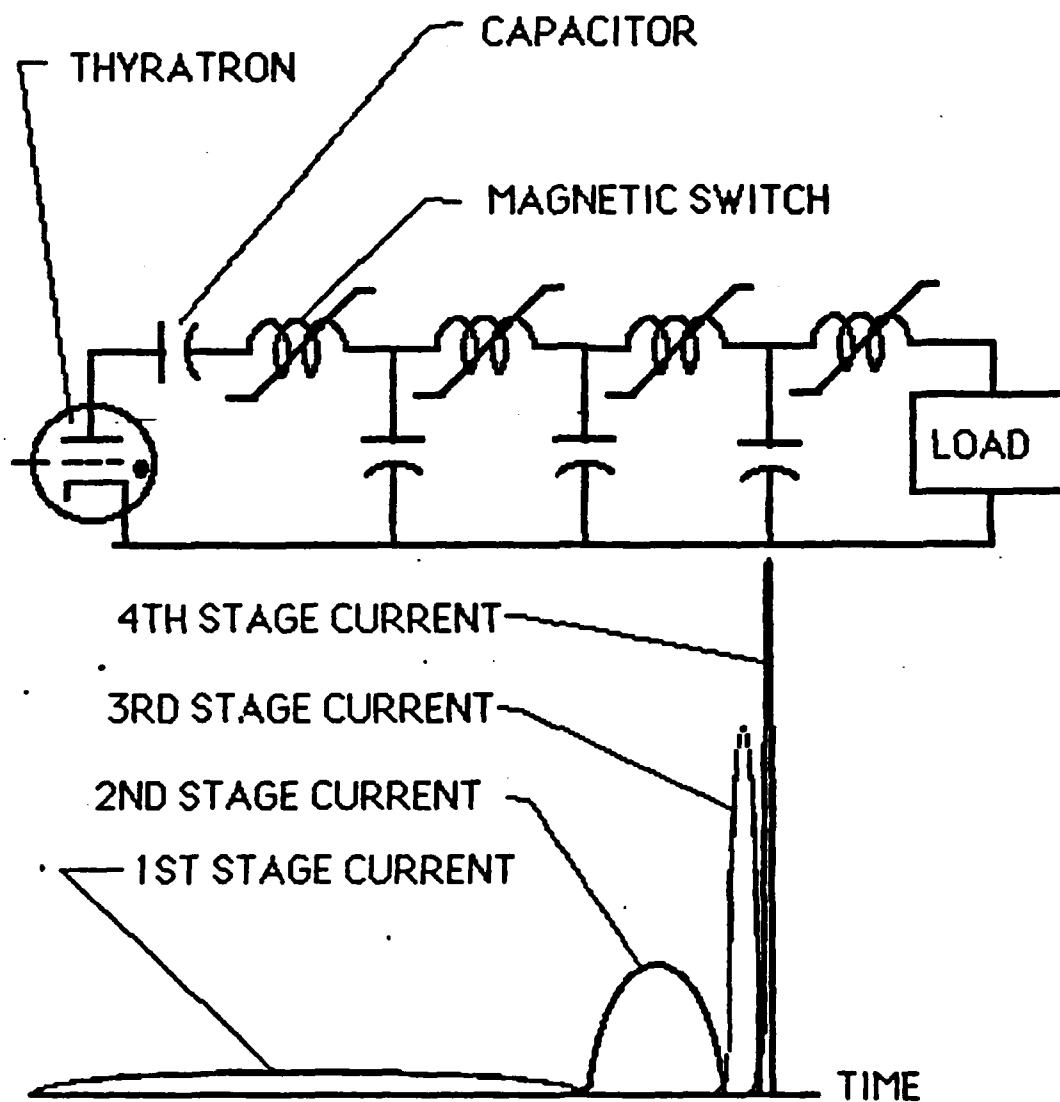
Los Alamos

**CONVENTIONAL POWER SYSTEM:
INERTIAL CONFINEMENT FUSION
HIGH CURRENT ACCELERATORS
EMP SIMULATION**



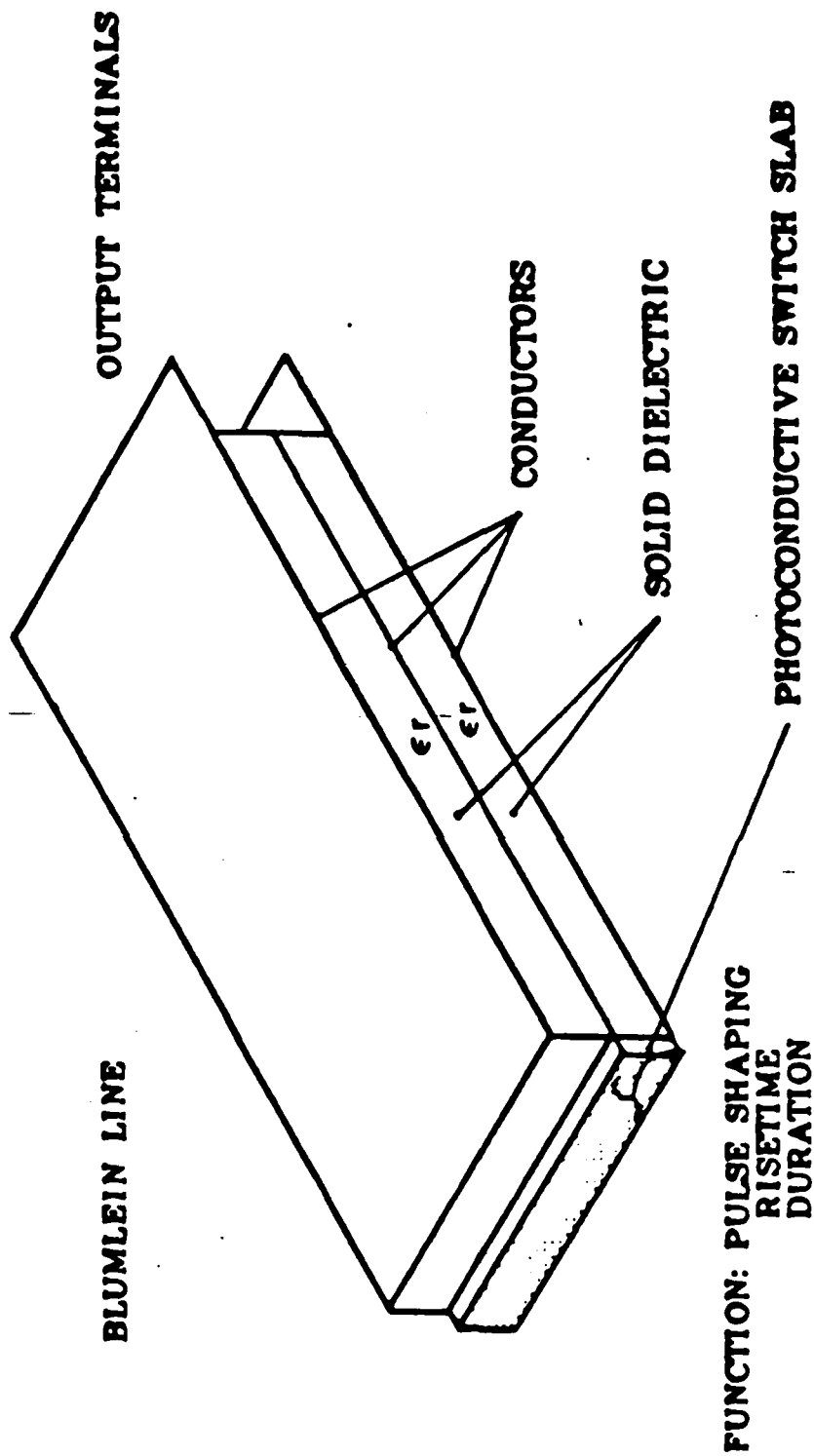
UTA-ECRC-PCL
ELECTRICAL ENGINEERING

CONVENTIONAL HIGH PULSE RATE, HIGH POWER SYSTEM



UTA-ECRC-PCL
ELECTRICAL ENGINEERING

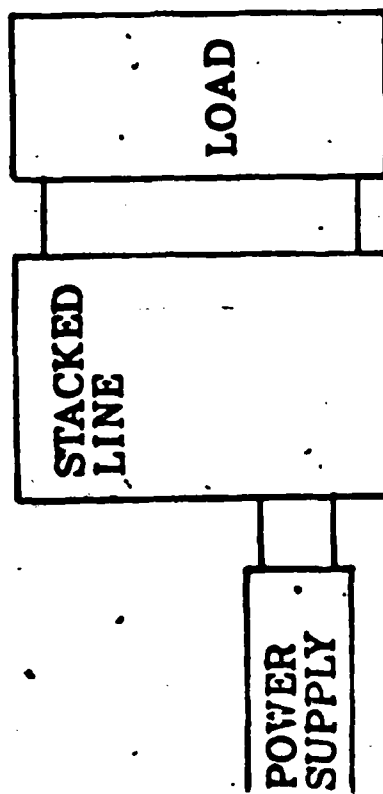
PULSE GENERATOR MODULE



Electronics Division

Los Alamos

ALTERNATE POWER CONDITIONING CONCEPT

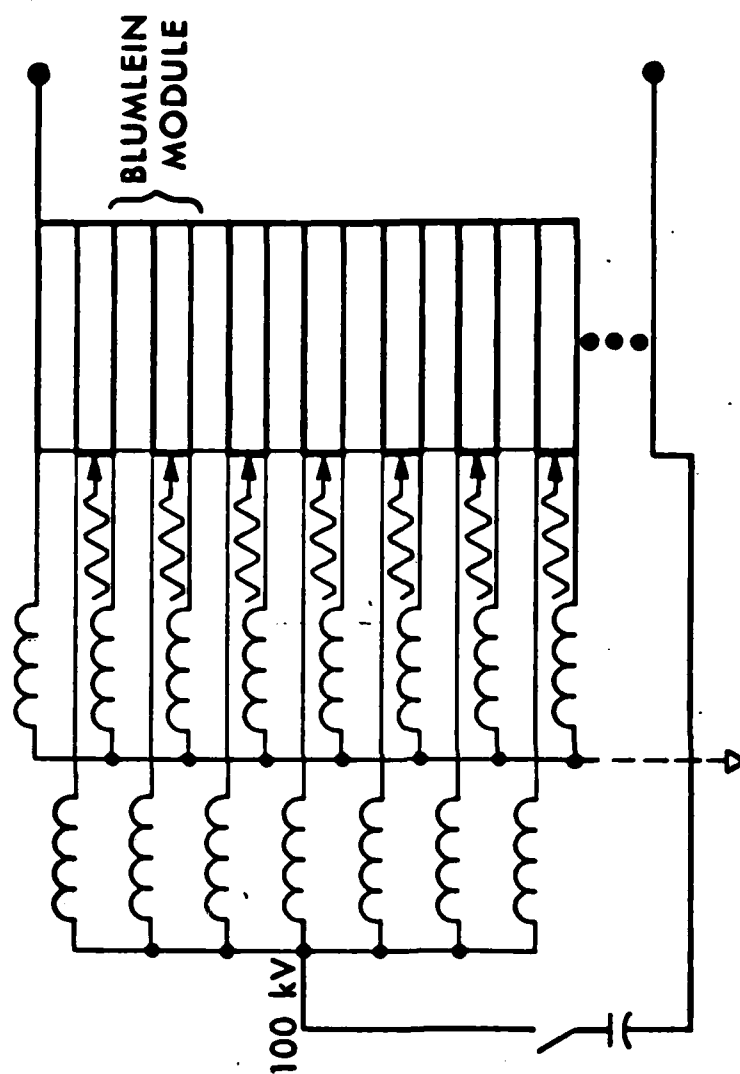


VOLTAGE MULTIPLICATION
PULSE SHAPING
SYNCHRONIZATION

Electronics Division

Los Alamos

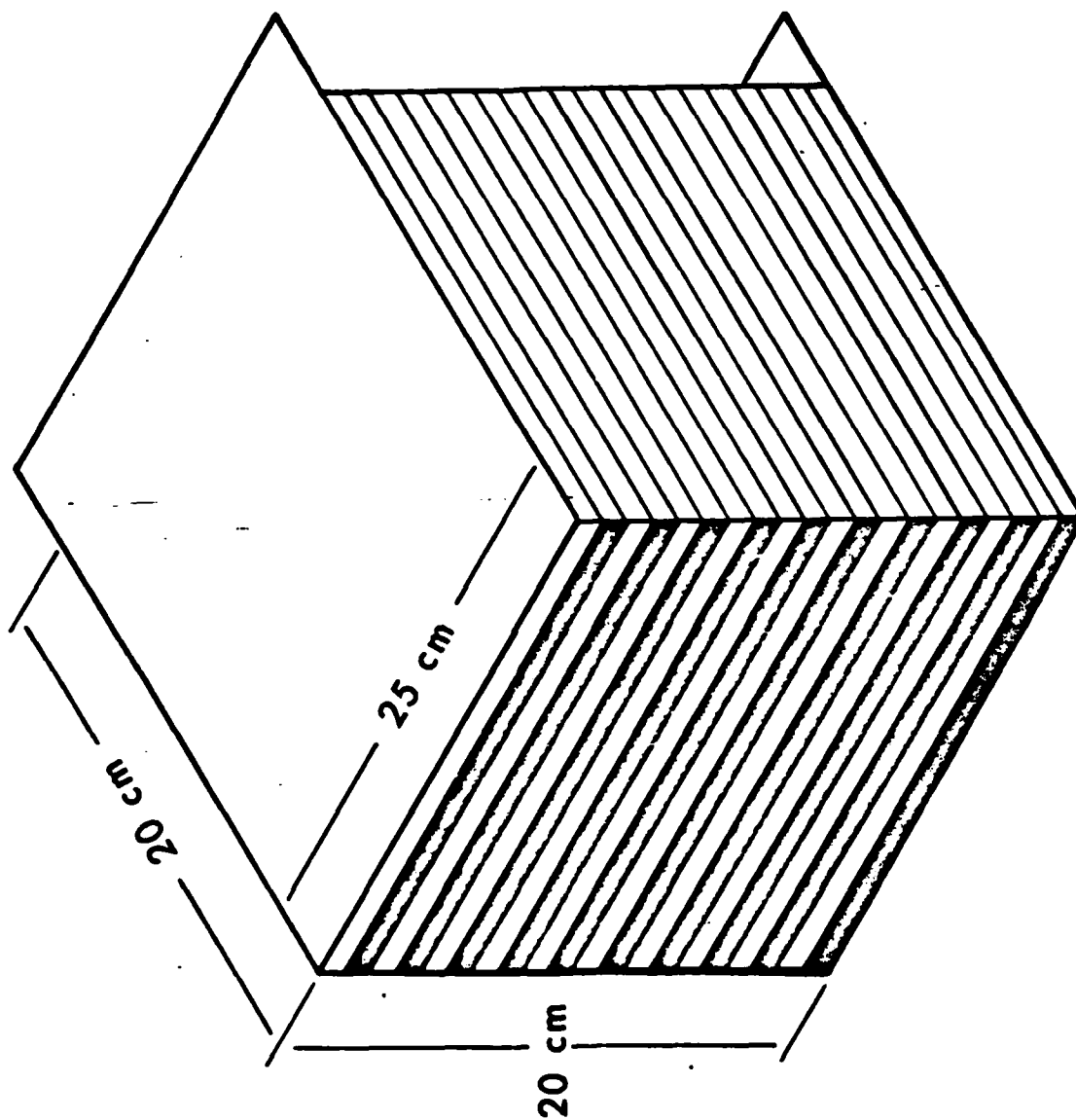
STACKED BLUMLEIN LINES



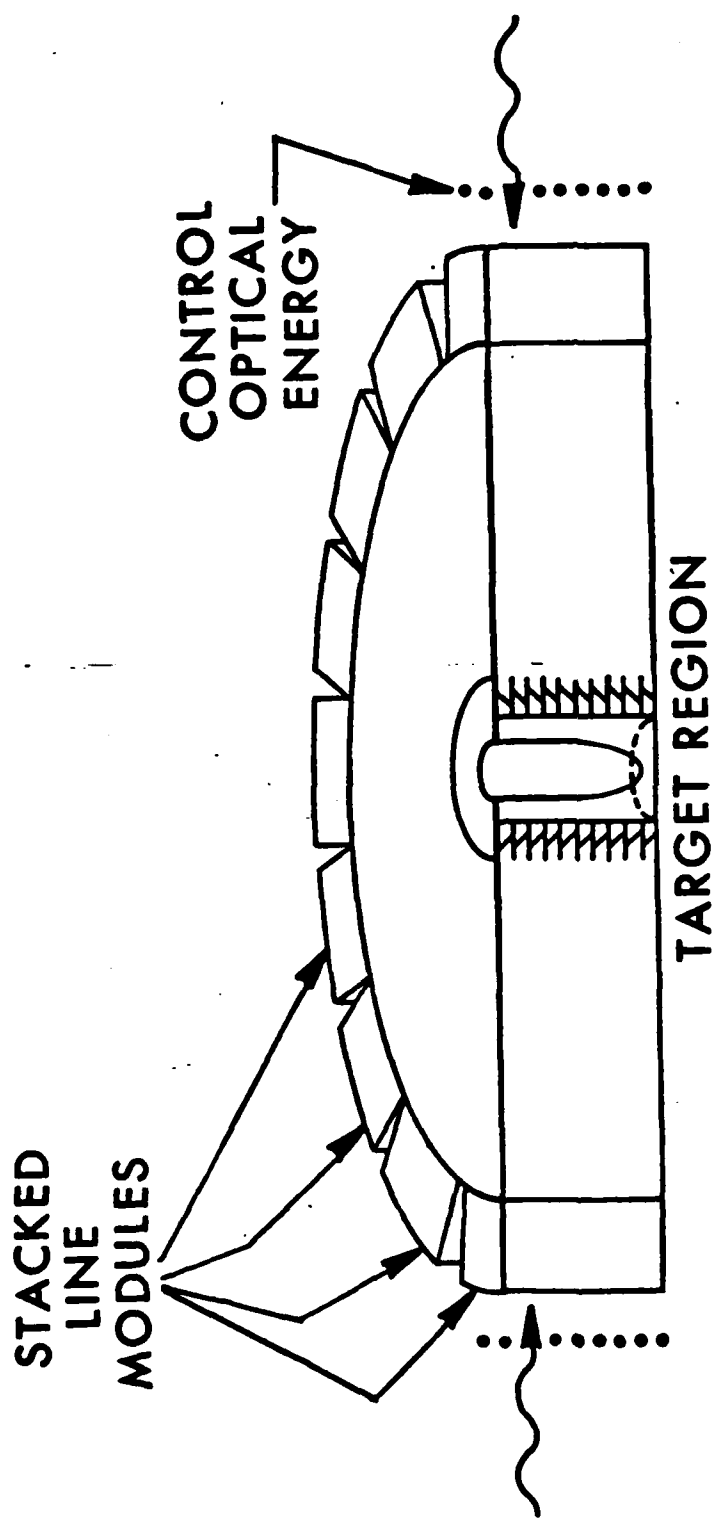
FUNCTION: VOLTAGE MULTIPLICATION

Electronics Division

Los Alamos



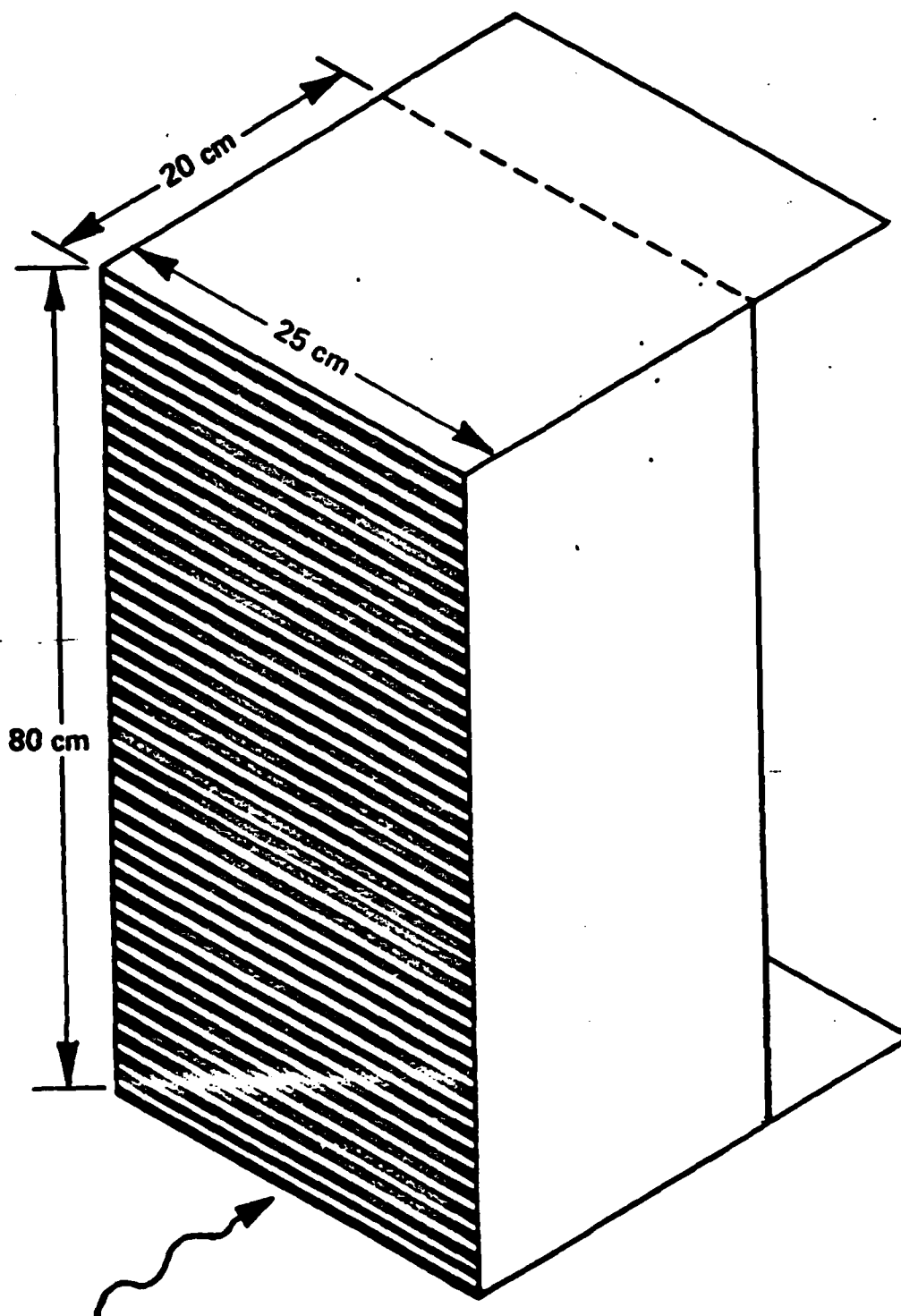
1 MV, 100 kA STACKED LINE MODULE



HIGH CURRENT WEAPONS EFFECT SIMULATOR CROSS SECTION

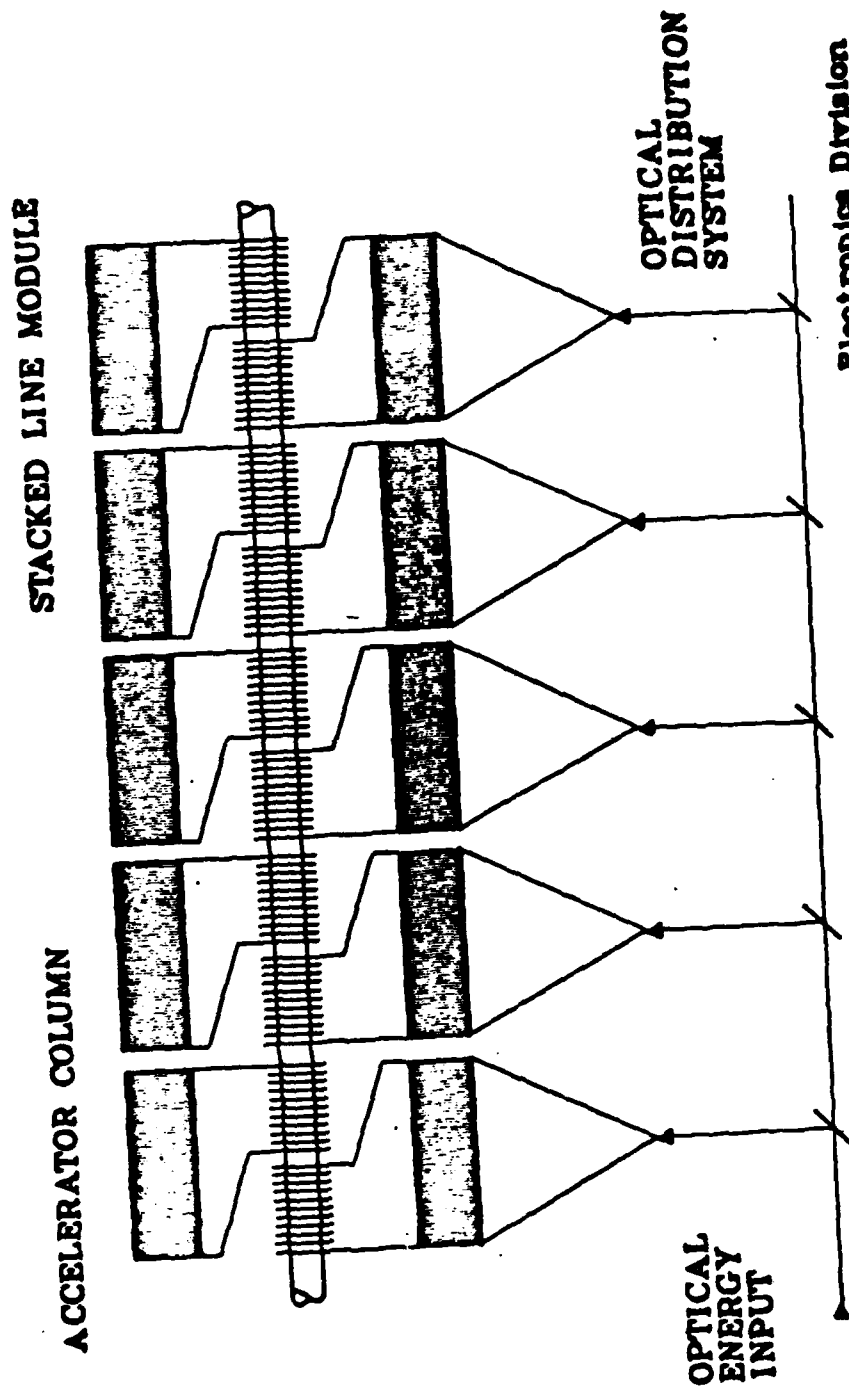
Los Alamos

Los Alamos National Laboratory/Operated by University of California



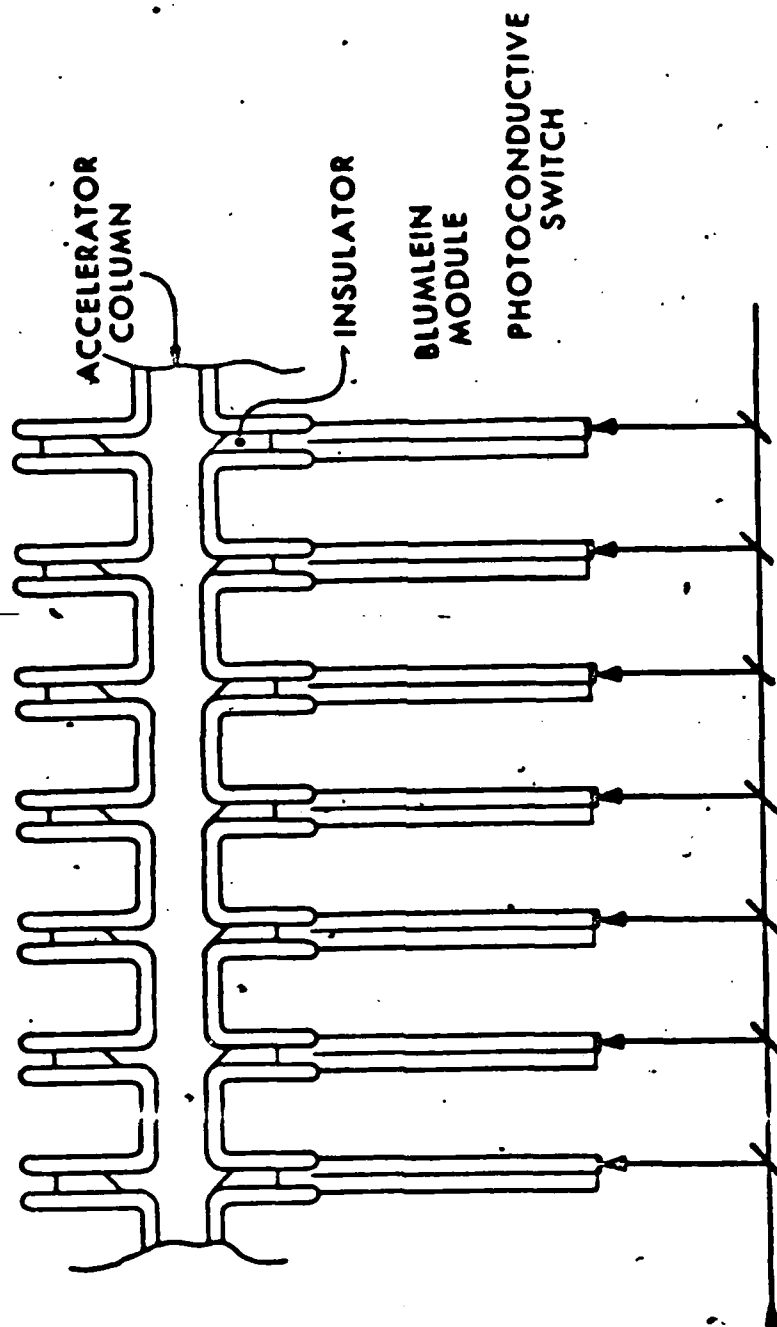
4 MV, 100 kA STACKED LINE MODULE

STACKED LINE INDUCTION ACCELERATOR



Los Alamos

DISTRIBUTED ACCELERATOR USING DISTRIBUTED BLUMLEIN MODULES



Los Alamos

Los Alamos National Laboratory/Operated by University of California

WHY USE PHOTOCONDUCTIVE POWER SWITCHES ?

- **FASTER RISETIMES**
RESISTIVE PHASE
INDUCTANCE
- **PRECISE CONTROL**
SEQUENTIAL
SIMULTANEOUS
- **NEW POWER CONDITIONING APPROACHES**
PHASED ARRAYS
STACKED LINES

UTA-ECRC-PCL
ELECTRICAL ENGINEERING

WHERE ARE PHOTOCONDUCTIVE SWITCHES APPROPRIATE ?

- **SHORT ELECTRICAL PULSES**
- **FAST RISETIMES**
- **LOW IMPEDANCE CIRCUITS**
- **PRECISE CONTROL**
- **LOW PULSE RATES-LASER LIMITED**

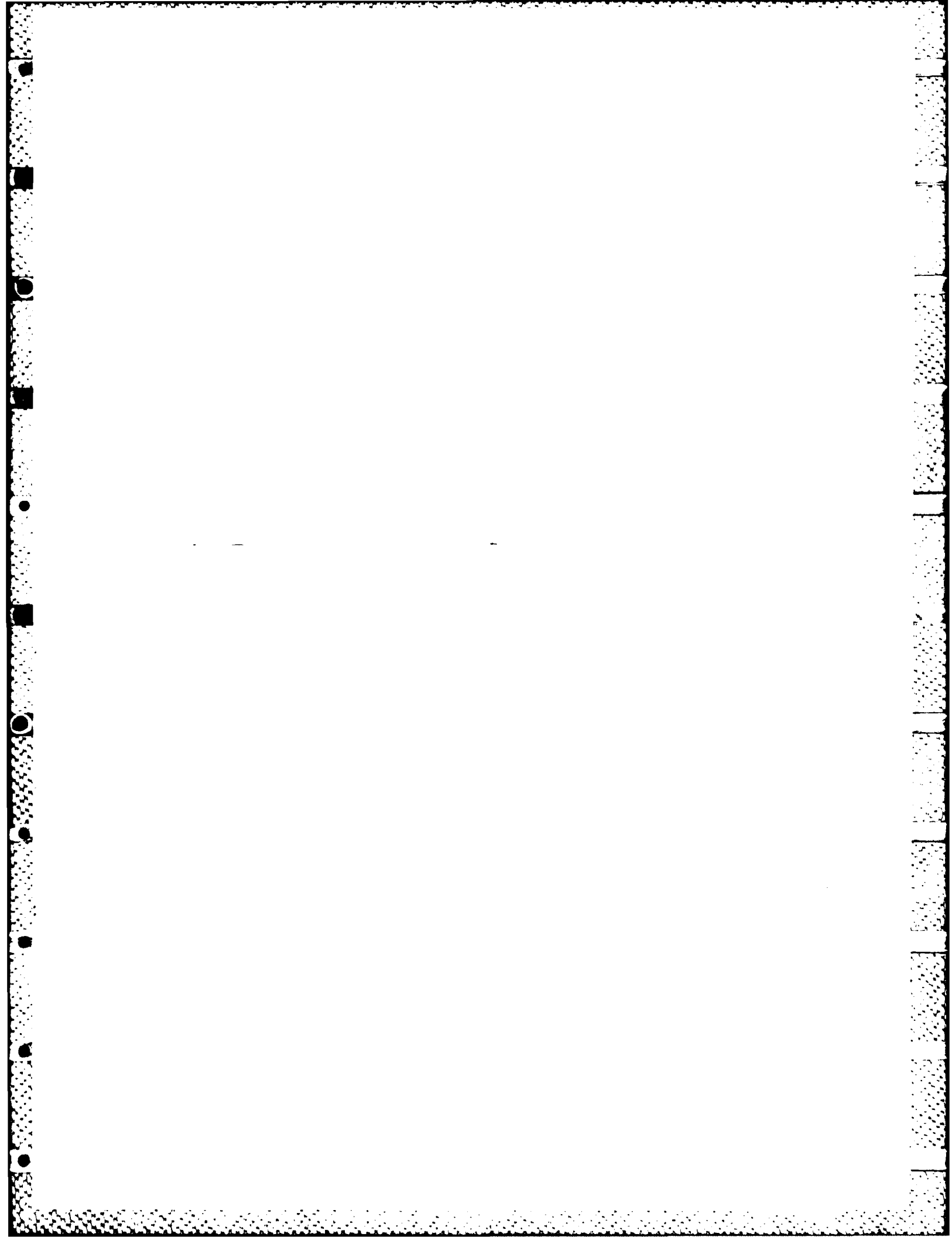
UTA-ECRC-PCL
ELECTRICAL ENGINEERING

AREAS FOR ADDITIONAL DEVELOPMENT

- ⊕ SURFACE FLASHOVER
- ⊕ MATERIAL: RECOMBINATION TIME AND RESISTIVITY
- ⊕ LARGE PHOTOCONDUCTOR DEVICE FABRICATION
- ⊕ POLYCRYSTALLINE SILICON ON SAPPHIRE SUBSTRATE
 - ⊕ EDGE GROWN THIN FILMS
- ⊕ OPTICAL SOURCES
- ⊕ CRYOGENIC SILICON DEVICES

Electrical Engineering

UTA-PCL



OPTICALLY ACTIVATED SEMICONDUCTORS AS REPETITIVE OPENING SWITCHES

E. A. Chauchard, M. J. Rhee, Chi H. Lee
Electrical Engineering Department
University of Maryland
College Park, Maryland 20742

ABSTRACT

We demonstrate for the first time the operation of a semiconductor repetitive opening switch. A semiconductor is maintained in a conductive state by illumination with a cw argon laser light. The opening of the switch is obtained by interrupting the light. A turn-off time of 1 ns has been achieved.

PACS: 85.20.Vq, 84.60.Td, 85.30.Fg, 85.60.Me

The rapid progress of inductive energy storage circuits as pulsed power systems has required the development of new opening switches [1,2,3]. These switches should be fast, capable of handling high voltages, and, in many applications, jitter free. Among the switches being commonly used, many have the following drawbacks: slow turn-off time, single-shot operation, short closing period, low repetition rate, inaccurate triggering. The unique characteristics of light-activated solid state switches make them prime candidates for repetitive opening switches. Since the switch is activated by laser using the photoconductivity effect, it is jitter free. Using bulk semiconductors, these switches can withstand high voltages and high current, as it has already been demonstrated for closing switches [4,5]. In this paper, we demonstrate for the first time the operation of semiconductor opening switches, and we show that the turn-off time can be as fast as 1 ns.

In this work, two planar switches are examined. The two gold electrodes are deposited on the surface of a piece of bulk semiconductor. One device is a 200 μm gap GaAs switch and the other is an interdigitated 4 μm gap InGaAs:Fe switch. To keep the switch closed, its gap is continuously illuminated with argon laser light at 514 nm. The opening is achieved by interrupting the light by means of a Pockels cell placed between two parallel polarizers (Fig. 1). The electrical pulse delivered to the Pockels cell is 200 ns long; its rise time and fall time are < 1 ns. To demonstrate the operation of the opening switch, we use an inductive storage circuit as shown in Fig. 1. The circuit is built in a shielded box to avoid the electromagnetic interference from the Pockels cell power supply. The temporal shape of the transient signal obtained when the switch opens is observed on the oscilloscope using a 50 Ω plug-in.

In the circuit represented in Fig. 1, the current $I(t)$ through the load as the switch opens may be described by the following equation:

$$C \frac{d^2 I(t)}{dt^2} + \frac{1}{R_L} \frac{dI(t)}{dt} + \frac{1}{L} I(t) = 0, \quad (1)$$

where C is the capacitance, L is the inductance, and R_L is the load resistance ($R_L = R + 50 \Omega$). The solution of this equation with initial current I_0 at $t = 0$ is:

$$I(t) = k I_0 [\exp(S_1 t) - \exp(S_2 t)], \quad (2)$$

where $k = (2R_L C \sqrt{\Delta})^{-1}$, $S_1 = -(1/2R_L C) + \sqrt{\Delta}$, $S_2 = -(1/2R_L C) - \sqrt{\Delta}$, and $\Delta = (1/2R_L C)^2 - 1/LC$. I_0 in this case represents the amplitude of the current difference in the switch when it opens: $I_0 = V(1/R_{on} - 1/R_{off})$, where V is the applied voltage and R_{on} and R_{off} are the switch resistances at the on-state and the off-state, respectively. The waveforms described by equation (2) are of three types: Δ positive corresponds to overdamped solutions, Δ negative to oscillatory solutions, and $\Delta = 0$ corresponds to the critical damping. One can calculate the following features of the current waveforms. In the oscillatory case, the period of oscillation is

$$T = 2\pi/\sqrt{-\Delta}. \quad (3)$$

In the damped case, the slope of the current waveform at $t = 0$ is

$$dI/dt = I_0/R_L C, \quad (4)$$

and the fall time for the overdamped case is:

$$\tau = (1/2R_L C - 1/\sqrt{\Delta})^{-1}. \quad (5)$$

If no capacitance is used in the circuit, a similar treatment leads to a fall time of

$$\tau = L/R_L. \quad (6)$$

The voltage signal observed on the oscilloscope is: $u(t) = 50 \times I(t)$.

The dark (off) resistances of the GaAs and InGaAs:Fe switches respectively are 2 M Ω and 150 k Ω . When illuminated with a 2 watts argon laser beam focused on the gap, their resistances decrease to 10 k Ω and 150 Ω . Fig. 2 shows the 200 ns long cut-off of the light, and the waveforms observed with the GaAs switch for different parameters of the circuit during this 200 ns period. No capacitance is used. To understand those waveforms for the values of V, R, L, R_{on} , and R_{off} given, one must take into account the stray capacitances of the circuit. Part of it (9.7 pF) is due to the 10 cm semi-rigid 50 Ω coaxial cable connecting the switch to the circuit. For the oscillatory case (Fig. 2b), equation (3) allows to deduce a value of 22 pF for the capacitance. In the overdamped cases (Fig. 2c, d, and e), the fall time of the signal is in good agreement with equation (6), which holds if the capacitance is very small. Equation (4) allows us to calculate a value of the capacitances of 30 pF in Fig. 2e, where the slope of the rising current at $t = 0$ can easily be measured. This value implies a fall time $\tau = 260$ ns, in good agreement with the measured value. The fastest rise time observed with the GaAs switch was 5 ns (Fig. 2c). This is in accordance with the expected carrier recombination time in this undoped material. In the case of the InGaAs:Fe switch, the carrier recombination time is only of the order of 300 ps. The switch turn-off speed is then limited by the Pockels cell rise time (1 ns). We indeed observe a 1 ns turn-off time (Fig. 3). The waveforms obtained with this second switch show the same characteristics as those with the GaAs switch. In this experiment, no attempt has been made to further decrease the resistances of the switches at the on-state. This can be achieved by using higher laser power or longer wavelength. Indeed, the absorption depth of 514 nm wavelength light in GaAs is only 0.1 μ m [6]. This is not suitable for obtaining a low on-state resistance, since it

reduces the electron path to a very thin layer. Another development of these switches would be to use larger gap sizes capable of withholding higher voltages.

In conclusion, we have demonstrated for the first time the operation of a 1 ns rise time semiconductor repetitive opening switch. Although in this work only 10 hz repetition rates have been achieved, these switches are potentially capable of operating at very high repetition rates.

ACKNOWLEDGEMENT

We wish to acknowledge V. Diadiuck from the MIT Lincoln Laboratory for supplying the InGaAs:Fe switch, and A. Rosen of RCA for supplying the GaAs switch. This work was supported by the Air Force Office of Scientific Research.

REFERENCES

1. K. H. Schoenbach, M. Kristiansen and Gerhard Schaefer, Proc. IEEE 72, 8 (1984).
2. R. A. Meger, R. J. Comisso, G. Cooperstein and Shyke A. Goldstein, Appl. Phys. Lett. 42, 943 (1983).
3. M. J. Rhee and R. F. Schneider, IEEE Trans. Nucl. Sci. NS-30, (4) 3192 (1983).
4. W. C. Nunnally, R. B. Hammond and R. S. Wagner, paper WM13 of CLEO Conference, Baltimore (1985).
5. Chi H. Lee (ed.), Picosecond Optoelectronic Devices, Academic Press.
6. S. M. Sze, Physics of Semiconductor Devices, 2nd edition, Wiley-Interscience.

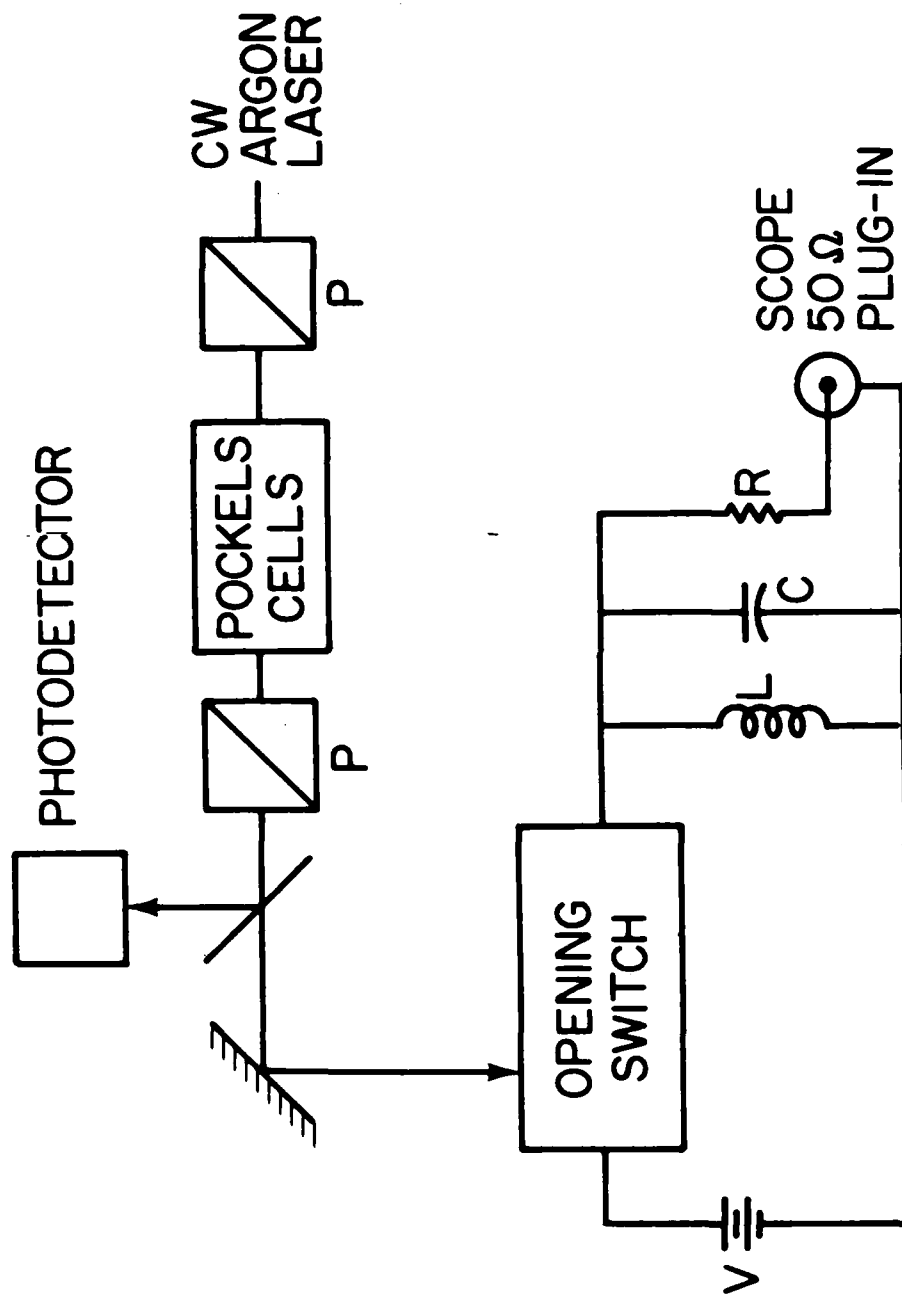
FIGURE CAPTIONS

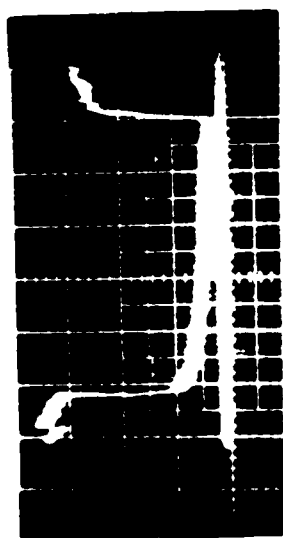
Fig. 1. Experimental set-up. P is a polarizer.

Fig. 2. Measured waveforms. (a) 200 ns long cut-off of the light.

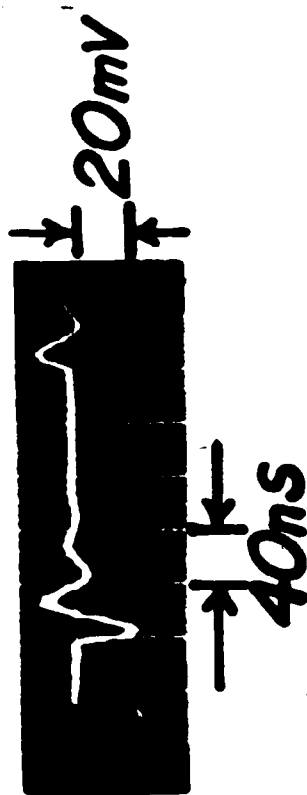
(b,c,d,e) output voltage waveforms obtained with the GaAs switch for $V = 20$ volts, $R_{on} = 12.5 \text{ k}\Omega$, and $R_{off} = 85 \text{ k}\Omega$. No capacitance was used. (b) $R_L = 573 \text{ }\Omega$, $L = 1.8 \text{ }\mu\text{H}$; (c) $R_L = 50 \text{ }\Omega$, $L = 20 \text{ }\mu\text{H}$; (d) $R_L = 573 \text{ }\Omega$, $L = 20 \text{ }\mu\text{H}$; (e) $R_L = 573 \text{ }\Omega$, $L = 156 \text{ }\mu\text{H}$.

Fig. 3. Output voltage waveform obtained with the InGaAs:Fe switch for $R_L = 50 \text{ }\Omega$ and $L = 20 \text{ }\mu\text{H}$ showing a 1 ns rise time.





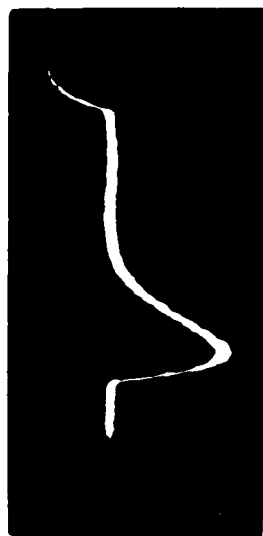
a



b



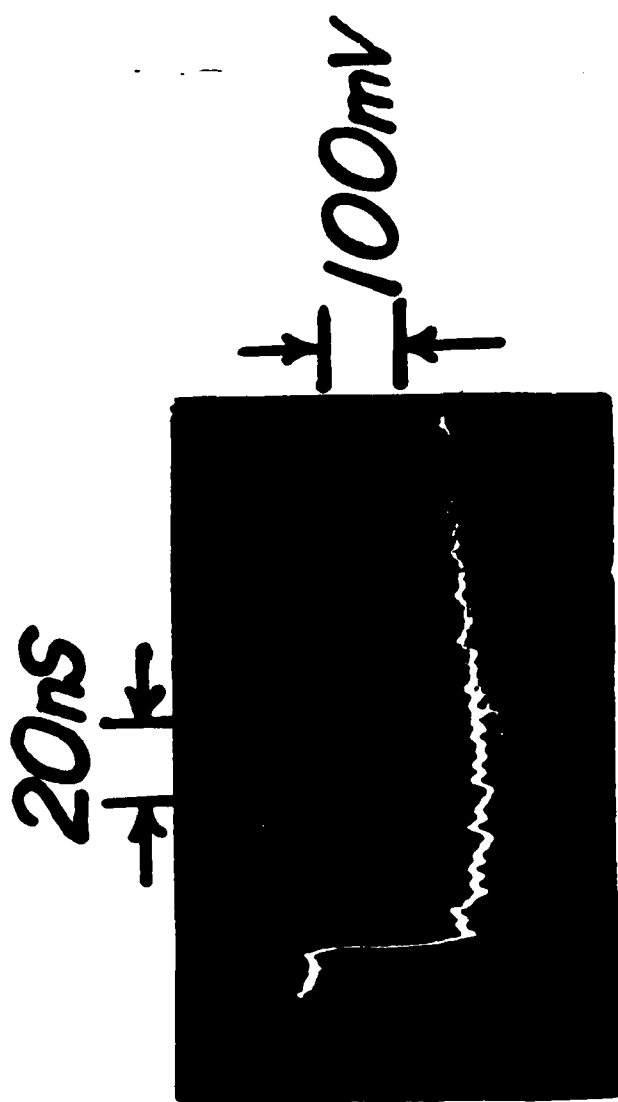
c



d



e



CHAUCHARD / RHEE / LEE
FIG. 3

VIEWGRAPHS

OPTICALLY ACTIVATED SEMICONDUCTORS AS
REPETITIVE OPENING SWITCHES

CHI H. LEE, E. A. CHAUCHARD, M. J. RHEE

OPTICALLY ACTIVATED SEMICONDUCTORS AS
REPETITIVE OPENING SWITCHES

CHI H. LEE, E.A. CHAUCHARD, M.J. RHEE

ELECTRICAL ENGINEERING DEPARTMENT
UNIVERSITY OF MARYLAND
COLLEGE PARK, MARYLAND 20742

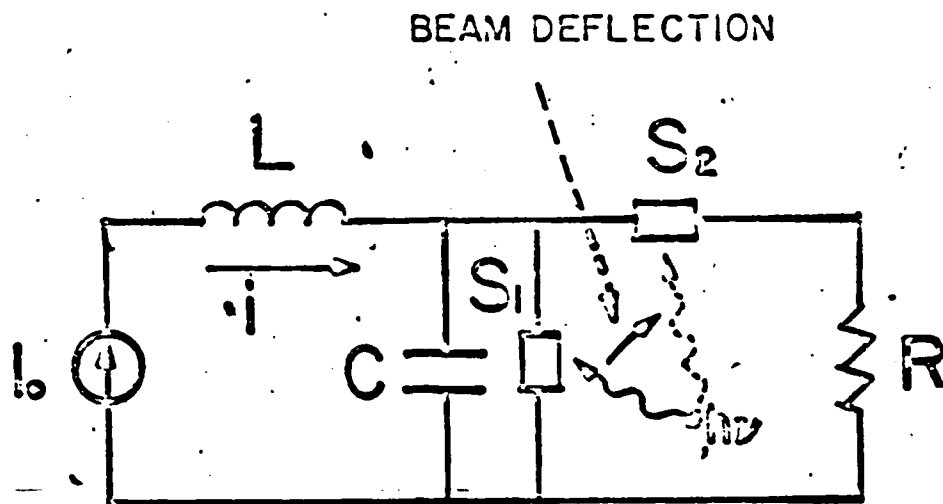


Fig. 5. Schematic representation of an inductive storage system with light activated semiconductor switches.

THE UNIQUE CHARACTERISTICS OF LIGHT ACTIVATED SEMICONDUCTOR SWITCHES MAKE THEM PRIME CANDIDATES FOR REPETITIVE OPENING SWITCHES:

- FAST TURN-OFF TIME
- JITTER FREE OPENING
- HIGH VOLTAGE, HIGH CURRENT WITHHOLDING CAPABILITY
- HIGH REPETITION RATE CAPABILITY.

WE DEMONSTRATE FOR THE FIRST TIME THE OPERATION OF A SEMICONDUCTOR REPETITIVE OPENING SWITCH. A TURN-OFF TIME OF 1 NS AND A REPETITION RATE OF 10 HZ HAVE BEEN ACHIEVED.

Type	CONTROL ELEMENT, GAIN	CURRENT DENSITY (A/cm ²)	HOLD-OFF (V)	VOLTAGE DROP (V)	OPENING TIME (ns)	COMMENTS
Bipolar	Base, 10 5 3	10 ⁵ 1000 10	100 500 1000	1-2	0.1-1 0.5-1 1-2	Trade-off between voltage & current
MOSFET	Gate, 4-5	50 10	500- 1000	2-3	<0.1	Turn-off limited by gate depletion capacitance
GTO	Gate, 3-5	100 100	1000 2600	2-3 2-3	1-2 1-2 (85%)	Possible problem with voltage rate of rise during turn-off
Thyristor	Gate, 1	100-300	5000	1.5-2	100-200	Mature technology, easy to parallel and series
GaAs JFET	Gate, 1	100	1000	2-3	<0.1	Under development
Optically activated switch	Light, electron beam	1000	5000	100	Si: 10 GaAs: 10 ns (undoped)	Low gain, scalable
Hall	Magnetic field	3000	1000	8	<1	Low resistance ratio, 10 ⁴ -1000
(OI) ²	Gate or light	500	1000	3.5	1-10	Under study to determine scalability

TABLE II. Opening switches.

TABLE III. Basic Research Issues.

Basic Research Problems	Research Approach
1. Surface breakdown mechanism on semiconductor surface.	Investigate various coatings for resistance to breakdown.
2. Development of new materials suitable for light activation.	Choose candidate materials and characterize mobility, quantum efficiency, and recovery mechanism.
3. Light source development, including laser and other light sources.	Compare performance of the switch under single photon and double photon absorption. Study carrier distribution under various conditions.
4. Light source modulation.	Devise method of modulation to terminate the light on the target quickly. Deflection of beam with electro-optic device may be needed.
5. Modeling and simulation.	Use both lumped circuit and transmission line models.
6. Opening time versus voltage drop.	Investigate effect of doping with deep level impurities on opening time and dark resistivity. Investigate methods of reducing the recombination time of carriers without sacrificing mobility.
7. Scalability.	Experimental verification of scalability.

Problems with High Voltage Switches

Breakdown

Intrinsic $E_B \sim 5 \times 10^5 \text{ V/cm}$

Extrinsic

residual joule heating \rightarrow thermal runaway

carrier injection \rightarrow initiate avalanche

surface breakdown

Contacts

How to make good Ohmic contact
on high resistivity semiconductor
with small contact resistance?

Two different types of applications

(1) Low voltage application

High speed optical detector, sampler

τ_e as small as possible

Switch. transfer efficiency not important

μ may be quite small

(2) High voltage application

Such as pulse power sources

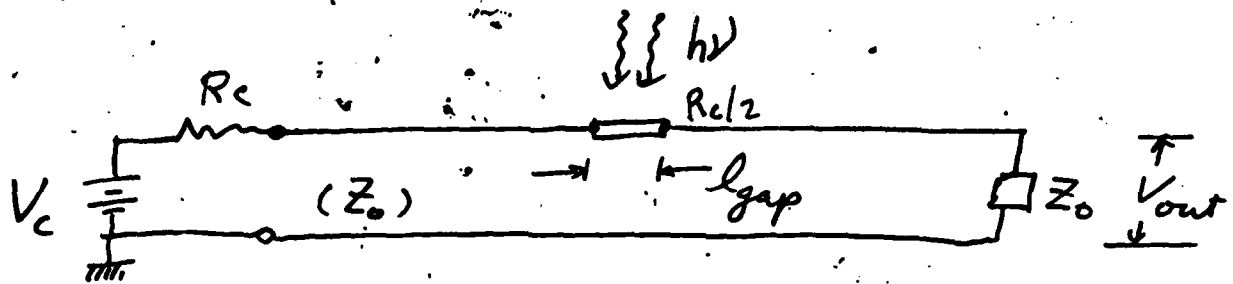
τ_e need not be small

transfer efficiency important

μ should be reasonable

Must have high dark resistivity
and high intrinsic breakdown
field.

Switching application:



$$V_{out} = V_c \frac{Z_0}{2Z_0 + R_s(\lambda)}$$

R_s = resistance of the switch under laser

$$\text{illumination} = \frac{l_{gap}^2}{N e \mu} + R_c$$

↑ contact resistance

N :: total number of the optically induced
... charge carriers

$N \propto$ optical energy.

$$\text{Scaling: } V_{max} = l_{gap} E_{Br}$$

↑ Breakdown field

(1) Using as a switch, one needs

$$R_s \ll 2Z_0$$

(2) as an optical detector

$$R_s \gg 2Z_0$$

TABLE I. Semiconductor materials investigated for kilovolt photoconductive switching.*

Semiconductor	E _g (ev)	Carrier Lifetime (ns)	Dark Resistivity
Si (intrinsic)	1.16	10 ⁴	5 × 10 ⁴
*Cr:GaAs	1.42	< 1	> 10 ⁷
Fe:InP	1.29	< 1	> 10 ⁷
*CdS _x Se _{1-x}	1.8 ~ 2.4	> 10	> 10 ⁷
GaP	2.24	> 1	> 10 ⁷
*Diamond (IIa)	5.5	< 1	> 10 ¹⁶

*First developed at the University of Maryland.

Diamond opto-electronic switch (Ho, Lee)

Diamond: insulating, type IIa

size: $3 \times 3 \times 0.5$ mm

$$\rho = 10^{14} \sim 10^{16} \text{ } \Omega \cdot \text{cm}$$

$$? E_{BR} > 10^7 \text{ V/cm}$$

$$\mu_e \sim 1800 \text{ cm}^2/\text{V}\cdot\text{s}$$

$$\mu_h \sim 1200 \text{ cm}^2/\text{V}\cdot\text{s}$$

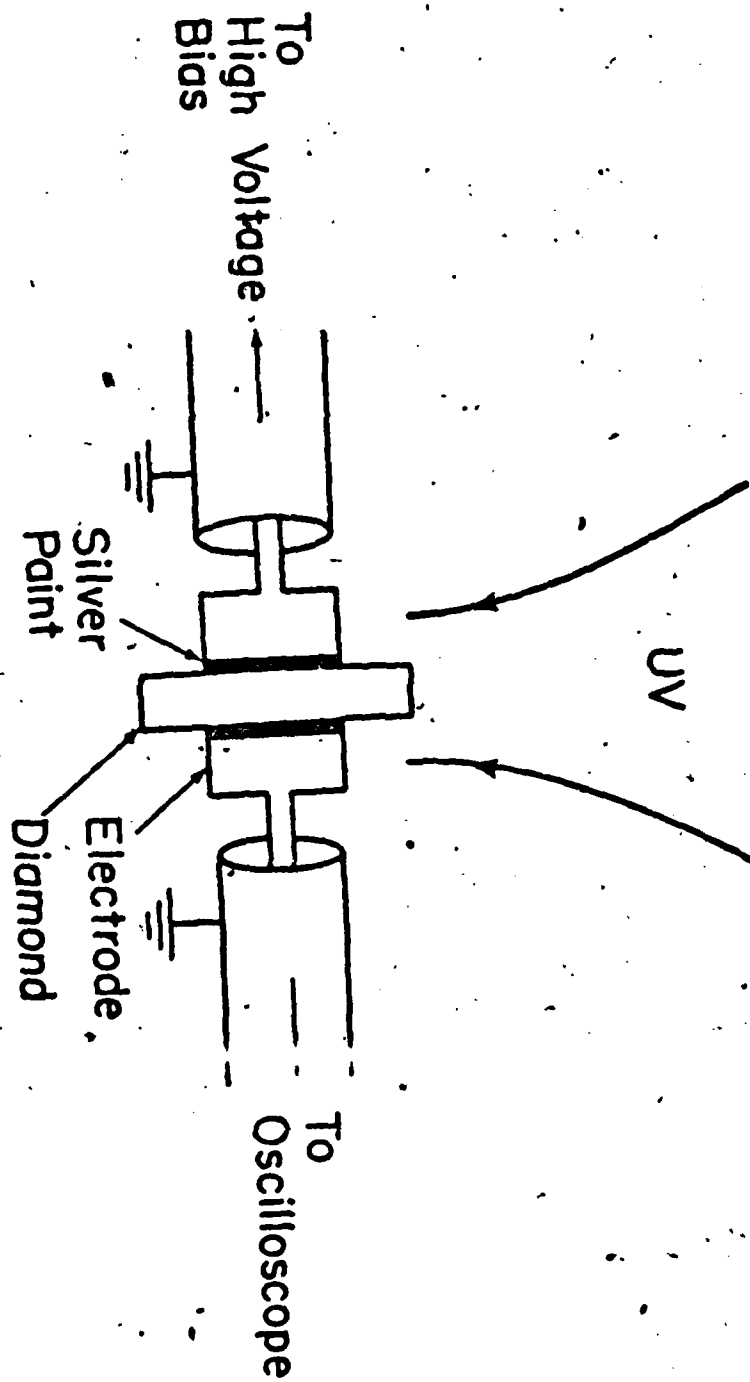
good thermal conductivity

switching efficiency $\sim 80\%$

Change of resistance

$$R_{off} > 20 \text{ M}\Omega$$

$$R_{on} \sim 30 \Omega$$

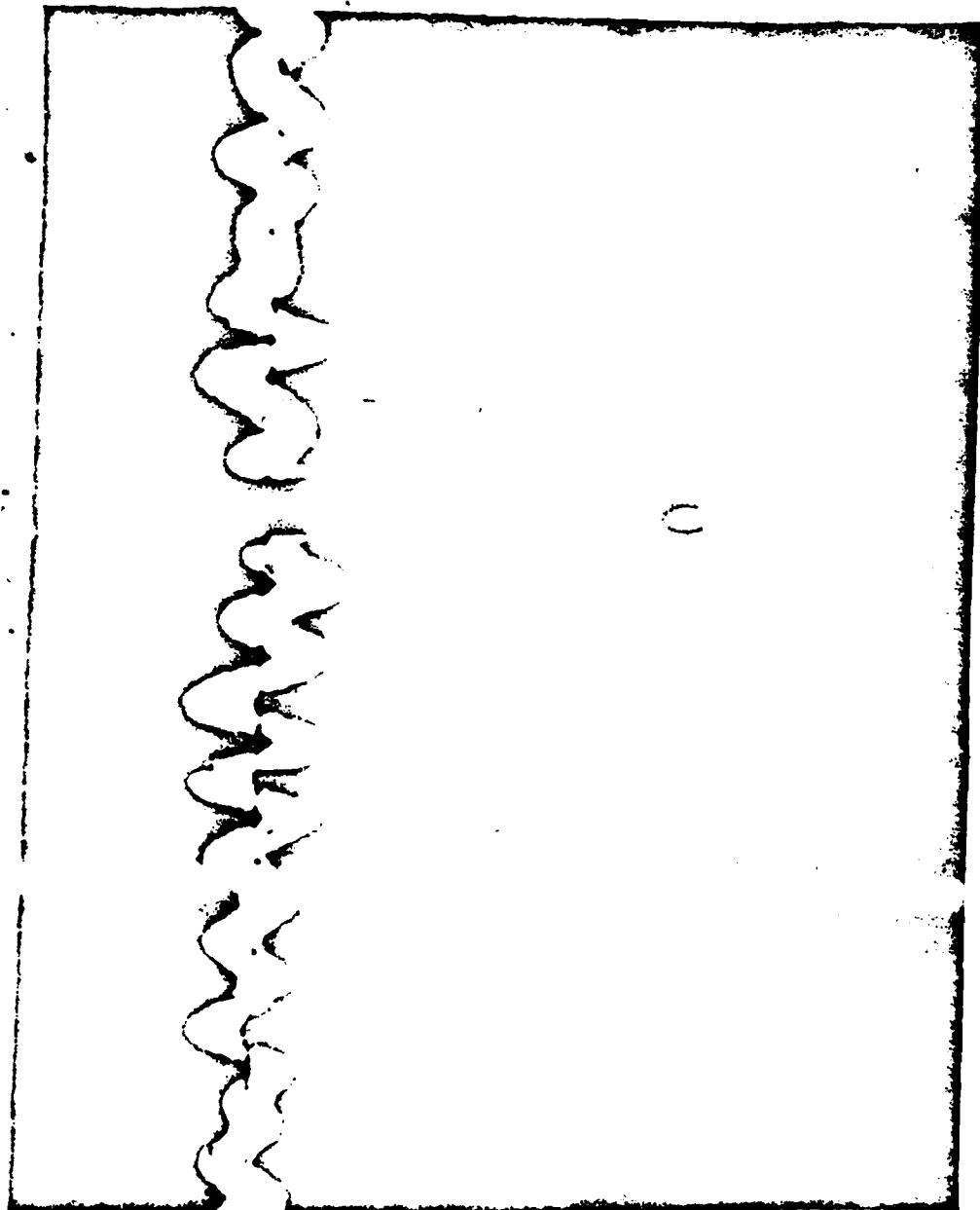


A diamond opto-electronic switch

200 V

800 volts out of a
possible max of 1 kv

2 NS



Depth of penetration of the
optical beam = thickness of the
plasma layer

$$d = \frac{1}{\alpha_e}$$

For single photon absorption

$$\alpha_e = \alpha$$

For two photon absorption

$$\alpha_e = \beta I$$

$$\beta \text{ cm/MW} \quad I \text{ in MW/cm}^2$$

-5 T

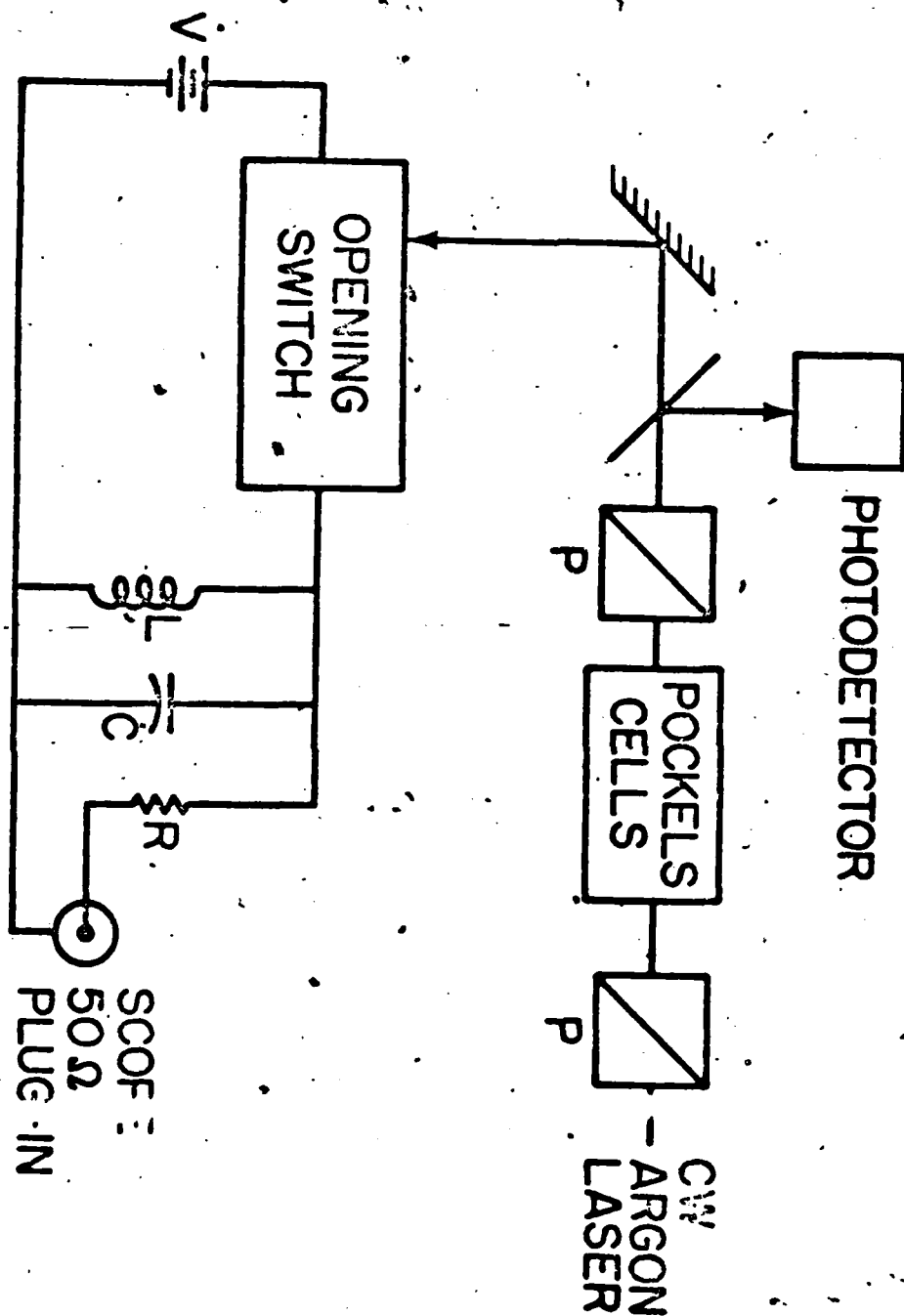
TWO PLANAR SWITCHES ARE USED:

- GaAs SWITCH, 200 μ m GAP

- InGaAs:Fe SWITCH, INTERDIGITATED, 4 μ m GAP

TO KEEP THE SWITCH CLOSED, ITS GAP IS CONTINUOUSLY ILLUMINATED WITH ARGON LASER LIGHT AT 514 nm. THE OPENING IS ACHIEVED BY INTERRUPTING THE LIGHT BY MEANS OF A POKELS CELL PLACED BETWEEN TWO PARALLEL POLARIZERS. TO DEMONSTRATE THE OPERATION OF THE OPENING SWITCH, WE USE AN INDUCTIVE STORAGE CIRCUIT.

Lamped Circuit



Circuit Modelling

In the inductive storage circuit, the current through the load as the switch opens may be described by:

$$C \frac{d^2 I(t)}{dt^2} + \frac{1}{R_L} \frac{dI(t)}{dt} + \frac{1}{L} I(t) = 0$$

where $R_L = R + 50 \Omega$

Solution:

$$I(t) = k I_0 [\exp(S_1 t) - \exp(S_2 t)]$$

where $k = (2R_L C \sqrt{\Delta})^{-1}$, $S_1 = -(1/2R_L C) + \sqrt{\Delta}$, $S_2 = -(1/2R_L C) - \sqrt{\Delta}$,

$\Delta = (1/2R_L C)^2 - 1/LC$, $I_0 = V(1/R_{on} - 1/R_{off})$. R_{on} and R_{off} are the switch resistances at the on-state and the off-state respectively.

Three types of waveforms:

I. $\Delta > 0$: overdamped solution

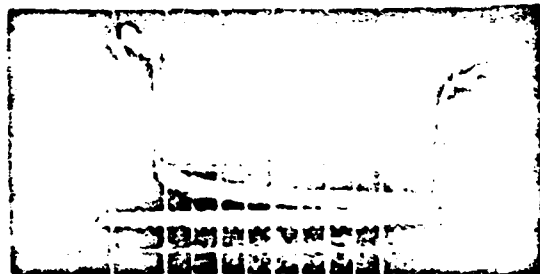
falltime: $T = (1/2R_L C - 1/\sqrt{\Delta})^{-1}$.

slope at $t = 0$: $dI/dt = I_0/R_L C$.

II. $\Delta = 0$ critical damping

III. $\Delta < 0$ oscillatory solution

period of oscillations: $T_1 = 2\pi/\sqrt{-\Delta}$



200 ns long cut-off of the
light (40 ns/div.)

Output voltage waveform obtained with the GaAs switch for $V = 20$ volts,

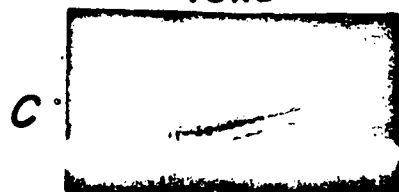
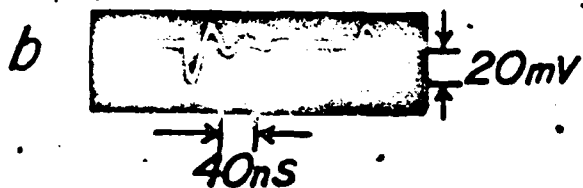
$$R_{on} = 12.5 \text{ K}\Omega, R_{off} = 85 \text{ K}\Omega$$

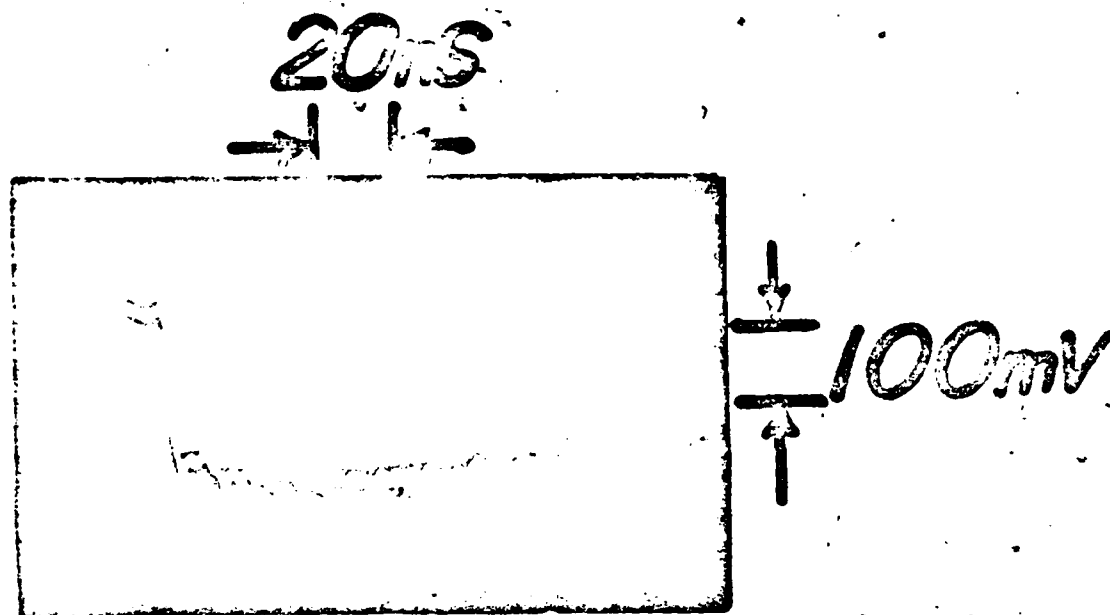
(b) Oscillatory case $R_L = 573 \Omega, L = 1.8 \mu\text{H}$

c } $R_L = 50 \Omega, L = 20 \mu\text{H}$

d } damped case $R_L = 573 \Omega, L = 20 \mu\text{H}$

e } $R_L = 573 \Omega, L = 156 \mu\text{H}$



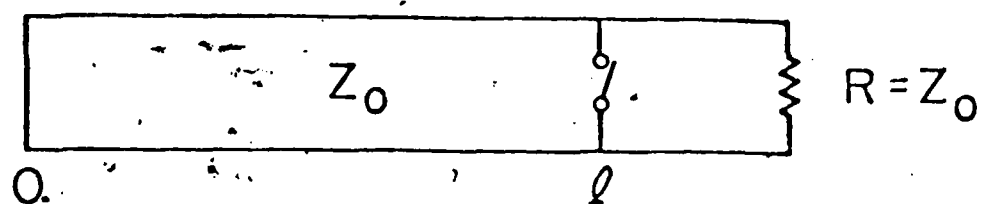


Output voltage waveform obtained with the InGaAs:Fe switch for $R_L = 50\ \Omega$ and $L = 20\ \mu\text{H}$ showing a 1 ns rise time.

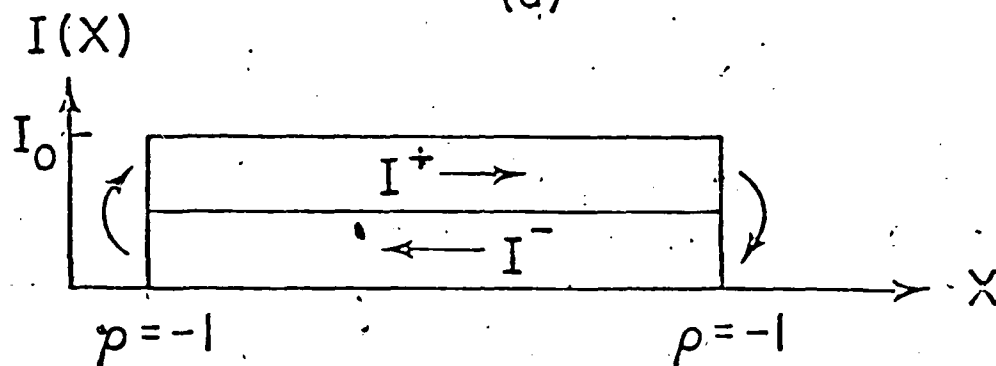
Current changed
transmission
line

I_0

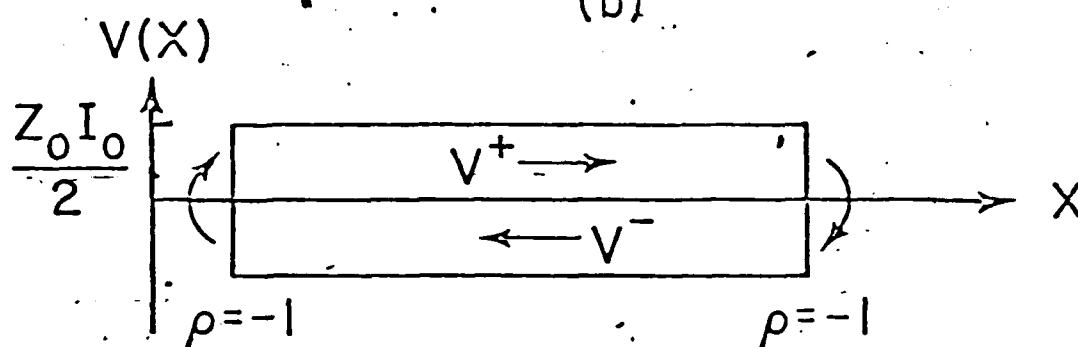
11



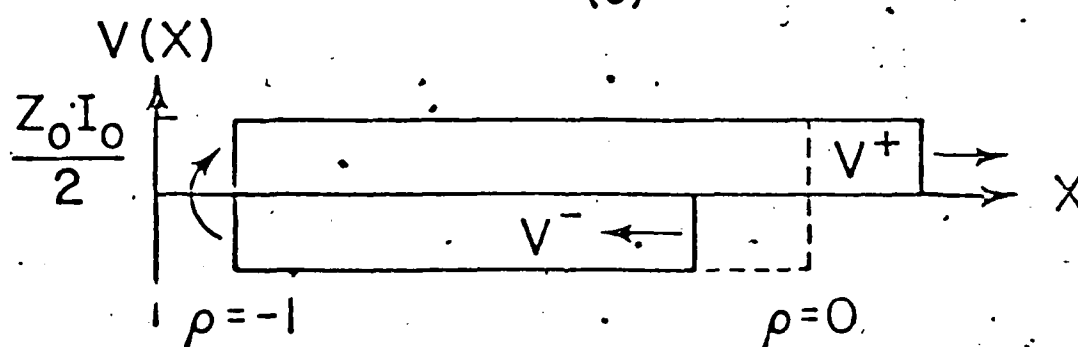
(a)



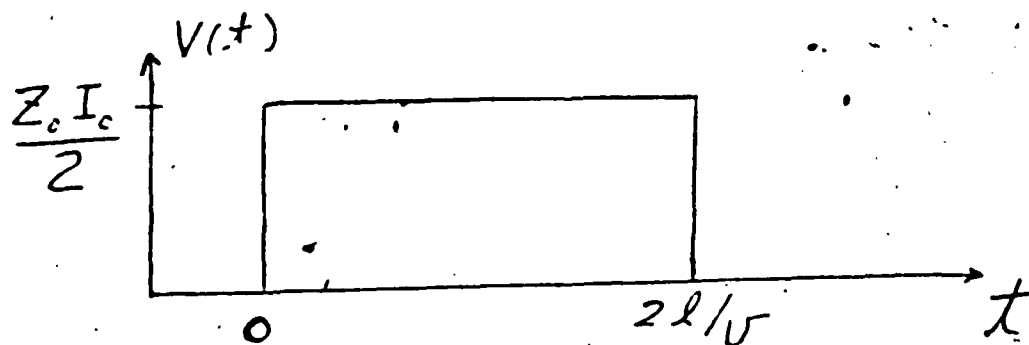
(b)

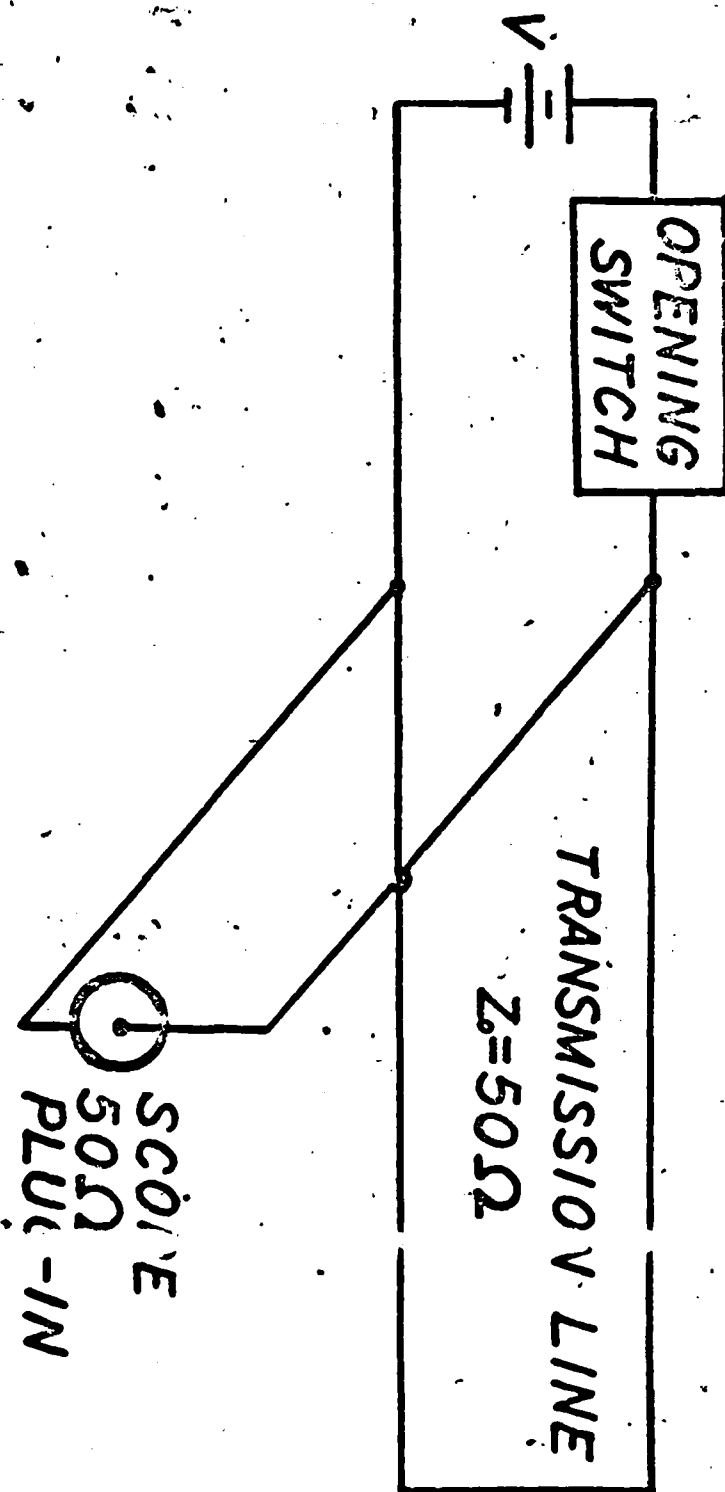


(c)



(d)





$$V_o = 10V$$

$$R_{on} = 10k\Omega$$

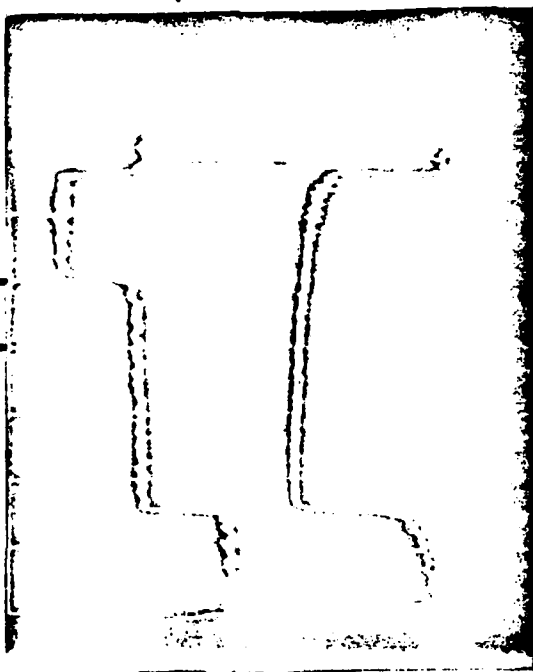
$$I_o = 1mA$$

$$V_{load} = 10^{-3} \times \frac{50}{2}$$

$$= Z_o \frac{I_o}{2}$$

$$= 25mV$$

40 ns



20 mV

Conclusion

We have demonstrated for the first time the operation of a semiconductor opening switch.

There are many fundamental issues need to be addressed.

VI. NON-PHOTOCONDUCTIVE SWITCHING

V.A.K. Temple

General Electric Company
Corporate Research and Development Center
Schenectady, New York 12345
(518) 385-8755

ABSTRACT

The feasibility of a new class of power devices which is based on an optimal combination of MOS and thyristor elements has been shown. Devices of this class function in the on-state and off-state in a manner indistinguishable from a thyristor, yet can switch from on-to-off or off-to-on by applying a voltage to its MOS gate. Thus, the devices exhibit extremely low forward drop, high surge current capability and enjoy negative thermal feedback. To turn off the device, one activates the gate so that FET's are turned on to effectively short one of the emitting junctions of the thyristor. These FET's need only block a maximum of about 1V when off and carry a sizable current for about a microsecond when on. To turn on the device, any of the normal methods may be employed. However, it is most convenient to use the same MOS gate electrode (and polysilicon layer) and a voltage of the opposite polarity to turn on the thyristor with another FET - just as if it were a normal MOS gated thyristor. The current density that can be turned off depends on the density and effective resistance of the turn-off FET's, while turn-on speed and di/dt rating depend on the initial turn-on area which, in turn, depends on the density of the on-FET's. If the off-gate voltage is maintained during the desired off-state period, the device has, effectively, an infinite dv/dt capability. Switching speed is most similar to, but somewhat faster than, that of GTO's (Gate Turn-Off thyristors) and, as in other bipolar devices, depends chiefly on carrier recombination time, device thickness and turn-off di/dt .

INTRODUCTION

There have been a number of investigations of various MOS-bipolar device alternatives described in the literature which benefit from either the high FET input impedance, as in the Darlington configuration, or from the high FET switching speed, as in the parallel MOS-bipolar transistor (MOS-BT) configuration. There are advocates, as well, for the series low voltage MOS-high voltage BT configuration to improve turn-off performance of the BT without the normal second breakdown phenomena. In all of these devices there are performance drawbacks. In the Darlington, forward drop is increased. In the parallel combination, we still have to drive the bipolar device (in concert now with the FET) to achieve faster less lossy turn-off. The BT, however, still limits the useful cut off frequency. In the series combination, forward drop is increased and two gates must be driven.

In the MOS-thyristor (MOS-T) combination there are two devices of note, as shown in Figure 1. One is the MOS-gated thyristor of Figure 1A, where one has a MOS element connected between anode and gate with an ability to turn on a large portion of the device simultaneously without having to supply the large (though short) gate current pulse that must be supplied to a typical inverter thyristor. In the recently described "Insulated Gate Transistor" (IGT)⁽¹⁾, illustrated schematically in Figure 1B, it is not clear that the device should be classified as a thyristor, since in the on-state the device effectively resembles a series diode - low voltage MOSFET. In the on-state, the thyristor is parasitic and, if it latches, will prohibit gate control. In the off-state and in device construction, the device is a thyristor and, therefore, blocks voltage in both directions. If the device is compared at the 600V level to a transistor (at a forced gain of 3), it can carry about three times the current density at a 2V forward

drop. Compared to a 600V MOSFET, it has about a 20 times higher current density at 2V. This is significant because the single control electrode is the MOS gate. However, the series FET, the electron spreading resistance, the modest level of modulation, and the nonuniform flow of current lead to a quite different story when its forward drop is compared to that of a thyristor. Now the IGT has a 10 times smaller current density at 1V and a 50 times smaller current density at 2V than a comparable 600V thyristor with the same doping profile and carrier lifetime profile. Obviously what is needed is a thyristor which can be MOS controlled in turn-off, as well as turn-on.

The key to accomplishing this turn-off function is to realize that thyristors have a holding current capability which is normally dictated by p-base resistivity and emitter short density, with low short density giving the lowest forward drop and holding current. What our FET's must do is to control the short density, making it very high when we want to turn off and very low (even zero) when we want to be on. Figure 2 indicates how this can be most easily accomplished. On the left, the FET element is seen to short the upper transistor emitter junction, while on the right we see a unit cell cross-section of a practical device.

TURN-OFF DESIGN

The key to turn-off is to break the latched condition in multiple parallel cells, such as that of Figure 2. For simplicity, the minimum design requirements estimate for breaking latching will now assume this to be an MCT composed of 1 cm long rectangular cells. To break the latching current, it is simply assumed that holes from the p-anode must prefer the FET path to the thyristor emitter junction path. In a worst case calculation, it is assumed necessary to divert nearly all of the hole current to the FET, while holding the maximum emitter-base junction voltage (V_j) below some threshold $V_{T,ON}$. This is somewhat similar to $V_{T,ON}$ in normal thyristor turn-on design, where it is assumed to be on if the V_j exceeds some critical voltage. $V_{T,OFF}$ was first conservatively assumed to be .5 E_g or ~.5V, but we later found to be better represented by the actual value of V_j before turn-off. Thus, turn-off current density J_{OFF} was first approximated as

$$J_{OFF} = V_j(J_{OFF})/\alpha_L(R_{CH} + R_{LAT} + R_{SP}) \quad (1)$$

where R_{CH} is the FET channel resistance, R_{LAT} is the lateral hole resistance in region 3 (the p-base of Figure 2), and R_{SP} is the FET spreading resistance. Due to modulation effects, R_{SP} and R_{LAT} are normally functions of device current and are quite a bit lower than what would be expected in a pure FET device. The term α_L is needed since $\alpha_L I_A$ is the hole current reaching the p-base layer from the anode. Note that "L" and "U" refer to lower and upper transistor, respectively.

Computer modeling and actual device measurements showed that (1) was an underestimate. As in the GTO⁽²⁾, it is only required that the gain of the upper transistor (NPN in the MCT) be sufficiently reduced to make α_{NPN} (or α_U) insufficient when added to α_L (or α_{PNP}) to add to unity. Stated differently, I_{FET} must be larger than that value for which dI_A/dI_{FET} is negative infinity. Various complex calculations may be made, but the most useful in comparing with our computer calculations was

$$J_{OFF} = V_j(J_{OFF})/\alpha_L R \Delta\alpha_U \quad (2)$$

where R is the effective hole resistance in $\Omega\text{-cm}^2$ and $\Delta\alpha_U$ is the value of $\alpha_{NPN}(J_{OFF}) - \alpha_{NPN}(0)$, i.e. the difference between low and high level gain of the upper transistor. Here, it is assumed that α_L does not change much in the first part of turn-off.

DEVICE TURN-ON ALTERNATIVES

The unit cell of Figure 2 has been shown without any turn-on capability, partly because the on-state can rapidly spread to this cell from a remote part of the device through a plasma spread that, due to the lack of emitter shorts, is even more rapid than normal, and partly because there are so many on-gate alternatives as illustrated in Figure 3. In A, one or more cells include what will be termed an on-FET which, when turned on, initiates thyristor action. Those cells latch on and plasma spreads from those cells to the remaining device area. Figure 4 shows an example of a cell which would accomplish the purpose. If this cell and that of Figure 2 are compared, it can be seen that by including an on-gate on one side of the cell, the cell size has been increased in that direction. This will later be seen to lower the current density that can be turned off in that cell.

In Figure 3B, the device is turned on by light which infers either a transparent electrode, a portion of the device with the metal emitter electrode removed in selected areas, or cells with the emitter electrode removed entirely. Figure 3C shows the normal thyristor turn-on, while 3D shows one of the most interesting turn-on methods, that of noise or leakage current turn-on which can occur where all unit cells look like that of Figure 2. In other words, with the off-FET's off, there are no emitter shorts so that leakage current or dv/dt current can turn on the device if it exceeds a critical amount. This amount is roughly being given by the 1V leakage current of the off-FET.

In such noise-triggered devices, in contrast to devices with one or more permanent shorts where the off-gate FET's need be on for only a few microseconds, the off-gate FET's now must be maintained in the on-state to keep the device off. However, unlike the MOS on-gate structure of Figures 3A and C, only a single polarity gate signal is required with respect to the emitter. Actually, with appropriate fixed interface and oxide charge, it is theoretically possible to control both the on-FET and off-FET of Figure 3 with three voltage levels of a single polarity. The same result, namely sufficiently different threshold voltages of the same polarity, could be achieved if one FET were made a depletion FET, while the other were made an enhancement FET. Because, in a more complex process, both on- and off-FET's can be chosen to be enhancement or depletion and because, to some degree, we can control fixed surface and oxide charge, it is possible to gate the device with a single polarity, either positive or negative, or with both polarities.

COMPUTER CALCULATIONS

In this section the forward drop and turn-off of an MCT unit cell was considered. Both of these calculations were done using a one-dimensional model. In the case of forward drop, this can be easily understood because the only place that current is somewhat constricted is in the upper emitter region which, however, is so highly doped that little increase in emitter drop is possible. In addition, cell size is a small fraction of total thyristor base thickness so that even in the base regions the current flow is quasi-one dimensional.

FORWARD DROP MODELING

Figure 5 shows a comparison of 600V turn-off devices with the FET, bipolar transistor and IGT data taken from the comparison curves of Reference 1 and the MCT and C-MCT (complementary MCT) taken from this work. The IGT curve is a calculated curve fitting the actual IGT device very closely. For the most accurate comparison between MCT and IGT, in calculating the MCT curve in Figure 5 the entire doping and carrier lifetime profiles of the parasitic thyristor inherent in the IGT were modeled as an MCT in the on-state. This profile is shown schematically in Figure 6. For the complementary MCT or C-MCT of Figure 5, the profiles were again those of Figure 6 but with the n- and p-labels reversed. Because of the fact that transistors block voltage in one direction only, the IGT (and MCT) devices were chosen to be asymmetric.

TURN-OFF MODELING

The on-state calculations were relatively simple. However, turn-off calculations were more complex. What was done was to add resistors (admittances) between the upper base nodes and upper emitter contact in the one-dimensional version of the program which would only allow upper base majority carrier current flow - in this case, holes. The admittance values were given a gaussian distribution with an abrupt cut-off at the n-emitter and n-base boundaries and a net resistance R which was then varied. Since the program assumes 1 cm^2 of area, R is then in $\Omega\text{-cm}^2$.

Figure 7 shows the result with various quantities of interest plotted as a function of R from its initial value of 60 to a final value of about $10 \text{ m}\Omega\text{-cm}^2$, at which time the program would no longer converge even with a very, very small reduction in R. This point was taken as the point at which latching was broken. It was also inferred, from our convergence problem, that the transition from latched thyristor to unlatched open-base transistor would be very fast, of the order of several base transit times.

An R of $60 \text{ m}\Omega$ is seen to have little or no effect with I_{HB} (the hole current entering the p-base from the n-base), I_{HE} (the hole current reaching the emitter), I_E , I_T and V_J (plotted as V_{BE}) asymptotically approaching their fully unshorted values. At this point, for example, $I_{HB} = .38 I_T$ and $I_{HE} = .30 I_T$ while $V_J = .838 \text{ V}$. At the final stable operating point in Figure 11, $I_{HB} = .41 I_T$ while I_{HE} has dropped to $.16 I_T$ - i.e., the upper transistor emitter efficiency has increased to help keep the device on with the shorting resistor in place. This partially offsets the resistor so that a smaller increase in the lower transistor gain is sufficient to keep the device on. The resistor (FET) current is interesting, having increased from 13 A at $R = 60 \text{ m}\Omega$ to 81 A at the turn-off point where it comprises only 24% of the net device current. Further, from considering V_J , it has only been necessary to reduce the upper emitter junction voltage to $.814 \text{ V}$ to turn off the device at its 338 A final operating point, a change of only 25 mV . Careful examination of the currents at this point reveals that the total current of 338 A at the last stable operating point is composed of 34 A hole and 213 A of return electron current into the emitter and 81 A of hole current in the resistor (FET) path, whereas at $R = 60$ one has 413 A total current composed of 131 A of hole current into the emitter, 269 A of return electron current and a resistor current of 13 A . These give injection ratios, r_E , of 3.94 and 2.05 , respectively, leading to injection efficiencies of $.80$ and $.67$. From taking the ratio of I_{EB}/I_{EE} where I_{EB} is the electron current reaching the n-base - p-base junction, one gets the effective upper transistor base transport factors, α_T , and multiplying by the injection efficiency, the transistor current gain.

A similar calculation was done for the C-MCT (complementary MCT) structure at a 1 V forward drop to look at turn-off from this same current density. Here it was found necessary to divert 117 A of electron current into the FET instead of 81 A , as in the MCT case. This increase is just due to α_L being larger with the n+ anode than with the p+ anode.

A further comparison of C-MCT and MCT was done at 1.25 V forward drop where current density was nearly 2000 A/cm^2 . In the MCT case, the necessary FET hole current to cause turn-off was about 250 A/cm^2 , while about 310 A/cm^2 FET electron current was needed to turn off the C-MCT. These results compare well to the prescription given in equation (2) if $V_{J, \text{OFF}} = .85$, $\Delta\alpha_L$ is about $.5$ and α_L is $.4$ and $.6$ for the MCT and C-MCT, respectively.

DEVICE RESULTS

A series of small 1200V (ideal breakdown voltage) C-MCT devices were fabricated with the geometry of Figure 2, but with square cells having a p-base ρ measured at 500 Ω/\square and ρ at about 1.5 $\Omega\text{-cm}$. The devices had no on-gates but were turned on, in the absence of emitter shorts, by leakage current. They were principally intended to see if a latched thyristor could be turned off. Some of the results on the one-, four- and sixteen-cell devices will be described briefly, with a more complete description of the device processing and larger device results on the wafer to be given in a later paper.

The device, unlike the modeled example, had a 100 μ lower base (region 6) which, with proper termination, would have blocked voltage in both polarities. As it was for results described here, devices were tested on a probe station, unpassivated and in wafer form, where they blocked 400V in the forward direction and at least 50V in the common reverse blocking junction. Figure 8 shows the forward drop, which to about 1.25V follows that of a similarly doped thyristor. After that point, current falls below that of the thyristor, most likely due to probe resistance.

Figure 9 shows a turn-off of 1000A/cm² using a 15V gate signal with a resistive load and a 50V anode-cathode potential. Turn-off is similar to the GTO or IGT, having an initial rapid fall as the latched condition is broken, and then a recombination tail.

Turn-off densities in the one cell device, which, therefore, does not have uneven turn-off problems, were typically 6000A/cm² at $V_G = 60$ and 2000A/cm² at $V_G = 15$. The $V_G = 15$ value of about 2000A/cm² is about twice the typical thyristor surge current rating and about 5 times the current density that can be turned off in a GTO. This compares well with the various predictions of Equation (2) using an R value, calculated from the geometry and profile of 1.6 m $\Omega\text{-cm}^2$.

SUMMARY

A new power device concept has been presented which combines thyristor power handling capability with MOS turn-on and turn-off control. Turn-off is accomplished by a MOS-gated emitter "short" in every cell of the device. To reduce the resistance of this short requires a high short density, a short FET channel length and a high FET g_m .

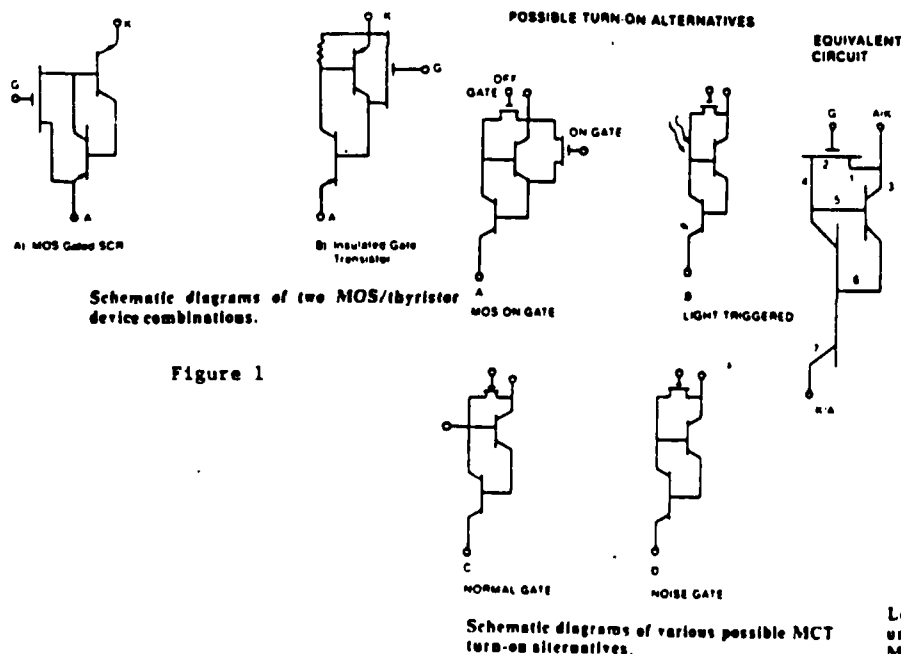


Figure 1

Figure 2

Figure 3

The analysis presented, along with computer model turn-off, indicates that under resistive load conditions, or conditions under which the device voltage is relatively constant, the current density that can be turned off is of the order of $V_{OFF}/5R\alpha_L$.

No temperature dependent or load dependent analyses were given, although several predictions can be made. First, V_{OFF} will fall as $1/T$ where T is in K. Second, R will increase as T increases through reduced carrier mobility. In going from 250K to 1250K, this might amount to a 2.5 derating factor. Third, if device voltage increases substantially with little reduction in current, we will find that α_L will increase. Probably a further factor of 2 derating would be appropriate.

Device results at 250C and turning off a resistive load at 50V showed that turn-off current density in the better devices ranged from 2000A/cm² with a 15V gate to 6000A/cm² with a 60V gate. Note that this indicates that the prime contributions to R are in channel and spreading resistance, both of which are reduced with FET gate bias.

Elevated temperature and circuit dependent modeling, as well as further device results, will be presented in a later paper.

REFERENCES

1. B.J. Baliga et al., "The Insulated Gate Transistor: A New Three Terminal MOS-Controlled Bipolar Power Device," IEEE Trans. on Electron Devices, ED-31, p. 821 (1984).
2. Duane Wolley, "Gate Turn-off in PNP Devices," IEEE Trans. on Electron Devices, ED-13, p. 390 (1966).

Left: Circuit schematic of the typical MCT unit cell. Right: Cross section of a typical MCT unit cell.

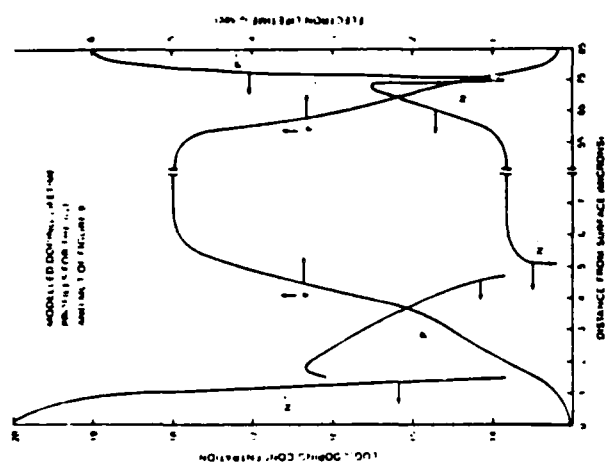


Fig. 6 Doping and lifetime profiles used in the computer model in generating the MCT and IGT J-V curves. (The C-MCT was calculated by changing the sign of the doping.)

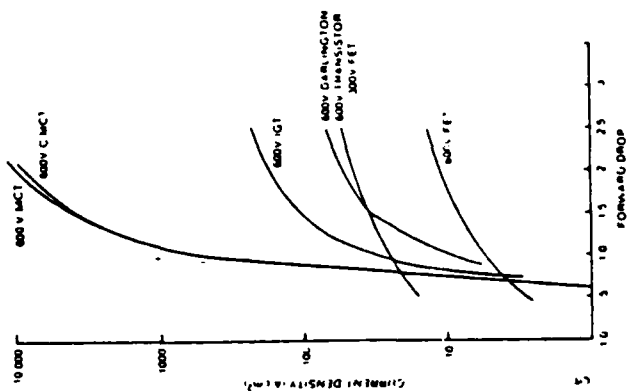


Fig. 5 Comparison of high gain turn-off device forward drop. The IGT and MCT are calculated based on the same identical doping and lifetime profiles.

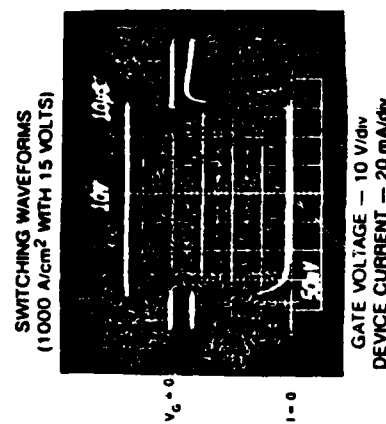


Fig. 9 Measured turnoff in a 50 volt resistive circuit with a 16 cell device using a 15 volt gate. The turn-off limit for size device at $V_G = 15$ ranged from 1000 to 2000 A/cm² at room temperature for this test circuit.

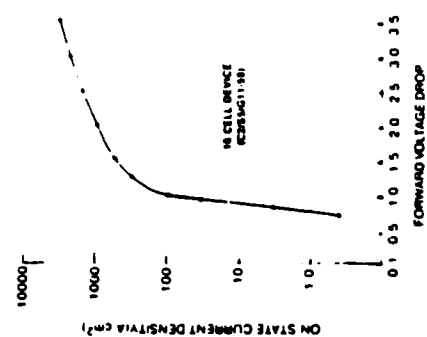


Fig. 8 Forward drop of a 16 cell device with $V_{G11} = 15$ volts. This device was made with twice the lower base thickness of the device of Fig. 9 so that it could block voltage in both polarities.

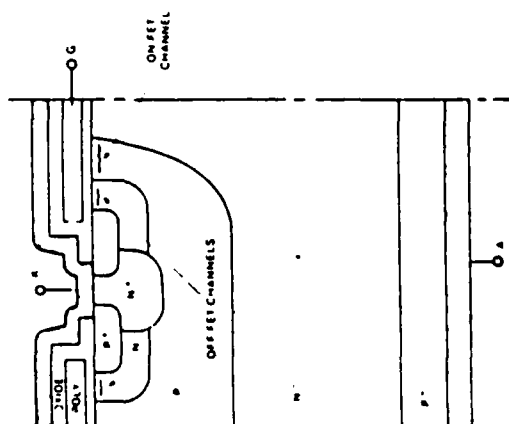


Fig. 4 Cross section of an MCT unit cell with both turn-on and turn-off FET's.

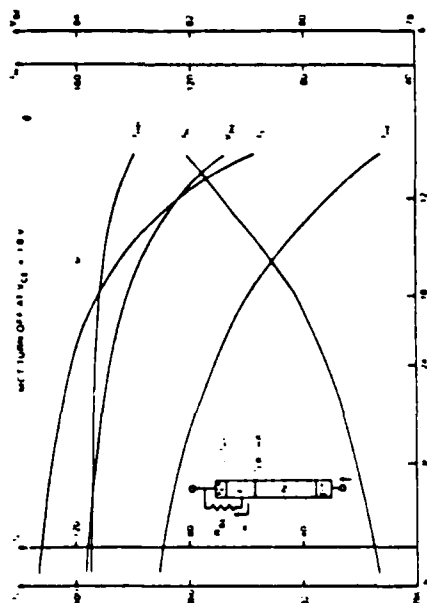


Fig. 7 Base-emitter voltage and various device currents (see inset diagram) during turnoff as a function of I_E . Note that I_B only carried hole current for MCT devices and only electron current for C-MCT devices. At $I_E = 0$, I_B was 400 A/cm.

VIEWGRAPHS

MOS CONTROLLED THYRISTORS (MCT'S)

V. A. K. TEMPLE

ADVANCED HIGH VOLTAGE DEVICE TERMINATIONS

- PLANE JUNCTIONS
 - NEGATIVE BEVEL, EFFECTIVENESS $\sim 1/\sqrt{2}$
 - POSITIVE BEVEL, GOOD FOR LARGE DIODES
- PLANAR JUNCTIONS
 - FIELD RINGS, NEEDS LARGE EDGE AREA
 - JTE, NEEDS MINIMAL EDGE AREA

V.A.K. TEMPLE
8/26/85

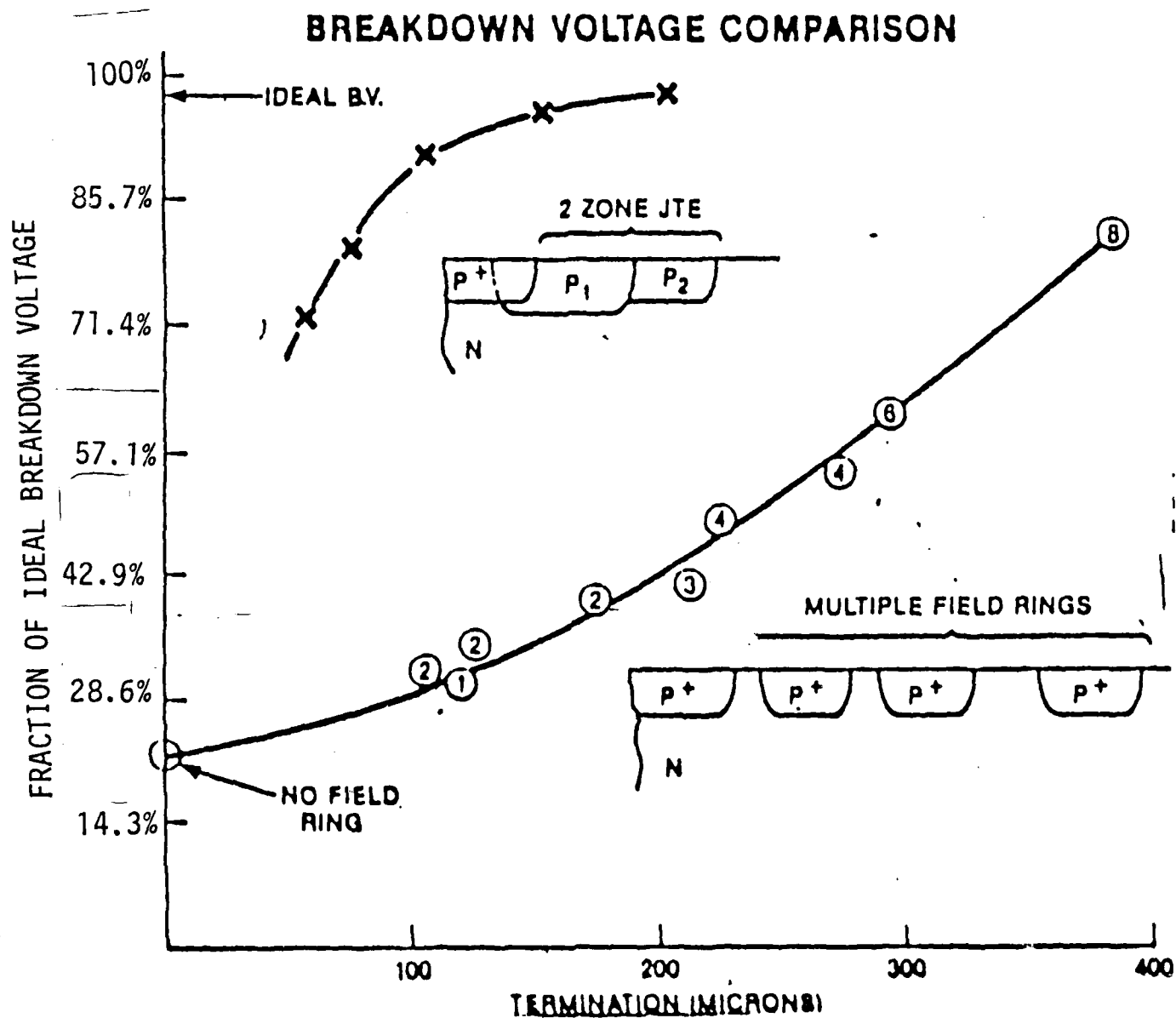


FIGURE 3: Breakdown voltage vs. termination extension for field rings and JTE. Circled numbers indicate the number of rings.

AD-A165 039

WORKSHOP ON NEW DIRECTIONS IN SOLID STATE POWER
SWITCHES HELD AT FARMINGD. (U) POLYTECHNIC INST OF NEW
YORK FARMINGDALE WEBER RESEARCH INST. B SEMITZKY

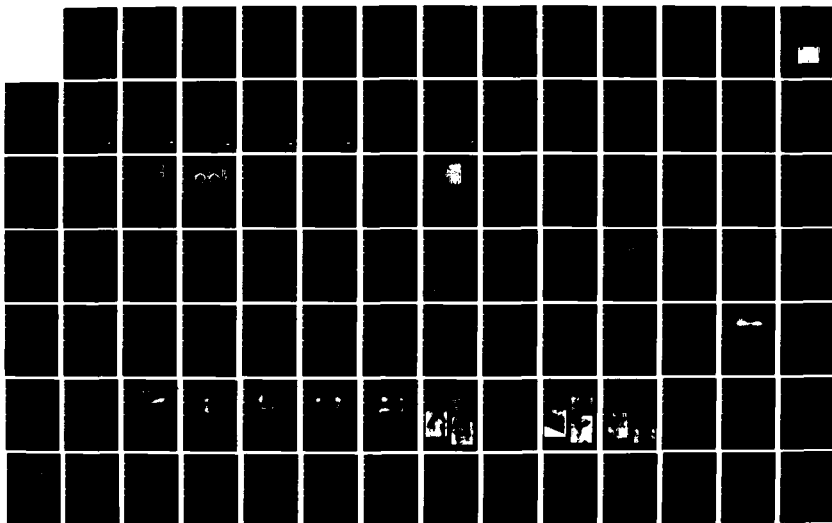
5/6

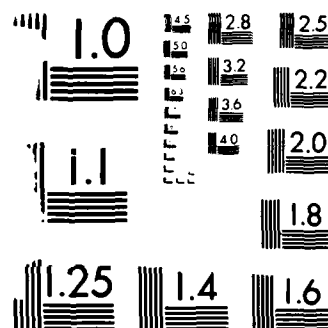
UNCLASSIFIED

24 DEC 85 N00014-85-G-0236

F/G 9/5

NL

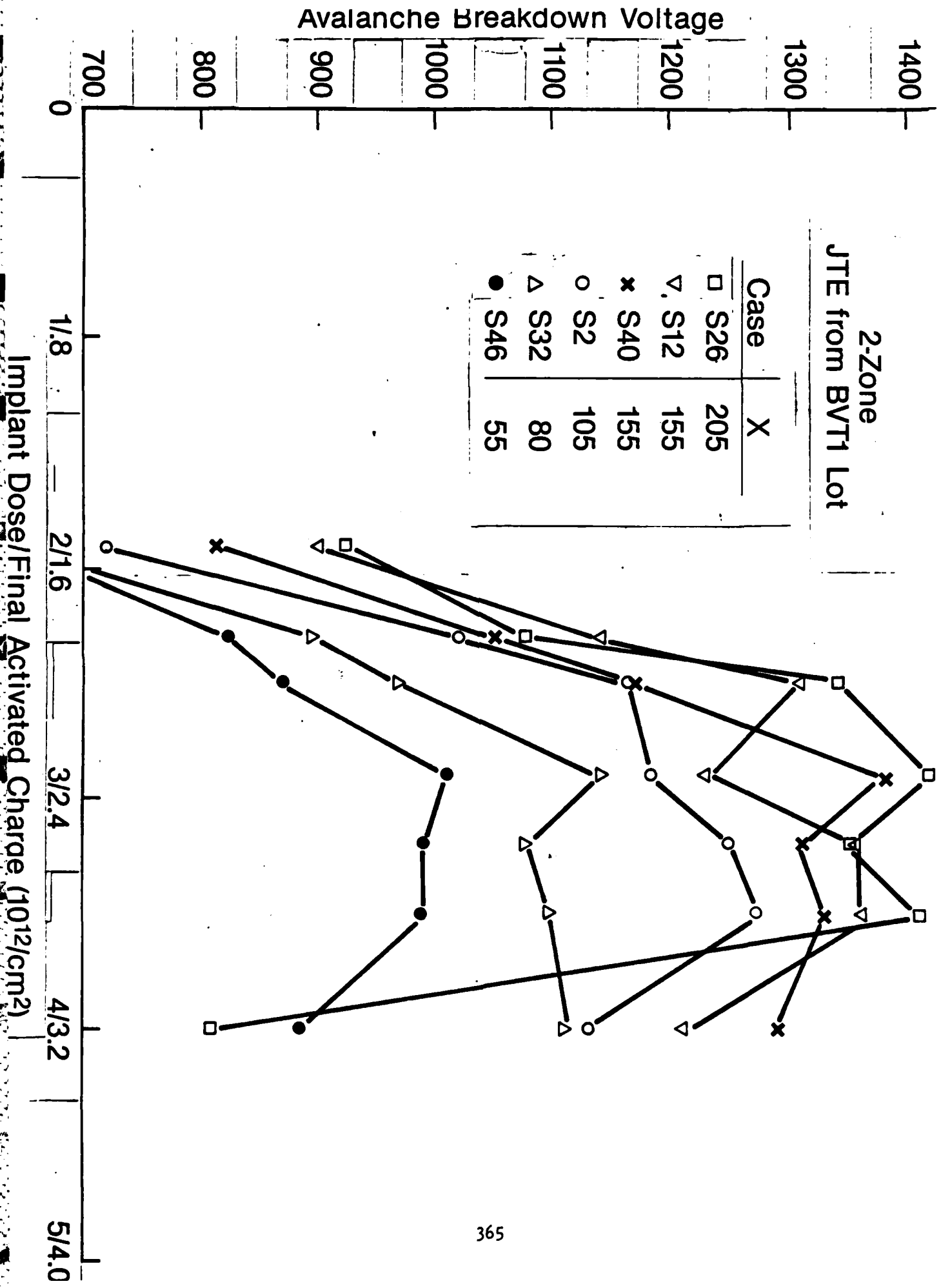


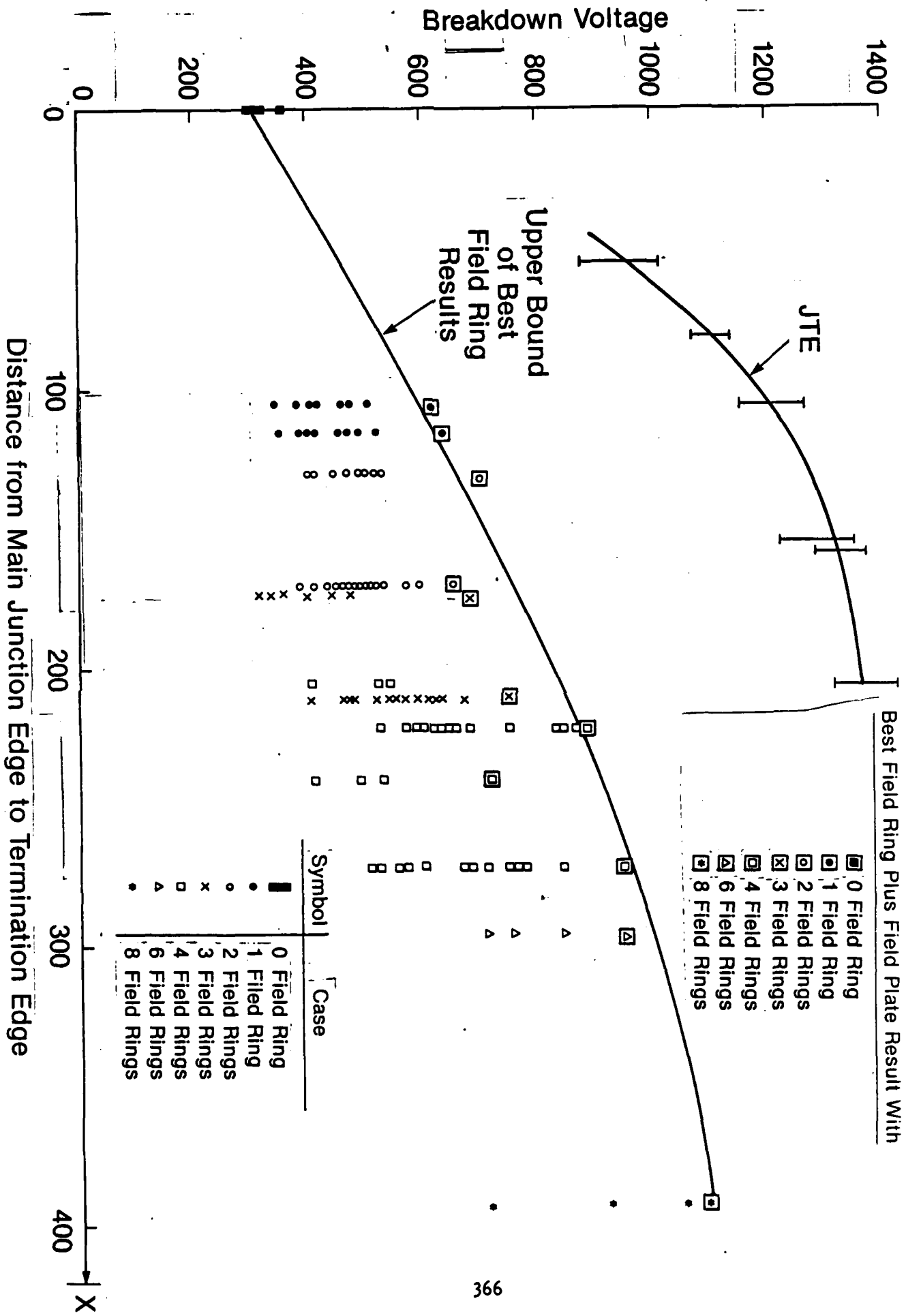


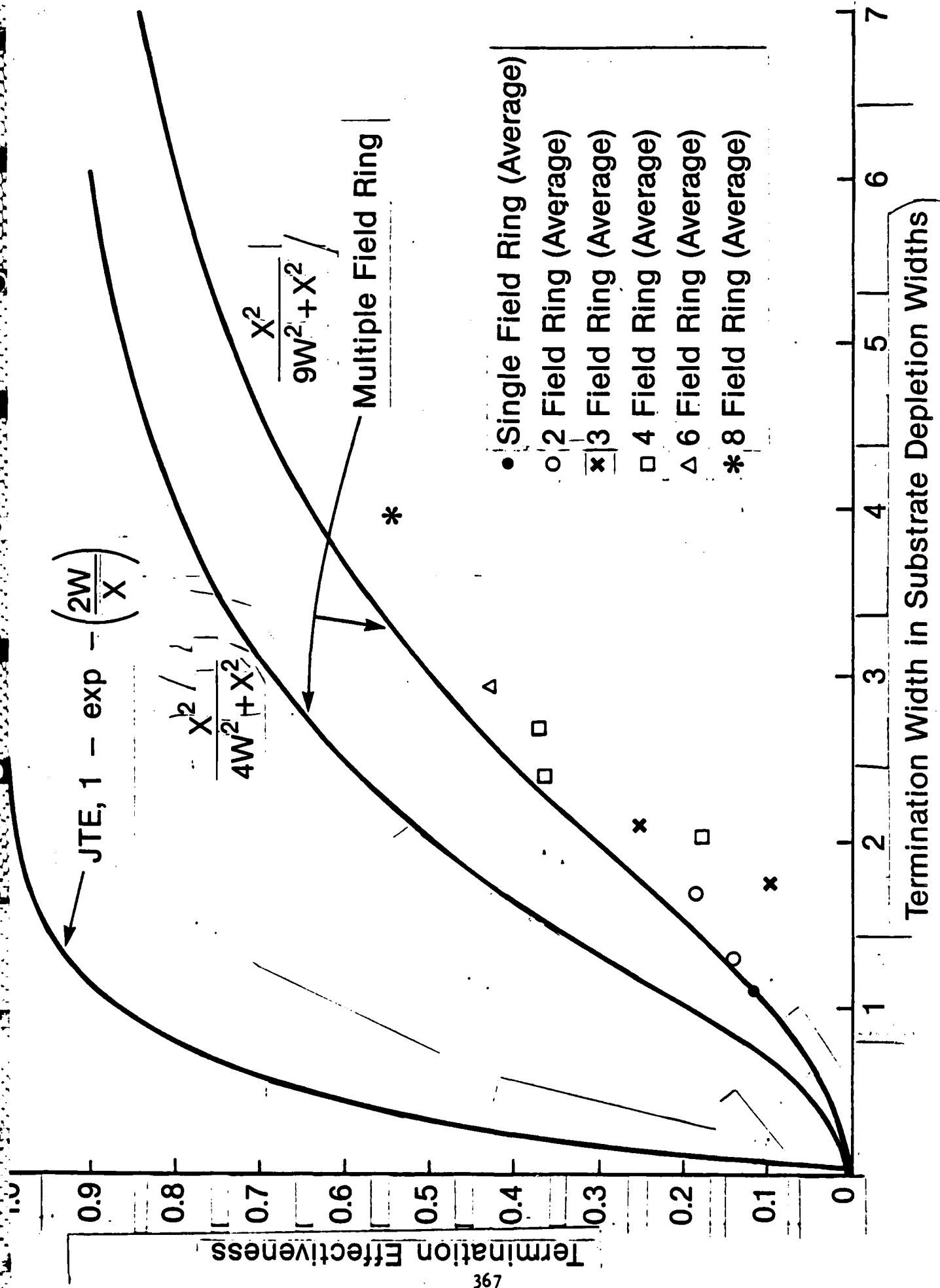
MICROCOPY RESOLUTION TEST CHART
NATIONAL BUREAU OF STANDARDS 1963-A

2-Zone JTE from BVT1 Lot

Case	X
□ S26	205
▽ S12	155
× S40	155
○ S2	105
△ S32	80
● S46	55

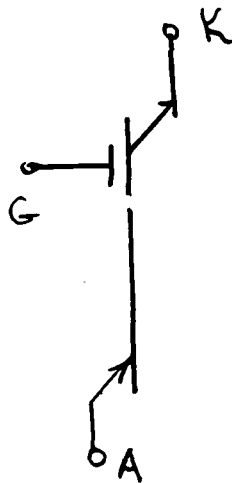






MOS CONTROLLED THYRISTOR, A NEW CLASS OF POWER SWITCHING DEVICES

- SCR I & V CAPABILITY AND FORWARD DROP
- MOS GATED ON AND OFF
- SUB MICROSECOND TURN-ON AND TURN-OFF



V.A.K. TEMPLE
8/26/85

TABLE 2 POWER DEVICE COMPARISON AT 600, 1200 AND 2500 VOLTS

Device	Forward Drop (A)		Turn-off Time (μs)	Recombination Charge (D) (μC/cm ²)	Turn-on Drive ₂ per cm	Turn-off Drive ₂ per cm	Turn-off Current (A/cm ²)	di/dt (A/μs)	dv/dt (V/μs)	Losses/cm ² at 60 Hz			Losses/cm ² at 1 kHz			Losses/cm ² at 10 kHz		
	Rated Current	Peak Densities								Conduction	Switching (F)	Total	Conduction 40 A/cm ² 50%	Switching (F)	Total	Conduction 40 A/cm ² 50%	Switching (F)	Total
600 Volt Asymmetric Blocking																		
1. GE D66 Power Darlington	2.5 (40 A/cm ²)	8 (100 A/cm ²)	6	30 (40 A/cm ²)	2A	-5A	100	Large (B)	Large (B)	30 (40 A/cm ²)	12.6	62.6 (40 A/cm ²)	30 (40 A/cm ²)	22	72	30 (40 A/cm ²)	11.2	162
2. GE IGT TICRI	1.3	1.7	3	30	.004 mJ	.004 mJ	400	Very (B)	Very (B)	26	0.6	26.6	26	10	30	26	100	126
3. MCT (Fast Turn-off)	0.7	0.85	< 1	2	.004 mJ	.004 mJ	900	Very (B)	Very (B)	14	0.04	14.2	14	0.6	14.6	14	6	20
1200 Volt Symmetric Blocking																		
4. C138 GE Thyristors	1.8 (100 A/cm ²)	3.8 (1000 A/cm ²)	23(C)	20 (100 A/cm ²)	0.2 mJ	NA	NA	500	500	90 (100 A/cm ²)	1.0	91 (100 A/cm ²)	90 (100 A/cm ²)	17	107	90 (100 A/cm ²)	170	260
5. Toshiba GTO (I) (based on SG1000EX23)	2.0	7	11+	100	1.2 mJ	60 mJ	200	250	400	100	7.4	107	100	123	223	100	1223(E)	1325
6. GE IGT - 121	1.9	8	3	200	.004 mJ	.004 mJ	400	Very (B)	Very (B)	95	7.2	102	95	120	215	95	1200(E)	1295
7. Fast Turn-off MCT	0.8	1.0	< 1.5	2.5	.004 mJ	.004 mJ	900	Very (B)	Very (B)	40	0.1	40.1	40	1.6	41.6	40	15.6	55.6
2500 Volt Symmetric Blocking (Except the diode, of course)																		
8. C702 GE Thyristor	1.8 (100 A/cm ²)	3.5 (1000 A/cm ²)	125(C)	120 (100 A/cm ²)	0.12 mJ	NA	NA	125	500	90 (100 A/cm ²)	9.0	99 (100 A/cm ²)	90 (100 A/cm ²)	150	240	90 (100 A/cm ²)	1500(E)	1590
9. SG 899EX21 Toshiba GTO	2.7	10	30+ 70 (tail)	100	2.5 mJ	60 mJ	150	100	500	135	11.5	146	135	171	264	135	1911(E)	2046
10. A540 GE Diode	1.0	2.3	30	100	NA	NA	NA	NA	NA	50	7.5	57.5	50	125	175	50	1250(E)	1300
11. Fast Turn-off MCT	0.8	1.2	< 2	3.2	.004 mJ	.004 mJ	900	Very (B)	Very (B)	40	0.24	40.2	40	4	44	40	40	80

NOTES:

- 600 volt device comparisons are made at 40 and 100A, for forward drop and 40 A/cm², for dissipation, due to the limitations of the power transistor.
- Because of their highly interdigitated structures, di/dt and dv/dt ratings are very large.
- Turn-off time in the diode, thyristor, IGT and MCT includes the tail time. In the transistor and GTO, turn-off time is the sum of storage plus tail time.
- With the possible exception of the GTO, switching loss is dominated by recombination charge which has been assumed to recombine at half the device rated voltage.
- For this frequency, a better trade-off between switching loss and forward could lower total losses by factor of about 2. This trade-off would reduce surge and RMS rating about a factor of 2.
- Switching losses do not include turn-on di/dt losses, except in the GTO where they are large.

TABLE 1

MOS CONTROLLED THYRISTOR ADVANTAGES

FEATURE	COMMENT
NEAR IDEAL THYRISTOR FORWARD DROP.	NO SHORT WHEN ON.
TURN-OFF OF SURGE LEVEL (OR HIGHER) CURRENT WITH A MOS GATE.	FET SHORTS INTERNAL TRANSISTOR STRUCTURE.
NEARLY UNLIMITED DI/DT AND AND DV/DT CAPABILITY.	VERY SMALL CELLS, EACH ACCESSED BY A FET.
TURN-OFF TIME NOT LIMITED BY NORMAL BIPOLAR RECOMBINATION TAIL.	SHORTING FET SHORTS THE HIGH VOLTAGE TRANSISTOR PORTION OF THE MCT.
BUILT-IN FET'S VERY RUGGED.	VERY LOW DUTY, REMOVES ONLY MINORITY CARRIERS.

Avalanche Breakdown Mechanisms and Application to Switching Devices

Michael D. Pocha
Lawrence Livermore National Laboratory
P.O. Box 808, Mail Stop L-156
Livermore, California, 94550

August 20, 1985

Introduction:

The purpose of this report is threefold. 1) to present a discussion of avalanche breakdown which is the primary high voltage limiting mechanism in semiconductor junction devices. 2) to discuss surface field effects on avalanche breakdown and junction termination techniques for reducing these surface effects. 3) to present a discussion of avalanche second breakdown and its application to high voltage, high speed, switching devices. One of the goals of these discussions is to present the current state-of-the-art in the area of junction breakdown and high voltage junction devices. Since only a cursory description of the subjects can be given in this short report, a large list of references is compiled to help the reader pursue these areas further.

Avalanche Breakdown:

Junction breakdown in high voltage semiconductor devices is almost always determined by the avalanche breakdown process. Avalanche breakdown occurs when a carrier moving in the reverse bias electric field of the depletion layer can gain sufficient energy to knock another carrier out of the conduction or valence band during a collision. This process is strongly dependent on the electric field in the depletion layer. The probability of breakdown for a given electric field distribution is calculated by the ionization integrals which integrate the ionization coefficients across the depletion layer [1-2]. Fig. 1 shows the ionization coefficients for electrons and holes as functions of electric field and temperature. The curves for the higher temperatures are extrapolated from the lower temperature data and may not be entirely accurate. Because of the strong electric field dependence of breakdown, all techniques for increasing breakdown voltage involve the reduction of electric field in the depletion layer. In the one dimension into the bulk the task is relatively simple very high breakdown voltage can theoretically be achieved by simply making the

p and n regions lightly doped and very wide. The real limiting effects are the two and three dimensional electric field effects at the edge of the semiconductor device where the junction comes to the surface.

Surface Breakdown:

Surface breakdown, as referred to here, is the effect of a reduced p-n junction breakdown because of a higher electric field across the junction at the surface of a semiconductor device [3]. The causes of this increased surface electric field are many, including dangling bonds at the surface of the semiconductor material, differences in dielectric constant between the semiconductor and the material surrounding it, fixed charge in the material coating the semiconductor surface, and curvature of diffused junctions. A variety of techniques have been suggested to reduce the surface electric field and thereby increase breakdown voltage [4]. These include beveling and etching the surface to change the charge distribution near the junction edge [5-9], field limiting diffusions [10], and field plates covering the junction edge [11-13]. Among these reports, the highest breakdown voltage was 10 KV, achieved using a semi-insulating polysilicon (SIPOS) field plate [13].

Second Breakdown and Switching:

If the current through a device is allowed to increase after breakdown is reached, a second breakdown is seen wherein the voltage across the device collapses to a much lower value as shown in Fig. 2. This negative resistance region of the characteristic is very useful for very high speed switching. A switching device called the "Avalanche Transistor" is based on this phenomenon [14]. Switches capable of holding off up to 1000 V and conducting several 10s of amps of current have been made with switching times of less than 5 nanoseconds [15]. This second breakdown phenomenon is not very well understood. Recently, two distinct regimes of second breakdown were described [16], one called thermal mode is relatively slow (microseconds), the other called current mode is fast (nanoseconds). One explanation of second breakdown is that it is a feed back effect in which carriers generated by avalanche multiplication forward bias the emitter base junction of bipolar transistors [17]. The discovery of a similar second breakdown in diodes tends to shed some doubt on this theory [18-19]. In fact the switching speed in diodes is substantially faster than in transistors. Fig. 3 is a pulse generated, by a circuit using one of these diodes, in our laboratory having a peak amplitude of 2800 volts (56 Amps.) and a rise time of less than 0.5 ns. These devices are

extremely useful for generation of high voltage pulses where low jitter and electrical triggering are a requirement.

References:

1. R. van Overstraeten and H. de Man, "Measurement of the ionization rates in diffused silicon p-n junctions," Solid-State electronics, Vol. 13, P. 583, 1970.
2. W. N. Grant, "Electron and Hole Ionization Rates in Epitaxial Silicon at High Electric Fields," Solid State Electronics, Vol. 16, P. 1189, 1973.
3. A. S. Grove, Physics and Technology of Semiconductor Devices, Sec. 10.5, P. 311, John Wiley and Sons, New York 1967.
4. Adolph Blicher, Field-Effect and Bipolar Power Transistor Physics, Chapter 4, P. 52, Academic Press, New York, 1981.
5. R. L. Davies, F. E. Gentry, "Control of Electric Field at the Surface of P-N Junctions," IEEE Transactions on Electron Devices, ED-11, P. 313, 1964.
6. V. A. K. Temple, M.S. Adler, "The Theory and Application of a Simple Etch Contour for Near Ideal Breakdown Voltage in Plane and Planar p-n Junctions," IEEE Transactions on Electron Devices, ED-23, P. 950, 1976
7. V.A.K. Temple, M.S. Adler, "Calculations of the Diffusion Curvature Related Avalanche Breakdown in High-Voltage Planar p-n Junctions," IEEE Transactions on Electron Devices, ED-22, P. 910, 1975.
8. V.A.K. Temple, "Increased Avalanche Breakdown Voltage and Controlled Surface Electric Fields Using a Junction Termination Extension (JTE) Technique," IEEE Transactions on Electron Devices, ED-30, P. 954, 1983.
9. K.P. Brieger, W. Gerlach, J. Pelka, "The Influence of Surface Charge and Bevel Angle on the Blocking Behavior of a High-Voltage P^+-n-n^+ Device," IEEE Transactions on Electron Devices, ED-31, P. 733, 1984.
10. M.S. Adler, V.A.K. Temple, A.P. Ferro, R.C. Rustay, "Theory and Breakdown Voltage for Planar Devices with a Single Field Limiting Ring," IEEE Transactions on Electron Devices, ED-24, P. 107, 1977.

11. F. Conti, M. Conti, "Surface Breakdown in Silicon Planar Diodes Equipped with Field Plate," Solid State Electronics, Vol. 15, P. 93, 1971.
12. F.A. Selim, "High-Voltage, Large-Area Planar Devices," IEEE Electron Device Letters, EDL-2, P. 219, 1981.
13. T. Matsushita, T. Aoki, T. Ohtsu, H. Yamoto, H. Hayashi, M. Okayama, Y. Kawana, "Highly Reliable High-Voltage Transistors by use of the SIPOS Process," IEEE Transactions on Electron Devices, ED-23, P. 826, 1976.
14. D.J. Hamilton, J.F. Gibbons, W. Shockley, "Physical Principles of Avalanche Transistor Pulse Circuits," Proceedings of the IRE, P. 1102, June 1959.
15. J. C. Koo, M. D. Pocha, "High Voltage, High Speed Switching Transistors Using Current-Mode Second Breakdown," Proceedings, 33rd Electronic Components Conference, IEEE Catalog No. 83CH1904-2, P. 178, 1983.
16. K. Koyanagi, K. Hane, T. Suzuki, "Boundary Conditions Between Current Mode and Thermal Mode Second Breakdown in Epitaxial Planar Transistors," IEEE Transactions on Electron Devices, ED-24, P. 672, 1977.
17. J.E. Carroll, P.J. Probert, "Current/voltage characteristics of transistors operating in current-mode second breakdown," Solid-State and Electron Devices, Vol. 3, P. 41, 1979.
18. I.V. Grekhov, A.F. Kardo-Sysoev, L.S. Kostina, S.V. Shenderoy, A.F. Ioffe, "High Power Subnanosecond Switch," Technical Digest, 1980 International Electron Devices Meeting, Washington D.C., P. 662.
19. I.V. Grekhov, A.F. Kardo-Sysoev, L.S. Kostina, "Breakdown delay and excitation of ionization waves in p-n junctions," Soviet Tech. Phys. Letters, Vol. 5, P. 399, Aug. 1979.

This work was performed under the auspices of the U.S. Department of Energy by Lawrence Livermore National Laboratory under contract No. W-7405-Eng-48.

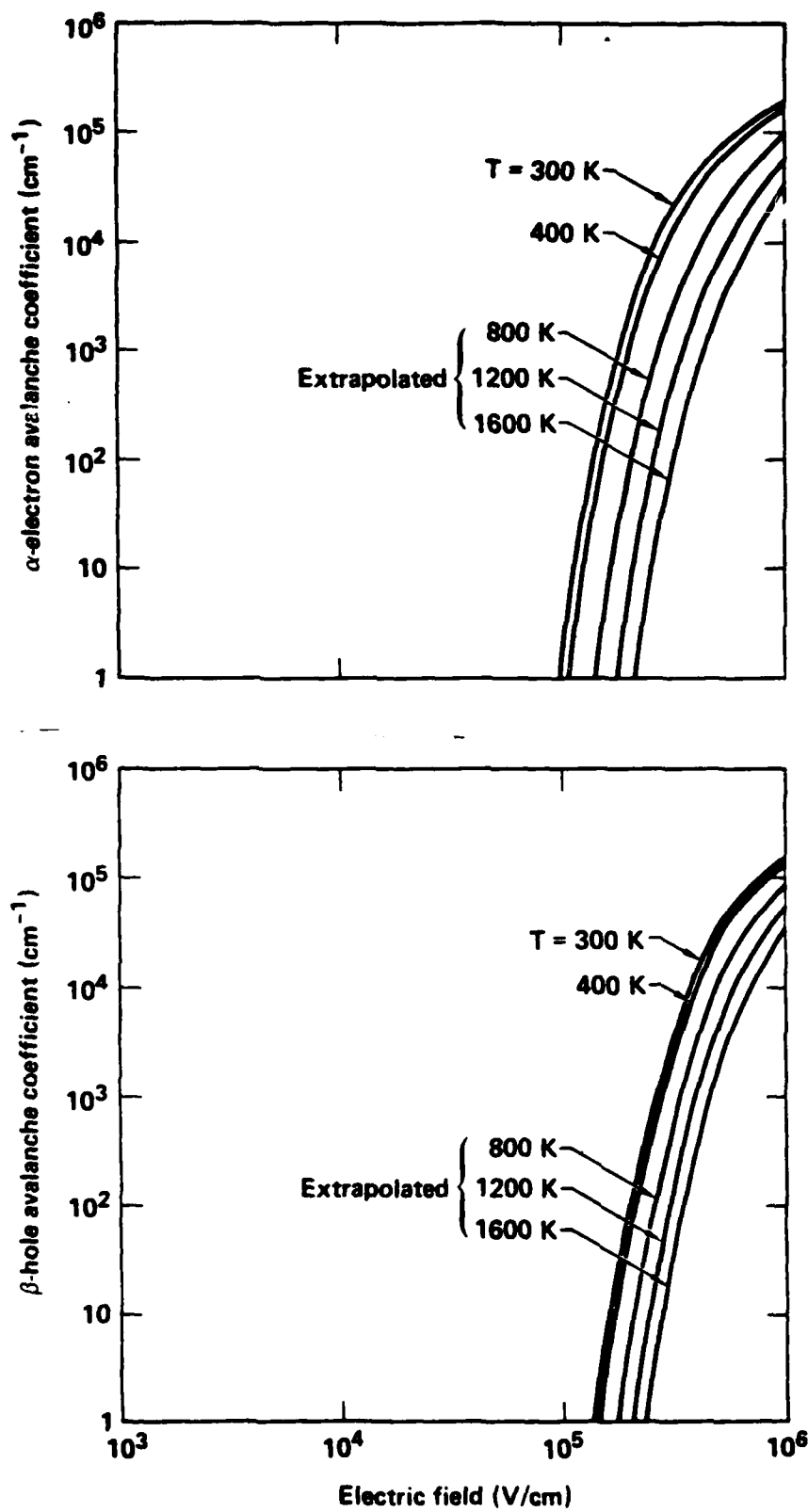


Figure 1. Ionization coefficients verses electric field for several temperatures.

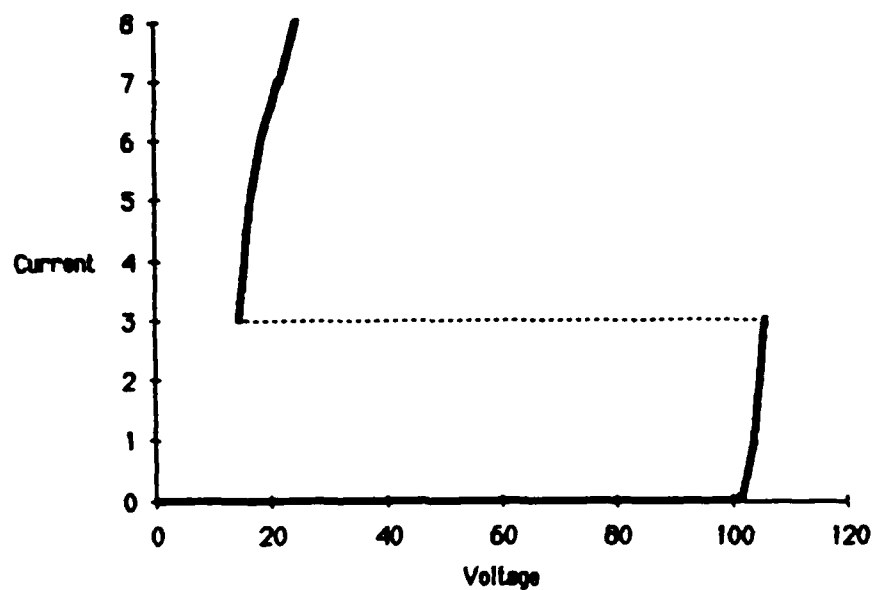


Figure 2. Current/voltage characteristics illustrating second breakdown in a junction semiconductor device

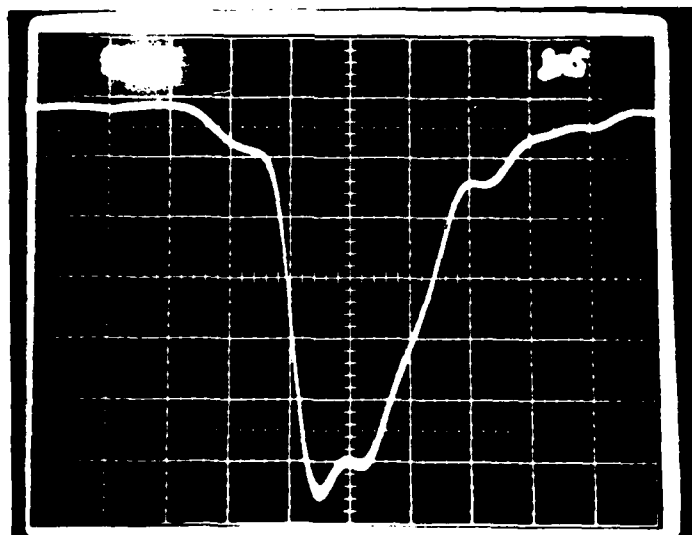


Figure 3. A 2800 volt 300 picosecond rise time pulse generated using the fast second breakdown effect in a silicon diode.

VIEWGRAPHS

AVALANCHE BREAKDOWN MECHANISMS AND APPLICATION
TO SWITCHING DEVICES

M. D. Pocha

Avalanche Breakdown Mechanisms and Switching Device Applications



Michael D. Pocha

**Lawrence Livermore
National Laboratory**

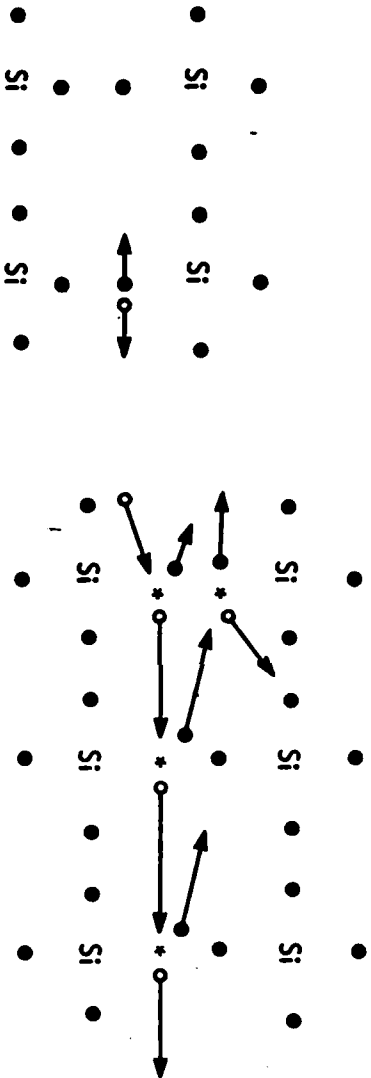
**Workshop on New Directions
in Solid State Power Switches**

**Aug. 28-30, 1985
Farmingdale, New York**

Topics

- **Avalanche Breakdown**
- **Surface Breakdown**
- **Second Breakdown**

Avalanche is the primary breakdown mechanism in high voltage devices



a. Zener breakdown--
high electric field

b. Avalanche breakdown--low electric
field

In general the avalanche integrals must be calculated



$$1 - \frac{1}{M_p} = \int_0^w \alpha_p \exp \left(- \int_0^x (\alpha_p - \alpha_n) d\eta \right) dx$$

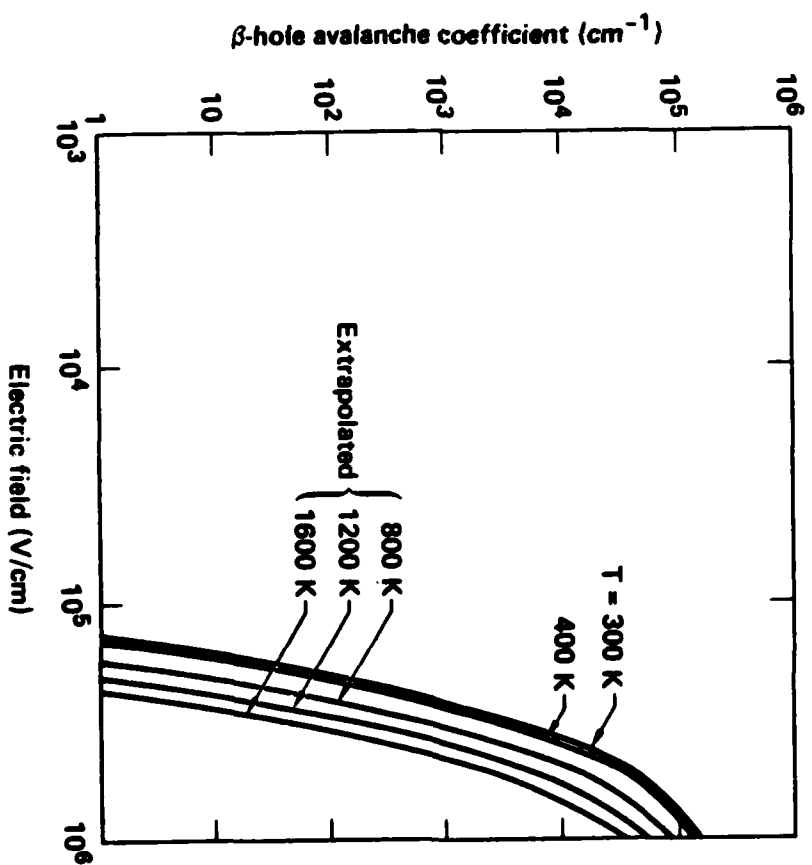
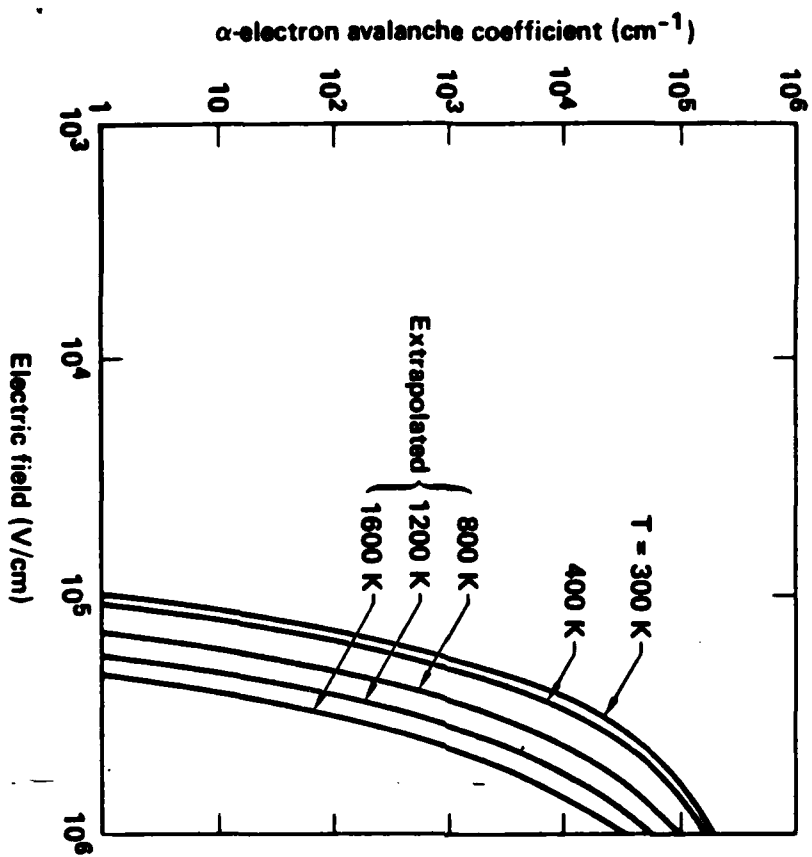
$$1 - \frac{1}{M_n} = \int_0^w \alpha_n \exp \left(- \int_x^w (\alpha_n - \alpha_p) d\eta \right) dx \quad (6)$$

w represents the width of the space-charge layer. The equation

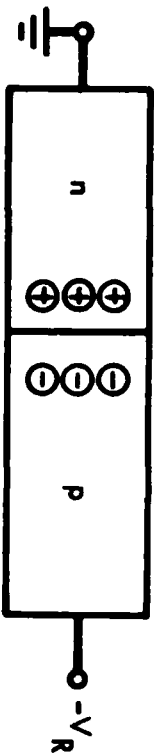
$$1 - \frac{1}{M} = 1 \quad (7)$$

is used as the criterion for breakdown.

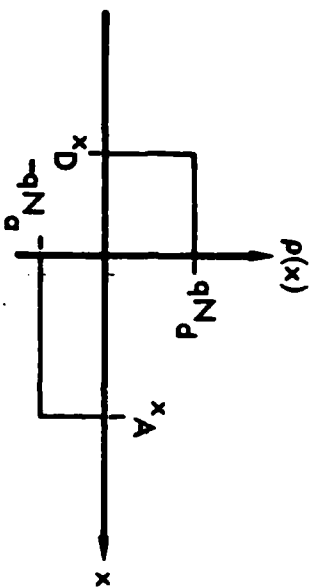
Ionization coefficients are a strong function of electric field



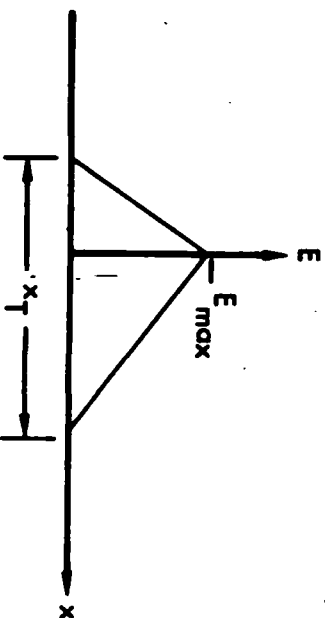
Electric field is the key to avalanche breakdown in a p-n junction



a. Charge distribution

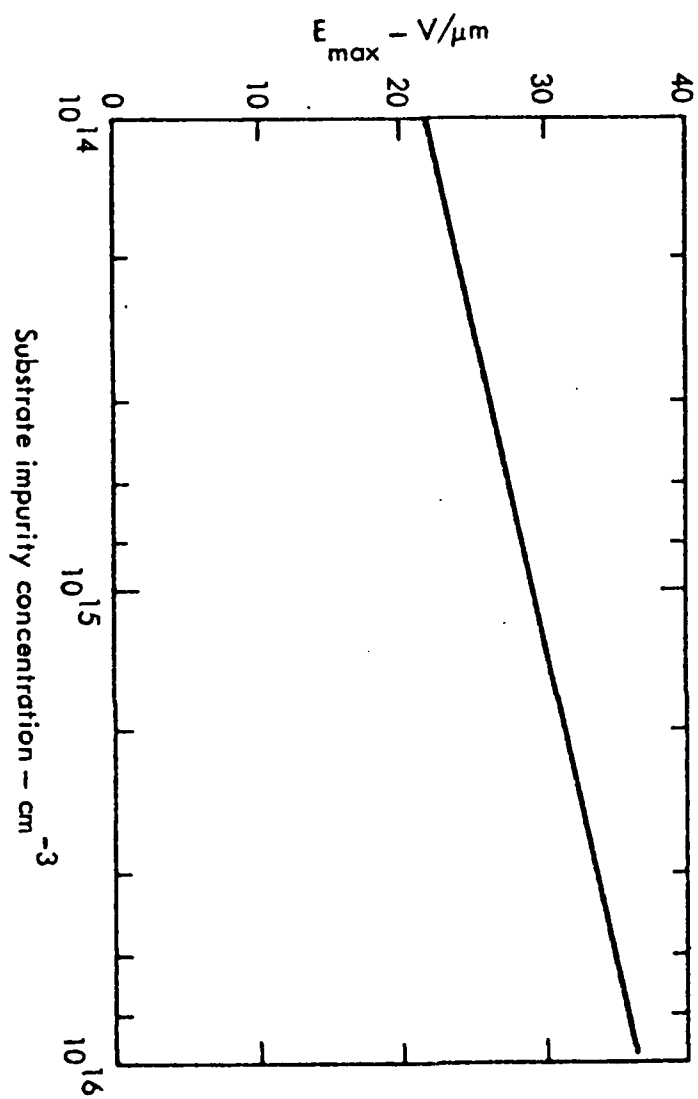


b. Charge distribution

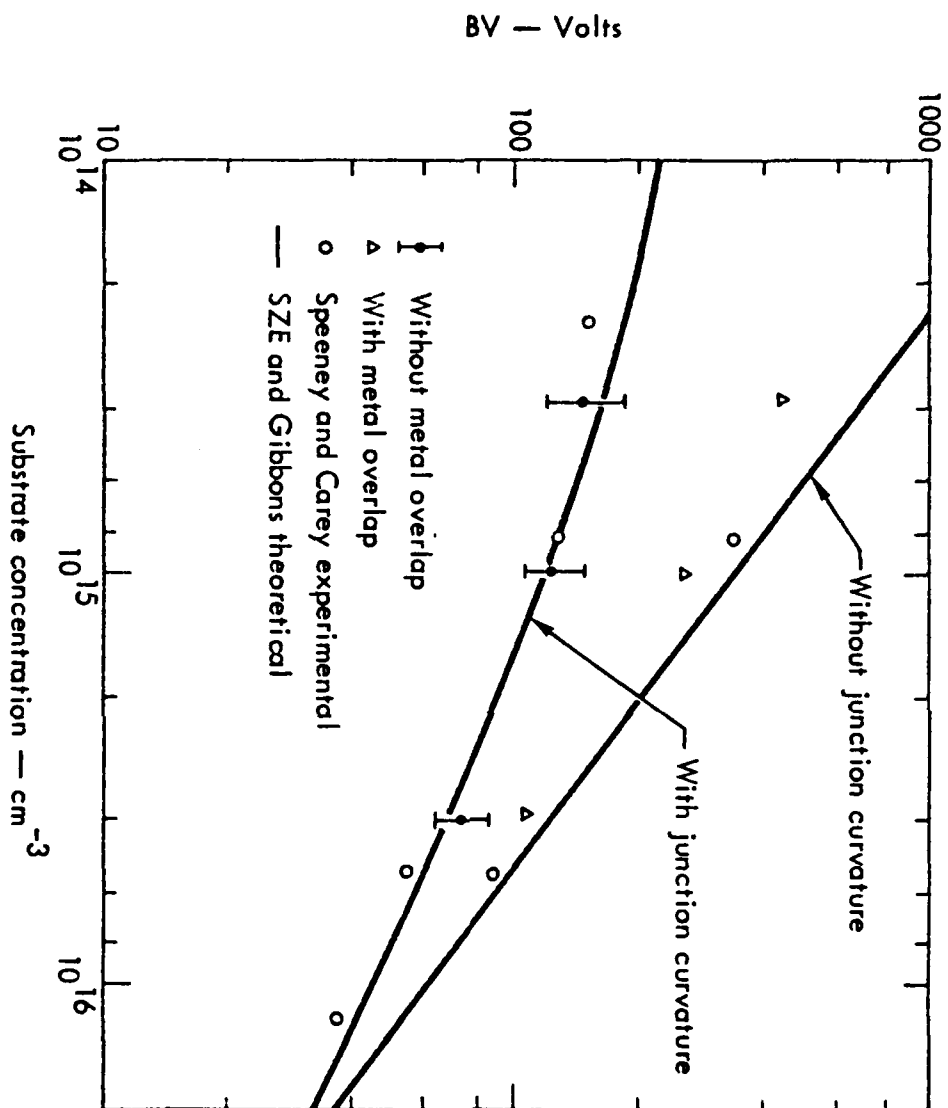


c. Electric field distribution

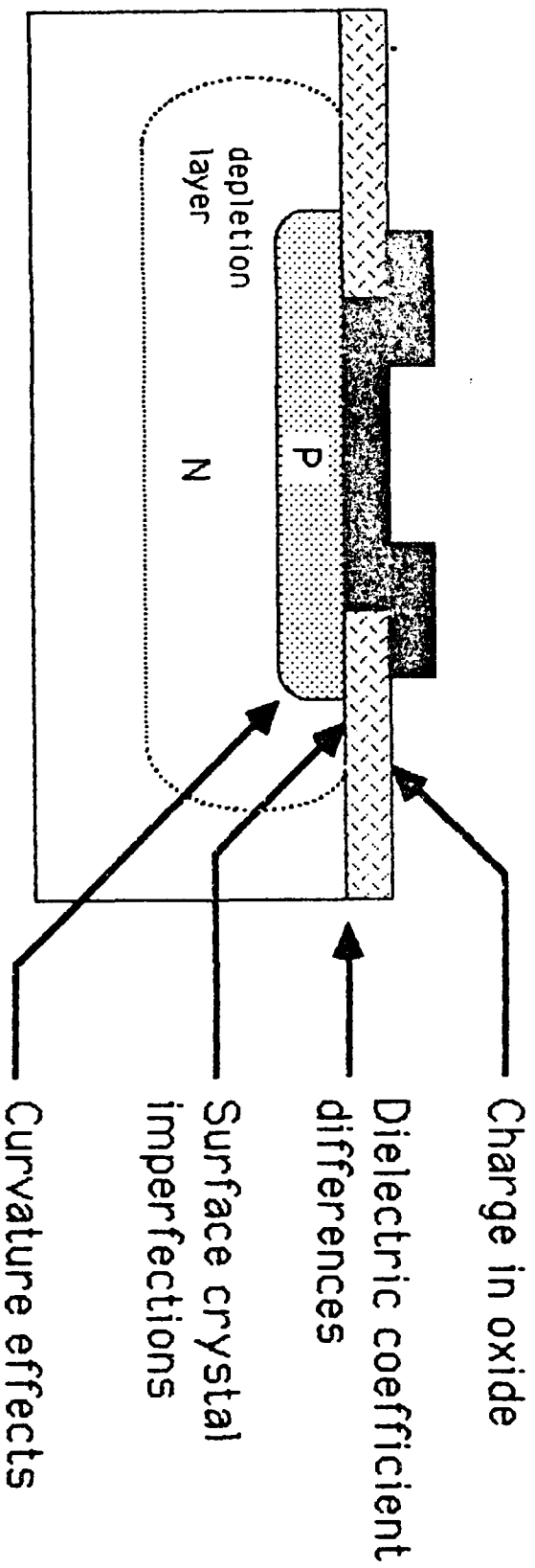
A critical field rule of thumb can be used
for quick calculations



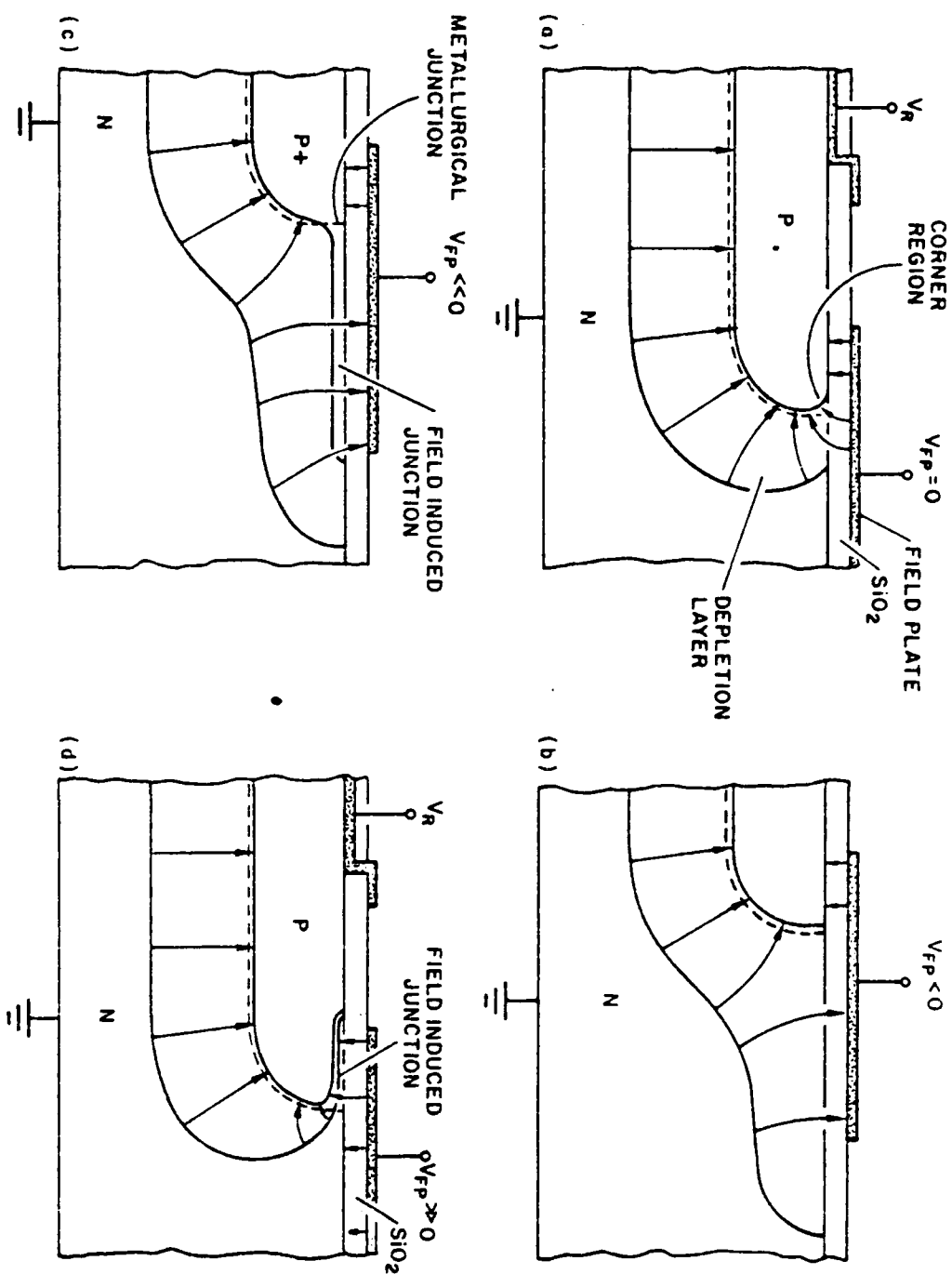
Without surface effects, avalanche breakdown can theoretically be very high



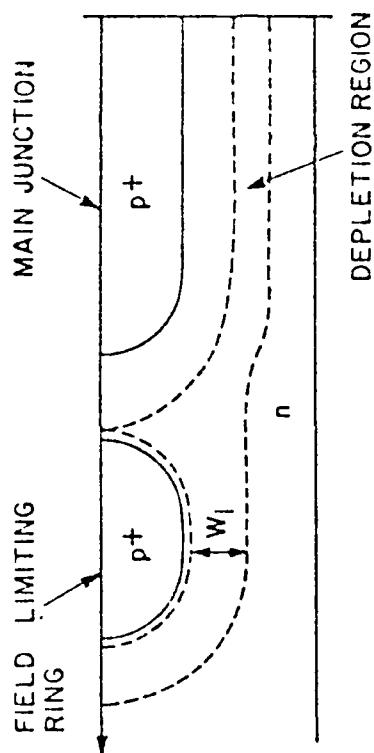
Surface breakdown – the limiting factor in junction devices



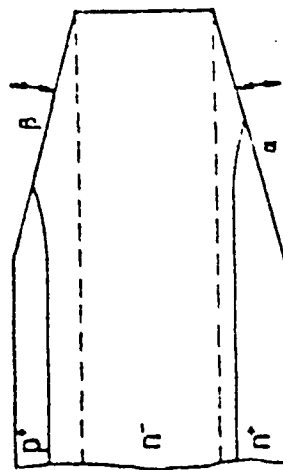
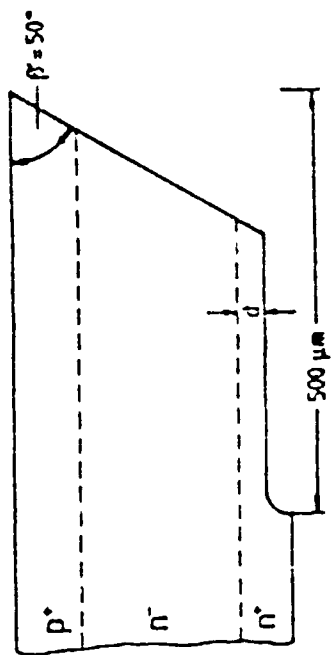
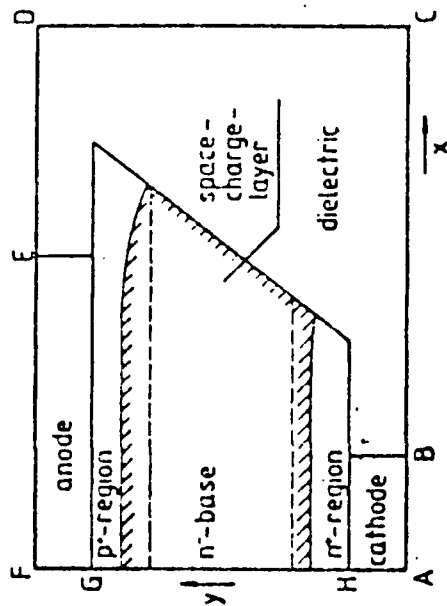
Field plates – easy to implement but limited to lower voltages



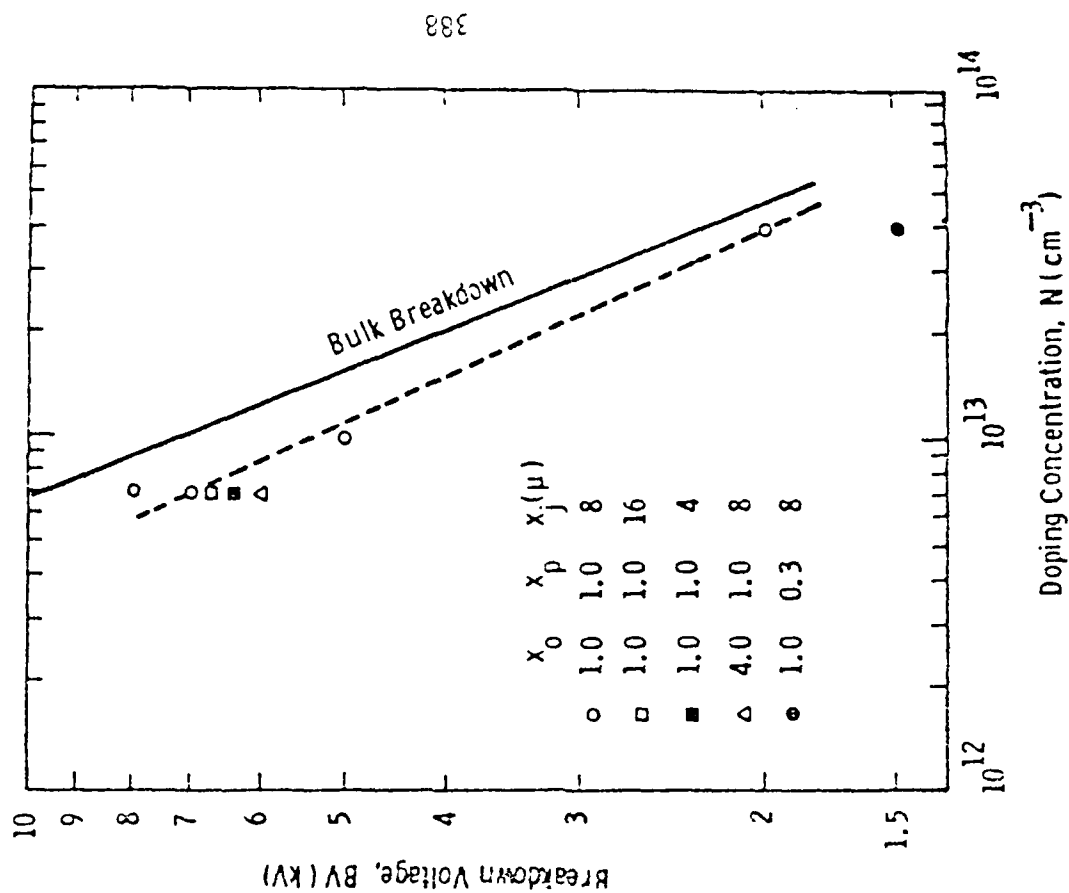
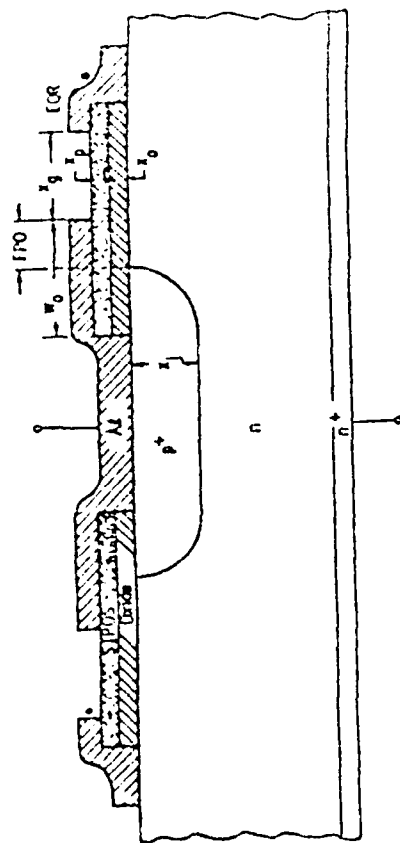
Diffused field limiting rings - limited to lower voltages



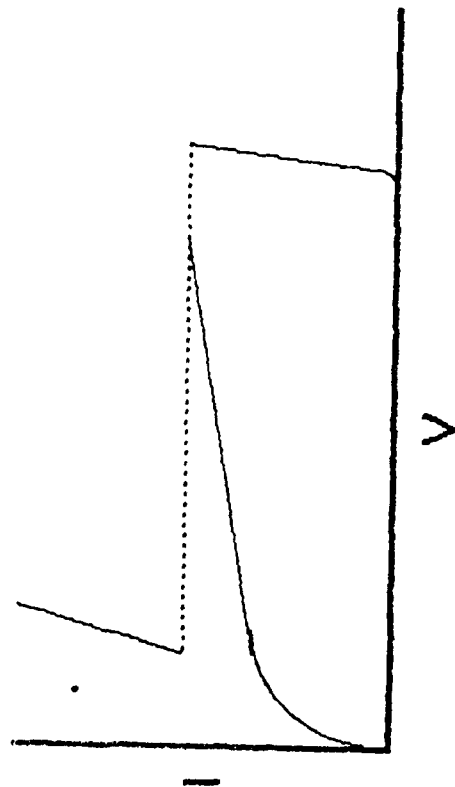
Edge profiling - effective but difficult to implement



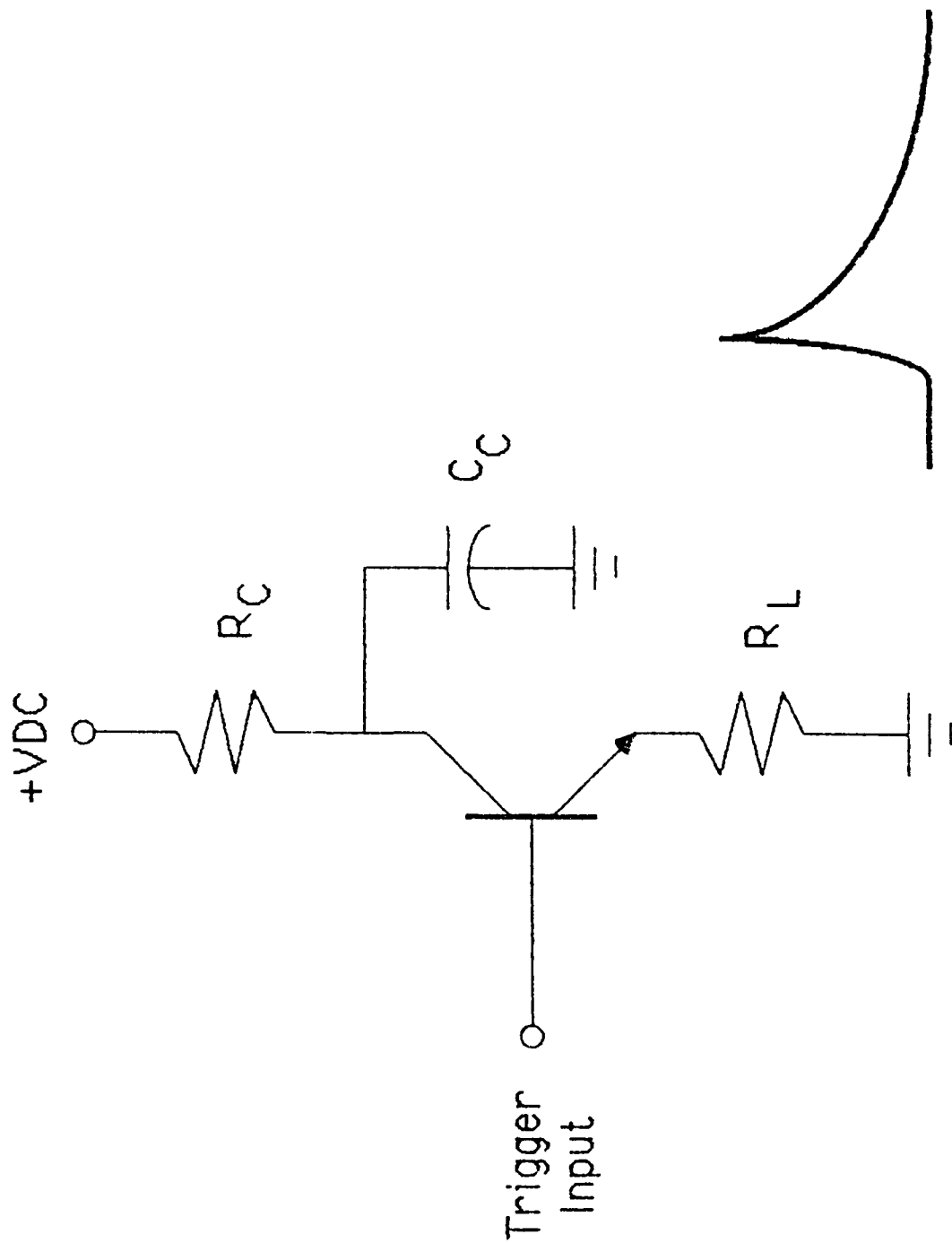
Resistive field plates – highest reported breakdown voltage



Second breakdown occurs when current flow reaches a high enough level



If energy is externally limited second breakdown
can be used to generate fast high voltage pulses



Commercial Devices are not Generally Designed for Avalanche Operation



Some available transistors (for the time being)

Mfg. & Model	BV (Volts)	Rise time (ns)
* Raytheon RS3500	(200)	280
Motorola 2N4014	(80)	140
Fairchild 2N3904	(60)	110
Texas Ins 2N2222	(75)	120
National 2N3700	(140)	220

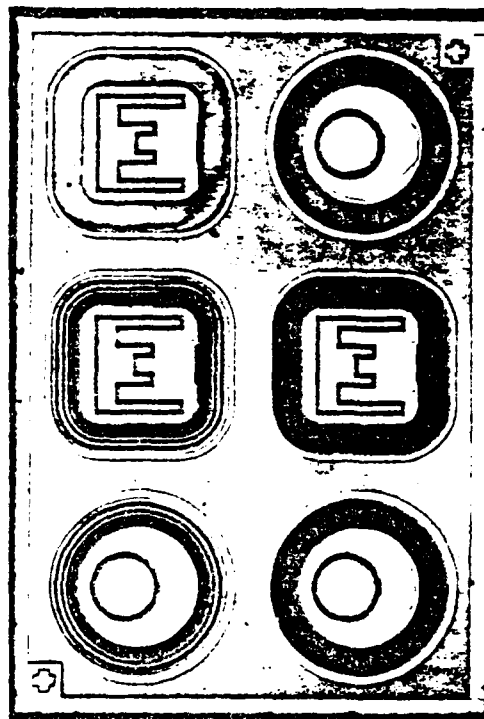
0.7-0.8
0.4-0.6
0.6-0.7
0.8-0.9
0.9-1.1

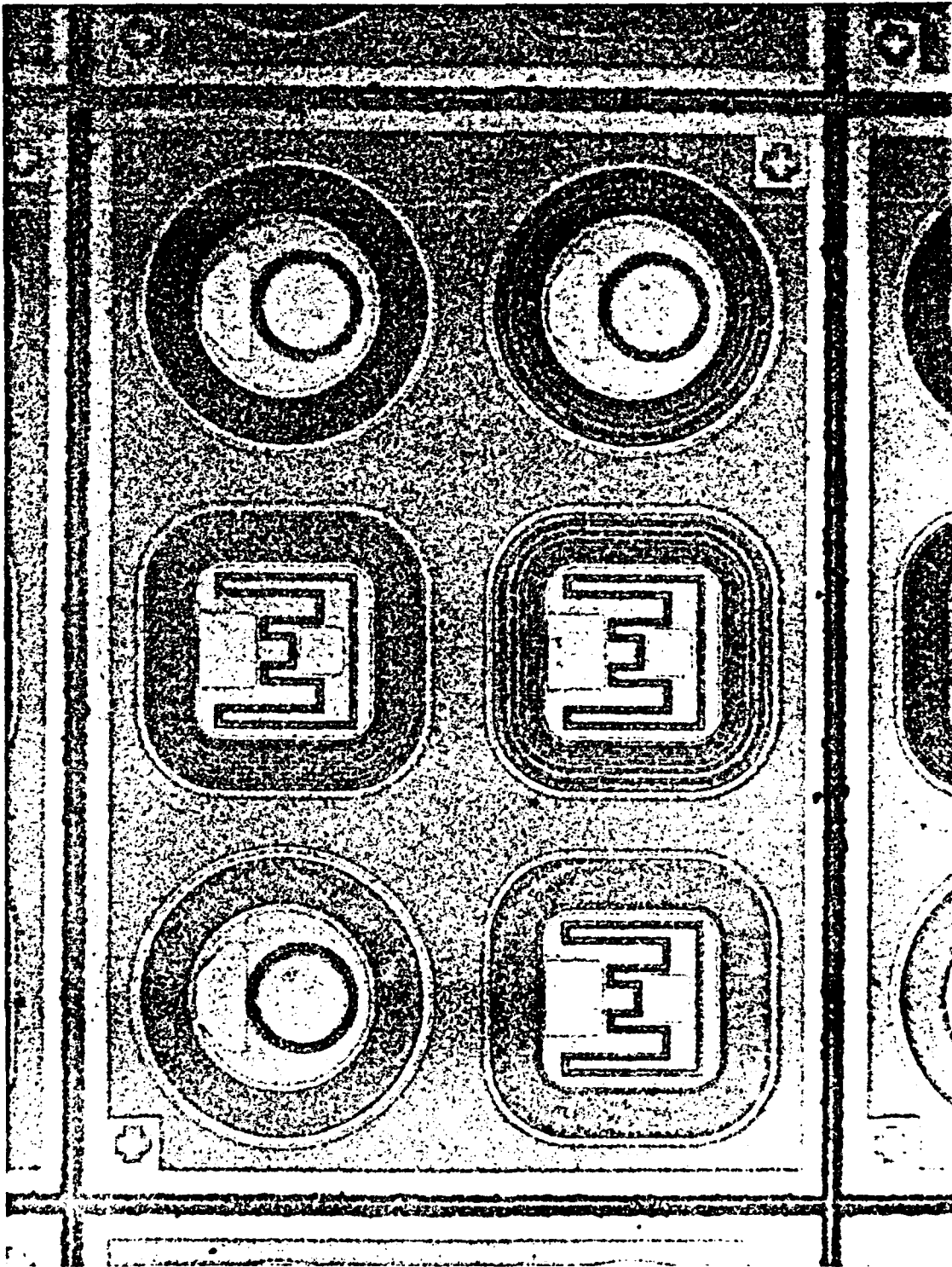
* The only transistor sold for avalanche application

Unreliability is the primary problem
Higher Voltage is desirable



800 Volt Avalanche Transistor



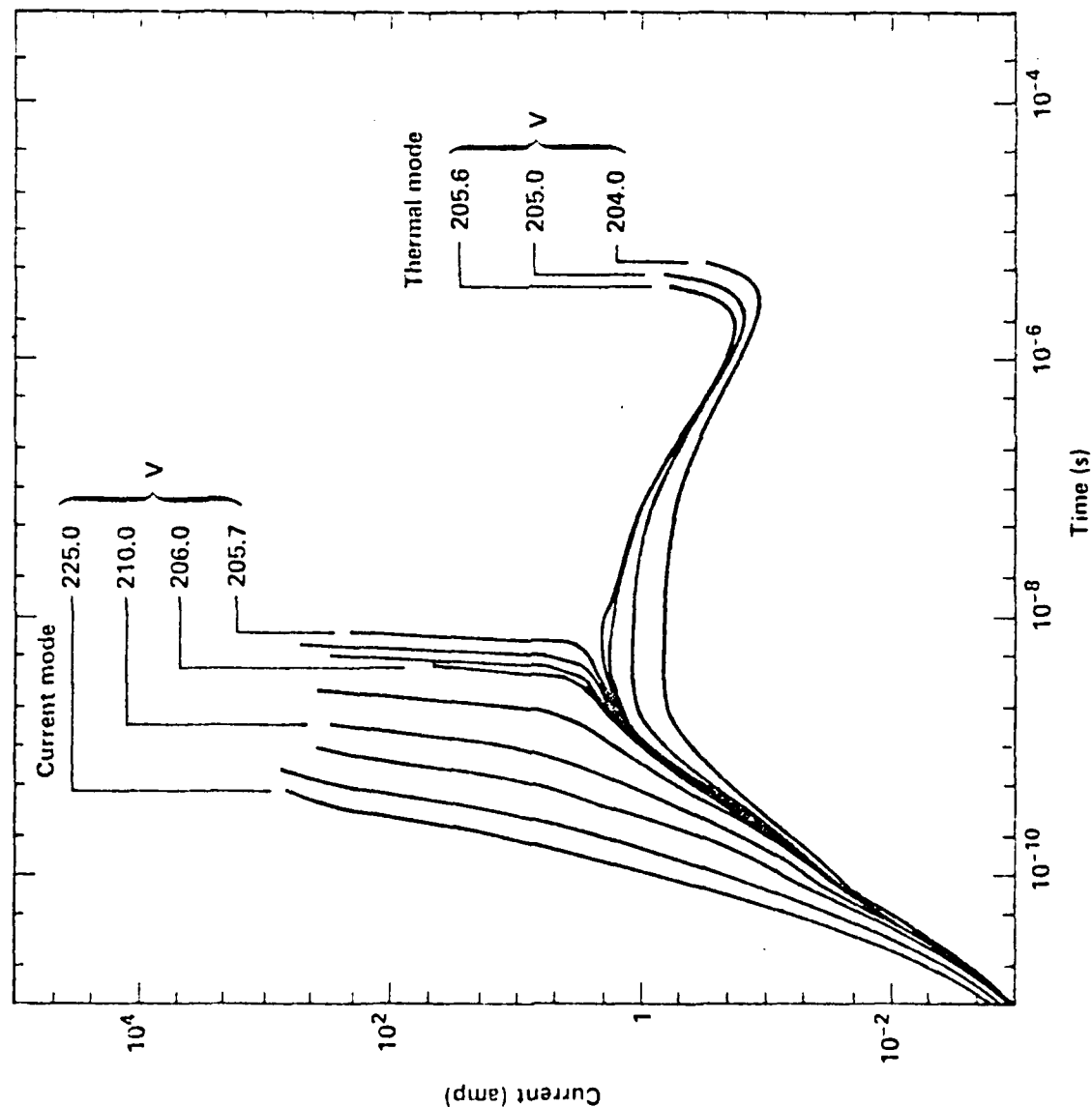


We have succeeded in achieving reliable
operation by design

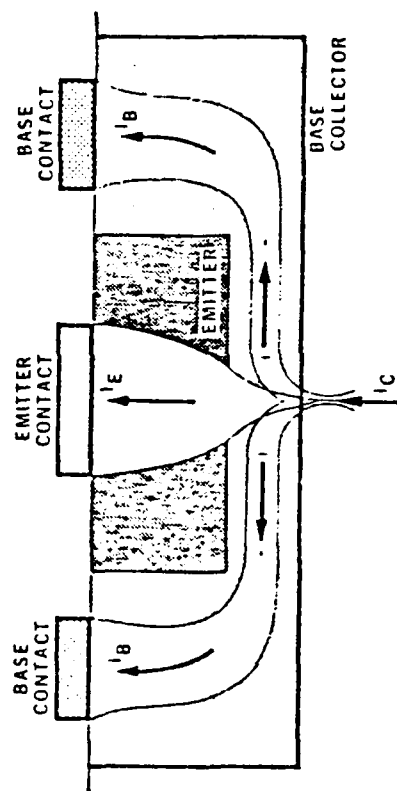


- Only normal D.C. Testing required
- Breakdown voltage > 800 Volts
- Voltage is limited by surface fields
- Rise time trade-off 200 V/ns .

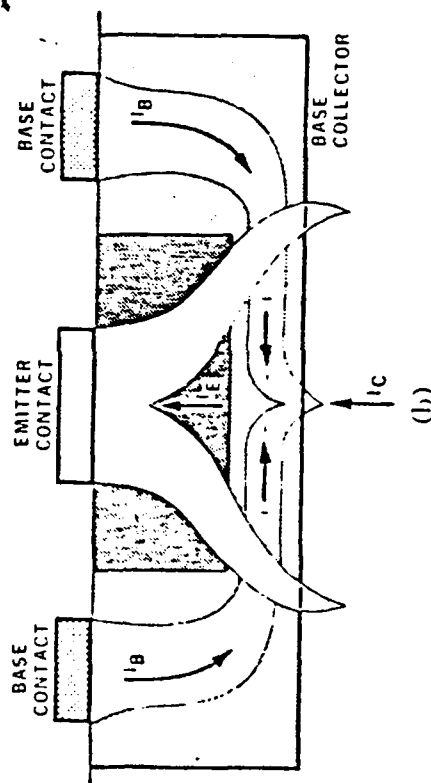
There appear to be two modes of second breakdown - current mode and thermal mode



Based on recent results, feedback model of current mode second breakdown may not be correct

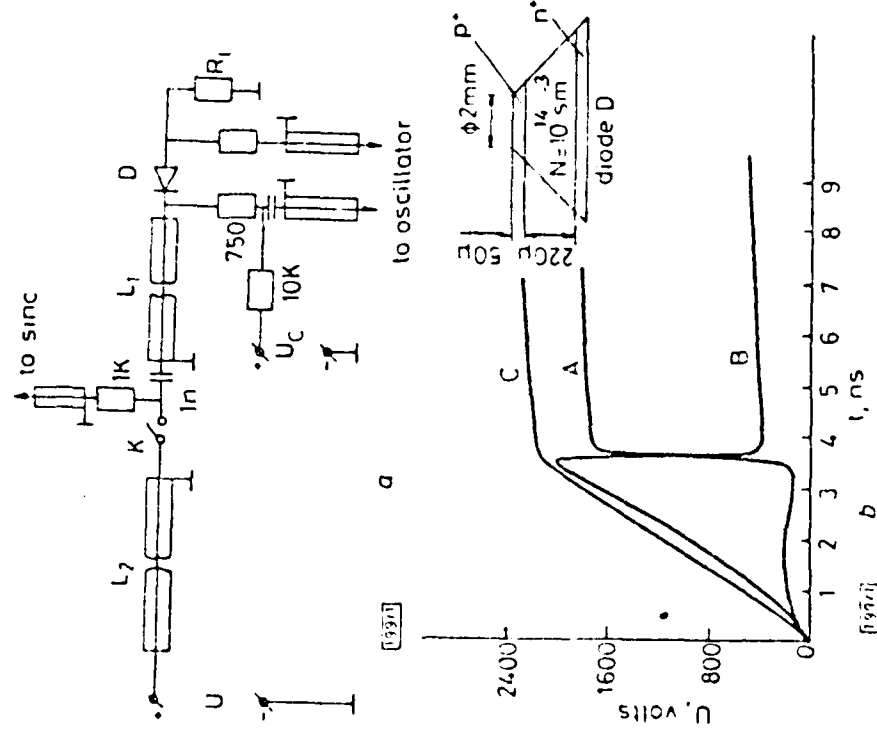


(a)

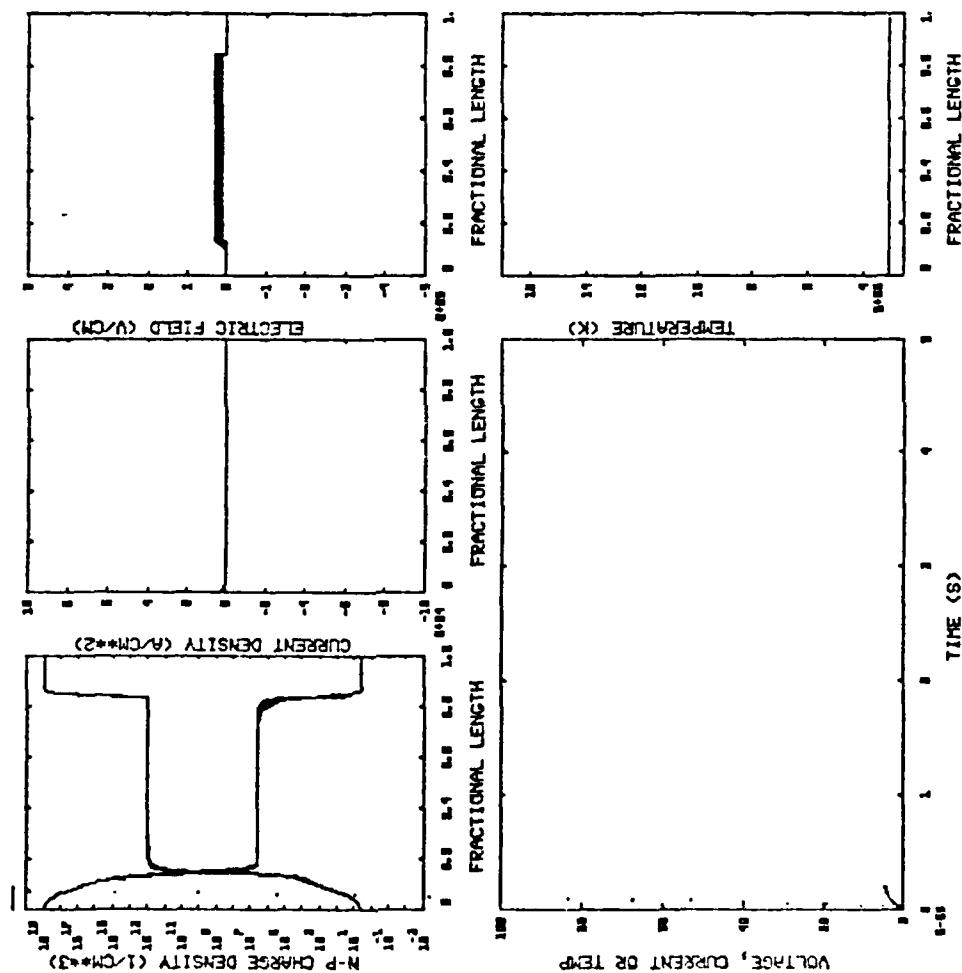


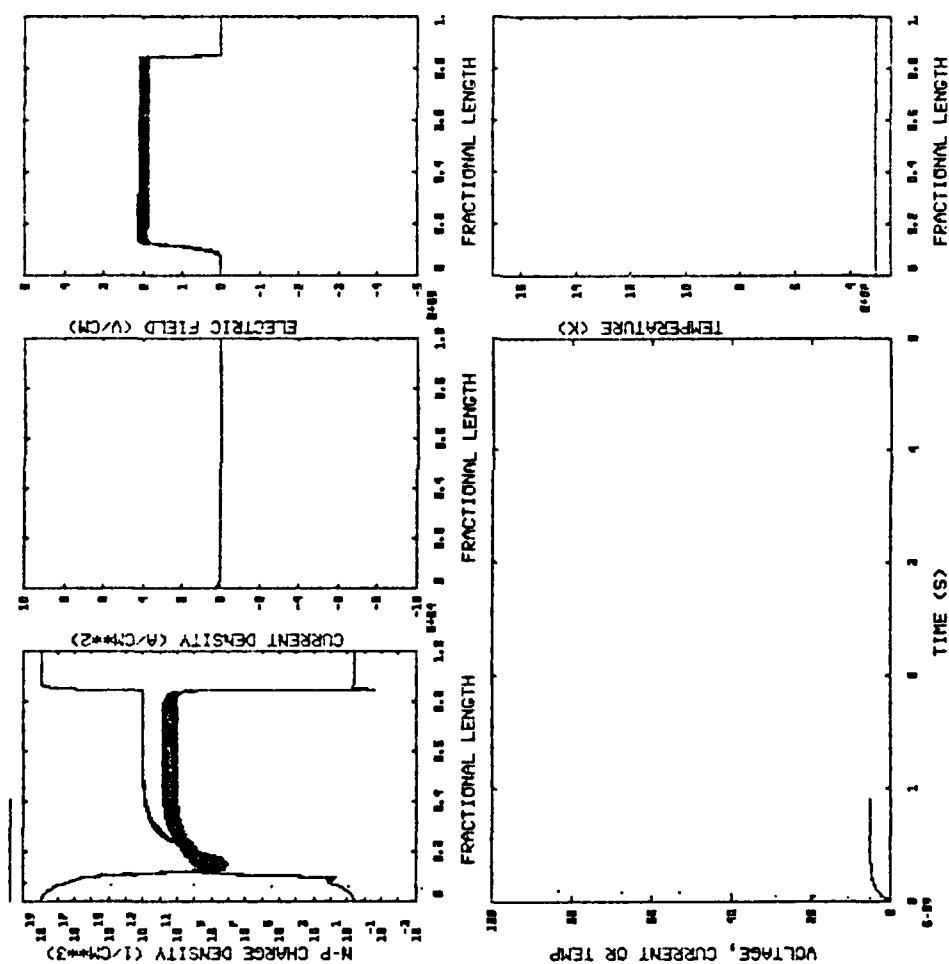
(b)

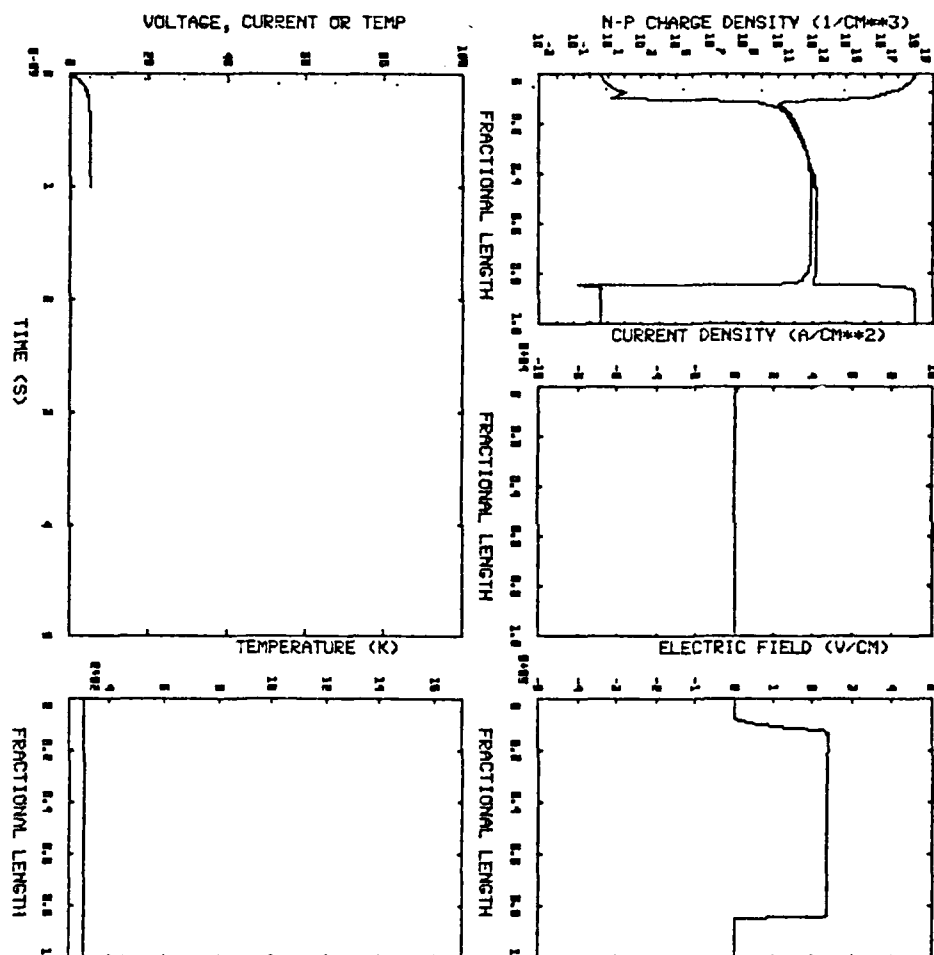
Second breakdown has been observed in diodes - and
rise times are much faster

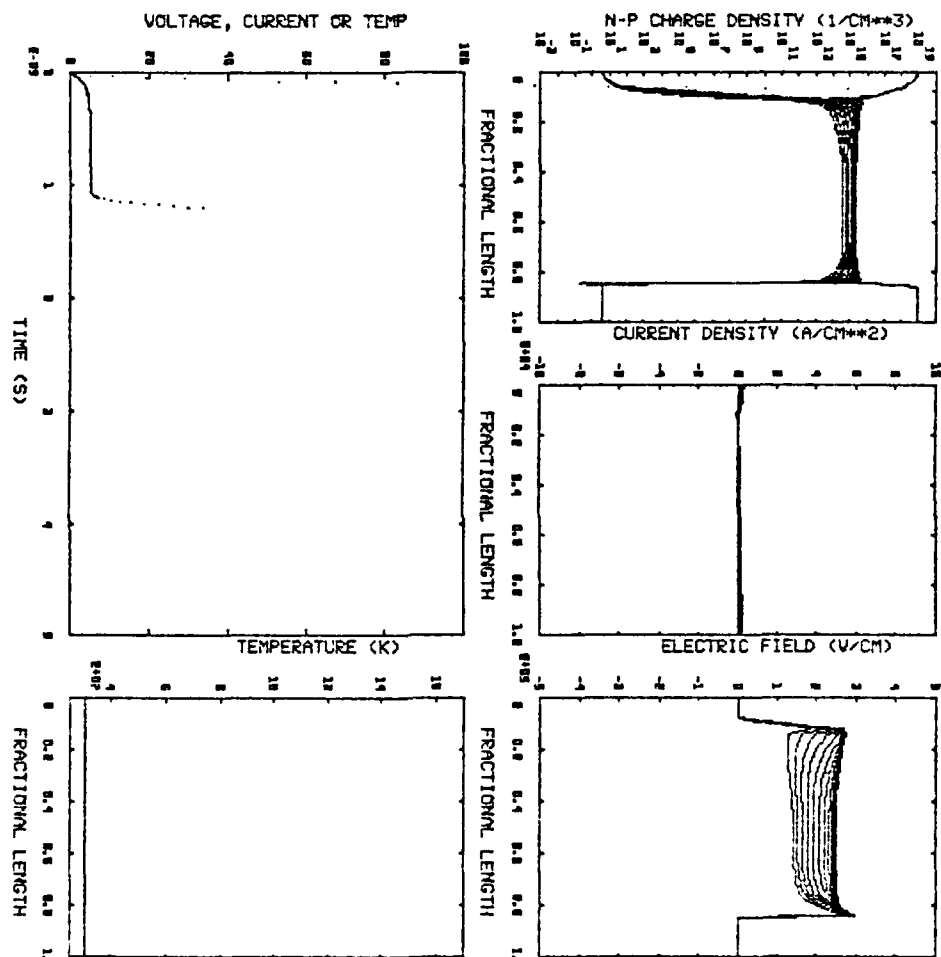


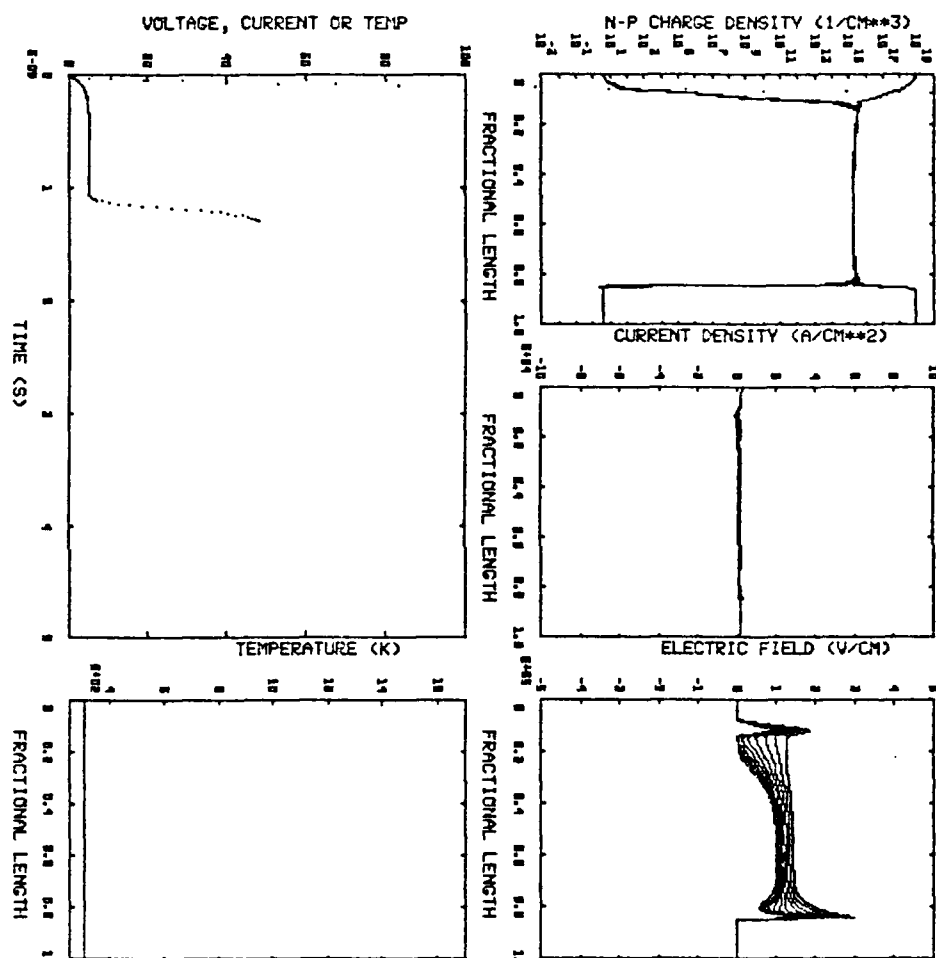
One dimensional numerical model shows the pulse sharpening diode effect

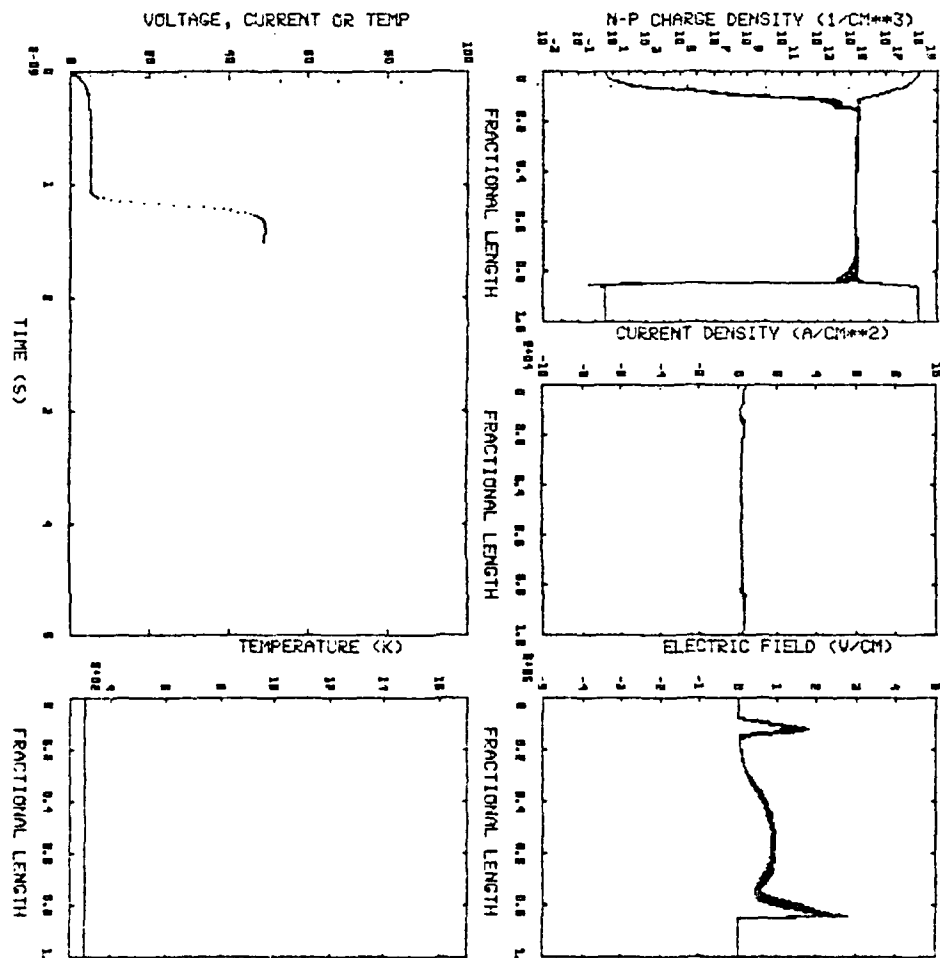








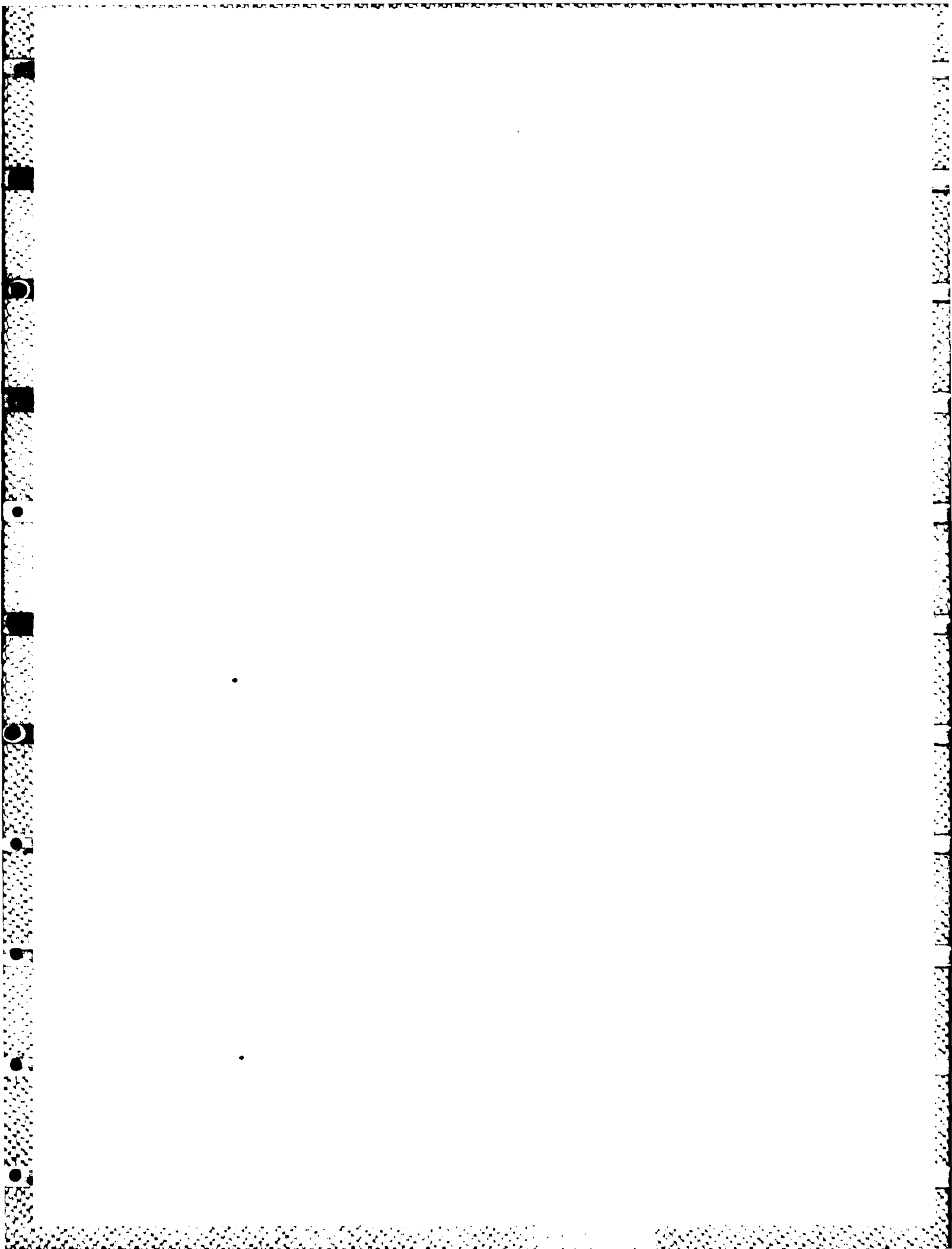




Concluding remarks



- Bulk avalanche breakdown
 - Very high voltages possible
- Surface breakdown
 - Approximately 10kV per junction
 - Surface field limiting structures take up space
- Current mode second breakdown
 - Very fast switching
 - If one dimensional effect - current may be scalable
 - Generation of incident pulse is non trivial



THERMAL SWITCHES FOR PULSE POWER

R. Ford
Code 4775

M. Kahn
Code 6363

Introduction

Inductive storage power supplies require the opening of the initial current storage circuit. This is shown in Fig. 1.

To perform this function, resistors that are sensitive to temperature are used here.

Figure 2 shows the small signal resistivities of conductive polycrystalline Barium Titanate and of a carbon filled polymer (polyethylene) switch material as they depend upon temperature.

Figure 3 shows the appearance of some PTC resistors as tested here. Three types of tests were used to evaluate these:

1) Steady State Voltage Test

The purpose of this test is to determine the maximum steady state voltage that can be applied. The circuit shown in Fig. 4 was used for it.

2) Maximum Current Test

The maximum current that a device is capable of interrupting was determined by applying a step function of voltage and observing the parameters of the current pulse passed by the PTCR.

A large battery bank comprised of 120 two volt cells, capable of delivering short circuit currents to 2000 amps, was used for this (see Fig. 5).

3) High Source Impedance Pulse Test

This test is designed to measure the maximum (short term) switched voltage for a PTCR when driven from a high impedance source. A large air core coil was connected to a D.C. supply as shown in Fig. 6. If the inductively stored energy is sufficient, the test device will be heated by essentially a

constant current, until it reaches switching temperature. The rapidly increasing resistance will then lower the current and produce a corresponding voltage increase.

Results and Discussion

Table #1 shows that the carbon filled polymer PTCR devices are able to switch single pulses up to 700 A, more than four times as much as the ceramic based devices. The ceramics on the other hand withstood more than three times the backvoltage, up to 600 V per device.

Figure 7 shows the small and the large signal resistances of a polymer-carbon composite PTCR (Type 6) measured before and during each current pulse. Figure 8 shows the large signal cold resistances of six of these parts. They show an irreversible increase in resistance after switching pulses in excess of 750A. At that point the current pulse is only about 3 milli-sec long and has a fall time of 0.2 milli-sec (see Fig. 9). As one would expect from a variable resistor, the voltage rise time has about the same duration as the current fall time (see Fig. 10).

Similar data are shown in Figs. 11 and 12 for the large signal resistances and switching times of the Type 1 carbon filled polymer PTCR devices. These devices appear to switch somewhat faster, with current fall times (at 700A) down to 100 microsec or less.

Figure 13 shows the small signal as well as the cold large signal resistances of two groups of barium titanate PTCR's, Types #4 and Types #7. These are also shown also in Table 1.

Figures #14 and #15 give the pulse durations and pulse fall (current shut off) times for these two types of barium titanate devices. They can be switched in milliseconds before failures are encountered.

Figures 16 and 17 show the resistances and pulse duration for the small (Type 2) ceramic PTCR devices. They tolerate only 60 amperes. Switching times of a millisecond or less seem allowable.

Failure Mechanisms:

Continuous application of excess voltage to Barium Titanate PTC resistors caused thermal runaway.

In the carbon filled polymer devices on the other hand, there was voltage breakdown at the edge of the electrodes. This is shown for a Type 6 (round) carbon filled polymer device in Fig. 18 and for a Type 1 (rectangular), carbon filled polymer device in Fig. 19. The latter broke down at 265 V D.C.

The resistivity increases shown in the various resistance plots were caused by pulse currents and were accompanied by physical damage. Figure 20 shows a failure generated by a current of 780A in a round, carbon-filled polymer PTCR.

The current switching capability of the thicker Barium Titanate based PTCR devices are often limited by temperature gradients. This is indicated schematically in Fig. 21, and can lead to thermal expansion cracking at the external edge. This is shown in Fig. 22 in a small Barium Titanate based PTCR (Type 2) that had been subjected to 60A. Such a crack can propagate through the ceramic, parallel to the major surface and split it in two, as can be seen in Fig. 23, or it can curve towards a major surface and terminate as shown in Fig. 24. The latter type of crack usually appears only on part of an edge, often before or coincidental to a more destructive breakdown as shown in an overall view in Fig. 25.

Some locations in the region of destructive breakdown showed considerable evidence of melting and resolidification. This is shown in Figs. 26, 27a, 27b and 27c. Some stalagmitic structures inside the cavity shown are also notable, see Fig. 28.

Figure 29 shows the breakdown region of another Type 7 sample that failed at just above 100 A. What appears like a resolidified and partially crystallized molten region formed about 10 mils from the edge of the ceramic, extending from the upper to the lower electrode. Figure 29c shows at a higher magnification some of the dendritic structures that were formed in the breakdown zone.

Figure 30a shows a failure in a Type 4 sample at 200 amps. The failure discharge melted a smoothwalled, 12-18 mil diameter tubular channel through the ceramic. It terminated in a 12 mil hole through the lower electrode surface. This is shown in Fig. 31 that further illustrates its smooth wall features, residues of frozen liquified Barium Titanate around it on the surface and cracks extending from it. Figure 30b shows most of the wider

section of the channel at a higher magnification: the dendritic surface is reproduced in more detail in Fig. 30c and it is similar to that shown in the resolidified section of the Type 7 sample in Fig. 29c. What looks in Fig. 30b like little balls is reproduced in Fig. 32. These balls seem to have an enhanced lead content.

A typical voltage spike generated in the high source-impedance test is shown in Fig. 33. In the lower voltage, Type 4 ceramic PTCR's it caused some circumferential axial cracking as shown in Fig. 34. Figure 34 also shows the formation of multiple, round shorting paths, similar to the single round hole that was found in some of the low impedance test failures.

In summary the present data show pulse current capabilities above 650 A for carbon-filled polymer PTCR's and up to 1/3 of this for Barium Titanate devices.

Switching speeds of milliseconds are easily attainable, even without triggering. The large scale availability of commercially made PTC resistors should make their early application in pulse switching circuits feasible.

•

VIEWGRAPHS

THERMAL SWITCHES FOR PULSE POWER

R. FORD and M. KAHN

**THERMAL
SWITCHES
FOR
PULSE POWER**

**R. FORD
AND M. KAHN**

**NAVAL
RESEARCH LAB**

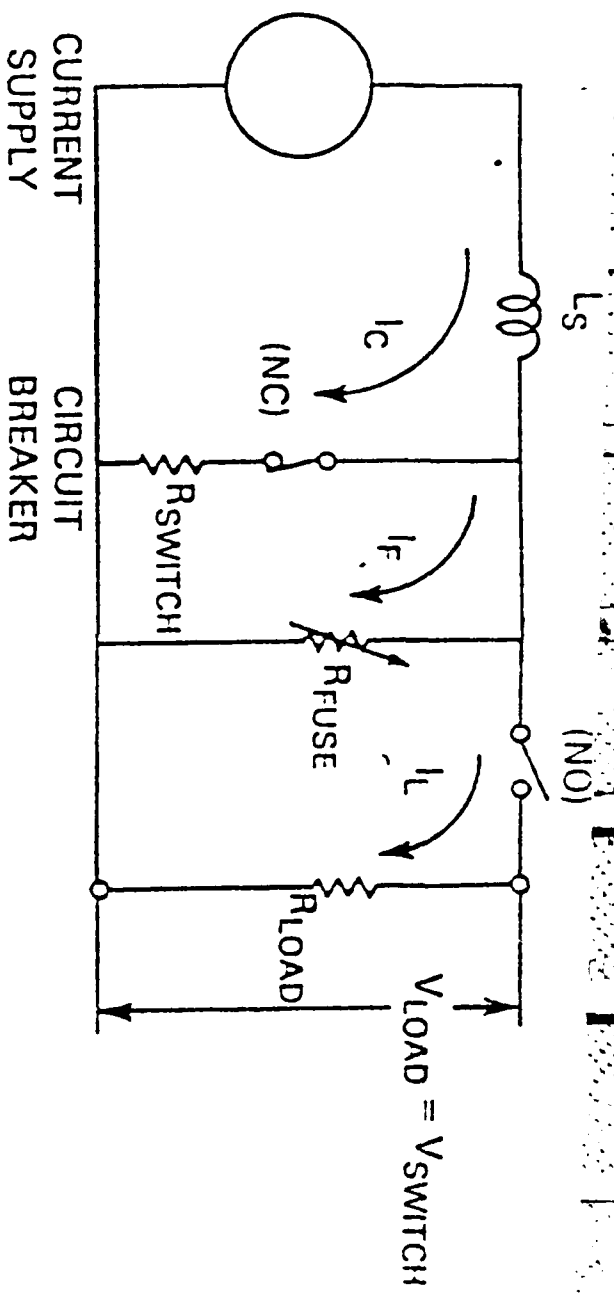


FIG. 1
PULSE POWER GENERATOR
AND WAVE FORMS

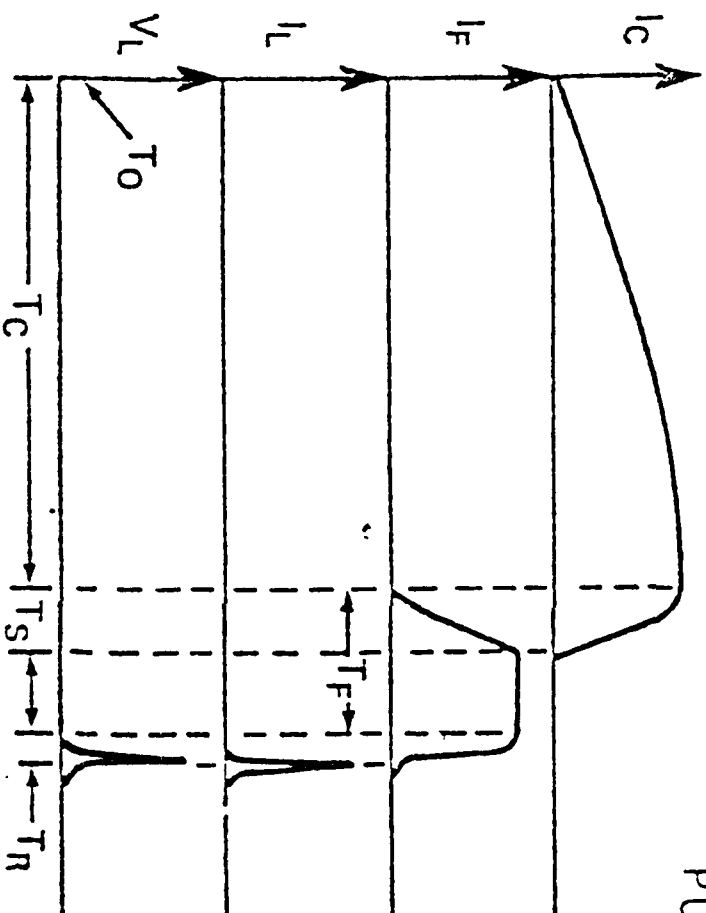
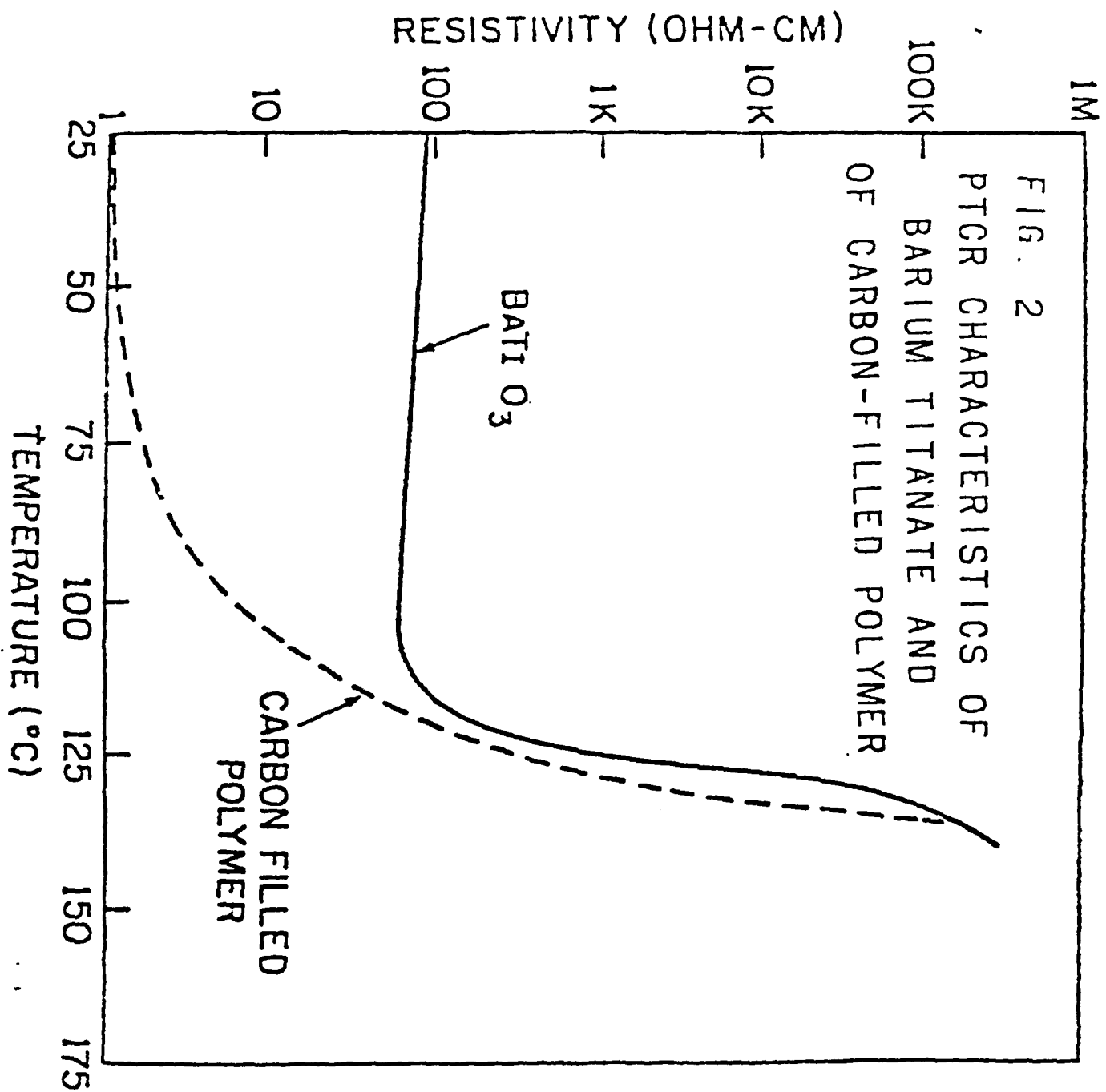


FIG. 2
PTCR CHARACTERISTICS OF
BARIUM TITANATE AND
OF CARBON-FILLED POLYMER



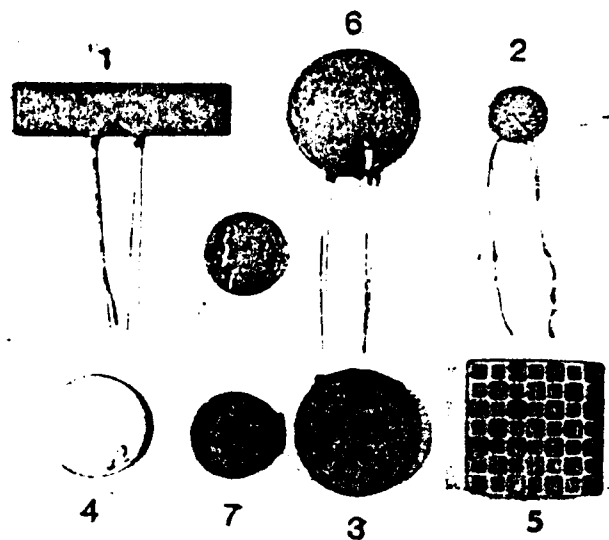


FIGURE 3 - PTC RESISTORS

- 1 CARBON FILLED POLYMER, EPOXY COATED
- 2 BARIUM TITANATE CERAMIC DISC, SOLDERED LEADS
- 3 BARIUM TITANATE ELECTRODED CERAMIC DISC
- 4 BARIUM TITANATE ELECTRODED CERAMIC DISC
- 5 BARIUM TITANATE ELECTRODED CERAMIC HONEYCOMB
- 6 CARBON FILLED POLYMER, EPOXY COATED
- 7 BARIUM TITANATE ELECTRODED CERAMIC DISC

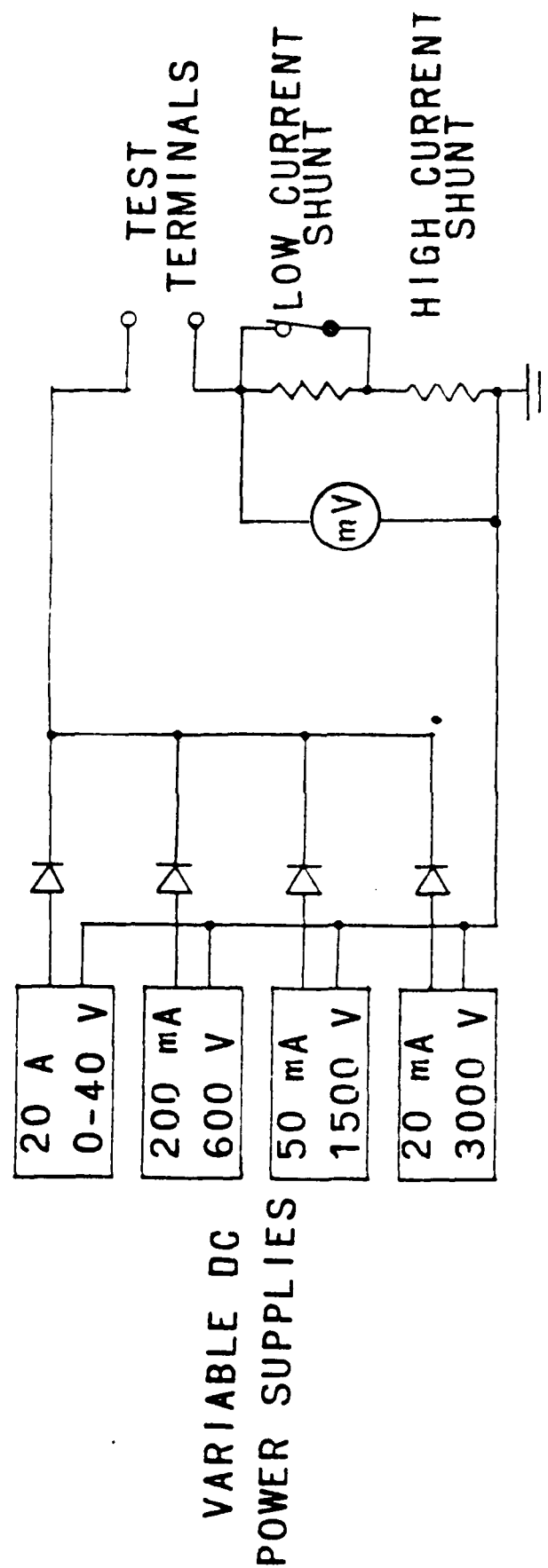


FIGURE 4
STEADY STATE MAXIMUM VOLTAGE TEST CIRCUIT

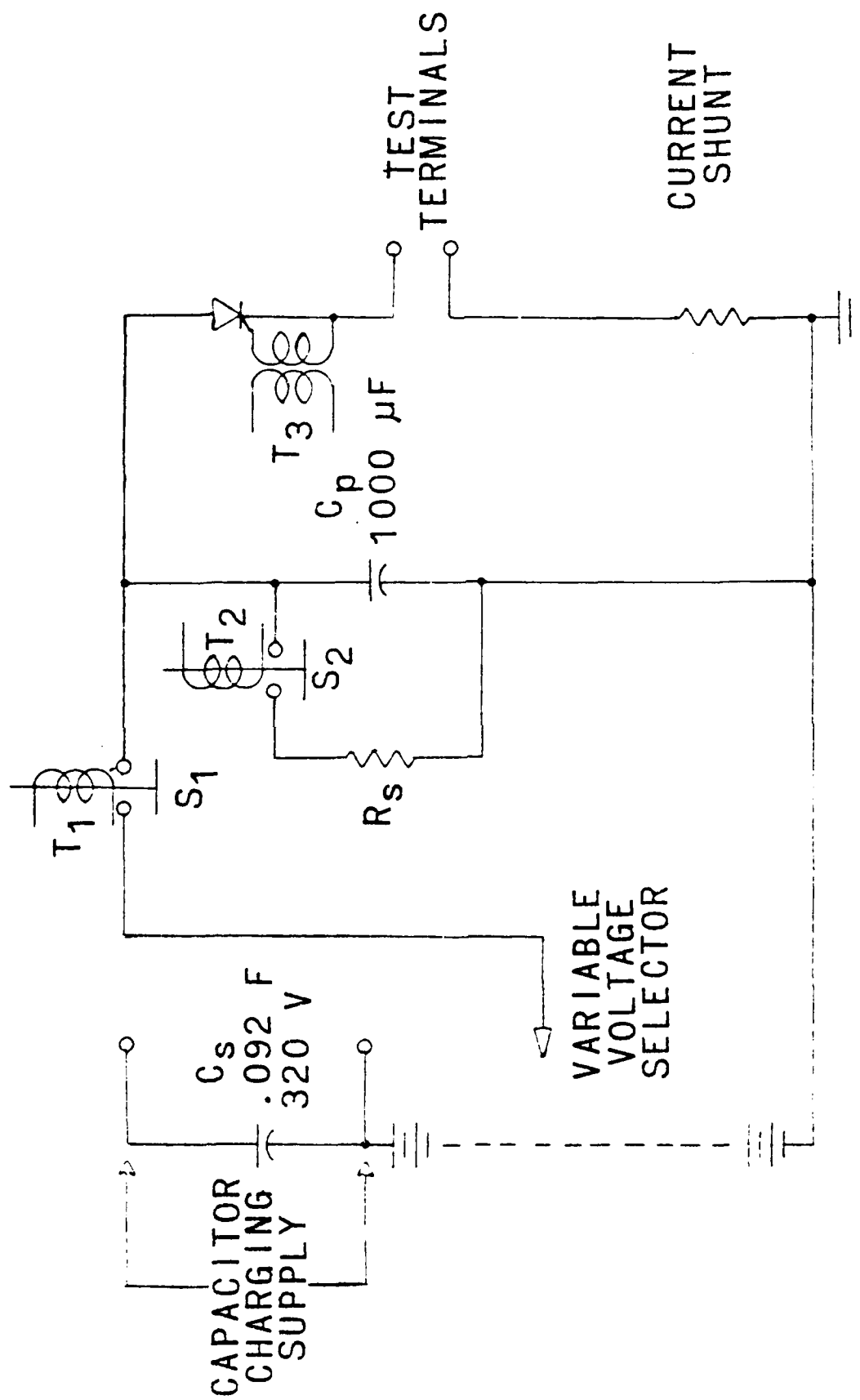


FIGURE 5
LOW IMPEDANCE, CURRENT FAILURE TEST CIRCUIT

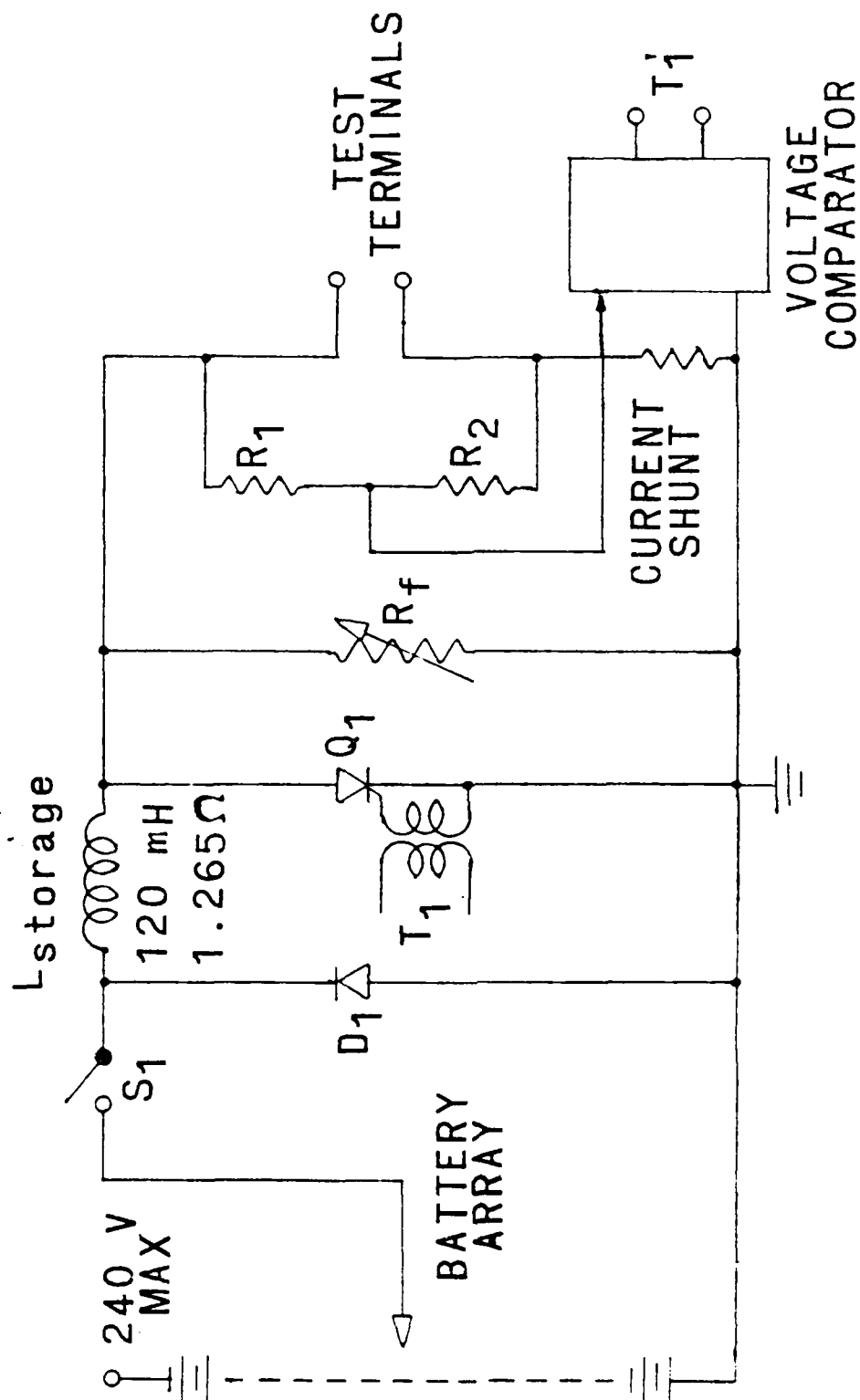


FIGURE 6
HIGH IMPEDANCE, CONSTANT CURRENT TEST CIRCUIT

TABLE #1

TYPES, DIMENSIONS, RESISTANCES AND FAILURE LEVELS OF PTCR DEVICES

Device Material	Type	Dimensions		Initial Cold Resistance		Max ¹ Steady State Voltage	Pulse Test Failure Levels		
							Low imp. test		
							I	V	high imp. test
		(in)		Small Signal	Large Signal	(V)	(A)	(V)	(A) (V)
				(Ω)	(Ω)				
carbon filled polymer	6	1.25 dia	0.065 ¹	7×10^{-3}	8×10^{-3}	55	760	120	
	1	2.13x0.5	0.09 ¹	17×10^{-3}	25×10^{-3}	215	700	>100	
Barium Titanate	4	1 dia	0.125	2.2	1.8	400	>150	250	360
	7	0.875 dia	0.125	6.9	5.2	595	90	420	600
	2	0.56 dia	0.063	17.5	25	215	60	86	

¹ Thickness of carbon filled polymer film is about .016"

FIGURE 7

COLD-RESISTANCES VS. PEAK PULSE CURRENT
FOR CFP TYPE#6 PTCR#8

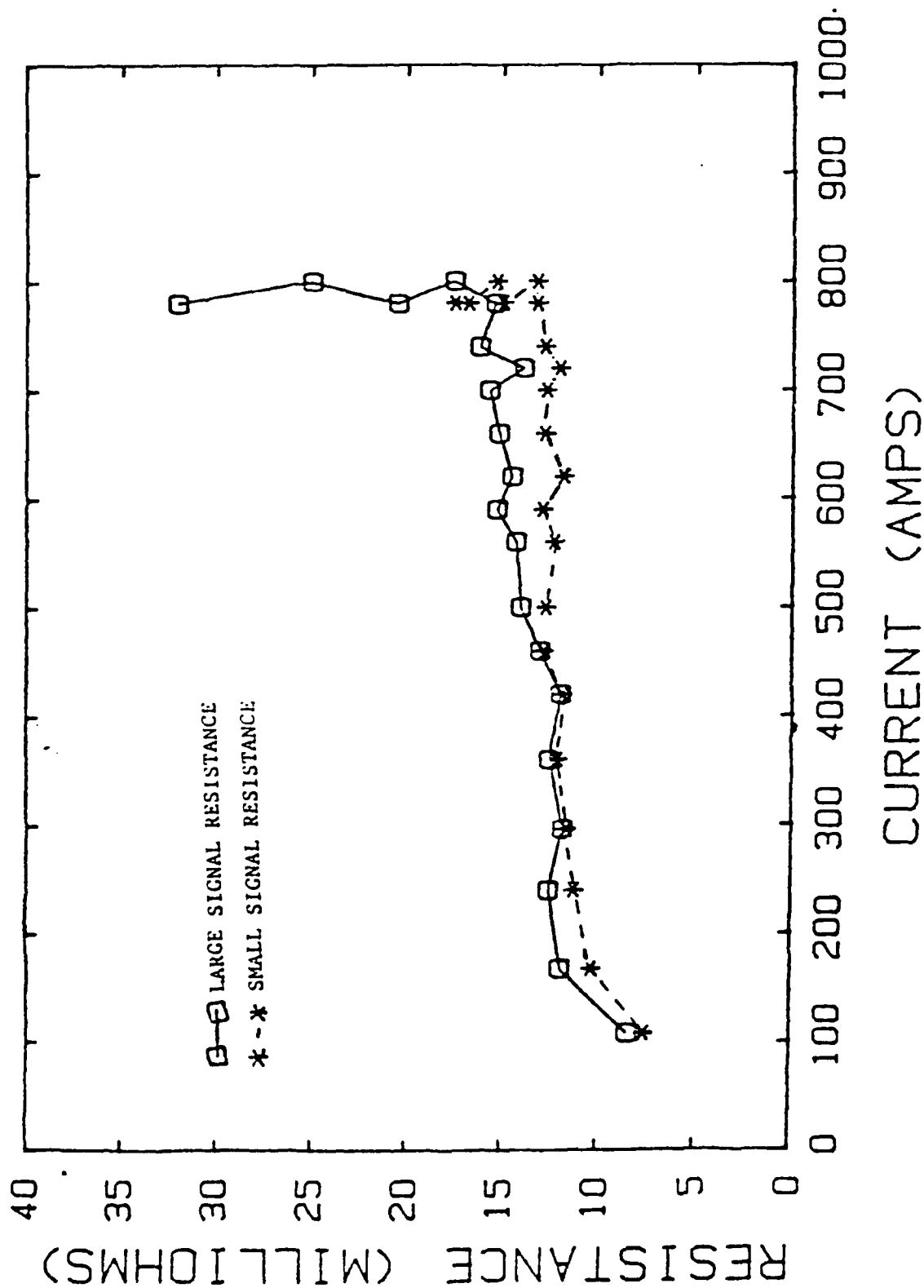


FIGURE 8
COLD LARGE-SIGNAL RESISTANCE VS PEAK PULSE CURRENT
FOR SIX CFP TYPE#6 PTCR'S

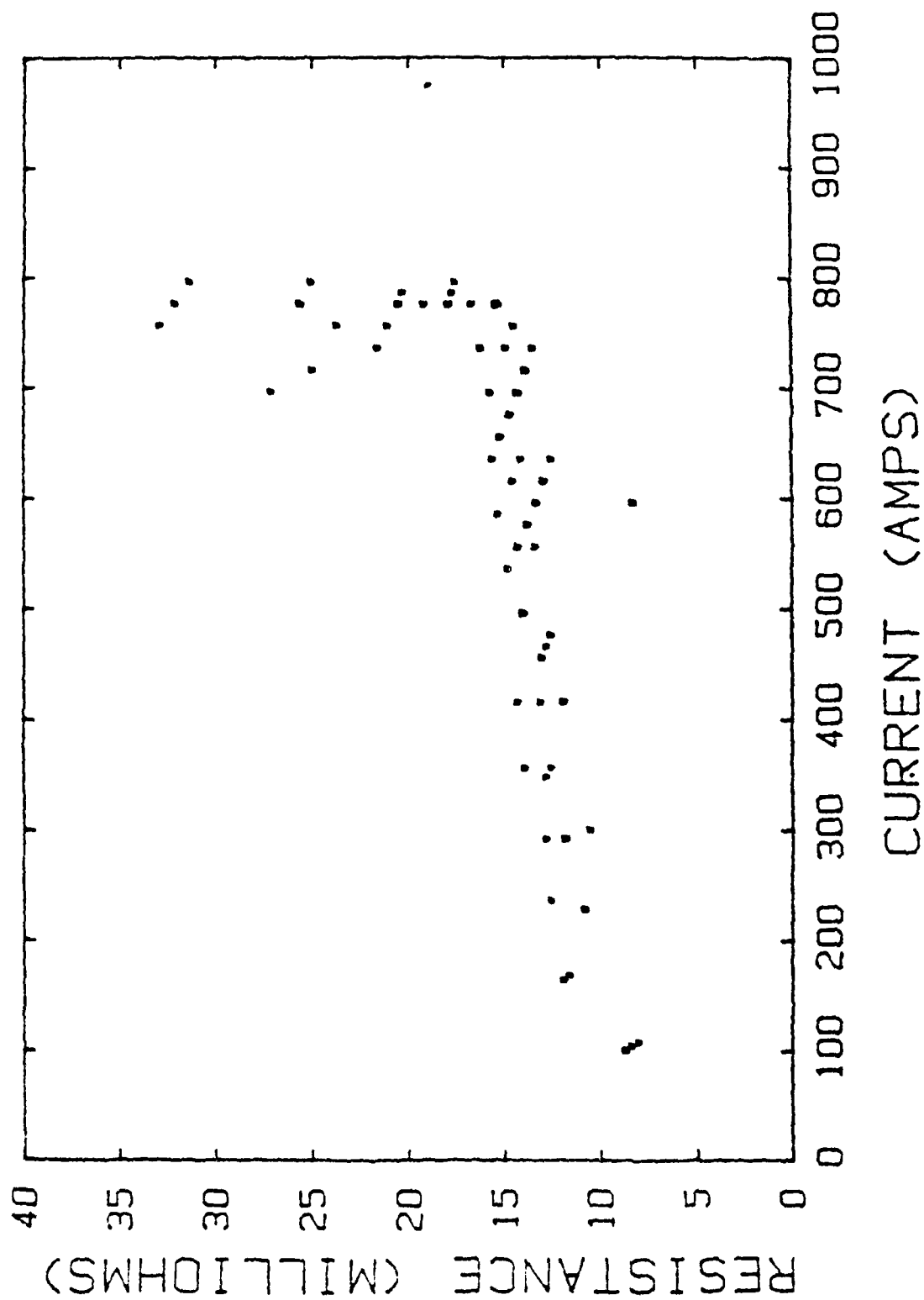


FIGURE 9
DURATION OF CURRENT PULSE AND CURRENT FALL-TIME VS
PEAK PULSE CURRENT OF SIX CFP TYPE #6 PTCR'S

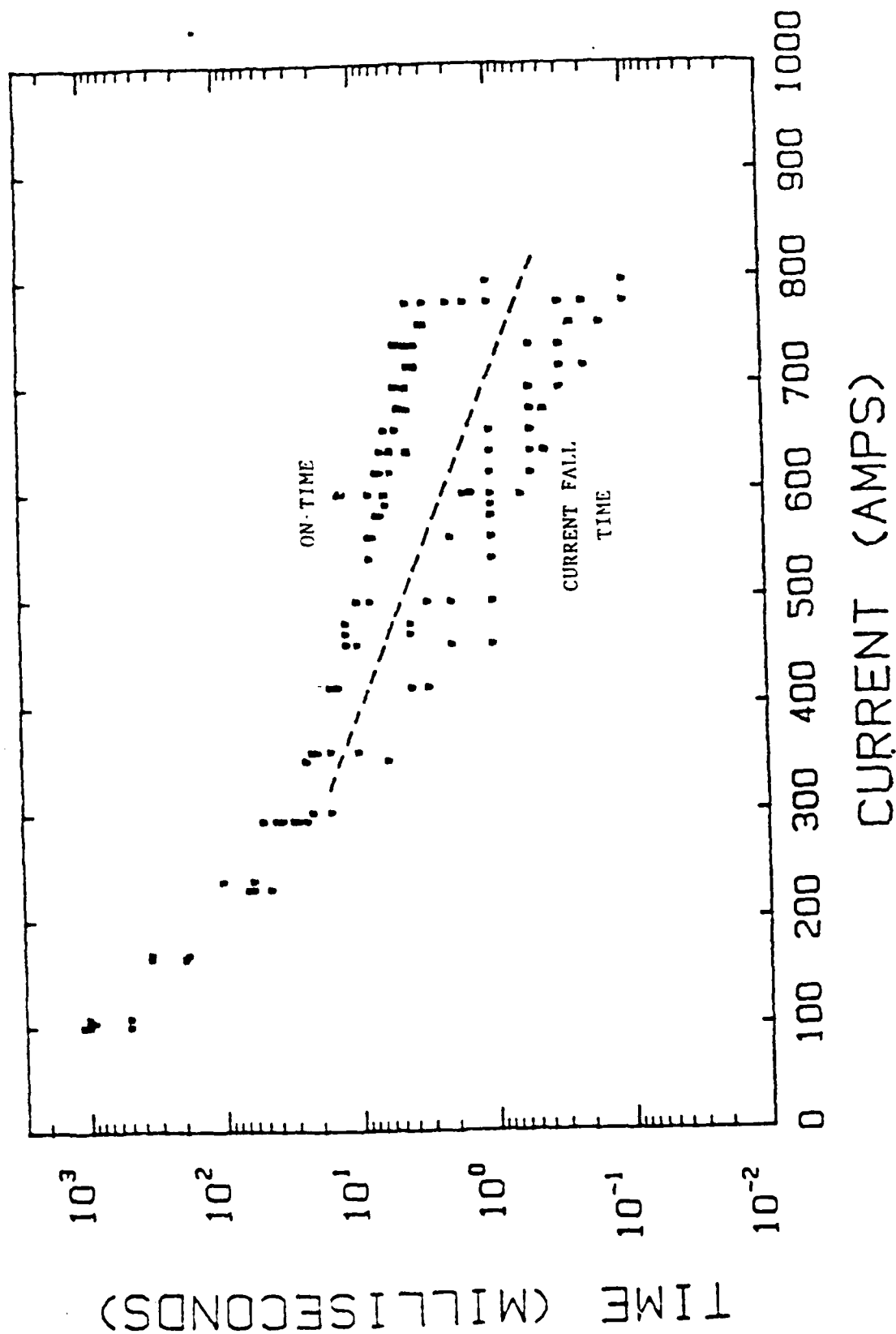


FIGURE 10

DURATION OF CURRENT PULSE AND VOLTAGE RISE-TIME
VS PEAK PULSE CURRENT OF SIX CFP TYPE # 6 PTCR'S

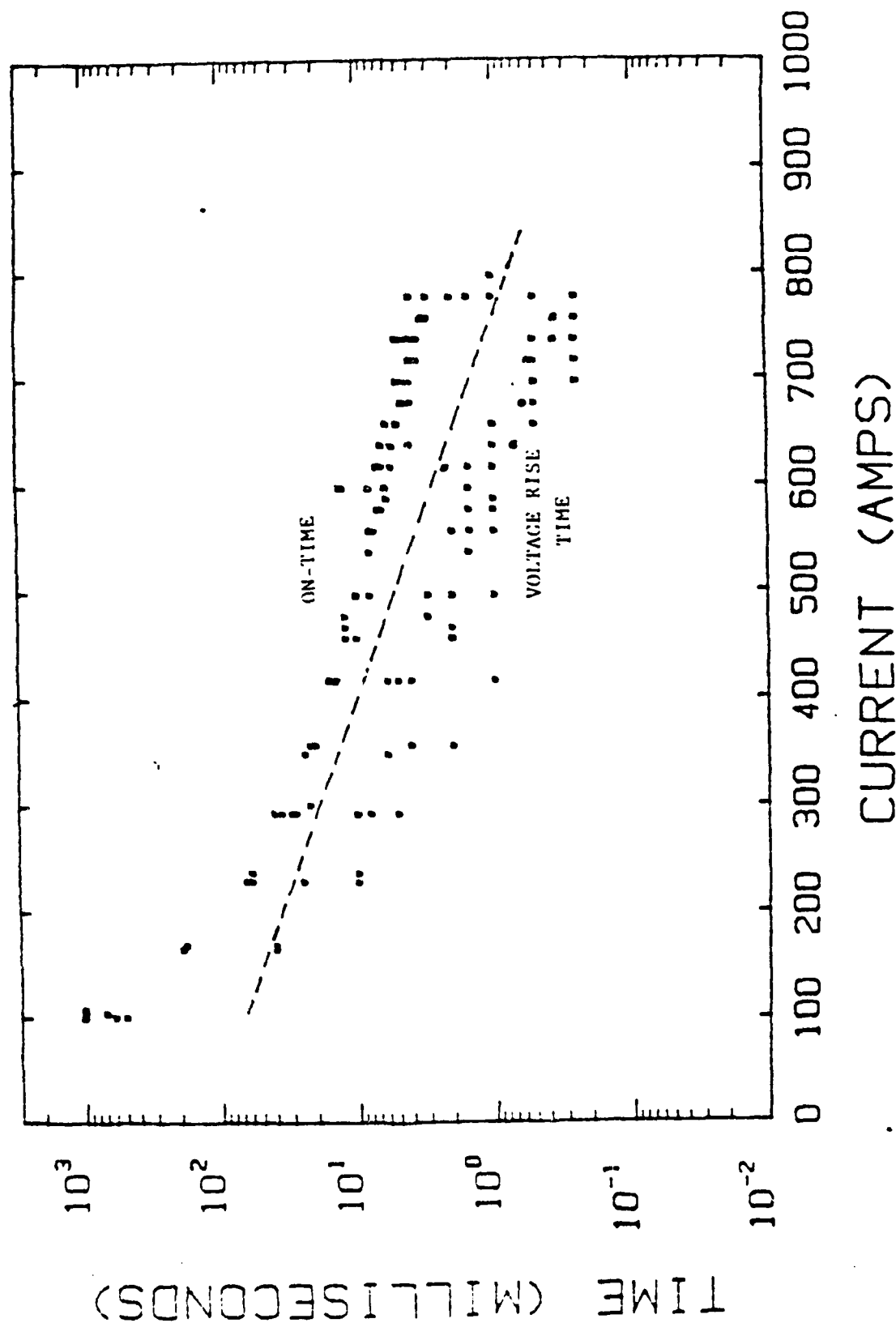


FIGURE 11
COLD LARGE SIGNAL RESISTANCE VS PEAK PULSE
CURRENT FOR FOUR CFP TYPE#1 PTCR'S

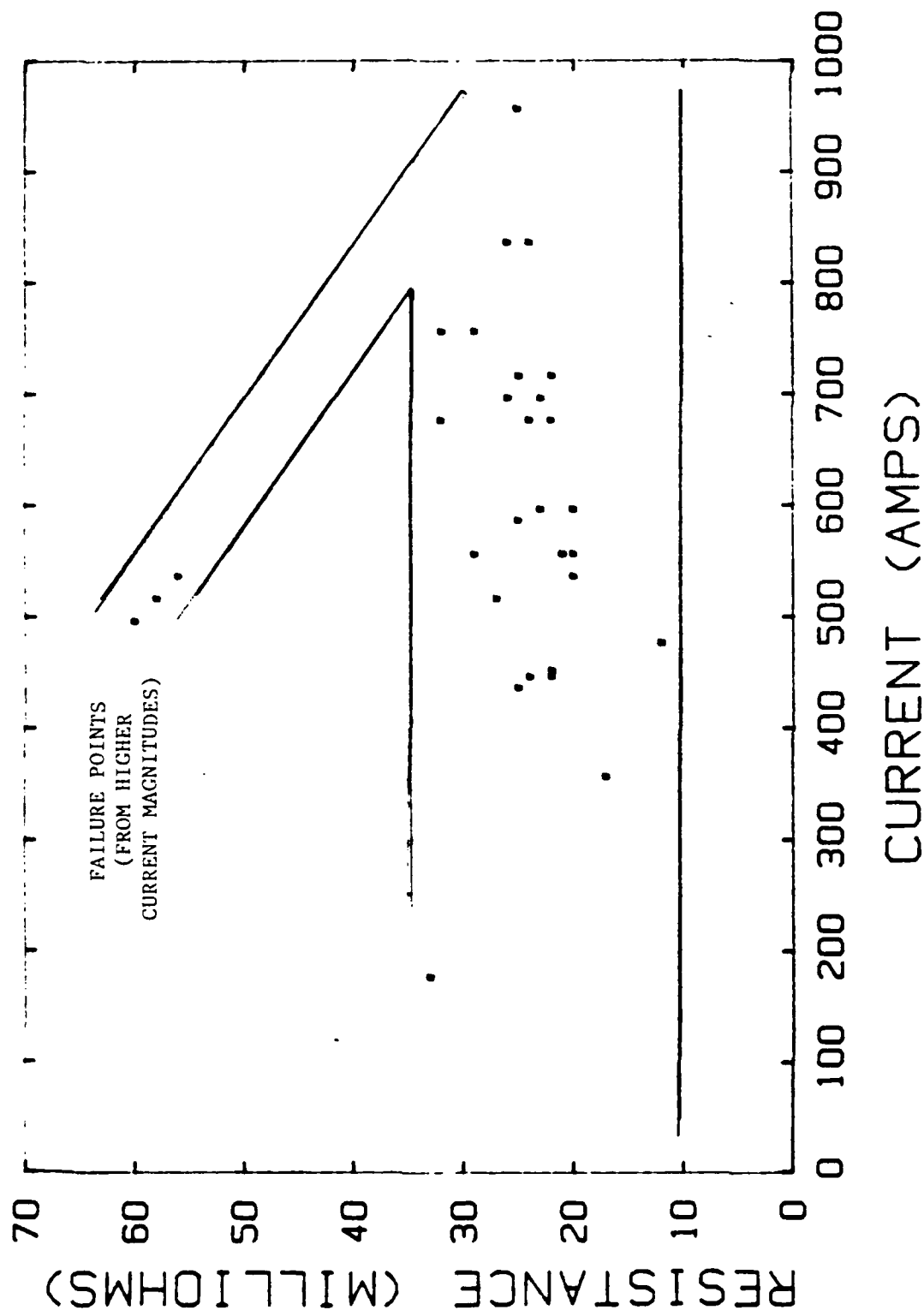


FIGURE 12
 DURATION OF CURRENT PULSE AND CURRENT FALL TIME
 VS PEAK PULSE CURRENT OF FOUR CFP TYPE#1 PTCR'S

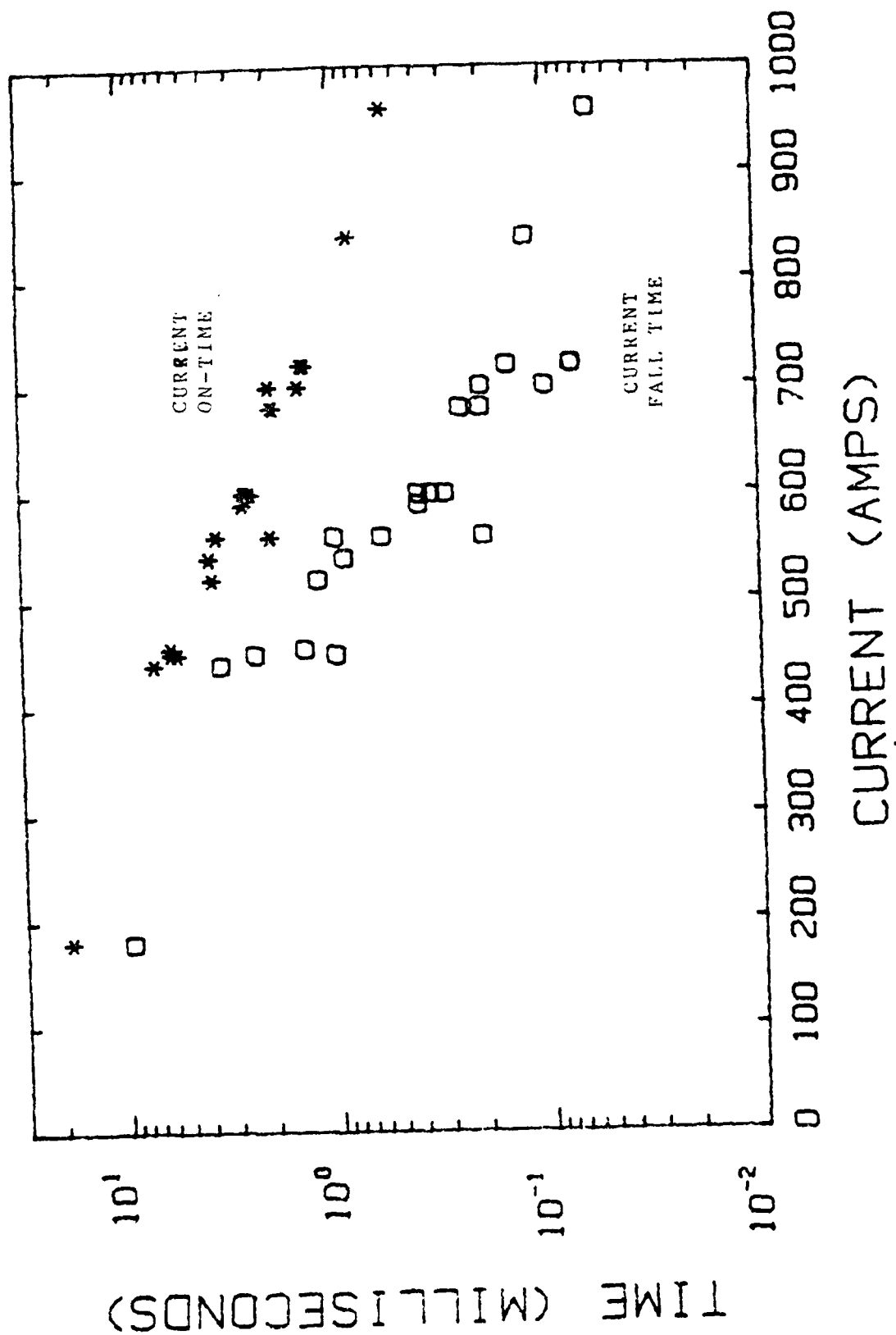


FIGURE 13

SMALL AND LARGE SIGNAL RESISTANCES VS APPLIED PULSE CURRENT FOR BaTiO₃ TYPES 4 AND 7 PTCR'S

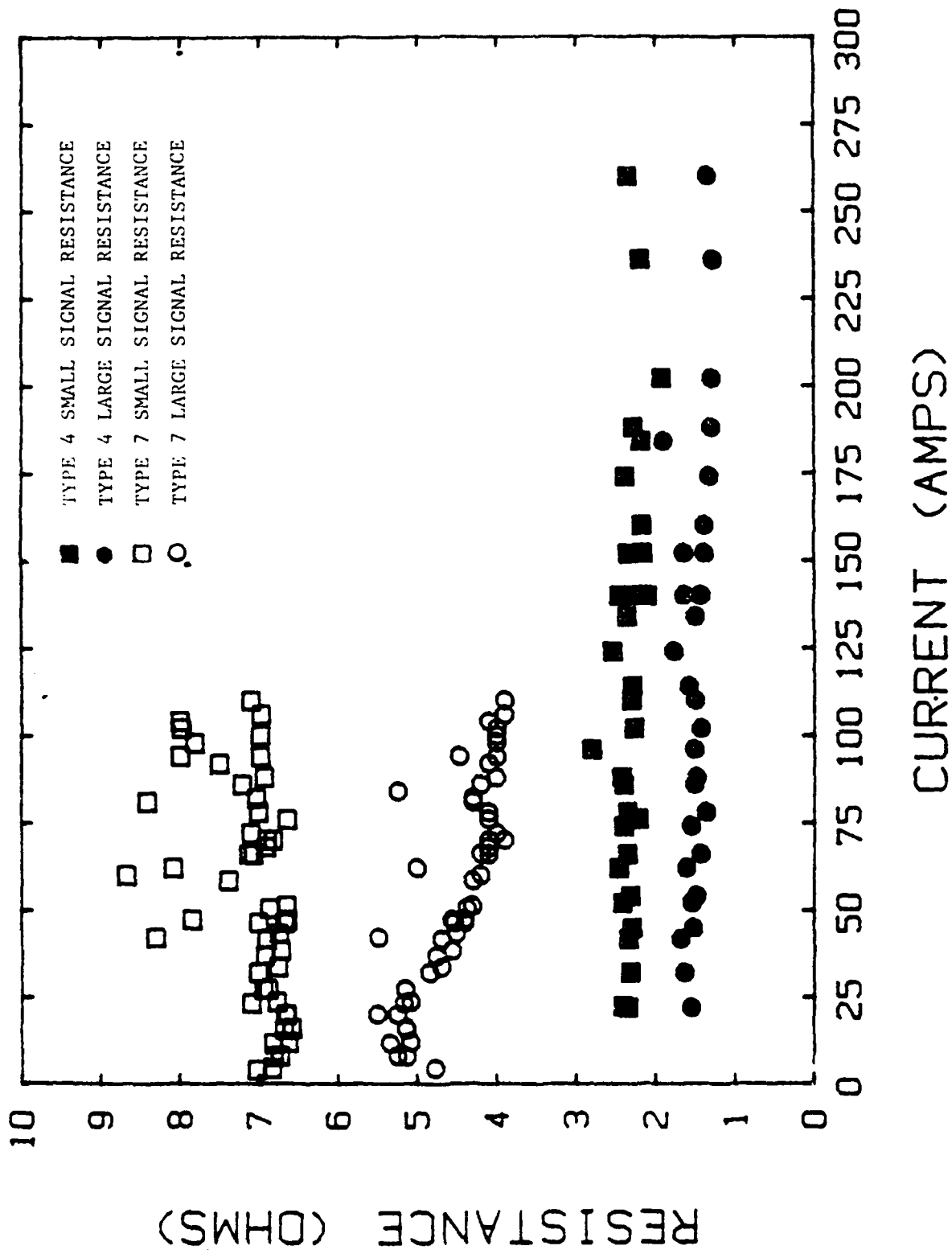


FIGURE 14
DURATION OF CURRENT PULSE VS PEAK PULSE CURRENT
FOR BaTiO₃ TYPES#4 AND#7 PTCR'S

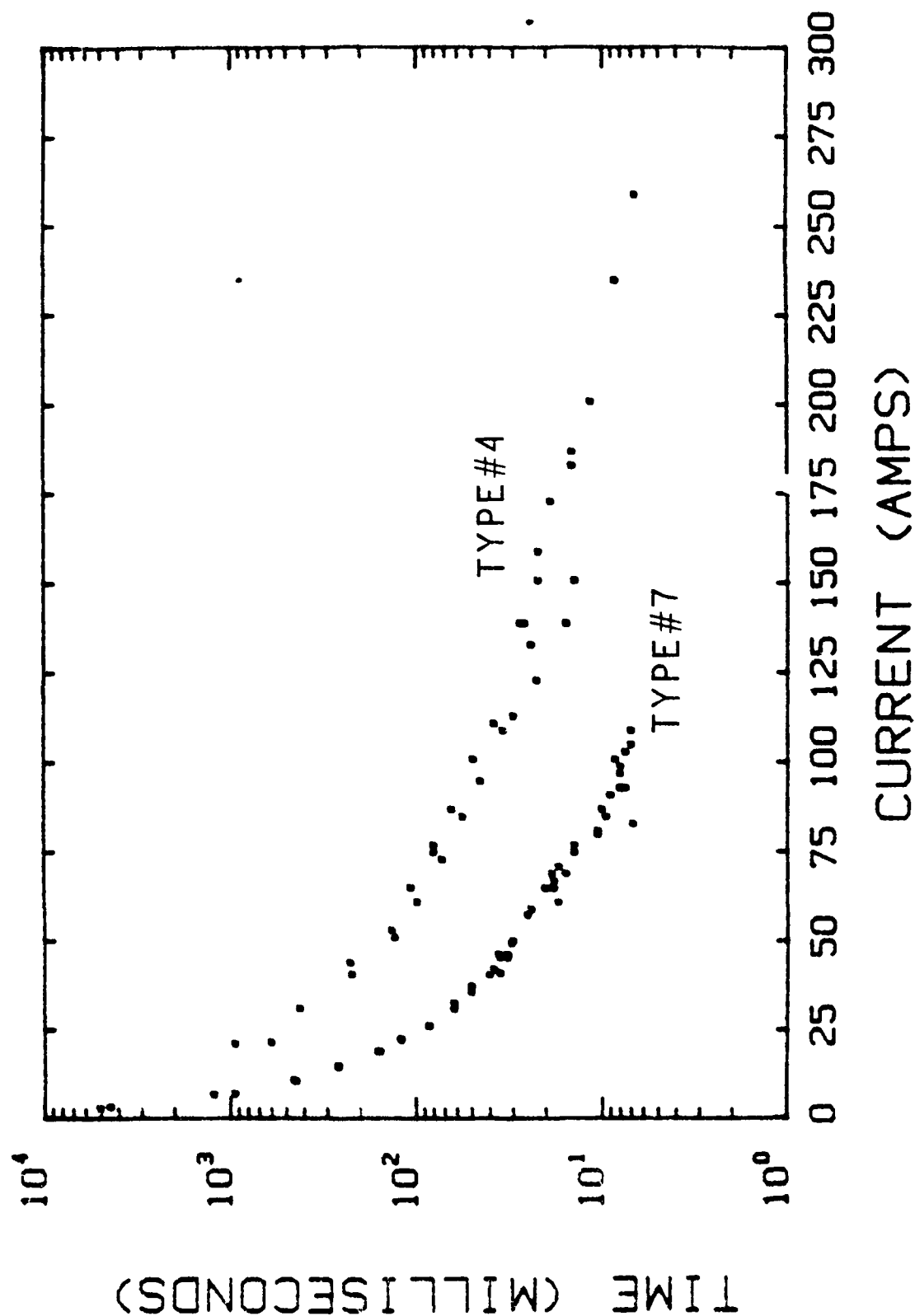


FIGURE 15
CURRENT FALL TIME VS PEAK PULSE CURRENT
FOR BaTiO₃ TYPES#4 AND#7 PTCR'S

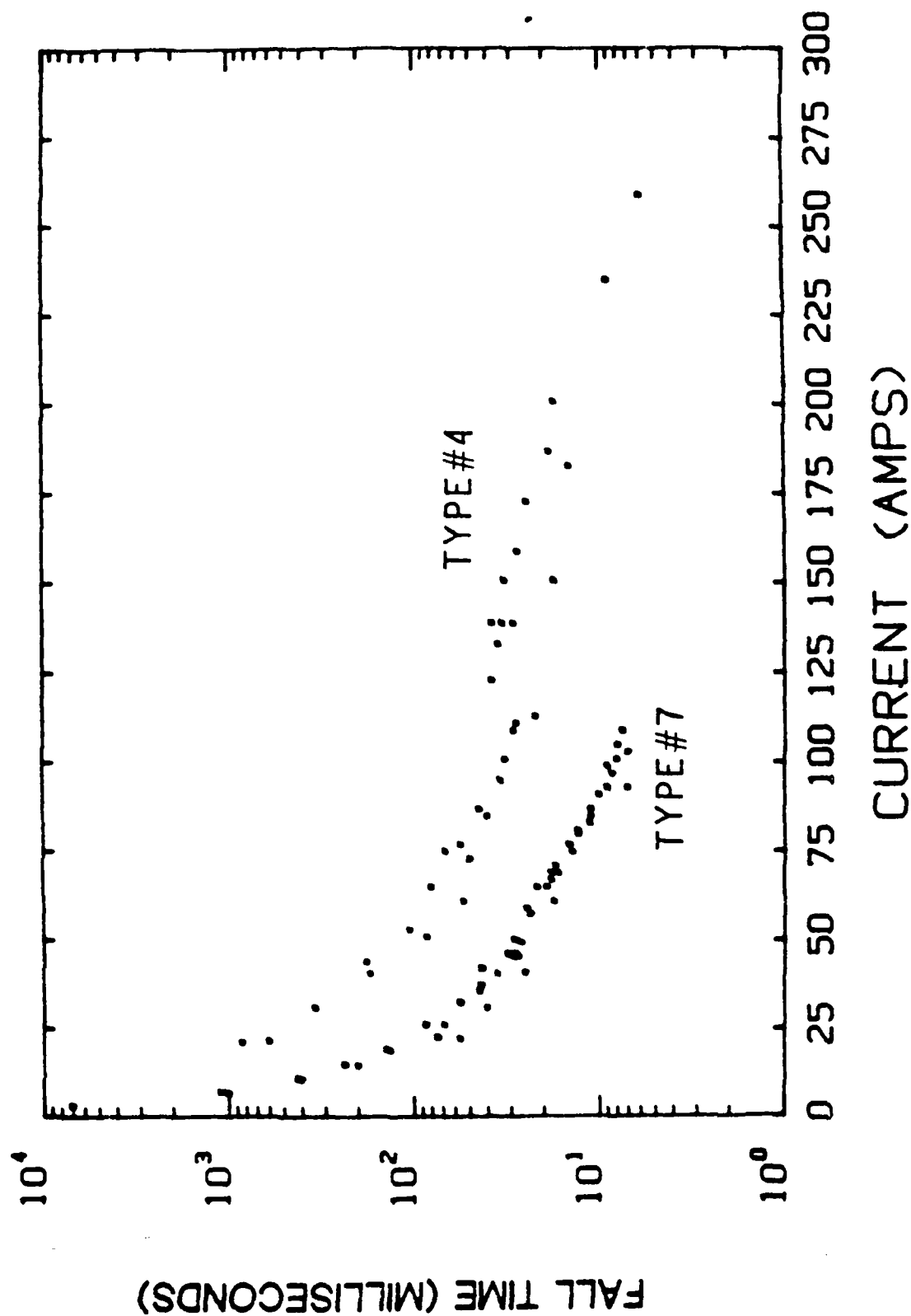


FIGURE 16
COLD RESISTANCE VS. PEAK PULSE CURRENT
FOR BaTiO₃ TYPE#2 PTCR#4

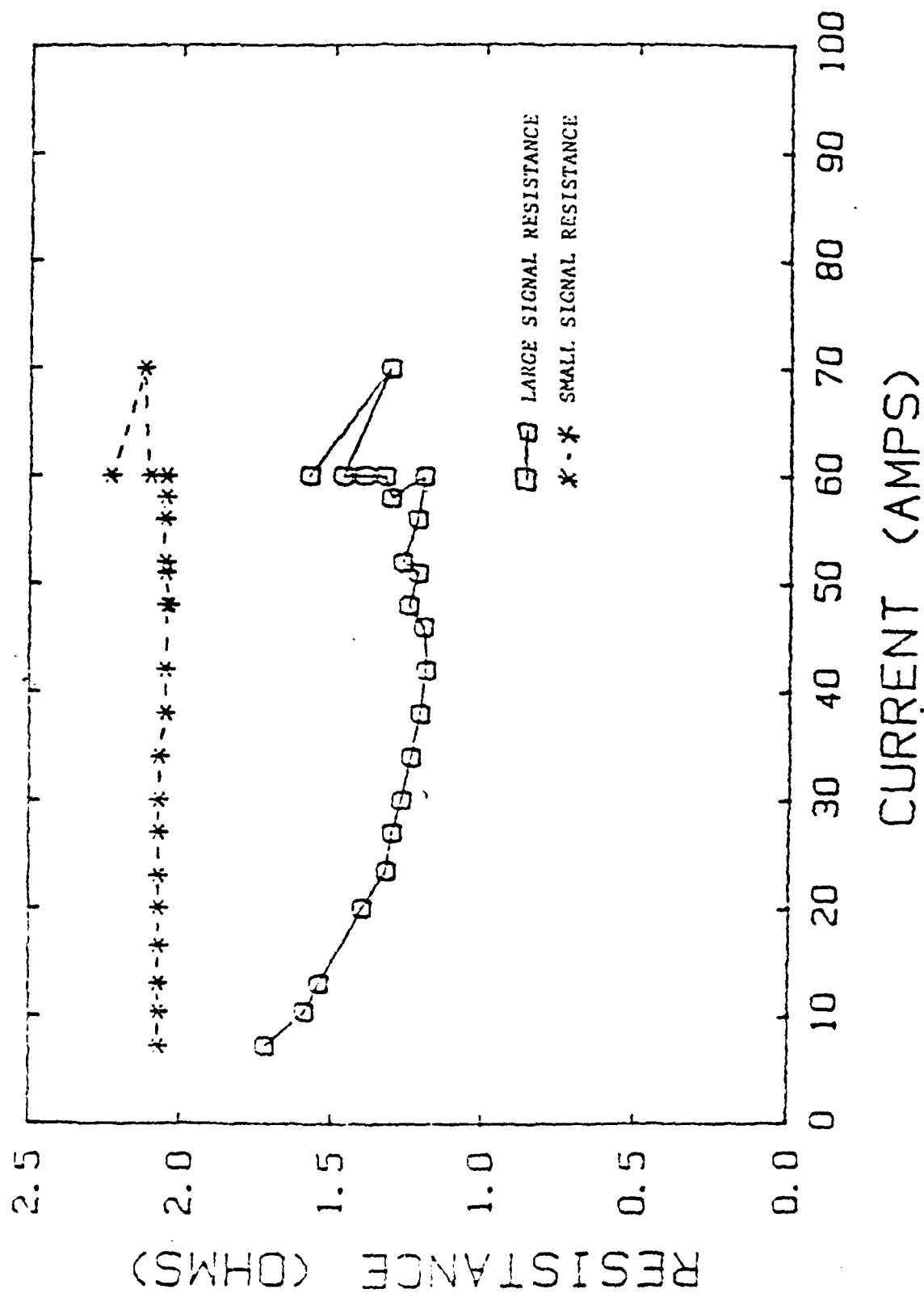
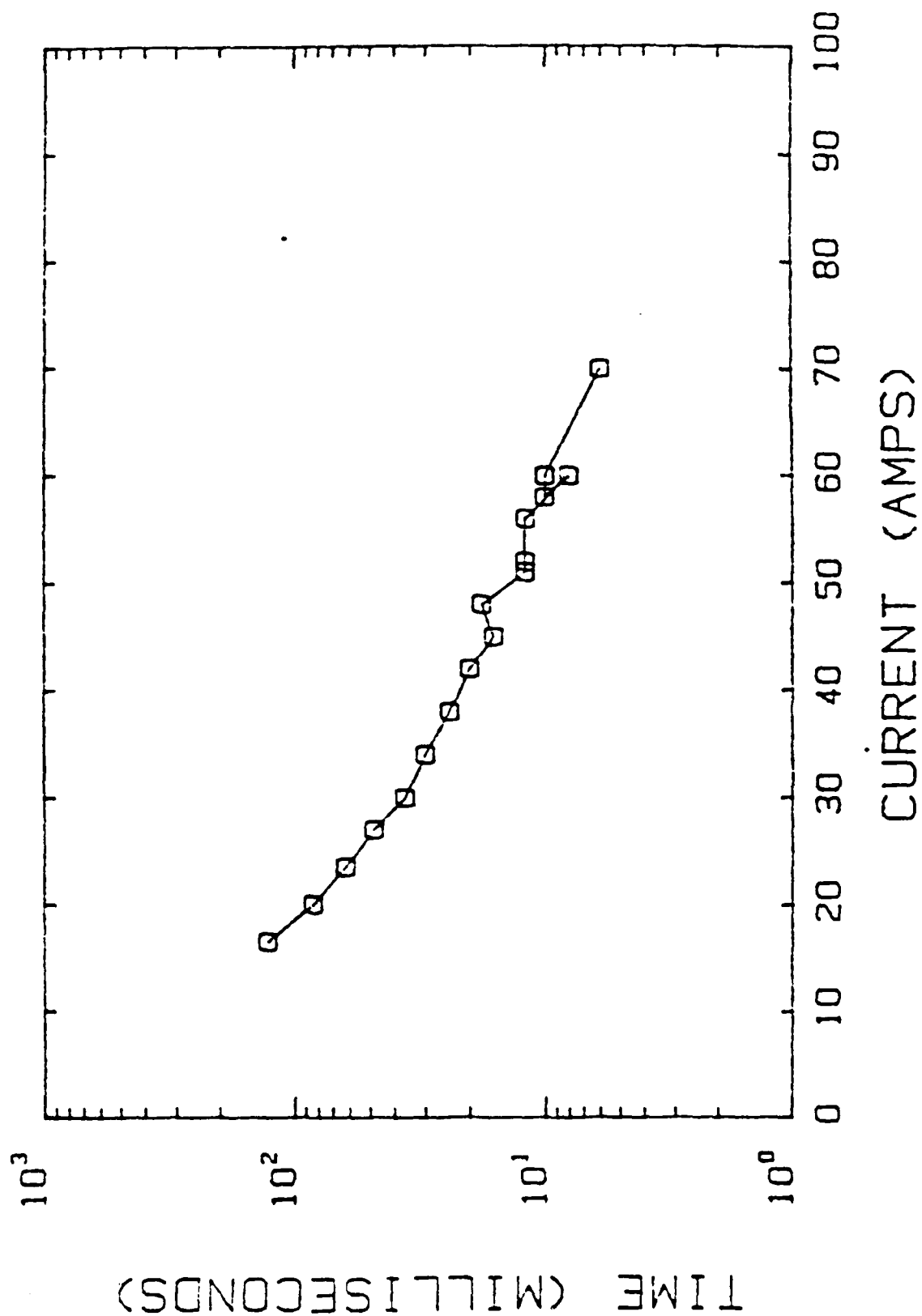


FIGURE 17
DURATION OF CURRENT PULSE VS PEAK PULSE
CURRENT FOR BaTiO₃ TYPE#2 PTCR#4



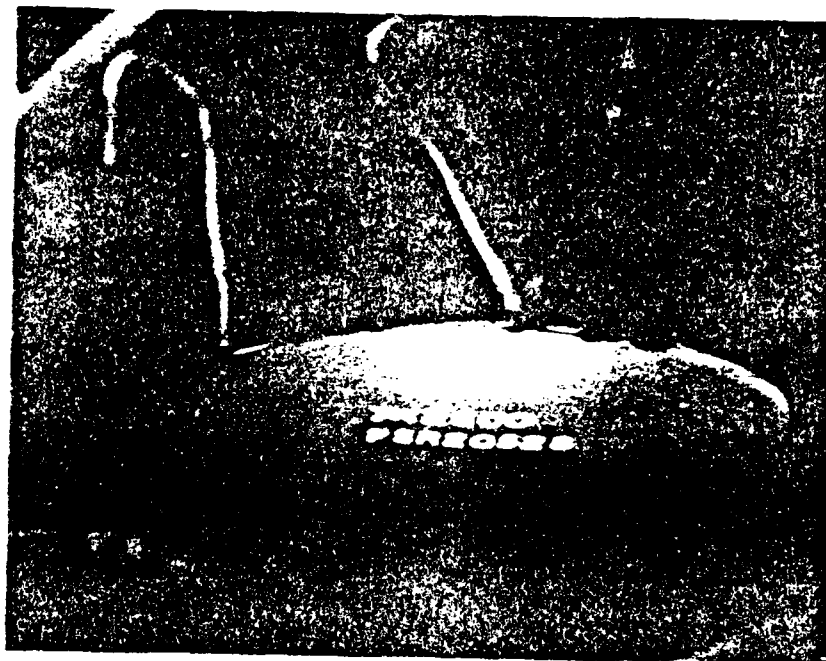


FIGURE 18
APPEARANCE OF VOLTAGE BREAKDOWN IN
CFP TYPE#6 PTCR#5

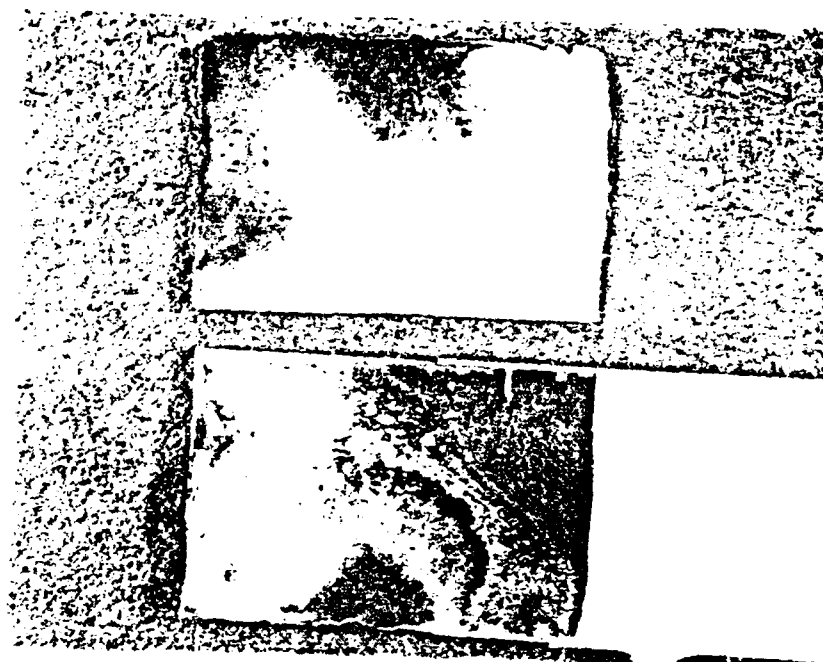


FIGURE 19
VOLTAGE BREAKDOWN IN TWO SPOTS
IN CFP TYPE#1 PTCR THERMAL RUNAWAY TEST#2

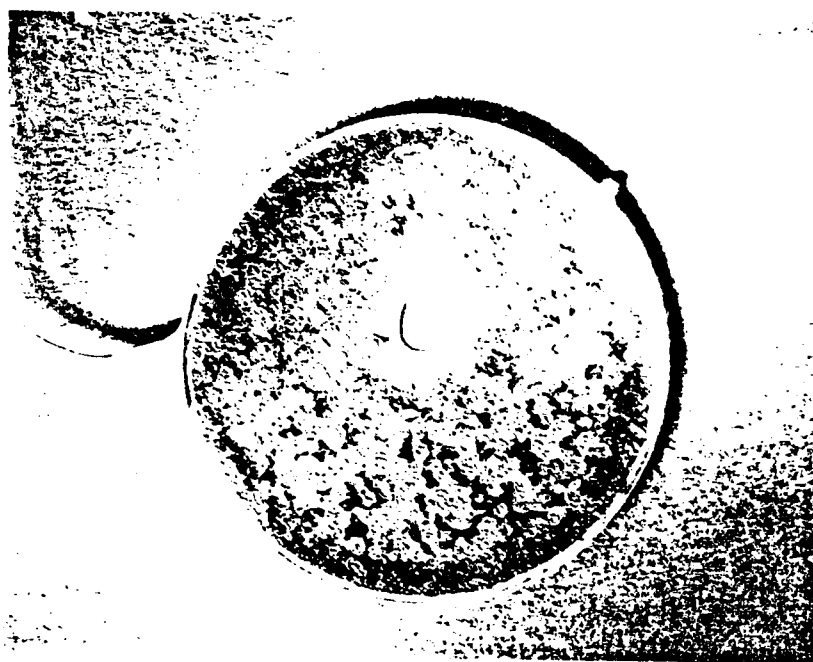


FIGURE 20
CURRENT FAILURE IN
CFP TYPE#6 PTCR

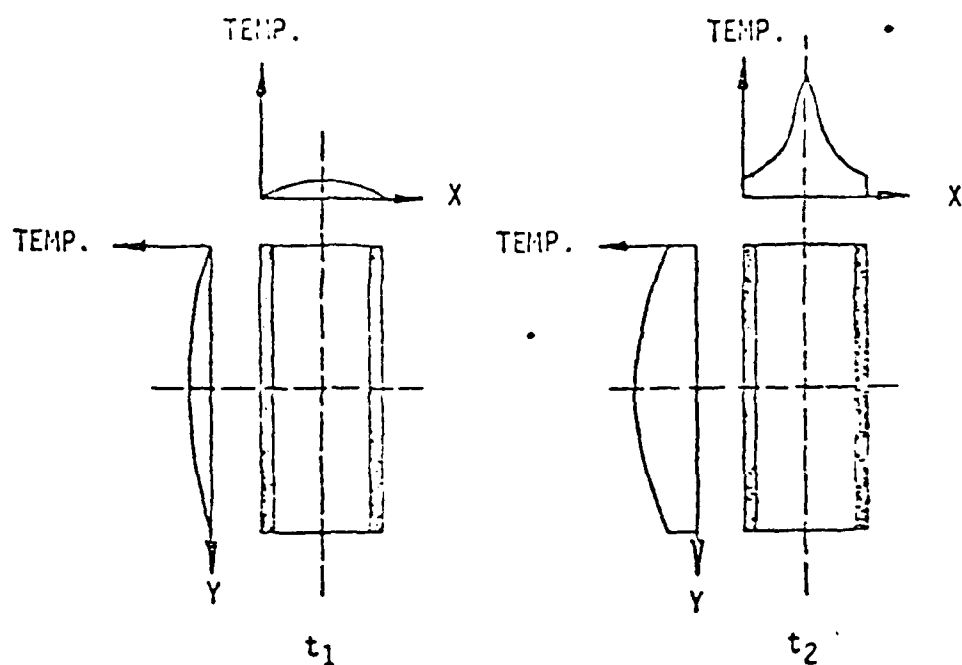


FIG. 21

Temperature distribution in a discoidal PTCR during fast heat-up. Y is the radial direction and X is the thickness, t_1 is the instant before the center of the part attains 85°C . At t_2 the resistivity increase in the central Y plane causes most of the power dissipation to be concentrated there, with an accompanying cumulative localized temperature rise.



FIGURE 22
CURRENT FAILURE (EDGE CRACK)
IN BaTiO_3 TYPE#2 PTCR#5

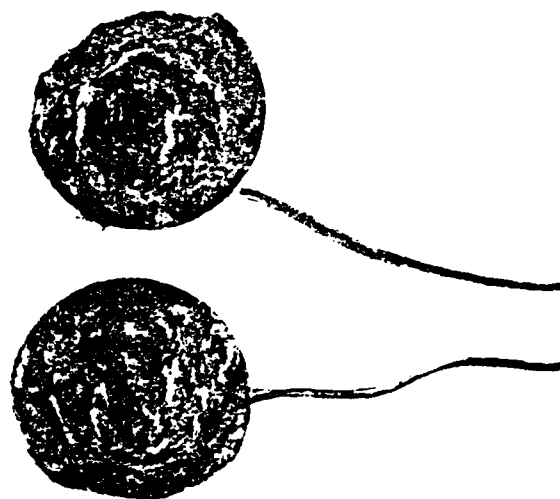


FIGURE 23
COMPLETE SPLIT DUE TO CURRENT FAILURE
IN BaTiO_3 TYPE#2 PTCR#5



FIGURE 24
EDGE CRACK CURVING TO MAJOR SURFACE
DUE TO EXCESS CURRENT IN BaTiO_3
TYPE#7 PTCR#3

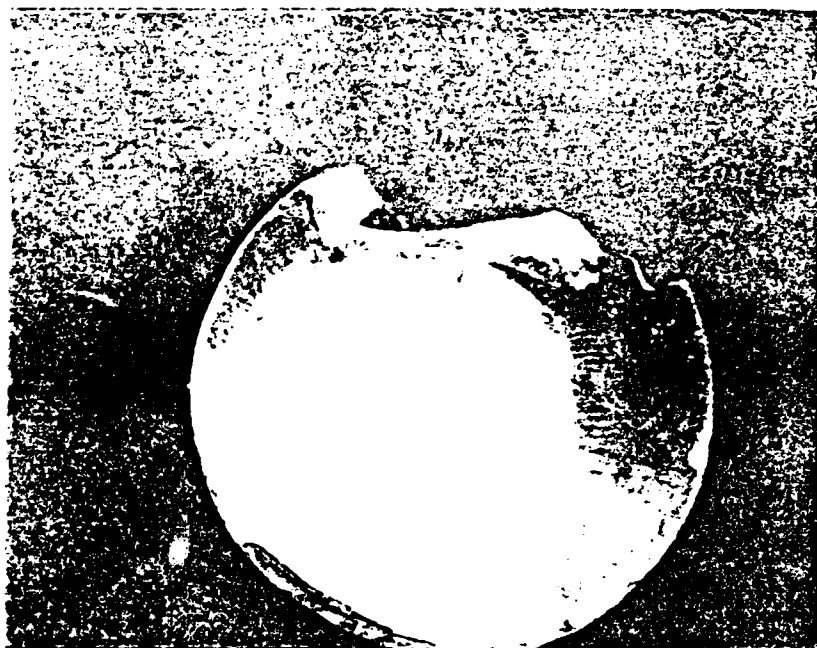


FIGURE 25
EDGE CRACK (LOWER LEFT) AND SEVERE
SHORTING DAMAGE (UPPER RIGHT) ON
 BaTiO_3 TYPE#4 PTCR#9

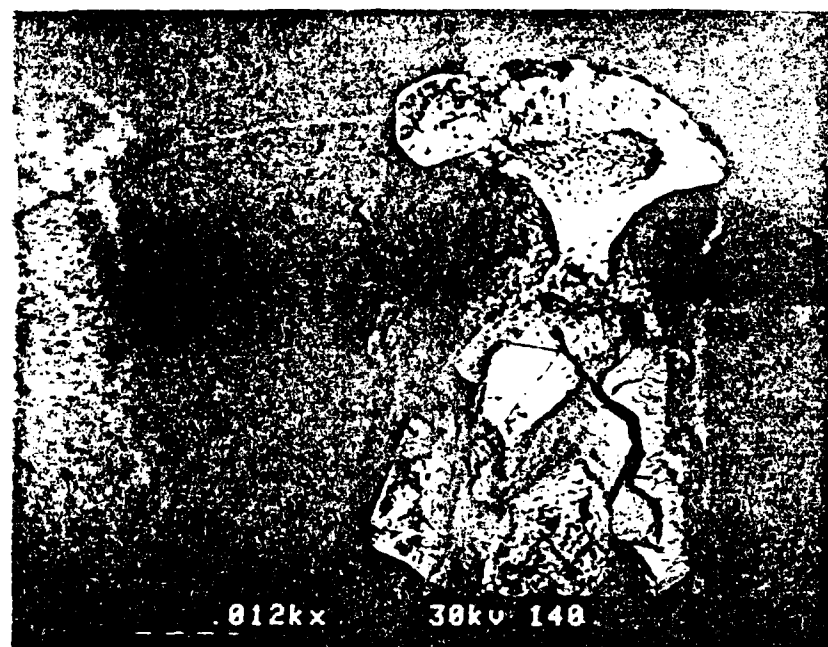


FIGURE 26
CROSS-SECTION OF SHORTING DAMAGE
IN BaTiO_3 TYPE#7 PTCR#3

FIGURE 27
MOLTEN AND RESOLIDIFIED
MATERIAL IN REGION OF
SHORTING DAMAGE IN
BaTiO₃ TYPE#7 PTCR#3



A



B



C



FIGURE 28
STALAGMITIC STRUCTURES HANGING FROM
CAVITY CEILING IN REGION OF SHORTING
DAMAGE IN BaTiO_3 TYPE#7 PTCR#3

FIGURE 29

"NEAR EDGE" BREAKDOWN.
WITH FROZEN AND
RECRYSTALLIZED MATERIAL IN
BaTiO₃ TYPE#7 PTCR#1

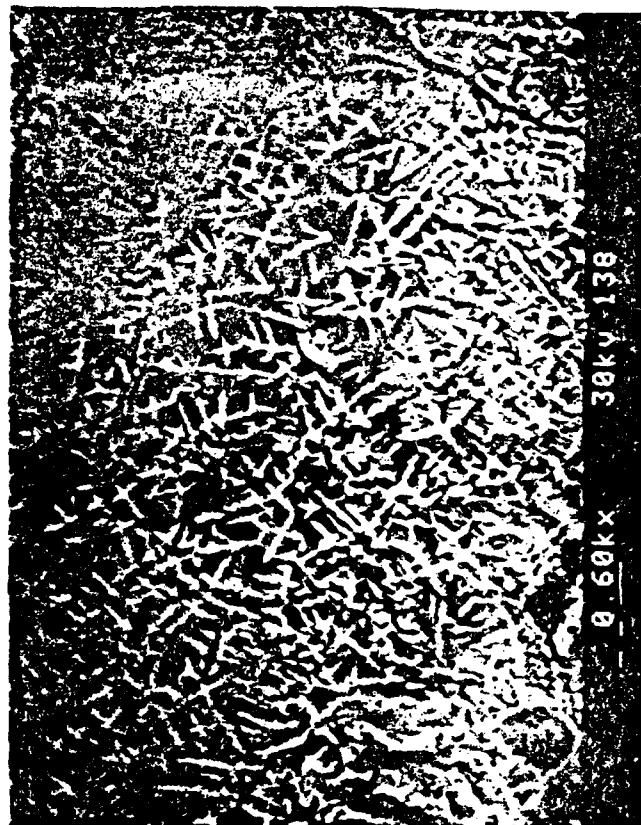
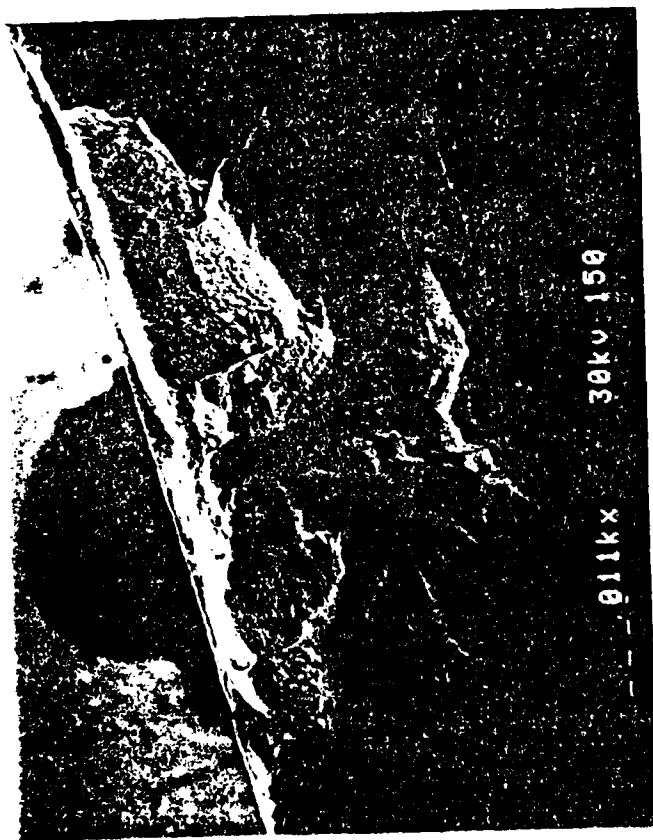
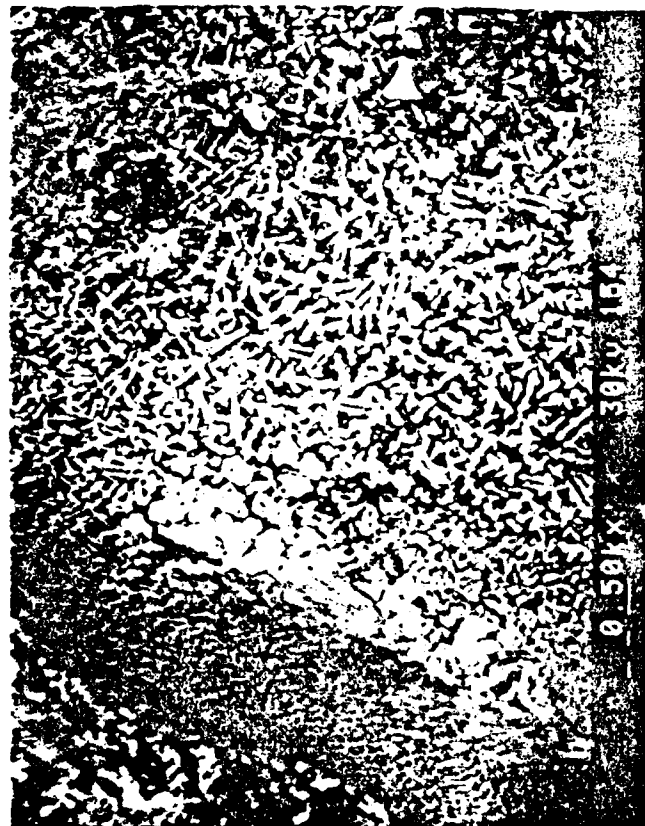


FIGURE 30

"NEAR EDGE" BREAKDOWN.
APPEARANCE OF RESOLIDIFIED
CHANNEL SURFACE IN BaTiO₃
TYPE #4 PTCR#7



A



047

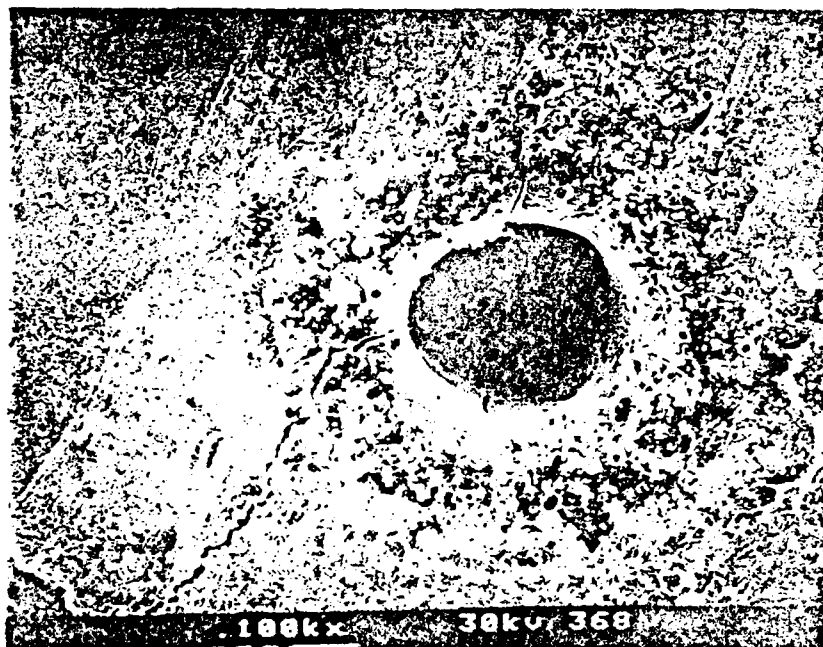


FIGURE 31
TERMINATION OF BREAKDOWN CHANNEL
ON ELECTRODED SURFACE, SHOWING HALO OF
RESOLIDIFIED BaTiO_3 , CRACKS AND
SURROUNDING ELECTRODE SURFACE IN
 BaTiO_3 TYPE#4 PTCR#7

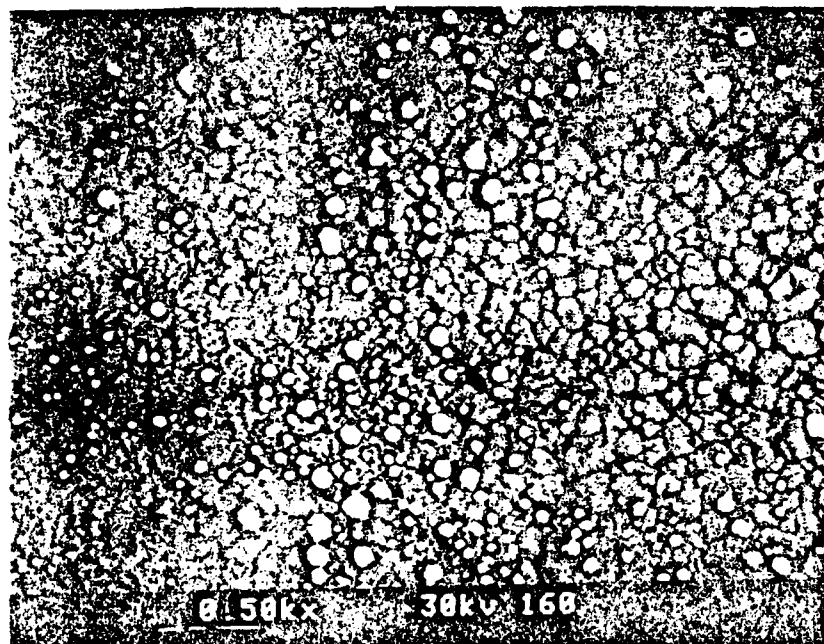
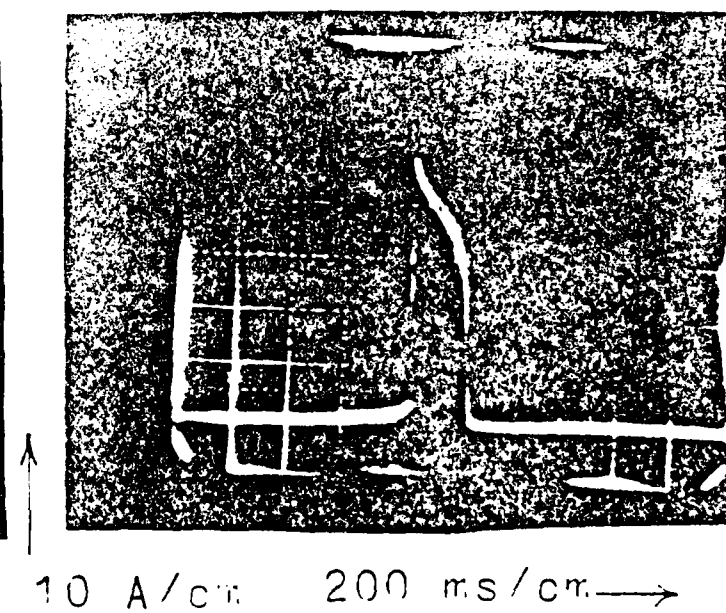
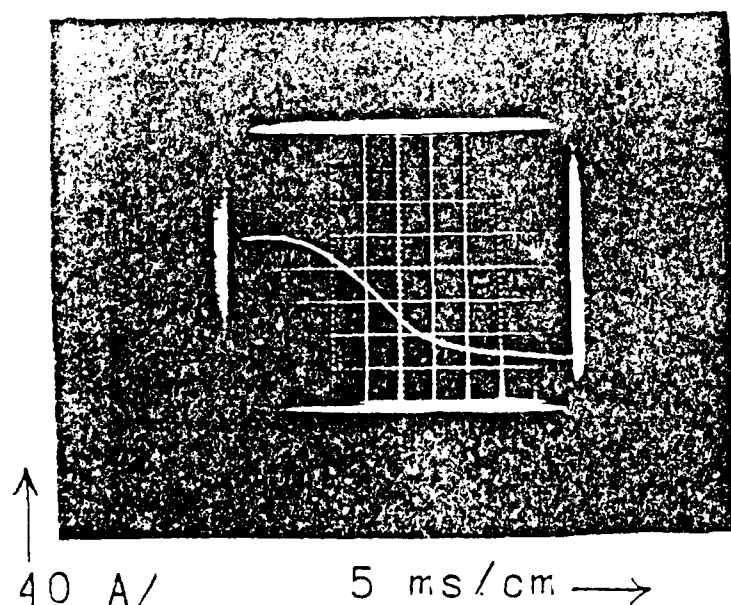
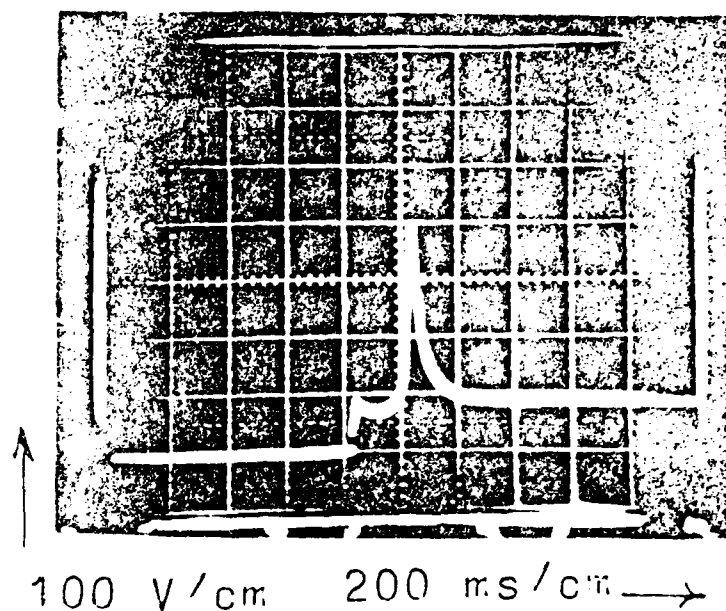
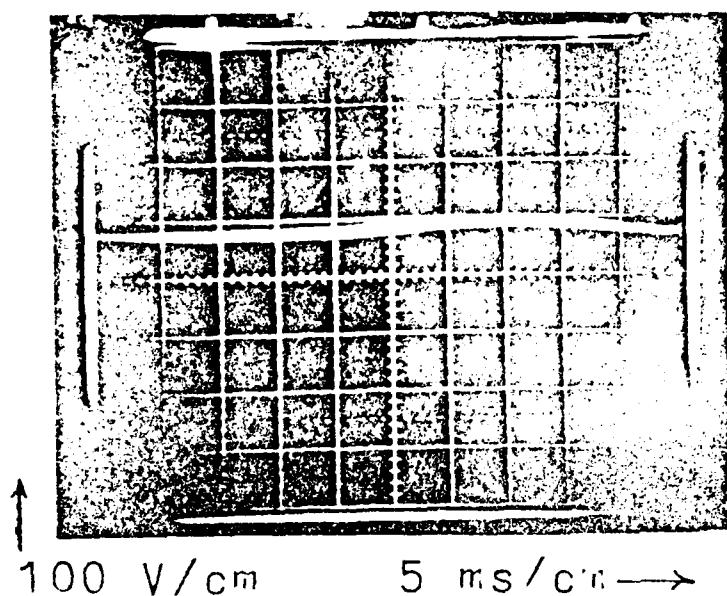


FIGURE 32
SURFACE APPEARANCE OF NARROWER CHANNEL
SECTION, SHOWING HIGH LEAD CONTENT
SPHERICAL STRUCTURES



LOW IMPEDANCE
SOURCE TEST

HIGH IMPEDANCE
SOURCE TEST

FIGURE 33
VOLTAGE AND CURRENT WAVESHAPES
BaTiO₃ TYPE#4 PTCR#7

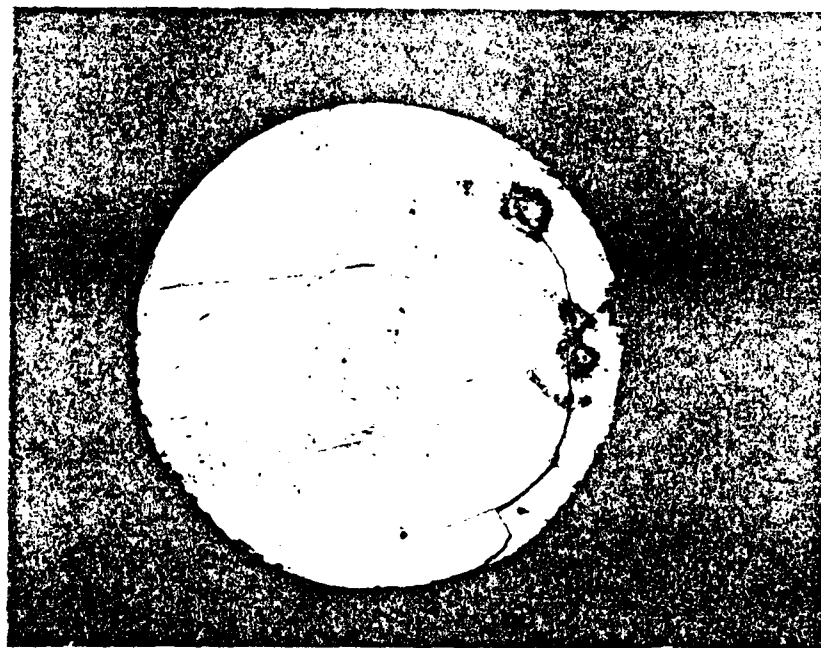


FIGURE 34
CIRCUMFERENTIAL CRACKING AND
MULTIPLE BREAKDOWN AFTER HIGH
IMPEDANCE PULSE TEST OF BaTiO_3
TYPE#4 PTCR#5

VII. GROUP DISCUSSIONS

GROUP 1

POTENTIAL MATERIALS FOR SOLID STATE SWITCHES

R. DAVIS
R. FORD
M. KAHN
W. NUNNALLY
M. O'MALLEY
T. RAO
R. REDIKER
J. SCOTT
G. SUNDBERG, CHAIRMAN

Potential Materials for Solid State Switches

Gale R. Sundberg, Chairman

NASA Lewis Research Center

Objective

The objective of this group was to briefly review the present state-of-the-art of semiconductor materials useful for switching applications, assess the status of selected materials for photoconductive and power switching applications, and identify the research areas where work is needed on the semiconductor materials.

Approach

After some discussion the group decided to put together a chart giving an overview of semiconductor materials that are presently being used for switching applications. The chart shown as Table 1 also includes potential new materials known to the group. The numbers and listed parameters are, in general, order of magnitude since we did not have access to correct values. They were, however, sufficient for comparison purposes.

The next step was to examine the desired characteristics for photoconductive closing switches and for power switches. Tables 2 and 3 show the important parameters and four of the leading candidates for each type of switch.

Finally, the group selected six candidate materials with interesting characteristics for future space power switching applications. Table 4 shows the status of six materials and a brief summary of the research directions required to improve ratings, characteristics and/or to move material in research into the arena of application.

Material Requirements

Material requirements for photoconductive switches are high resistivity and high carrier mobility. Also desirable are a long recombination time (at least much larger than the pulse duration), optical absorption depths about equal to electrical skin depth, low resistance, injecting, ohmic contacts to the material and low cost. From Table 2 we see some interesting tradeoffs between Si and GaAs. The higher resistivity and mobility makes GaAs look attractive for higher switch efficiency, power handling and lower heating, but Si has greater flexibility in control of carrier lifetime leading to a greater energy gain and much lower cost. Material requirements for power switches are based on the criteria for defining a good switch. A good switch has two stable states - open (OFF) and conduction (ON) -

and two transitional (switching) states that correspond to moving from one state to the other. The OFF state requires high breakdown voltage and high resistivity (low leakage currents), while the ON state requires low voltage drop, low resistivity and high current density. For highly efficient operation the transition (or switching) states require high mobility and short recombination times as the device switches from one state to another. Another desirable feature is low drive power to control the switching action from OFF to ON or vice versa. For high power devices thermal limiting factors of maximum temperature, thermal conductivity and thermal resistance to a heat sink are also critical for stability and reliability. Cost is also a driver.

From Table 3 the trade-offs are quite interesting. Si presents the most mature and functional technology for today's power switching applications using junction devices. Better material processes and new topologies permit higher voltage, current switches that are faster and more efficient. New work on deep impurity, double injection techniques in bulk silicon show promise to push the switching voltages up by a factor of 10 with operation at temperatures to 300°C and in radiation environments approaching a gigarad. Direct bandgap materials, though they have attractive high resistivities, high mobilities and short recombination time have many fabrication and stability problems for power switches. Thus, they have not challenged Si. SiC looks very attractive as a high temperature switch (500°C) with very good thermal conductivity. The technology, however, is yet in its infancy.

Summary

Si is still the material of choice as a baseline material for both photoconductive and power switches. Si technology is highly developed, the processes well known and devices characterized for many applications. Table 4 summarizes the groups findings during the time available for discussion. SiC shows much promise for high temperature applications if it can be processed reproducibly, doped adequately and suitable ohmic contacts can be devised. Other materials shown in addition to GaAs are fundamentally still laboratory devices requiring much work and further demonstrations to prove their feasibility as switches.

Someone in our group summarized the discussion with the statement, "The best material is the one that fits the application!" For most applications that best material as of today is still silicon. Even as new materials appear on the horizon to challenge its position much work on silicon material and new devices continue to push it to higher voltages, higher power, faster switching speeds with more efficient operation in all types of switching applications.

1. Photoconductive
2. Junction
3. Opening
4. Closing
5. Thermally Activated
6. Magnetically Activated
7. Phase Transition

448

TABLE 2. PHOTOCONDUCTIVE CLOSING SWITCH CHARACTERISTICS

Material	Intrinsic Resistivity $\Omega \cdot \text{cm}$	Mobility Electron and Hole cm^2/volt	Recombination Time, τ_R	Energy Gain $\frac{V_{IR}}{(\text{Optical})}$	Optical Absorption depth cm	Cost
Desired	$>10^5$	High	Large $\tau_R \gg \tau_{\text{pulse}}$	High*	About Equal to electrical skin depth	Low
Si	2.3×10^5	1925	ns to ms	10^5	1 for 1.06μ	Lowest
GaAs	10^9	9300	ns	10	1 for 1.06μ	High
SiC	10^9	525	no to μs	?	?	Higher, should decrease
GaP	10^7	450	ns	?	?	High

* Highly dependent on laser wavelength

TABLE 3. POWER SWITCHES: JUNCTION AND BULK DEVICES

Material	Intrinsic Resistivity, $\Omega \cdot \text{cm}$	Mobility Electron and Hole cm^2/volt	Recombination Time, τ_R	Breakdown Field, V/cm	Current Density, A/cm^2	Cost
Desired	$>10^5$	High	Low	High	High	Low
Si	2.3×10^5	1925	ns to ms	10K: Junction 65K: Bulk	50K	Lowest
GaAs	10^9	9300	ns	40K: Bulk	50K	High
SiC	10^9	525	ns to μs	3×10^6 : Bulk	50K	High
Si-Metal Composite	10^5	1925	ns to ms	10K	10^4	High, could decrease to Silicon

TABLE 4. SUMMARY AND NEEDS

<u>Material</u>	<u>Status</u>	<u>Research Directions Needed</u>
Si	Highly developed, processes known characterized.	Potential for epi cap to increase V_{BR} Various studies - deep impurities, radiation, contacts, thermal, etc., - are needed.
SiC	First samples of β -SiC . Processes developing.	Characterizations, process reproducibility, new substrates, switch demonstration, ohmic contacts, thermal.
GaAs	Moderate Development, Characterized Continuing problems.	Same as for silicon, except its potential for use as a power switch needs to be established.
Ga·In·As·P	Fabricated only in thin films	Total development of compound for this application. Determine if thick film is feasible.
Super-Ionic	Lab processes. Not characterized. Curiosity.	Characterizations of basic parameters is required, many physics type studies needed.
Si Composite TaSi ₂ doped	First lab samples early studies	Characterizations, studies of transport mechanics, need switch demonstration.

BEST MATERIAL IS THE ONE THAT FITS THE APPLICATION!

GROUP II

PERTINENT RELAXATION MECHANISMS

P. DELFYETT
M. FIELDS
J. HALBOUT
R. HAMMOND, CHAIRMAN
R. JAIN
A. JOHNSON
C. LEE

RELAXATION MECHANISMS - WORKING SESSION REPORT

CHAIRMAN: Robert B. Hammond, Los Alamos National Laboratory

SESSION MEMBERS: Peter Delfyett - CCNY
Mike Fields - Sandia
Jean-Marc Halbout - IBM
Ravi Jain - Amoco
Anthony Johnson - AT&T
Chi Lee - Univ. Maryland

Introduction

Because of the expertise represented in our working group we decided to focus our discussions on carrier-relaxation mechanisms in photoconductors. We considered carrier-relaxation mechanisms important in photoconductors for either closing or opening power-switch applications. We did not consider other forms of solid-state relaxation processes and thus our discussions are most relevant to photoconductor power switching. We considered carrier-relaxation mechanisms in 6 categories:

Dielectric Relaxation

Carrier Trapping and Thermal Emission

Carrier Recombination

Carrier-Transit-Time-Related Relaxation Mechanisms

Time- and Intensity-Dependent Optical Absorption

Filament Formation

We based our discussions on the importance of these classes of relaxation mechanisms to the following switch characteristics:

Risetime (Closing)	→ 1 nsec
Falltime (Opening)	→ 1 nsec
On-time (Pulse length)	→ 10 nsec to 10 msec
Current	→ 10 kA to 1 MA
Voltage	→ 10 kV to 1 MV
Power	→ 1 GW to 1000 GW
Efficiency	→ HIGH
Repetition Rate	→ 10 to 1000 Hz

II. Dielectric Relaxation

Dielectric-relaxation time is defined as the product of resistivity and dielectric constant in a material. It is the time necessary for the electric field in a material to respond to an externally-applied electric field. Currents can be generated by the photoconductor due to this relaxation and these currents can be affected by temporal variations in the bias. Non-uniform electric fields near contacts or surfaces can introduce these currents and they may be important to photoconductor switch performance.

It is important to recognize that the dielectric-relaxation time in a photoconductor can change by many orders of magnitude during pulsed-laser excitation. Orders of magnitude changes can also occur after laser excitation from carrier trapping and recombination. These changes occur simply due to the very large changes in free-carrier concentrations.

It is also important to recognize that the dielectric-relaxation time is a macroscopic property of the semiconductor just as resistivity and dielectric constant are macroscopic quantities. Since conductivity and dielectric

constant can change locally, it has been suggested that a more general formula for dielectric-relaxation time is:

$$\tau = (\int \epsilon(x) E(x)^2 dx^3) / (\int \sigma(x) E(x)^2 dx^3)$$

One should also consider frequency dependence in the dielectric constant.

III. Carrier Trapping and Thermal Emission

Optically-created free carriers can be trapped and emitted from defect sites that have energy levels within the forbidden bandgap of the semiconductor. These carrier-trapping and emission processes can affect carrier mobility and thus switch efficiency. They can also affect switch on-time and pulse shape particularly during the transition from initial transient-trapping behaviour to steady-state trapping and emission.

There can be a strong electric-field dependence to these processes particularly in thermal emission, i.e. the Poole-Frenkel effect. Since the field in the photoconductor will change with time, the analysis of these effects may be quite complex.

IV. Carrier Recombination

Recombination of the optically-created free carriers in a photoconductor can affect closing-switch on-time, opening-switch faltime, and opening-switch efficiency. Nearly always, this recombination occurs at defect sites in the bulk of the photoconductor, i.e. by trap-assisted recombination.

Recombination can also occur by Auger recombination, through defect sites at the surface of the photoconductor, i.e. by surface recombination, or at the contacts.

Carrier recombination is usually of central importance to

photoconductor-power-switch function. Despite the many modeling studies of photoconductivity in semiconductors over the past 40 years, there have been few studies of the transient recombination processes occurring under the highly-excited conditions found in a photoconductor power switch.

V. Carrier Transit-Time Effects

There are a number of carrier-relaxation processes associated with the transit of free carriers across the photoconductor. These processes are critically important because they reduce closing-switch on-time.

The separation of electrons and holes due in the electric field in the photoconductor can lead to the build-up of space charge. Space charge build up normally occurs because carriers lost by recombination at a contact are not reinjected at the other contact. The resulting space charge shields the conductive volume of the photoconductor from the applied electric field thus shutting off current flow. Space charge build up in a photoconductor has never been studied for the transient conditions occurring in a photoconductor power switch.

VI. Time- and Intensity-Dependent Optical Absorption

During excitation, when free carriers are being produced in the photoconductor by the laser, many dynamical effects are occurring simultaneously that dramatically affect switch risetime and switch efficiency.

During the initial phase of optical excitation the Franz-Keldysh effect can enhance optical absorption because of the high electric field in the photoconductor. This is particularly true when the photon energy is near the bandgap energy of the photoconductor. However, as the electric field collapses the enhanced absorption continuously decreases.

As the free carrier concentration increases during excitation, optical

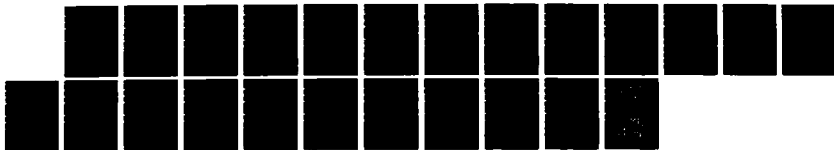
AD-A165 039

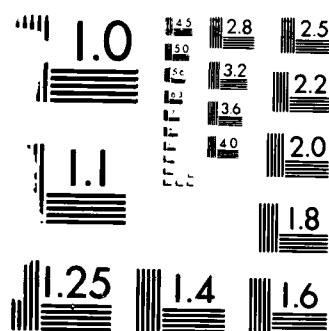
WORKSHOP ON NEW DIRECTIONS IN SOLID STATE POWER
SWITCHES HELD AT FARMINGD. (U) POLYTECHNIC INST OF NEW
YORK FARMINGDALE WEBER RESEARCH INST. B SENITZKY
24 DEC 85 N00014-85-G-0236 F/G 9/5

6/6

UNCLASSIFIED

NL





MICROCOPY RESOLUTION TEST CHART
NATIONAL BUREAU OF STANDARDS 1963-A

absorption can be enhanced due to a bandgap narrowing called the Burstein shift. This is important when the photon energy is close to the bandgap energy and when the free carrier concentration is $>10^{17} \text{ cm}^{-3}$.

Also, as the free carrier concentration increases during excitation, free-carrier absorption can become important. If the free-carrier absorption length becomes similar to or shorter than the band-to-band absorption length in the photoconductor, switch efficiency is compromised. This is because photons contribute to heating the free carriers rather than creating free carriers.

VII. Filament Formation

Nonuniformities in the photoconductor during conduction can lead to the formation of filaments of high current. These filaments experience local thermal runaway and can lead to catastrophic failure of the device. Filaments can form due to nonuniformities in the photoconductor material, nonuniformities in the electric field, spatial nonuniformities in the laser excitation, and nonuniformities in the contacts.

Filaments can also form during impact ionization breakdown and by the pinch effect due to magnetic fields.

VIEWGRAPHS

PERTINENT RELAXATION MECHANISMS

Relaxation Mechanisms

Photoconductors: Closing/Opening
(carrier relaxation)

- Dielectric Relaxation
- Trapping / Thermal Emission
- Trapping / Recombination
- Transit time
- Time/Intensity Dependent Absorption
- Filament Formation

Switch Characteristics

Risetime (Closing) \rightarrow 1 nsec

Fall time (Opening) \rightarrow 1 nsec

On-time (Pulse Length) \rightarrow 10 nsec - 10 msec

Current/Voltage/Power \rightarrow 10 kV - 1 M
10 kA - 1 m

Efficiency

Rep. Rate (Recovery) 10 - 1000 Hz

Dielectric Relaxation

$$\tau = \rho \epsilon$$

$$\tau = \frac{\int \epsilon(\omega) |E(x)|^2 dx^3}{\int \sigma(\omega) |E(x)|^2 dx^3}$$

? ↗

Frequency Dep.?
(carrier conc. dep.)

Risetime

- before/after exc.
- contact effects
non-uniform field
- band bending

TRAPPING / THERMAL EMISSION

$$\tau \sim \nu^{-1} e^{+EA/kT}$$

On-time - Pulse Shape

Efficiency - Mobility

Field Dependence, Poole-Frenkel

Trapping / Recombination

Shockley-Read-Hall
trap-assisted

Surface
Auger

On-time
Efficiency

TRANSIT time ?

" Dielectric relax time "

Space-charge Build-up
Contact Recombination

On-time

Contacts to:
high resistivity
highly excited

Time-dependent Absorption

Franz-Keldysh effect

Band-gap Narrowing (Burstein effect?)

Free-Carrier

Risetime

FILAMENT FORMATION

Non-uniformities

material, field, excitation
contact

Thermal Runaway:

catastrophic failure

Impact Ionization Breakdown

Pinch effect (Magfield)?

GROUP III

VOLUME AND SURFACE BREAKDOWN PROBLEMS

T. BURKES
R. DONALDSON
M. POCHA, CHAIRMAN
B. SENITZKY
V. TEMPLE
M. WEINER
F. ZUTAVERN

Final Report Group 3
Volume and Surface Breakdown Problems
M. D. Pocha
10/4/85

Preliminary considerations:

The study of volume and bulk breakdown in high voltage solid state devices is a very broad field with many potential areas of work. The first step taken by the group was to narrow the discussion to the areas which were felt to be of highest priority. It appears that surface breakdown is the limiting factor in high voltage devices since several researchers have observed arcing along the surface at electric field values as low as 0.2 - 0.4 those theoretically needed for volume breakdown. Several members of the group reported finding that a field lower than 6×10^4 V/cm was needed to prevent breakdown of either a silicon or GaAs switch. If, however, the photoconductive switch was replaced by a dielectric, like quartz, electric field strengths as high as 2×10^5 V/cm could be reached before arcing was observed. The highest breakdown field reported for a switch was 8×10^8 V/cm for a silicon switch in a vacuum.

We also concluded that surface breakdown is an important area for study to all classes of semiconductor devices including junction devices such as thyristors and diodes, and bulk devices such as photoconductive switches. Surface breakdown is the limiting factor for both closing and opening switches.

Physics Concepts:

We next attempted to identify the key physical mechanisms that could contribute to surface breakdown and therefore should be studied. It appears that surface breakdown is not well understood, and there is much fundamental study needed

- 1) Surface thermal runaway may occur at lower power levels than bulk thermal runaway and may therefore be a limiting factor for high voltage devices.
- 2) Avalanche breakdown at the surface could be lower than in the bulk because of geometrical effects or crystal imperfections near the surface or at the interface between the bulk semiconductor and surface coatings.

- 3) Nonuniformities may exist in the surface electric field, again due to geometric effects or crystal imperfections. Also possible nonuniformities in conduction and charge trapping phenomena could contribute to nonuniform electric fields.
- 4) Stray emissions of optical, secondary electron, or R.F. energy from other components in the system could enhance the conductivity at the surface and lower the breakdown voltage.
- 5) Charge trapped in passivation dielectric coatings could cause enhancement or depletion of the semiconductor surface and contribute to lower breakdown.
- 6) Contact effects such as corona or charge injection may be a factor in initiating surface breakdown.

Physics issues:

The basic purpose of the study of surface breakdown is to find a way to increase it to a value higher than bulk breakdown so that it is no longer the limiting factor. For comparison, at atmospheric pressure, in a high breakdown strength atmosphere such as sulphur hexafluoride, the highest reported field with a switch in place is 6×10^4 V/cm. If, in the course of research, someone discovers a way to achieve a higher field, it is something new and worthy of publication.

The following is a list, in approximate order of priority, of the physics issues or "things to do" that were felt to be important by the group. While surface breakdown is important to all classes of semiconductor devices, the group felt that the photoconductive switch is the simplest device to fabricate and therefore the most appropriate vehicle for this study.

- 1) Determine intrinsic bulk breakdown at high voltage. The numbers used for bulk breakdown are extrapolated from measurements of ionization coefficients at low voltage, and may not be accurate at high voltage. A test structure with very long surface area should be used to measure and verify bulk breakdown fields in high resistivity semiconductor materials used for photoconductive switches. Carrier lifetime effects may also be important in determining breakdown fields and should be studied.
- 2) Develop experimental procedures and map surface electric field distributions, especially near the contact regions, to determine how nonuniform they are and to find techniques for making them more uniform if necessary.

- 3) Develop non-destructive testing techniques need to be to allow many repeated tests to be performed on individual samples, thereby eliminating sample to sample variations from complicating the experiments. One technique suggested was to use thyristors to crowbar the current once breakdown is initiated.
- 4) Develop techniques to image the breakdown (optically or electromagnetically) so that the dynamics of the process could be modeled.
- 5) Explore the effect of various surface coating materials, especially semi-insulating or superionic (negative photoconductivity).
- 6) Explore the time dependence of breakdown. If pulse bias voltage is applied at time scales short compared to the dielectric relaxation time, it is conceivable that higher electric field strength could be achieved.

Initially, we felt, that most of the studies should be experimental to establish a working data base, but ultimately a sound theoretical understanding must be developed. Development of theoretical models of the breakdown process should also be one of the goals of any future work.

GROUP IV

SOLID STATE PLASMA TRANSPORT AND MODELLING

M. GUNDERSON

K. JUNGLING

E. KUNHARDT, CHAIRMAN

J. MEYER

P. WILLIAMS

Solid State Plasma Transport and Modelling

M. Gunderson
K. Jungling
E. Kunhardt, Chairman
J. Meyer
P. William

The plasma transport and modelling group sought to identify: a) the highest level of detail required of an analytical model to satisfactorily describe the dynamics of a yet to be determined solid state switch for pulse power applications, b) availability of fundamental data required in the analytical model, c) physics issues that need to be addressed in this area, and d) numerical techniques and algorithms which may exist to analyze similar problems in other areas and that may be applicable to this problem. These four topics are discussed below.

It was agreed that the carrier (electrons and holes) dynamics in a solid state switch can be satisfactorily described by macroscopic equations of the conservation type (continuity equations). This is due to the fact that in a semiconductor, the dominant characteristic time scales at which the carrier distributions approach a local equilibrium are sufficiently short that, for the time scales of interest in pulse power, transport and rate parameters (such as mobility, ionization rate, etc.) are well defined. The question then is, are these transport coefficients and rate parameters (to be called "macroscopic parameters") known as a function of electric field and material properties? If not, how can they be determined?

In pulse power applications, carrier densities in solid state switching devices are $\geq 10^{15} \text{cm}^{-3}$. At these densities, carrier-carrier scattering plays an important role in shaping the carrier distribution functions. Thus, the macroscopic parameters are also dependent on the carrier concentration. Analytic expressions

role in shaping the carrier distribution functions. Thus, the macroscopic parameters are also dependent on the carrier concentration. Analytic expressions and/or experimental values for these parameters are known for some materials. This information, however, pertains primarily to the low carrier density regime. A data base of transport and rate coefficients as a function of field, material and carrier density need to be developed for use in pulse power applications. Tools are available to provide this information. It entails the solution of kinetic equations for the carrier distributions taking carrier-carrier scattering into account. This approach requires the knowledge of the various carrier scattering crosssections. These crosssections are in general known, except for the trapping crosssection. In any case, a crosssection data base should also be developed. In addition, attention should be given to obtaining the unknown crosssections for the materials of interest.

Given the analytical framework, what are the physics issues that need to be addressed? We focused on three issues. These are: 1) carrier (plasma) dynamics at high densities and high fields in the bulk and in the contact regions, 2) filamentation instabilities, and 3) the tailoring of the transport properties and rate parameters. The relevance of these topics are discussed subsequently.

A major problem in the development of high power solid state switching devices is surface breakdown. The threshold voltage for breakdown along a semiconductor-insulator interface appears to be lower than along a surface between two insulators. What is it about a semiconductor that causes this lowering of the surface flashover voltage? Does the carrier distribution play a role in this? For example, the carrier distributions in configuration space (free and bound) immediately after the voltage is applied to a device may affect the field distribution in a manner that lowers the threshold voltage for surface flashover.

Given that the device holds off the applied voltage, the study of the switching cycle (off-on-off) entails an investigation of carrier dynamics in a semiconductor including space-charge fields and trap dynamics. Particular attention should be directed to the contact regions (and junctions if present), since in these regions large fields are normally present, thus enhancing the probability that instabilities develop. These instabilities may lead to filamentation and subsequently to device failure.

The analysis of the switching cycle should be done in more than one dimension (1-D), since geometric effects only appear in such situations. These effects are in general very important. Previous investigations of carrier dynamics in solids have been restricted to the low density range, where space-charge fields and trap dynamics need not be taken into account and to 1-D.

The maximum length of the on state of a switching device is in general restricted by the formation of instabilities which lead to device failure. Of importance are instabilities which lead to the formation of current filaments. Since these instabilities will eventually determine the range of pulse lengths for which solid state devices may be used, it is important to understand the threshold conditions and growth rates of these instabilities. Very little is known about them.

The role of space-charge redistribution and impact ionization in the operation and stability of a device should also be considered. Moreover, from a practical point of view, "power loading" curves should be obtained. That is, curves that show the maximum current (or power) that a device can carry for a given length of time before destructive instabilities develop. This will help in mapping out the parameter space for which a given device may be used (until the phenomena is better understood and perhaps techniques are developed for expanding the domain of operation).

A final topic of discussion, and one that attracted considerable attention was that of the tailoring of the transport properties and rate coefficients of a semiconductor. That is, by manipulating the carrier distribution in $(\underline{r}, \underline{k})$ space as a function of electric field, the macroscopic parameters can be made to have a desired field dependence. The manipulation can be either active or passive. Active manipulation implies the use of external agents (photons, electric and/or magnetic fields) to change the scattering processes or the carrier trajectories and thereby changing the distribution function. Passive manipulation implies that non-uniformities in \underline{r} (such as in hetero-structures) and/or the properties in \underline{k} space of the scattering centers are initially arranged so as to achieve a desired field dependence of the macroscopic parameters. The tailoring in \underline{k} space will require detail knowledge of the scattering crosssections. This "engineering" of the properties of the medium may be useful for a number of applications. The group recommended that the physics issues that were discussed should be directed at understanding the physics of three promising technologies: high power photo conductor switches, Fast SCR's, and DI^2 switches.

It was agreed that numerical techniques and algorithms exist that can readily be modified and used in these investigations, if the incentive exists. Finally, any investigation should provide the fundamental limitations of any given technology and the scaling laws for increasing the power handling capabilities of a given device.

UNCLASSIFIED

SECURITY CLASSIFICATION OF THIS PAGE (When Data Entered)

REPORT DOCUMENTATION PAGE		READ INSTRUCTIONS BEFORE COMPLETING FORM
1. REPORT NUMBER 1	2. GOVT ACCESSION NO. AD-A165039	3. RECIPIENT'S CATALOG NUMBER
4. TITLE (and Subtitle) WORKSHOP ON NEW DIRECTIONS IN SOLID STATE POWER SWITCHES		5. TYPE OF REPORT & PERIOD COVERED FINAL- 7/1/85 - 12/31/85
7. AUTHOR(s) Benjamin Senitzky		6. PERFORMING ORG. REPORT NUMBER
9. PERFORMING ORGANIZATION NAME AND ADDRESS WEBER RESEARCH INSTITUTE POLYTECHNIC INSTITUTE OF NEW YORK FARMINGDALE, N.Y. 11735		8. CONTRACT OR GRANT NUMBER(s) N00014-85-G-0236
11. CONTROLLING OFFICE NAME AND ADDRESS DEPT. OF NAVY, OFFICE OF NAVAL RESEARCH 800 N. Quincy St. Arlington, Virginia 22217-5000		10. PROGRAM ELEMENT, PROJECT, TASK AREA & WORK UNIT NUMBERS
14. MONITORING AGENCY NAME & ADDRESS (if different from Controlling Office) OFFICE OF NAVAL RESEARCH 715 Broadway New York, N. Y. 10003-6896		12. REPORT DATE DECEMBER 24, 1985
		13. NUMBER OF PAGES 530
		15. SECURITY CLASS. (of this report) UNCLASSIFIED
		15a. DECLASSIFICATION/DOWNGRADING SCHEDULE
16. DISTRIBUTION STATEMENT (of this Report) See Attachment Number 1 (attached)		
17. DISTRIBUTION STATEMENT (of the abstract entered in Block 20, if different from Report)		
18. SUPPLEMENTARY NOTES No supplementary notes.		
19. KEY WORDS (Continue on reverse side if necessary and identify by block number) pulse power workshop, photoconductive switching, switching		
20. ABSTRACT (Continue on reverse side if necessary and identify by block number) The Workshop on New Directions in Solid State Power Switching was conducted on August 28 - 30, 1985, by the Weber Research Institute of the Polytechnic Institute of New York. The workshop invited people from different areas to discuss the relevant properties of solid state power switches. (continued on reverse)		

DD FORM 1473

JAN 73

EDITION OF 1 NOV 65 IS OBSOLETE

UNCLASSIFIED

SECURITY CLASSIFICATION OF THIS PAGE (When Data Entered)

UNCLASSIFIED

SECURITY CLASSIFICATION OF THIS PAGE(When Data Entered)

Two new materials were discussed. R. Davis pointed out the beneficial characteristics of silicon carbide, and J. Scott described optically activated super-ionic conductors. J. Meyer treated the transport properties in photoexcited semiconductors.

Photoconductive switching in low power picosecond ranges was discussed by D. Auston and A. Johnson. Higher power picosecond devices were considered by W. R. Donaldson and G. Mourou. The physical mechanisms underlying photoconductive switching were presented by R. B. Hammond. Very high power photoconductive switching techniques were summarized by W. C. Nunnally and a repetitive opening switch was described by C. H. Lee, et al.

A new non-photoconductive switching device - An MOS controlled thyristor was presented by V. Temple. Avalanche breakdown phenomena, both bulk and surface, was summarized by M. Pocha. M. Kahn and R. Ford discussed opening switches for inductive storage power supplies.

Four groups were formed to identify research directions in the following areas: (1) Potential Materials for Solid State Switches, (2) Relaxation Mechanisms, (3) Volume and Surface Breakdown, and (4) Solid State Plasma Transport.

UNCLASSIFIED

SECURITY CLASSIFICATION OF THIS PAGE(When Data Entered)

GRANT NUMBER: N00014-85-G-0236

ATTACHMENT NUMBER 1

DISTRIBUTION LIST FOR REPORTS

ADDRESSEE

NUMBER OF COPIES

Head, Physics Division
Code 412
Office of Naval Research
800 North Quincy Street
Arlington, VA 22217-5000

3 copies of proceedings

ACO
Office of Naval Research
Resident Representative
715 Broadway 5th Floor
New York, N.Y. 10003-6896

1 copy of proceedings

Defense Technical Information
Center
Building 5, Cameron Station
Alexandria, VA 22314

1 copy of proceedings

END
DTIC
FILMED
4-86